



NUI MAYNOOTH
Ollscoil na hÉireann Má Nuad

Geophysical Characterisation and Evolutionary Model of the Quaternary sediments in the North Offaly region of Central Ireland

Xavier Mir Pellicer

Supervisor: Doctor Paul Gibson

Thesis submitted for the degree of Ph.D

Faculty of Social Sciences

Department of Geography

National University of Ireland, Maynooth

March 2010

CONTENTS

ABSTRACT.....	XV
ACKNOWLEDGEMENTS.....	XVI

CHAPTER 1

INTRODUCTION.....	1
1.1 – AIMS AND OBJECTIVES	1
1.2 – GEOGRAPHICAL SETTING	3
1.3 – THESIS STRUCTURE.....	5

CHAPTER 2

LITERATURE REVIEW.....	8
2.1 – INTRODUCTION.....	8
2.2 – BEDROCK GEOLOGY	9
2.3 – GLACIAL GEOLOGY.....	11
2.3.1 - <i>Glaciations in Ireland</i>	11
2.3.2 - <i>Glaciations in the research area</i>	15
2.3.3 - <i>Glacial and Post glacial Morphostratigraphy</i>	17
2.4 – GEOPHYSICAL TECHNIQUES	26
2.4.1- <i>Overview</i>	26
2.4.2- <i>Electrical resistivity methods</i>	27
2.4.3 - <i>Electromagnetic Methods</i>	30
2.5 – SUMMARY	36

CHAPTER 3

RESEARCH METHODOLOGICAL APPROACH AND THEORETICAL CONCEPTS.....	38
3.1 – INTRODUCTION.....	38
3.2 – QUATERNARY GEOLOGICAL METHODS.....	39
3.2.1 - <i>Introduction</i>	39
3.2.2 – <i>Desktop Compilation</i>	40
3.2.3 – <i>Quaternary Geological Mapping</i>	42
3.2.4 – <i>Morphological Mapping</i>	47
3.2.5 – <i>Depth to Bedrock (DTB)</i>	48
3.3 – ELECTRICAL RESISTIVITY	50
3.3.1 – <i>Introduction</i>	50

3.3.2 – Theoretical Concepts.....	51
3.3.3 – Electrical Resistivity Tomography (ERT).....	56
3.3.4 – 3D Modelling	68
3.3.5 – Time-lapse Resistivity.....	70
3.3.6 – Azimuthal Resistivity	73
3.4 – GROUND PENETRATING RADAR (GPR)	75
3.4.1 – Introduction.....	75
3.4.2 – Theoretical Concepts.....	76
3.4.3 – Data Collection	82
3.4.4 – Data Processing	89
3.4.5 – Time/Depth Slices.....	98
3.4.6 – Data Interpretation	100
3.5 – ELECTROMAGNETIC VERY LOW FREQUENCY (VLF).....	103
3.6 – SUMMARY	105

CHAPTER 4

RESULTS OF GEOLOGICAL MAPPING107

4.1 - INTRODUCTION	107
4.2 – PHYSIOGRAPHIC UNITS	107
4.2.1 - <i>The Shannon Basin esker-dominated landscape</i>	109
4.2.2 - <i>The Shannon - East basin watershed area</i>	110
4.2.3 - <i>The East basin</i>	111
4.2.4 - <i>The Brosna River basin</i>	112
4.3 – QUATERNARY GEOLOGICAL MAPPING RESULTS.....	112
4.3.1 – Introduction.....	112
4.3.2 - <i>The Shannon Basin esker-dominated landscape area</i>	114
4.3.3 - <i>The Shannon and the East Basin watershed area</i>	123
4.3.4 - <i>The East Basin</i>	125
4.3.5 - <i>The Brosna River basin</i>	127
4.4 – RESULTS OF LABORATORY ANALYSIS OF FIELD DATA	129
4.5 – DEPTH TO BEDROCK (DTB)	133
4.6 – SUMMARY	134

CHAPTER 5

FORWARD MODELLING OF GEOPHYSICAL DATA AND TRAINING SITES STUDY136

5.1 – INTRODUCTION.....	136
5.2 – ELECTRICAL RESISTIVITY	137
5.3 – GPR	159
5.4 – GEOPHYSICAL TECHNIQUES TRAINING SITES T1, T2 AND T3.....	178
Site T1	178
Site T2	186
Site T3	193
5.5 – SUMMARY	199

CHAPTER 6

RESULTS OF GEOPHYSICAL SURVEYS.....201

6.1 – INTRODUCTION.....	201
6.2 – SITE S1.....	204
6.2.1 – Introduction.....	204
6.2.2 – Electrical Resistivity Data.....	210
6.2.3 – Ground Penetrating Radar (GPR).....	250
6.2.4 – Very Low Frequency Data (VLF).....	272
6.2.5 – Evaluation of Geophysical techniques.....	277
6.3 – SITE S2.....	281
6.3.1 – Introduction.....	281
6.3.2 – Electrical Resistivity Data.....	283
6.4 – SITES S3 AND S4.....	285
6.4.1 – Introduction.....	285
6.4.2 – Electrical Resistivity Data.....	289
6.4.3 – Ground Penetrating Radar (GPR).....	293
6.5 – SITE S5.....	304
6.5.1 – Introduction.....	304
6.5.2 – Electrical Resistivity Data.....	306
6.5.3 – Ground Penetrating Radar (GPR).....	308
6.6 – SITE S6.....	313
6.6.1 – Introduction.....	313
6.6.2 – Ground Penetrating Radar (GPR).....	314
6.7 – SITE S7.....	318
6.7.1 – Introduction.....	318
6.7.2 – Electrical Resistivity Data.....	319
6.8 – SITE S8.....	321
6.8.1 – Introduction.....	321
6.8.2 – Electrical Resistivity Data.....	323
6.8.3 – Ground Penetrating Radar (GPR).....	324
6.9 – SITE S9.....	327
6.9.1 – Introduction.....	327
6.9.2 – Electrical Resistivity Data.....	328
6.9.3 – Ground Penetrating Radar (GPR).....	329
6.10 – SITE S10.....	333
6.10.1 – Introduction.....	333
6.10.2 – Ground Penetrating Radar (GPR).....	335
6.11 – SITE S11.....	340
6.11.1 – Introduction.....	340
6.11.2 – Electrical Resistivity Data.....	342
6.12 – SITE S12.....	345
6.12.1 – Introduction.....	345
6.12.2 – Electrical Resistivity Data.....	347
6.12.3 – Ground Penetrating Radar (GPR).....	347
6.13 – SITE S13.....	351
6.13.1 – Introduction.....	351
6.13.2 – Electrical Resistivity Data.....	354
6.13.3 – Ground Penetrating Radar (GPR).....	356
6.14 – SITE S14.....	359
6.14.1 – Introduction.....	359
6.14.2 – Electrical Resistivity Data.....	361
6.14.3 – Ground Penetrating Radar (GPR).....	362
6.15 – SITE S15.....	366
6.15.1 – Introduction.....	366

6.15.2 – Electrical Resistivity Data.....	367
6.15.3 – Ground Penetrating Radar (GPR)	368
6.16 – SITE S16.....	371
6.16.1 – Introduction.....	371
6.16.2 – Electrical Resistivity Data.....	372
6.16.3 – Ground Penetrating Radar (GPR)	373
6.17 – SITE S17.....	377
6.17.1 – Introduction.....	377
6.17.2 – Ground Penetrating Radar (GPR)	378
6.18 – SUMMARY	381

CHAPTER 7

DISCUSSION OF RESULTS AND EVOLUTIONARY MODEL.....	385
7.1 – GEOPHYSICAL METHODS	385
7.1.1 - Electrical Resistivity Methods.....	385
7.1.2 - Electromagnetic Methods	390
7.1.3 - Comparative analysis of GPR and ERT.....	393
7.2 – GEOLOGICAL CHARACTERISATION OF SITES	395
7.3 – QUATERNARY GEOLOGY AND EVOLUTIONARY MODEL OF DEGLACIATION.....	401

CHAPTER 8

CONCLUSIONS AND FURTHER RESEARCH.....	411
8.1 – CONCLUDING REMARKS.....	411
8.2 – FURTHER RESEARCH.....	415

APPENDIX A	416
-------------------------	------------

Borehole logs and Particle size analysis data

APPENDIX B	428
-------------------------	------------

Measured and calculated pseudosections and inverse resistivity model

BIBLIOGRAPHY	434
---------------------------	------------

INCLUDED IN FOLDER

MAP 1:	<i>Quaternary geology map for the research area</i>
MAP 2:	<i>Depth to bedrock map for the research area</i>
ENCLOSURE 1:	<i>Geophysical data for Site S1</i>
ENCLOSURE 2:	<i>GPR results for a range of geomorphological features</i>

List of Figures

Figure 1.1 – Location of the study area.	4
Figure 1.2 – Map of the study area.	5
Figure 2.1 – Two main models of glaciation for Ireland	14
Figure 3.1 – Lithofacies coding scheme	43
Figure 3.2 – Histograms for DTB and Rock Elevation data	49
Figure 3.3 – Resistivity range of geological materials	52
Figure 3.4 – Generalised array of electrode configuration for resistivity survey	54
Figure 3.5 – Resistivity electrode configurations	56
Figure 3.6 – Electrical resistivity meter Campus Geopulse and Geopulse Tigre	57
Figure 3.7 – Electrode deployment for 2D electrical resistivity pseudosection	58
Figure 3.8 – Sensitivity functions for Wenner, Schlumberger and Dipole-Dipole arrays	59
Figure 3.9 – Measured apparent resistivity pseudosection	60
Figure 3.10 – Model block used for inverse modelling	62
Figure 3.11 – Calculated and measured resistivity pseudosection and inverse model	63
Figure 3.12a – Measured apparent resistivity pseudosections for profile S1-L04-5m	64
Figure 3.12b – Inverse model resistivity sections for profile RS1-L04-5m	66
Figure 3.13 – Flow diagram for ERT data collection, processing and interpretation	67
Figure 3.14 – Two modes of data collection for 3D resistivity survey	69
Figure 3.15 – Time-lapse seasonal resistivity variation	72
Figure 3.16 – Methodology for Azimuthal resistivity data collection	74
Figure 3.17 – Artefact in GPR radargram	82
Figure 3.18 – GPR data collection components, amplitude and time are measured	83
Figure 3.19 – Common offset and common mid point data collection methods	84
Figure 3.20 – Average amplitude-frequency plot for 100 MHz antenna frequency	86
Figure 3.21 – Three types of antenna deployment	88
Figure 3.22 – Time Zero adjustment	90
Figure 3.23 – Difference of GPR radargram after application of a number of gains	93

Figure 3.24 – Difference of GPR radagram after application of a number of filters	94
Figure 3.25 – Hyperbolic reflection from point features and dipping reflectors	95
Figure 3.26 – GPR data processing outcome	96
Figure 3.27 – Flow diagram for GPR data collection, processing and interpretation	97
Figure 3.28 – Time/Depth slice analysis of GPR dataset using a 50ns time range	99
Figure 3.29 – Terminology for radar surfaces, radar packages and radar facies	101
Figure 3.30 – Coding scheme for radar surfaces and radar facies	102
Figure 3.31 – VLF data collection mode	105
Figure 4.1 – Distribution of physiographic units for the research area	108
Figure 4.2 – Spatial distribution and names of the main esker ridges in study area	114
Figure 4.3 – Cross-section of glaciofluvial sediments overlying Clara Esker	118
Figure 4.4 – Ballyduff Esker longitudinal profile	119
Figure 4.5 – Exposure showing glaciodeltaic sediments	121
Figure 4.6 – Particle size distribution ternary diagrams for collected samples	130
Figure 4.7 – Spatial distribution of petrography analysis data results	132
Figure 5.1 – Theoretical resistivity models of two layers with horizontal contact A	140
Figure 5.2 – Theoretical resistivity models of two layers with horizontal contact B	141
Figure 5.3 – Theoretical resistivity model of two layers with erosive contact	142
Figure 5.4 – Theoretical resistivity model of two layers with vertical contact	143
Figure 5.5 – Theoretical resistivity model of three layers with horizontal contact A	146
Figure 5.6 – Theoretical resistivity model of three layers with horizontal contact B	147
Figure 5.7 – Theoretical resistivity model of three layers with horizontal contact C	148
Figure 5.8 – Theoretical resistivity model of three layers with horizontal contact D	149
Figure 5.9 – Theoretical resistivity models for moist and dry sand lenses	151
Figure 5.10 – Theoretical resistivity models for sand lens with gradational contact	152
Figure 5.11 – Theoretical resistivity models for small moist and dry sand lenses	153
Figure 5.12 – Theoretical resistivity models for sand filled channels on diamicton	155
Figure 5.13 – Theoretical resistivity model of esker ridge	156
Figure 5.14 – Theoretical resistivity model encompassing 5 sediment types	157

Figure 5.15 – GPR theoretical model produced in GPRSIM	160
Figure 5.16 – GPR theoretical models for layers with horizontal contact and boulders	164
Figure 5.17 – GPR theoretical models illustrating distortions of the radagrams	167
Figure 5.18 – GPR theoretical models for channel features	168
Figure 5.19 – GPR theoretical model illustrating response of high attenuation material	169
Figure 5.20 – GPR theoretical models illustrating threshold of sub-vertical reflectors	170
Figure 5.21 – GPR theoretical model illustrating resolution of horizontal layers	173
Figure 5.22 – GPR theoretical model to depict low permittivity values	174
Figure 5.23 – GPR theoretical model to depict infinitesimal permittivity variation	175
Figure 5.24 – GPR theoretical models for several geomorphological settings	177
Figure 5.25 – Location of GPR survey and borehole and exposures in Site T1	179
Figure 5.26 – Comparison of exposure ET1 and radagram GT1-L01-200MHz	183
Figure 5.27 – Comparison of radagrams collected in Site T1	184
Figure 5.28 – Comparison of results for three different antenna orientations in Site T1	185
Figure 5.29 – Location of GPR survey and borehole and exposures in Site T2	186
Figure 5.30 – Comparison of exposure ET2 and radagram GT2-L01-200MHz	190
Figure 5.31 – Comparison of radagrams collected in Site T2	191
Figure 5.32 – Comparison of results for three different antenna orientations in Site T2	192
Figure 5.33 – Location of GPR and resistivity profile and exposure in Site T3	193
Figure 5.34 – Comparison of exposure ET3 and ERT profile RT3-L01-1m	196
Figure 5.35 – Comparison of exposure ET3 and GPR profile GT3-L01-200MHz	197
Figure 5.36 – GPR profile GT3-L02-200MHz	198
Figure 6.1 – Location of the sites in the research area	202
Figure 6.2 – Borehole data classification scheme based in Folk (1954)	203
Figure 6.3 – Location of boreholes and exposures in Site S1	207
Figure 6.4 – Interpretation of exposures ES1A and ES1B	208
Figure 6.5 – Location of 2D ERT profiles within Site S1	211
Figure 6.6 – ERT profile RS1-L01-10m	215
Figure 6.7 – ERT profile RS1-L03-5m	216
Figure 6.8 – ERT profile RS1-L04-5m	217

Figure 6.9 – ERT profile RS1-L05-10m	217
Figure 6.10 – ERT profile RS1-L06-10m	218
Figure 6.11 – Location of time-lapse ERT profiles	219
Figure 6.12 – Time-lapse ERT profile RTS1-L01-5m	220
Figure 6.13 – Time-lapse ERT profile RTS1-L01-2m	221
Figure 6.14 – Time-lapse ERT profile RTS1-L02-5m	222
Figure 6.15 – Time-lapse ERT profile RTS1-L02-2m	223
Figure 6.16 – Effective Recharge for sandy loam for year 2006	224
Figure 6.17 – Time-lapse ERT profile RTS1-L01-5m collected for several seasons	227
Figure 6.18 – Time-lapse ERT profile RTS1-L01-5m seasonal variation	228
Figure 6.19 – Time-lapse ERT profile RTS1-L01-2m seasonal variation	229
Figure 6.20 – Time-lapse ERT profile RTS1-L02-5m seasonal variation	230
Figure 6.21 – Time-lapse ERT profile RTS1-L02-2m seasonal variation	231
Figure 6.22 – Resistivity variation of 5 points for ERT profile RTS1-L01-5m	234
Figure 6.23 – Resistivity variation of 5 points for ERT profile RTS1-L01-2m	235
Figure 6.24 – Resistivity variation of 5 points for ERT profile RTS1-L02-5m	236
Figure 6.25 – Resistivity variation of 5 points for ERT profile RTS1-L02-2m	237
Figure 6.26 – Location of azimuthal resistivity points within Site S1	239
Figure 6.27 – Cartesian plot of the six VES collected at Point 1 (Site S1)	240
Figure 6.28 – Cartesian plot of the six VES collected at Point 2 (Site S1)	241
Figure 6.29 – Cartesian plot of the six VES collected at Point 3 (Site S1)	242
Figure 6.30 – Cartesian plot of the six VES collected at Point 4 (Site S1)	243
Figure 6.31 – Average values for points surveyed with Azimuthal Resistivity (Site S1)	244
Figure 6.32 – Location of the ERT profiles recorded for 3D model at Site S1	245
Figure 6.33 – Resistivity 3D model horizontal depth slices	247
Figure 6.34 – Resistivity 3D model vertical slices	248
Figure 6.35 – Multi-frame sequence of the resistivity 3D model	249
Figure 6.36 – Location of GPR profiles within Site S1	251
Figure 6.37 – GPR profile GS1-L01-50MHz	252
Figure 6.38 – Time slice diagram for radargram GS1-L01-50MHz	253
Figure 6.39 – GPR profile GS1-L01/L02-200MHz	255

Figure 6.40 – GPR profile GS1-L03-200MHz	256
Figure 6.41 – GPR profile GS1-L04-200MHz	259
Figure 6.42 – GPR profile GS1-L05-200MHz	260
Figure 6.43 – GPR profile GS1-L07-100MHz	261
Figure 6.44 – GPR profile GS1-L08-100MHz	262
Figure 6.45 – Location of the GPR 3D model recorded in Site S1	264
Figure 6.46 – CMP Surveys carried out within the GPR 3D Model	265
Figure 6.47 – Depth slices at 1m intervals for GPR 3D Model	268
Figure 6.48 – Vertical slices at 1m intervals for GPR 3D Model	269
Figure 6.49 – Fence diagrams for the GPR 3D Model	270
Figure 6.50 – Isosurfaces depicted for GPR 3D Model	271
Figure 6.51 – Location of VLF profiles	272
Figure 6.52 – Results of VLF profile VLFS1-L01	273
Figure 6.53 – Results of VLF profile VLFS1-L02	274
Figure 6.54 – Results of VLF profile VLFS1-L03	275
Figure 6.55 – Results of VLF profile VLFS1-L04	276
Figure 6.56 – Location of profiles recorded in Site S2	282
Figure 6.57 – ERT profile RS2-L01-10m	285
Figure 6.58 – ERT profile RS-L02-10m	285
Figure 6.59 – Location of profiles recorded in Site S3	286
Figure 6.60 – Location of profiles recorded in Site S4	288
Figure 6.61 – ERT profiles RS3-L03-2m and RS3-L01-10m	291
Figure 6.62 – ERT profile RS3-L02-2m	292
Figure 6.63 – ERT profile RS4-L01-10m	292
Figure 6.64 – GPR profile GS3-L01-100MHz	294
Figure 6.65 – Time-slice analysis for GPR profile GS3-L01-100MHz	295
Figure 6.66 – GPR profile GS3-L01-200MHz	296
Figure 6.67 – GPR profile GS3-L04-200MHz	297
Figure 6.68 – GPR profile GS3-L06-100MHz	299
Figure 6.69 – GPR profile GS3-L05-200MHz	299
Figure 6.70 – GPR profiles GS4-L01-200MHz and GS4-L01-100MHz	302

Figure 6.71 – Time-slice analysis for GPR profile GS4-L01-200MHz	303
Figure 6.72 – GPR profile GS4-L02-200MHz	303
Figure 6.73 – Location of profiles recorded in Site S5	306
Figure 6.74 – ERT profile RS5-L01-10m	307
Figure 6.75 – GPR profile GS5-L01-100MHz	309
Figure 6.76 – Time-slice analysis for GPR profile GS5-L01-100MHz	309
Figure 6.77 – GPR profile GS5-L02-100MHz	311
Figure 6.78 – GPR profile GS5-L03-100MHz	312
Figure 6.79 – GPR profile GS5-L03-200MHz	312
Figure 6.80 – Location of profiles recorded in Site S6	314
Figure 6.81 – GPR profile GS6-L01-100MHz	316
Figure 6.82 – GPR profile GS6-L02-100MHz	317
Figure 6.83 – GPR profile GS6-L03-100MHz	317
Figure 6.84 – Location of profiles recorded in Site S7	318
Figure 6.85 – ERT profiles RS7-L01-10m and RS7-L02-10m	320
Figure 6.86 – Location of profiles recorded in Site S8	322
Figure 6.87 – ERT profile RS8-L01-10m	323
Figure 6.88 – GPR profile GS8-L01-100MHz	325
Figure 6.89 – GPR profile GS8-L01-100MHz velocity calibration	326
Figure 6.90 – Time-slice analysis for GPR profile GS8-L01-100MHz	326
Figure 6.91 – Location of profiles recorded in Site S9	328
Figure 6.92 – ERT profile RS9-Merge-10m	331
Figure 6.93 – ERT profile RS9-L5-10m	331
Figure 6.94 – GPR profile GS9-Merge-100MHz	332
Figure 6.95 – GPR profile GS9-Merge-100MHz velocity calibration	333
Figure 6.96 – Location of exposure, borehole BH- and GPR profiles in Site S10	335
Figure 6.97 – GPR profile GS10-L01-100MHz velocity calibration	337
Figure 6.98 – GPR profile GS10-L01-100MHz	337
Figure 6.99 – GPR profile GS10-L02-100MHz	338
Figure 6.100 – GPR profile GS10-L03-100MHz	339
Figure 6.101 – Location of surveyed profiles and exposures recorded in Site S11	341

Figure 6.102 – ERT profile RS11-L01-10m	343
Figure 6.103 – ERT profile RS11-L02-10m	343
Figure 6.104 – ERT profiles RS11-L03-10m and RS11-L04-10m	344
Figure 6.105 – Location of profiles in Site S12	346
Figure 6.106 - ERT profile RS12-Merge-10m	349
Figure 6.107 - GPR profile GS12-Merge-100MHz	350
Figure 6.108 – Location of profiles in Site S13	353
Figure 6.109 - ERT profile RS13-L01-5m	354
Figure 6.110 – GPR profile GS13-L01-100MHz	356
Figure 6.111 – GPR profile GS13-L02-100MHz	357
Figure 6.112 – GPR profile GS13-L03-100MHz	358
Figure 6.113 – Location of profiles in Site S14	360
Figure 6.114 - ERT profile RS14-L01-5m	361
Figure 6.115 – GPR profile GS14-L01-100MHz	363
Figure 6.116 – GPR profile GS14-L02-100MHz	364
Figure 6.117 – GPR profile GS14-L03-100MHz	365
Figure 6.118 – Location of profiles surveyed in Site S15	367
Figure 6.119 - ERT profile RS15-L01-5m	368
Figure 6.120 – GPR profile GS15-L01-100MHz	370
Figure 6.121 – GPR profile GS15-L02-100MHz	370
Figure 6.122 – Location of profiles in Site S16	372
Figure 6.123 - ERT profile RS16-L01-5m	373
Figure 6.124 – GPR profile GS16-L01-100MHz	375
Figure 6.125 – Time-slice analysis for GPR profile GS16-L01-100MHz	375
Figure 6.126 – GPR profile GS16-L02-100MHz	376
Figure 6.127 – Location of profiles in Site S17	377
Figure 6.128 – GPR profile GS17-L01-100MHz	379
Figure 6.129 – GPR profile GS17-L02-100MHz	380
Figure 7.1 – Resistivity variation for time-lapse profiles RTS1-L02-5m and RTS1-L02-2m	 389

Figure 7.2 – Schematic cross-section illustrating the sequence of deposition in the study area	409
Figure 7.3 – Proposed evolutionary model of deglaciation for the study area	410
Figure A1 - Borehole log for BH-S1E	417
Figure A2 - Borehole log for BH-S1F	418
Figure A3 - Borehole log for BH-S1G	419
Figure A4 - Borehole log for BH-S1H	420
Figure A5 - Borehole log for BH-S3A	421
Figure A6 - Borehole log for BH-S4A	422
Figure A7 - Borehole log for BH-S5A	423
Figure A8 - Borehole log for BH-S6A	424
Figure A9 – PSA cumulative graph for samples collected in BH-S1E	425
Figure A10 – PSA cumulative graph for samples collected in BH-S1F	425
Figure A11 – PSA cumulative graph for samples collected in BH-S1G	426
Figure A12 – PSA cumulative graph for samples collected in BH-S1H	426
Figure A13 – PSA cumulative graph for samples collected in BH-S3A	426
Figure A14 – PSA cumulative graph for samples collected in BH-S4A	427
Figure A15 – PSA cumulative graph for samples collected in BH-S5A	427
Figure A16 – PSA cumulative graph for samples collected in BH-S6A	427
Figure B1 – Pseudosection and inverse model of profile RS1-L01-10m	429
Figure B2 – Pseudosection and inverse resistivity model of profile RS1-L04-5m	429
Figure B3 – Pseudosection and inverse resistivity model of profile RS1-L06-10m	430
Figure B4 – Pseudosection and inverse resistivity model of profile RTS1-L01-5m	430
Figure B5 – Pseudosection and inverse resistivity model of profile RTS3-L01-10m	431
Figure B6 – Pseudosection and inverse resistivity model of profile RTS5-L01-10m	431
Figure B7 – Pseudosection and inverse resistivity model of profile RS9-Merge-10m	432
Figure B8 – Pseudosection and inverse resistivity model of profile RS13-L01-5m	432
Figure B9 – Pseudosection and inverse resistivity model of profile RS14-L01-5m	433
Figure B10 – Pseudosection and inverse resistivity model of profile RS16-L01-5m	433

List of Plates

Plate 2.1 – Glacial sediments typically occurring in the research area	19
Plate 2.2 – Geomorphological features typically occurring in the research area	21
Plate 3.1 – VLF system used for this thesis	104
Plate 4.1 - Esker ridge forming part of Split Hill Esker complex	109
Plate 4.2 – Meltwater channel south of Ballinagar	110
Plate 4.3 – View of the south slope of Croghan Hill	111
Plate 4.4 – Moate Esker, a symmetric continuous subglacial tunnel fill	117
Plate 4.5 – Glaciolacustrine sediments overlying Ballyduff Esker	120
Plate 4.6 – Organic rich alluvial clays (marl)	125
Plate 4.7 – Well-rounded boulders deposited within Esker Ridge	126
Plate 4.8 – Interstratified glaciofluvial sand and gravel deposited on a kame terrace	127
Plate 4.9 – Exposure of glacial diamicton with silty sandy matrix	128
Plate 4.10 – Exposure of glaciofluvial sediment underlying peat	128
Plate 4.11 – Exposure of clayey diamicton	129
Plate 6.1 – Morphological features within Site S1	205
Plate 6.2 – Exposure ES2A	282
Plate 6.3 – Morphological expression along profile RS2-L01-10m	284
Plate 6.4 – Morphological expression of Site S3	287
Plate 6.5 – Recording a GPR profile in Site S4 using a 200MHz antenna	289
Plate 6.6 – Morphological expression of Site S5	305
Plate 6.7 – Exposure ES5A	305
Plate 6.8 – Exposure ES7A	319
Plate 6.10 – Exposure ES8A	322
Plate 6.11 – View of Site S9	327
Plate 6.12 – Exposure ES10A	334
Plate 6.13 – Exposure in Site 11 (ES11A)	340
Plate 6.14 – Exposure in S11 (ES11B)	341
Plate 6.15 – Ongoing GPR data collection in Site S12	345
Plate 6.16 – Tree trunks buried peat	348

Plate 6.17 – View of Site 13	351
Plate 6.18 – Exposure in S13 (ES13A)	352
Plate 6.19 – View of Site 14	359
Plate 6.20 – Exposure in S14 (ES14A)	360
Plate 6.21 – View of Site 15	366
Plate 6.22 – View of Site 16	371

List of Tables

Table 3.1 – Parameters recorded during fieldwork for exposure description	44
Table 3.2 – Datasets used for production of DTB map	48
Table 3.3 – Geometry of the measured and inverted pseudosections for four electrode configurations	64
Table 3.4 – Subsurface electrical properties of some common geological materials	78
Table 3.5 – Reflection coefficients of soft sediments occurring within the study area	79
Table 5.1 – Parameters for GPR forward modelling	162
Table 6.1 – Borehole records for Site S1	210
Table 6.2 – Time-lapse resistivity surveys: date, weather and temperature	219
Table 6.3 – Azimuthal resistivity data collected for L01 (0 degrees) of Point 1	238
Table 6.4 – Correlation between ERT data, GPR and VLF data for Site S1	280
Table 7.1 – Lithology, resistivity and EM amplitude for a range of geomorphological features	387

ABSTRACT

Data from field mapping of 133 exposures, 57 boreholes and 190 petrographic and particle size analysis samples were used to produce Quaternary geological and depth to bedrock maps for the 600 Km² research area located in the North Offaly region of central Ireland. Based on the mapping, the area was subdivided into four physiographic units with specific landscape characteristics, namely: Shannon Basin esker-dominated landscape; Shannon - East Basin watershed area; East Basin and the Brosna River Basin. The capabilities of geophysical techniques were tested as Quaternary sediments mapping tools and the geophysical results obtained, combined with field mapping, were used in the production of an evolutionary model of deglaciation. The geophysical methods employed were Electrical Resistivity Tomography (ERT), time-lapse resistivity imaging, azimuthal resistivity, Ground Penetrating Radar (GPR) and Very Low Frequency (VLF). Forward modelling with GPRSIM and RES2DMOD software and geophysical ground truth evaluation in three test sites aided in the selection of the most efficient data collection, processing and interpretation methods, evaluation of the potential and limitations of the techniques and inversion models and yielded a better interpretation of the geophysical data. Seventeen sites were geophysically surveyed in association with borehole and exposure data where available. GPR proved to be an excellent technique for the classification and characterisation of sedimentological and deformational structures within low conductivity soft sediments, expressed as esker and morainic ridges, glaciodeltas, sub-aqueous fans or raised bog. A centre antenna frequency of 200MHz gave a better spatial resolution than 100MHz but a lower penetration and also took longer to collect the data. Amplitude analysis of 2D GPR data assisted in the lithological classification of these sediments. ERT data permitted accurate depth to bedrock detection and lithological classification of soft sediments. ERT and GPR data combined yielded the best results. Monthly time-lapse resistivity showed that effective recharge, lithology and depth influenced the observed variation in resistivity. Geophysical data and field mapping suggest that a glacial lake expanded westwards, confined to the east by the Shannon Basin watershed and to the west by two ice-sheets, one retreating northwest and the other south-southwest.

ACKNOWLEDGEMENTS

The geophysical equipment used for this thesis and training required has been provided by the National University of Ireland, Maynooth Environmental Geophysics Unit. This project would have not been possible without their assistance. The Geological Survey of Ireland (GSI) was a key player providing me with all the equipment for exposure recording, borehole drilling and particle size analysis. I would like to thank all the GSI staff that has supported me and shared their knowledge during this research study.

I want to thank all the landowners that facilitated me the entrance to their properties and assisted me in the various occasions I got stuck in the mud! I would especially like to mention Mr. Cox for his patience and kindness.

I cannot extend enough thanks to my supervisor Paul Gibson, for all his support and encouragement during my time as his research student, thanks for taking the risk and the time. Special thanks also go to my co-supervisor William Warren for his good humor and for his very helpful comments on my research. This project would have not been possible without the friends and colleagues that assisted me in the field during the last four years. I list them hoping I do not forget any one: Francesco, Ester Mir, Jotes, Shane, Meritxell, Ariadna, Natalia, Michael, Claire, Beatriz S, Carlos and Helen. I would like to mention especially Silvia Caloca and Beatriz Mozo for their priceless assistance and good humor, either under the rain or in front of the numerous upset cows we came across. I would also like to thank Shane Murphy and Xavier Monteys for their valuable advice in geophysical data processing, Ester Toribio for help on image enhancement, Ramonet and John Brennan for their fieldwork engineering ideas and developments, Ronnie Creighton and John Butler for their support and Michael Sheehy for his support and vivid insights in both geology and coffee beans.

Finally, I wish to acknowledge the support of my partner Ana Rodriguez, thanks for your patience and understanding.

This Thesis is dedicated to my mother, Angela Pellicer Fité.

La feina feta no fa destorb.

CHAPTER 1

Introduction

Geophysics has been increasingly used for the study of Quaternary sediments during the last three decades (Telford et al., 1976; Reynolds, 1997; Jol and Bristow, 2003). However, the use of a number of geophysical techniques on genetically diverse Quaternary sediment types and a systematic evaluation of their potential as a Quaternary geological mapping tool has not yet been undertaken in Ireland. In this study a 600 Km² area in the Irish midlands, in the vicinity of Tullamore (Co Offaly), has been selected to remedy this deficit (Figure 1.1).

Numerous uncertainties about the nature, thickness and distribution of the Quaternary sediments arose during the geological field mapping phase of this research because of the limited exposure. A drilling program was undertaken to augment the field mapping in order to improve the sedimentological interpretation. However, drilling surveys only provide point data that, although of a high resolution in depth, is of a coarse spatial resolution. Consequently, a range of geophysical techniques were applied to aid in the interpretation of the Quaternary sediments.

1.1 – Aims and objectives

This thesis is focused on the application of ground-based geophysics for the study and interpretation of Quaternary sediments in the Irish Midlands. The research has three main aims.

The first aim of the research is to produce a Quaternary geology map for the 600 Km² study area located in the south County Westmeath and northeast County Offaly region, see Figure 1.1. A number of objectives have to be accomplished in order to fulfil the aim:

- to recognise, map and classify geomorphological features in the area using aerial photography and Digital Elevation Model data interpretation and field mapping;
- to delineate the distribution of Quaternary sediments along the surface and their thickness variation. Moreover, in key areas, to establish the 3D relationship between different sediment types;
- to identify the main features contributing to ice flow dynamics and formulate a preliminary interpretation of the glacial history of the area;
- to establish the location of sites suitable for geophysical surveying on Quaternary sediments. These will be selected on the basis that a broad range of geomorphic features and sedimentological settings are represented and that their results add to the construction of an evolutionary model of glaciation and deglaciation of the area.

The second aim is to assess the potential of Electrical Resistivity Tomography (ERT) and Ground Penetrating Radar (GPR) for mapping Quaternary sediments in Ireland. It is intended to establish a methodology to integrate these techniques in the Quaternary geology mapping process and the construction of an evolutionary model of deglaciation for the area. In order to fulfil this aim a number of objectives should be achieved:

- to recognize the best data collection mode, finest calibration and most efficient post-processing methodology for the mentioned geophysical techniques to assess the nature, the spatial distribution and the sedimentological setting of Quaternary sediments;
- to discuss and compare the results obtained by both geophysical systems against each other and against additional geophysical systems (e.g. Very Low Frequency Electromagnetics) and traditional mapping techniques (e.g. borehole and exposure data);
- to establish a systematic data processing and interpretation methodology for both geophysical systems, assess the potential and limitations of both methods in depicting

lithological and sedimentological variations within the subsurface in the field and in a theoretical environment by means of forward modelling software packages;

- to characterise a number of sites using both geophysical and traditional mapping techniques to aid in the production of an evolutionary model of deglaciation for the study area.

The third aim of the research is the construction of an evolutionary model of deglaciation for the North County Offaly – South County Westmeath region of the Irish Midlands.

The research will be focussed in glacially derived deposits, as these are the most complex in nature and most widespread in Ireland, covering 90% of its land surface (Edwards and Warren 1985). However, postglacial deposits, such as alluvium, lacustrine deposits and peat will be also addressed as they cover over 30% of the study area.

1.2 – Geographical Setting

The study area is located in the Irish Midlands (Figure 1.1) covering parts of north County Offaly and south County Westmeath. The main towns within it are Tullamore, Daingean and Kilbeggan. The Brosna, tributary of the Shannon River, is the main drainage system in the area running south-westwards from Lough Ennell to the southwest corner of the research area. The area forms a rectangle, the corners of which are marked by the following points on the Irish National Grid: NW - E220000, N240000; NE - E250000, N240000; SW - E220000, N220000; SE - E250000, N220000. The total area covered is 600 Km². The study area has been divided into four geomorphologically homogeneous units with specific landscape characteristics as set out by geomorphology, geology, land use and vegetation. The distribution of the physiographic areas and of main towns, roads and other geographical features referred to in this thesis are presented in Figures 1.2 and 4.1.

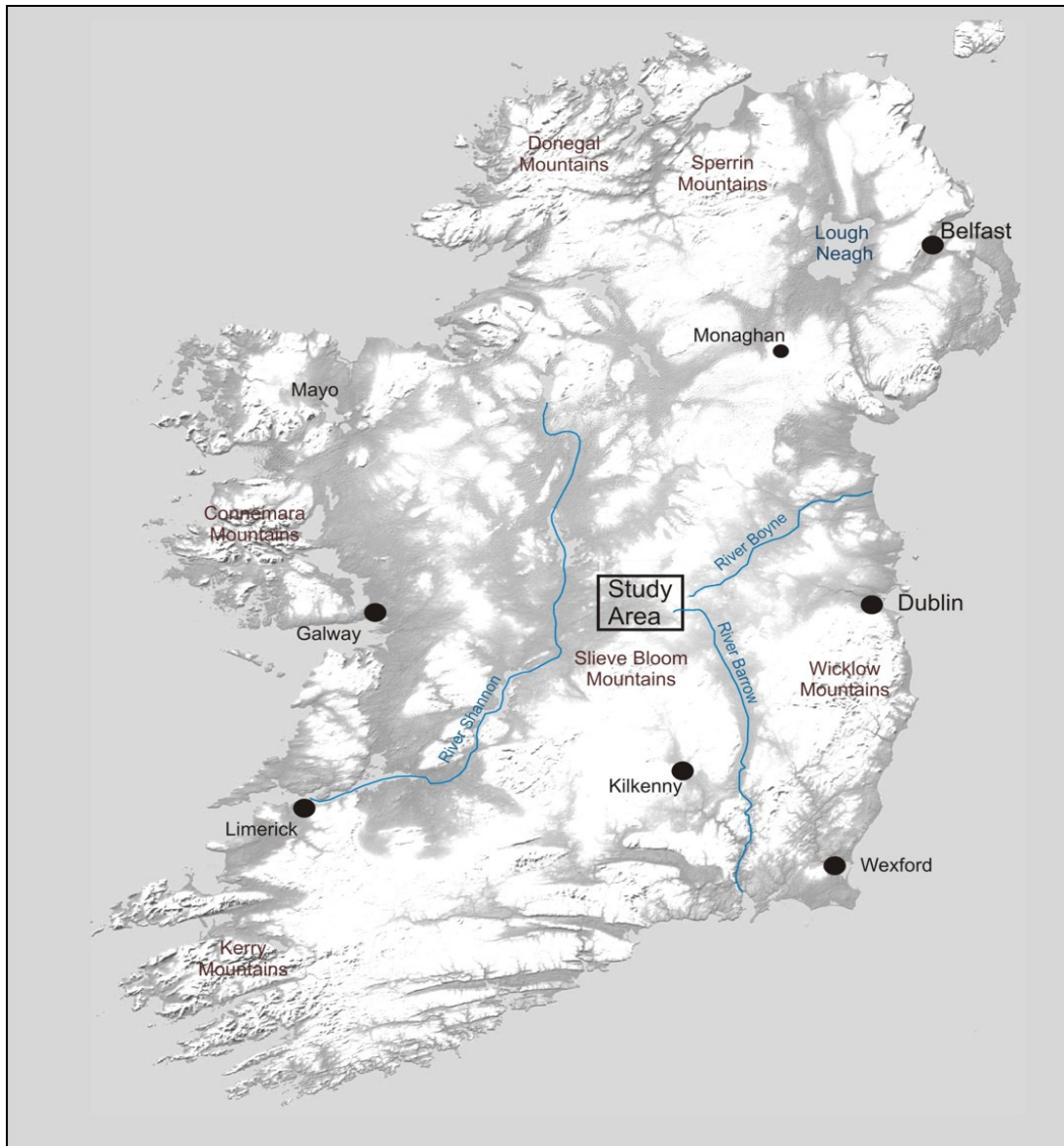


Figure 1.1 – Location of the study area in Ireland and geographical locations referenced in the thesis.

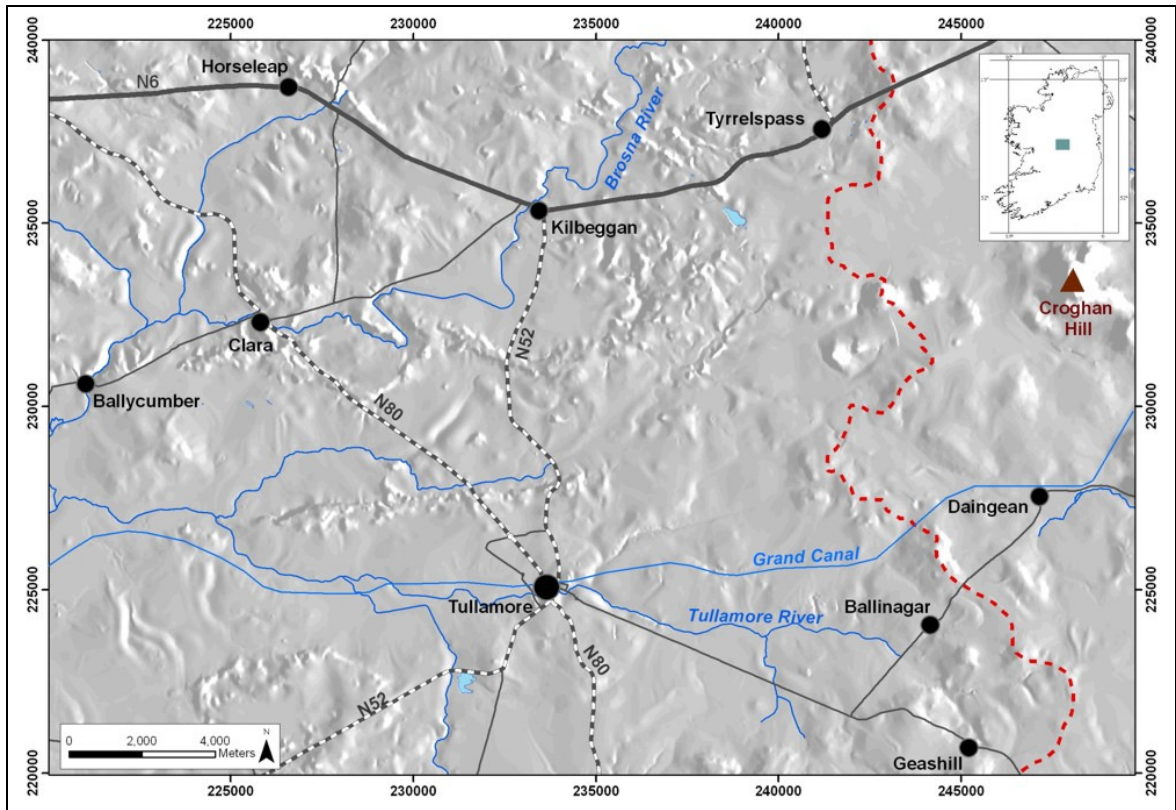


Figure 1.2 – Map of the study area. Dashed line in red indicates location of watershed between the Shannon and the Boyne/Barrow Basins.

1.3 – Thesis Structure

The layout of this thesis is structured as follows. In Chapter 1, the geographical setting for the study area is outlined and the aims and objectives to be achieved are presented.

The literature review for the thesis is presented in Chapter 2 and is divided into three main parts. Firstly, the Bedrock Geology in the study area and its surroundings is discussed. Secondly, this is followed by a review of previous research on the Quaternary geology undertaken in the Midlands of Ireland and a description and review of the sediment types and landforms occurring in the region. Thirdly, the development of the geophysical techniques used for this thesis and the application of such techniques for the study of Quaternary sediments is presented.

The methodologies used during this thesis are presented in Chapter 3. An account of the Quaternary geology mapping techniques used, including: desktop compilation, geomorphological analysis, fieldwork mapping, sampling methods, depth to bedrock map production and sample laboratory testing is presented. In addition, the geophysical techniques employed during the thesis are presented and explained. Two geophysical techniques are widely used during this thesis, Electrical Resistivity Tomography (ERT) and Ground Penetrating Radar (GRP), Very low frequency (VLF) electromagnetic survey has also been tested at one of the sites of interest to evaluate its performance against the other techniques.

The description and analysis of the nature and provenance of the Quaternary sediment types is presented in Chapter 4. Sedimentary and erosive geomorphologic features within the area are identified, illustrated and interpreted. The data are presented as a Quaternary Geology Map (Map 1) to the reconnaissance standard of the Geological Survey of Ireland. This will facilitate the reconstruction of a model of deglaciation in the study area. It will also be an instrument for the identification of potential sites to test the geophysical techniques used for this thesis. Furthermore, desktop compilation and field data available have been used to construct a depth to bedrock map for the study area (Map 2).

Chapter 5 focuses on theoretical forward modelling of ERT and GPR data and geophysical investigations at test sites where correlations could be made between geophysical response and sedimentary structures. Computer-based theoretical models of the subsurface can be produced using a number of software packages, which allow the theoretical capabilities and limitations of these geophysical techniques to be tested and aids in the interpretation of geophysical field datasets. Moreover, surveys carried out in areas of known geology help in the refinement of the ideal settings for data collection for the sediment types located in the study area, help determine limitations of the techniques and help in understanding the geophysical response where there are no exposures.

A total of 17 sites have been surveyed by means of geophysics and the results of each surveyed site are presented and explained in Chapter 6. The geomorphological description

and the Quaternary sediments distribution along the surface is firstly presented, followed by borehole or exposure data collected at the site (when available). Each ERT, GPR and VLF profile or 3D model is thoroughly described and interpreted using a previously established systematic classification.

Chapter 7 focuses on the discussions of the results from Chapters 4, 5 and 6. The discussion is divided in two main parts. The first part focuses on the geophysical techniques. The results obtained for each technique are assessed and compared to each other and based on these results the different sites are geologically characterised. The second part considers the Quaternary Geology and depth to bedrock mapping results and the distribution of Quaternary sediments and geomorphological features. Furthermore, an evolutionary model of deglaciation in the study area is constructed based on data compiled from traditional mapping and geophysical mapping data collected during this thesis and from supplementary data compiled from the literature.

Final conclusions are drawn in Chapter 8. The conclusions are related to: the Quaternary Geology mapping results, to findings on the capabilities of the geophysical techniques and to the glacial history of the study area. Moreover, a number of topics for further research following the line of investigation of this thesis are proposed.

Two appendices are included within the thesis:

- Appendix A shows a detailed log of some of the boreholes drilled for this thesis and a particle size analysis distribution (PSAD) results for some of the samples collected for each borehole.
- Appendix B displays some ERT profiles with the measured apparent resistivity pseudosection, the calculated apparent resistivity pseudosection and the inverse model resistivity section.

CHAPTER 2

Literature Review

2.1 – Introduction

The literature relevant to this thesis is considered in three separate sections: the first two relating to the bedrock and glacial geology of the study area (sections 2.2 and 2.3) and the third which relates to the geophysical techniques used in the research especially when applied to sediment analysis (section 2.4). The geographical locations (i.e. mountain ranges, rivers, lakes, towns and counties mentioned in the literature review are presented in Figure 1.1.

The 1 to 100,000 scale Bedrock Geology Map Number 15 published by the Geological Survey of Ireland (Hitzman, 1992) covers the study area and this is the main source of information for the bedrock geology types presented below. A discussion of the bedrock types and their spatial extent is important as the glacial (and most of the postglacial) sediments covering most of the Irish Midlands are derived from them. Thus, their identification in field mapping of the sediments (see Chapter 4) was important for reconstructing the glacial events.

The glacial geological literature section is itself further divided into three parts. The first part focuses on the history of Glaciations in Ireland. The naming of the stages in Ireland has historically differed from the standard North West European Stages (NWES), these are presented and correlated to each other. Since the earliest work reported in the literature (middle-late 19th century) on the study of glacial geomorphology and stratigraphy in Ireland, two differing schools of thought on the glacial history of Ireland have evolved based on two evolutionary models of glaciation and deglaciation. The two models are presented and discussed as well as the most recent publications on the Geology of Ireland. The second part reviews the literature related to the Geology of the Irish Midlands, this is presented in chronological order and discussed thoroughly; yet again the main discussion in the literature is related to the model of glaciation and deglaciation in the region proposed

by different authors. The third part of this section centres on the description and discussion of the glacial and postglacial geomorphological features and sedimentological structures typically encountered in the Irish Midlands. The main geomorphological features shaping the landscape are explained in detail and their characteristic stratigraphic record presented. The terminology and definitions are employed throughout the thesis.

The historical background and reported applications of the geophysical techniques utilised for this thesis are presented in the second section. Firstly, a range of geophysical techniques historically used on the study of the subsurface are presented, principally focussing on Electrical Resistivity (ER) and Electromagnetic Methods (EM). Secondly, the use and evolution of electrical resistivity methods for the study of the near subsurface (0-50m) are described. These have significantly evolved since the early 1900s and a wide range of data collection methods have been tested since. The introduction of Electrical Resistivity Tomography (ERT) and computer based post-processing techniques during the 1980s significantly broadened the applications of this method in geological research. Thirdly, the evolution of the EM methods used for this thesis (GPR and VLF) and the range of applications within geology for the study of the subsurface since their introduction are explained and discussed. Finally, the sparse research carried out in Ireland using these techniques is presented.

2.2 – Bedrock Geology

The research area is largely covered by soft sediments such as till, sand and gravel, and peat. Bedrock outcrops or comes close to the surface, in 84 locations, covering a total of 11.02 Km² representing only 1.83% of the study area. However, as mentioned above, the description and classification of the bedrock geology in the area is important as most of the sediments are derived from them.

Different types of limestone rocks are the dominant petrology underlying about 97% of the area. However, volcanic rocks occur in the region around Croghan Hill, north of Daingean,

represent about 3% of the bedrock within the area. Sandstone is present near Ballycumber, near the western margin of the study area.

As part of the mapping undertaken for this thesis, the till and gravel units are defined and mapped according to their most commonly (dominant) contained stone type. A number of formations with limestone as the dominant rock type have been grouped as Lower Carboniferous limestone. Other dominant petrologies encountered during the mapping were Devonian sandstones and Dinantian volcanic rocks.

Devonian rocks located west and northwest of Ballycumber consist of Old Red Sandstone (ORS) (360 to 408 MA), which were deposited in a drier, warmer climate than that of the present. They have mainly been mapped on borehole records (Hitzman, 1992). These rocks are composed of reddish conglomerates, sandstones, siltstones and mudstones with minor greenish equivalents (McConnell and Philcox, 1994). Numerous sandstone erratic boulders, cobbles or pebbles have been identified on the land surface and enclosed within glacial sediments. Their spatial distribution relative to their bedrock source provides a good indication for ice movement in the region.

Lower Carboniferous rocks (327 to 354 MA) consist of different types of limestone. The formations composing the sequence are the following: Navan Group, Ballysteen Limestone Formation, Waulsortian limestones, Allenwood Formation, Visean limestones and Lucan Formation.

The Navan Group was deposited during Dinantian time and consists of open marine to near tidal carbonates with minor shale and locally calcareous sandstones (Hitzman, 1992). It has been mapped surrounding Old Red Sandstone rocks in low ground in the Shannon Basin area as part of an anticline with the axial plane running in a SW-NE direction. The Ballysteen Formation consists of well-bedded relatively clean limestone in the lower beds, which gradationally pass up into finer-grained and muddier limestone (McConnell and Philcox, 1994). It has been mapped surrounding the formations described as ORS and the Navan Group. It outcrops 4 Km west of Ballycumber. The Waulsortian Limestones

underlies nearly 29% of the study area; they mainly consist of pale grey (microcrystalline) limestone, which commonly form individual and coalesced mounds (Lees, 1964). Waulsortian limestone passes laterally into the Allenwood Formation (McConnell and Philcox, 1994) covering about 12% of the study area. It is a hard locally dolomitized limestone (Hitzman, 1992) whose main surface expression is to be found in the hills as exposed reef forms e.g. Knockastia Hill located outside the study area, 5 Km north of Horseleap. The Allenwood Formation is known to be locally overlain by the Lucan Formation (McConnell and Philcox, 1994). The Edenderry oolite member (regarded as a member of the Allenwood Formation), interdigitates with basinal limestones of the Calp and with shelf limestones of this formation. The Visean Limestones underlie more than 15% of the area, these are predominantly composed of pale coarse grained limestone which is dolomitized in a number of deformation zones (Hitzman, 1992). The most prominent esker systems in the region develop their widest expression on top of this formation. Finally, the Lucan Formation, which underlies more than 38% of the area, is predominantly composed of clayey limestone and calcareous shale. Limestone (locally sandy) turbidites, underlie the region in the eastern part of the study area (Hitzman, 1992).

Different types of volcanic rocks outcrop on Croghan Hill and surrounding areas. The hill constitutes the largest exposed area of Dinantian volcanics in the Irish Midlands. Lavas are alkali basalts and associated rocks are both pyroclastic and extrusive deposits. The extension of volcanic rocks ranges from 3-4 Km² of agglomerate and basalt around Croghan Hill itself to several small circular occurrences, which correspond to the 2.3% of the study area. Tills derived from mafic igneous rocks and erratic volcanic pebbles and boulders encountered near the eastern margin of the research area provide a good indication of ice direction.

2.3 – Glacial Geology

2.3.1 - Glaciations in Ireland

The Quaternary Period is the most recent period of geological time and it is generally taken to cover, approximately, the last 2.6 million years (Gibbard and Cohen, 2009). It is

subdivided into two epochs: Pleistocene (2.6 million to 10,000 years ago) and the Holocene (10,000 years ago to the present). The Holocene, in Ireland, is the postglacial period. The Pleistocene may also be subdivided into the Early, Middle and Late. The Early Pleistocene runs from 2.6 to 0.78 millions of years ago, the Middle Pleistocene extends as far as 130,000 years ago. The Late Pleistocene stretches from 130,000 years ago to the present. During this late stage most of the surficial sediments were deposited in Ireland.

Most sediments in Ireland owe their genesis in one way or another to the action or melting of ice. Ireland was covered by ice for long periods during the Quaternary. The last glaciation had a huge influence on both the current landscape and shaping of underlying geology of the country (Mitchell et al., 1973). The early stages of the last glaciation commenced 115,000 years ago and extended until the Holocene (Coxon and Brown, 1989), during which, the action of modern rivers and the infilling of lakes, along with the formation of peat bogs, have been the main natural processes affecting the landscape.

The Glaciations in Ireland have traditionally been named in the literature as Midlandian (younger) and Munsterian (older) (Coxon, 1993; Mitchell et al., 1973) For the purpose of this thesis they have been named in accordance with the internationally recognised North West European Stages (NWES). The Midlandian (Oxygen Isotope Stage – OIS- 2-5d) is the equivalent of the Weichselian stage, while the Munsterian (OIS 6-8) is analogous to the Saalian stage (Mitchell et al., 1973). The interglacial stage between them is the Eemian (OIS 2-5e). Organic rich deposits recorded in Co. Monaghan have been inferred to have been deposited during this stage (McCabe, 2008). The pre-Munsterian interglacial was defined as the Gortian interglacial (Holsterian in the NWES) by Watts (1964) based on a number of interglacial deposits identified in South Ireland, However, Warren (1979, 1985) challenged such an interpretation and proposed that these sediments were of Eemian origin

A broad range of glacial features has been mapped and described in the Irish Midlands since the end of the 19th century with varied and contradictory interpretations as to their nature and evolution. These are of significant interest in order to understand the glaciation in Ireland during Weichselian times and have been a centre of discussion within the

geological community throughout the 20th century (Charlesworth, 1928, 1963 and 1973; Flint, 1930; Farrington, 1947; Watts, 1964; Mitchell, 1976; Synge, 1979; Warren, 1985, 1991a and 1992; McCabe, 1987; Bowen et al., 2002). The extent of the outer margins of the ice sheet covering Ireland during the last glaciation is still under debate, and numerous models have been presented. The study area for this thesis is a key region in the interpretation of models of glaciation in Ireland.

The first proposed model of glaciation in Ireland presented by M.H. Close (1867) was based on drumlin direction, striae and erratic carriage. It was suggested that the Irish ice sheet was made up of smaller ice-bodies that extended from a number of well-defined centres, each deflecting the flow pattern of the other where they met and coalesced. Other models of glaciation evolved from a map produced by Hull (1878). These models proposed by Charlesworth (1928) and Flint (1930) suggested an ice divide or ice divides located in the area between Galway/Mayo and Lough Neagh and radiating ice in all directions from it. This ice lobe was proposed to terminate at an end moraine, originally mapped by Lewis (1894), formerly named by Wright (1914) as the Southern Irish End Moraine (SIEM) and further developed and presented as a map by Charlesworth (1928). The interpretation of this large discontinuous feature running across Ireland from the Irish Sea, near Wexford, to the Atlantic, south of the Shannon river mouth, was mainly based on morphostratigraphic evidence. Deposits south of the feature were considered as being of Munsterian (Saalian) age. This view was supported by the presence of a smoother landscape with gentle slopes and the dominance of periglacial features (Mitchell, 1976) and the lack of limestone clasts within the sediments, which would have weathered out under periglacial conditions (McCabe, 1987). This model (Figure 2.1a) was supported and refined by most of the scientific community throughout the 20th century (Charlesworth, 1963 and 1973; Farrington, 1947; Synge and Stephens, 1960; Synge, 1979; Mitchell et al., 1973; McCabe 1985 and 1987; Bowen et al., 2002; Knight et al., 2004). Warren (1985, 1991 and 1992) presented a model of glaciation (see Figure 2.1b) in accordance with ice directions plotted by Close (1867). It consisted of three main ice centres, the first expanding from Connemara mountain range, the second from the Sperrin Mountains in Northern Ireland and the third spreading from Scotland and running down the Irish Sea. Moreover, there

were three secondary ice masses located in the Donegal, Wicklow and Kerry mountains. These Ice domes coalesced during ice advance at a number of points and reciprocally influenced their spreading out direction (Warren, 1985). It has also been stated by O’Cofaigh (2007) that an end moraine occurred offshore from Cork and that there was no stratigraphic evidence to support the view that the SIEM did indeed mark the southern limit of the Midlandian Glaciation. Hegarty (2004) rejects the morphostratigraphic evidence for the SIEM on the basis of the occurrence of primary lodgement tills with preserved limestone clasts in the southern areas of County Kilkenny. Research by Ballantyne et. al. (2006) proposes that the Wicklow ice dome was encircled by thick converging ice masses from the Irish Midlands and the Irish Sea Basin that met at an altitude of approximately 600 metres Ordnance Datum (OD), which would support ice extending offshore. Furthermore, radiocarbon dating by O’Cofaigh (2007) of the Irish Sea till overlain by Inland Irish till also suggests Last Glacial Maximum (LGM) extending offshore, as far as the Scilly Islands (6° W, 50°N).

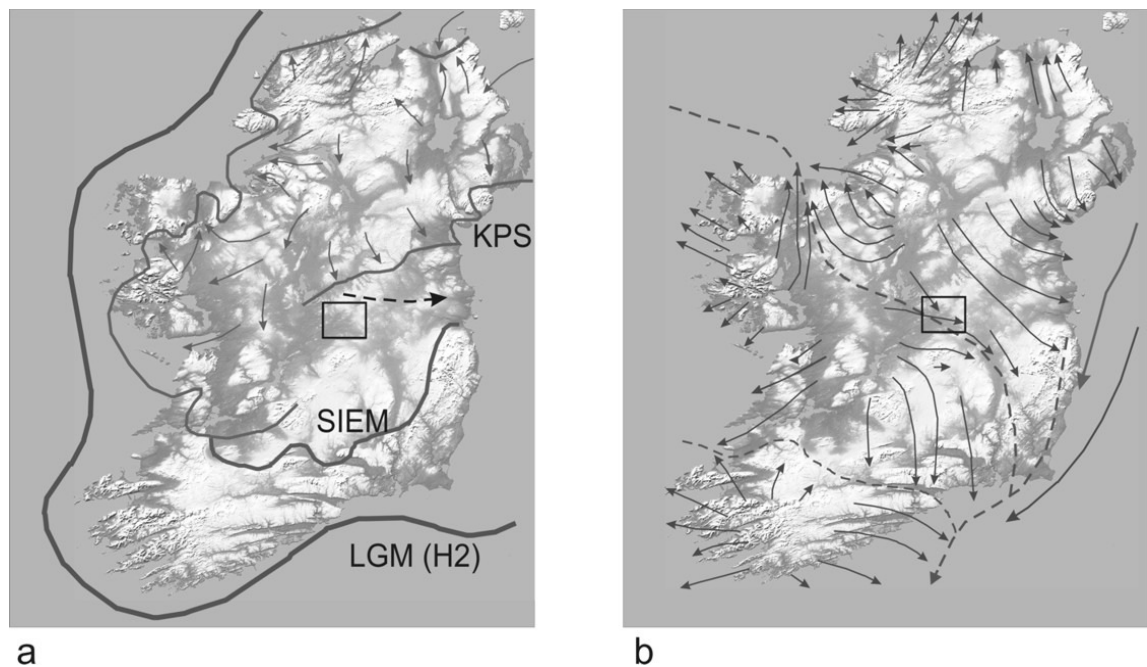


Figure 2.1 – Two main models of Glaciation in Ireland. Arrows indicate Ice flow. Continuous lines are ice maxima or ice retreat stages, discontinuous lines are discharge outlets. Study area outlined in black. a) Model of glaciation based on McCabe and Clark (2003). LGM – Last Glacial Maximum; SIEM – South Irish End Moraine; KPS - Killard Point Stadial (14K ¹⁴C yrs BP). b) Model of glaciation derived from Warren (1992) and Warren and Ashley (1994) based on drumlin orientation and esker distribution.

Evidence on ice thickness and isotope cosmogenic dating of ice scoured bedrock presented by Ballantyne et al. (2007 and 2008) supports the Ice dome model and the Donegal and Central ice domes extending offshore during the LGM in the areas west of Counties Donegal, Galway and Mayo. Greenwood and Clark (2009a and 2009b) propose a model of glaciation and deglaciation for the last Irish Ice Sheet based on landforms distribution (Greenwood and Clark, 2008) mapped from digital elevation models (DEM) and dates compiled from published literature. They propose an initial stage of glaciation dominated by a British Ice Sheet invading Ireland from the northeast, coalescing with minor local ice domes, growing as a unique body and reaching its maximum close to the continental shelf margin about 24,000 y.B.P. Ice sheet subsequently decayed as an independent body towards several ice centres located along the western parts of Ireland.

2.3.2 - Glaciations in the research area

Research on the glacial history of the Midlands of Ireland and in particular on the area around Tullamore since the beginning of the last century has mainly focused on the east-west aligned esker system (commonly named the Esker Riada) cutting across the Irish Midlands. The main ideas and interpretations that emerged from that research are presented below.

Several large ridges running across the study area north and south of Tullamore in an east to west direction have been interpreted in the past as ice marginal ridges associated with an ice sheet retreating northwards. Charlesworth (1928) visualized the large east-west orientated ridges as recessional moraines; with smaller north-south ones as subglacial/subaerial ice walled tunnel fill deposits. Farrington and Synge (1970) interpreted the ridge system as esker ridges composed of subaqueous fans deposited sequentially from subglacial conduits at the ice margin with associated morainic mounds. This suggests an ice-sheet withdrawing towards the west and southwest, the moraines marking standstill stages in that retreat. The model of glaciation and deglaciation during Weichselian times presented by Warren (1991, 1992) and recently supported by cosmogenic isotope dating by Ballantyne et al. (2006, 2007 and 2008), envisaged the two

main ice centres, the Northern Dome (centred on the north Midlands) and the Central Dome (centred on the central and west Midlands) coalescing in areas close to north County Offaly and advancing as a single ice sheet flowing in an east-southeast direction. The ridges running east-west were interpreted as eskers deposited during ice retreat and under subaqueous conditions. Further research pursued on the Midlands esker ridges by Warren and Ashley, (1994) reinforced this model and presented a detailed morphostratigraphic description of the main features which shows the polygenetic nature of some of the eskers, which were found to encompass continuous tunnel fill partially buried by ice marginal fan moraines in places. Glaciolacustrine sediments identified by Glanville (1997) in a region 50Km east from the study area were associated with two ice margins retreating west and north. Sedimentological work by van der Meer and Warren, (1997) on late glacial clays in lacustrine basins shows sedimentation of rhythmites and clays in an unstable environment and the presence of floating ice in a glacial lake environment. Moreover, smaller esker ridges located north of the main east-west trending eskers are associated with a change in the ice retreat direction subsequent to the splitting of the central and northern ice domes. Delaney (2002a) envisaged a two-phase model of esker formation involving eastward drainage of ice and water initially into a glacial lake with water level at 92m ordnance datum (OD) for at least part of its existence, followed by retreat and readvance from the northwest. Geological and geomorphological mapping using both traditional and remote sensing methodology on the eastern margin of the Shannon Basin presented by Pellicer and Warren (2005) identified a clear pattern of deglacial sedimentation into a large and expanding interdomal lake (Glacial Lake Riada). Two main directions of ice retreat are identified from the pattern of esker, ice-marginal delta and subaqueous fan sedimentation. Initially two conjoint ice dome fronts decayed westward forming the western wall of the ice dammed lake. The two domes then began to separate opening an ever-widening inlet, which progressed westward to separate the domes. This resulted in a profound change in the pattern of ice retreat, with two ice fronts, one decaying toward the northwest and the other to the southwest. Latest research in the Irish Midlands by Delaney (2008) focuses on the deposition of glaciolacustrine varved sediments deposited during Late Weichselian times (22-10Ka BP) in a proglacial lake recognized as glacial Lake Riada. The outline and

the water level of this lake changed rapidly during deglaciation, this is further discussed in Chapter 7.

2.3.3 - Glacial and postglacial Morphostratigraphy

Sediments deposited during the Quaternary Period cover more than 90% of the land surface of Ireland (Edwards and Warren, 1985) and over 98% of the study area. An important part of this research was the mapping and recording of available outcrop data as this yielded important information in its own right but also provided ‘ground truth’ for the geophysical techniques. A brief description of the different sediment types and geomorphological features mapped during fieldwork and adopted nomenclature presented below. The field mapping results are described in detail in Chapter 4.

Till (Boulder Clay)

Till is sediment deposited by or from glacier ice. Glacial ice is the principal depositional agent, but gravity and, in some cases, water, also plays a part. Tills are often over consolidated, or tightly packed, unsorted or unbedded. They can possess many different particle and clast (stone) sizes, and commonly have sharp, angular clasts. Tills have often been referred in the past as ‘boulder clays’.

An intense discussion on a genetic classification of tills has persisted for the last three decades. Dreimanis (1988) proposed a till classification as follows: lodgement tills, melt-out tills, deformation tills and flow tills. According to Dreimanis (1988), the lodgement process involves the plastering of glacial debris from the sliding base of a moving glacier by various mechanical processes. The term ‘melt-out till’ proposed by Boulton (1970) was described as sediment derived from slow release of debris from the lower or upper surface of stagnant ice, widely produced during periods of marked ice retreat. Deformation tills are shaped by the shearing of existing sediment beneath the ice due to the action of the sliding of an active glacier, whereas, flow tills are derived debris produced from glacier ice release or from redeposition by sliding and/or gravity flow of freshly deposited till (Dreimanis

1988). Menzies et al. (2006) used micromorphology to study the internal architecture of tills and established that deformation is the main factor shaping the internal architecture of tills. A new approach to classification of tills based on their level of deformation and the term tectomict was proposed to differentiate the old classification of tills from a deformation based one. An exposure showing till typically deposited in the research area is presented in Plate 2.1a.

Interstratified Tills with Gravel

Classification of a deposit as interstratified till with gravel is designated when clear interstratifications between unsorted (diamicton) and well-sorted (sands and gravels) sediments are recognized.

This sediment association is, by and large, morphologically expressed by hummocky moraines deposited in ice contact areas. Hummocky moraines are the end product of topographic inversion cycles during the ablation of ice overlain by debris. Several cycles of debris reworking and topographic inversion may occur before debris is finally deposited in a series of irregular mounds and ridges (Benn and Evans 1998). Typical facies association consist of interbedded debris flows, laminated lacustrine sediments and glaciofluvial sands and gravel in varying degrees of disturbance where there is deposition of till locally washed by water released from the ice sheet (Eyles, 1979; Paul, 1983). Very dynamic changes in the depositional regime, due to changes in water source position, are expected when ice front advance and retreat takes place a number of times in the same area. An exposure showing interstratified till with gravel deposits occurring northwest of Tyrrellspass is presented in Plate 2.1b.

Glaciofluvial/Glaciolacustrine sediments

Glaciofluvial sediments occur extensively within the study area and are morphologically expressed by a variety of landforms. The most striking geomorphological features composed of glaciofluvial sediments are the numerous east-west esker ridges cutting across the Irish Midlands. These landforms will be discussed later due to their importance in the area. Other morphological features identified, chiefly formed of glaciofluvial

sediments and genetically differentiated, are sandar, kame and kettle topography, subaerial and subaqueous fans and glacier fed deltas. An exposure showing glaciofluvial sediments occurring north of Tullamore along the Ballyduff Esker is presented in Plate 2.1c.

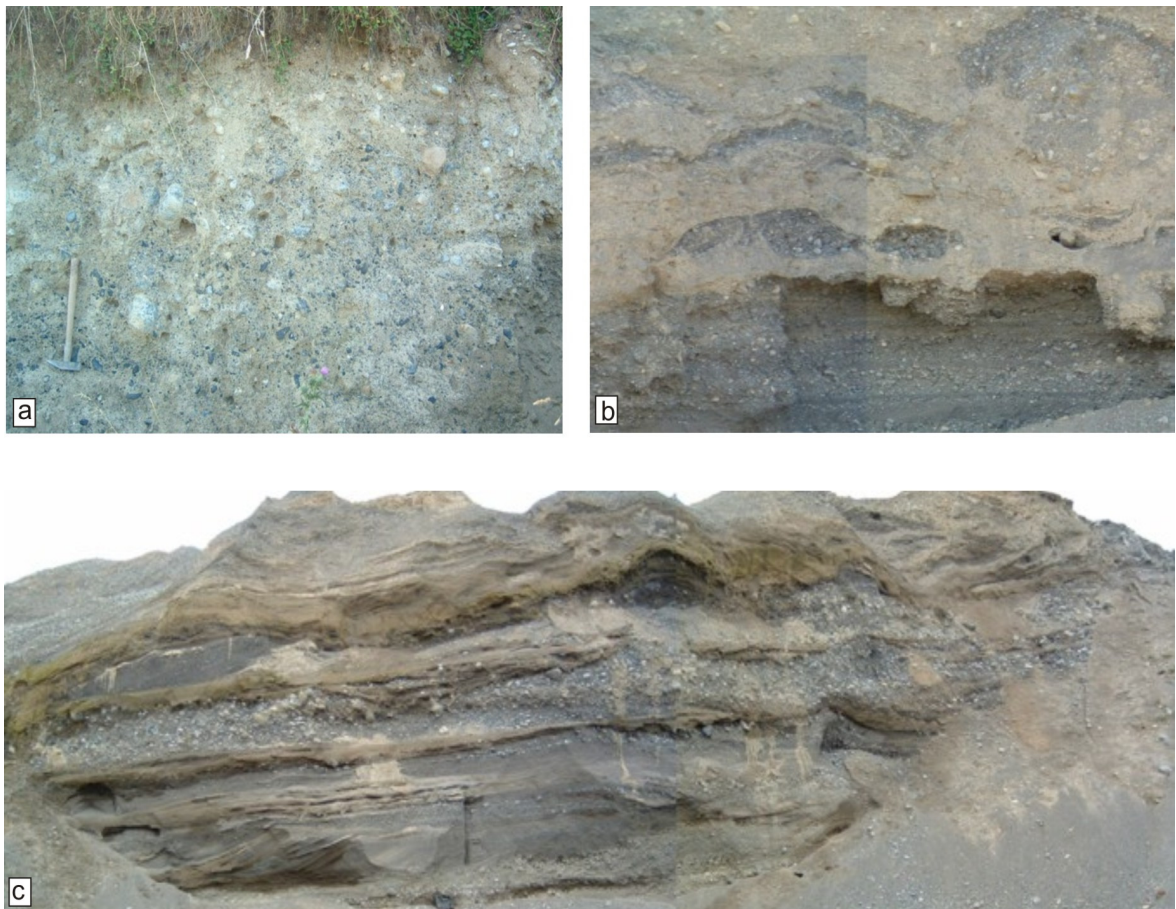


Plate 2.1 – Glacial sediments typically occurring in the research area. **(a)** Diamicton derived from Lower Carboniferous limestone with sandy matrix. **(b)** Interstratified till with gravel. **(c)** Glaciofluvial sediments consisting of interstratified sand, gravel and silt.

Sandar are gently sloping outwash plains deposited in a subaerial proglacial environment where proglacial streams carry large amounts of suspended sediment and bedload (Benn and Evans 1998). They occur in braided streams and develop from a combination of steep gradients, abundant bedload, and fluctuating discharges (Miall, 1992). Sediments consist of well-sorted sands and gravels. In some cases they may grade into deltaic and distal

lacustrine environments. Morphologically, sandar can be expressed by very flat to very hummocky landscape.

Kame and Kettle topography comprises a morphological assemblage of mounds (kames) and hollows (kettles); it forms where large quantities of debris are reworked by supraglacial and englacial drainage systems during the final steps of glacial decay (Clayton, 1964). A good example of this type of topography has been recognized along the east end of the main esker ridges south of Tyrrellspass. Kettle holes may be represented by lakes and represent areas of subsidence caused by the melting of buried ice (Benn and Evans 1998). Kame mounds are steep-sided, variously shaped mounds composed chiefly of sand and gravel, formed by subglacial or ice-contact glaciofluvial deposition (Holmes, 1947). However, kame terraces have been defined as gently sloping depositional terraces perched on valley sides and are deposited by meltwater streams flowing between glacier margins and the adjacent valley walls (Flint, 1957). These occur along the northeast slopes of Croghan Hill located in the eastern part the study area. An example of Kame and Kettle topography is presented in Plate 2.2a.

Morainic ridges are morphological features running parallel to the former ice margin providing an indication on readvance or standstill episodes of the ice sheet during its retreat. Moraines occurring in the area of interest could be defined as recessional moraines, because they are formed during overall glacier recession, even though they may have been deposited or pushed up during standstills or minor ice readvances. Benn and Evans (1998) classify ice-marginal moraines as four main types, glaciotectonic landforms, push and squeeze moraines, dump moraines and latero-frontal fans and ramps. However, commonly moraines are composite in nature. Glaciotectonic landforms are generated by the deformation of bedrock or sediment underlain by the ice sheet. Push moraines are small ridges, usually less than 10m in height, produced by minor glacier advances (Rabassa et al., 1979). Dump moraines will form where the ice margin remains stationary during debris accumulation (Boulton and Eyles, 1979), they can become push moraines if subsequent ice readvance occurs. Latero-frontal fans and ramps consist of coalescing debris fans associated with the ice front, are asymmetrical in cross-section, and have steep inner and gentle outer slopes, which can develop into sandar under favourable glaciofluvial

conditions (Benn and Evans, 1998). As part of this thesis, morainic ridges have been surveyed southwest of Tullamore by means of ground-based geophysical techniques (see Plate 2.2b).



Plate 2.2 – Examples of geomorphological features typically occurring in the research area. (a) Kame and Kettle topography occurring west of Ballycumber. (b) Morainic ridge surveyed using geophysical techniques located southwest of Tullamore. (c) Subaqueous fan located south of Ballinagar.

Subaqueous and subaerial fans are commonly found in the study area. They are deposited at an ice front environment. Sediments transported by the glacier hydrologic system at the ice margin in standing water conditions are deposited as subaqueous fans or deltas (Ashley and Warren, 1995). The direction of transport of the sediments is perpendicular to the ice margin, but several point sources can create a continuous or segmented ridge indicating the former position of the ice margin. These features have been termed ‘delta-moraines’ by Synge (1950) referring to the Galtrim moraine in Co. Meath, and by Flint (1971) relating to the Ronkonkoma moraine in Long Island, New York (USA). These features are also referred to as subaqueous moraines and described as transverse moraines deposited at or close to the grounding lines of water terminating glaciers, with highly variable morphological and sedimentological settings (Benn and Evans, 1998). An example of a subaqueous fan morphological expression is presented in Plate 2.2c. Subaerial ice-contact alluvial fans have been described by Ashley and Warren (1995) on elevated ground east of Kinnegad, Co. Westmeath, approximately 40 km east of the research area. The perpendicular to oblique paleocurrent direction across the beads and the lack of lacustrine evidence, have been interpreted as features derived from ice front deposition under subaerial conditions.

Deltas may form as glacier-fed deltas, receiving the sediment from glacial meltwater streams on the land surface or as ice-contact deltas or built up directly from ice-contact margins evolved from subaqueous fans that in time reached the lake water level (Benn and Evans 1998). Glacier fed deltas are analogous to fluvial deltas. Postma (1990) presented a classification showing delta morphology as a function of basin depth and gradient of the feeder river system. However, glacial environments are very unstable depositional landscapes, rapid changes in lake/sea level or sediment discharge can occur, which can often result in a combination of delta types forming within a single feature. Ice contact deltas are fed by subglacial or englacial tunnels. High energy, coarse-grained systems mainly develop as ‘Gilbert’ type deltas whereas, low energy; fine-grained systems tend to evolve into ‘Hjulstrom’ type deltas with shallower dipping foresets. In both systems, glaciers act as a support for the glaciofluvial sediments. The removal of support during ice

retreat delivers a characteristic steep coarse grained ice-contact face on the up ice side and a gentle depositional slope down ice. The sediments on the down ice slope are composed of medium to fine-grained sands, silts and clays, which accumulate as delta foresets when depositional activity is low. Furthermore, bottomsets dominated by laminated fine sediments occur in the distal delta front (Ashley, 1995). Some of the geophysical surveys carried for this thesis have been performed on these types of sediments; see Chapter 5 – Section 5.4.

Eskers are the dominant geomorphological within the study area (see Figure 4.2, Chapter 4) laid down by glacial meltwater in tunnels and crevasses in stationary or retreating ice sheets, and are seen on land as long, narrow, sinuous ridges. They commonly possess rounded boulders and cobbles. Clasts are usually much larger overall than in other glaciofluvial deposits and sand may or may not be present. The esker alignment usually shows a close correspondence with the ice flow direction. The gravels are usually bedded, the beds often slump towards the flank of the esker, indicating collapse as the confining ice walls melted. Examples of the morphology and internal characteristics of the eskers investigated in this research are given in Chapter 4. An esker classification based on eskers mapped in the Irish Midlands presented by Warren and Ashley (1994) has been largely accepted by the scientific community and the one used during the mapping for this thesis. It categorises eskers into the four different types described below:

Continuous subglacial tunnel fill represents deposition within tunnels underneath or within an ice body originally used as water escape conduits. When there is a blockage of the tunnel perhaps because of ice collapse, large boulders become trapped within the tunnel. Sediment carried by the water in the tunnel accumulates at the front of the blockage and a ridge starts forming, pro-grading upstream. The sediments can range from well-sorted to very poorly-sorted depending on the hydraulic conditions that obtained at the time of deposition. Classically, such deposits are, for the most part, very coarse and may in extreme cases contain boulders up to 5 metres in diameter. This type of feature can be deposited within days or months (occasionally tens of years).

Continuous fluvial ice-channel fill is deposited in channels cut into the ice on top of the glacier or down to the substrate and are subsequently infilled by sediment. Thus the sediment is either deposited on ice and subsequently lowered to the substrate by ice melt, or deposited directly on the substrate between ice walls. This type, though less common than others, can form components of eskers that are largely tunnel fill deposits. They also occur on higher ground that emerged through the ice sheet as it downwasted.

Long beads - subglacial tunnel fill are segmented ridges or beads representing sequential deposition near or at the ice margin as the ice sheet retreats. Long beads are defined by the ratio of their length to their width, usually in the range of 5:1 to 10:1. They are often distinct landforms and are of a uniform size along their length. They are usually offset and may exist as multiple parallel ridges (Warren and Ashley, 1994). The older beads are those farther away from the ice centre.

Short beads are deposited within a lake. These have been interpreted as sequential deposition of ice-contact subaqueous outwash fans below the water surface or up to the water surface level. Having reached surface level, these become equivalent to deltas (Warren and Ashley, 1994). They do not appear as long ridges with long beads but instead are shaped as fans, caused by being deposited in a water body (Benn and Evans, 1998). They too are younger in the ice retreat direction.

Postglacial sediments

Postglacial sediments in the research area are mainly of lacustrine, alluvial and organic (e.g. peat) origin.

Lacustrine sediments are deposited contemporaneously with deglaciation or during postglacial times in depressions left behind by the ice during ice retreat. These deposits are usually composed of silts and clays and occasionally of fine sands. The presence of varves (thin laminar beds of fine sands grading upwards to thinner bands of silts) indicates the origin of the sediments as being associated with a proglacial environment. Peat deposits

usually overlay them. Numerous studies have been carried out on lacustrine and glaciolacustrine sediments in Ireland attempting to develop a proxy for climate evolution during the late Quaternary (e.g. Mitchell 2006, Diefendorf et al., 2006 and 2007). Van der Meer and Warren (1997) examined the micromorphology of lacustrine sediments in the Irish Midlands, and concluded that these were deposited by turbidity currents within a glacial lake and presented deformation structures related to water escape, slumping and probably iceberg scouring.

Alluvium is a postglacial deposit and may consist of gravel, sand, silt or clay in a variety of combinations and often consists of a fairly high percentage of organic carbon (10%-30%). Alluvium is mapped only on modern day river floodplains. The alluvial deposits are usually bedded, consisting of many complex strata of water-lain material left both by the flooding of rivers over their floodplains and the meandering of rivers across their valleys. In terms of physical properties, (grain size) alluvial deposits are very dynamic systems, presenting strong variations in small areas. Alluvial sediments are especially dominant in the area along the Brosna River Basin.

Peat is also a postglacial deposit, consisting mostly of vegetation, which has only partially decomposed. This non-decomposed layer accumulates and compacts mostly on poorly drained low ground and small lakes carved out and left by ice sheets (raised bogs, fens), but also in elevated areas with excessive rainfall, occurring as blanket bog. Peat within the research area is mostly represented by raised bogs. These developed in old basins that were gradually filled by decomposed organic matter as fen peat, which prevents the input of nutrients into the system. This facilitates the growth of plants that develop under low nutrient conditions, such as sphagnum mosses and heathers ultimately developing into raised bogs (Gibson, 2007a). In the last few centuries, much of Ireland's peat has been cut away for burning as solid fuel or is oxidized as the result of dewatering of the peat in an attempt to make the land arable. An account of the extraction of peat from the Irish Midlands bogs is presented by Gibson (2007a). Moreover, research on peat bogs in Ireland has provided valuable palaeoclimate data from the Holocene (e.g. Blackford and Chambers, 1995; Pilcher, 1973).

2.4 – Geophysical techniques

2.4.1- Overview

Geophysics is a broad science that involves the study of the physical properties of the Earth and other planets. In a more restricted form, it is the study of the physics of the Earth's interior. Applied geophysics is concerned mainly with the study of the near surface (0 to 1000m depth) and covers a number of fields such as, engineering, oil and mineral exploration, environmental sciences and archaeological mapping (Reynolds, 1997). An important advantage in the use of applied geophysics for the study of the subsurface is that the techniques employed are non-intrusive, environmentally friendly surveying methods.

Geophysics has historically been related to important findings in the study of subsurface, such as the discovery of the Mohorovicic discontinuity in 1909 or the delineation of the Earth's core by Guttenberg in 1912. The acceptance of the plate tectonic model in 1967 extensively increased the use of geophysics for geological research (Fowler, 1990). There is a broad range of geophysical methods available, each one has been usually developed for the investigation of a particular field and subsequently applied, if suitable, to others. Gibson and George (2004) list the basic geophysical methods and their main applications. Gravity was developed to detect changes in density of the crust and is mainly used for hydrocarbon exploration and regional geological mapping. Magnetic susceptibility is highly effective at detecting metallic objects and ore bodies and can also be applied to geological mapping and archaeology. Seismic refraction and reflection have been extensively used for regional geological mapping and particularly focussed on mapping oil reservoirs. Electrical Resistivity has been applied to the study of a broad range of environmental studies such as contaminant plumes or cavity mapping. Electromagnetic methods encompass a broad range of systems; which measure the conductivity or relative permittivity of the subsurface and can be used for either regional or local investigations.

The use of several suitable geophysical techniques in the study of the same area will narrow down the possible geological settings and considerably improve a final interpretation. Several techniques have been used during the thesis combined with other

traditional mapping data in order to achieve a good understanding of the local and regional sedimentological setting of the area. The geophysical methods employed have been selected on the basis of their availability for the project and their suitability for delineation of sediment distribution, as well as water table detection and depth to bedrock mapping. The techniques utilized are electrical resistivity including ERT, time-lapse and azimuthal resistivity and electromagnetic encompassing Ground Penetrating Radar (GPR) and Very Low Frequency (VLF).

Further discussions on the theoretical concepts underpinning the geophysical techniques applied during the research and the methodological approach adopted are considered in Chapter 3.

2.4.2- Electrical resistivity methods

Electrical Resistivity was originally developed in the 1900s. Wenner (1915) was the first to suggest the use of four electrodes for geophysical prospecting (see Figure 3.4, Chapter 3) and in 1921, Schlumberger started to use resistivity for oil and gas exploration. A number of methods and electrode arrays have been developed since then, although the Wenner and Schlumberger methods remain widely used. In the research for this thesis, a combined Wenner-Schlumberger array was employed – see Chapter 3. The availability of computers for data processing during the 1970s prompted the wide use of electrical resistivity methods in the study of hydrogeology, cavity location for mining, geotechnical investigations and environmental studies (Reynolds, 1997). Resistivity profiling and vertical electrical sounding (VES) have been the two main methods used for electrical resistivity surveying until the 1980s. Resistivity profiling involves moving the four fixed electrodes in a line, mostly using the Wenner or Schlumberger arrays in order to detect lateral variations on the subsurface. VES measures the changes of the electrical resistivity with depth at a given point by increasing the distance between the electrodes. VES has been widely employed for the detection of vertical changes in the subsurface (Larson, 1995; Carpenter, 1996; Guglielmin et al., 1997).

The introduction of multi-electrode survey systems during the 1980s, commonly named Electrical Resistivity Tomography (ERT), using 25 to 50 electrodes, allowed the collection of lateral and vertical resistivity variations substantially quicker than previously (Barker, 1981). This approach produces a 2D image of the subsurface, named a pseudosection (Gibson and George, 2004). Loke and Barker (1996) presented a methodology and software (RES2DINV) for data post processing by the use of a least-squares algorithm which would reduce the Root Mean Square error between the measured and the calculated apparent resistivity (Gibson and George, 2004). Electrical Resistivity Tomography (ERT) was applied to hydrogeological studies by Overmeeren and Ritsema (1988). It allows the recording of multiple data points along a line at different depths. ERT has been widely used (Maule et al., 2000; Hauck et al., 2003; Comas et al., 2004; Kilner et al., 2005; Martinho and Alomeida, 2006) and it is considered in greater detail in Chapter 3. The data can be collected in a line by combining the Schlumberger and Wenner arrays increasing the spatial resolution of the final dataset, this array has been named by Loke (2004) as the Wenner-Schlumberger array. For this thesis, 25 electrodes were employed to give 157 data points for each profile at different depths, some of which were collected in the Wenner array format and some by means of the Schlumberger array. This method has been used to collect electrical resistivity data for this thesis. Other methods with fixed electrodes for 2D imaging of the subsurface are also available such as the dipole-dipole, or pole-pole but are used less frequently (Griffiths and Turnbull, 1985; Overmeren and Ritsema 1988; Dahlin, 1996). Another resistivity data recording method presented by Sorensen (1996) consist of a set of electrodes dragged over the ground at a constant velocity, which allows the acquisition of a large profile in a short time period. This method yields a high resolution according to Moller and Sorensen (1998) when compared to the method presented by Overmeeren and Ritsema (1988). However, its use is rarely encountered in the literature.

Some electrical resistivity work has been published for Ireland. Smyth (1994) applied VES to geological mapping and to detect peat thickness and water table levels in peatlands of north Co. Offaly. George and Gibson (2000) used it for detection of contamination plumes in disused landfill sites in County Monaghan and to locate a suitable site for groundwater extraction in Maynooth, Co. Kildare (Gibson and George, 2001). Gibson et al. (2004) and

Gibson (2005) used resistivity for the detection of karstic features and time-lapse resistivity for the investigation of landfill plumes. Caloca (2006) has employed resistivity to identify and describe a range of glacially derived geomorphological features in north County Offaly. A number of reports have also been published by Gibson and George (2004, 2006) and Gibson (2007b,c) using geophysical techniques including electrical resistivity, applied to archaeology and by O'Sullivan et al. (2004) on the use of geophysics to assess potential waste disposal sites. The 2D time-lapse resistivity was first employed in Ireland by Gibson (2003) for the detection of seasonal changes in the subsurface. Moreover, a number of private companies use resistivity as a tool for detection of archaeological sites, depth to bedrock, karst features, landfill leakage monitoring etc. Furthermore, a number of MA theses from the Department of Geography of National University of Ireland, Maynooth University have focused on the use of geophysical techniques applied to the study of glacial and postglacial sediments (Callaghan, 2002; Breen, 2003; Doughan, 2004). O'Rourke and O'Connor (2009) produced a classification of the median resistivity values recorded on the different types of Carboniferous limestone occurring in Ireland and concluded that median values were highly related to depositional environment. However, the research attained in the Irish context on resistivity surveys applied to the study of a broad range of sediment types is fairly limited. The research carried out in this thesis aims to provide a wider understanding of the use of the electrical resistivity method applied to the study of surficial sediments in Ireland.

Azimuthal resistivity consists of the use of VES methodology to collect data at different depths and in a number of directions around a unique point with the aim of detecting anisotropy within the sediments. A quadrangular array was introduced by Haberjam and Watkins (1967) who stated that this is a more sensitive system for the detection of rock anisotropy and uses less space for surveying than the standard collinear array. Risk (1975) used a collinear array to characterize fissures in a region with geothermal activity. Baker (1981) introduced an offset Wenner method for the study of anisotropy of an homogeneous subsurface by using a five collinear electrodes with the first reading taken by the first four and the next by the second to the fifth electrodes. The use of azimuthal resistivity surveys has been used since by a number of authors (Taylor and Flemming, 1988; Watson and

Barker, 1999; Busby and Jackson 2005) mainly for detection and characterization of anisotropy such as bedrock jointing. Applications to the study of surficial sediments is very limited, Boris and Merrian (2002) attempted to map fractures in till by using this method. This technique has been scarcely used in Ireland; Breen (2003) used the technique with very small fixed electrode spacing for the study of an esker. The application of azimuthal resistivity employing variable orientations and electrode spacings in the study of surficial sediments will be tested in this thesis.

Time-lapse resistivity is a time consuming methodology which attempts to detect variations in the electrical properties of the subsurface with time introducing a 4th dimension to data collection. This technique can be carried out through short time periods (several day)s with readings taken every few hours) to evaluate the migration of contamination plumes from waste disposal sites in order to optimize remediation costs (Radulescu et al., 2007), detection and monitoring of concentration of a conductive contaminant within an unconfined aquifer (Oldenborger et al., 2007) or quantification of superficial water infiltration rates into the subsurface (Barker and Moore, 1998). Long term time-lapse resistivity surveys have been applied to monitor seasonal variations on seepage rates through a dam (Johansson and Dahlin, 1996), seasonal change of the salinity within aquifers (Leroux and Dahlin, 2006), safety assessment for storage of nuclear waste (Yaramanci, 2000) or estimation of subsurface temperature variation (Morard et al., 2008). The use of time-lapse resistivity surveying in Ireland is fairly limited. Gibson (2003, 2005) presented some surveys carried out on limestone bedrock.

2.4.3 - Electromagnetic Methods

Some electromagnetic surveying techniques measure subsurface variations in the conductivity (σ), which is inversely proportional to resistivity. Conductivity is measured in Siemens per metre (S/m), although for environmental surveying, the readings are taken in mS/m, as the values recorded are rather small. Conductivity values for geological materials range from 10^5 mS/m for sulphides to 10^{-2} mS/m for some igneous rocks, see Figure 3.3, Chapter 3.

Numerous electromagnetic methods have been developed since the 1960s, the ones discussed in this chapter are those used in the thesis. These are the following:

- Ground Penetrating Radar (GPR)
- Very Low Frequency Survey (VLF)

Ground Penetrating Radar (GPR) records discontinuities in the subsurface by the emission, propagation, reflection and reception of high frequency electromagnetic waves, generally between 25 MHz and 1000 MHz (Neal, 2004). The most commonly used frequency range, for the study of sediments, is 50 MHz to 500 MHz (Jol and Bristow, 2003).

Ground Penetrating Radar was originally developed during the early 20th century by German scientists interested in the investigation of buried features (Reynolds, 1997). Improvements in antennae design and electronics, mainly during the 1970s, produced a tool for the detection of subsurface discontinuities with a higher spatial resolution than seismic methods (Neal, 2004). The technique has been successfully used in the investigation of ice thickness, water depth in lakes, depth to bedrock and water table levels, as well as the detection of karst features and bedrock fabric (Davis and Annan, 1989). The use of GPR in geological studies has increased greatly since the early 1980s as a result of its commercial availability, the rapid acquisition of data and the potential of its interpretation (Neal, 2004). A methodology for the study of radar profiles, encompassing, data processing and interpretation has been adapted from previous seismic stratigraphy interpretation presented by Mitchum et al. (1977). Furthermore, a terminology to describe, define and interpret radar reflectors and radar facies has been developed and is presented by Neal (2004).

The correct use of this technique during data collection can highly influence the subsequent interpretation of the profiles. The antenna frequencies used for

sedimentological mapping for this thesis are 200 MHz, 100 MHz and 50 MHz. High frequency antennae provide a high spatial resolution of subsurface features but low penetration, whereas low frequency antennae give a lower resolution but deeper penetration. Work carried out by Davies and Annan (1989), Jol (1995) and Smith and Jol (1995) show the resolving limitations of different antennae and their maximum penetration. The use of several antenna frequencies for the same survey area is recommended by Jol and Bristow (2003) in order to resolve sedimentological structures at different scales. Other factors to take in to account during data collection are the type of geophysical reflection survey, the antennae orientation and separation, the step size (distance between consecutive data collection points), the location and orientation of the profile with respect to the feature recorded and the time window. These concepts are further considered in Chapter 3.

Another important step before data interpretation is the post-processing of the GPR survey data. Many of the post processing techniques have been adapted from highly sophisticated seismic data processing software packages (Annan, 1999). The most common post-processing techniques are briefly presented below and will be considered in more detail in Chapter 3. *Timezero drift* is performed when the first break in the radar profile changes position from trace to trace and is usually due to a colder temperature for the console electronics compared to air temperature (Sensors and Software, 1999). A number of gains and filters are often applied to the raw data in order to eliminate artefacts by mathematical manipulation of the data, though the use of the wrong filters could lead to the introduction of unwanted artefacts (Annan, 1999). *Signal saturation correction (wow)*, dewow is a filter applied to suppress low frequency “wow” (Sensors and Software, 1999). The most commonly applied gains are Automatic Gain Control (AGC), which applies a gain to the data inversely proportional to signal strength in order to equalize the profile (Sensors and Software 1999) and Spreading and Exponential Compensation (SEC), which applies an exponential gain to the profile enhancing deeper data which compensates for wave spreading and attenuation effects. Other filters enhance horizontal or sub-horizontal reflectors while diminishing the signal for vertical reflectors (e.g. migration). Topographic correction is recommended when a survey is carried out and is best recorded by using total

station or differential GPS (Jol and Bristow, 2003). A Ground Penetrating Radar transmitter antenna propagates the energy at right angle to the surface and therefore an increase of the slope dip, will amplify the error on the location of subsurface features, Lehmann and Green (2000) noted that the misalignment of underground features becomes a problem on slopes greater than 6°.

Ground Penetrating Radar has been used in the study of glacial and postglacial sediments since the early 1980s (Ulriksen, 1982; Smith and Jol, 1992; Lonne and Lauritsen, 1996; Busby and Merrit, 1999; Bristow et al., 1999; Beres et al., 1999; Bano et al., 2000; Overgard and Jacobsen, 2001; Bakker and van der Meer, 2003; Kostic et al., 2005). Ulriksen (1982) recognised a high attenuation rate related to clay-rich sediments and that the water table within glaciofluvial sediments was detected as a very strong reflector. Fisher et al. (1992) used several post- processing methods before data interpretation and was the first to apply the technique of the Common Mid Point (CMP) in sediments, The CMP technique is used to calculate the sounding velocity for the surveyed sediment type, which is used to convert the radargram time measurements to depth measurements. Velocity usually varies with lithology and most GPR software incorporate velocity analysis tools (Sensors and Software, 1999). The use of pseudo 3D surveys, which involves the collection of lines in perpendicular directions and displayed as fence diagrams was used by Gawthorpe et al. (1993), Bristow (1995) and Bristow et al. (1996, 1999, 2000). The generation of 3D data cubes collected during time-consuming 3D surveys has been employed by Beres et al. (1995, 1999). Several methods have been developed to shorten the process by the integration of GPR and Global Positioning System (GPS) for data collection (Urbini et al., 2001 and Jol and Bristow, 2003). Appropriate processing of the data collected and the use of radar stratigraphy for sedimentological interpretation is recommended by Jol and Bristow (2003) and Neal (2004). The concept of radar stratigraphy is derived from principles employed in seismic stratigraphic analysis. It allows the delineation of radar surfaces, which bound radar packages that can, in turn, be interpreted as radar facies (Neal, 2004). This methodological approach yields a consistent interpretation of the data. Further discussion is presented in Chapter 3 – Section 3.4.6.

Numerous examples of research on glacial and postglacial sediments mapping and interpretation using GPR are available in the literature. Steinen et al. (2001) described the anatomy of a buried esker ridge, Bakker and van der Meer (2003) and Jakobsen and Overgaard (2002) revealed deformation structures within a push-moraine complex. Kostic et al. (2005) used a combination of borehole data, 3D GPR data and flowmeter data to characterise the sedimentology and hydraulic heterogeneities in deltaic sediments. Ayotte (1994) mapped the spatial distribution of glaciolacustrine sediments and depicted their underlying till and bedrock surfaces. Beres et al. (1999) characterized glaciofluvial sediments by the use of 3D and 2D georadar mapping and concluded that 3D mapping leads to a more accurate interpretation of the data. Bano et al. (2000) depicted water table level, stratigraphic facies and tectonic activity in the Rhine Basin. Dehls et al. (2000) studied the effect of postglacial neotectonic faulting on glacial sediments while Cassidy et al. (2003) characterized the architecture of jokulhlaup deposits. Leopold and Volkel (2003) tested 100 MHz and 200 MHz antennae for detection and 2D mapping of periglacial slope deposits overlain by peat, successful results were obtained with the 100 MHz, the 200 MHz antenna did not allow enough penetration for this type of survey. They estimated the velocity for peat as 0.042m/ns and of 0.06m/ns for slope deposits by using a CMP Survey. On the other hand, surveys carried out in Ireland by Trafford (2009) and Murphy and Clark (2009) for the detection of peat thickness on raised and blanket bog respectively, estimated velocity in peat between 0.035m/ns (for raised bog) and 0.037m/ns (for blanket bog).

GPR applied to geological studies has not yet been extensively used in Ireland though various geophysics companies have used the technology to locate underground services. Pringle et al. (2003) used this technique to depict channel architecture in Carboniferous turbiditic sediments, Caloca (2006) used GPR to identify and describe the sedimentological settings of glacial and postglacial deposits in part of the Midlands of Ireland. Gibson and George (2004, 2006) and Gibson (2007b,c) used a range of multidisciplinary geophysical surveys including GPR for the location of buried archaeological features in the Irish Midlands. The most recent research carried out in Ireland was presented in the EAGE Conference 2009 in Dublin. Trafford (2009) used GPR to record peat thickness in the Irish Midlands and produced a 3D peat thickness map.

Murphy and Clark (2009) tested the use of GPR to identify peat stability features in a peat slide; abandoned subsurface water conduits probably conditioning the peat failure were identified. Finally, Lombard (2009) recognised peat thickness and depth to bedrock using this technique.

Very Low Frequency (VLF) is an electromagnetic surveying technique that uses an external source of radiation (VLF Transmitter stations) provided by military installations, which broadcast within the frequency range of 15 – 30 KHz (Beamish, 2000). These frequencies are approximately 3 orders of magnitude less than those employed in GPR. The energy radiated by the transmitter induces eddy currents in conductive geological units or structures. The eddy currents produce a secondary magnetic field and the VLF receiver measures the primary and the secondary magnetic fields together and the distortion of the primary magnetic by the secondary. Steeply dipping features (e.g. faults) with strong conductivity contrasts with their surroundings which are orientated parallel to the direction of the transmitted pulse are most easily detected by this method as the strength of secondary magnetic field produced is large enough to be measured (Gibson and George, 2004). VLF is particularly effective at mapping electrical conductivity contrast between geological units. The depth of investigation ranges between 40-60 metres in high resistivity sediments to 4-5 metres on very conductive subsurface (Northwest Geophysical Associates, 2000).

VLF surveying is usually carried out by measuring collinear data points every 10 metres in lines parallel to the subsurface structures measured in the field (O'Connor, 2007 - personal communication). Beamish (2000) proposed that data should be collected with a high lateral density (1-5 metres) in order to infer the main elements of the subsurface resistivity distribution.

VLF has been rarely used in the Irish context, though discussions with geophysical companies indicate that it has been employed on occasions mainly for the detection of subsurface water. Gibson (1991) employed it to investigate the Tow Valley Fault system in Northern Ireland, George and Gibson (2000) and Gibson and George (2001) used VLF as a

secondary technique for the detection of groundwater sources in water bearing fractures in several sites in County Monaghan and in Maynooth, Co. Kildare. Moreover, Krahn (2009) used this technique to investigate the ground conditions on a proposed landfill site; a NW-SE trending structure was identified and interpreted as a dolerite dyke with the aid of other geophysical techniques.

2.5 – Summary

Two evolutionary models of glaciation and deglaciation for Ireland have been in debate during the last century. However, most recent research points to the Ice Dome Model proposed by Warren (1985) following Close's (1867) interpretation of drumlin distribution. This consists of a number of coalescing ice domes with well-defined ice centres shaping the whole of the Irish landscape during the last glaciation.

The distribution of sediments in Ireland has been mapped in the past by means of conventional mapping techniques including geomorphology, which can often link the morphological expression of a feature to its lithological composition, and sedimentology. However, the latter requires the existence of field exposures and in non-exposed regions, costly drilling programs or trenching is necessary to assess the composition and distribution of the subsurface sediments, as well as the depth to the solid bedrock. Geophysical techniques are an inexpensive, non-intrusive and fast data collection method for subsurface mapping. Their application to soft sediments and depth to bedrock mapping has been widely used from the 1900s, especially from the 1970s, when the introduction of computer based data collection methods greatly improved the quality of collected data.

The literature review has shown a shortage of reported geophysical investigations in the Irish context applied to sediments, as well as a high potential for the use of geophysical methods for the study of the subsurface.

A range of electrical resistivity techniques (2D, azimuthal and time-lapse resistivity) can be used to assess the electrical properties of the subsurface, which can be directly

correlated to variations in the subsurface lithological composition, moisture contents or mineral composition. Moreover, the use of electromagnetic methods, especially GPR, has been widely used for mapping the internal architecture of soft sediments in 2D along a profile and at a smaller scale in 3D. VLF has been used in the past for mapping of conductivity contrast between geological units. The combination of the three methods has significant potential for lithological and sedimentological characterisation of the subsurface, which could lessen the environmental impact and the cost of soft sediment mapping in regions where the subsurface is composed of low to medium conductivity materials.

CHAPTER 3

Research Methodological approach and theoretical concepts

3.1 – Introduction

A number of geophysical methods were tested to assess their applicability for the systematic mapping of glacial and postglacial sediments in the Irish Midlands. The differentiation of the lithology and the detection of the sedimentological settings within the subsurface by means of geophysical surveying can aid in the construction of an evolutionary model of glaciation and deglaciation for the research area. Conventional mapping techniques were used to map the Quaternary geology of the research area before geophysical surveying,

A number of steps are involved in conventional geological mapping techniques. The desk compilation phase consisted of gathering archival data and literature related to the study area and the analysis of the available satellite imagery and aerial photography. Later fieldwork focused on morphological mapping, site investigation, borehole drilling and sampling. This was followed by the description and analysis of field-collected samples. However, as mentioned previously, exposed sediments for data collection are rather sparse in the Irish Midlands and drilling and trenching are invasive and very expensive data collection methods. Geophysical techniques are non-invasive, fast and inexpensive data collection methods which can counteract these difficulties.

As reported in Chapter 2, Electrical Resistivity, Ground Penetrating Radar (GPR) and Electromagnetic Very Low Frequency (VLF) were the geophysical techniques used in this research. Electrical Resistivity methods have a common theoretical background; however, there are a number of modes of data collection and display that have been used for this thesis. Data can be collected and displayed as 1D, 2D or 3D models. Azimuthal resistivity consists of data collection at a single point at a number of depths and at various orientations. Electrical Resistivity Tomography (ERT) involves the collection of a vertical 2D grid of data points along a survey line on the surface that can subsequently be

interpolated and inverted to obtain a profile showing the electrical properties of the subsurface materials underlying the given survey line. A 2.5D representation of the electrical properties of the subsurface can be obtained by interpolating the data collected from ERT profiles at a regular distance and parallel to each other. Data collection, processing and interpretation methods for all of these are presented later in the Chapter.

GPR methodology has been greatly refined during the last two decades (Neal, 2004). An account of the theoretical background of the propagation of electromagnetic waves through the subsurface is presented. The different methods encountered in the literature review for collection, processing, interpretation and display of GPR data are presented and discussed in detail in order to recognize the most suitable methods to be used for the present research. The methodology is presented later in this chapter as a flow chart indicating the data collection, processing and interpretation methods generally followed for this thesis.

VLF has seldom been utilised in Ireland and has been mainly used for the identification of large geological structures. The correlation of VLF data with the data obtained from the other two (main) geophysical techniques employed during this thesis may clarify the potential of this technique for soft sediment and depth to bedrock mapping. It was employed on Site S1 (see Chapter 6). A short account of the theoretical background supporting this technique, as well as a brief description of the system and some of its applications for geological mapping are presented later. Furthermore, the methods utilised for data collection, processing and interpretation are explained in detail.

3.2 – Quaternary Geological Methods

3.2.1 - Introduction

The geological mapping techniques used for this study are described chronologically. Firstly, the desk compilation of literature in the study area and thematic and digital datasets relevant to the research, are presented. Secondly, the geological mapping techniques, which include, exposure description, sediment sampling and analysis, sedimentological analysis and classification, borehole logging and geomorphological mapping methods are

described in detail. Thirdly, data processing of borehole, rock outcrop and exposure data to obtain a depth to bedrock map for the area using geostatistical analysis is presented

The Quaternary Geology map produced from this research (see Map 1 enclosed with thesis) distinguishes between the following broad categories of deposits: diamicton, sand/gravel, peat, alluvium, lacustrine sediments, marl and made ground. Both sand/gravel and diamicton are further divided to show the dominant lithology type. The mapping program involved an extensive field-mapping component to check existing information and draw up the final boundaries. Additionally, sampling and drilling programme have been carried out.

3.2.2 – Desktop Compilation

The six-inch Bedrock Geology maps (Geological Survey of Ireland, 1871) show where rock outcropped at the surface at that time. Some of the maps indicate areas of bog and alluvium and it proved to be a valuable dataset in the preliminary identification of postglacial deposits. The maps also portray the location of gravel pits at that time. While many are now closed or filled in, they are indicative of where areas of gravel may lie.

A glacial and postglacial deposits map for the area in digital format (largely compiled from archival data and remote sensing) has been used as a starting point for the geological mapping exercise. Although, some of the data were found to be inaccurate at detailed scale, it provided valuable information as a first approach to identify the main geomorphological features and sediment distribution.

Data for the production of the depth to bedrock (DTB) map (see Map 2 enclosed with thesis) have been obtained from a number of sources: the Geological Survey of Ireland (GSI) digital rock outcrop maps, the borehole database within the same organization, consisting of well records, mineral prospecting borehole records and geotechnical investigations and results from the drilling program carried out for this thesis. In addition, data obtained from private surveys carried out in the research area in relation to mineral

prospecting, infrastructure such as the M6 road or gas pipeline and from Offaly County Council, percolation test were also used.

Esker boundaries were identified at a preliminary stage using data available for the surficial and postglacial deposits map for County Offaly (Warren and Hammond 1999) and from the one mile to six inches scale digital compilation from the Geological Survey of Ireland for County Westmeath. Both datasets were used as a foundation for the geological mapping and have subsequently been enhanced and corrected where necessary during the mapping program for this thesis.

A Digital Elevation Model at 10 metres spatial resolution and at metric altitudinal resolution combined with colour digital aerial photography from 2000 (1m spatial resolution), were supplied by the Ordnance Survey of Ireland and were used to obtain a 3D expression of the area in digital format and to identify and classify the main morphological features. Black and white aerial photography from 1965 was stereoscopically analysed to support the morphological analysis.

A Landsat 7 satellite image was used by Jordan (2002) for the differentiation of Quaternary landscapes in Western Ireland. Landsat 7 imagery for study area gathered on the 15th of June of 2001 was georeferenced to the Irish Grid and subsequently processed to obtain a 15m spatial resolution multi-band image. This dataset was used to identify main vegetation types in the area. Vegetation can sometimes be directly correlated to the underlying sediment type. Even though it has a relatively coarse spatial resolution compared to the aerial photography, the dataset was especially valuable at differentiating between glacial and postglacial deposits. The delineation of peat deposits was mainly obtained by means of satellite image analysis. Areas that would have been mapped as grassland when analysed using aerial photography were categorised as peat dominated when examined via the infrared bands of the Landsat imagery.

Finally, the Discovery Series Map sheet 48 of the Ordnance Survey of Ireland at 1:50,000 scale was used as a navigation tool during fieldwork and as a reference map when operating Geographical Information Systems (GIS).

3.2.3 – Quaternary Geological Mapping

The fieldwork for the geological mapping programme involved several methods, which are discussed below. The 600 Km² study area was divided into 15 fieldwork sheets, each at a scale of 1:20,000 and covering an area of 40 Km². The field sheets were derived from the combination of colour aerial photography at 1m spatial resolution (pixel size) and a hillshaded DEM at 20m spatial resolution. The final product was digitised using ArcGIS 8.3 software and has subsequently been edited down and is presented at a 1 to 40,000 scale.

Reconnaissance mapping involved thoroughly covering the field area, on foot and by car, and surveying all quarries, gravel pits, stream cuttings, drains, house foundations, trenches, or any other cutting into the subsurface originated by human or natural causes, of use in determining the nature of the underlying sediments. In some cases, it was possible to infer the sediment type from the geomorphology; e.g. eskers are composed of gravel, as are deltas; river floodplains are composed of alluvium; and in-filled lacustrine basins are usually made up of clay and or silt. In almost all cases, however, it was essential to find exposures where sedimentological analyses could be completed.

The broad genesis, complexity and limited exposure of the glacial tills, meant that it was virtually impossible to map according to matrix composition. The dominant clast type can, to a large extent, be used as a proxy for outline matrix composition, e.g. diamicton derived from sandstone bedrock will be likely to have a sandy matrix.

Eskers were the most studied feature during fieldwork. The relationship of the esker distribution to other sediment types has been taken into account. The esker bodies and exposures within them were systematically photographed and recorded. The eskers were classified into four main types following the classification of Warren and Ashley (1994).

Sedimentological classification. A standard classification has been used in order to identify and describe lithofacies types within exposures as well as their relationship to one another. The lithofacies coding scheme from Benn and Evans (1998) was used to classify sediments during exposure description (Figure 3.1).


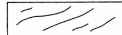
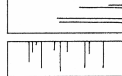
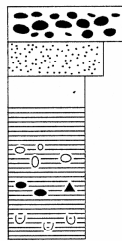
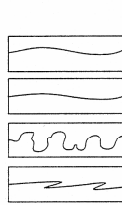
Code	Description	SYMBOLS		
<u>Diamictions</u>	Very poorly sorted admixture of wide grain size range			
Dmm	Matrix-supported, massive.		Diamict	
Dcm	Clast-supported, massive.			stratified
Dcs	Clast-supported, stratified.			sheared
Dms	Matrix-supported, stratified.			jointed
Dml	Matrix-supported, laminated.			
--- (c)	Evidence of current reworking.			
--- (r)	Evidence of resedimentation.			
--- (s)	Sheared.			
--- (p)	Includes clast pavement(s).			
<u>Boulders</u>	Particles > 256 mm (b-axis)			
Bms	Matrix-supported, massive.		Gravel	
Bmg	Matrix-supported, graded.		Sand	
Bcm	Clast-supported, massive.		Fines	
Bcg	Clast-supported, graded.		Laminations	
Bfo	Deltaic foresets.		with interclasts	
BL	Boulder lag or pavement.		with dropstones	
			with loading structures	
<u>Gravels</u>	Particles of 8–256 mm			
Gms	Matrix-supported, massive.			Contacts
Gm	Clast-supported, massive.			Erosional
Gsi	Matrix-supported, imbricated.	Conformable		
Gmi	Clast-supported, massive (imbricated).	Loaded		
Gfo	Deltaic foresets.	Interbedded		
Gh	Horizontally bedded.			
Gt	Trough cross-bedded.			
Gp	Planar cross-bedded.			
Gfu	Upward-fining (normal grading).			
Gcu	Upward-coarsening (inverse grading).			
Go	Openwork gravels.			
Gd	Deformed bedding.			
Glg	Palimpsest (marine) or bedload lag.			
<u>Granules</u>	Particles of 2–8 mm			
GRcl	Massive with clay laminae.	Sfl	Flasar bedded	
GRch	Massive and infilling channels.	Se	Erosional scours with intraclasts and crudely cross-bedded.	
GRh	Horizontally bedded.	Su	Fine to coarse with broad shallow scours and cross-stratification.	
GRm	Massive and homogeneous.	Sm	Massive.	
GRmb	Massive and pseudo-bedded.	Sc	Steeply dipping planar cross-bedding (non-deltaic foresets).	
GRmc	Massive with isolated outside clasts.	Sd	Deformed bedding.	
GRmi	Massive with isolated, imbricated clasts.	Suc	Upward-coarsening.	
GRmp	Massive with pebble stringers.	Suf	Upward-fining.	
GRo	Open-work structure.	Srg	Graded cross-laminations.	
GRruc	Repeating upward-coarsening cycles.	SB	Bouma sequence.	
GRruf	Repeating upward-fining cycles.	Scps	Cyclopsams.	
GRt	Trough cross-bedded.	--- (d)	With dropstones.	
GRcu	Upward coarsening.	--- (w)	With dewatering structures.	
GRfu	Upward fining.			
GRp	Cross-bedded.			
GRfo	Deltaic foresets.			
<u>Sands</u>	Particles of 0.063–2 mm			
St	Medium to very coarse and trough cross-bedded.	<u>Silts & Clays</u>	Particles of <0.063 mm	
Sp	Medium to very coarse and planar cross-bedded.	Fl	Fine lamination often with minor fine sand and very small ripples.	
Sr(A)	Ripple cross-laminated (type A).	Flv	Fine lamination with rhythmites or varves.	
Sr(B)	Ripple cross-laminated (type B).	Fm	Massive.	
Sr(S)	Ripple cross-laminated (type S).	Frg	Graded and climbing ripple cross-laminations.	
Scr	Climbing ripples.	Fcpl	Cyclopels.	
Ssr	Starved ripples.	Fp	Intraclast or lens.	
Sh	Very fine to very coarse and horizontally/plane bedded or low angle cross-laminated.	--- (d)	With dropstones.	
Sl	Horizontal and draped lamination.	--- (w)	With dewatering structures.	
Sfo	Deltaic foresets.			

Figure 3.1 – Lithofacies coding scheme from Ben and Evans (1998).

The following parameters have been recorded for each individual bed during fieldwork:

- Type of contact: conformal, erosive, etc.
- Consolidation: 1(very poorly) to 5(extremely consolidated)
- Sorting: 1(very poorly) to 5(very well-sorted)
- Lenses: presence, shape and dimensions.
- Structures: collapse features, lamination, pebble imbrication, etc.
- Matrix: percentage, size and colour.
- Clasts: Size and petrology.
- Erratics: presence, type, size.

Exposure description is based on the parameters shown in Table 3.1. The grid coordinates for every exposure described during fieldwork were recorded using a Global Positioning System (GPS) Garmin GPS72 that attains horizontal and vertical metric precision. These data were input into a spatial database for subsequent analysis and presentation by means of a Geographical Information System (GIS).

Type	Condition and Age	Face Steepness	Topography	Vegetation
Ditch	Good- Recent	Horizontal	Hill side	Crops
Gravel Pit	Poor - Recent	Gentle	Hill top	Forests
River cut	Good- Old	Steep	Moundy	Grass
Road cut	Poor - Old	Vertical	Ridge	Rushes
Trench	Very poor – Old	Overhanging	Valley	Marshes
Trial Pit	Very poor –Recent		Flat	Shrubs
			Etc.	Etc.

Drainage	Dominant Petrology	Field Interepretation	Presence of
Very good	Limestone	Moraine	Iron Pan
Good	Sandstone	Esker ridge	Calcrete
Medium	Shale	Delta	Seepage
Poor	Acid Volcanic Rocks	Kame mound	Organic matter
Very poor	Etc.	Etc.	Etc.

Table 3.1 - Parameters recorded during fieldwork for exposure description.

The data, systematically collected during fieldwork for every exposure and for every individual bed on some occasions (dominant petrology), have been valuable when describing sediment types and interpreting their depositional environments.

Sediment Sampling and Analysis has been carried out throughout the field mapping programme. Petrography analysis has been undertaken by the author on clasts retained in the 5-10 mm size range to determine the dominant petrology (stone type) within the sample. This was a necessary exercise for the thematic subdivision of diamictons and glaciofluvial sediments into petrologically differentiated zones. In some occasions stone counts have been performed in the field to ascertain preliminary till dominant petrology.

Samples were gathered from exposure faces and from boreholes. Most of these were collected from till deposits. They were also taken from glaciofluvial, glaciolacustrine and alluvial deposits when considered relevant. Exposures were sampled behind the vertical surface of the face, below the weathering profiles of postglacial times and at least 1 metre above bedrock. The sample size obtained was at least of 5 Kg, the minimum sample size recommended by the BS5930:1999 for laboratory test purposes for a maximum grain size of fine to medium gravel.

Samples were gathered at depth from the drilled boreholes. Drilling was carried out in areas with little or no depth to bedrock information or where sediment (petrological and/or lithological) composition was not certain. Although the information on sedimentary structures and architecture is particularly limited, the lateral extent of buried lithofacies can often be determined from borehole data (Evans and Benn, 2004). The drilling system used for this survey was the continuous flight auger drilling method. The debris from drilling only gives a very coarse indication of the levels and character of the strata (BS 5930:1999). A sample was collected when a change in the sediment type was observed. In the majority of cases, the boreholes ended before bedrock was reached. Samples were retained from all the boreholes. A total of 70 boreholes were drilled, 57 to support the Quaternary Geology

mapping exercise and 13 to assist in the interpretation of geophysical data. Logs produced for the boreholes are recorded in hardcopy and digital format.

The samples collected during field mapping were subsequently described by the author in the laboratory using the following parameters: matrix colour (based in the Munsell soil colour chart, 2000), lithology, petrology, clast size and clast shape. This preliminary analysis was used as the baseline to make a decision on the samples to be sent for Particle Size Distribution Analysis (PSA). In all, 129 samples were selected for PSA. PSA was carried out by Metlab International Ltd. at the minimum standards accepted by the BS EN ISO 22476-2:2005 (2006). Hydrometer analysis was performed on 53 samples where fine grain size was the dominant lithology. The data collected from particle size analysis were plotted on cumulative logarithmic graphs to illustrate the grain size distribution, most sediments exhibit a characteristic skew on their particle size distribution so data shown on a logarithmic scale produce a normal distribution in the ideal case of a log-normally distributed population (Evans and Benn, 2004). The samples were classified under the Folk's (1954) classification scheme using Sedclass software (Poppe et al., 2003).

The 5 to 10 mm clast size has been used by the Geological Survey of Ireland (GSI) for the last few decades for petrography analysis. Brigland (1986) suggests that the use of a consistent size range is necessary to allow comparisons between sample sets. Therefore, 5 to 10 mm clasts from each sample were retained for this thesis to carry out petrography analysis on 100 pebbles. A total of 33 samples were analysed using a hand lens and a reflected light binocular microscope when larger magnification was necessary to recognize the dominant petrology and possible erratic carriage within each sample. Although in most cases, the clast assemblage is controlled by the provenance of the sediment, lithologies less resistant to mechanical and chemical weathering may be underrepresented in the sample (Evans and Benn, 2004), e.g. limestone clasts are more resistant to mechanical weathering than the basic igneous rocks occurring in the area. Petrographic analysis results are presented in Chapter 4 (Figure 4.7). The results are summarized as percentages; hence the

spatial distribution of the dominant lithology and erratic carriage within each sample can be evaluated.

3.2.4 – Morphological Mapping

A detailed morphological analysis of the area has been undertaken with the aim of identifying features such as possible esker and morainic ridges, meltwater channels, kame and kettle topography, fluvial and glaciofluvial terraces. A 10 metre spatial resolution Digital Elevation Model (DEM) with 1 metre altitudinal resolution has been chiefly used. A 20 metres spatial resolution DEM with 1m height resolution was utilized in areas where the 10m resolution dataset was not available. These datasets were hillshaded or sun-illuminated. Colour and black and white digital aerial photography were overlaid on the hillshaded DEM to produce a 3D model to be subsequently analysed using ArcGIS software. Black and white aerial photography from 1965 in hard copy was stereoscopically analysed in places to support and extend the geomorphological dataset. The integration of both methods was a time-consuming process, but helped in creating an overall picture of the distribution of morphological features and at defining morphological units. The landforms, added to the geology, help in the reconstruction of the glacial and deglacial pattern in the area, which provides a better understanding of the stratigraphy and sedimentology of the deposits. Furthermore, breaks in slope estimated from the DEM have been used to identify boundaries between different deposits, as morphological delineations often relate to lithological boundaries.

Fieldwork, focussing on geomorphological mapping was carried out after the aerial photographic analysis. Geomorphological features were depicted and classified by means of 3D digital analysis of the landscape; fieldwork was mainly directed towards the recognition of the features previously classified and to reclassification when necessary. Over 250 sites were visited during the geomorphological mapping process. Approximately 20% of the features had to be reclassified following this fieldwork exercise. The height of the features recorded during fieldwork was calculated by the use of an abney level. Width, length and orientation of macro-scale features were measured by means of digital image

analysis using Geographical information Systems and dimensions of mesoscale and microscale features were measured in the field with measuring tape and a millimetric scale ruler respectively. The orientation of the features was measured with a Silva compass and their location determined using a Garmin GPS 72 Global Positioning System.

3.2.5 – Depth to Bedrock (DTB)

The depth to bedrock map was the result of the compilation of several available datasets (Table 3.2). Datasets or individual data that presented inconsistencies were discarded for this exercise. The data were input into a single database with the following attributes: grid coordinates depth to bedrock, elevation and bedrock elevation. In areas where no data were available, DTB estimations were made on the basis of morphological analysis (i.e. knowledge of an esker ridge height and morphology facilitates assigning a minimum DTB value within the ridge area), fieldwork experience and the mapped sediment type.

Dataset type	Source	Bedrock met	Bedrock not met
Borehole	Geotechnical database	502	529
Borehole	Quaternary Drilling program	10	161
Borehole/Trenching	Offaly CoCo	6	1,032
Borehole	Private Geotechnical companies	143	284
Exposures	Quaternary Mapping	5	0
Rock outcrop map	Bedrock Section	376	0
Rock close to the surface	Quaternary Section	4,195	0
Geophysics	This thesis and Smyth (1994)	166	0
Estimates of DTB	This thesis	9,006	n/a
TOTAL		14,409	2,006

Table 3.2 - Datasets used for production of DTB map. Data points used for interpolation is under Bedrock met. Bedrock not met data were used for Quality Control of the final dataset.

Rock outcrops mapped from the bedrock section of the GSI and rock close to the surface delimited during the mapping program were classified as areas where DTB was less than 1 metre. The data were originally available as polygons but these were converted to point data at 60m spacing in order to have all the datasets in the same format. Points within rock

outcrops were sampled with a DTB of 0.3m and points within rock close to the surface were assigned values of 1m.

Geostatistical analysis was employed to process the point data available and to produce the DTB Map. This was the result of a geostatistical exercise using the ArcGIS Kriging interpolation method. Rock elevation data points were used for the geostatistical analysis exercise and these were derived by subtracting DTB values for each borehole from the 20m resolution DEM. Rock elevation data avoid the interference of the sediment morphological expression during the interpolation exercise in the setting presented in the Irish Midlands (Clark, 2004), where topography is fairly subdued at a regional scale. The distribution of the data in a histogram of the two datasets (Figure 3.2) shows how DTB data are particularly skewed compared to the Rock Elevation data. Interpolation using the kriging method is recommended when using normally distributed data (Clark, 2004 – Personal Communication).

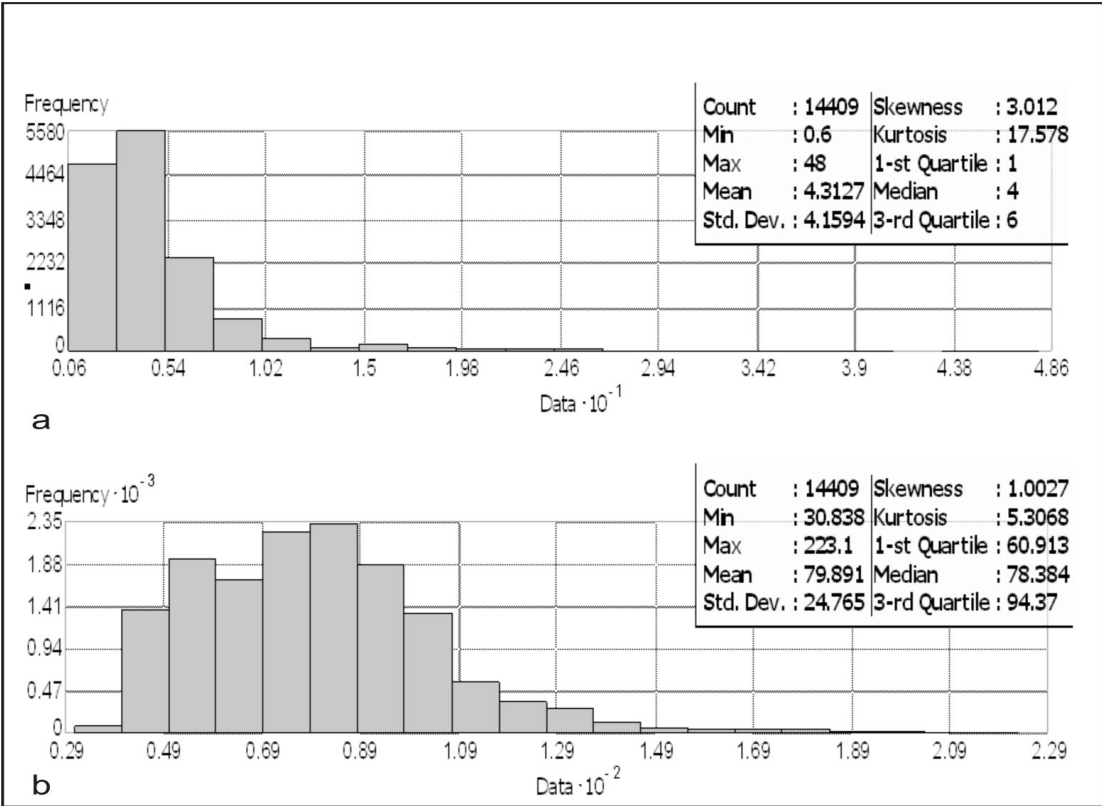


Figure 3.2 – (a) distribution of DTB data, the histogram is right skewed. (b) Distribution of the Rock Elevation data shows a histogram normally distributed slightly right skewed.

Therefore, the Rock elevation map was calculated using the kriging interpolation method, the map obtained was subsequently subtracted from the DEM and a DTB map was obtained. The dataset was edited manually where inconsistencies within it could not be solved by means of geostatistical analysis (e.g. DTB within areas of known bedrock outcrop were on occasions estimated as negative because of the DEM resolution and accuracy). The Depth to Bedrock Map is enclosed as Map 2. The results of this study are further discussed in Chapter 4.

3.3 – Electrical Resistivity

3.3.1 – Introduction

Electrical resistivity methods detect variations in the electrical properties of a body, which can be linked to its physical properties. When a low frequency alternating current is transmitted into the ground, the current flow affects the potentials in the earth (Koefoed, 1979). Two electrodes are used for the transmission of electrical energy into the earth (source and sink electrodes) and two others to measure the potential distribution (potential electrodes). The apparent resistivity is computed from the magnitude of the current, the potential difference and the distance between the electrodes. In a homogenous subsurface, the apparent resistivity would correspond to the true resistivity; however, in a heterogeneous environment it is the average of the subsurface materials through which current flows.

A number of methodologies for data collection, processing and presentation have been employed for this thesis. The following section describes in detail the theoretical concepts and methods related to electrical resistivity data collection, processing and interpretation, focussing on the electrical resistivity tomography (ERT). This is followed by a section describing the data collection techniques, processing and display of 3D models. Furthermore, time-lapse resistivity, consisting of collection of a dataset for the same location at several time periods, is described in detail. Finally, a data collection method named azimuthal resistivity, which consists of data collection for different orientations with several electrode spacings, is presented and discussed.

3.3.2 – Theoretical Concepts

If a potential difference, measured in volts (V) is applied across a body, then a current measurement in Amperes (A) will flow in the circuit. Increasing the voltage results in an increased current and they are related thus:

$$V = RI \qquad \text{equation (3.1)}$$

This is known as Ohm's Law, where R, the resistance measured in Ohms, is the constant of proportionality. R is proportional to L, the length of a wire and inversely proportional to A, its cross-sectional area. Thus:

$$R \propto \frac{L}{A} \qquad \text{equation (3.2)}$$

or

$$\rho = R \frac{A}{L} \qquad \text{equation (3.3)}$$

where ρ is the resistivity.

The resistivity of a substance is an intrinsic characteristic, like its density, however, unlike density; the resistivity can vary over many orders of magnitude, Figure 3.3.

Electrical conduction will occur via fluids within the rock, except for clay and metallic ores. Resistivity of materials varies from $10^{-2} \Omega \text{ m}$ for graphite to $10^{16} \Omega \text{ m}$ for pure sulphur (Reynolds, 1997). Disagreements arise in the literature on the resistivity ranges for the same geological materials from several authors reviewed (Reynolds 1997, Bernstone et al., 2000 and Guerin et al., 2004). A compromise from the information gathered is presented in Figure 3.3.

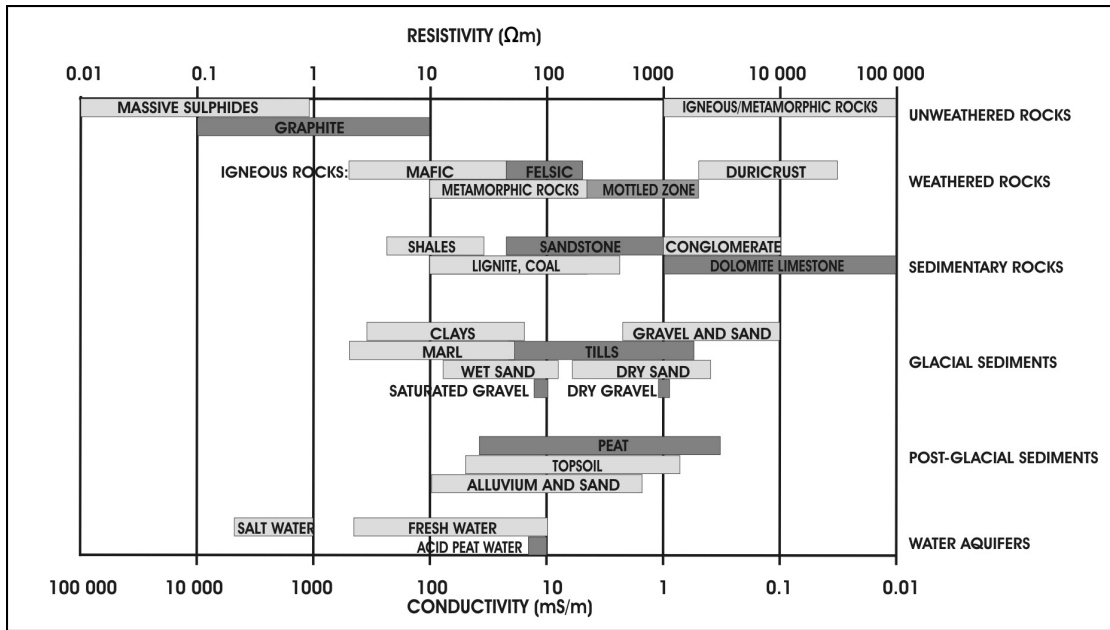


Figure 3.3 – Resistivity range of some geological materials, modified from Palacky (1987) with data from Reynolds (1997), Pozdnyakova (2002) and Gerin et al. (2004).

It has to be noted that values can be extremely variable depending on the effective porosity and the degree of saturation of the sediment. Resistivity values for unconsolidated sediments vary greatly depending on their moisture content, i.e. water saturated gravel have resistivity values of around $100\Omega\text{m}$, whereas dry gravel resistivity values are around $1400\Omega\text{m}$ (Reynolds, 1997). Poorly-sorted sediments such as till can range from $80\Omega\text{m}$ to $2000\Omega\text{m}$ (Palacky, 1987). This variation depends on the dominant lithology and its moisture content, stony till will usually yield very high resistivity values, whereas saturated clayey till will have low resistivity values. Mapping the subsurface resistivity variations obtained during an electrical survey provides information on the variations in the subsurface geology.

As mentioned above, when conducting a survey, four electrodes are employed in practice, two current electrodes and two potential electrodes. Electrical current is injected into the ground at C1 (source) and removed at C2 (the sink electrode) and the potential difference is measured between the two potential electrodes, P1 and P2. It is not possible to simply measure the potential difference between the current electrodes because of the high contact resistances between the ground and the electrodes.

When the current enters the ground, it radiates outwards and for a theoretical homogeneous medium, it can be shown for the source and sink electrodes that the potential at any point is given by

$$V = \rho \frac{I}{2\pi r_1} - \rho \frac{I}{2\pi r_2} \quad \text{equation (3.4)}$$

where r_1 , the distance from the source electrode and r_2 , the distance from the sink (Gibson and George, 2004). The potential difference between P1 and P2 electrodes (ΔV) is measured in reality and re-arranging equation 3.4 gives

$$\rho = \frac{2\pi \Delta V}{I} \left[\frac{1}{\frac{1}{r_1} - \frac{1}{r_2} - \frac{1}{r_3} + \frac{1}{r_4}} \right] \quad \text{equation (3.5)}$$

Where $r_1 - r_4$ are as shown in Figure 3.4. Thus measuring the distances and ΔV and using a known current, the resistivity can be obtained. Equation 3.5 can be rewritten thus:

$$\rho_a = K \frac{\Delta V}{I} \quad \text{equation (3.6)}$$

where K is known as the geometric factor.

$$K = 2\pi \left[\frac{1}{\frac{1}{r_1} - \frac{1}{r_2} - \frac{1}{r_3} + \frac{1}{r_4}} \right]$$

However, in the field, the subsurface is not homogenous and the electrical current will have passed through sediments with different resistivities but only one value of resistivity

is recorded. Thus what is recorded in the field is not the true resistivity (ρ) but the apparent resistivity (ρ_a).

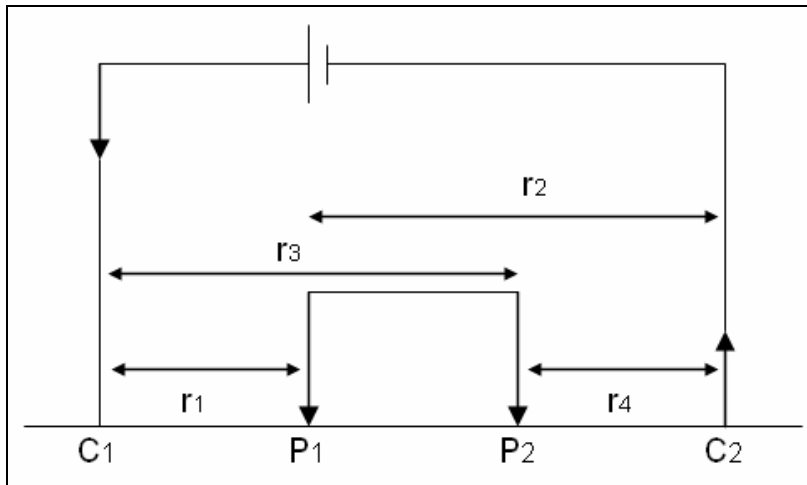


Figure 3.4 - Generalised array of electrode configuration for resistivity survey from Gibson and George (2004).

Electrode arrays

In order to determine the apparent resistivity, the geometric factor has to be obtained and this involves measuring 4 distances ($r_1 - r_4$) for every measurement. Such an approach would greatly increase the time need for surveys and consequently a number of standard electrode configurations have been developed, for which the geometric factors have been calculated. The most commonly used ones are the Wenner, Schlumberger (named after their creators) and the Dipole-Dipole array (Figure 3.5). There are other less commonly employed electrode configurations (pole-pole, pole-dipole) that will not be discussed in this thesis.

The Wenner array consists of four electrodes with equal distance 'a' between them. It is possible to have 3 variations of this array. The most commonly used one, is that shown in Figure 3.5 where the potential electrodes are located between the current electrodes (C1 P1 P2 C2). This is the Wenner alpha array (and is generally just called the Wenner array). The Wenner beta array is C1 C2 P1 P2 and the Wenner gamma is C1 P1 C2 P2.

The geometric factor for the Wenner array can be determined from equation 3.6 where $r_1 = r_4 = a$ and $r_2 = r_3 = 2a$.

Substituting yields a geometric factor

$$K = 2\pi \left[\frac{1}{\frac{1}{a} - \frac{1}{2a} - \frac{1}{2a} + \frac{1}{a}} \right]$$

Which reduces to $2\pi a$, thus the apparent resistivity for the Wenner array is

$$\rho_a = 2\pi a \left[\frac{\Delta V}{I} \right] \quad \text{equation (3.7)}$$

For the Schlumberger array, the potential electrodes are again between the current ones but the distance between them is much less, typically 'n', the distance from C1-P1 is 6 times the P1-P2 distance. The apparent resistivity for this array is

$$\rho_a = 2\pi a n(n+1) \left[\frac{\Delta V}{I} \right] \quad \text{equation (3.8)}$$

and for the Dipole-Dipole

$$\rho_a = 2\pi a n(n+1)(n+2) \left[\frac{\Delta V}{I} \right] \quad \text{equation (3.9)}$$

In order to obtain resistivity data with, for example the Wenner array, one could simply take a single reading, (with ‘a’ electrode spacing) then move the array on a short distance, take another reading and repeat to obtain data at fixed points along a line. If the process is repeated for the same line but with an electrode spacing of ‘2a’ then a greater depth of the subsurface is analysed as the depth of penetration increases with electrode spacing. Such an approach would be very time consuming and a multi-electrode recording system was introduced by Barker (1981), which speeded up electrical resistivity surveying.

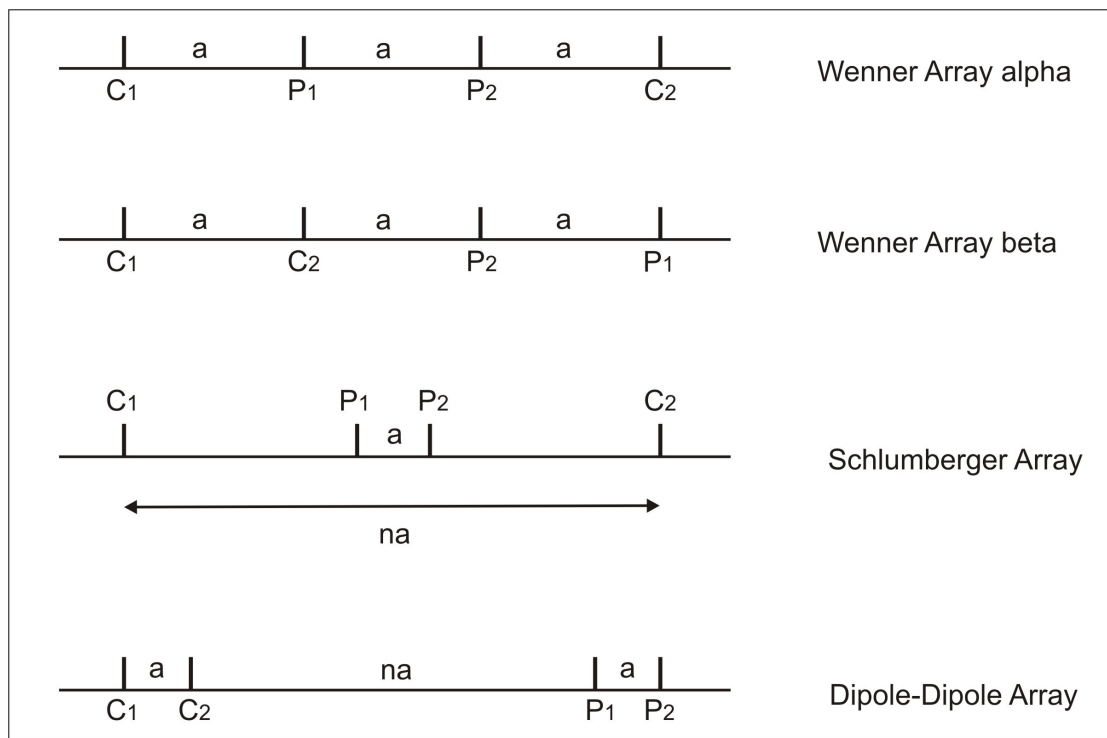


Figure 3.5 – Resistivity electrode configurations.

3.3.3 – Electrical Resistivity Tomography (ERT)

The ERT method consists of a number of electrodes that are inserted into the ground at equal spaced intervals. Two different electrical resistivity meters have been used for the thesis. Most of the field data have been collected with a Campus Geopulse resistivity meter, which has 25 electrodes (Figure 3.6a). A more advanced Geopulse Tigre resistivity meter with 32 electrodes became available in 2008 (Figure 3.6b) and has been used to

collect data for the electrode configuration test, described later within this section and for Sites S13 to S16.

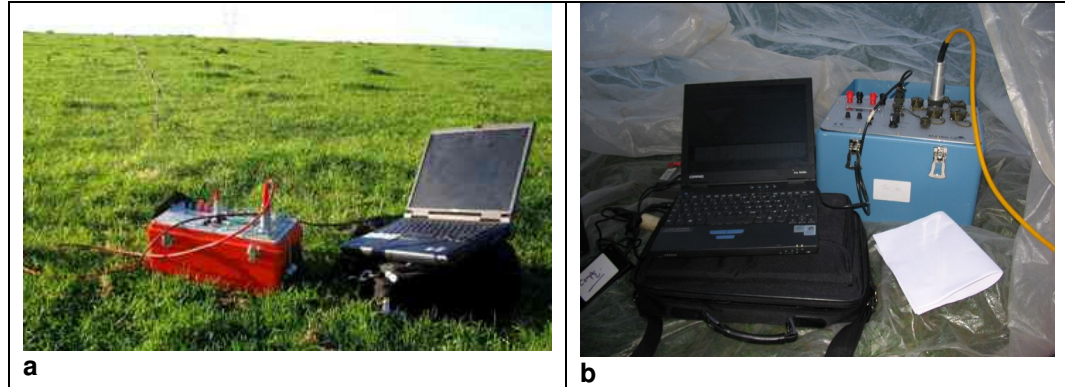


Figure 3.6 – (a) Electrical resistivity meter Campus Geopulse. (b) Electrical resistivity meter Geopulse Tigre.

The cable is connected to each electrode and to the resistivity meter, which is connected to a computer, Figure 3.7. A parameter file was created and loaded into the computer which specifies, the number of repeat readings taken (N), the current (mA) to be used, electricity transmission time length (On), time between readings (Off), which four electrodes are to be used and which are to be current and which potential, see below.

N	C(mA)	On	Off	C1	P1	P2	C2
5	2.0	1.0	0.5	1	2	3	4
5	2.0	1.0	0.5	2	3	4	5
5	2.0	1.0	0.5	3	4	5	6

The readings are taken one at a time starting with the minimum electrode spacing, (which will give information on shallow depths) until all the electrodes have been employed. On the next recording level, electrode spacing is increased, therefore a deeper part of the subsurface is imaged, but fewer readings can be recorded, see Figure 3.7. The survey continues until the maximum electrode spacing is reached. Data collected in this format are conventionally plotted as a pseudosection in which the horizontal position is the mid point

for the particular set of four electrodes being used and the vertical position is the median depth of investigation for the particular array being employed (Barker, 1989). The median depth (or pseudodepth) is the level at which 50% of the recorded signal is obtained from above and below that level.

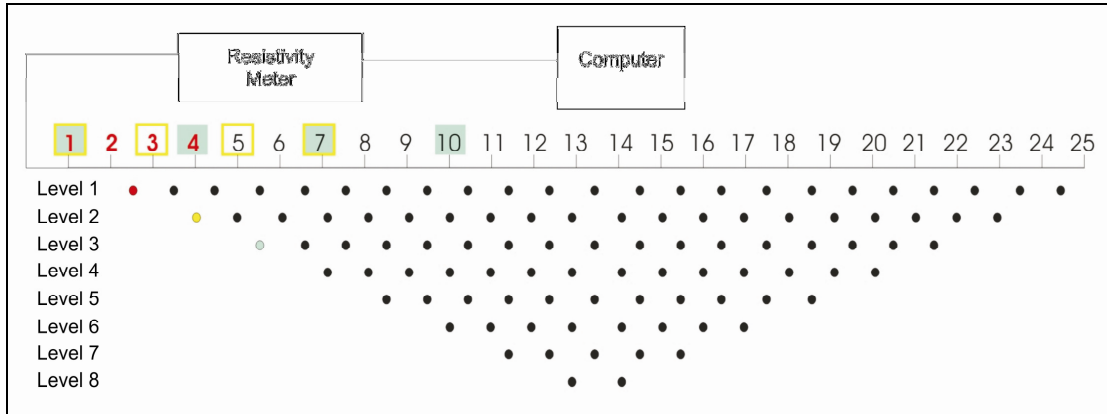


Figure 3.7 – Electrode deployment to construct a 2D electrical resistivity pseudosection using the Wenner electrode configuration. Red point recorded by electrodes in red, yellow point recorded by electrodes outlined in yellow etc.

An important point to consider when undertaking a resistivity survey is which of the various available array types should be employed and what are the differences between them. These questions are best answered by considering the sensitivity functions of the different arrays which can be obtained from the Fréchet derivative for a homogeneous half-space (McGillivray and Oldenburg, 1990). The sensitivity functions for the Wenner, Schlumberger and Dipole-Dipole arrays are shown in a standardised graphical format in Figure 3.8. For each array, the most ‘sensitive’ parts are shown in blue or red, and these are the regions where the subsurface has the greatest effect on the measure apparent resistivity. The Wenner array has horizontal contours (and high sensitivity) under the centre of the array, thus it is good at resolving vertical changes (horizontal layers) but poor at resolving vertical features. Note the high negative sensitivities at C1-P1 and C2-P2, this means a feature with lower true resistivity in this area than the background would yield a higher apparent resistivity reading. Noise does not affect this array much and the median depth of investigation is 0.519 times the electrode spacing. The Schlumberger array has a slightly different sensitivity function depending on the ‘n’ level used (for ‘n’ = 1 it is the same as the Wenner array). This array is sensitive to both horizontal variations when ‘n’ is low and

to vertical features when 'n' is high (Loke, 2001). Additionally, the horizontal coverage for each recorded level is greater for the Schlumberger array and the median depths of investigation is about 10% greater, thus more information can be obtained from deeper levels.

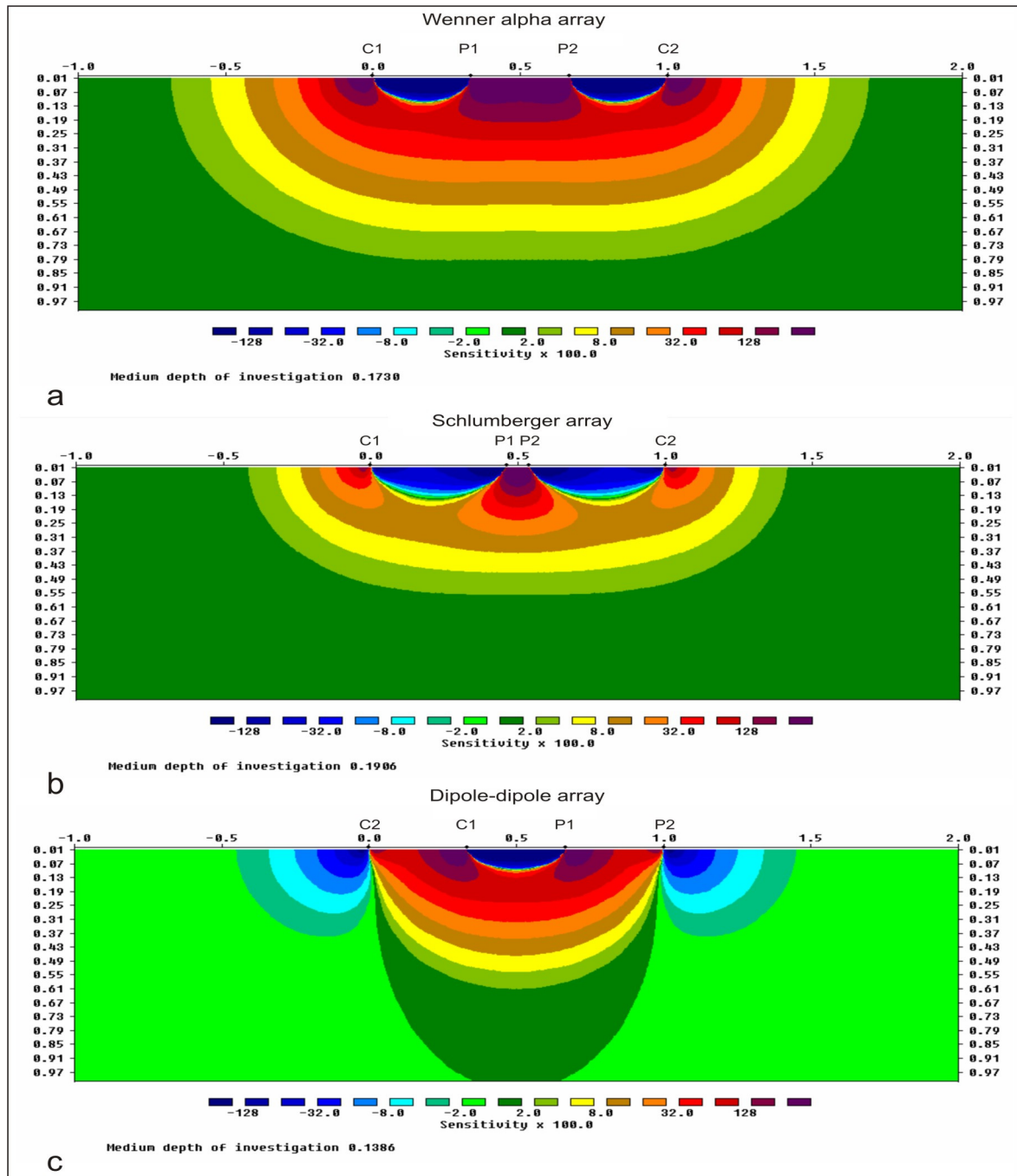


Figure 3.8 – Sensitivity functions for the (a)Wenner, (b)Schlumberger and (c)Dipole-Dipole arrays. Derived from RES2DMOD Software.

The sensitivity function for the Dipole-Dipole array also varies with the ‘n’ value but it clearly has a different pattern to those of the Wenner and Schlumberger arrays. The greatest sensitivities are below C1-C2 and P1-P2 and this array is mostly used for the investigation of vertical features (e.g. detection of cavities with vertical walls, periglacial wedge casts etc). The resolution in a vertical direction would be rather poor compared to the Wenner or the Schlumberger arrays, thus it would not be recommended for detecting horizontal features. Also, the median depth of investigation is the lowest of the three arrays and it is very sensitive to noise, especially at high ‘n’ values, though it does have a good horizontal coverage. Moreover, glacial and postglacial sediments are generally characterised by horizontal, subhorizontal or oblique contacts, vertical contacts are rarely expected in this kind of sediments. The use of an array with high vertical resolution is more appropriate for this thesis.

In the light of these characteristics, a combined Wenner-Schlumberger array was used in the collection of the resistivity data as it was felt that such an array would image the subsurface more accurately. With 25 electrodes it is only possible to obtain 92 readings using the Wenner array. The parameter file for the Wenner-Schlumberger array used in this research allowed 157 readings to be obtained (70% more than for the Wenner) using a range of overlapping ‘n’ values, mostly 1-7. This approach provided more data, especially at deeper levels which helped constrain the models produced. Assuming an electrode configuration of 25 electrodes at 5m, the length of the line is 120m (first electrode at 0) and the depth of investigation is about 22m and the area covered is more than 1500 m². An example of the measured apparent resistivity pseudosection is presented in Figure 3.9.

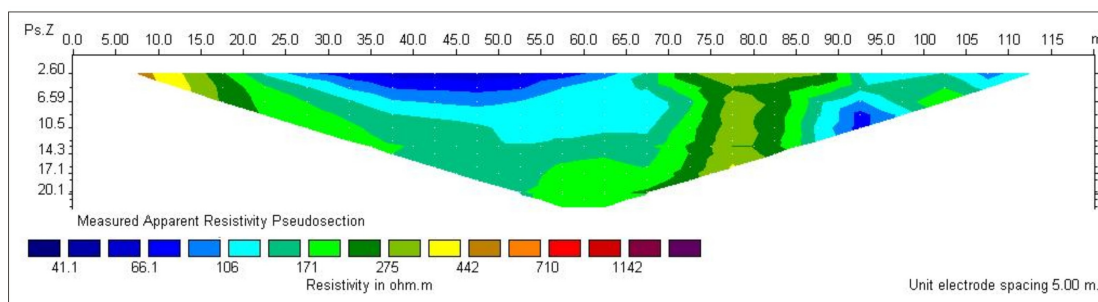


Figure 3.9 – Sample of a 5m electrode spacing measured apparent resistivity pseudosection using the Wenner-Schlumberger array.

The pseudosection is useful in that it gives some information on the nature of the subsurface, however, it should be realised that the values measured are those of apparent resistivity, the depths are only pseudodepths and the image is not a true reflection of the nature of the subsurface. To determine true resistivity and true depth it is necessary to model the data using an inversion program.

RES2DINV Inversion modelling program

RES2DINV is an inversion modelling program which allows the variation of true resistivity with depth to be obtained using the apparent resistivity values that have been measured in the field. The program is based on the smoothness constrained least squares method of deGroot-Hedlin and Constable (1990) which solves the partial derivatives of the Jacobian matrix. The process is speeded up using a quasi-Newton optimisation approach (Loke and Barker, 1995, 1996). A number of steps are involved in the procedure.

- The subsurface is divided into a number of rectangular cells, the deepest of which extends to the median depth of investigation for the maximum electrode spacing employed in the survey, Figure 3.10. The number of blocks do not exceed the number of data points and the blocks increase in thickness with depth (usually by 10%), as the resolution decreases with depth.
- Each block is initially assigned a single resistivity value. For the initial model, a homogeneous earth model is assumed based on the measured apparent resistivity values.
- The apparent resistivity distribution that this model would produce is **calculated**, based on the array type and sensitivity functions discussed earlier and compared with the **measured** apparent resistivity values and the RMS error between them is calculated. The resistivity values of the cells are then iteratively altered, in order to reduce the RMS error between the measured and calculated apparent resistivities. In order to prevent a continual loop, a minimum change between iterations (usually 5%) is set. The process is generally complete after about 6 interactions.

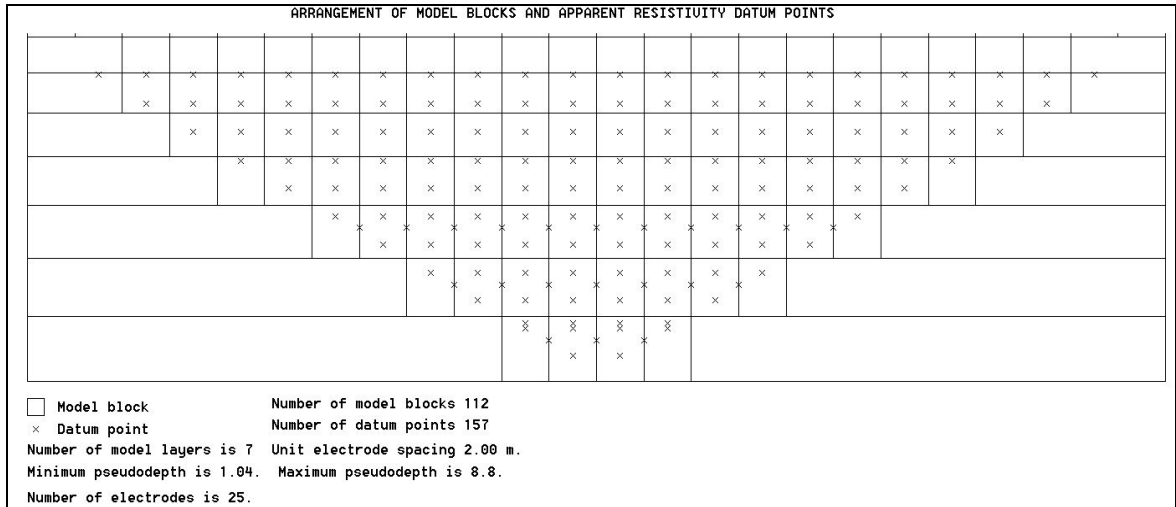


Figure 3.10 – Model block used for inverse modelling. Some blocks contain two apparent resistivity readings. Size of blocks increases in depth by 10% to compensate for the decrease in resolution.

An inverse model of the apparent resistivity pseudosection is finally obtained (Figure 3.11), together with the measured and the calculated apparent resistivity. The inverse model presented in Figure 3.11 shows two areas with high resistivity values, of up to $1300\Omega\text{m}$, from 5 - 15m and 75 - 85m probably related to sand and gravel. On the other hand, a low resistivity area ($30 - 70\Omega\text{m}$), related to saturated fine sediments occurs on the surface from 20 - 65m.

The settings employed within RES2DINV were the same for nearly all the sections recorded, thus the final results were kept consistent. Software was set on finest mesh refinement to enhance accuracy of calculated apparent resistivity values (Loke, 2004) and a total of 6 iterations were calculated. The least-square inversion method with a robust constraint is recommended for datasets with sharp boundaries (Loke, 2004) and was used for inversion of the recorded apparent resistivity. Higher errors were obtained when the logarithm of apparent resistivity was used as the data parameter to carry out the inversion, although Loke (2004) recommends it. It was ultimately decided to use the apparent resistivity values to perform the inversion. Finally, a model with the thickness of the layers increasing by 10% was picked. These settings were only altered for profiles that had high standard errors; the smoothness standard constraint was used in such situations.

If there were significant variations in topography, then a distorted finite-element grid with uniform distortion was used to create the topographic model (Loke, 2004). The

topographic values were obtained from the Ordnance Survey of Ireland 10m pixel size Digital Elevation Model (DEM). Topography was incorporated into the final results where necessary.

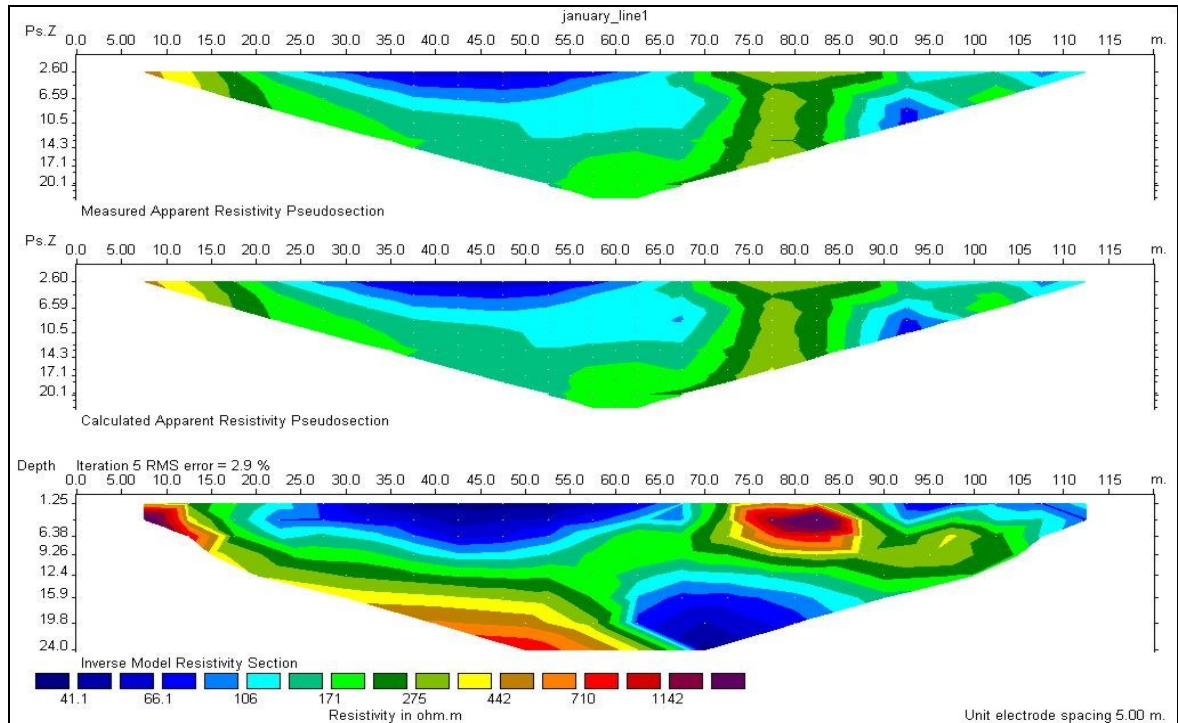


Figure 3.11 – RES2DINV produces an inverse resistivity model from the measured apparent resistivity pseudosection. A calculated apparent resistivity pseudosection is generated from the inverse model. The error obtained (2.9%) is the difference between the measured and the calculated pseudosections.

Electrode Configuration test

Several arrays were assessed in a test profile named RS1-L04-5m. The aim was to compare the resulting measured apparent resistivity and the derived inverse model resistivity section for different electrode configurations. The profile was recorded using the Geopulse Tigre resistivity meter with 32 electrodes at 5m spacing. The four profiles were recorded during the same day, within a time range of five hours. The line is located in Site S1 (see Map 1) where a number of sediments had been previously mapped (esker gravel, lacustrine clays, subaqueous fan sands). The electrode configurations used and the geometry of the measured and inverted pseudosections are presented in Table 3.3 and the results shown in Figure 3.12a.

5m spacing	Data	Measured			Inversion Model		
	Points	Length (m)	Depth (m)	Area (m ²)	Length (m)	Depth (m)	Area (m ²)
Wenner alpha	155	140	25.5	1650	140	26.2	2100
Wenner beta	155	140	20.75	1350	140	21.4	2100
Wenner-Schlumberger	210	140	26.8	1700	140	31.3	2100
Dipole-dipole	289	120	24	1640	120	25.2	2050

Table 3.3 – Geometry of the measured and inverted pseudosections for four electrode configurations.

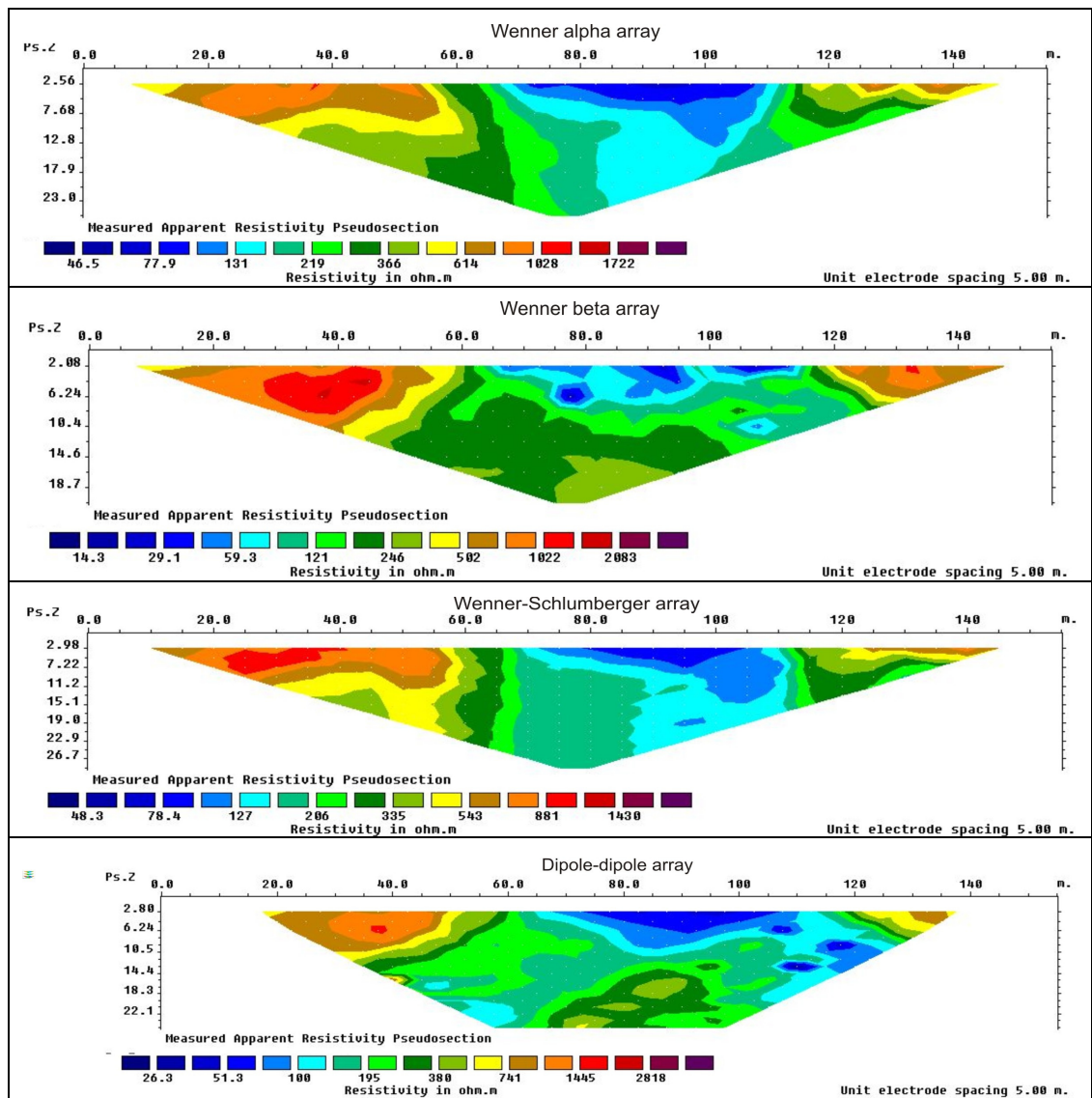


Figure 3.12a – Measured apparent resistivity pseudosection for profile S1-L04-5m recorded in Site S1 with the Geopulse Tigre resistivity meter with 32 electrodes at 5m spacing, using four different electrode configurations.

Wenner alpha and beta arrays measure 155 data points each, Wenner-Schlumberger array records 210 and the Dipole-dipole array pseudosection has 289 data points. Maximum depth of penetration is attained by The Wenner-Schlumberger array with 28.6m, Wenner alpha pseudosection is 25.5m, Dipole-dipole reaches 24m and Wenner beta penetration is 20.75m. The profiles for the Wenner and Wenner-Schlumberger arrays are triangular in shape; the measured readings cover a length of 140m on the higher level and only 5m at the lower one. On the other hand, the Dipole-dipole stretches for 120m on the higher level and 40m on the lower. The area covered by the measured pseudosections is particularly small for the Wenner beta array. Visual analysis of the measured pseudosections (Figure 3.12a) show three differentiated resistivity regions; two high resistivity areas occur on the upper area of the left and right margins of the profile ranging between 700 Ω m and 1200 Ω m. A lower resistivity region occurs at 65 - 115m with values lower than 100 Ω m.

The different inversion models show similar area coverage of over 2000 m². Wenner alpha and beta arrays use less data points than Wenner-Schlumberger and Dipole-dipole. Dipole-dipole is the one using the largest number of measured data points for the inversion, which may improve the resolution of features. However, Wenner-Schlumberger array provides 31.3m depth of penetration, a few metres deeper than the other three. The inverted resistivity models obtained (Figure 3.12b) show the main features in all the arrays, the smoother contacts between features are observed on the Wenner-Schlumberger array. A high resistivity area occurring in the lower central region at 70 - 100m of the profile is observed on all the Wenner arrays, whereas, the Dipole-dipole displays it in the bottom left margin at 40 - 60m.

Loke (2001) describes the Wenner-Schlumberger array as a good compromise between the Wenner and the Dipole-dipole arrays, which provides a good balance between vertical and horizontal resolution. The inverse model of the pseudosection derived from the Wenner-Schlumberger provides a deeper penetration of investigation, see Figure 3.12b. Furthermore, Wenner and Schlumberger sensitivity functions (Figure 3.8) have higher sensitivity than Dipole-dipole in the areas around the recorded point.

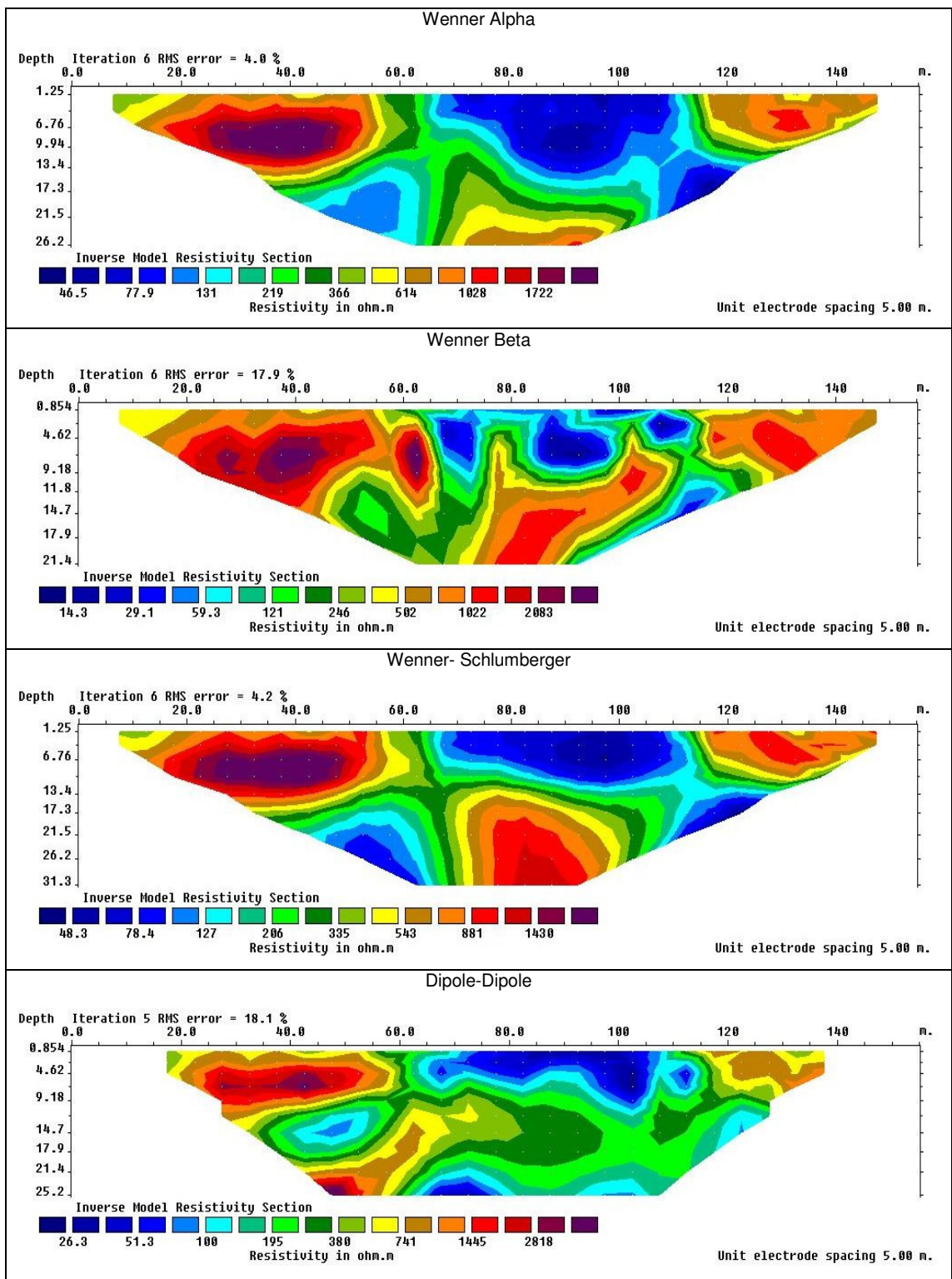


Figure 3.12b – Inverse model resistivity sections for profile RS1-L04-5m recorded in Site S1 with the Geopulse Tigre resistivity meter using four different electrode configurations.

Data collection to data interpretation

All the ERT profiles for this thesis have been collected with the Wenner-Schlumberger array, with the exception of the electrode configuration test presented above. Figure 3.13 shows a flow diagram indicating the methodology steps followed to generate the final model of the pseudosection prepared for data interpretation.

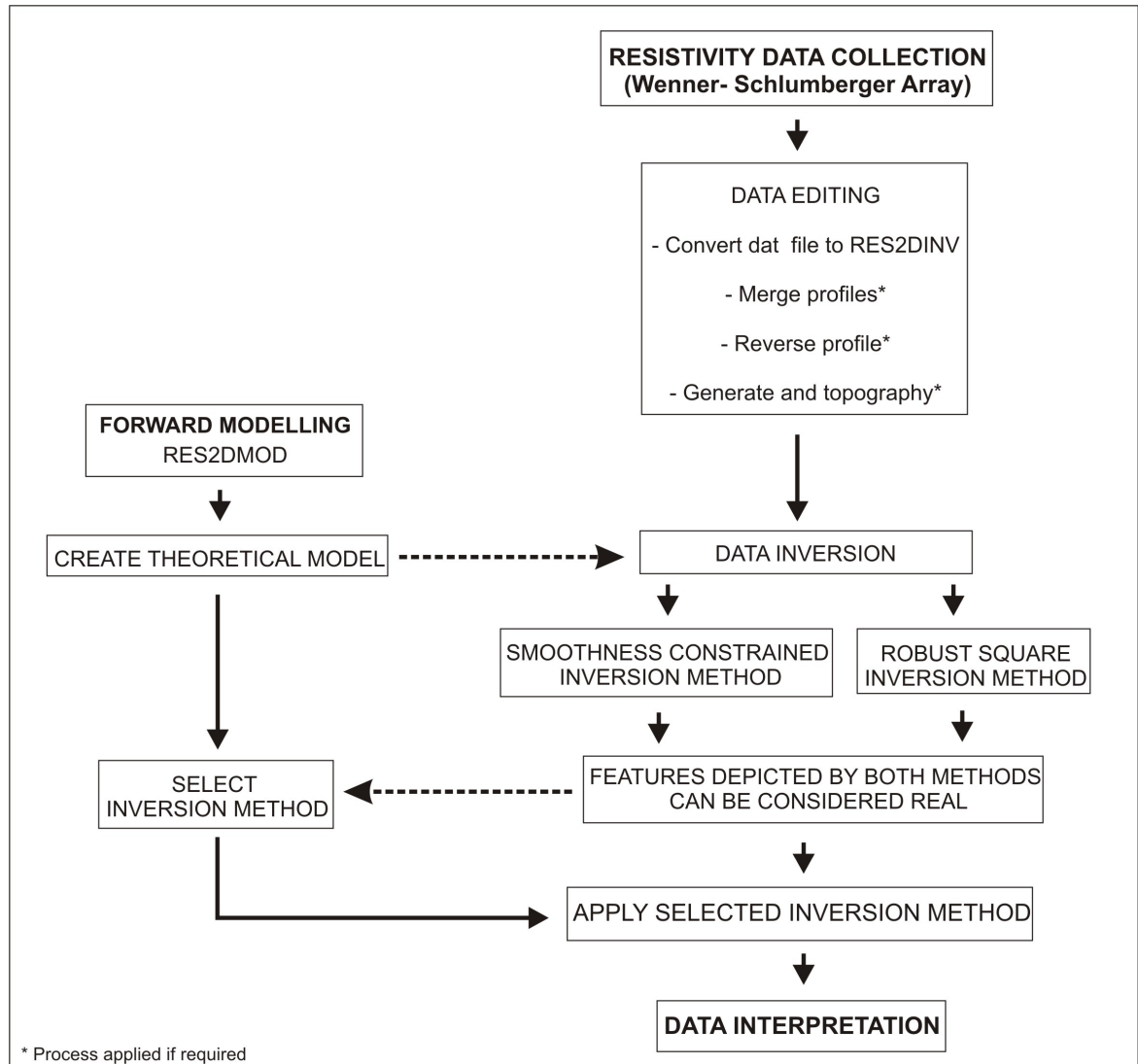


Figure 3.13 – Flow diagram illustrating the steps followed for ERT data collection to data interpretation, emphasizing the steps followed for data processing.

Firstly, the raw data collected in the field is prepared for inversion, on some occasions data editing had to be performed before data processing. The editing stage includes:

- Merging of inline profiles. ERT profiles collected inline during the same day have been merged in order to process them as a unique entity.
- Reverse profiles. Data may have been collected in the field in different directions in order to speed the data collection exercise. Some of the original datasets were reversed when necessary in order to present the data in this thesis in a consistent direction.
- Generate topography. Topography data extracted from OSI DEM at 10m spatial resolution has been added to the profiles when considered valuable for their final interpretation.

Secondly, datasets have been inverted by using the smoothness constrained and the robust square inversion methods, features depicted by both inversion methods can be considered real (Loke, 2004).

Thirdly, the field data were compared to the theoretical datasets produced during the forward modelling exercise (Chapter 5) and the adequate inversion method was selected. The data were inverted again to generate the final model of the pseudosection ready for interpretation. The final interpretation is based on the resistivity range of some geological materials presented in Figure 3.3 and general knowledge of the geological settings in the study area.

3.3.4 – 3D Modelling

3D electrical resistivity surveying has not yet been widely adopted by researchers as it is quite a time consuming costly exercise. The method used for this thesis is often referred to as 2.5D surveying. It consists of a group of parallel profiles at fixed distance from each other that are subsequently processed as one entity. Figure 3.14 shows the layout for a full 3D data collection compared to a 2.5D resistivity survey. The parameter file for a 3D

layout is such that data can be collected using any 4 electrodes along a line (y direction), across a line (x direction) or diagonally.

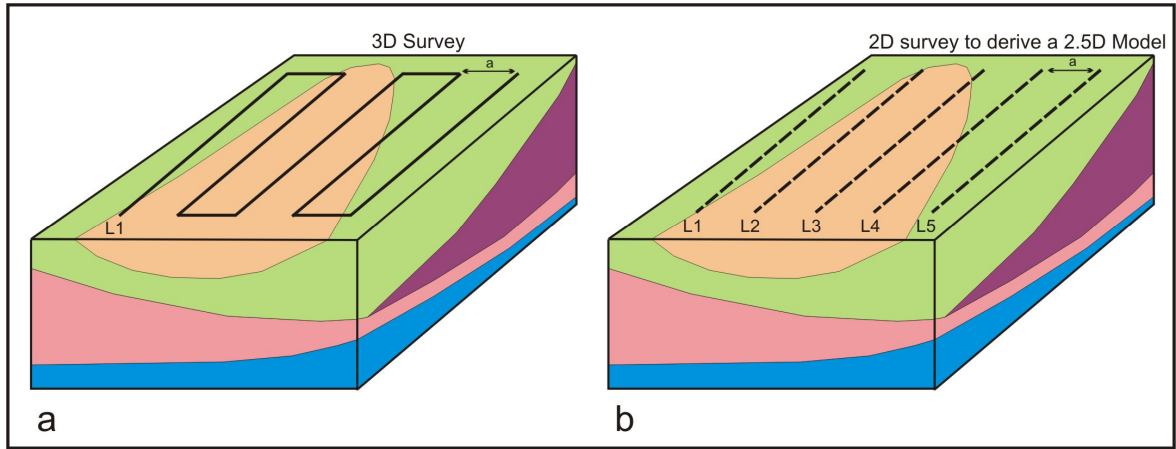


Figure 3.14 – Two modes of data collection for 3D resistivity survey. **(a)** A 3D survey needs of longer cables to cover the same area but provides with a complete 3D model with readings taken along the line and at diagonal directions. **(b)** Data are collected as 2D pseudosections and subsequently compiled and inverted as a unique 2.5D model, less detail is obtained using this method.

This approach allows different parts of the subsurface to be sampled. However, a great drawback is that a very large number of electrodes are required to collect a meaningful amount of data. For example, only 2 data points can be collected along or across any line using 25 electrodes as there are only 5 along or across a line. It is possible to use a pole-pole or pole-dipole array which involves remote electrodes to provide better coverage at the edges of the surveyed grid but even then the area covered for the survey is often too small (Maule et. al. 2000). In addition, very long cables need to be run to the remote electrodes and the sensitivity functions of these arrays are different from the Wenner-Schlumberger one. However, as the electrical resistivity data for this thesis have been collected mainly using the Wenner-Schlumberger array, it has been decided to collect data for 2.5D modelling with the same array configuration, as it will maintain consistency with the data collected and will facilitate correlations between datasets.

It is possible to undertake a 3D survey in which the electrodes are located along fewer parallel lines, but each line can be considerably longer e.g. a system with 50 electrodes will allow 5 parallel lines of 10 electrodes each. This set up is then moved across the survey

area. This approach increases the number of data points along the line, however, the depth of investigation is greatly reduced.

The approach used in this research was to obtain parallel lines of data employing all 25 electrodes along each line (Figure 3.14b). These data were then subsequently combined into a 2.5D dataset and inverted using RES3DINV software (Loke, 2005). Although this method is not a full 3D modelling technique, it allowed a large number of data points to be collected and gave a good depth of investigation. This is considered the most cost effective method to produce 3D electrical resistivity models, until a multi-channel resistivity system is available (Maule et al., 2000, Loke, 2001).

Nine parallel resistivity lines spaced six metres apart, were collected using the Wenner-Schlumberger array at two metres spacing at Site S1 in order to produce a 2.5D model and to determine the heterogeneous nature of the middle region of a fan. The total area surveyed was 48 x 48m (2304 m²) and 1413 readings were collected. Two boreholes were drilled within this site in order to constrain the model and to provide ground truth (BH-S1B and BH-S1C, see Table 6.1). The location of the dataset within Site S1 can be viewed in Chapter 6, Figure 6.5.

The collected resistivity data were inverted using the smoothness constrained inversion method (deGroot-Hedlin and Constable, 1990) within RES2DINV. Depth slices consisting of layers showing the variation of resistivity at different depths were derived from the model and the 3D data processed with SlicerDicer software to produce the final 3D model.

The final 3D Model is described in detail and interpreted in Chapter 6.

3.3.5 – Time-lapse Resistivity

Time-lapse resistivity imaging involves the collection of electrical resistivity data at a selected location at different times. This helps monitor changes in the nature of the subsurface through time. This type of survey can be carried out for short time periods (a

few days with readings taken every few hours) or for long term time-lapse resistivity surveys to monitor seasonal variations.

A time-lapse resistivity survey can assist on the accurate interpretation of the distribution of sediments in the subsurface, as seasonal variations occurring in the subsurface (water table, moisture content) can slightly or greatly change the response of the sediments to electrical resistivity surveying. For example, a similar high resistivity response may be obtained in the summer over a sand/gravel subsurface and a subsurface composed of cobbles and boulders. A similar high response may be acquired over the free draining cobble subsurface in winter, whereas the presence of water within slower draining gravels would yield a considerably lower value.

Time-lapse resistivity surveys have been carried out as part of this thesis to measure monthly and seasonal variations of electrical resistivity for four profiles at site S1. Two of the profiles have electrode spacing of 5m in order to yield information to a depth of approximately 24m. The other two profiles have electrode spacing of 2m (maximum depth of investigation of 9m), and are co-linear with the 5m spacing profiles in order to obtain more detailed profiles within them. The profiles have been surveyed on a monthly basis from January 2006 to January 2007. The locations of these profiles and three boreholes drilled along them (BH-S1A, BH-S1E and BH-S1F, see Appendix A) are presented in Figure 6.11.

The surveyed profiles are located in areas where a range of glacial and postglacial sediments occurs. These include subglacial till, glaciofluvial sediments such as esker sands and gravel and sand dominated subaqueous fans, and postglacial lacustrine silts and clays with a thin drape of peat in places. Ideally, the electrodes would have been installed permanently on site for the entire survey (Johansson and Dahlin, 1996 and Yaramanci, 2000). Due to logistical impediments, permanent electrodes could not be installed for a year duration period. However, the two ends of the profiles were marked by the installation of permanent wooden posts.

RES2DINV software allows the production of inversion models for resistivity data collected at different times. The software provides the option of using a joint inversion technique, where the inversion of the first measured resistivity data is used to constrain the datasets collected at a latter stage (Loke, 2001). The use of this method allows the identification of possible errors derived from the inversion of the files. The final product from this process is a profile showing two of the datasets collected at different times, together with the percentage variation in resistivity. Figure 3.15 shows an example, courtesy of Gibson (2003).

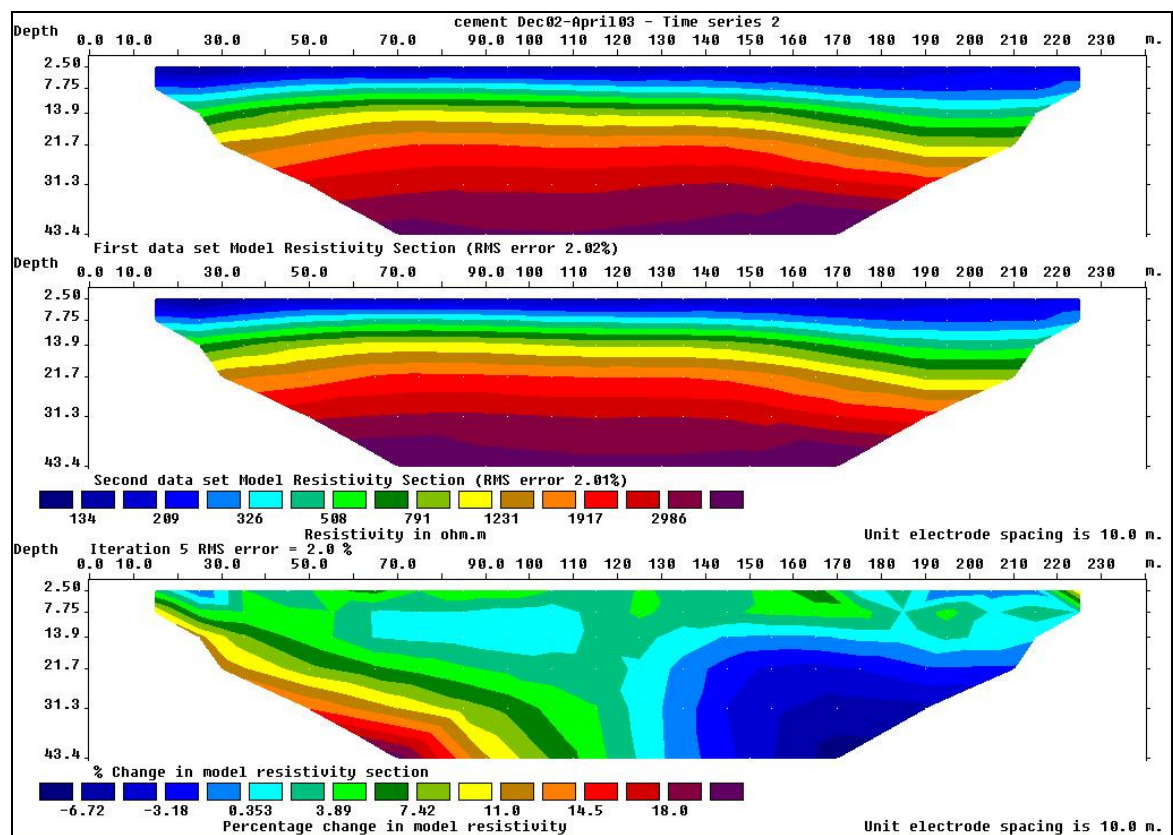


Figure 3.15 – The bottom profile illustrates the time-lapse seasonal resistivity variation between the two profiles above. The profiles were collected December 2002 and April 2003 on a limestone bedrock area in Co. Meath. Reproduced by permission, Gibson (2003).

Seasonal changes in a profile were monitored. Significant variations can be observed between the profiles collected in December 2002 (above) and April 2003 (below). A general increase in the resistivity values of around 10% is observed in the left part of image, while the region to the right experiences a decrease of up to 7%. The observed

variations can provide useful information which helps in understanding the nature and internal structure of the subsurface and to detect features overlooked by standard a electrical resistivity survey.

Weather data from Derrygreenagh and Mullingar weather stations, located 17 km northeast and 30 Km north respectively from site S1, has been supplied by Met Eireann. These data will help determine the influence of rainfall and temperature on electrical resistivity seasonal variations. Seasons with heavy rainfall and low temperatures are expected to reduce the electrical resistivity values obtained as moisture content of the sediments in the subsurface should increase thus enhancing their conductivity. However, dry seasons with higher temperatures are expected to show an increase in the average resistivity values. The time-lapse resistivity results are presented in Chapter 6.

3.3.6 – Azimuthal Resistivity

A resistivity sounding shows the variation in apparent resistivity with depth for one point and is conventionally collected by increasing the electrode spacing for an array symmetrically over the central point of the array (see Gibson and George, 2004). However, this approach assumes that there are vertical changes in resistivity but that the subsurface is laterally homogenous. Thus increasing the array spread in any direction should yield the same results if the subsurface is homogeneous. Azimuthal resistivity consists of the collection of electrical resistivity data for a given point using several electrode spacings in a number of directions, in order to determine the apparent resistivity variation with orientation (Busby, 2000), see Figure 3.16a. This technique has been widely used on the identification of sub-vertical geological structures (Flemming, 1986; Watson and Barker, 1999; Busby and Jackson 2005) but has been rarely employed for sediment analysis.

The most popular arrays for data collection are the collinear Wenner and Schlumberger array and a range of square arrays, which according to Habberjam and Watkins (1967) are more sensitive to anisotropy and involve 65% less area than a collinear array.

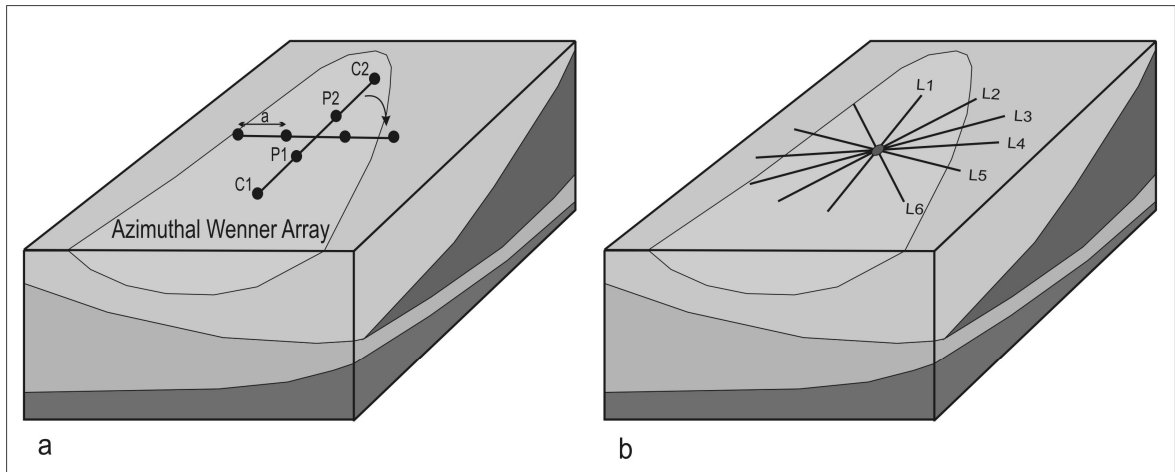


Figure 3.16 – Sketch diagram illustrating methodology for Azimuthal resistivity data collection using the Wenner electrode configuration.

The apparent resistivity data obtained can be plotted on Cartesian diagrams as a function of azimuth, however, they can also be plotted on a polar diagram and a shape is portrayed by joining the data with a continuous line. Elliptical shapes are interpreted as anisotropy of the subsurface, the long axis indicating the strike direction of subvertical fractures.

Boris and Merrian (2002) attempted to use azimuthal resistivity to identify anisotropy within homogeneous till caused by fractures, with only partial success. It is known from previous geological mapping and from other geophysical techniques used in this study that the glacial and postglacial sediments present in the study area are typically heterogeneous in nature. Changes in the physical properties of the sediments surveyed for this thesis often occur within tens of metres both laterally and in depth. A Wenner array was used to test the potential of the azimuthal resistivity for the study of the internal architecture of heterogeneous soft sediments compared to other geophysical techniques utilised for this thesis.

A total of 6 lines revolving around a point at angles of 0°, 30°, 60° etc were recorded for this thesis (Figure 3.16b). The results are plotted as Cartesian diagrams. The X-axis showing the electrode spacing and the apparent resistivity value obtained on the Y-axis. The visual analysis of the plot has been used to interpret the azimuthal variation of the physical properties of the subsurface at the surveyed point.

Four points with different sedimentological settings have been surveyed at Site S1 (see Map 1) using this technique; the results are presented and interpreted in Chapter 6.

3.4 – Ground Penetrating Radar (GPR)

3.4.1 – Introduction

GPR data collected in the field yield a profile that displays the subsurface sediment architecture of the near surface (less than 50m depth), in the form of reflectors. The depth of penetration and the resolution of the system vary with the frequency used for data capture. In general, higher frequencies provide better resolution but less penetration than lower frequency systems. Subsequent to data capture, the data need to be processed in order to maximize the information extraction. No single radargram displays all the information obtained on a GPR survey. A number of processing techniques such as the application of various gains or filters, time/depth slice amplitude analysis or migration of the data need to be applied to the raw GPR data. In addition, where there is a large variation in relief for a radar profile, topographic corrections are also necessary. The processed data are interpreted visually and visual interpretation of GPR data is derived from the principles of seismic stratigraphy (Neal, 2004). The concepts of radar surface, radar package and radar facies, developed by various authors since the 1970s (for example, Mitchum et. al, 1977; Davis and Annan, 1989; Baker, 1991; Neal et al., 2002) has resulted in a systematic approach to the interpretation of GPR data. Moreover, the use of time slice analysis permits differentiate between main dominant lithologies (sand and gravel from silts and clays etc) encountered in a profile.

A number of methodologies for data collection, processing and presentation have been used for this thesis. The following section explains in detail the theoretical concepts for Ground Penetrating Radar. This is followed by two sections presenting the main data collection and processing techniques available in the literature, the techniques selected to be used for this thesis are described in further detail. Furthermore, the time/depth slice

analysis method is introduced and discussed. Finally, the methodology used for systematic data interpretation and the coding system used for classification of the data collected for this thesis are considered.

3.4.2 – Theoretical Concepts

This technique consists of the transmission of electromagnetic pulses at a (supposed) constant frequency into the ground from an electronic transmitter. These pulses are reflected back from subsurface interfaces and read by a receiver located a short distance from the transmitter. Two parameters are read: the strength (amplitude) of the reflected signal and the time at which these signals are received. The longer it takes for a returned signal to appear, the deeper the layer it has been reflected from. High resolution instrumentation is needed to measure the travel time of an electromagnetic wave from the transmitter to a receiver as it varies between ten and more than thousand nanoseconds (10^{-9} seconds). Discontinuities in the subsurface are identified and can be interpreted as changes in moisture content, lithology, sedimentology or anthropogenic structures.

Subsurface properties control the behaviour of electromagnetic energy transmitted through it. This behaviour is influenced by a number of factors such as the frequency (f) of the wave and the material involved. Energy propagation through a body depends upon its relative permittivity (ϵ_r), also referred to as dielectric constant, electrical conductivity (σ), magnetic permeability (μ) and scattering and geometric spreading of the energy (Neal, 2004). The relative permittivity is the capacity of a material to store electrical charge, the electrical conductivity is its ability to transport an electrical charge, and the magnetic permeability is the capacity of storing magnetic field energy, which is equivalent to the relative permittivity. Furthermore, scattering and geometric spreading of the energy influence the transmission of electromagnetic energy:

- The presence of particles in the subsurface with similar dimensions to the wavelength induces the scattering of the energy, decreasing the transmission into the ground.

- The geometric spreading of the energy transmitted into the subsurface as an expanding cone yields a decrease of energy with depth by a factor of $1/r^2$, where r is the travelled distance (Reynolds, 1997).

The velocity (v) of propagation of electromagnetic waves in a vacuum is the speed of light ($c = 0.3\text{m/ns}$). However, the velocity of propagation through a body (V_m) is a function of the angular frequency ($\omega = 2\pi f$), ϵ , σ and μ . This is mathematically expressed by Neal (2004) as:

$$V_m = \frac{c}{\sqrt{\epsilon_r \mu_r \left[\frac{\left(1 + \left(\frac{\sigma}{\omega \epsilon}\right)^2\right) + 1}{2} \right]}} \quad \text{equation (3.10)}$$

The influence of σ on the GPR frequency ranges (50-1000MHz) is considered minimal for materials such as well-sorted sand and gravel (Reynolds, 1997). Moreover, μ_r is given the typical value for a non-magnetic body ($\mu_r = 1$). So equation 3.10 can be simplified as follows:

$$V_m = \frac{c}{\sqrt{\epsilon_r}} \quad \text{equation (3.11)}$$

The velocity is inversely proportional to the square root of the relative permittivity. Water saturated materials, which have high relative permittivity will have a lower velocity of propagation than unsaturated sediments.

Another important factor resulting in the loss of energy with depth is the attenuation of the waves. The exponential decrease of the original amplitude (A_0) of the wavelength occurring at a given depth z depends on the attenuation factor (α). This is expressed by Neal (2004) as follows:

$$A = A_0 e^{-\alpha z} \quad \text{equation (3.12)}$$

The attenuation factor is frequency independent for materials with a very low loss factor ($P = \sigma/\omega\epsilon$) and can be expressed as follows (Conyers, 2004).

$$\alpha = \frac{\sigma}{2} \sqrt{\mu/\epsilon_r} \quad \text{equation (3.13)}$$

The attenuation factor is highly dependent on the conductivity of the subsurface and inversely proportional to the square root of the relative permittivity. Thus, attenuation values for saturated sediments (low permittivity) are higher relative to unsaturated ones.

Subsurface properties such as conductivity, relative permittivity, attenuation and velocity will condition the resulting GPR profile. These properties have been categorized for a range of geological features (Davis and Annan, 1989; Reynolds, 1997; van Overmeeren, 1994). Neal (2004) summarised them, Table 3.4 is a modified form of his values relevant to the present study area. Attenuation values are very large for fine sediments (silts and clays), which affects the depth of penetration, usually low in these types of sediments. Moreover, less penetration is expected under water table levels as saturated sediments have larger attenuation values than dry sediments.

Medium	Permittivity (Er)	Conductivity σ (mS/m)	Attenuation α (dB/m)	Velocity v (m/ns)
Air	1	0	0	0.3
Dry sand	2.55-7.5	0.01	0.01 – 0.14	0.1 – 0.2
Saturated sand	20 – 31.6	0.1 – 1	0.03 – 0.5	0.05 – 0.08
Dry sand and gravel	3.5 – 6.5	0.007 – 0.06	0.01 – 0.1	0.09 – 0.13
Saturated sand and gravel	15.5 – 17.5	0.7 – 9	0.03 – 0.5	0.06
Dry silt	2.5 – 5	1 – 100	1 – 300	0.09 – 0.12
Saturated silt	22 – 30	100	1 – 300	0.05 – 0.07
Dry clay	2.5 – 5	2 – 20	0.28 – 300	0.09 – 0.12
Saturated clay	15 – 40	20 – 1000	0.28 – 300	0.05 – 0.07
Dry till	7.4 – 21.1	1 – 20 (b)	0.1 – 3.67 (a)	0.1 – 0.12
Saturated till	24 – 34	20 – 500 (b)	1.71 – 51(a)	0.1 – 0.12
Peat	57 – 80	< 40	0.3	0.03 – 0.06
Bedrock	4 – 6	10^5 – 40	7×10^6 – 24	0.12 – 0.13

Table 3.4 – Subsurface electrical properties of some common geological materials. Modified from Neal (2004). (a) Values calculated by equation (3.4) assuming $\mu = 1$. (b) Values obtained from thesis data.

Reflection of the energy occurs when a change in the properties of the subsurface occurs. Given two neighbouring layers with different properties, which are expressed by different relative electrical permittivities (ϵ_{r1} and ϵ_{r2}), a reflection coefficient (R) can be calculated thus (Reynolds, 1997):

$$R = \frac{\sqrt{\epsilon_{r2}} - \sqrt{\epsilon_{r1}}}{\sqrt{\epsilon_{r2}} + \sqrt{\epsilon_{r1}}} \quad \text{equation (3.14)}$$

The relative permittivity within sediments is controlled by the moisture content, lithology, sediment packing or sorting. Therefore, lithological changes, deformation structures or water table level should be detected by the use of GPR (Neal, 2004). Reflection coefficients will range between +1 and -1, the polarity of the reflected wave is indicated by the sign. Reflection coefficients for a number of geological settings typically occurring in the study area are presented in Table 3.5.

Feature detected	MATERIAL 1	MATERIAL 2	E1	E2	Reflection Coefficient
Till overlaid by Gravel	Dry Gravel	Till	6	10	-0.13
Till overlaid by Clay	Dry Silts and Clays	Till	5	10	-0.17
Till over Bedrock	Till	Limestone	10	4	0.23
Change in Moisture content	Dry Sand	Moist Sand	6	8	-0.07
Peat overlying Gravel	Peat	Gravel	25	6	0.34
Peat overlying Clay	Peat	Clay	25	5	0.38
Water Table (Sand)	Dry Sand	Saturated Sand	4	22	-0.40
Water Table (Gravel)	Dry Gravel	Saturated Gravel	6	17	-0.25
Water Table in Peat	Dry Peat	Saturated Peat	25	45	-0.15
Fault in Till	Dry Till	Saturated Till	10	24	-0.22

Table 3.5 – Reflection coefficients obtained from a number of examples encountered in soft sediments which typically occur within the study area. Permittivity values extracted from Davis and Annan (1989), Daniels et al. (1995) and Neal (2004). E1 and E2 indicate permittivity for top and bottom layer respectively.

The highest reflection coefficients are obtained from sharp contacts in the subsurface such as presence of water table, unconsolidated sediments on bedrock or peat overlying unsaturated sediments or bedrock. These settings would be represented in a radargram as very strong reflectors. Minute changes in the relative permittivity between adjacent layers will be represented as weak reflectors. Annan et al. (1991) stated that the sharpness of the reflection is also a function of the wavelength and the thickness of the transition zone,

which has to be at least three times the wavelength. Van Dam and Schlaeger (2000) confirmed that relative electrical permittivity is the main factor controlling reflection in soft sediments and those primary reflections are often related to primary depositional structures. On the other hand, the presence of jointing, faulting or folding is often detected as reflectors in the GPR profile. As stated above, very high reflection coefficients imply the feature being represented by a very sharp reflector. However, a drawback from this is that more energy is reflected to the surface, which entails less energy being transmitted through the feature, reducing the depth of penetration.

GPR unprocessed data encompass a number of limitations that have to be taken in account before processing and interpretation. These are presented and discussed below.

The common offset **data collection mode** has been used for this thesis, see next section (GPR data collection). It has to be borne in mind that the antenna separation between the transmitter and receiver means that reflectors detected close to the surface are deformed, as the electromagnetic waves detecting the object travel at an angle, which implies that the depth of the feature is overestimated; this type of deformation is reduced for deeper reflectors (Neal, 2004).

As mentioned above, the **depth of penetration** depends on a number of factors. A lower antenna frequency will usually yield a deeper penetration depth. However, the **vertical resolution** of a dataset obtained increases with the antenna frequency, the higher the frequency the smaller the wavelength. Wave theory from seismic reflection states that vertical resolution is $\frac{1}{4}$ of the wavelength (λ) (Sheriff, 1977). Knowing the following: $\lambda = v / f$. The minimum vertical resolution (Δ_{mV}) is:

$$\Delta_{mV} = \frac{v}{4f} \quad \text{equation (3.15)}$$

Neal et al. (2003) were able to detect beds of 0.2 m thickness in low-loss material using a 900MHz antenna. Another factor to take in account is the **horizontal resolution**, it has

been defined by Rial et al. (2008) as the minimum distance required between neighbouring reflectors located at the same depth to detect the two as separate features. Heinz (2003) stated that horizontal resolution also decreases with depth. Gracia (2008) and Kathage (2008) present horizontal resolution as the diameter of the first Fresnel zone, which is represented by the following formula:

$$\Delta_H = \sqrt{\frac{\lambda^2}{4} + L\lambda} \quad \text{equation (3.16)}$$

Where Δ_H is the length of the feature resolved, λ is the wavelength based on centre frequency and L is the depth of the object, thus there is a decrease of resolution in depth. Moreover, the **step size** between traces will limit the horizontal resolution. Woodward et al. (2003) stated that in order to detect a horizontal feature, at least 10 adjacent radar traces should cover it; thus, using a 200 MHz antenna with the recommended 0.1m step size, only features larger than 1m will be resolved. However, features smaller than these have been detected (Gibson, 2009 personal comm.).

The presence of **noise** associated with external factors has to be taken in account before data collection. Radio waves from various sources or any external equipment employing frequencies close to the operating GPR frequency may distort the data. Moreover, natural features, such as presence of saline groundwater or very conductive clays may produce a highly attenuated signal in the radargram (Neal, 2004; Gibson and George, 2004).

The presence of **artefacts** is fairly common in GPR profiles; these can be derived either from surface or subsurface elements. Artefacts caused by surface features such as electric fences, poles, trees, walls or irregular topography close to the recorded profile may result in recording reflectors which are not caused by real subsurface features, Figure 3.17 shows a dipping reflector related to an operating electric fence located 10m from the start of the line. These have to be avoided if possible, otherwise noted during fieldwork and taken into account during the data interpretation stage. The presence of high conductivity reflectors in the subsurface can originate “ringing” which displays as a reflector systematically repeated

in depth, this is due to EM waves bouncing back and forth between the antenna and the reflector (Sensors and Software, 1999). Such features can mask deeper subsurface discontinuities, an example of this artefact has been gathered in Site S1 and is shown in GS1-L04-200MHz from 0 - 40m (Figure 6.41).

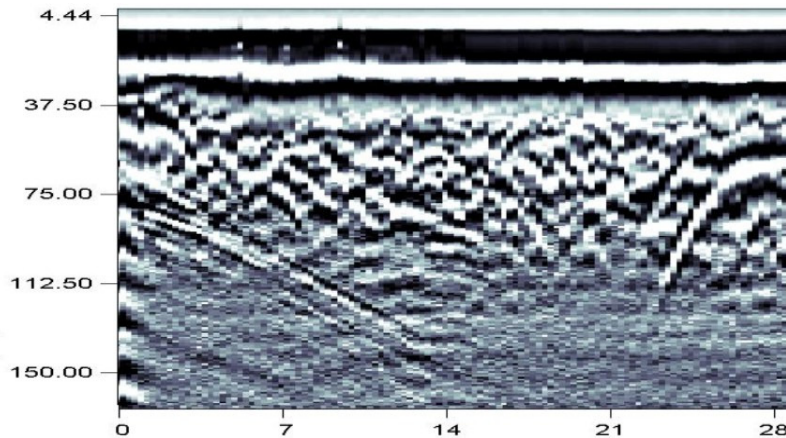


Figure 3.17 – Artefact in GPR. Note continuous sloping reflector starting at the left margin at 75ns of the profile. The reflector is associated with live electrical wire situated 2.5m from line start (0m).

3.4.3 – Data Collection

The GPR used for data collection for this research is a Sensors & Software pulseEKKO 100. The system is equipped with a transmitter and a receiver connected with fibre optic cables to a console measuring time and reflection strength, which is connected to a computer that displays a profile of the subsurface on site (Figure 3.18).

There are a number of parameters that have to be set up before data collection starts. These are:

- Survey type
- Data collection mode
- Frequency
- Step size
- Antenna separation
- Time window
- Time sampling interval

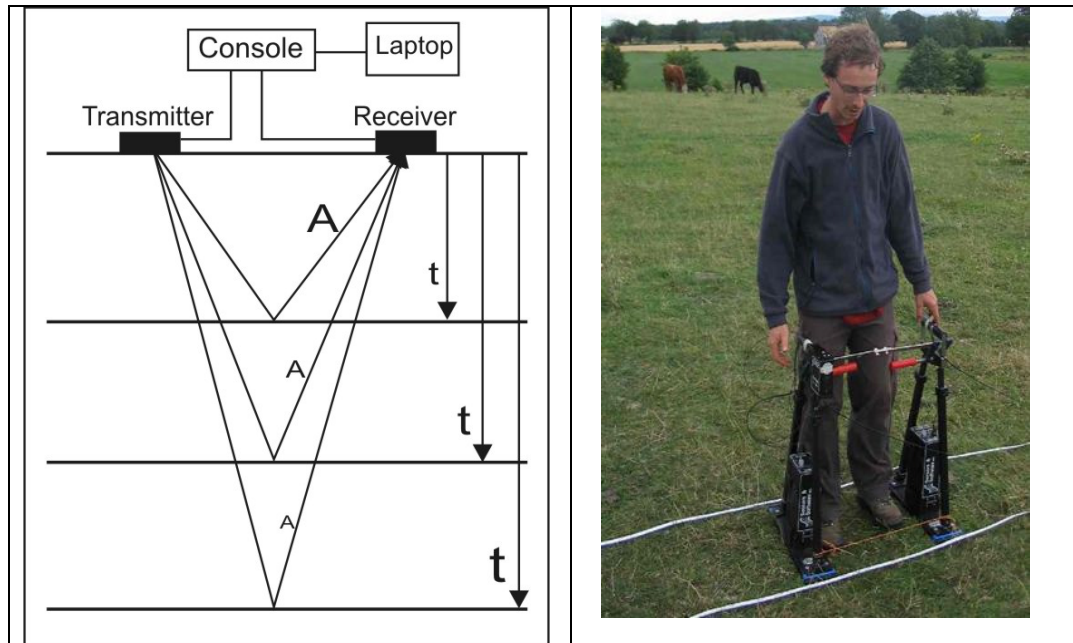


Figure 3.18 – Left - Diagram showing GPR components and data collected at a single point. Time and amplitude of the reflected wave are collected by the receiver, measured by the console and displayed with the laptop on site. Right - GPR data collection using 200MHz antennae.

The most common **survey type** for data collection is the common offset in which the transmitter and the receiver antennae are separated by a fixed distance and moved along the survey line. However, variations in lithological conditions in the subsurface may produce significant changes in velocity, which will influence the shape of the reflectors detected and their true position within the recorded profile. Velocity differences of up to 50% have been measured in unsaturated sediments (Neal, 2004). The use of Common Mid Point (CMP) soundings is recommended before extensive survey work is commenced in order to identify changes in velocity within the subsurface (Jol and Bristow, 2003). A CMP sounding is produced by obtaining data over a central position at different antennae spacing. Figure 3.19 illustrates common offset and CMP survey types and the difference between the datasets collected for the same line. The CMP profile (Figure 3.19b) can be used to compute the velocity for a given reflector, knowing time difference ($TX2 - TX1$) and distance difference ($X1 - X2$) the velocity for the reflector can be computed. However, EkkoView DeLuxe software includes a tool to convert the CMP radargram to a velocity profile for different depths (see Figure 3.19c), which has been used for velocity calculation for this thesis. The X axis indicates the dominant velocity and Y axis indicates depth.

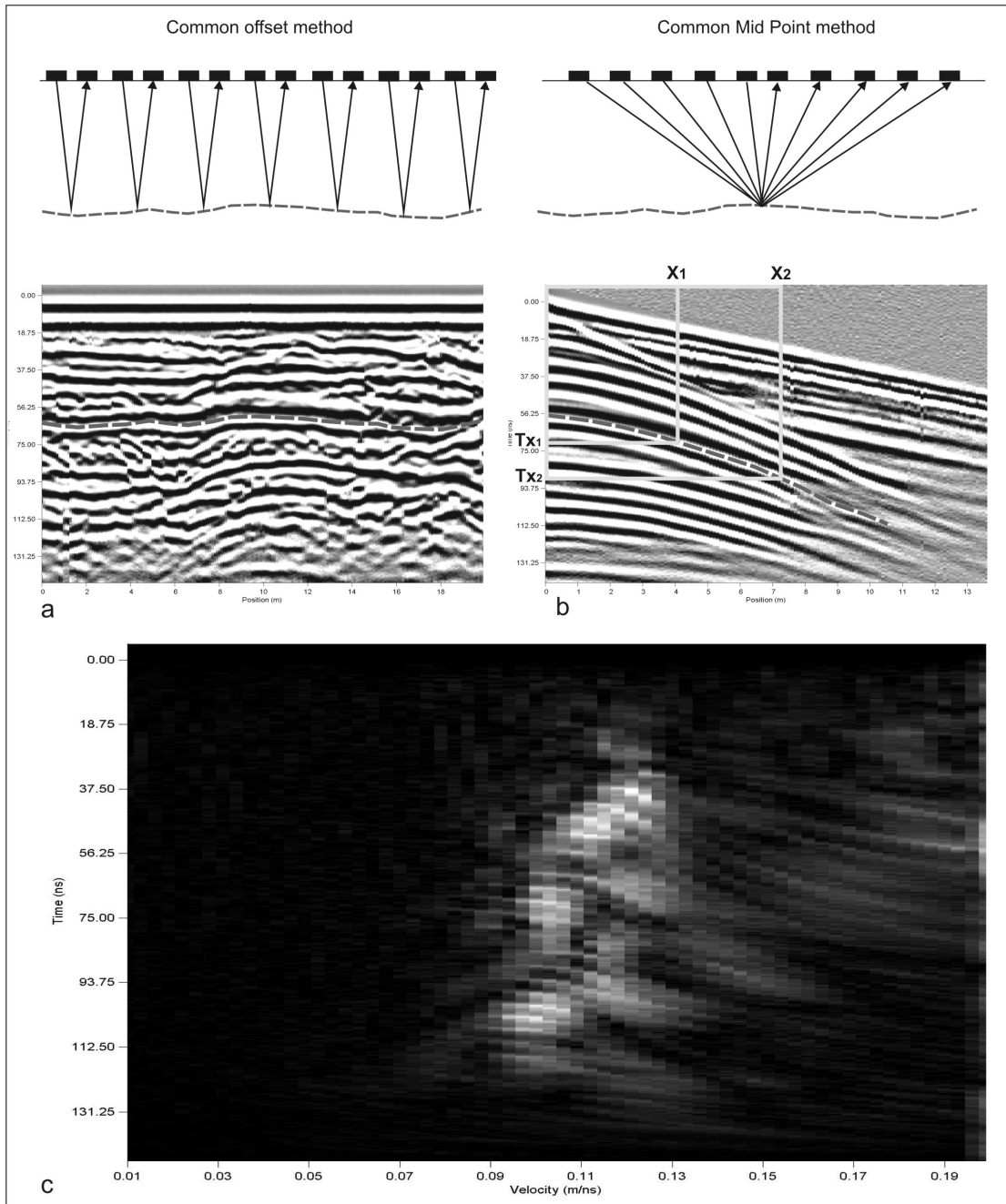


Figure 3.19 – Data collection methods used for this thesis and results obtained for a profile in site S1. (a) Common offset records the location and shape of reflectors. (b) Common Mid Point allows the velocity of the electromagnetic waves at different depths to be calculated. (c) A velocity diagram produced from CMP radargrams with the EkkoView DeLuxe software.

White areas show the dominant velocity at depth and it can be observed how velocity ranges 0.10 - 0.12m/ns, thus a velocity of 0.11m/ns would be used to calculate depth for this profile.

Two **data collection modes** can be used. The step mode consists of taking the first reading with the antennas separated by a fixed distance, then the system is moved at a predetermined distance along a line and a second reading is taken, this is repeated until the line surveyed is recorded. Continuous mode consists of moving the antennae at a constant velocity along the line and readings are taken at preset time intervals. The step data collection mode has been the one adopted for this thesis, this data collection mode is more time consuming, however, the accuracy of the dataset collected is higher using this method (Jol and Bristow, 2003).

As mentioned in the theoretical background section, there is a trade off between frequency used, depth of penetration and resolution. The higher is the antenna frequency, the lower the penetration and the better the resolution. Surveys carried out on sediments usually use antennas frequencies between 50 and 500MHz (Jol and Bristow, 2003). A further concept to take in account is the difference between centre/nominal frequency and dominant frequency.

The centre or nominal frequency is the average frequency broadcasted by the antenna, a GPR antenna broadcasts EM waves within a “two octave bandwidth” (Conyers, 2004), e.g. an antenna with a centre frequency of 200MHz is in fact broadcasting approximately within the 100 - 400MHz range. Moreover, a loading down of frequency occurs when recording GPR data, high frequency energy is more easily attenuated in the shallow subsurface; therefore, the dominant frequency will usually be lower than the nominal frequency. A diagram showing the dominant frequency of a nominal 100MHz antenna used in this research is presented in Figure 3.20 which shows that the dominant frequency ranges 60 - 70MHz. This results in an important decrease of the expected resolution for a nominal 100 MHz antenna frequency.

Three antennas with centre frequencies of 50MHz, 100MHz and 200MHz were available for the pulseEKKO 100 system used for this thesis. The knowledge of the study area and the level of detail required for the data acquired have facilitated the selection of the right antenna frequency. Occasionally, the same line has been recorded using two (or all) of the

antenna frequencies in order to depict and discuss the variation in penetration and resolution of the resulting datasets.

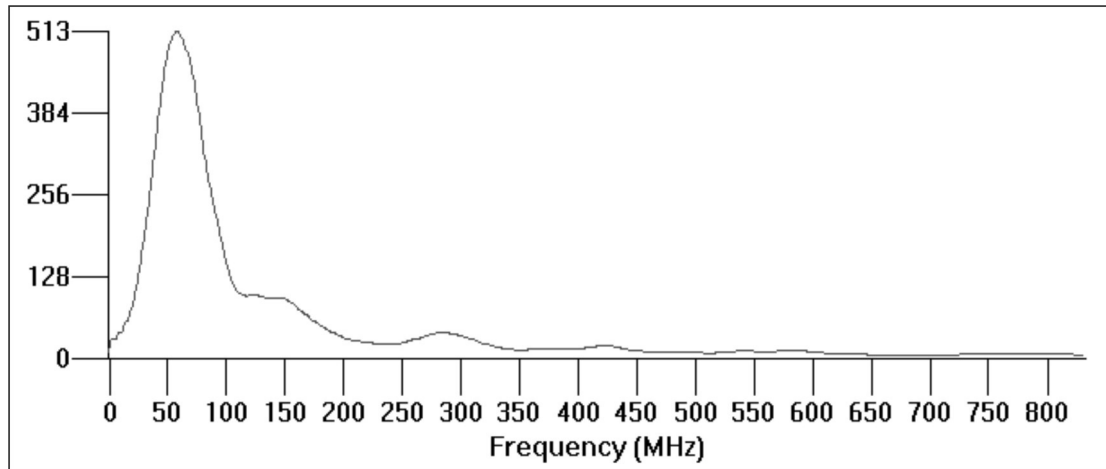


Figure 3.20 – Average amplitude-frequency plot for 100 MHz nominal antennae frequency.

The **step size** is the distance between adjacent data collection points. It is dependent on the antenna frequency and the size of the feature one wishes to locate. Jol and Bristow (2003) recommend that the Nyquist sampling interval consisting of $\frac{1}{4}$ of the wavelength of the investigated body should not be surpassed. Sensors and Software (1999) recommends the use of a step size of 0.1m for a 200MHz, 0.25m for a 100MHz and 0.5m for a 50MHz. These were considered suitable for this thesis and systematically used for data collection.

The **antenna separation** should be at least half a wavelength of the frequency used. Therefore, it is wider for low frequencies. The antenna separations used for this survey are those recommended by Sensors and Software (1999) for the pulseEkko 100 GPR system: 0.5m for the 200MHz, 1m for the 100MHz and 2m for the 50MHz antennae. Antenna coupling occurs on the shallow subsurface which obscures the shallower region along the subsurface creating a dead zone where no information is recorded, the larger the antenna separation, the deeper the dead zone is. According to Conyers (2004) this dead zone is around 1.5 wavelengths of the centre frequency used, thus it would approximately be of 1.5m for a 200MHz, of 3m for a 100MHz and of 6m for a 50MHz. However, radargrams recorded for this thesis using a 50 MHz antenna resolve features from 2m depth. See Chapter 5 (Figure 5.27) and Chapter 6 (Figure 6.37).

Time window represents the length of time over which data will be collected for each individual GPR trace. Thus if one assumes a velocity of 0.1m/ns a time window of 100ns means that reflectors within the top 5m will be recorded. (Two-way travel time has to be taken into account). Setting too short a time window means deeper reflectors are not recorded. However, if subsurface conditions are such that penetration is of the order of 5m then setting a time window to collect data at greater depths is inefficient. The time window is set according to the frequency used. Annan (2002) recommends the use of a time window exceeding by 1/3 the target depth. Typically, for subsurface conditions within the research area, a time window of 150ns has been assigned to a 200MHz, 250ns for a 100MHz and 300ns to a 50MHz antenna. However, potential depth of penetration of the electromagnetic waves usually exceeds the default time windows in low-loss materials such as unsaturated, well-sorted sands and gravels, Jol and Bristow (2003) recommend the use of larger time windows in such conditions. Therefore, time windows of 250ns for a 200MHz and of 350ns for a 100MHz antenna have been used for this thesis when appropriate subsurface conditions were encountered.

Time sampling interval is the time allocated for each reading taken by the receiver, a sample is a digital value defining a section of the waveform. The greater the number of samples recorded, the more accurately the waveform is defined. A higher sampling interval will be needed with decreasing frequency. Sampling intervals defaulted by Sensors & Software have been used during this survey. These are 800 picoseconds (10^{-12} seconds) for the 200MHz and 100MHz antennas and 1600ps for the 50MHz antenna. An additional number of factors such as, line orientation and location, antenna orientation and topography have been taken in account during data collection.

Line orientation and location has been decided independently for every site. Typically, lines have been collected parallel and perpendicular to the surveyed feature (e.g. for morainic ridge a line cutting across and another along it have been recorded) in order to image the reflectors, that can aid in the understanding of the internal architecture of the surveyed feature, at different angles. Jol and Bristow (2003) recommend the collection of grid data for construction of fence diagrams and if possible collection of 3D data. A 3D

dataset has been gathered in Site S1 for a small rectangular test area. Closely spaced lines 0.5m apart were collected using a 200 MHz antenna, to produce a high resolution 3D model; the results are presented in detail in Chapter 6.

Antenna orientation has to be selected before survey is carried out. The antennae are dipolar and transmit the EM waves through the surface with a preferred polarity, therefore, the type of antenna deployment used (Figure 3.21) will influence the signature recorded in the radargram. Horizontal-perpendicular polarization (*EH*) is defined by *E* (Electric Vector) being contained within a horizontal plane perpendicular to the plane of incidence, on the other hand vertical parallel polarization (*EV*) is defined by *E* (Electric Vector) being contained within a vertical plane parallel to the plane of incidence (Baker et al., 2007). Perpendicular broadside to survey direction (PR-BD) is designed to collect *EH* polarization data, it is the most commonly used antenna orientation as its elliptical Fresnel zone is inline with the line surveyed (Baker et al., 2007). Parallel broadside (PL-BD) is designed to collect *EV* polarization data, its Fresnel zone runs across the survey line and is more susceptible to noise from features adjacent to it (Baker et al., 2007), however, it has been recommended by van Overmeeren (1994) for water table detection. Cross polarization (XPOL) is designed to collect both *EH* and *EV* polarization data. Two test sites on exposures in gravel pits in an esker ridge and in glaciodeltaic sediments have been surveyed to select the preferred antenna orientation by using the three types of antenna deployment presented in Figure 3.21. PR-BD provided the best results and has been consistently used for this thesis. Further details are presented in Chapter 5.

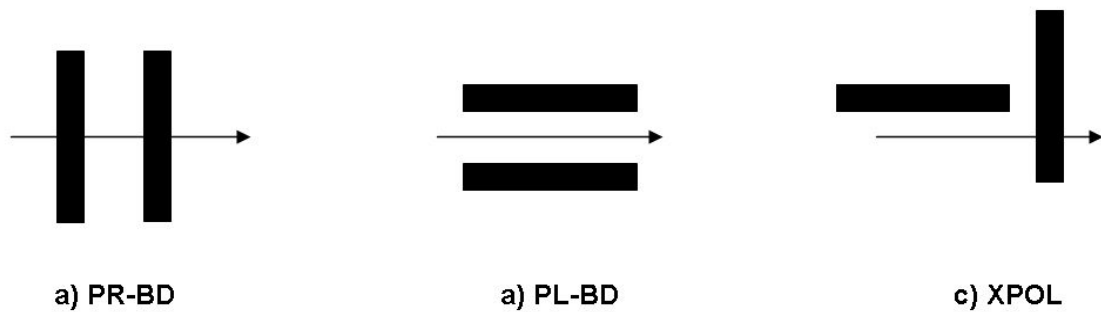


Figure 3.21 – Three types of antenna deployment: (a) PR-BD – Perpendicular broadside, (b) PL-BD – Parallel broadside and (c) X-POL – Cross polarization. Arrow indicates survey direction.

Topography has to be recorded and added to the recorded profile in order to correctly position the subsurface reflectors to properly interpret the data. The 10m spatial resolution DEM for the study area has been used to collect elevation data along the surveyed lines at 10m intervals. The elevation data has been added to the profiles subsequent to data processing and before the final interpretation.

Some GPR profiles gathered for this thesis cut across each other in order to produce fence diagrams for interpretation. Moreover, a 3D data block for a small rectangular area 30m long by 20m wide has been surveyed within Site S1 where electrical resistivity data had been previously gathered. 102 lines were collected using the step data collection mode and the 200 MHz antenna frequency to produce the 3D model. 41 parallel lines 30m long with a 0.5m separation have been surveyed in a south to north direction; furthermore, 61 lines (20m long separation 0.5m) have been collected at right angles. Two CMP surveys have been carried out within the 3D block in order to evaluate changes of velocity with depth.

3.4.4 – Data Processing

Data processing techniques for GPR data have been mainly derived from methods previously applied for seismic reflection studies. Software for seismic data processing has frequently been adapted for GPR data manipulation (Jol and Bristow, 2003). The software EkkoView and EkkoView Deluxe have been used to organize and process the GPR data gathered for this project. The characteristics and functions of the applications, filters and gains available in this software for data processing are presented below. The software EkkoMapper3 has been used for processing data collected along parallel lines and for the display of time/depth slice maps. Voxler software has been used to produce a 3D model. All GPR data were subjected to a range of processing procedures such as different gains, filters, background removal, instantaneous phase/frequency and absolute amplitude as some subsurface features only become apparent when specific processing is applied. In addition, migrated and non-migrated radargrams were analysed. Interpretation of radar sections are based on all processing, though not all processed radar data are shown in the

thesis. In addition, in some instances two or three different radargrams taken along one line have been merged into a single dataset. Velocity correction has been applied to the datasets where a CMP survey had been performed.

Processing techniques can be categorized as data correction, gains and filters. Three types of data correction have been identified by Neal (2004), time zero adjustment, dewow and topographic correction.

A time delay in the first arrival is usually recorded due to the distance between the transmitter and the receiver. EkkoView DeLuxe allows the amplitude of individual GPR traces to be displayed showing the position of time zero. Time zero has to be adjusted to the first break of the trace in order to yield a correct calculation of velocities (Figure 3.22). All other traces are automatically referenced to it. Moreover, misalignment of the first break of the wave received may occur when working in extreme conditions or due to technical problems with the system (Sensors and Software, 1999), this did not occur during this research. However, when individual radargrams were examined, it was found that the time zero position sometimes varied. The time zero for these lines were standardised before they were employed in the production of time/depth slices.

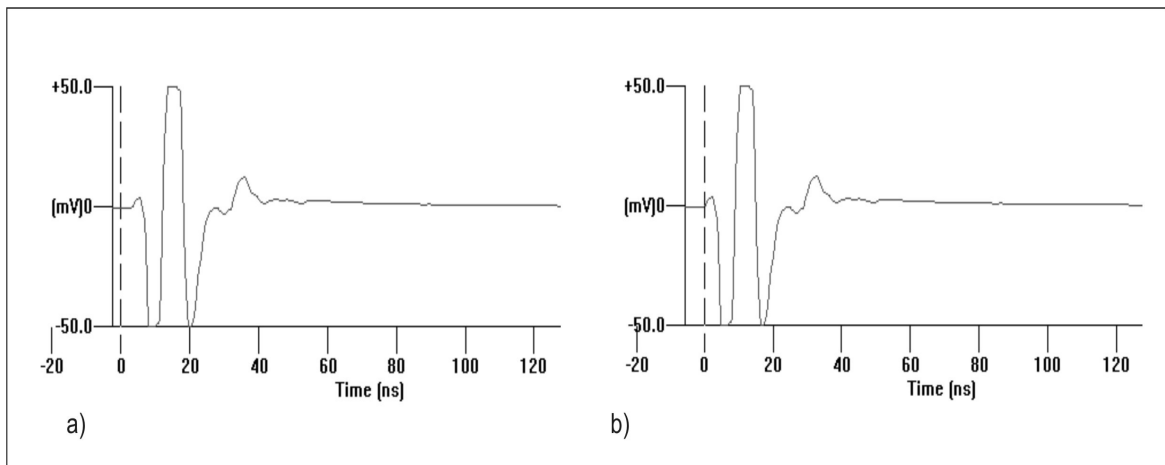


Figure 3.22 – Time Zero adjustment. (a) Shows the plot of a trace prior to Time Zero adjustment. Time Zero has been adjusted for the same trace in (b) by setting it to the first break.

GPR data have a low frequency component that diffuses into the subsurface instead of propagating through it. This produces low frequency signal saturation (“wow”) of the collected data. In order to remove it, EkkoView DeLuxe uses a high pass filter (Dewow) which is run on each trace individually. The filter applied to the data permits the centre frequency to pass with fidelity while suppressing the low frequency “wow” (Sensors and Software, 2001). This processing step is a standard procedure for all GPR data.

Topographic correction is performed at the end of the data processing procedure. This is performed in an automatic manner by the software EkkoView DeLuxe, by assigning an elevation value to a number of traces along the line. This correction has not been applied where the profile has been collected on relatively flat lying ground.

Attenuation of the radar signal is quite variable depending on the nature of the subsurface. However, an exponential decay of the radar signal occurs with time (depth). Therefore, reflectors at depth will yield a weak signal, as less energy is available for reflection, producing small amplitudes compared to the shallower reflectors. The equalization of the radar signal is attained by the application of time gain functions to the radargram. A number of gains available in the EkkoView software and described below were employed during processing.

A Constant Gain consists of multiplying all the amplitude values by a constant. This enhances the response obtained equally through all the profile. Use of a large number can mask the detail for shallow reflectors (due to saturation as they had an initial high amplitude), while use of a small number may be insufficient to reveal weak reflectors at large depth. However, the relative amplitude signal is preserved for the radar profile.

Autogain uses the average decaying curve function of the radar signal strength to calculate a tailored gain to the data collected. It provides a good result for profiles where subsurface conditions are relatively homogeneous. However, it tends to overestimate or underestimate gain values when localized changes occur.

Automatic Gain Control (AGC) applies a function to each trace that is inversely proportional to the signal strength for each reflector, a maximum value is applied to avoid very large gains. This emphasise weak reflectors in the deeper areas and subdues stronger reflectors at shallow depths and tends to equalise the response for the full depth range. However, it does not show the relative signal strength of the displayed reflectors.

Spherical and Exponential Gain Compensation (SEC) estimates the velocity and attenuation of energy through the ground and aims to compensate for the spherical spreading and the exponential energy dissipation. This is performed by applying an exponential function to the data, increasing with time. The steepness of the curve is dependent on a selected attenuation value. The curve is capped with a chosen maximum value as in the AGC gain.

The gains described have been applied to a previously “dewowed” profile collected in Site S5 (Figure 3.23). The results for the profile with no gain applied are very poor. Virtually nothing from depth can be determined. Similar results are achieved by applying Autogain and a Constant Gain using a value of 100. The AGC and SEC gains show the best results. Most of the reflectors in the profile are depicted and slightly better resolution is attained with the AGC. Although, the relative reflector strength is lost by using this method, by viewing the dataset with another method (SEC), the reflectors can be categorized by their strength. Furthermore, it has to be taken in account that although the use of gains amplifies reflectors in the subsurface, it also amplifies systematic noise or reflections from surface features.

AGC is the gain mainly used for display purposes this thesis, as it generally provides a better delineation of the reflectors, though all datasets were analysed using a range of gains. SEC has been applied to radargrams where time depth/slice analysis has been performed, since it preserves the relative amplitude strength, which is lost when an AGC gain is applied to a dataset.

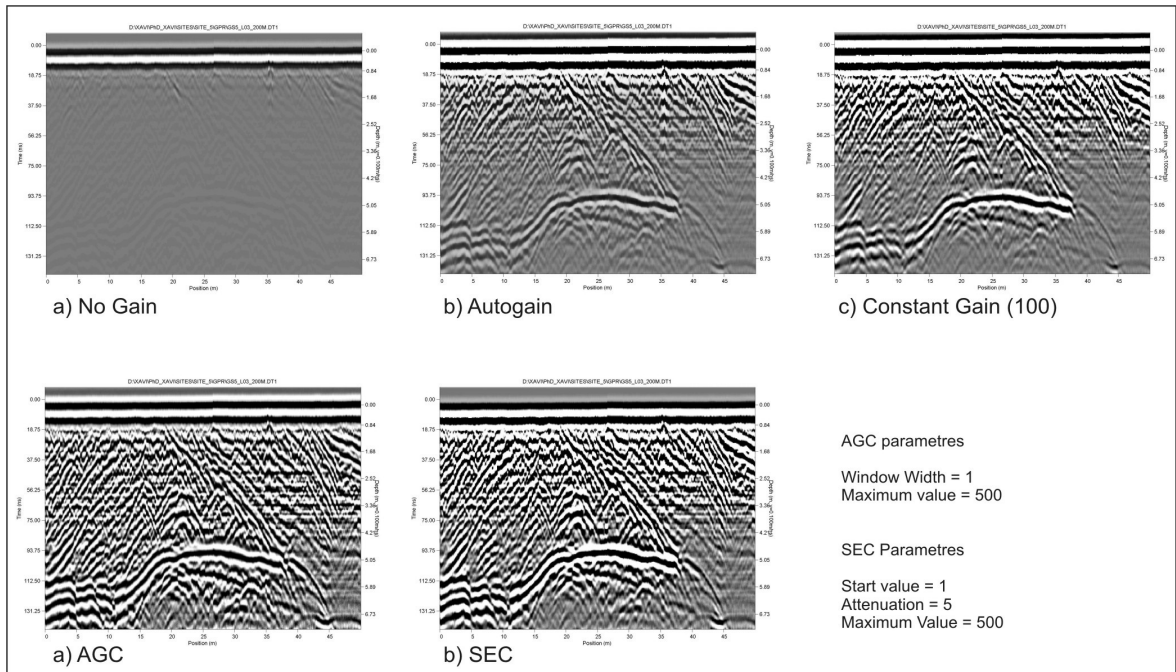


Figure 3.23 – Difference shown for a radagram subsequent to the application of a number of gains. Radagram has been previously dewowed.

The use of time and spatial filters is recommended by Jol and Bristow (2003) and a number of these are available in EkkoView DeLuxe. Time filters are applied to each trace individually, whereas spatial filters use adjacent traces to enhance or eliminate certain features (Sensors and Software, 2003). Time filters alter the shape of every individual trace. A band pass filter lets through the portion of the spectrum that is needed to enhance a particular feature and filters out the noise in the profile. Low pass frequency preserve low frequencies in the dataset filtering out high frequencies in the trace. Conversely, high pass filter eliminates unwanted low frequencies. Spatial filters use adjacent traces to emphasize the wanted spatial variations. Horizontal filter consists of producing a trace from the average of the neighbouring ones. This enhances the continuity of horizontal or low angle reflectors and eliminates highly dipping reflectors. On the other hand, applying a trace difference filter emphasises the local rapidly dipping reflectors by subtracting the trace analysed from the previous one (Sensors and Software, 2003). Background subtraction uses a window to create an average trace value which is subtracted from the window centre trace. The operation is repeated for all traces, and it tends to emphasize deviations from the norm. The use of these filters has to be applied carefully as they reduce the horizontal and vertical resolution of the profile. Some of the filters described applied to a unique dataset

are presented in Figure 3.24. A loss of resolution often occurs with application of filters. The use of several filters to look at the data can augment the number of subsurface features depicted.

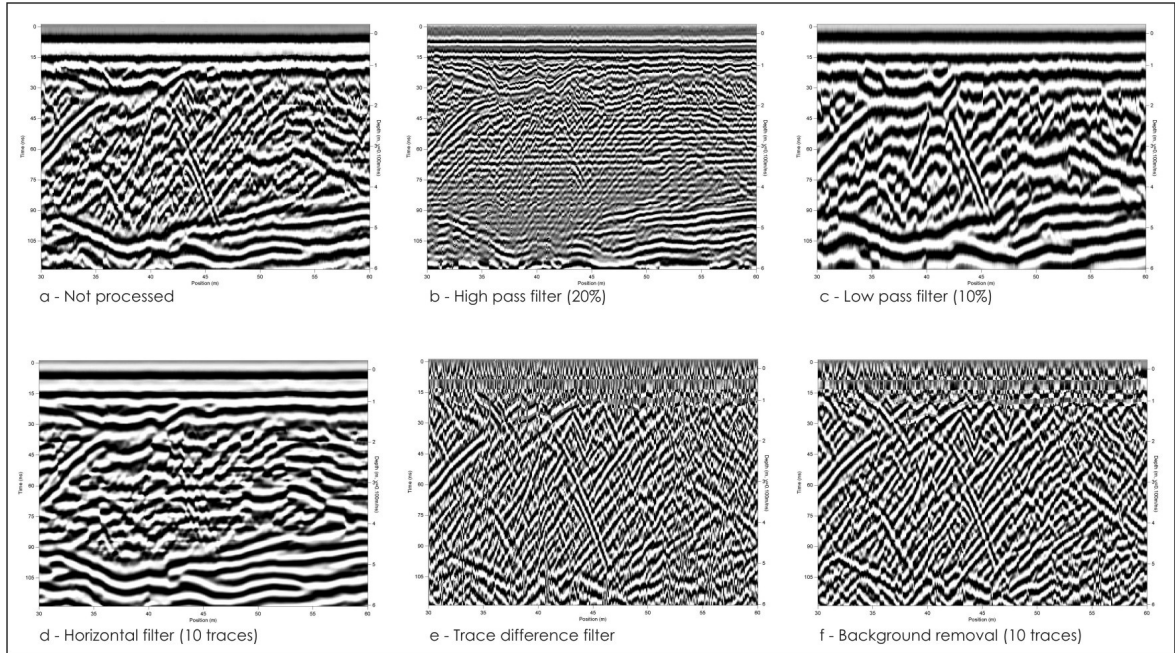


Figure 3.24 – Difference shown for a radagram subsequent to the application of a number of filters. Radagram has been previously dewowed.

Migration is widely used as a processing technique in sedimentological studies. It is a filtering process that attempts to remove distortions within the dataset derived from energy reflected from features that are outside the profile surveyed, as the energy radiated from the transmitter propagates as a 3D cone. The aim of this process is to achieve an image that represents a geological profile through the ground along the surveyed line. A number of distortions usually occur to features frequently encountered in the subsurface.

The dip of oblique recorded reflectors, such as foresets in deltaic sediments, is generally underestimated and has to be subsequently corrected. The presence of isolated point features, for instance buried boulders, is usually recorded as hyperbolae (Figure 3.25). The shape of the hyperbola can be used to estimate the velocity of propagation of the EM waves within the surrounding sediments, the narrower the hyperbolae the slower is the velocity. Channel features produce a number of reflectors, depending on the complexity of

the bedding, which do not represent the feature in the subsurface, for example a “bow-tie” pattern Neal (2004), see Figure 5.18 in Chapter 5. Reflections from the flanks and the base of the channel may result in three different reflectors. Migration of the data using the appropriate velocity collapses hyperbolic reflections, corrects the displacement of continuous dipping reflectors and enhances continuity of horizontal and dipping reflectors. Figure 3.26 shows the difference between a non migrated GPR section and the same profile following migration. Continuity of horizontal and oblique reflectors is enhanced, a large number of hyperbolic reflections have collapsed subsequent to migration. Migration has been applied to most of the profiles for this thesis. However hyperbolic reflections are often related to the presence of boulders in the subsurface, which is indicative of some sedimentological settings (e.g. push moraine). Under these circumstances the profiles presented have not been migrated.

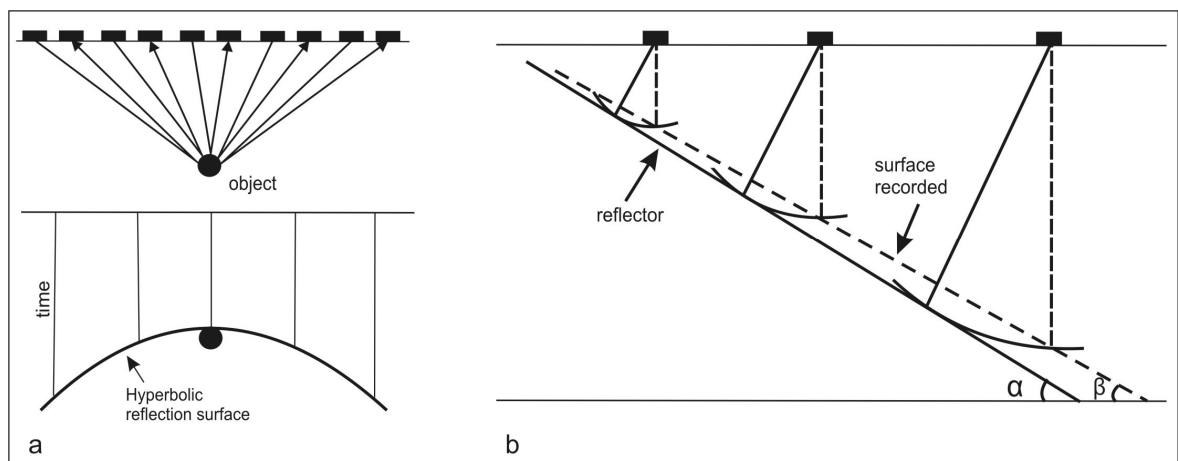


Figure 3.25 – (a) Hyperbolic reflection from point features and (b) angle underestimation of continuous dipping reflectors are common occurrences within GPR radargrams. Hyperbolae can be collapsed and dip angle corrected by migrating the dataset using the adequate velocity.

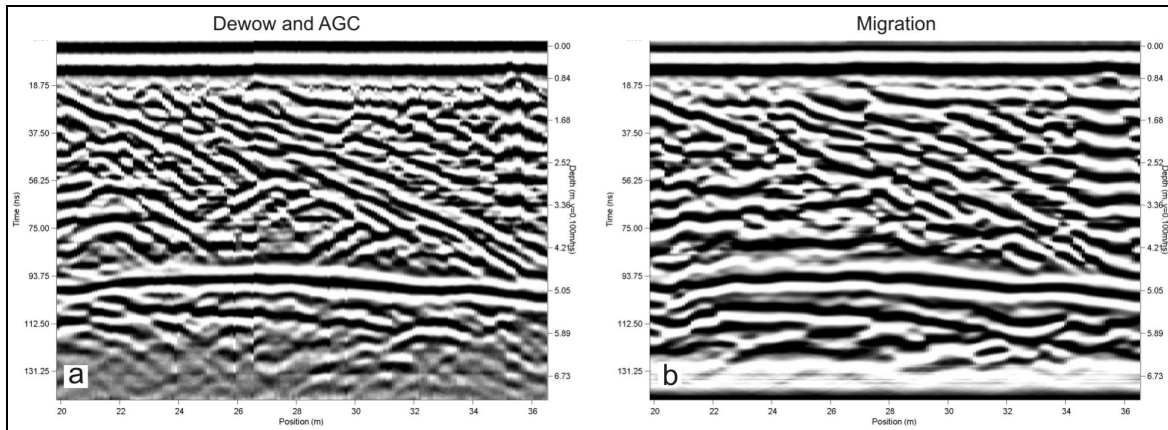


Figure 3.26 – Result obtained following data processing a) Dewow and AGC and b) same profile after migration.

Envelope is a processing technique that converts all the negative wavelets to positive values within each trace of a profile. This technique is useful for time/depth slices amplitude analysis, see Section 3.4.5. Slices are generated by averaging amplitude values in thickness range. Data have to be enveloped; otherwise, the existing positive and negative values in the trace may cancel each other out, producing misleading amplitude values (Sensors and Software, 2007).

The methodology followed for data processing varied depending on the type of feature analysed. However, there is a set of fixed initial steps that has been applied to all the files recorded for this thesis. The final steps vary, depending on the basis of the information required from the radargrams. The methodology has been derived from reviewed literature, mainly Neal (2004) and Jol and Bristow (2003). A flow diagram indicating the data processing steps followed to generate the radargrams prepared for data interpretation is presented in Figure 3.27. Most of the data have been systematically processed using this methodology. In some instances, slight variations of this methodology have been applied to a number of radargrams in order to improve their interpretation. These variations are described in Chapter 6 while presenting the radargrams on a case by case basis.

A 3D Model has been produced for Site S1, the data processing and display involves three different software packages. GFP Edit software is used to organize the profiles collected to produce the 3D Model, Ekko Mapper 3 software is used to process, view and export the

data into 3D format. Finally, Voxler software permits to display the data as a 3D view, as fence diagrams or isosurfaces. These will be presented in further detail in Chapter 6.

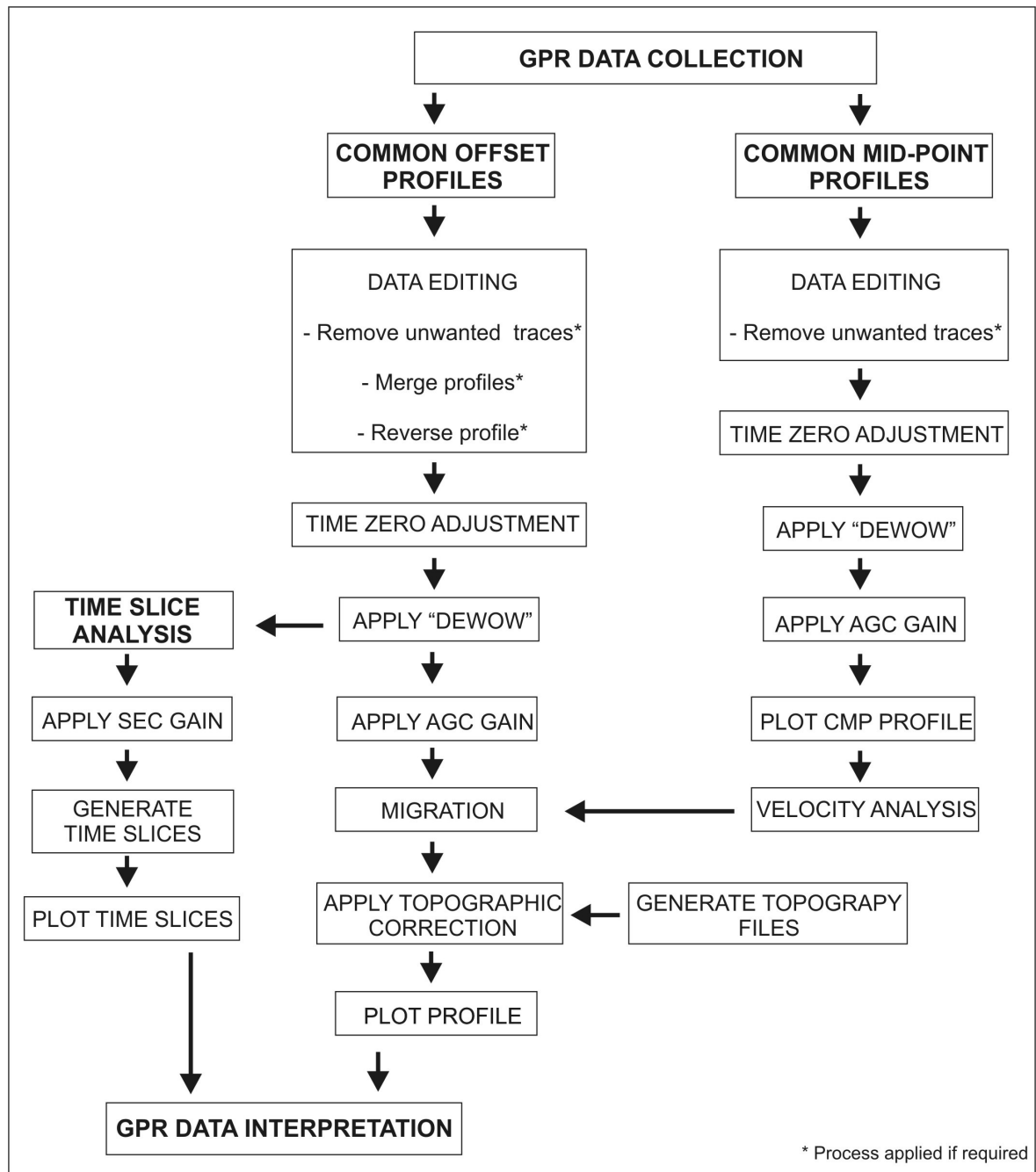


Figure 3.27 – Flow diagram illustrating the steps followed from data collection to data interpretation, emphasising the steps followed for data processing.

3.4.5 – Time/Depth Slices

The conventional method for displaying radargrams is as black and white (or colour) images such as shown in Figure 3.24. However, a substantial amount of detailed information may be lost by this approach. A different way to plot GPR data is by the production of time/depth slices. Time slice analysis consists of plotting the amplitude values of a radargram for a selected time range. The amplitude values along this time range are averaged or summed for each trace, thus a unique amplitude value for each trace is obtained for the selected time range and the data can be plotted as a line showing changes of amplitude along the profile. The data are previously normalised using the envelope processing technique presented in Section 3.4.4 by converting all negative values to positive.

Figure 3.28 shows an example of 200MHz, 100m length radargram analysed by means of Time Slice Analysis using three time ranges: 0 - 50ns, 50 - 100ns and 100 - 150ns. Three situations are presented: 1) not processed dataset, 2) the dataset after AGC gain plus migration and 3) following SEC gain plus migration. Large differences can be observed in the non-processed dataset from 0 - 50ns time range compared to the lower ones, presenting values almost an order of magnitude larger, the use of a gain improves the visualization of the data. The relative amplitude values are lost when applying an AGC gain to the data, which means that they can not be related to lithological changes as the amplitude is distorted by the gain. On the other hand the SEC gain preserves the relative amplitude through the profile, therefore, the SEC gain has been selected for this thesis. Following data processing, the three time slices range within amplitude values from 5000 - 30000. The large variations occurring along the x axis for each time slice can be correlated to lithological changes along the profile at different levels. Higher amplitude correlates with sediments with a high reflectivity, low attenuation of the EM waves. Regions with fine or saturated sediments will respond with large attenuation values of the EM waves producing less reflectivity, yielding lower amplitudes expressed in the graph. A number of time ranges can be tested in a single profile in order to obtain data at different levels of detail, a combination of all time slices greatly aids the interpretation of the data collected.

Time Slice Analysis

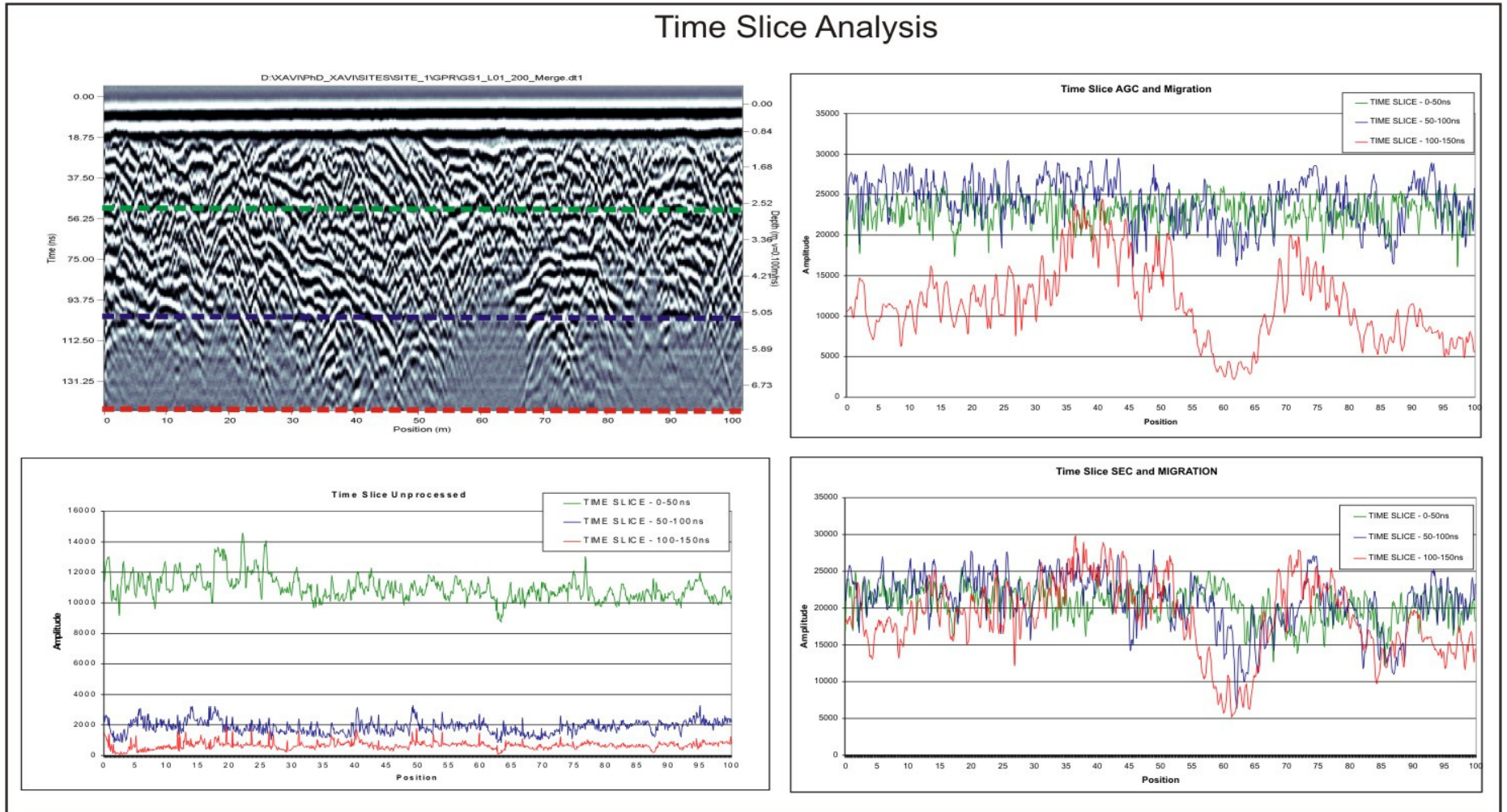


Figure 3.28 – Time/Depth slice analysis on 200MHz GPR dataset using a 50ns time range. Slice analysis is presented for the radagram prior to processing (bottom left), after processing by means of an AGC Gain + Migration (top right) and after processing with a SEC Gain + Migration (bottom right).

The amplitude data shown in Figure 3.28 is for a single radargram. However, if the same time slices are applied to a number of parallel radargram, then a series of 2D amplitude slices at different depths for an area can be constructed. Time slice analysis is widely used in the display and interpretation of 3D models. Ekko Mapper software allows the user to construct and plot time/depth slices for selected ranges of time or depth as colour maps indicating the amplitude values varying across the subsurface. An example of this is presented in Chapter 6 for a 3D dataset collected in Site S1.

3.4.6 – Data Interpretation

As mentioned earlier, GPR data interpretation has been mainly derived from the principles of seismic stratigraphy. The development of a systematic methodology for the interpretation of seismic data was undertaken by the petroleum industry from the 1970s. This was subsequently adapted for GPR data interpretation by Gawthorpe et al. (1993) and other authors (Baker, 1991 and Jol and Smith, 1991), who also defined the relationship between the seismic stratigraphy and the new concept of radar stratigraphy.

Radar stratigraphy has been developed through the 1990s. Neal et al. (2002) introduce and define the concepts of radar surfaces, radar packages and radar facies, which have been commonly used in the literature since then. The terminology used for GPR data interpretation for this thesis is derived from Neal (2004) and is presented graphically in Figure 3.29. The reflections presented by radargrams are described by their shape, dip, relationship to each other and continuity.

Neal (2004) presents a code format for radar surfaces and radar facies that allows the creation of a relative chronology within each radargram as well as with adjacent ones. It differentiates between radar surfaces and radar facies with subgroups for each category (Figure 3.30). The coding format has been adapted and modified for this research by adding a number of sedimentological and structural codes not contemplated in Neal's

coding scheme. The coding scheme attempts to represent the potential situations presented by glacial, glaciofluvial, glaciolacustrine and postglacial sediments existing in the study area.

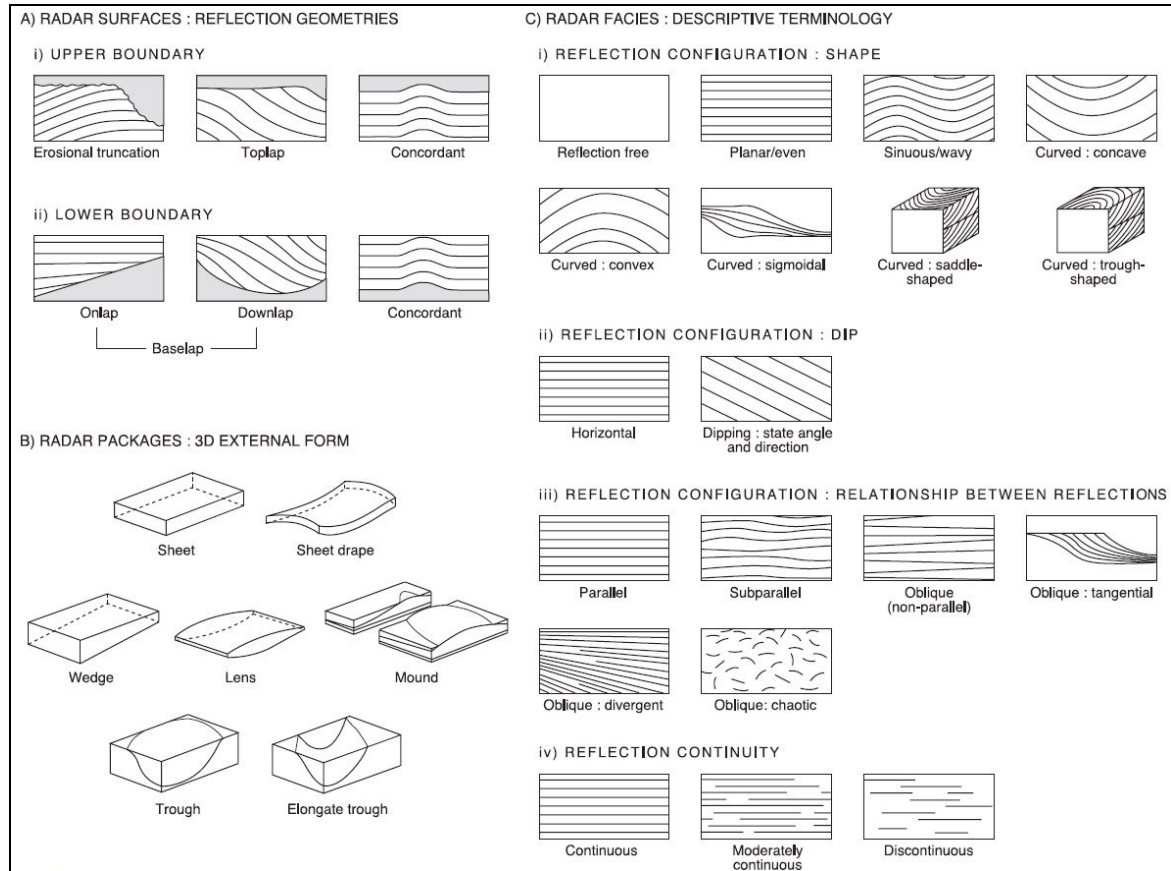


Figure 3.29 – Terminology for description of radar surfaces, radar packages and radar facies, from Neal (2004).

The existence of numerous reflectors within the profiles that are not directly related to sediment deposition (e.g. water table, faulting, folding, hyperbolae derived from point features, noise...) has forced the production of a terminology for the characterization of these reflectors. These have been described by their shape, dip and continuity. However, the coding system differentiates them from the interpreted sedimentological bounding surfaces (Figure 3.30).

Subsequent to the systematic description of the radar surfaces and radar facies within a radargram, its sedimentological interpretation is presented, supported by borehole data or exposure description (when available), morphological data, time slice analysis and knowledge of the regional geology.

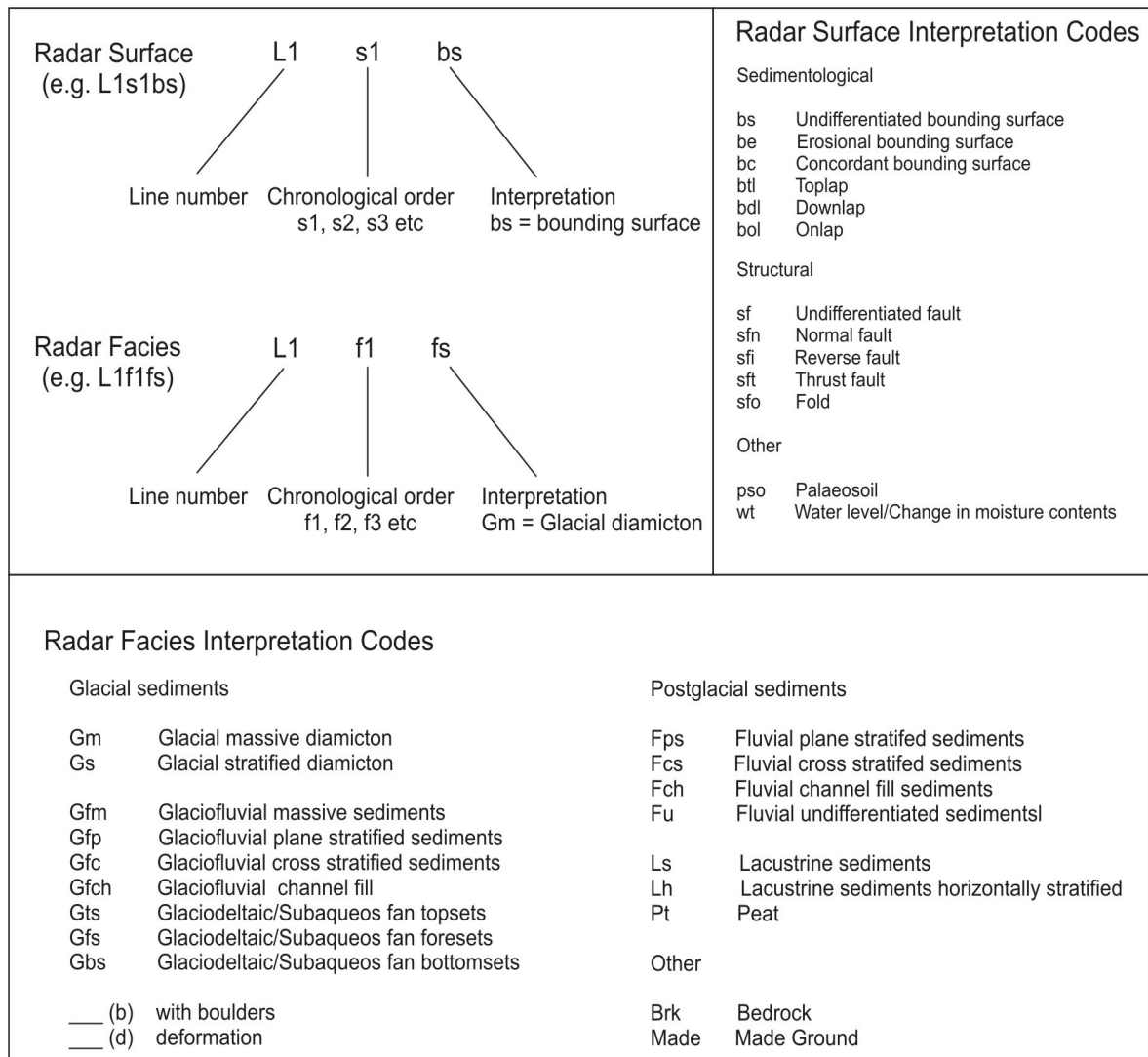


Figure 3.30 – Code format for radar surfaces and radar facies, modified from Neal (2004). Radar surfaces/facies interpretation coding scheme used for this thesis.

3.5 – Electromagnetic Very Low Frequency (VLF)

Electromagnetic waves broadcast by military stations within a frequency range of 15 - 30 KHz and derived secondary waves formed from the interaction of these waves with the subsurface are sensed by Very Low Frequency (VLF) systems. Such systems have been used for the detection of geological structures within the shallow subsurface (Soocochof, 1979; Beamish, 1998 and 2000; Jeng et al., 2004; Oskooi and Pedersen, 2005 and 2006). VLF is a low cost, light and easy to operate instrument which makes it a suitable tool for affordable and quick reconnaissance of the shallow subsurface (Monteiro Santos et al., 2006). Depth of investigations reaches a maximum of about 100m (Oskooi and Pedersen, 2005) in highly resistive subsurface and 4 - 5m in conductive ground (Northwest Geophysical Associates, 2000). A good knowledge of the subsurface structures being mapped is necessary; measurements recorded depend on the shape and disposition of the subsurface elements mapped and the direction of the transmitter (Oskooi and Pedersen, 2005).

An Abem Wadi VLF system has been used for this thesis (Plate 3.1). It consists of a portable system mounted on a belt, which is worn by the operator. It is composed of four components:

- A handheld microcomputer for data storage composed of a monitor and a customized keyboard.
- A measuring unit containing the radio receiver and batteries to power the system
- An antenna unit composed of an antenna reading data from the horizontal field and a second one sensing the vertical field.
- An in-built digital inclinometer that informs the operator that the reading is collected within a narrow range from the vertical.

Prior to data collection, the closest station with the most powerful signal is automatically detected by the system. The closest stations to the research area are in the UK, the station located in Anthorn (GBZ = 19.6 KHz), was the one used for this thesis. The system measures the ratio of the strength between the vertical: horizontal magnetic fields. The operator has to travel along a line in the direction of the surveyed structure or feature and if

possible towards the broadcasting antenna. The Anthorn antenna is located approximately in a northeast direction from the study area. Data are collected at regular intervals along the line. A number of lines over 300m long with a reading taken every 10m were recorded.



Plate 3.1 – Abem Wadi VLF system used for this thesis.

Two readings are collected for each point, the raw in-phase value (RR) records the ratio between the primary field and the secondary field in phase with it (Figure 3.31), anomalies in the subsurface will be indicated by changes in the RR value. A second reading is the raw out-of-phase imaginary (RI) value, which records the phase displacement with the primary field. Data are presented in graphical format with the distance of the profile on the X-axis and % variation along the Y-axis. Filtering of the data are recommended before plotting, as the profiles obtained are usually asymmetric and changes are difficult to relate to anomalies in the subsurface (Gibson and George, 2004). The Wadi system uses a filtering method developed by Karous and Hjeltdt (1983) consisting of a linear average of the three readings at either side of the filtered one. Filtered data are also plotted, filtered real (FR) and filtered imaginary (FI) provide a more accurate location of the structure or feature mapped. After data filtering, the percentage variation recorded will be situated over the subsurface structure that caused it.

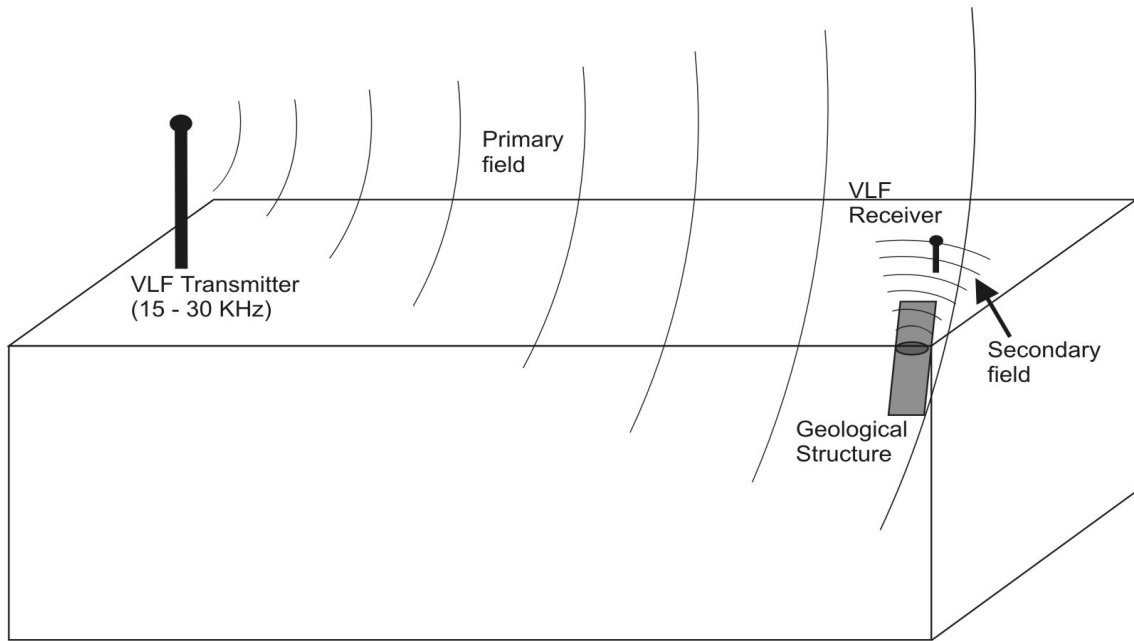


Figure 3.31 – VLF transmitter broadcasts a primary field. A secondary field is generated when a conductor (e.g. geological structure) is encountered. Both fields are sensed by the VLF receiver and the distortion from one another is calculated. Larger anomalies are recorded where conductor detected strikes in the direction of an imaginary line between the transmitter and the receiver.

Data collected have been interpreted using both, the raw and the filtered data. Weak conductors suggest the presence of fractures conducting groundwater (George and Gibson, 2000) or low resistivity sediments (saturated silts and clays). On the other hand, high conductivity may be related to presence of ore bodies. The interpretational software for VLF data is fairly limited, which restricts the capacity to extract further information from the collected data.

3.6 – Summary

A broad range of conventional geological mapping techniques including desktop compilation, use of DEM applied to morphological mapping, exposure data recording and sampling, drilling methods and laboratory sample analysis including particle size distribution and petrographic analysis have been presented and discussed in this chapter. Furthermore, the use of a geostatistical analysis method for the production of a depth to bedrock map is also described and proposed.

The three geophysical techniques used for this thesis are Electrical Resistivity (ER), Ground Penetrating Radar (GPR) and Very Low Frequency Electromagnetics (VLF). The theoretical background for each of these methods has been presented and discussed. Moreover, a systematic methodology for data collection, data processing and data interpretation has been established for ER and GPR.

ER methods used encompass a number of techniques. Electrical Resistivity Tomography (ERT) consists of a number of electrodes that are inserted into the ground at equalled spaced intervals along a survey line providing a vertical 2D section of the subsurface as a final result. 3D models can be generated from 2D parallel profiles, the production of 3D datasets has been presented and discussed. Time-lapse resistivity data collection, consisting of the collection of a unique survey line at different time, and the processing techniques used for this type of datasets has been introduced. Finally, the azimuthal resistivity data collection method consisting of collection of point data along a number of directions is presented and its potential for soft sediment mapping is considered.

GPR data can be presented in different formats. Data collected can be presented as topographically corrected 2D subsurface profiles along the survey line or as 3D models when data are collected in grid format. The two methods were discussed and compared as well as a broad range of processing techniques applicable to these datasets. Furthermore, a methodology is presented, discussed and established for time/depth slice analysis, for both 2D and 3D datasets. The relevant processing steps have been set out on a methodology flow chart for a precise interpretation of the generated dataset.

The survey data collection procedure for VLF and basic theoretical background is presented. The processing and interpretation techniques for the data collected are shown.

The use of the geophysical techniques together with the more conventional soft sediment mapping techniques can greatly improve the efficiency and accuracy of the interpretation of geology data and aid on the reconstruction of an accurate model glaciation and deglaciation in the research area.

CHAPTER 4

Results of Geological Mapping

4.1 - Introduction

The results of the desk compilation, field mapping and laboratory testing have been compiled and are presented below. The research area has been divided into four main physiographic units. These are regions within the study area with comparatively homogeneous landscape characteristics. The mapping results are presented separately for each unit in three sections.

Firstly, a number of characteristics of the physiographic units are presented: the area covered for each unit, their topographic expression and the main features that characterize them. Secondly, the Quaternary Geology for each physiographic unit is described in detail. The description of key geomorphological features or exposures occurring in the region is presented, discussed and their genesis interpreted. The spatial distribution of sediments is presented in Map 1 (enclosed with thesis). Thirdly, the results obtained from laboratory testing for samples collected during field mapping sampling and borehole drilling are presented. The samples collected were described by the author. Moreover, particle size distribution analysis results carried out by Metlab Ltd. and petrography analysis results carried out by the author are presented and discussed. In addition, the results of a depth to bedrock map produced using geostatistical analysis for the research area are presented in Map 2, (enclosed with thesis). Results obtained show the estimated soft sediments thickness and the volume of sediments deposited during the Quaternary in the study area.

4.2 – Physiographic Units

Previous to field mapping, the study area was subdivided by the author into four physiographic units with specific landscape characteristics based on geomorphology, geology, land use and vegetation. These are:

- The Shannon Basin esker-dominated landscape
- The Shannon - East Basin watershed area
- The East Basin
- The Brosna River Basin

The area covered by each unit and the location of the main towns, roads and other geographical features referred to in this thesis are presented in Figure 4.1 and the spatial distribution of main eskers systems shown in Figure 4.2. A brief account of the main characteristics and the dominant landforms occurring in each physiographic unit is presented below.

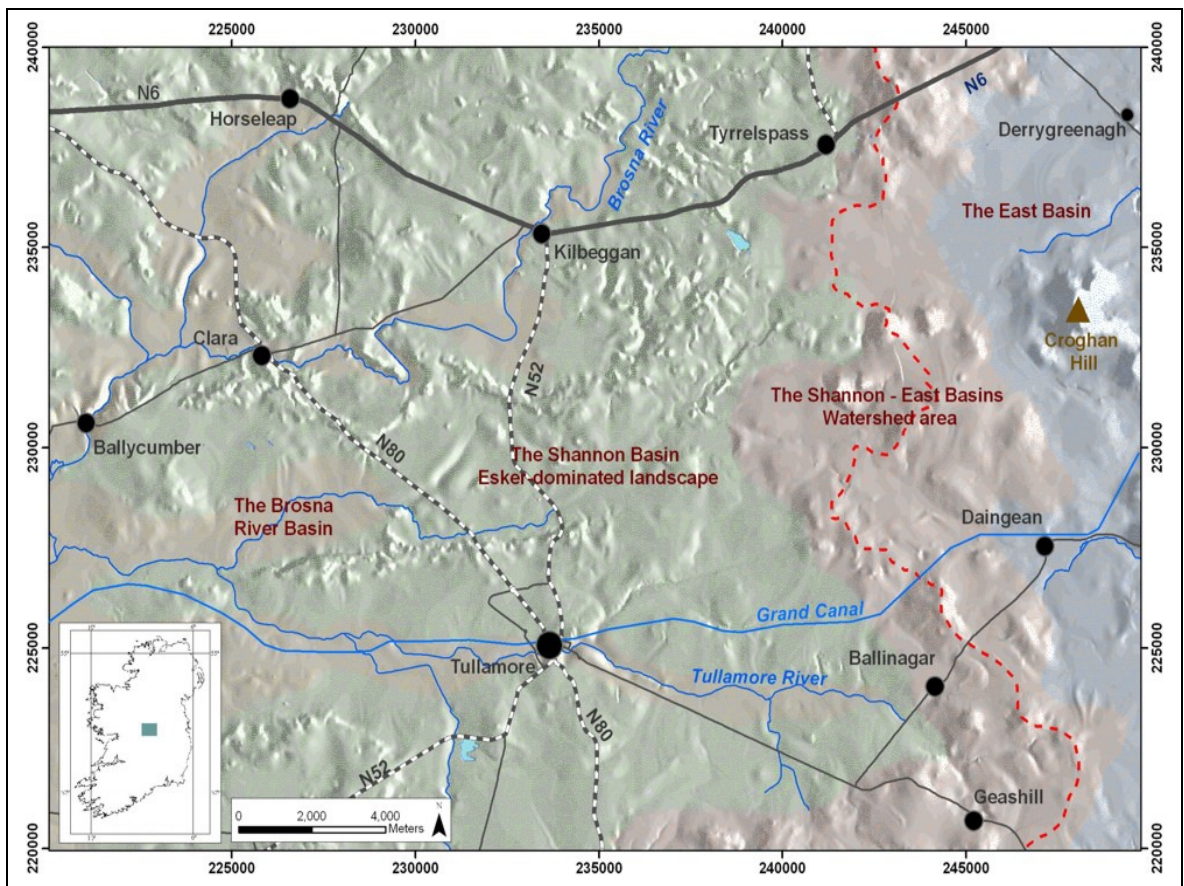


Figure 4.1 – Distribution of physiographic units for the research area. Dashed line in red indicates location of watershed between the Shannon and the Boyne/Barrow Basins.

4.2.1 - The Shannon Basin esker-dominated landscape

This physiographic unit covers just over 320 Km² and is mainly dominated by esker ridges running east to west and northeast to southwest. Some small hills related to ancient reef forms occur where Waulsortian Limestone outcrops. Four main esker complexes dominate the topography within the area and from south to north are: Ballyduff Esker, Clara Esker, Split Hill Esker (Plate 4.1) and Moate Esker. These features started forming in a small area southeast from Kilbeggan along the east margin of the Shannon Basin and spread west, southwest and northwest from this point (Ashley and Warren, 1995). They range between 10 - 30 metres in height and 50 - 500 metres in width. The surrounding landscape often exhibits kame and kettle topography, which develops on glaciofluvial sediments associated with ice front deposition or esker development. Other areas, with gently undulating ground, are usually dominated by till (boulder clay) with some very gentle ridges being interpreted as rogen moraines (Clark and Meehan, 2001; Greenwood and Clark, 2008). Postglacial sediments such as raised peat bog and lacustrine sediments have developed in former glacial lake basins and these are generally underlain by diamicton and by well-sorted sediments in places.



Plate 4.1 - Esker ridge forming part of Split Hill Esker complex. The photograph has been taken at (232560E, 238641N).

A significant feature in this area is a glaciolacustrine fan/delta associated with the Kilcormac Esker at its eastern end. The Kilcormac Esker is a narrow, continuous ridge, symmetrical in cross-section, which terminates in a spread of horizontally bedded gravel. The gravel spread has a frontal slope 18 - 25 metres above the surrounding landscape and extends for more than 1.6 Km in length in a north easterly direction (Farrington and Synge 1970). The feature has a maximum altitude of over 80 metres OD, agreeing with the lowest levels of the meltwater channels occurring in the eastern Shannon Basin watershed.

4.2.2 - The Shannon - East Basin watershed area

The watershed area covers an area of just over 110 Km² and stretches in a narrow band along the watershed divide between the Shannon Basin and the Boyne/Barrow Basins. The Boyne/Barrow Basins are treated as a unique entity and it will be referred to as the East Basin from this point forward. Subglacial sediments and raised bog dominate the landscape. The topography gradually drops in height from north to south reaching its lowest watershed pass at 84.5 metres OD 3 Km west of Daingean. A number of channels cutting across the watershed have been recognized during field mapping for this thesis in the slightly more elevated landscape between the Shannon and East Basins and have been interpreted as meltwater channels. Some examples of these features occur southeast of Geashill along the Tullamore to Portarlinton Road running south-eastwards and south of Ballinagar running north-eastwards, see Plate 4.2.



Plate 4.2 – Meltwater channel running north-eastwards across the watershed between the Shannon and the Barrow River Basins. The feature occurs 2 Km south of Ballinagar. Arrow indicates former meltwater direction.

These channels were shaped by glacial meltwater flowing eastward from the decaying ice sheet to the west during the closing stages of the last glaciation and lie between 80 - 100 metres above OD. Several channels have been identified from Geashill to south of Tyrrelspass. The landscape is, in the main, gently undulating and underlain by diamicton. Several limestone bedrock outcrops are located on the higher ground and a number of large raised bogs extend from the lower parts of the watershed.

4.2.3 - The East Basin

This region covers less than 70 Km² and is dominated by raised peat bogs (generally cut away) often overlying extensive glaciofluvial sediments and till plains shown as gently undulating ground. Some small hills can be identified, usually associated with limestone bedrock outcrops, (Lucan Formation and Waulsortian Limestones). A small esker has been mapped east of Daingean running eastwards.

The most prominent feature in the area is Croghan Hill (Plate 4.3). This is the highest point within the study area reaching 226 meters OD. This hill has a volcanic origin and is mainly composed of basalt and tuffs and was formed during the Lower Carboniferous c.350 MA (Hitzman, 1992). Several ice-marginal (kame) terraces have been identified on its hill slope. Small hills occur where bedrock is close to the surface; these are composed of Lower Carboniferous limestone and encircled by peat chiefly underlain by diamicton.



Plate 4.3 – View of the south slope of Croghan Hill.

The area north of Croghan Hill is mainly draped by cutaway peat bog overlying lacustrine silts and clays, which are underlain by glaciofluvial sand and gravel. The glaciofluvial sediments infill depressions in the landscape, probably formed during the last glaciation, and are directly related to the meltwater channels referred to in the watershed physiographic region. A large gravel pit under cut-away peat is currently being quarried in the lowland area north of Croghan Hill.

4.2.4 - The Brosna River Basin

This unit covers just over 100 Km². The Brosna River runs south-westwards along Kilbeggan Village and southwards in the region south of Ballycumber. Flat plains covered by fine alluvial sediments, lacustrine deposits, marl and raised peat bog are the major morphological features in the area. Most of the basin is susceptible to flooding.

This area was morphologically shaped during postglacial times. The Brosna River cuts across the esker-dominated landscape at several points. Alluvial flats around the main channels are surrounded by raised bogs generally developing on lacustrine sediments deposited in shallow lake basins shaped during the last glaciation.

4.3 – Quaternary Geological Mapping Results

4.3.1 – Introduction

Three systematic mapping programs carried out in Ireland have provided datasets that have been used to identify some of the main geomorphological features in the research area.

- The six-inch Bedrock Geology maps (Geological Survey of Ireland, 1871) for Counties Westmeath and Offaly show bedrock outcrops at the surface at that time. These maps outline some of the main esker ridges cutting across the landscape, illustrate kame mounds and kettle holes and show the location of

gravel pits, which provide information on the distribution of glaciofluvial sediments in the area.

- Furthermore, the surficial glacial and postglacial deposits map for County Offaly (Warren and Hammond, 1999) at a scale of 1 inch to the mile (1:126,720) to accompany the soil survey bulletin number 43 outlines the main glacial and postglacial sediments for County Offaly.
- Finally a systematic National scale soil parent material survey was carried out by Spatial Analysis Group from Teagasc (Meehan et al., 2006). The maps are derived from 1995 black and white digital stereo-photography interpretation and previously existing maps, specifically Warren and Hammond (1999). The resulting soil parent material maps classify sediment types with similar criteria to the reconnaissance mapping classification established by the Geological Survey of Ireland.

The existence of these datasets and the literature available for the Irish Midlands facilitated the selection of sites of interest for fieldwork mapping. As mentioned earlier, the study area has been divided into four physiographic units each with distinctive geomorphological characteristics. The Quaternary geology and morphological setting in the area will be described for each of the four areas separately. Some examples of the morphological and sedimentological features dominant in the area are presented. Some of the evidence found for ice advance and retreat is also discussed within this chapter.

A total of 133 exposures were recorded in the study area as part of the field mapping exercise. Furthermore, 57 boreholes were drilled in the area to investigate regions where exposures were absent. 190 samples were collected in the field from exposures and boreholes for further analysis.

The Quaternary geological mapping results are presented in Map 1 (scale 1:40,000), which shows the dominant sediment types within 1m of the surface. Moreover, relevant morphological data, location of investigated sites, boreholes drilled and locations of

geophysical surveys are also displayed. Furthermore, particle size distribution analysis data and petrography analysis results are presented and discussed within this chapter.

4.3.2 - The Shannon Basin esker-dominated landscape area

Esker ridges are the dominant landscape features in the research area. Six main esker ridges and their associated glaciofluvial sediments have been mapped and described. Each is briefly described (from north to south) as they are important geomorphological features with a unique spatial distribution. Figure 4.2 shows the spatial distribution of the main eskers cutting across the research area. Each individual esker is described from the ice margin to the ice centre in order to be consistent with the time sequence of deposition of the features. A total of 101 exposures were visited and 34 boreholes drilled in this area as part of the field mapping exercise.

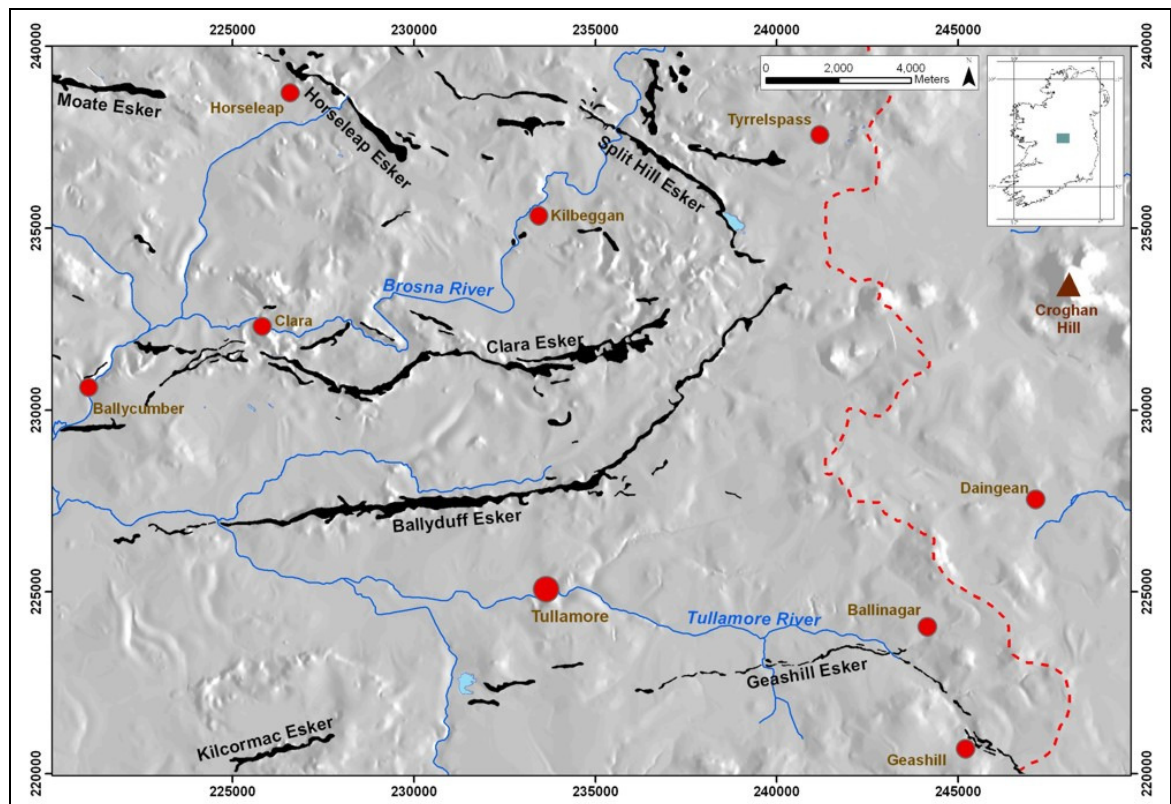


Figure 4.2 – Spatial distribution and names of the main esker ridges in study area. Dashed line in red indicates location of watershed between the Shannon and the Boyne/Barrow Basins.

Split Hill Esker starts south of Tyrrelspass at a height of 101 metres OD. It runs north-northwest gradually turning northwest towards the ice centre. The ridge can be traced on the ground for 12.5 Km. The average width is about 120m, ranging between a minimum of 50m and a maximum of 250m where the ridge is cut by the N6 road. Its relative topographic expression above the surrounding ground varies in height from 5 - 40m. Plate 4.1 shows a southeast view of the esker 4 Km north of Kilbeggan, where a sudden change in the topographic expression of the feature can be observed. The ridge reaches a maximum height of 6m above the surroundings in the foreground and in the background; the esker suddenly increases its height and width reaching heights of 20 - 30m.

Based on the classification given by Warren and Ashley (1994) and outlined in Chapter 3, the Split Hill Esker can be classified as a continuous ridge tunnel fill formed after infilling of a subglacial tunnel. Several subaqueous fans can be identified along the esker, deposited under thin ice conditions. The ice becomes so thin that the tunnel loses its competence to withstand the hydrostatic pressures causing fans to be deposited along the main esker ridge (Warren and Ashley, 1994). Some esker ridges parallel to the main feature have been mapped. They mainly consist of long and short beaded eskers, which could either represent temporal diversions of the main tunnel or independent tunnel fills contemporaneous with the main feature.

Horseleap Esker runs for 5 Km in a southeast to northwest direction, reaching a maximum height of 30 to 35 metres above the surrounding landscape north of Horseleap. It has a maximum width of 250 metres at its southeast end. The ridge starts 4 Km west of Kilbeggan as a fan shaped feature running along the national road N6 and gradually narrows towards the west. The fan shaped feature at the southeast is composed of interstratified sand and gravel and is interpreted in this thesis as glaciodeltaic sediments delivered by a meltwater subglacial conduit, which subsequently formed the esker ridge after blockage of the subglacial channel. The fan/glaciodelta reaches a maximum altitude of 92 metres OD and is probably associated with the early stages of glacial Lake Riada. A possible outlet of the glacial lake runs eastwards along a raised peat bog 1.5 Km south of Tyrrelspass. The channel is at an altitude of 93 metres OD, however, knowledge on the

thickness of the peat along the outlet may provide a better correlation with the mentioned glaciodeltaic sediments (see Chapter 6 – Site 9). The esker ridge, mainly composed of boulder and coarse gravel, runs west-north-west as a continuous tunnel fill. Caloca (2006) carried out a geophysical survey in the area within this esker north and west of Horseleap, the ridge was interpreted at this point as a complex continuous tunnel fill composed of several interconnected infilled conduits. Moreover, an isolated mound south of the main ridge has been interpreted as a kame mound, probably of subglacial genesis. A linear feature 500m wide and 1.7 Km long was identified north of the esker and trending at right angles to it. It is composed of well-sorted sand and gravel and reaches a maximum height of 92 metres OD. This is interpreted by the author as a subaqueous/subaerial ice marginal fan associated with the esker, probably indicating standstill conditions of the ice margin at this point. Farther west, the esker loses its topographic expression for 3 Km northwest from Horseleap. The esker complex extends outside the study area as a ridge starting at E224600, N240500. It runs west-northwest for 1.5Km and displays a suite of associated ridges running parallel and across the main feature. Sand and gravel has been mapped in some small exposures. It has little topographic expression reaching a maximum height of 10m above the surrounding landscape.

Moate Esker can be traced for over 10 Km from Ardnurcher (E224000, N238200) in Co. Offaly to Mountemple (E215000, N242000) located in Co. Westmeath 7 Km to the northwest, outside the study area. It runs in a west-northwest direction as a continuous tunnel fill. The feature starts at its eastern margin as an ice marginal ridge with fan shape morphological expression with flat top at 85m OD composed of interstratified sand and gravel. It reaches a maximum width of 400m at its eastern margin and gradually narrows westwards. A morainic ridge, probably associated with this feature at its maximum width is expressed topographically 2 Km south of it. This moraine runs northeast-southwest as a continuous but wide ridge. The esker extends west reaching heights of 20 - 30m above the surrounding landscape at the northwest margin of the study area; a number of exposures recorded along it show coarse to cobble gravel as the dominant lithology. The esker runs as a continuous tunnel fill 100 to 150m wide with minor changes in topography reaching maximums of 30m above the surrounding ground northwest of the study area. Plate 4.4

illustrates the morphological expression of the ridge. An exposure recorded in a gravel pit shows a long section of the esker. This has been used for the geophysical survey as one of the sites to test the resolution and penetration of ground penetrating radar (see Chapter 5, Site T2). A number of exposures within the gravel pit show a dominance of coarse gravel, cobble and boulder gravel and some deformed sand lenses derived from Lower Carboniferous limestone with the presence of calcrete in places.



Plate 4.4 – Moate Esker behaves as a symmetric continuous subglacial tunnel fill in the region north of Moate Town. The ridge reaches 8 to 10m height over the surrounding landscape and is between 80m and 100m wide.

Clara Esker is a broad undulating feature which is 100 to 500m wide in places. It has been interpreted as being composed of at least of 3 esker ridge tunnel-fills separated by large kettle holes and locally blanketed with sand and gravel (Warren and Ashley, 1994). The ridge complex runs in a southwest direction for the first 5 Km, but it gradually changes direction and runs east to west from this point. It can be traced from Sonagh (E238600, N234200) to 6 Km west of Ballycumber (E212000, N231500), it covers a total distance of 22 Km within the study area, though in some areas the ridge loses its surface expression. Kame and kettle topography has been recognized during field mapping along the ridge, especially in the region south of Clara. Glaciolacustrine sediments are present where these morphological features are dominant. Glaciolacustrine sediments were deposited after esker deposition as ice from the Northern Dome receded towards the northwest and ice from the Central Ice Dome retreated in a south-westerly direction, Glaciofluvial sediments with paleocurrents inferred from gently dipping foresets dipping 5

to 10 degrees northwards overlying the esker ridge have been recorded south of Clara Village (Figure 4.3). A large number of exposures have been recorded along the ridge and it has been interpreted as a continuous subglacial tunnel fill for 12 Km from its east margin to Clara Town. The feature loses continuity in the Ballycumber area where it is interpreted as a long bead subglacial tunnel fill. Several ridges mapped in this area (see Map 1), mainly parallel to each other and running westwards, may express a dynamic subglacial environment with tunnels being used and subsequently abandoned during ice retreat.

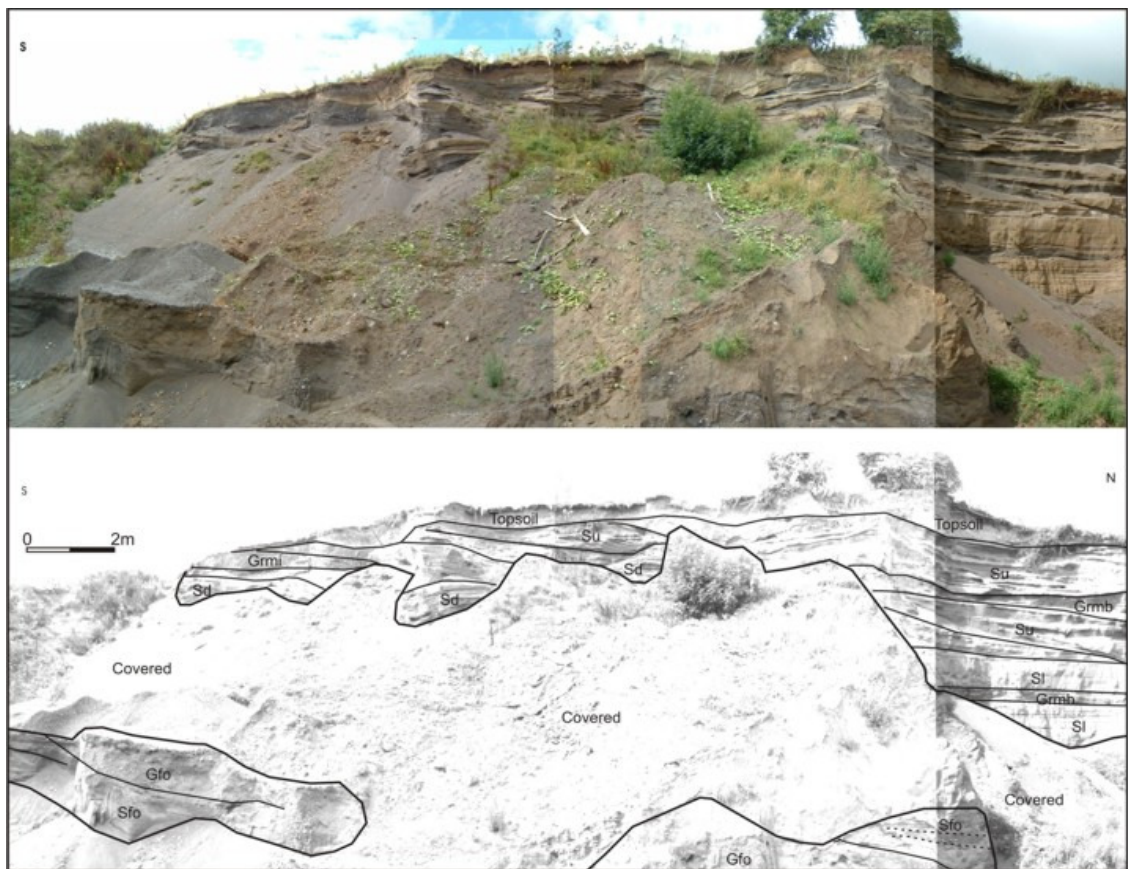


Figure 4.3 – Cross-section of glaciofluvial sediments overlying Clara esker ridge. Interstratified sand and gravel beds with bedding generally dipping north and deformed in places.

Ballyduff Esker was first recorded by Sollas (1896) and it can be traced as a continuous ridge for 20 Km. It starts in Cappanrush in Co. Westmeath (E240000, N233330) and runs in a west-southwest direction to Tinnycross (E235100, N228200). This section has all the characteristics of a true esker, being a narrow winding ridge of symmetrical cross-section (Farrington and Synge, 1970). A number of sites recorded along this part of the ridge show

coarse gravel with numerous rounded to subrounded boulders as the dominant lithology indicating a high energy depositional environment. An exposure recorded in the region is presented in Figure 4.4. The section shows crudely bedded boulder/cobble gravel dipping westwards on the lower parts overlain by sub-horizontally bedded coarse gravel with some boulders.

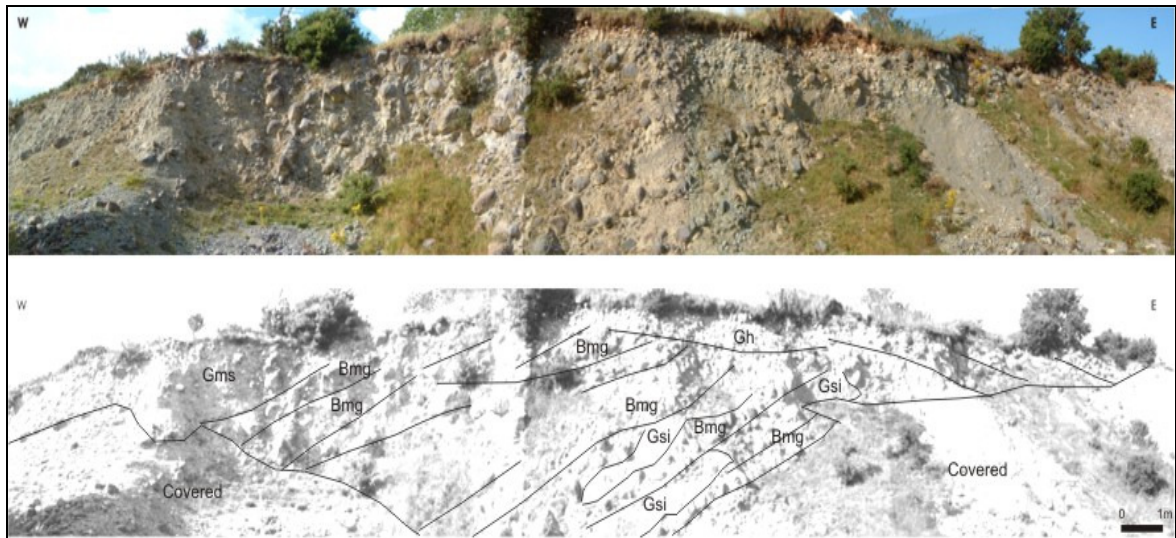


Figure 4.4 – Ballyduff Esker ridge longitudinal profile, 40 metres length, 5 metres height. There are boulder gravel beds dipping 20 to 25 degrees west interstratified in places with imbricated gravel beds. Coarse gravel beds horizontally crudely bedded overlie them in places.

The ridge changes its direction 3 Km north of Tullamore and runs westwards from this point, see Map 1. Moreover, it increases its width to 300m in places and its topographic expression reaches a maximum of 40m above the surrounding ground. This occurs mainly around Tullamore where the esker is expressed as a complex esker ridge overlain in places by glaciolacustrine sediments. Boulder gravel is dominant in the tunnel fill. The dominant petrology is Lower Carboniferous limestone; boulders are generally very well rounded and their size can reach up to 3m in diameter. The core esker ridge was probably deposited while the Northern and Central ice domes still formed a single ice body, which was retreating in a westerly direction (Warren, 1991). Tunnel morphology is well expressed and can be observed from the eastern esker end and towards the east-southeast direction where it forms a very steep sided narrow continuous ridge. Glaciolacustrine sediments, in the form of a series of large coalescing subaqueous fan lobes, are built up on its southern side along the east – west trending stretch north of Tullamore. These overtop the tunnel

deposits in places, towards the western extent of the feature. The fan sediments were probably deposited by meltwater flowing from the Central Dome into the ice-dammed Lake Riada after the two domes had separated during deglaciation. These have been recorded during this research in several gravel pits along the ridge in the region north and northwest of Tullamore. An example of it is presented in Plate 4.5. The fans are formed of sand and fine gravel dipping up to 20 degrees north. Some of the lobes show very clear point sources whilst others coalesce to form an irregular topography observed on the western part of the ridge (Warren and Ashley, 1994).



Plate 4.5 – Exposure of Ballyduff Esker complex showing glaciolacustrine dipping sediments deposited as deformed foresets composed of interstratified sand and gravel gently dipping northeast.

Kilcormac Esker runs for 2 Km within the study area in a west-southwest direction, a glaciolacustrine gravel body occurs at its easternmost end. The ridge is 15 - 20m high and 50 - 100m wide. South of the east end of the esker, a morainic type ridge crosses the esker body transversally; the morainic topography and the esker topography merge into one another with no recognisable break, indicating that the deposition was probably contemporaneous (Farrington and Synge, 1970). A number of exposures within the esker show the core to be composed mainly of very well rounded Limestone boulder/cobble gravel with sandy matrix. This esker ridge was interpreted as a continuous subglacial

tunnel fill deposited simultaneously with ice retreat, as can be inferred from the morainic ridges crossing it transversely (Farrington and Synge 1970).

A complex ice-marginal glaciodeltaic system was deposited with sediment supplied through the esker tunnel before the esker formed. This feature has been recorded in a number of exposures north of Kilcormac Esker. Several exposures recorded from a gravel pit within the glaciodeltaic complex north of Blackwood (E227000, N223000) show that the deposits are dominated by well-sorted glaciofluvial sand and gravel. Topsets, foresets and bottomsets were recognized in a face-orientated north-northeast – south-southwest (Figure 4.5). Paleocurrents, inferred from foresets dipping 30 degrees north, indicate water flowing north. Kettle and kame topography on the fan/delta top (see Map 1) indicates feature development associated with dead ice. The top of the fan/delta reaches a maximum altitude of 82 meters OD. This elevation is in accord with a number of outlets of the Glacial Lake Riada located along the watershed between the Shannon and the Barrow Basins from Daingean to Geashill. The glaciodeltaic system has been also recognized around Derrinvullig (E224000, E222500). Topsets and foresets dipping west-northwest indicate paleocurrents flowing west-northwest and it appears that the feature grew, migrating as a fan, from east to west.

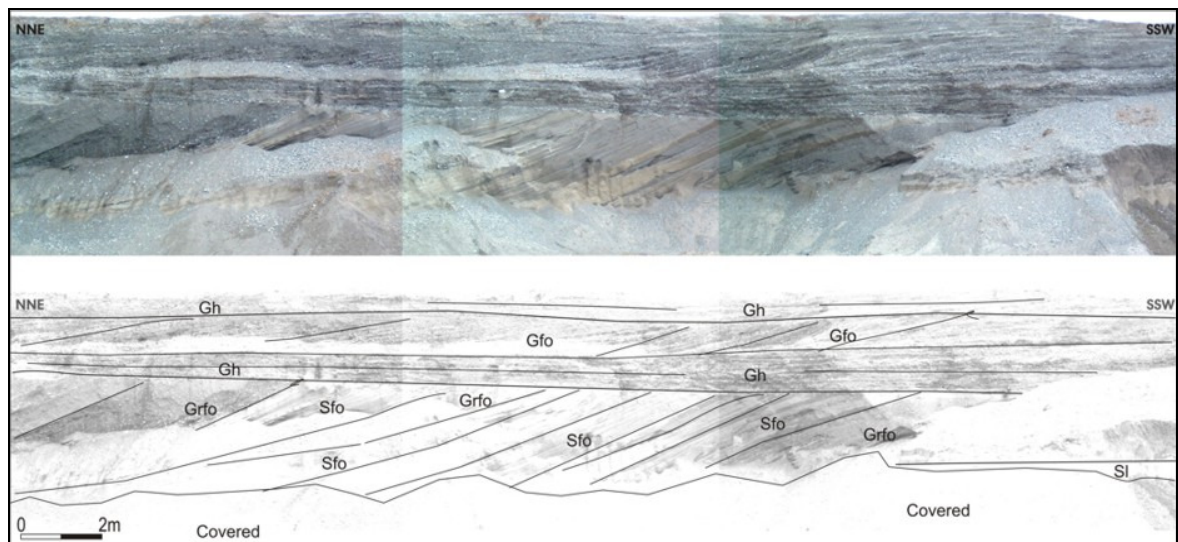


Figure 4.5 – Exposure illustrating very well developed topsets and foresets overlying bottomsets recorded on gravel pit excavated on glaciolacustrine sediments deposited north of Kilcormac Esker. Paleocurrents indicate water flowing north-northeast.

Geashill Esker runs in a northwest direction in the region south of Geashill marginal to a meltwater channel draining towards the southeast. There is an abrupt change of direction around Ballycue (E244000, N223000) where the feature trends westwards as far as the area north of Brackagh (E231000, N222000). Its topographical expression decreases towards its western end, yet there is continuity of the ridge towards the east. Height varies from 3m in Brackagh to 10m above its surroundings in Annagharvey (E240500, N222800). Its width varies between 10m, where it is at its lowest, to 200m where it is at its highest. Its highest expression (up to 20m) is reached east of Geashill. Exposures recorded along the esker show well-sorted sand and gravel with well-rounded cobbles and pebbles mainly derived from Lower Carboniferous limestone. A change on the grain size of the sediments recorded in exposures along the ridge has been observed after the direction shift towards the west; gravel becomes more sorted in places with a predominance of interstratified sand and gravel. In contrast, it is dominated by large well-rounded boulders and cobbles along the ridge in the region northwest from Geashill. Moreover, glaciofluvial sediments associated with the esker have been recognised around Site S1 (see Map 1). These deposits run parallel to the ridge and would have been laid down during ice retreat towards the west. The feature behaves as a continuous subglacial tunnel fill in the east and evolves into a segmented tunnel fill or long beads towards the west.

Diamicton is another main glacial sediment type within the area. It is morphologically expressed as very gently to gently undulating ground. It presents some topographic expression in the form of frontal moraines running southeast - northwest in the region north of the Kilcormac Esker (E225790, N220680). Furthermore, a series of very gentle ridges located 2 to 7 Km east of Tullamore running parallel to each other from north to south occurs in a region of thin Quaternary sediments (see Map 1). These ridges are interpreted as recessional moraines related to a period of ice retreat towards the west. Exposure and borehole data for these ridges show that they are composed of sandy silty diamicton.

Lower Carboniferous limestone is the dominant petrology in the glacial tills. Samples collected in the region show that silty sandy till is the dominant lithology. A number of

erratics have been recognised in the petrographically analysed samples; the most common being sandstone, calcareous sandstone and chert. Based on field mapping, two small areas between Moate and Clara and Moate and Kilbeggan have been classified as tills derived from Devonian sandstone.

The postglacial deposits occurring in this region are lacustrine sediments, alluvium and peat. The landscape associated with the postglacial sediments has no topographic expression and the area is generally prone to flooding. Alluvial sediments often cover large extensions around riverbeds and are mainly composed of silt and clay. Lacustrine sediments occur in the area south of Tullamore and in areas around the Clara Esker. The sediments recorded are dominated by interstratified silt and clay. Small angular limestone pebbles have been identified in some locations and interpreted as dropstones from icebergs drifting on the former glacial Lake Riada. Lacustrine sediments are often observed underlying peat deposits. The peat deposits are cut away in most of the area, with only Clara bog being partially preserved. This organic deposit commonly develops on top of alluvial flats, lacustrine plains and glacial till. Its thickness can vary from 1 - 12m.

4.2.3 - The Shannon and the East Basin watershed area

The morphological features dominating this landscape and distinguishing it as a unique region are the numerous lake overflow channels flowing eastwards and cutting through the watershed at approximately right angles (see Map 1). These channels released meltwater towards the East Basin from Glacial Lake Riada, located in the Shannon Basin (Pellicer and Warren 2005). The height of the channels can be correlated to the highest point of several glaciofluvial/glaciolacustrine deposits associated with the Horseleap, Moate, Ballyduff, Clara and Kilcormac Eskers. The lower topographic points in this area occur within these channels. Heights in the area range from 84 metres OD in the channel along the Grand Canal west of Daingean to 145 metres OD along the N6 road 2 Km east of Tyrrelspass. An example of one of these channel features, located south of Ballinagar, is presented in Plate 4.2.

A total of 14 exposures were visited and 9 boreholes drilled in this area as part of the field mapping exercise.

The dominant sediment in the area is subglacial till derived from Lower Carboniferous limestone. It is morphologically expressed as very gently to gently undulating ground. Samples collected from boreholes or exposures show that the dominant lithological type in these deposits ranges from sandy silty to silty clayey diamicton. The exposures recorded exhibit well-consolidated sediments with thicknesses varying from 1m to more than 10m. Results from petrographic analyses show the presence of sandstone, calcareous sandstone and chert erratics. A number of ice marginal deposits interpreted as frontal moraines running south-southwest north-northeast have been mapped 4 Km north of Rochfordbridge. These are composed of sandy gravel and gravelly sand and were probably deposited during a standstill stage of an ice margin retreating north-westwards.

Glaciofluvial sediments are expressed in a number of morphological features. An esker ridge, with associated glaciofluvial fans, has been mapped along a meltwater channel running northwest - southeast around Geashill, which has been explained in detail in section 4.2.2. Other small isolated kame mounds and kettle holes occur south and east of Tyrrelspass and coarse gravel deposits overlain by peat have been observed in 2m deep ditches south of these features. Exposure availability is quite poor; however, these deposits have been interpreted as glaciofluvial sediments deposited by large westwards flowing subglacial streams, fed by an ice front situated at the confluence of the Split Hill, Clara and Ballyduff Eskers.

Postglacial sediments are dominated by peat and are often underlain by lacustrine sediments. Alluvial sediments develop along small river channels commonly as silts and clays. Lacustrine sediments include silt/clay and organic-rich fine sediments (marl), which occur in a number of locations; an example of marl has been mapped northwest of Geashill (E244100, N222600) and is presented in Plate 4.6. Lacustrine sediments outcrop mainly in areas that have been exposed during peat cutting and they seem to underlie most of the peat-covered areas. Peat deposits are mostly cutaway, only Raheenmore bog, located north

of Daingean is still partially preserved. On many occasions, these deposits developed on the abandoned meltwater channels (see Map 1), impeding the identification of the channel morphology and altitude.



Plate 4.6 – Exposure of organic rich alluvial clays (marl) deposited along the south margin of Geashill Esker.

4.2.4 - The East Basin

The dominant bedrock types in this region are Lower Carboniferous limestone, which outcrops on several hills east of Daingean and volcanic rocks which outcrop in the region around Croghan Hill and along the Grand Canal in Daingean.

A total of 8 exposures were visited and 6 boreholes drilled in this area as part of the field mapping exercise. The till within 1m of the surface in this area is mainly derived from Lower Carboniferous limestone, however, some samples taken at E251400, N237600 show a yellowish brown matrix. Petrography analysis performed on some samples indicates that this till is derived from basic igneous rocks occurring in some bedrock outcrops west of the site. An area of till derived from basic igneous rocks morphologically expressed as very gently to gently undulating ground has been delineated around and northeast of Croghan

Hill, see Map 1. Several erratics derived from volcanic rocks (Plate 4.7) have been recorded within glaciofluvial deposits east of Croghan Hill, which indicate meltwater flowing towards the east during deglaciation.



Plate 4.7 – Exposure recorded 4 Km east from Daingean showing well-rounded boulders deposited within esker ridge running east-west. See detail of erratic volcanic rock in the bottom right corner. See 40cm long pick on the middle right for scale.

Meltwater channels fed from an ice margin to the west of the eastern margin of the Shannon Basin watershed, described above, discharged, during ice retreat, large quantities of glaciofluvial sediment into the area north of Croghan Hill. Morphologically flat glaciofluvial deposits are located along the channels discharge area. These glaciofluvial sediments were originally overlain by peat (see Map 1); exploitation of the peat over the last few decades has revealed them. They are usually fairly thin with thicknesses from 1 - 7m and fining from coarse gravel to fine sand towards the east. These deposits have been interpreted as a sandur infilling former shallow glacial depressions left behind during ice retreat. Furthermore, several kame terraces composed of sand and gravel with occasional interstratified diamicton, occurring along the north and northeast facing slopes of Croghan Hill have been recognised by their morphology and their internal structure recorded in a number of gravel pits. The internal architecture of these deposits is presented in Plate 4.8.

Alluvium is the less abundant postglacial deposit in the area, only occurring along small streams in quite confined valleys usually as fine sediments. Lacustrine sediments in the region have been exposed under cut-away peat during peat extraction in a number of peat bogs located south and northwest of Croghan Hill and in very small patches north of

Daingean. These sediments are mainly composed of 1m to 2m thickness silt and clay and frequently overlie glaciofluvial sands and gravels. The peat in this area has mainly been harvested, generally a thin 1 - 3m thick layer of peat remains in some of the working bogs. This peat had mostly accumulated on lacustrine sediments deposited in lakes left behind after deglaciation.



Plate 4.8 – Exposure of deformed interstratified glaciofluvial sand and gravel dipping north-northeast deposited on a kame terrace positioned along the northwest slope of Croghan Hill.

4.2.5 - The Brosna River Basin

The dominant deposits in this area are of postglacial origin. However, large areas of glacial sediments within 1m of the surface also occur either as glacial or glaciofluvial deposits. Till derived from Lower Carboniferous limestone (Plate 4.9) is the dominant glacial deposit in the area. A small patch of till (1 Km²) derived from Devonian sandstone is also present in an area located 5 Km north-northwest from Clara (see Map 1), which is expressed on the surface by the presence of large subangular and subrounded sandstone and conglomerate boulders. This type of landscape varies from flat to gently undulating with some isolated mounds composed of diamicton. Glaciofluvial sediments are rare on the surface in this region; nonetheless, they have been mapped in places as gently dipping interstratified sand and gravel underlying peat deposits (Plate 4.10).

A total of 10 exposures were visited and 8 boreholes drilled in this area as part of the field mapping exercise. Alluvial sediments dominate the lower areas along the Brosna River channel. This deposit reaches a thickness of 7m in some places along the channel.

Exposures in this area are generally very poor (Plate 4.11). The sediments recorded are mainly composed of very dense blue to grey clay with occasional angular pebbles derived from limestone bedrock.



Plate 4.9 – Glacial diamicton with silty sandy matrix derived from Lower Carboniferous Limestone.



Plate 4.10 – Glaciofluvial sediment underlying peat in the Brosna Basin physiographic unit.



Plate 4.11 – Ditch in flat lying ground composed of waterlogged clayey diamicton.

Peat deposits are generally located on higher ground surrounding the flood plains. Most of these deposits are still being cut away and in some places have been totally harvested exposing glacial and glaciofluvial sediments. Marl deposits have been mapped during the field mapping exercise along the Tullamore River on a stretch 5 Km long and 1 Km wide. Bedrock outcrops in very few locations in this area.

4.4 – Results of Laboratory Analysis of field data

Particle size analyses have been carried out on a number of samples collected during fieldwork. A total of 205 samples were collected, 41 from exposures and 164 from boreholes. These were subsequently described and classified based on the following parameters: matrix colour, lithology, petrology and clast size and shape. This preliminary analysis was used to decide which samples should be sent for Particle Size Distribution Analysis (PSA). The samples selected for PSA numbered 129. All samples were wet sieved. Hydrometer analysis was done in 53 samples where fine grain size was the dominant lithology. PSA was carried out by Metlab International Ltd. at the minimum standards accepted by the BS EN ISO 22476-2:2005. Final classification of sediments is based on the results received from the PSA tests and the proportion of the different lithological components is presented in Figure 4.6.

A ternary diagram plot for all the samples showing gravel-sand-silt/clay percentages for the wet sieved samples is presented in Figure 4.6a. Figure 4.6b illustrates the particle size distribution of the matrix (sand-silt-clay) samples analysed using the hydrometer method. The proportion of gravel, sand and fine sediments displayed in Figure 4.6a shows sediments dominated by sand and gravel and a lower proportion of fines. However, it can be observed how the highest concentration of data points falls in the central area of the diagram where similar lithological percentages occur. On the other hand, samples analysed with the hydrometer method (Figure 4.6b) show a clear distribution along the sand – silt axis, indicating a very low percentage of clay within most of the samples in the area. According to these data, the dominating matrix compositions of the sediments in the study area are sandy silt and silty sand.

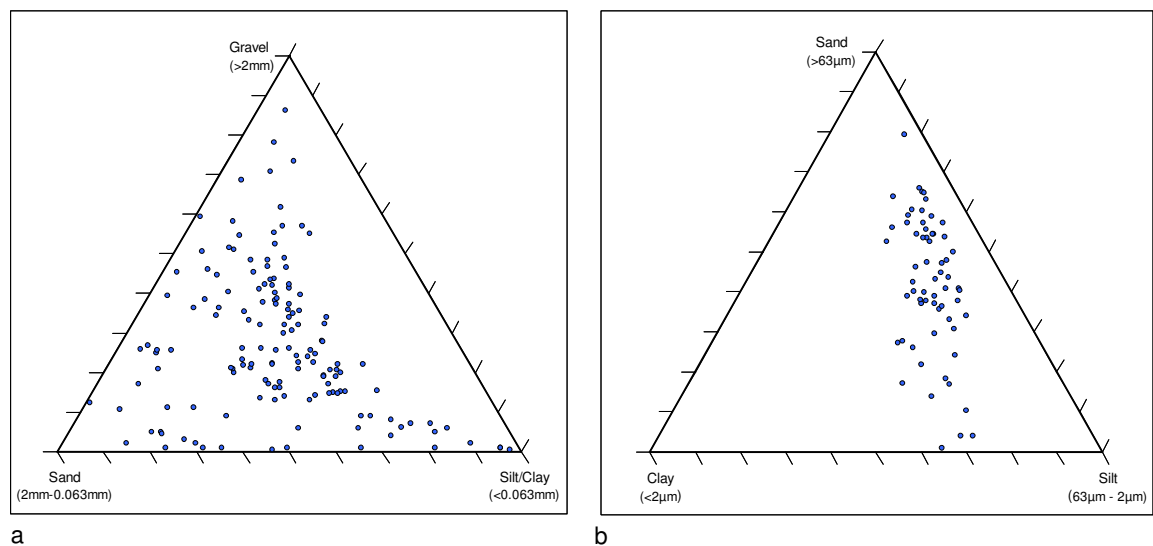


Figure 4.6 – Ternary diagrams for collected samples. a) Ternary diagram representing percentages adjusted to 20mm of gravel, sand and fines for each sample. b) Ternary diagram illustrating percentages adjusted to 2mm of sand, silt and clay.

Petrography analyses were carried out on 42 samples to determine their dominant petrography and their erratic carriage. The sample picked are evenly distributed through the study area and represent all the sediment types previously mapped, This information can subsequently be used to identify ice flow directions, as ice flowing over a bedrock substrate will pick up that particular type of bedrock and deposit the clasts farther down-

ice, perhaps on bedrock of another type. Only clasts within the 5 - 10mm size range were counted, and only counts from within the same fraction should be compared between sites (Ehlers, 1996). A total of 100 pebbles were identified for each sample. All petrologies found as bedrock within the study area were represented within the samples. The different types of Lower Palaeozoic lithologies were grouped together, as were the Upper Carboniferous rocks, due to the difficulty in telling different formations apart on such small samples. The results of the petrography analyses were used to subdivide areas of diamicton and gravels into petrographically similar zones of dominant clast lithology. The petrography analysis indicates glacial and postglacial sediments being chiefly derived from limestone bedrock with 87% of the pebbles identified derived from limestone bedrock. This result was not unexpected as limestone underlies 94% of the sediments in the study area. Other common pebbles identified are derived from chert and sandstone bedrock. Chert layers often occur within limestone bedrock as veins or thin beds. Sandstone, conglomerate and siltstone underlie sediments in two narrow elongated areas stretching southwest-northeast in the region of Moate and Ballycumber. Figure 4.7 shows the real distribution of petrographically analysed samples and their petrologic percentages in a pie chart format. These results have been used to delineate the boundaries of glacial and glaciofluvial sediments encountered in the study area by their dominant petrology. An exception to the rule are the samples collected in the region around Croghan Hill, which presented a higher percentage of limestone derived pebbles than basic igneous pebbles during the petrography analysis as the former are more difficult to grind down than the latter. However, the Quaternary sediments have been classified as till derived from basic igneous rocks as the matrix was dominated by this rock type.

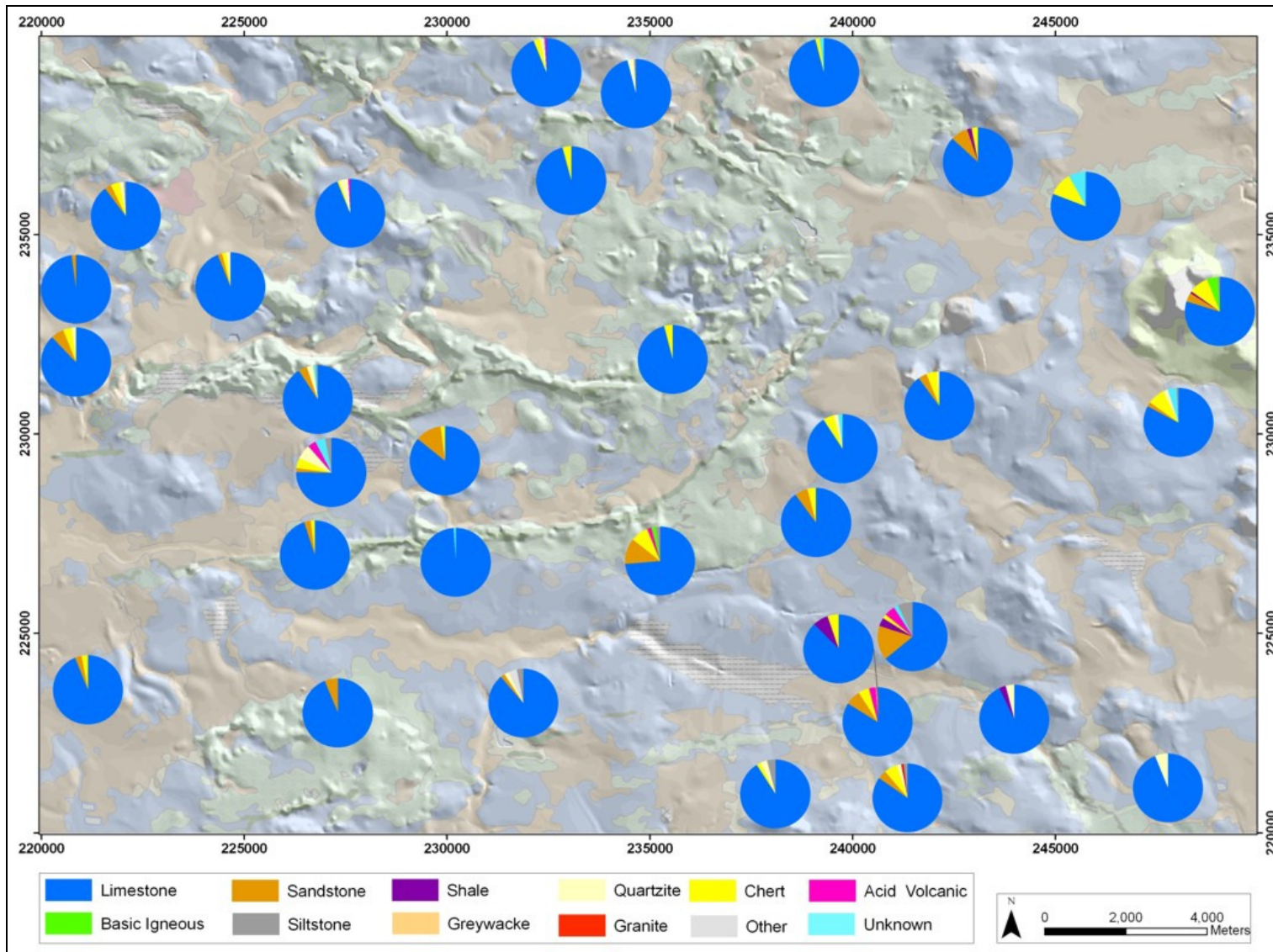


Figure 4.7 – Petrography analysis data results portrayed in pie chart format.

4.5 – Depth to Bedrock (DTB)

The methodology used to produce the Depth to Bedrock map has already been discussed in Chapter 3. The depth to bedrock map produced for this thesis is presented at 1 to 40,000 scale (Map 2 enclosed with thesis).

Depth to Bedrock (DTB) within the research area ranges between 0 and more than 40m. 1.8% of the area has bedrock within 1m of the surface and 3.3% of the study area has a DTB from 1 to 3m. These areas are predominantly located on relatively high ground north of Kilbeggan, around Croghan Hill and along the watershed between the Shannon and the East Basins. Erosion predominated over sedimentation on the hilltops. Depths to Bedrock of 3 - 5m cover 25.3% of the study area. These regions mostly occur in diamicton that is generally thin in the northern areas and thickens towards the topographically more depressed south region. The dominant depth to bedrock is 5 - 10m, it covers 53% of the area, and mainly occurs in diamicton, peat and alluvial sediments throughout the region. However, it is particularly dominant on the lower ground region along the Brosna River Basin. Furthermore, the flat landscape in the eastern and northern areas surrounding Croghan Hill is within this DTB range. The dominant sediments in this area are from discharge of glaciofluvial sediments through the meltwater channels along the watershed between the Shannon Basin and the East Basin, which were subsequently overlaid by peat. Thick sediments (more than 10m) cover 29.5% of the area, these mostly occur in areas dominated by glaciofluvial sediments, including: eskers and associated deposits, glaciodeltaic sediments, and interstratified tills with gravel. The depressed landscape in Co. Offaly within the Shannon Basin, encloses most of these thickly deposited sediments. Thick surficial sediments also occur in an area south of Ballinagar, which has been intensively surveyed by the use geophysics, as part of this thesis (see Chapter 6). Very deep DTB was recorded along a west-east channel feature cutting the limestone bedrock and running from the Kilcormac Esker towards the Geashill Esker and turning southeast, south of Ballinagar. Lack of depth to bedrock data for the region south of Tullamore does not allow the definition of the morphology of this feature westwards. Further geophysical surveying along this channel has been performed during this thesis and is presented in Chapter 6.

Enclosed Map 2 displays the distribution of thickness of soft sediment within the region as described above. The depth to bedrock map produced has a digital resolution of 30m pixel size. Every pixel has a depth to bedrock (DTB) value assigned. The sum of all the DTB values in metres attached to every pixel in the map multiplied by 900 m², which is the area covered by every pixel (30m x 30m = 900 m²), gives the volume of sediments covering the research area.

Pixel size is 30m x 30m = 900 m²

$$\sum DTB(m) \times Pixel\ size(m^2) = 4920773m \times 900 = 4428695700m^3$$

Total volume of sediments deposited within the area = **4.43 Km³**

The average thickness (At) of deposits can be calculated by dividing the volume of sediment accumulated by the research area (600 Km²).

$$600000000 \times At = 4428695700m^3; At = 4428695700m^3 / 600000000m^2 = 7.38m$$

Average thickness of sediment overlying Bedrock (At) = 7.38 m

The total volume of sediments accumulated over solid bedrock in the research area has been calculated at 4.43 Km³ and the average thickness of sediments in the area is estimated to be 7.38m.

The depth to bedrock map assists in the understanding of the sedimentary and depositional processes occurring in the area. Morphological features such as esker ridges and associated glaciofluvial deposits, subaqueous fans, glaciodeltas, meltwater channels and ice-moulded bedrock are clearly depicted in this dataset.

4.6 – Summary

The area mapped during this project is situated in the Irish Midlands around Tullamore Town. The final Quaternary geology map (Map 1) enclosed in this thesis displays the dominant sediment type within 1 metre of the surface classified by their dominant

petrology. Morphological features relevant to the shaping of the landscape are presented as symbols or as lines indicating ice or water direction. Boreholes drilled, exposures surveyed and geophysical sites are also presented.

The dominant deposits in the area are glacial and glaciofluvial sediments derived mainly from Lower Carboniferous limestone bedrock. Esker ridges and associated glaciofluvial/glaciolacustrine sand and gravel features are the dominant landforms in the area. Four main eskers, Split hill Esker, Moate Esker, Clara Esker and Ballyduff Esker splay westwards in a large fan shape. Other important glacial features in the area are meltwater channels draining from the Shannon Basin to the west into the Boyne/Barrow Basins to the east, and poorly developed drumlinised landscape north of Kilbeggan. Postglacial sediments in the area include lacustrine silts and clays, peat, alluvial clays, silts and sands and marl. Peat is the dominant deposit, human activity during the last century has dramatically reduced it. Alluvial sediments are extensive in low relief areas, especially along the Brosna River.

Petrographic analysis completed on 42 samples composed of 100 pebbles with size ranging between 5 to 10mm shows Lower Carboniferous limestone as the dominant petrology in the region. A small region around the Croghan Hill area has been classified as till derived from volcanic rocks, even though it is not the dominant petrology in the petrography analysis. The matrix content in samples collected in the region illustrates volcanic rocks as the dominant petrology. These results concur with the composition of the bedrock underlying the region.

The final Quaternary geology map (Map 2) presents the distribution of the Quaternary deposits thickness in the study area. The map has been produced using the krigging geostatistical method and the total volume of sediments overlying the bedrock is estimated to be 4.43 Km³, which represents an average thickness of Quaternary deposits of 7.38m.

CHAPTER 5

Forward modelling of geophysical data and training sites study

5.1 – Introduction

Forward modelling of geophysical data allows the testing of the potential and limitations of geophysical techniques for geological mapping. Moreover, it aids in making decisions on the data collection, processing and interpretation methods.

Electrical resistivity forward modelling of the subsurface has been carried out with RES2DMOD software. This software is used to produce simplified models of the subsurface to which varying electrical resistivity values are assigned, which can subsequently be inverted with the RES2DINV software and the results compared to the original field data.

GPRSIM software has been utilized to create a number of theoretical GPR models of the subsurface generally encountered in the Irish Midlands. Forward modelling of this data allows the evaluation of the limitations and potential of GPR for depiction of lithological, sedimentological and structural surfaces commonly found in the subsurface.

Ground truth evaluation of GPR and ERT was performed at three test sites (T1, T2 and T3) with good exposures in order to determine the usefulness of the techniques, optimum deployment methodology, limitations and to understand the obtained responses. For example, a number of GPR data collection modes and antennae frequencies were tested and compared to the in situ sedimentological analysis of the exposure. Site T1 is located in the study area (see Map 1), Sites T2 and T3 are located outside the study area 8 Km west-northwest from Horseleap and 6 Km east from Croghan Hill respectively.

5.2 – Electrical Resistivity

The inversion program RES2DINV was introduced in Chapter 3 and it allows the construction of a subsurface model with real resistivities and depths from the measured apparent resistivity distribution. Like other inversion programs, there is no unique solution to the equations used in the calculations, thus in theory a range of models could yield the same apparent resistivity distribution. Loke (2002) developed the forward modelling software RES2DMOD, in which theoretical subsurface models with set resistivity values can be constructed and their calculated apparent resistivity pseudosections produced.

A number of simplified theoretical models expected to occur in sediments in the study area have been produced for this research for three reasons. Firstly, by comparing apparent resistivity pseudosections created for known models, with apparent resistivity pseudosections obtained in the field, a better interpretation of the subsurface can be made. Secondly, the apparent pseudosections produced using the forward modelling program RES2DMOD can themselves be inverted using the RES2DINV inversion program and the model created compared with the original theoretical model. This tests the reliability and resolvability of the RES2DINV program for different situations and allows its limitations to be determined (Kilner et al., 2005). Thirdly, the inversion model of the resistivity section can be computed with RES2DINV software using a range of settings. A number of parameters available in the RES2DINV software were tested during this exercise in order to determine the ideal settings for the inversion process. The smoothness constrained inversion method (deGroot-Hedlin and Constable, 1990) and the Gauss-Newton robust constraint method (Claerbout and Muir, 1973) are available to produce the inversions, the former is recommended to be used to delineate gradational contacts between geological features. The latter may result in higher RMS errors, although is more accurate in detecting sharp contacts (Loke, 2001). The damping parameters, mesh refinement used and the increase in thickness of the layers in depth are other important parameters that can be altered in the inversion program and which can affect the resultant model (Loke, 2004).

The methodology used to analyse the outcome from theoretical models is as follows:

- Use RES2DMOD software to produce a theoretical model of the subsurface (e.g. Figure 5.1a (top) shows a theoretical model encompassing a 1.7m thick low resistivity layer ($100\Omega\text{m}$) over a high resistivity layer ($1000\Omega\text{m}$).
- Convert the theoretical model to RES2DINV format.
- Invert the file with a range of settings to observe the difference between the theoretical model and the derived inversion model. A dashed white line in the inversion model (Figure 5.1, bottom) shows the position of the contact between layers in the theoretical model.

The theoretical models considered are: channel features, eskers, faults/vertical contacts, sand lenses enclosed in poorly-sorted (low resistivity) sediments, several horizontal bedding examples and a more complex lithological setting composed of fine sediments overlapping an esker and associated glaciofluvial sediments, overlying tills.

The models constructed are mostly at 1m spacing. Increasing the electrode spacing by a factor of 10 simply increases the length and depth of the model by 10 but yields the same pattern. The forward modelling has been produced only for the Wenner-Schlumberger array as this was the selected array type (see Chapter 3, section 3.3.2) employed during fieldwork. Many more models (with varying layer thicknesses and resistivity values) were tested than are shown here, though the results of these tests are given when they prove relevant.

Two horizontal layers with different resistivity values

One of the simplest models is where two horizontal layers with different resistivities are present which would correspond to a simple vertical lithological change.

A number of theoretical models were tested.

Model 1 - Low resistivity layer ($100\Omega\text{m}$) over high resistivity layer ($1000\Omega\text{m}$).

Model 2 – Low resistivity layer ($100\Omega\text{m}$) over medium resistivity layer ($300\Omega\text{m}$).

Model 3 - High resistivity layer ($1000\Omega\text{m}$) over low resistivity layer ($100\Omega\text{m}$).

Model 4 – Medium resistivity layer ($300\Omega\text{m}$) over low resistivity layer ($100\Omega\text{m}$).

Each theoretical model was tested using different layer thicknesses. Moreover, the smoothness constraint inversion method and the Gauss-Newton robust constraint method were tested for every model.

Theoretical model 1 may correspond to a field situation of clayey silt overlying well-drained gravels or bedrock (see Figure 5.1a). Model 2 represents a clayey silty layer overlying sandy/silty till (See Figure 5.1b). Both derived inversion models have higher resistivity values occurring at the lower parts of the profile, which in a real situation may be misinterpreted as a change in lithology. The contact between the two layers in model 1 occurs at around $190\Omega\text{m}$, while model 2, which has a much lower difference between the original resistivity values, the contact is at $150\Omega\text{m}$.

A model with a thinner upper layer has been created in order to test the resolvability of the top layer equal to the electrode spacing or thinner. In a situation of a low resistivity layer over medium resistivity layer (model 2), the upper layer is resolved with thickness as thin as a quarter of the electrode spacing. The same resolution occurs in a case of a low resistivity layer overlying a high resistivity layer.

Theoretical model 3 corresponds to sand and gravel overlying fine sediments. Model 4 may be the equivalent of a diamicton overlying lacustrine sediments. The boundary between the two layers is detected half way between the resistivity values involved for both models. However, three layers are detected when using the smoothness constrained inversion method; whereas, the correct number is detected by the Gauss-Newton robust constraint method (Figure 5.2a).

The resolvability of the top layer with thickness equal to or less than the electrode spacing has also been tested for models 3 and 4. The upper layer is resolved in all occasions, even when very thin. However, a third non-existent layer is detected at the bottom of the profile when using both, the smoothness constraint and the Gauss-Newton robust constraint method. For model 3, this lower non-existent layer becomes more prominent as the upper layer is thinned (Figure 5.2a,b). The third layer appears when the thickness of the upper

layer is half of the electrode spacing. The same situation occurs for model 4, although on this occasion, the third layer appears in the inversion model when the thickness of the upper layer is only a quarter of the electrode spacing.

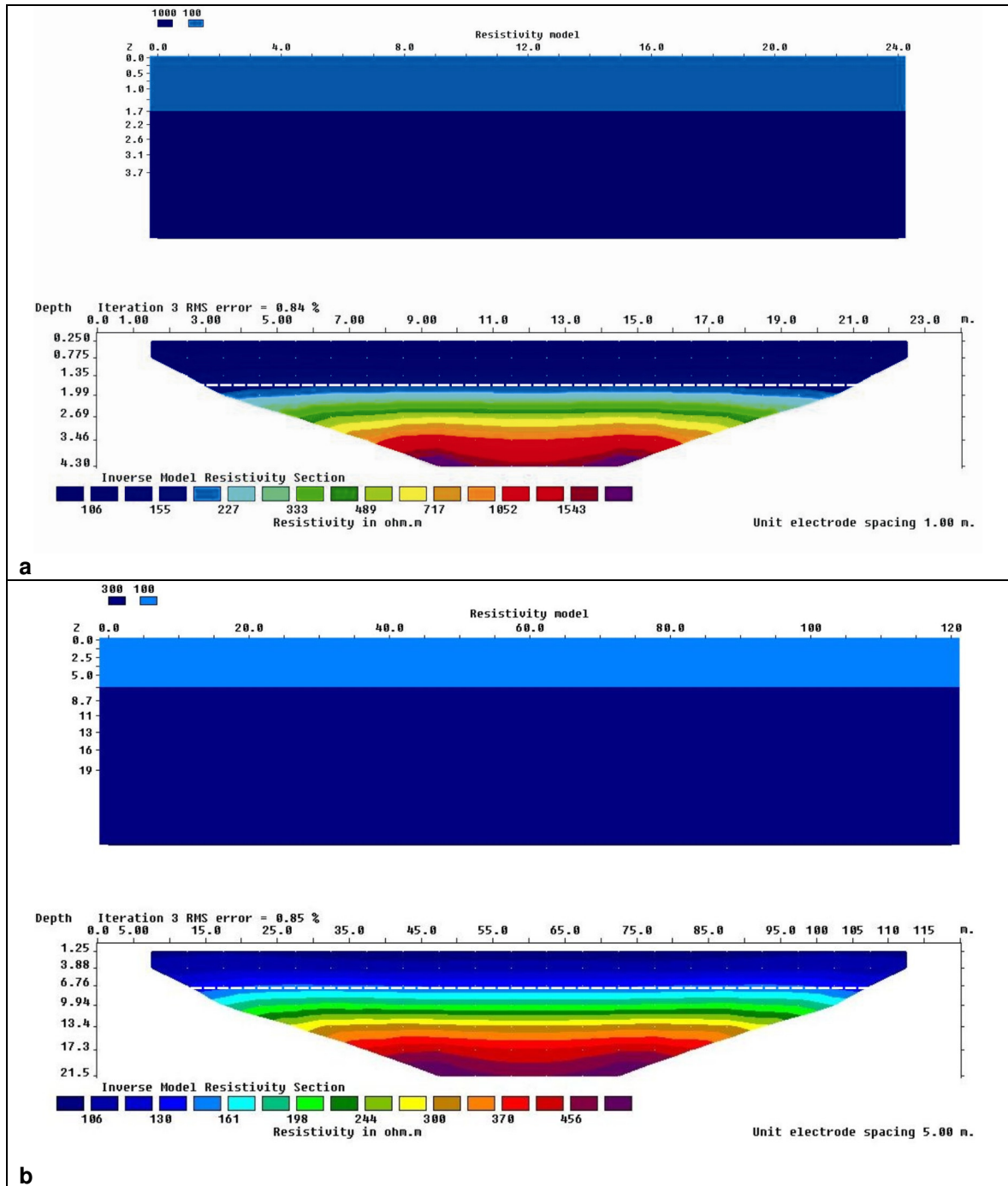


Figure 5.1 – Theoretical resistivity models presenting two layers with horizontal contact. **(a)** Low resistivity layer (clayey silt) overlying high resistivity layer (bedrock) and **(b)** Low resistivity layer (clayey silt) overlying medium resistivity layer (sandy diamicton).

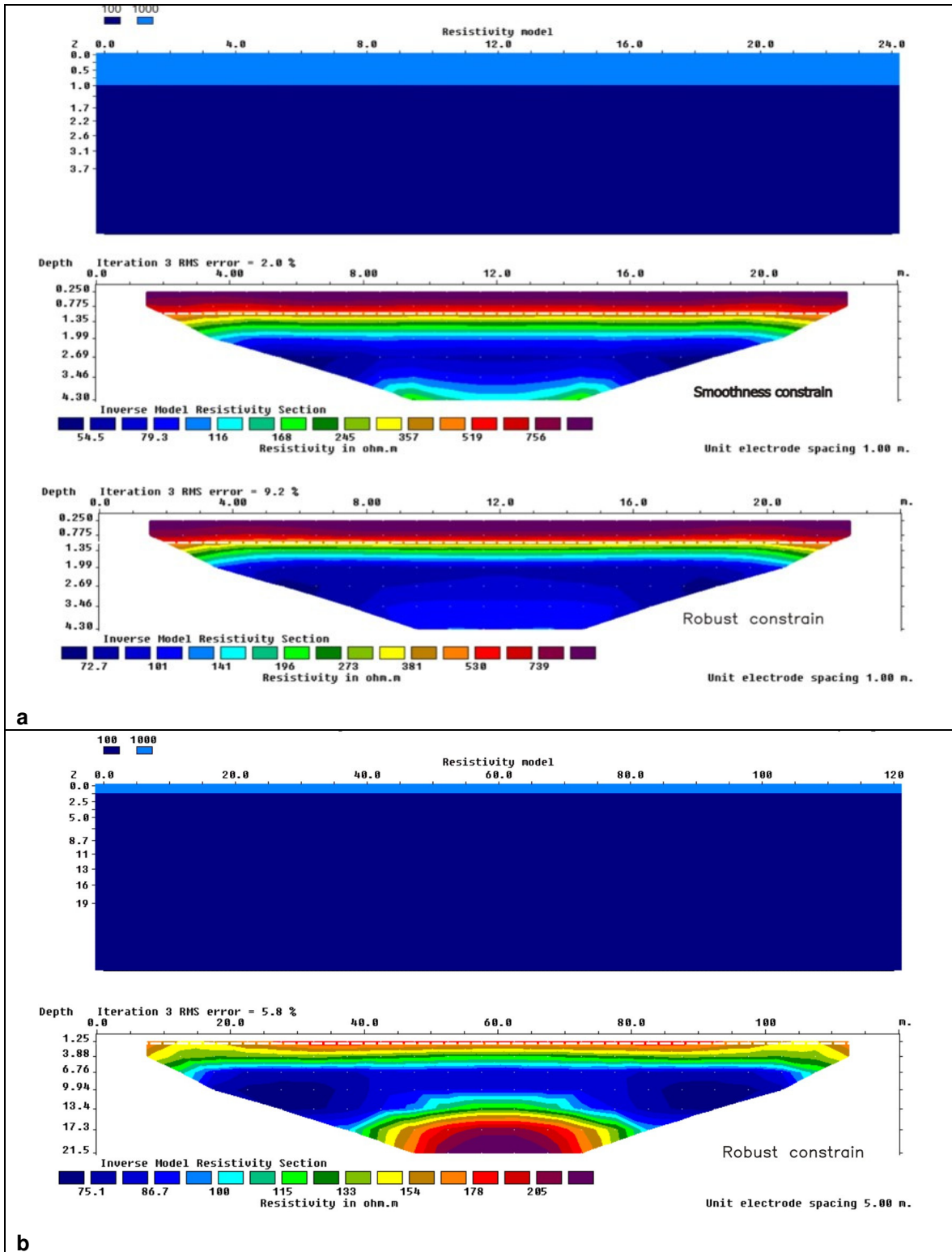


Figure 5.2 – Theoretical resistivity models presenting two layers with horizontal contact and their respective derived inversion models. **(a)** High resistivity layer (sand and gravel) overlying low resistivity layer (clayey silt) inverted using the smoothness constrained inversion method (above) and the robust constraint (below). **(b)** Thin high resistivity layer (sand and gravel) overlying low resistivity layer (clayey silt).

Till on bedrock

A theoretical model showing clayey silty tills ($300\Omega m$), which are the dominant tills in the study area; overlying high resistivity bedrock ($2000\Omega m$) is presented in Figure 5.3. The resulting inversion model provides a fairly smoothed contact between the two layers compared to the theoretical model. However, the shape of the feature is approximately preserved. The contact follows resistivity values ranging $500 - 800\Omega m$. The model has been inverted using the smoothness constraint inversion method and the Gauss-Newton robust constraint method. A more accurate fit is provided by the robust constraint method. This method is recommended where sharp lithological contacts occur, however, the use of the two methods is recommended by Loke (2001), as features depicted from both inversion methods are more likely to be real.

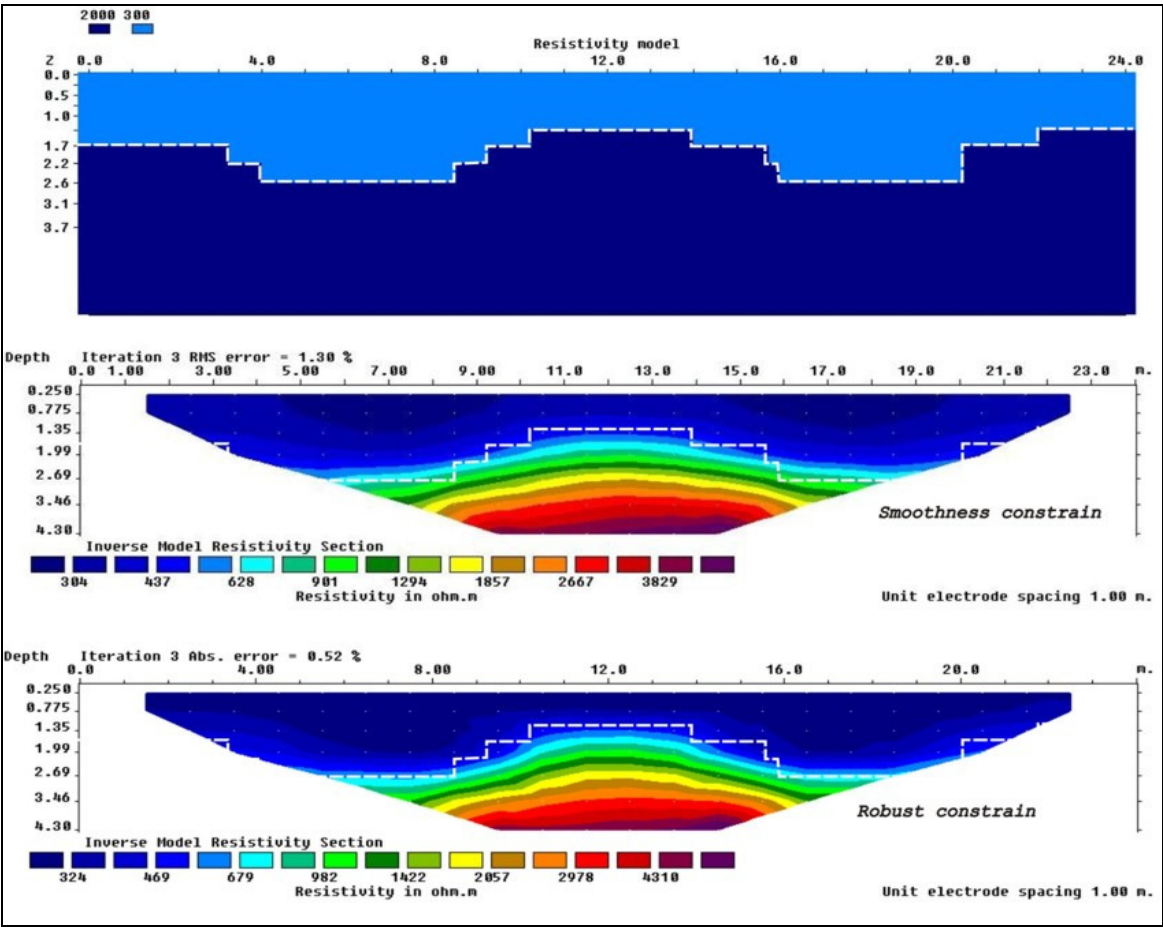


Figure 5.3 – Theoretical resistivity model presenting two layers with erosive contact for low resistivity layer (clayey silt) overlying very high resistivity layer (bedrock). White line indicates location of the layers contact. The model has been inverted using a smoothness constrained inversion method (above) and a robust constraint (below).

Fault/ vertical contact

A simple model representing a vertical fault or contact between two different lithologies with resistivity values of 100 - 400 Ω m is presented, Figure 5.4. The derived inverse model is a reasonably good approximation to the theoretical model in that a vertical contact is recorded, though it is slightly sinuous. Modelled resistivity values to the right of the contact, shown in blue on the inverted model are in the 100 - 120 Ω m range, similar to the theoretical model, though a greater range is shown to the left of the contact, though most values are 350 - 420 Ω m. The use of the dipole-dipole method is recommended by Loke (2001) to accurately detect vertical features. However, planar, sinuous and curved contacts are typically more common on glacial and postglacial sediments than vertical ones.

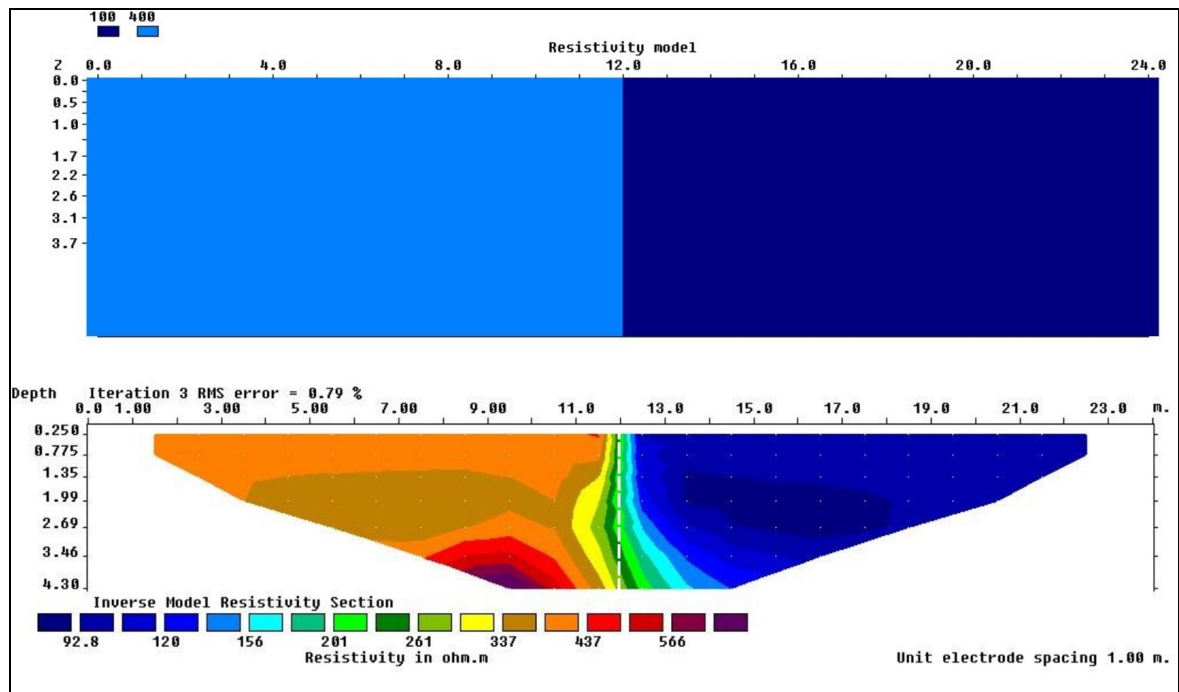


Figure 5.4 – Theoretical resistivity model presenting two layers with vertical contact.

Three horizontal layers with different resistivity values

Four situations with parallel horizontal layers with different relationships between resistivity values have been tested. These models allow the resolvability of horizontal layers relative to the electrode spacing to be tested.

1 - Low resistivity layer ($100\Omega\text{m}$) over medium resistivity layer ($400\Omega\text{m}$) over high resistivity layer ($1000\Omega\text{m}$).

2 - Low resistivity layer ($100\Omega\text{m}$) over high resistivity layer ($1000\Omega\text{m}$) over medium low resistivity layer ($200\Omega\text{m}$).

3 - Low resistivity layer ($100\Omega\text{m}$) over high resistivity layer ($1000\Omega\text{m}$) over medium resistivity layer ($400\Omega\text{m}$).

4 - High resistivity layer ($1000\Omega\text{m}$) over low resistivity layer ($100\Omega\text{m}$) over medium/high resistivity layer ($800\Omega\text{m}$).

All the inverse models derived from the Wenner-Schlumberger array encompass some slight deformation of the layering on both margins of the profile in the upper contact, and on the margins and the central areas for the lower contact. The software RES2DINV divides the subsurface into a number of rectangular cells; see Figure 3.10, before the interpolation procedure. Resistivity values are calculated by averaging the readings falling within each cell and an inversion model is derived from them. Deformation or artefacts often occurs at the edges of the profile, as there is no data to interpolate beyond its outer edge. Moreover, sharp contacts in the subsurface will display as gradual on the models as an interpolation method is used. This may result in misinterpretation of the data, see model 1 below.

The Inversion derived from model 1 is presented in Figure 5.5, and it does display an increase in resistivity with depth. The contact between upper and the middle layers occurs at resistivity values of $120\Omega\text{m}$ and of $800\Omega\text{m}$ between the middle and lower layers. However, the profile may be misinterpreted as a two layer situation, as the resulting profile is very similar to the 2 layer model shown in Figure 5.1.

The smoothness constrained inversion method and the Gauss-Newton robust methods have been tested with models 2, 3 and are shown in Figures 5.6a and 5.6b. In both models the upper contact is located within resistivity values ranging 150 - 180 Ω m. The lower contact for model 2 is located around 650 Ω m when using the robust inversion method, whereas it occurs at around 850 Ω m with the smooth inversion method. The inversion for model 3 displays a displacement of 1.1m of the lower contact when inverting by the smoothness constraint method, which accounts for a 25% error for the location of the lower contact. However, when using the robust inversion method, the lower contact in the inverted model agrees reasonably well with the original data.

A number of thicknesses for the middle layer have been tested for model 2. As expected, its detection becomes poorer as its thickness is reduced to less than the electrode spacing used. On the other hand, when increasing the resistivity value for the lower layer from 200 - 300 Ω m, the middle layer cannot be detected for a thickness less than 1.6m (electrode spacing = 1). The Gauss-Newton robust constraint method provides better results compared to the smoothness constraint inversion method.

Theoretical model 4 is presented in Figure 5.7 and for both, the smoothness constraint and the robust constraint, the resulting inversion models have a similar appearance. The contact between the very high resistivity upper layer and the low resistivity middle layer occurs at values around 500 Ω m for both inversion constrained models. This contrasts with the situation seen in models 2 and 3; where a low resistivity layer overlies a very high resistivity layer and the contact is located at around 180 Ω m. On the other hand, the lower contact occurs at 130 Ω m. Note that both methods have introduced a high resistivity artefact at depth.

The middle layer is still detected when its thickness is reduced to one third of the electrode spacing, however, its shape and position become more inexact as the thickness is reduced. Figure 5.8 shows a middle layer 0.7m thick for both high resistivity layer within low resistivity sediments (Figure 5.8b) and for a low resistivity layer enclosed within higher resistivity sediments (Figure 5.8c). The high resistivity layer is not depicted by the

inversion model, whereas, the low resistivity layer within higher resistivity values is detected, although its thickness in the inversion model is erroneous.

The situation of a low resistivity layer overlying a high resistivity layer tends to result in a contact between them situated within values closer to the low resistivity layer (e.g. 100Ωm over 1000Ωm, the contact has values of less than 200Ωm). In contrast, the situation of a high resistivity layer overlying a low resistivity layer, the contact between them tends to fall on the average between the two (e.g. 1000Ωm over 100Ωm, the contact is located in the region of resistivity values of 500Ωm). This has to be taken in account when delineating lithological changes from an inverse model. On the other hand, the Gauss-Newton robust inversion method seems to provide more accurate results compared to the smoothness constraint inversion method. However, this may be due to the constructed theoretical models which themselves have sharp contacts.

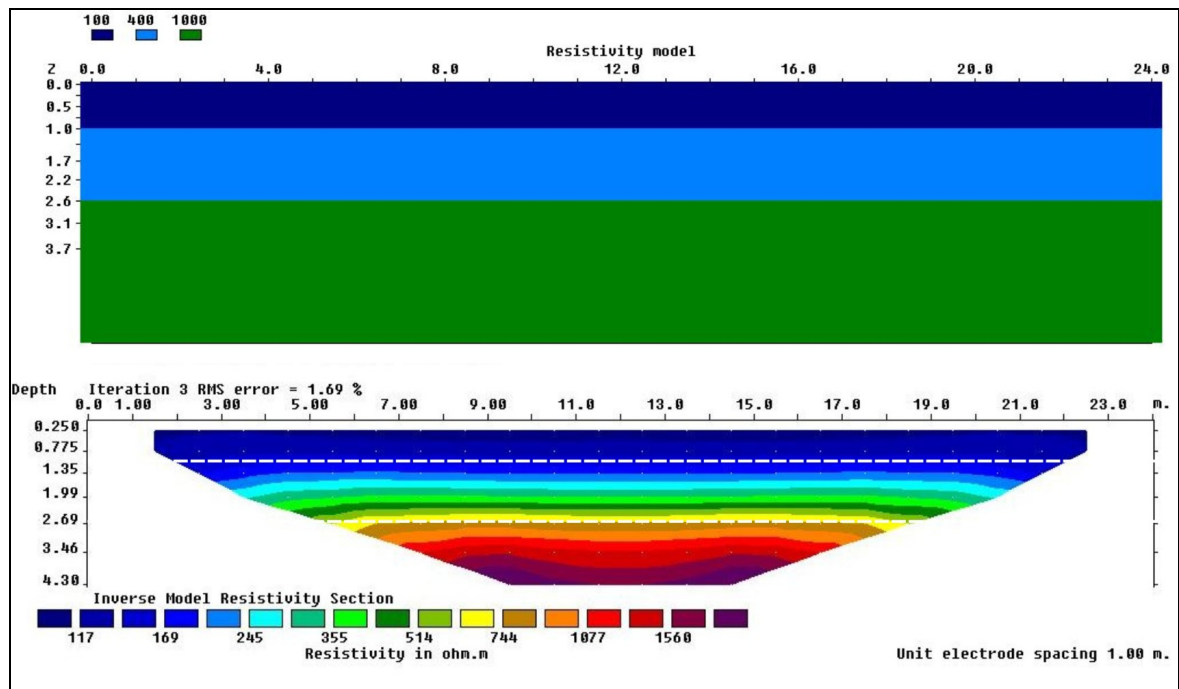


Figure 5.5 – Theoretical resistivity model for three layers, low resistivity layer (clayey silt) overlying medium resistivity layer (sandy diamicton) which overlies a high resistivity layer (bedrock). White lines indicate positions of the contacts.

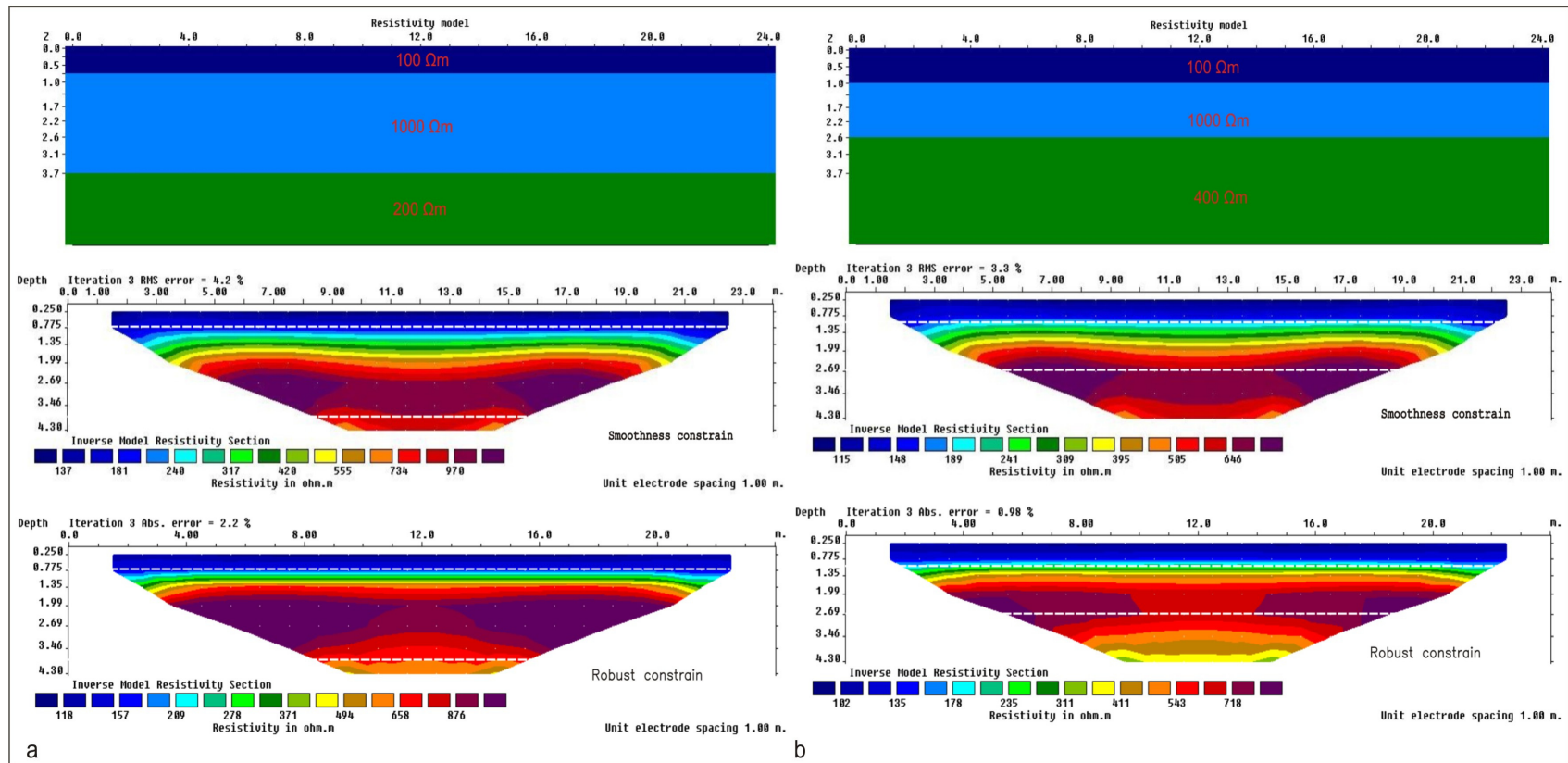


Figure 5.6 – Theoretical resistivity model for three layers, inverted using both, the smoothness constrained inversion method (above) and the Gauss-Newton constrain robust method (below). **(a)** Low resistivity layer (clayey silt) overlying a thick high resistivity layer (dry sand and gravel) which overlies a low/medium resistivity layer (silty diamicton). **(b)** Low resistivity layer (clayey silt) overlying a high resistivity layer (dry sand and gravel) which overlies a medium resistivity layer (sandy diamicton).

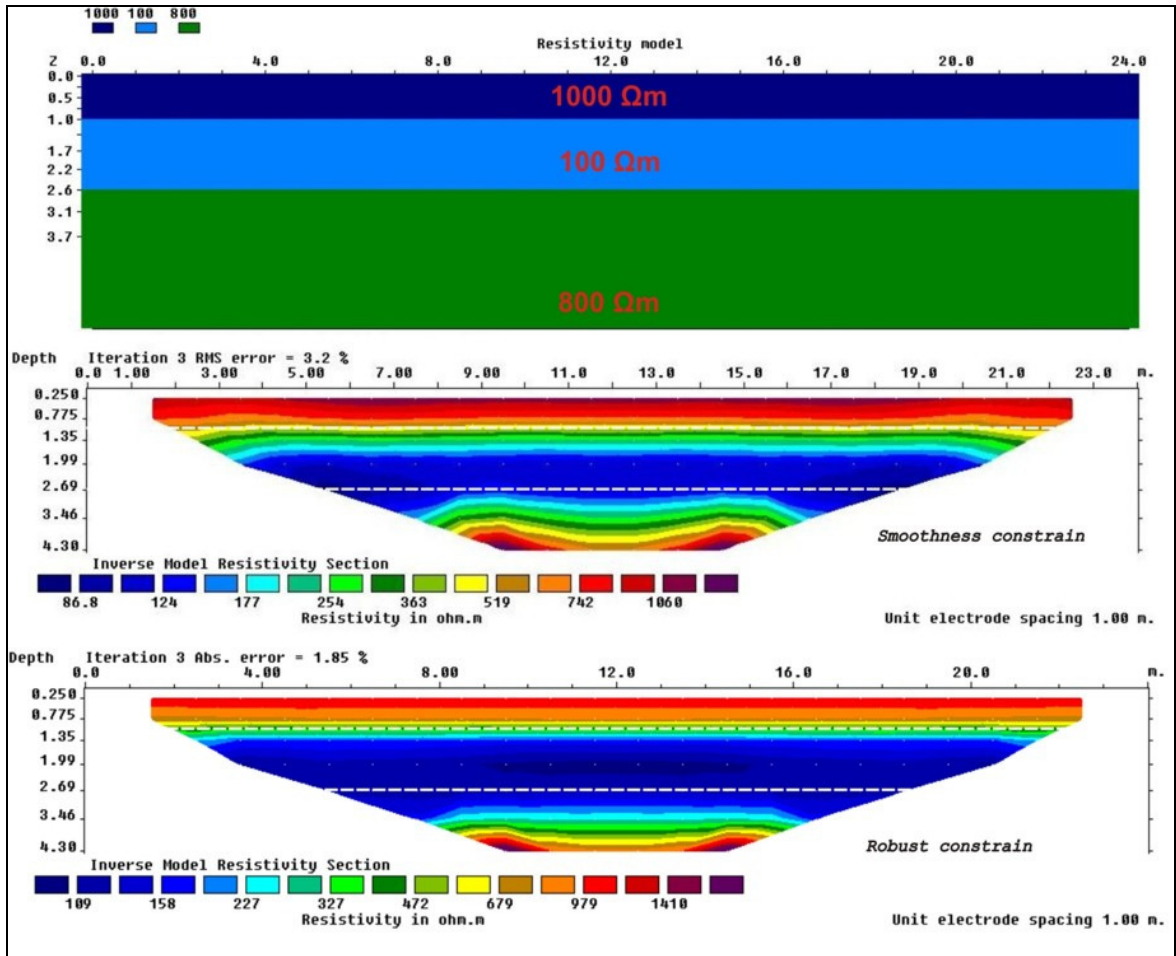


Figure 5.7 – Theoretical resistivity model for three layers, high resistivity layer (dry sand and gravel) overlying low resistivity layer (clayey silt), which overlies a high/medium resistivity layer (dry sand). The model has been inverted using both, the smoothness constrained (above) and the Gauss-Newton robust constraint (below).

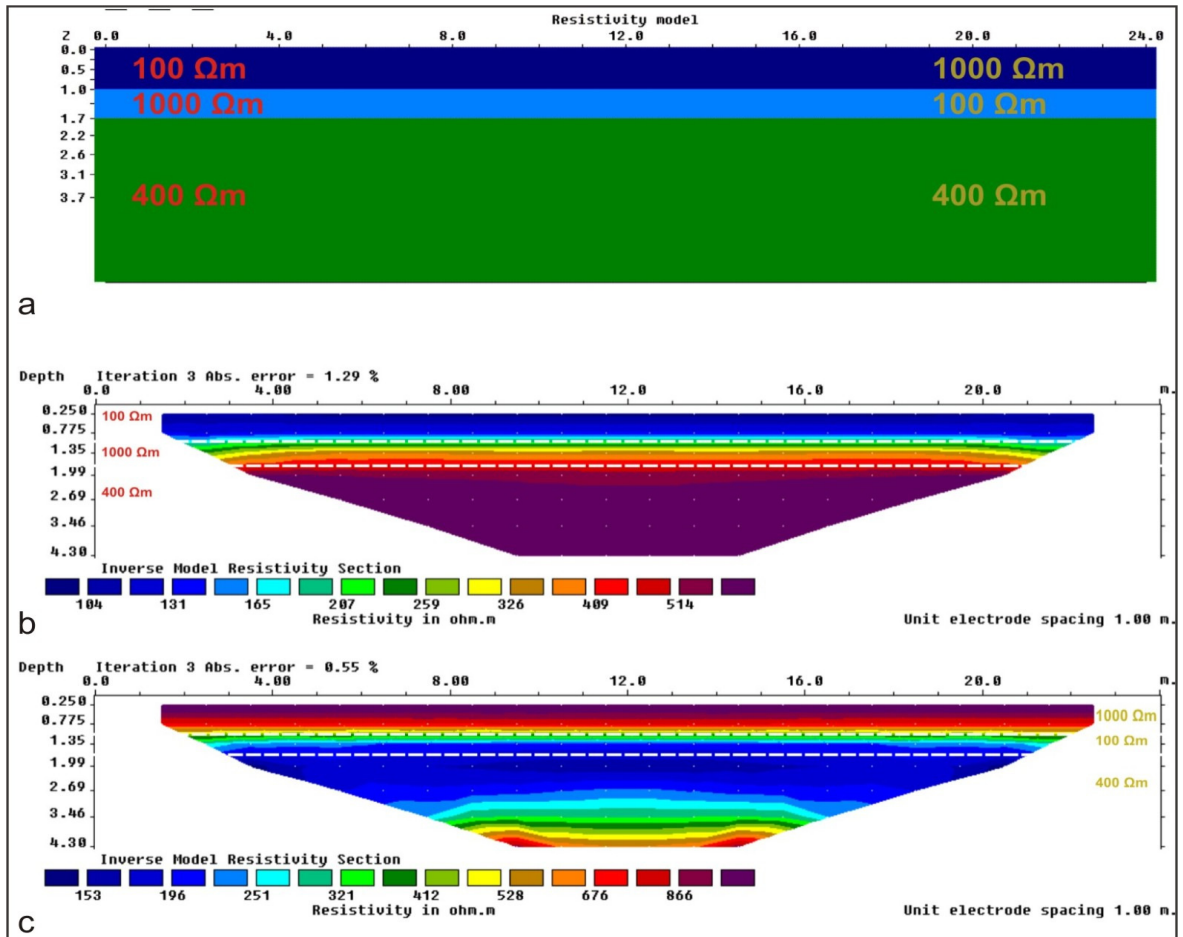


Figure 5.8 – (a) two theoretical resistivity models for three layers, with middle layer thinner than the electrode spacing. (b) inverse model for thin high resistivity layer within lower resistivity layers, middle layer is not depicted. (c) thin low resistivity layer within higher resistivity layers; middle layer is detected, though layer thickness is overestimated.

Sand and gravel lens enclosed in till.

Five different situations were tested for these lithological settings.

Large moist sand (200Ωm) lens within clayey till (100Ωm).

Large dry sand (1000Ωm) lens within clayey till (100Ωm).

Large sand (1000 - 400Ωm) lens within clayey till (100Ωm).

Thin Moist sand (200Ωm) lens within clayey till (100Ωm).

Thin dry sand (1000Ωm) lens within clayey till (100Ωm).

The upper and the lateral contacts of a large moist sand lens are well depicted by either the robust or the smoothness constrained inversion methods (Figure 5.9a), however, the lower

contact is not properly portrayed and could easily be interpreted as a vertical structure with continuity in depth. The dry sand lens sample is better depicted than the moist (Figure 5.9b), the contrast between resistivity values is ten times larger, which aids to the depiction of features. In both situations, the best resulting inversion is attained by the use of the robust constrain inversion method and increasing the layer thickness in the inversion model by 25%, instead of the standard 10%.

A large sand and gravel lens presenting a gradational decrease in resistivity from its centre to the edges has been processed by means of both inversion methods with layer thickness increasing by 25%. According to Loke (2001), gradational changes are better depicted by means of the smooth constrained inversion method. However, results presented in Figure 5.10 recognize the robust inversion model as a better fit to the original model.

The model for a thin sand lens (thickness is one third of the electrode spacing) has also been tested for both, saturated and dry lenses within till. The saturated sand lens within till is poorly depicted by using either the robust or the smoothness constraint method. In addition, a non-existent layer in the original model appears at the bottom of the inversion profile, which may be misinterpreted as a lithological boundary, see Figure 5.11a. The inversion results for both, the robust and the smoothness constraint, obtained from the small dry sand lens (Figure 5.11b) depict the upper and the lateral contacts with surrounding body. Nevertheless, the thickness of the layer is inaccurate and the resulting inversion model is similar to the one for the large dry sand lens (Figure 5.9b). The size of the feature cannot be properly resolved when large variations in resistivity values occur in the subsurface.

Two theoretical models: a sand lens 0.7m thick (just below electrode spacing) and a 1.2m thick (just above electrode spacing) have also been tested. As before, the lenses are depicted, although the thickness of the lens is not, resulting profiles are nearly identical to Figure 5.11b.

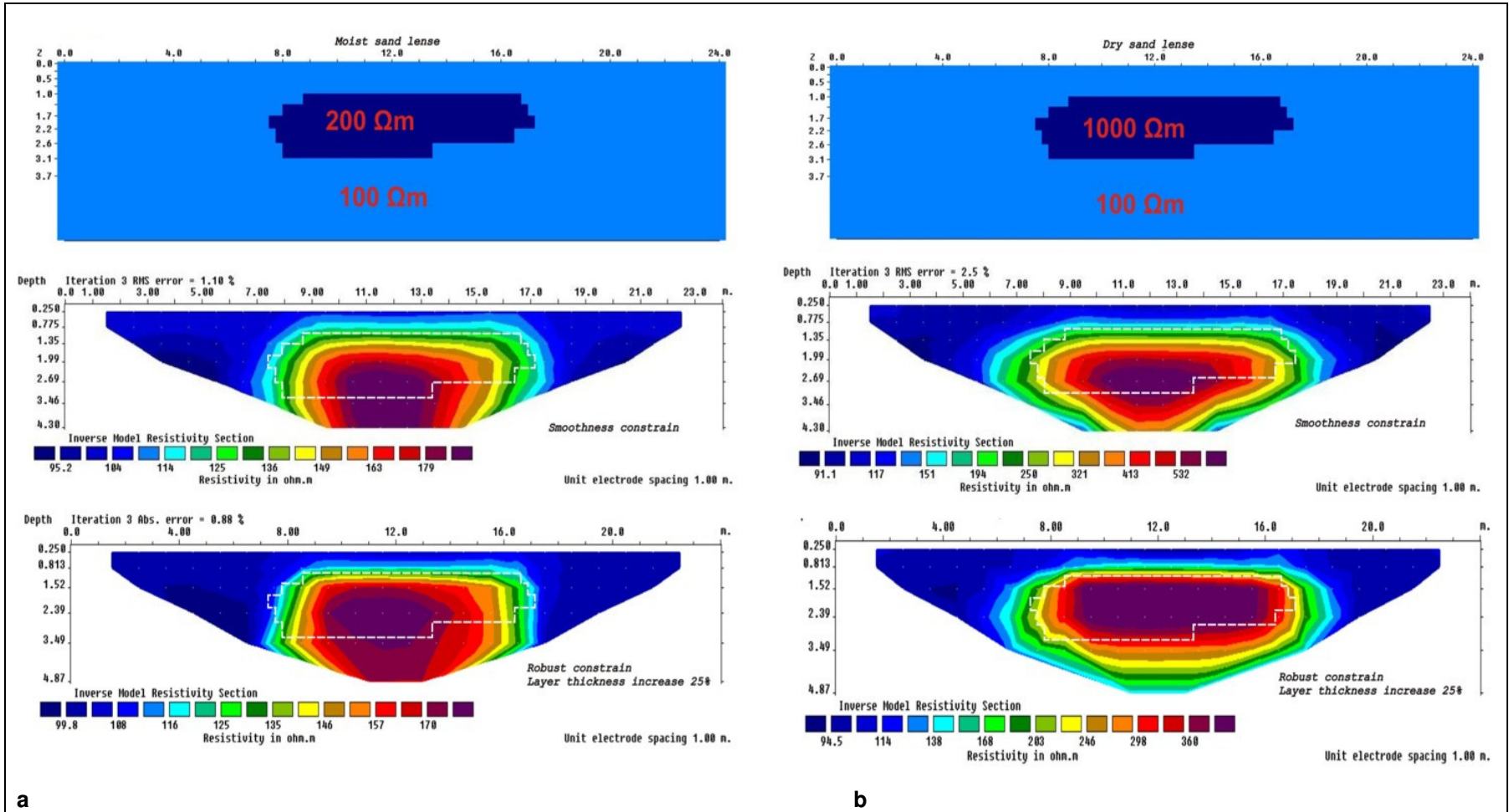


Figure 5.9 – Theoretical models for moist (a) and dry (b) sand lens incorporated within clay/clayey diamicton. Both models have been inverted by means of the smoothness constrained model (above) and the Gauss-Newton robust constrain model below with a layer thickness increase of a 25%. White line indicates location of the layers contact.

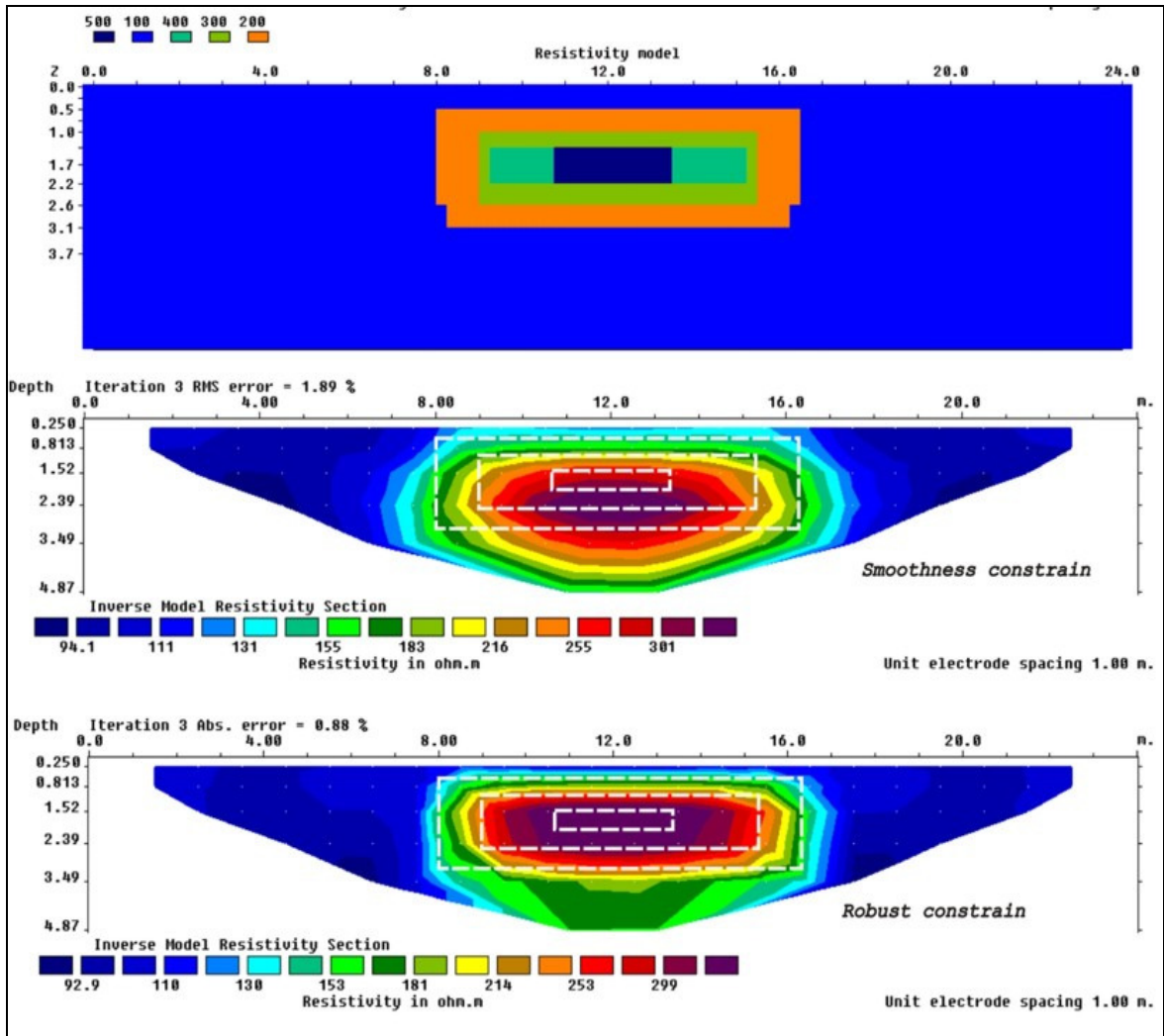


Figure 5.10 – Theoretical models for sand lens with gradational contact with clay\clayey diamicton. The models have been inverted by means of the smoothness constrained model (above) and the Gauss-Newton robust constrain (below).

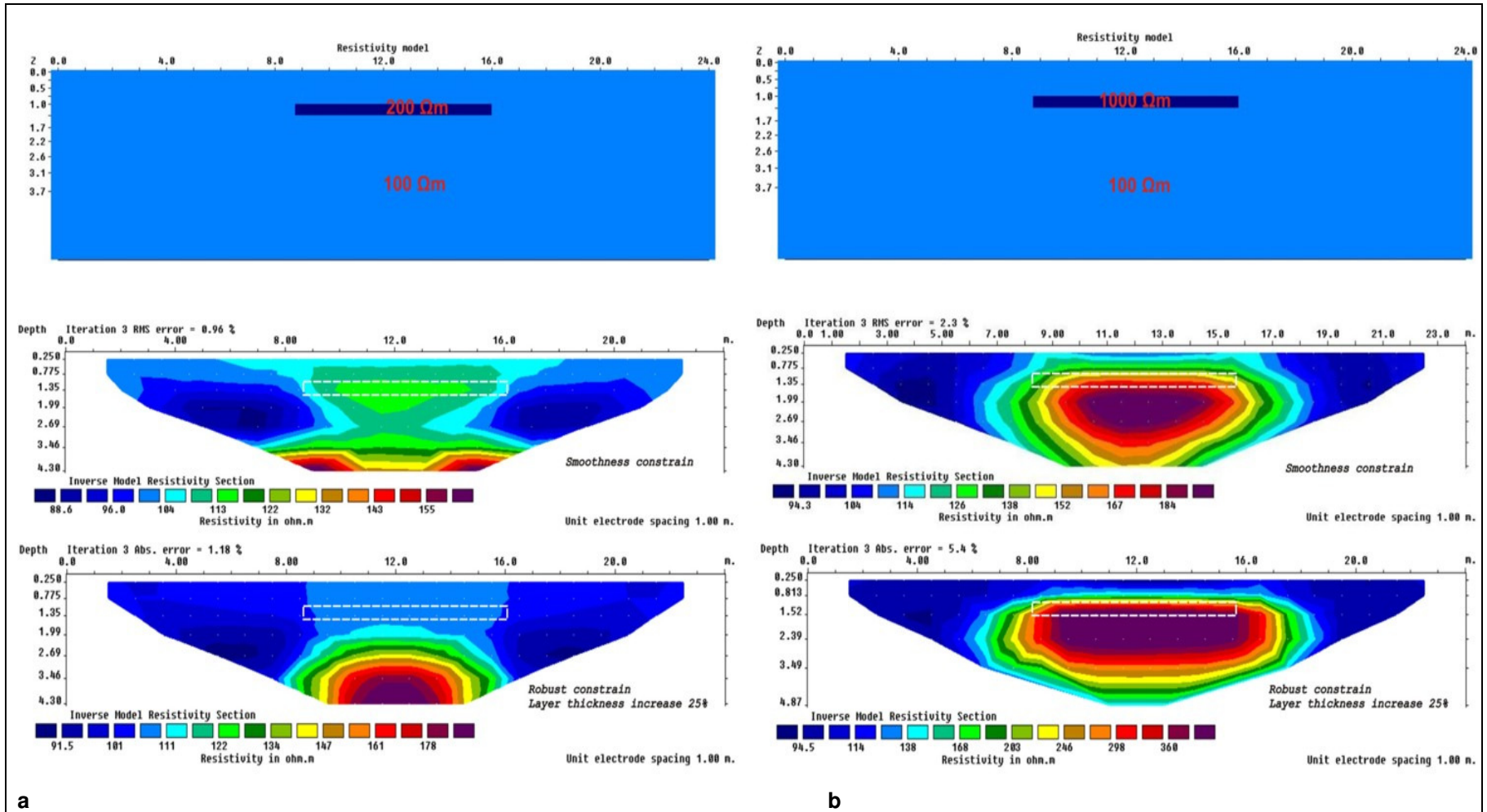


Figure 5.11 – Theoretical models for small moist (a) and dry (b) sand lens incorporated within clay/clayey diamicton. Both models have been inverted by means of the smoothness constrained model (above) and the Gauss-Newton robust constrain model (below) with a layer thickness increase of a 25%. White line indicates location of the layers contact.

Channel features

Four models for channel features have been constructed.

- 1 – Channel filled with dry sand and gravel ($1000\Omega\text{m}$) overlying poorly-sorted sediments ($300\Omega\text{m}$).
- 2 – Clay channel infill ($100\Omega\text{m}$) overlying poorly sorted sediments ($300\Omega\text{m}$).
- 3 – Set of parallel clay filled small channels ($100\Omega\text{m}$) cut into poorly-sorted sediments ($300\Omega\text{m}$).
- 4 – Series of sand filled channels ($800\Omega\text{m}$) cut into poorly-sorted sediments ($300\Omega\text{m}$).

All the models have been inverted using both, the smoothness constrained inversion model and the Gauss-Newton robust inversion model, however, the resulting models are alike and only the former is presented.

The inverse models derived for both clay channel infill and sand and gravel channel infill (Figure 5.12) show fairly good visual correlation with the four theoretical models. The shape of the main features is well preserved and the resistivity values obtained fit the original data. The contact between different lithologies occurs approximately at resistivity values in the middle range between the two lithologies. A theoretical model has also been tested for a 0.5m deep by 0.7m width channels (smaller than the electrode spacing). The shape of the features is still detected. High resistivity values which occur at the bottom corners of the derived inversion models, may be misinterpreted as a change in lithology are most likely due to edge distortion.

Comparable results are obtained by the clay infilled channels in till (Figures 5.12c and 5.12d). The shape of the features is not so accurately depicted, probably due to the lower difference between resistivity values assigned in the theoretical model. The derived models show slightly higher resistivity values than the original data, moreover, anomalies occur along the bottom of the model, which could be misinterpreted as a lithological change.

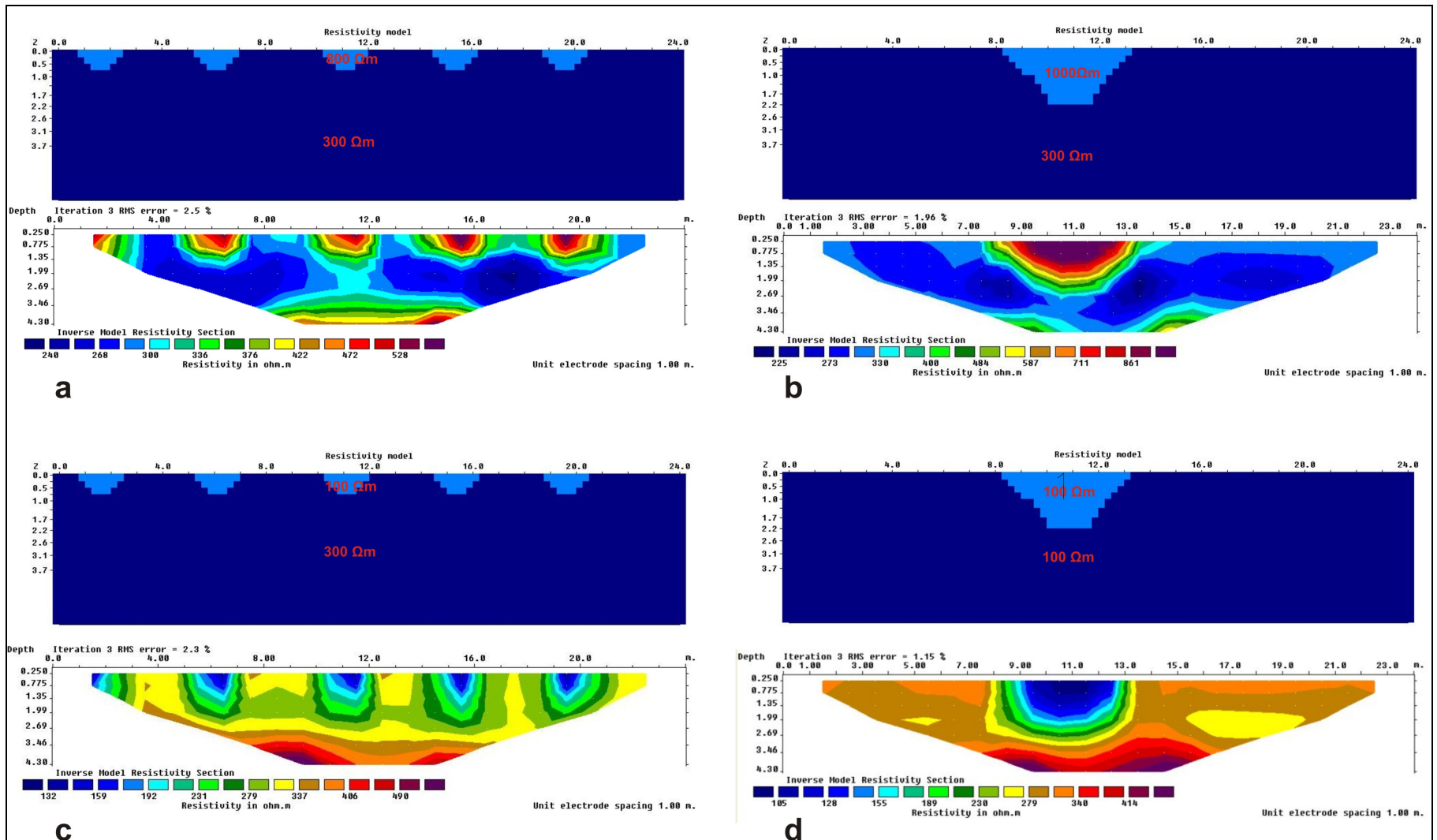


Figure 5.12 – Theoretical models for (a) small sand filled channels on diamicton, (b) large dry sand and gravel filled channel on diamicton, (c) small clay filled channels on diamicton and (d) large clay filled channel on diamicton. All models are inverted using the robust constrained inversion method.

Ridge overlapped by clay overlying till

This model consists of a cross-section of an esker ridge composed of sand and gravel (800Ωm) overlying till (300Ωm). Both overlain by postglacial silts and clays (100Ωm).

The best fit to the original is obtained by inversion with the robust constraint method, see Figure 5.13. The shape of the esker ridge is well-defined by this method. The contact between silts and clays and the till occurs at about 200Ωm. It is slightly deformed at the edges of the profile; however, in general terms, there is a reasonably good fit with the original model. As observed before in other models, some anomalous high resistivity values occur at the base of the inversion model, which are susceptible to misinterpretation.

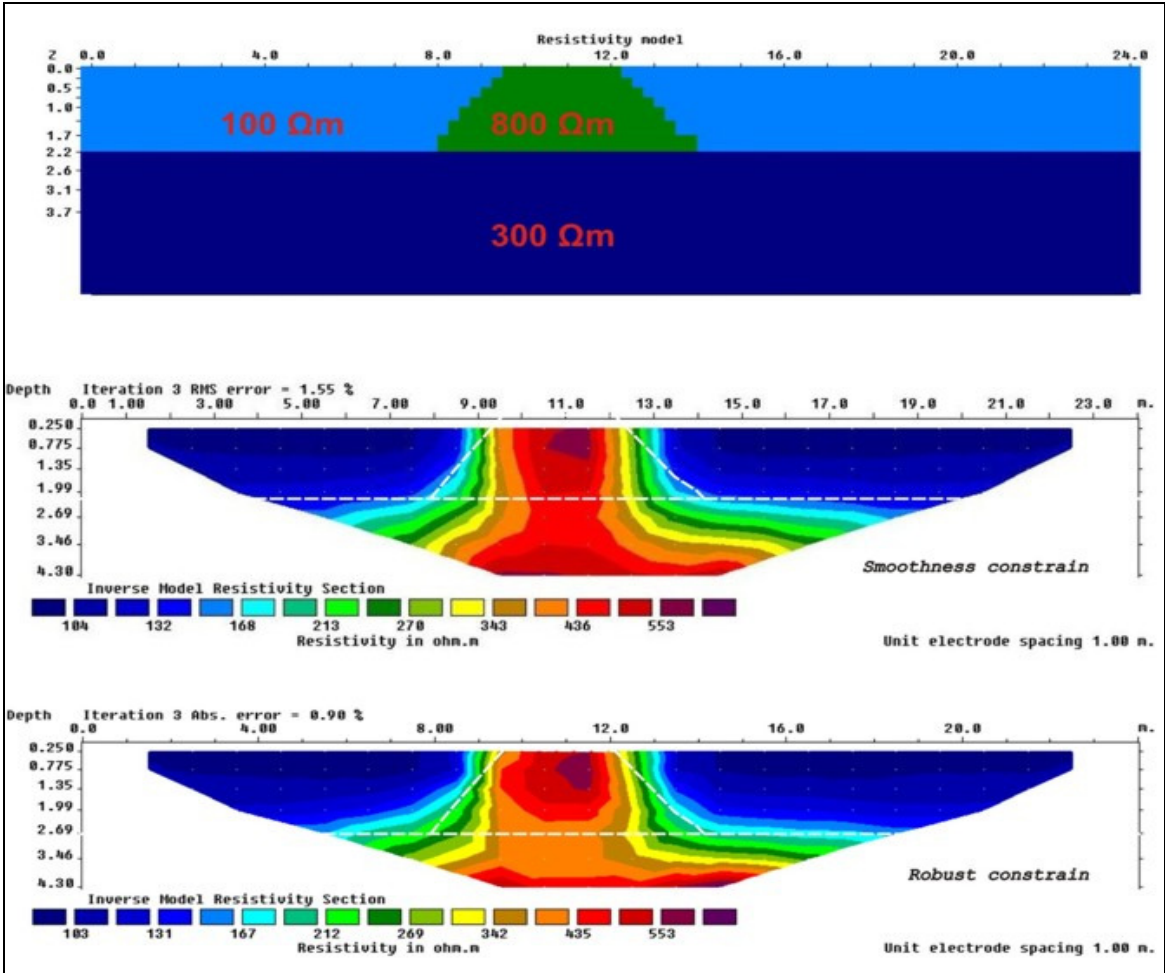


Figure 5.13 – Theoretical model of esker ridge (300Ωm) overlapped by lacustrine silts and clays (100Ωm), both overlying diamicton (300Ωm). The model have been inverted by means of the smoothness constrained model (above) and the Gauss-Newton robust constrain (below).

Line S1-L01-5m

A model has been produced simulating a profile collected as part of the time-lapse survey performed in site S1 (see Chapter 6 for results of time-lapse). This theoretical model is an approximation and is composed of 5 types of sediments with varying resistivity values: till ($250\Omega\text{m}$), lacustrine silts and clays ($100\Omega\text{m}$), glaciofluvial sand and gravel ($500\Omega\text{m}$), esker sand and gravel ($700\Omega\text{m}$) and glaciofluvial sands ($400\Omega\text{m}$).

Two derived inverse models using the smoothness constrained and robust constrained inversion methods are presented in Figure 5.14. The latter best preserves the lithological contacts. The shape of the esker in the inversion model may be misinterpreted as a channel feature. This shows how knowledge of the geomorphology and local geological settings of the areas around the field site will usually help in the interpretation.

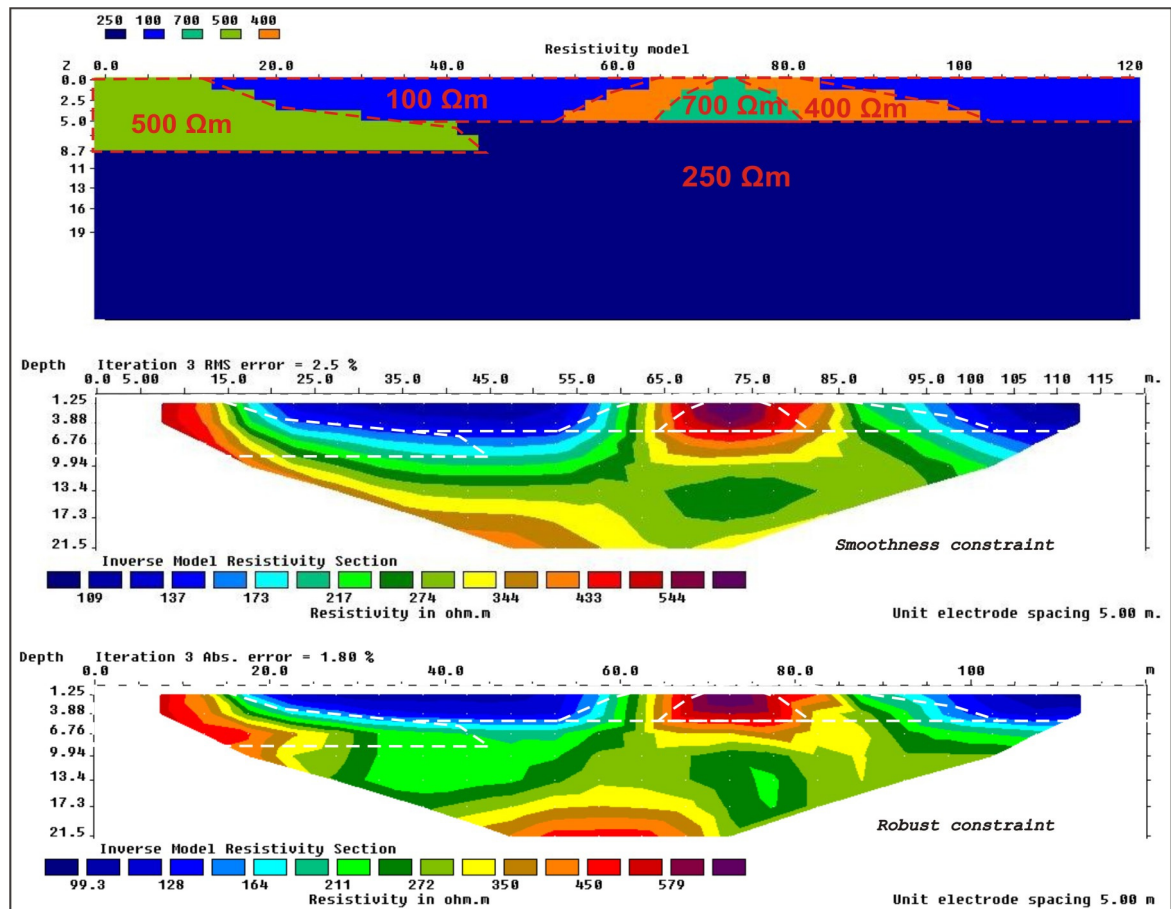


Figure 5.14 – Theoretical model consisting of 5 types of sediments with different resistivity values. Inversion with smoothness constrained method (above), robust constrain method (below).

Discussion

The results obtained for the theoretical models presented in this chapter show the potential and limitations of the RES2DINV software to produce inversion resistivity models of the subsurface.

The software has a large number of possible setting combinations that can be tested to obtain the most accurate final results. The type of inversion method picked for data processing appears to be the main factor to take in account. The two main inversion methods should be used for data inversion and as a general rule, features depicted for both methods can be considered real (Loke, 2001). However, the use of the Gauss-Newton robust constrained method is, in general, the one that provides the most accurate results.

As a general rule, the contact between a low resistivity layer ($100\Omega\text{m}$) overlying a high resistivity layer ($1000\Omega\text{m}$) is depicted in the inversion model at values closer to the low resistivity ($250\Omega\text{m}$) than to the high resistivity values. On the other hand, in a situation of a high resistivity layer overlying a low resistivity layer, the contact falls on the average values between the two ($500\Omega\text{m}$). This is more evident when the resistivity contrast between the two layers increases.

Horizontal layers with resistivity values higher than the surroundings and thicker than the electrode spacing are detected when the resistivity contrast between the layer and the host material is more than 70% (e.g. In order to be detected, a layer enclosed within a host material with resistivity of $300\Omega\text{m}$, requires a minimum resistivity value of $510\Omega\text{m}$).

Horizontal layers with resistivity values lower than the surroundings and thicker than the electrode spacing are detected when the resistivity contrast between the layer and the host material is more than 30% (e.g. In order to be detected, a low resistivity layer enclosed within a host material with resistivity of $300\Omega\text{m}$, requires a maximum resistivity value of $210\Omega\text{m}$).

Layers or lenses thinner than the electrode spacing are partially resolved when the resistivity contrast between the layer and the surrounding material is more than four times (e.g. Layer or lense has a value of 800 Ω and surrounding material has a value of 200 Ω m). However, although the upper and the lateral contacts are usually resolved, the thickness of the feature and the resistivity values are never properly resolved regardless of the resistivity values contrast.

Channel features and esker ridges are generally well depicted; Features of this nature, smaller than the electrode spacing, have also been detected. However, esker ridge can be misinterpreted as channels. A good understanding of the geology and geomorphology of the surveyed area should aid to the proper interpretation of the final inversion model.

Non-existent high resistivity artefacts may be generated by the inversion model at the bottom corners of the pseudosection when high contrast between layers occurs within the subsurface. These artefacts are generated during the interpolation of the data and have to be taken into account during interpretation of the generated inverse model.

5.3 – GPR

Electromagnetic waves transmitted through a body behave differently depending on a number of factors: frequency (f) of the transmitted wave, relative permittivity (ϵ_r), electrical conductivity (σ) and magnetic permeability (μ) of the body. These factors will influence the velocity and the amplitude of the waves detected by the receiver antenna. These concepts have already been discussed in Chapter 3 (see section 3.4.2).

Goodman (1994) presented a methodology for simulating GPR models using GPRSIM software. This software has been employed to create simplified models of the subsurface which have subsequently been modelling using a GPR simulator algorithm. The results of such modelling have greatly aided the interpretation of the GPR data collected in the field. The software allows a number of parameters to be entered for both subsurface properties and the survey settings. A model of the subsurface is initially interactively created by

digitising a theoretical subsurface structure, (see Figure 5.15 for an example). A number of modelling parameters can be assigned to each material within the profile: relative permittivity (ϵ), electrical conductivity (σ) and magnetic permeability (μ). Furthermore, a set of parameters, wave velocity (V), attenuation factor (α) and wavelength (λ) are calculated from these parameters.

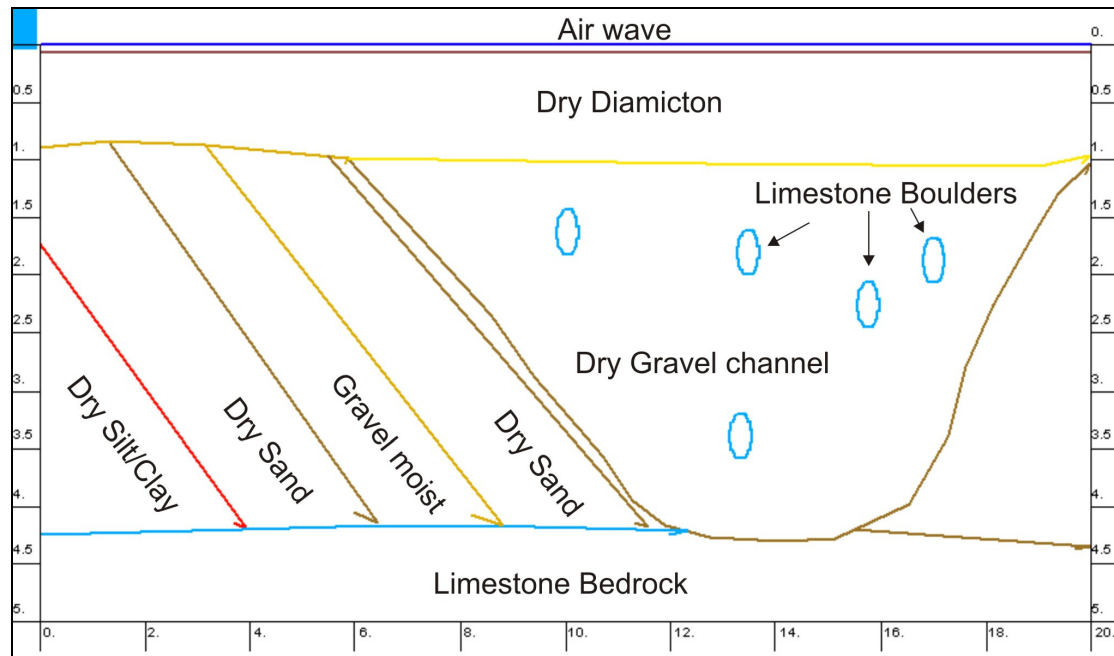


Figure 5.15 – Theoretical model produced in GPRSIM representing a diamicton underlain by a channel feature with associated foresets which overlies limestone bedrock.

The velocity of the electromagnetic waves within the material is calculated from equation 3.11, presented in Chapter 3.

The attenuation factor (α) is computed by

$$\alpha = \omega \left[\frac{\epsilon_r \epsilon_i}{2} \sqrt{1 + \left(\frac{\sigma}{\omega \epsilon_r \epsilon_i} \right)^2} - 1 \right]^2 \quad \text{from Goodman (2007)}$$

Where ω is the angular frequency = $2\pi f$ and ϵ_r and ϵ_i are the real and the imaginary relative permittivities, respectively.

Finally, the wavelength (λ) is calculated from the equation

$$\lambda = V/f$$

The survey settings parameters that can be entered are, antenna frequency, antenna separation, step size, wave polarization, antenna aperture and gains applied to the resulting profile.

Moreover, a large range of wave types (50) can also be set, these are coded as R, TRT, TTRTTT etc. where R stands for a direct reflected wave, TRT for a transmitted, reflected, transmitted wave and TTRTT for a wave transmitted through two layers, reflected from the top of the third and then transmitted through the upper two layers again. The correct wave types have to be selected in order to record all the features within the theoretical model. The more wave types that are used, the more complex the radargram will appear. Many more wave combinations than are shown in this section were tested. For example, the effects of ringing resultant from multiple reflections RRRRRR between two layers were examined in order to help identify artefacts in the data.

Forward modeling has been applied to several simple geological models reflecting the subsurface architecture recorded during data collection for this thesis. The physical properties for a range of materials typically found in the study area have been input into the software program for data modeling (Table 5.1). These have been extracted from a number of sources:

- Electrical permittivity from Table 3.4 (Neal, 2004) and Baker et al. (2007).
- Conductivity from Figure 3.3, Table 3.4 and conductivity values collected from electrical resistivity surveys carried out for this thesis.
- Magnetic permeability has been defaulted to 1, as materials with high magnetic mineral concentrations are not expected in the study area.

The wave type used has been customized for each theoretical model based on the number of layers modeled. The same geological setting has been modeled using different antennae frequencies, separation and step size utilized for data collection. Wave polarization and antenna aperture has been kept constant for all the simulations.

Material	Permittivity (Er)	Conduct. (S/m)	Velocity (cm/ns)	Wavelength (cm)	Attenuation (1/m)	Source
Air	1	0	30	150	0	Goodman (2007)
Esker dry	6	0.003	12.25	61.23	2.3x10 ⁻²	Neal (2004) and thesis
Esker moist	10	0.0008	9.49	47.43	4.76x10 ⁻²	Neal (2004) and thesis
Esker saturated	16	0.0017	7.5	37.5	0.08	Neal (2004) and thesis
Loam-sand dry	6	0.0014	12.25	63.1	0.108	Neal (2004) and thesis
Loam-sand moist	18	0.004	7.07	35.35	0.178	Neal (2004) and thesis
Gravel Dry	6	0.0007	12.25	61.23	5.38x10 ⁻²	Neal (2004)
Gravel Moist	12	0.0014	8.66	43.3	7.62x10 ⁻²	Neal (2004) and thesis
Gravel Saturated	17	0.005	7.28	36.38	0.229	Neal (2004) and thesis
Sand Dry	5	0.00001	13.42	134.16	8.42x10 ⁻⁴	Neal (2004) and thesis
Sand Moist	12	0.0002	8.66	86.6	8.42x10 ⁻²	Neal (2004) and thesis
Sand Saturated	20	0.0007	6.71	67.08	1.09x10 ⁻²	Neal (2004) and thesis
Soil Loamy	20	0.001	6.71	33.54	2.95x10 ⁻³	Goodman 2007
Pure water	81	0.0001	3.33	16.67	2.09x10 ⁻³	Goodman 2007
Water	81	0.01	3.33	16.67	0.209	Goodman 2007
Granite	5	1x10 ⁻⁸	13.42	67.08	8.42.10 ⁻⁷	Goodman 2007
Limestone	4	0.0001	15	74.99	9.42.10 ⁻³	Neal (2004) and thesis
Silt/Clay Dry	10	0.02	9.45	47.24	1.187	Neal (2004) and thesis
Silt/Clay Moist	20	0.035	6.69	33.43	1.47	Neal (2004) and thesis
Till Dry	10	0.01	9.48	47.39	0.595	Neal (2004)
Till Saturated	24	0.0125	6.12	30.61	0.481	Neal (2004)
Peat Dry	25	0.0025	6	30	9.42x10 ⁻²	Neal (2004)
Peat Moist	45	0.009	4.47	22.36	0.253	Neal (2004)

Table 5.1 – GPR forward model parameters. Material physical properties from Neal (2004), Baker et al. (2007), Goodman (2007) and geophysical field data collected for this thesis.

A number of theoretical models have been simulated using the GPRSIM software, these are the most common structures that have been observed during field mapping:

- Two horizontal layers with a small change of the material permittivity (10%).
- Two horizontal layers with a large change of the material permittivity (140%).
- V shaped channel feature
- U shaped channel feature
- Set of asymmetrical channel features
- Difference in response of limestone boulders within dry and saturated diamicton
- Deltaic sediments (topsets, foresets and bottomsets)
- Channel feature on bedrock with associated foresets overlain by till
- Esker ridge and associated glaciofluvial sediments on till
- Esker ridge within peat overlying till
- Fractures within glacial sediments
- Theoretical resolution of vertical layers
- Theoretical resolution of horizontal layers
- Resolution of neighboring materials with minute variation on their permittivity values.

Two layers with a small (10%) and a large (140%) change in relative permittivity are presented in Figure 5.16a, b. A horizontal reflector is well depicted in both cases. It is noticeable that reflectors are composed of three bands representing positive and negative oscillations of the electromagnetic wave. In the situation of a change from low permittivity material to higher permittivity (a) the reflector is composed of a negative pulse, represented in white, followed by a positive (black) and ending with a negative pulse (white). Neal (2004) represents this numerically (see equation 3.14) with the reflection coefficient, which would be negative in that situation. The reflection coefficient is positive in the situation of electromagnetic waves traveling from a high to a low permittivity material. A large difference in the relative permittivity values between two materials (Figure 5.16b) is expected to yield to a high reflectivity reflector, whereas a lower contrast

is expected to produce a reflector with lower intensity (Figure 5.16a), however, the expected difference in reflectivity contrast is not apparent because of the gain used in this simulation.

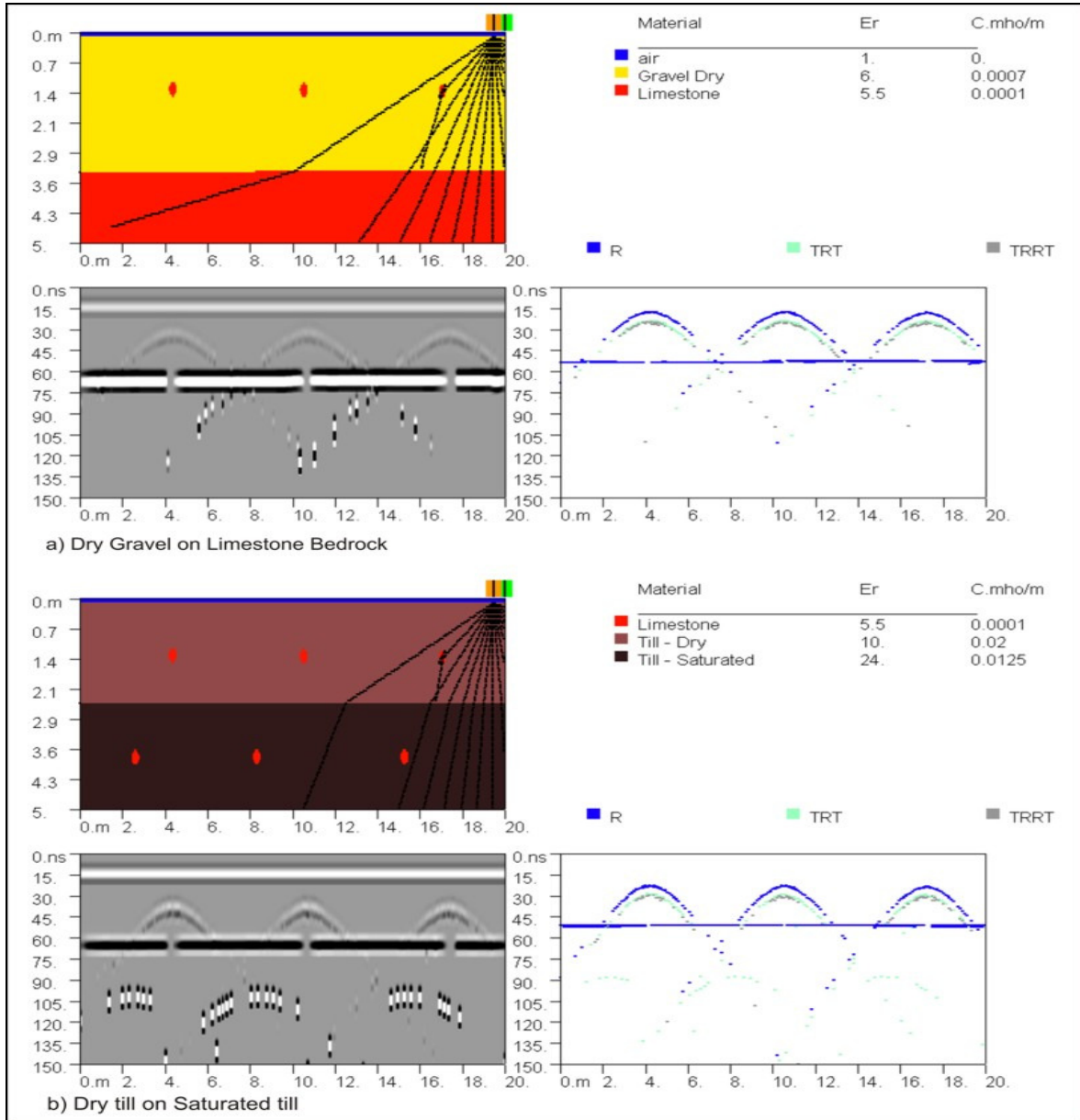


Figure 5.16 – Theoretical models for layers with horizontal contact and boulders enclosed in host materials with different permittivities and velocities. GPR data simulated with a 200MHz antenna.

Another feature identified from this model is the shape of the hyperbolae representing limestone boulders. The deeper the boulders are within the subsurface, the wider is the resulting hyperbola. This is mainly because of the travel time difference between the waves

reflected from the boulder with antennae vertically over it and the waves reflected with the antennae located oblique to it, which decreases with depth factors; moreover, the size of the Fresnel zone (equation 3.16), which increases with depth allows the detection of features farther away from the antennae. These result in narrower shaped hyperbolae associated with relatively shallow boulders when compared to the deeper ones. Moreover, a low relative permittivity contrast between the boulders and the host material (Figure 5.16b - top layer) is represented by poor reflectivity hyperbolae whereas a high permittivity contrast (Figure 5.16b - bottom layer) produces high reflectivity hyperbolae. The lower boulders are depicted as discontinuous hyperbolae; these are enclosed within saturated sediments with higher conductivity resulting in a higher attenuation factor.

A drawback of GPR software is that, in order to convert from time to distance, a unique velocity is used for data processing, thus it is assumed that no velocity changes occur in the subsurface within a profile. However, variation in the material properties causes changes in velocity, which can then produce important distortions of the radargram. A number of examples are presented to understand the nature of the distortions caused by velocity variations that would be expected in data collected during fieldwork (Figure 5.17). The velocity used for the simulation exercise is 0.1m/ns. Figure 5.17a presents a three layer setting consisting of peat overlying dry gravel on saturated gravel. When modeled, the thickness of the high velocity material (dry gravel) is reduced, while the low velocity material (peat) is increased. A boulder within a high velocity medium will produce a broader shaped hyperbola located in a shallower position than the real position (Figure 5.17b), in contrast, the same boulder within a low velocity medium will respond with a narrow hyperbola located at a deeper position than the true one. Note also that the sub-vertical boundary between the two host materials is not detected in the simulation because rays reflected from it are not recorded back at the receiver antenna. This reinforces the use of several methods, such steep contacts are well depicted with ERT (Figure 5.4). Deformation of the subsurface sedimentological architecture is illustrated in Figures 5.17c,d. An esker ridge overtopped by sediments with similar velocity, such as dry sand, is represented in the radargram as a good approximation to the shape of the actual feature. However, if the feature is overtopped by a low velocity material such as peat, the feature is

depicted on the radargram as a stretched ridge with thickening of areas overlain by peat and thinning of the region overlain by the esker, which results in significant deformation of the layers located under the esker ridge. Knowledge of this deformation is essential to correctly interpret data collected in the field.

Channel features are often present within glaciofluvial sediments and a number have been mapped in the study area. Three examples of the GPR signature of channel features simulated using GPRSIM are presented below. Figure 5.18a illustrates the response of a V shaped symmetric channel feature to GPR survey as a “bow-tie” pattern, previously presented in Chapter 3 – Section 3.4.4. This pattern shows a reflection from the channel wall underlying the antenna and another from the opposite wall underneath it, which cross each other at the lowest point within the channel. In addition, a pull up of the shape of the original channel is observed; this is because the channel infill is dry gravel, a high velocity material. On the other hand, the U shaped channel feature (Figure 5.18b) is represented as a less pronounced “bow-tie” pattern; however, the region of the channel wall with a vertical/sub-vertical dip is not recorded by the GPR system because reflected waves do not reach the receiver. A more realistic situation with irregular channel features infilled with dry gravel cut into diamicton with angular/subangular boulders is presented in Figure 5.18c. The channels are detected fairly accurately; the occurrence of the “bow-tie” pattern is not as clearly expressed as before. Furthermore, the point features digitized into the model as angular/subangular boulders are poorly depicted as discontinuous hyperbolae. It can be inferred from this that boulders depicted as continuous hyperbolae in the radargram would characteristically have a rounded/subrounded shape.

Materials which are highly conductive, such as silts and clays, have high attenuation values, which impede the penetration of electromagnetic waves through the subsurface. Figure 5.19 shows a dry layer of clay overlying saturated clay underlain by saturated gravel. It is known that clayey sediments tend to have high conductivity values. The gravel layer overlain by fine sediments cannot be depicted by the GPR simulation (at the gain employed) because of the high attenuation values associated to fine sediments, which diffuse the electromagnetic energy before the gravel bed is reached.

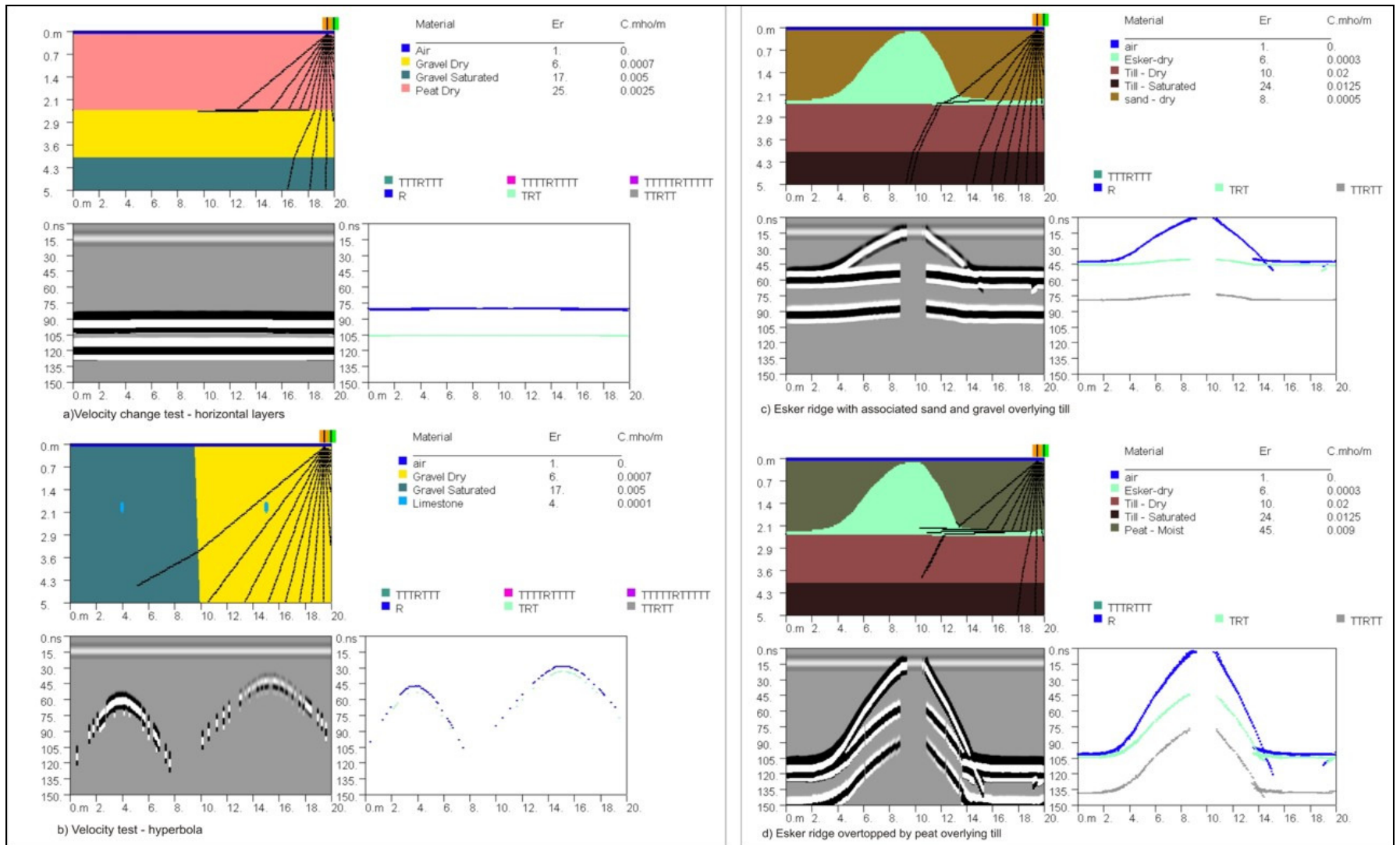


Figure 5.17 – Theoretical models illustrating distortions of the radagrams due to material velocity variations. Simulated with a 200MHz antenna.

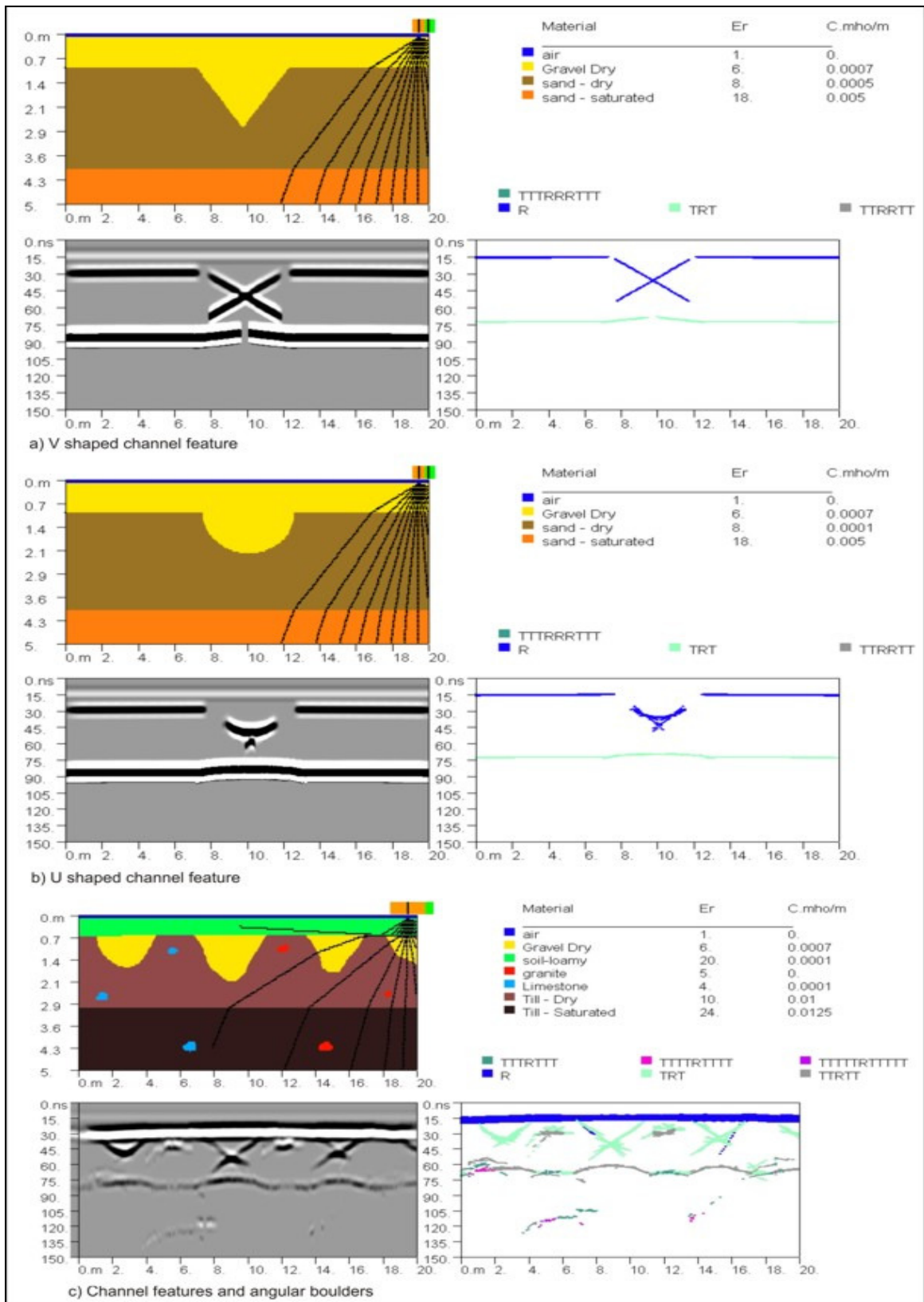


Figure 5.18 – Three theoretical models for channel features. Simulated with 200MHz antenna frequency.

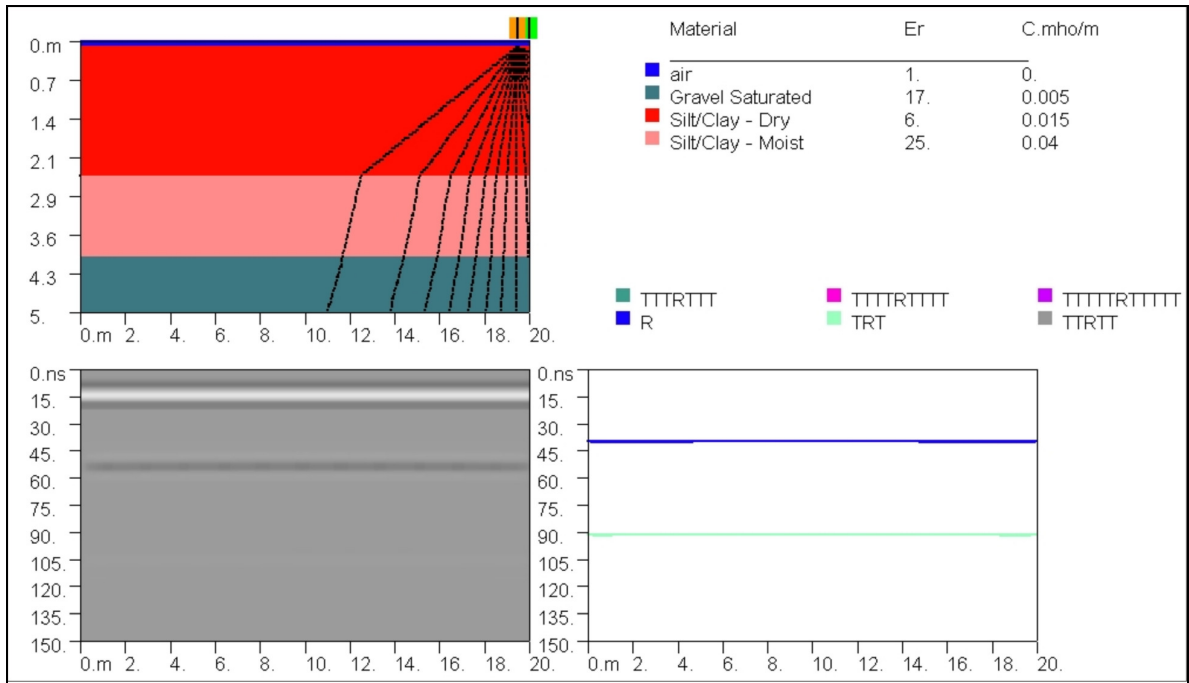


Figure 5.19 – Theoretical model illustrating high attenuation material response to GPR survey. Simulated with 200MHz antenna frequency.

Resolution of sub-vertical features has been assessed by constructing a theoretical model with continuous reflectors at increasing dipping angles (Figure 5.20). The same model has been simulated with 200, 100 and 50MHz antenna frequencies. Reflectors at angles dipping at greater than 82° are not depicted by any of the antennae on the simulation. Reflectors detected at lower angles show some distortions, mainly angle underestimation of continuous dipping reflectors (see Figure 3.25b, Chapter 3) and differences in the reflectivity strength. Reflectors at an angle of 80° and 79° in the model are represented in the radargrams by reflectors dipping 51° and 59° respectively, the distortion of the reflector can be correlated with the velocity of the material, thus the faster the velocity, the higher the dipping angle and the larger the distortion of the image. Antennae with 50 and 100 MHz frequency present better continuity of the reflectors detected, as transmitted and reflected waves (TRT) are recorded in the radargram. This is probably due to the higher penetration of low frequency antennae and to the larger antenna separation than the one used for the 200MHz antenna. TRT waves portray reflectors at slightly higher angles than the R waves, probably influenced by the overlying material. Additionally, TRT waves show stronger reflectors than the reflected (R) waves.

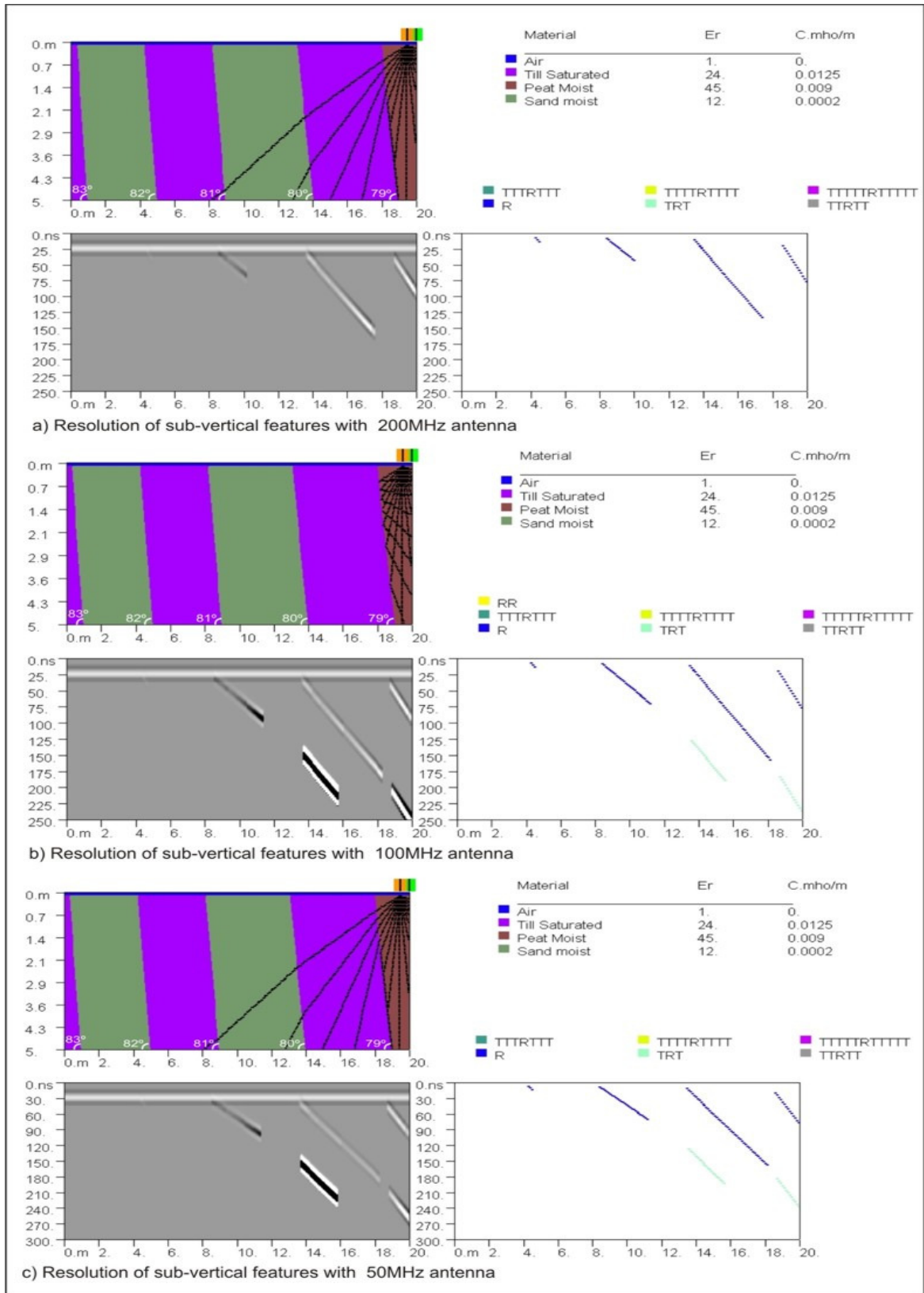


Figure 5.20 – Theoretical models illustrating threshold for detection of sub-vertical reflectors. Simulated with 200MHz, 100MHz and 50MHz antenna frequencies.

Resolution of horizontal features is tested for two situations using a 200MHz antenna. Figure 5.21a shows thin layers composed of low-loss material (e.g. dry sand), Figure 5.21b displays thin layers composed of low velocity material (e.g. peat). EM waves travel faster in low-loss materials, thus the thickness of layers composed of low-loss material is underestimated in the radargram, unless the velocity correction is performed by the velocity of propagation within this material using the velocity calibration tool in Ekko View DeLuxe, however, this software only allows a velocity correction for each radargram, thus for radargrams with diverse materials of differing velocities a decision has to be made on which velocity is to be used (i.e. average of velocities or velocity of predominant material). Horizontal layers with a thickness of 0.5m or more are resolved in all situations when using a 200MHz antenna. A 0.25m thickness layer is resolved when composed of low velocity materials such as peat. Nonetheless, the same layer cannot be resolved when composed of a high velocity material such as well-sorted dry sand (Figure 5.21a), however, it can be inferred from the presence of four polarization bands. A 0.1m thickness layer cannot be resolved, even though it can be inferred from the presence of four polarization bands. These values, do not agree with the theoretical resolution of a 200MHz antenna, which would be 0.18m for dry sand and 0.1m for saturated sand (Jol and Bristow, 2003). Moreover, the setting presented in Figure 5.21b has been also simulated using a 100MHz antenna (Figure 5.21c); no difference is noticeable from visual analysis of the obtained radargrams; a decrease in resolution would be expected according to GPR theoretical background discussed in Chapter 3; it appears that the software GPRSIM presents some limitations at representing the expected variation of resolution of different antenna frequencies.

As discussed in the GPR theoretical concepts in Chapter 3, differences in relative permittivity between adjacent materials result in a change in the behaviour of the EM waves, which is recorded as a reflector. However, the degree of difference needed between materials in order to obtain a reflector in a radargram has not been established. A number of simulations have been carried out in order to ascertain the minimum relative permittivity difference needed to obtain an observable reflection. Two situations have been tested: Figure 5.22 shows six materials with relative permittivity values varying between 5 and

5.5. Figure 5.22a shows that a relative permittivity difference of 0.02 in the shallow subsurface is not depicted. However, the same relative permittivity variation is detected as a strong reflector when the reflector is located in the deeper part of the radargram (Figure 5.22b), as the reflector is enhanced by an exponential gain. Figure 5.22c shows the same situation with an exponential gain of 2. In this situation, relative permittivity differences of more than 0.1 (1.81%) are detected. The same exercise has been performed with minute differences in materials with large relative permittivity values. Figures 5.23a and 5.23b show six materials with permittivity values varying between 30 and 30.5. The application of large exponential gains strongly enhances the reflectors and all the layers are depicted; however, the strength of the reflectors is rather smaller than that for layers with low relative permittivity values. Permittivity variations smaller than 0.25 (less than 1%) are not detected after applying an exponential gain of 2. A situation with extremely small permittivity variations between 30 and 30.0195 is presented in Figures 5.23c/d. Figures 5.23c shows how a permittivity variation of 0.0005 representing a 0.0016% difference is still detected when using an exponential gain of 10. On the contrary, no layers are depicted when an exponential gain of 2 is used. It is noticeable that changes in permittivity affect the strength of the reflectors detected, however, to establish a minimum value for which the change in permittivity between neighbouring bodies is not depicted by the use of GPR is not possible using the GPRSIM software as tiny (non realistic) changes in relative permittivity of 0.0016% are still detected using this software.

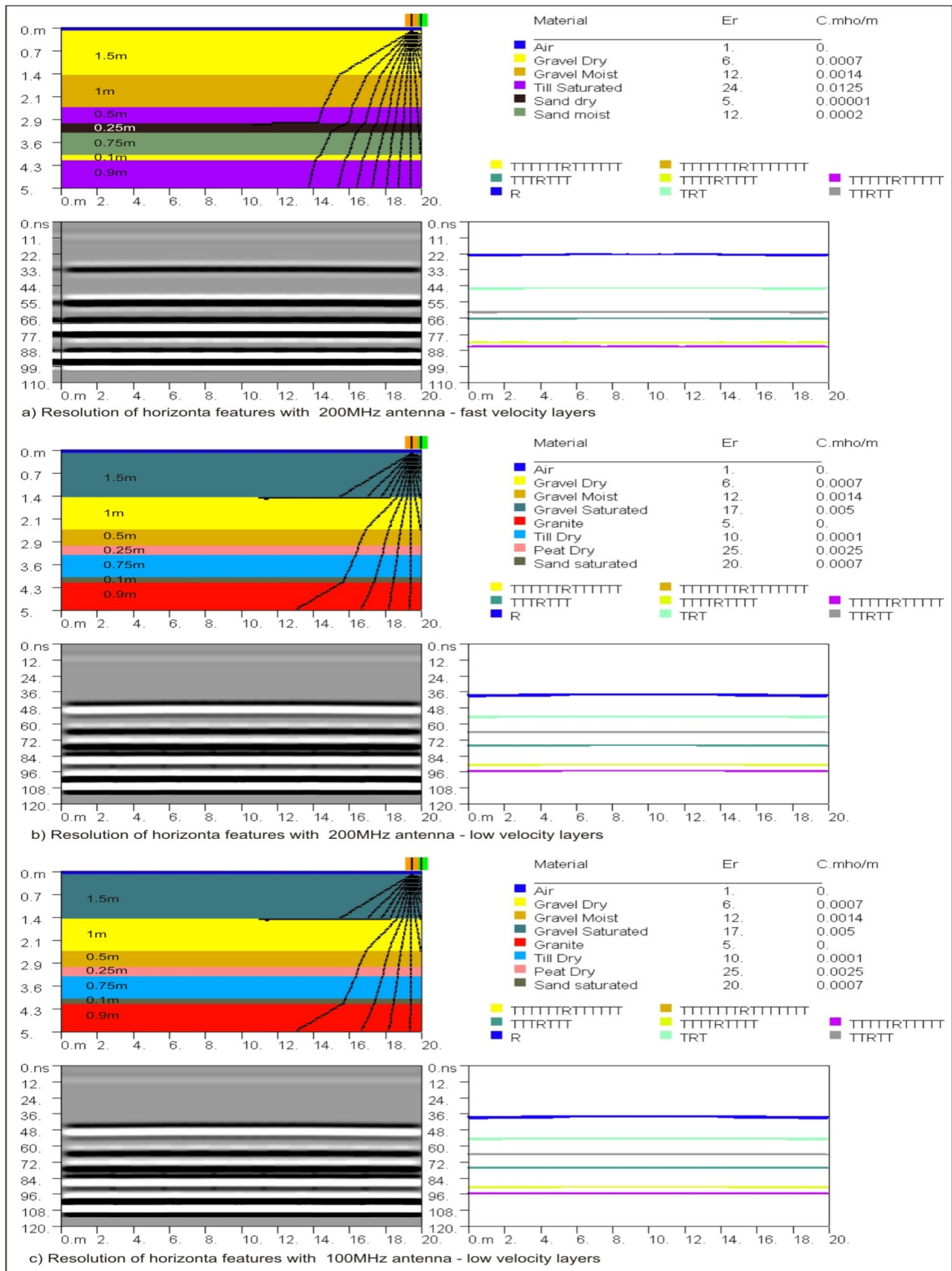


Figure 5.21 – Resolution of horizontal layers. (a) Diagram showing resolution of thin layers composed of high velocity material (dry gravel) compared to (b) resolution of thin layers composed of low velocity material (peat) using a 200MHz antenna. The theoretical model with thin layers composed of low velocity material (peat) has also been tested with a (c) 100 MHz antenna.

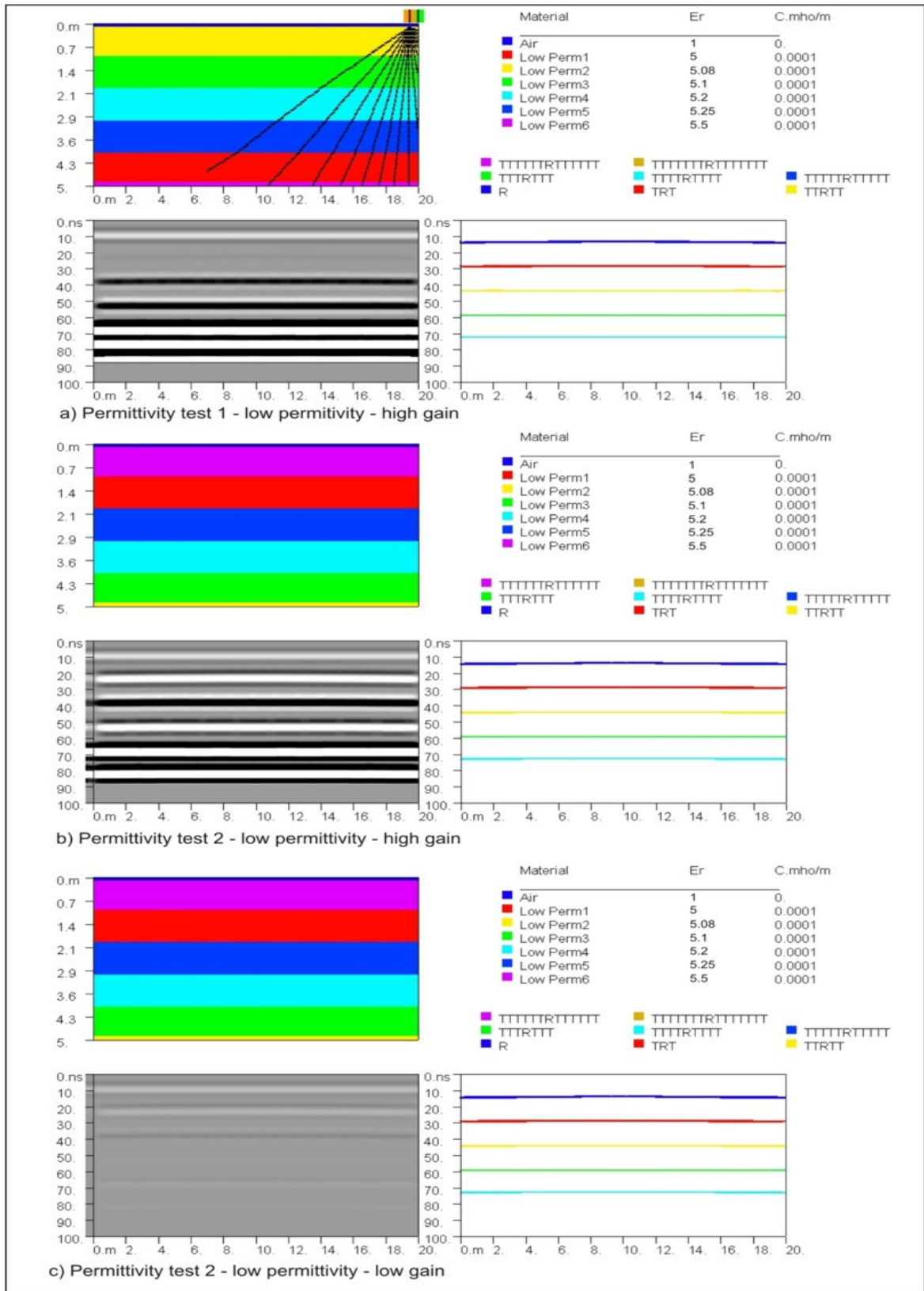


Figure 5.22 – Depiction of neighbouring materials with low permittivity values with minute permittivity variation between them.

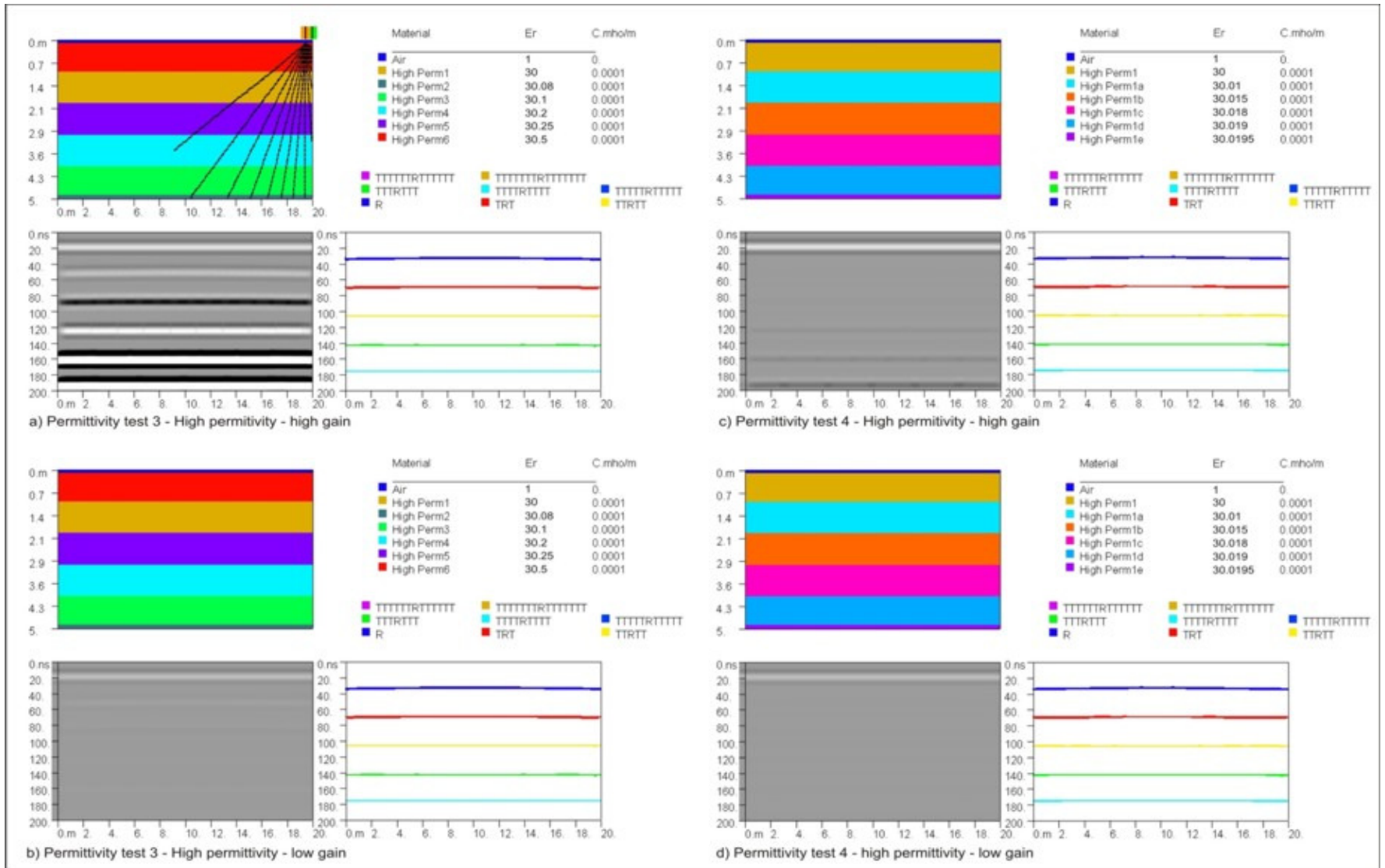


Figure 5.23 – Small (a,b) and infinitesimal (c,d) permittivity variation between materials with high permittivity values.

A typical setting expected in the study area is the presence of large boulders defining the core of esker ridges. Figure 5.24a displays such a theoretical model of an esker ridge with boulders and water table, which is marked by dry sediments overlying saturated sediments. The recorded radargram could be misinterpreted as a channel feature with boulders. This illustrates that knowledge of the geological setting and the topographic expression of the feature is essential to properly interpret GPR data. Figure 5.24b shows a large channel feature infilled with gravel and a number of boulders, overlying bedrock and flanked by foresets. The bedrock reflector is gradually pulled up in the area around the channel as sediments within the channel have a higher velocity. Deltaic sediments are common in the study area and consequently the resolution of foreset bedding has been tested and is presented in Figure 5.24c. Beds thinner than 2m cannot be resolved using the GPRSIM software. Reflectors with four polarization bands (white, black, white, black) indicate the presence of a thin bed (0.5m thick) rather than a single reflector which would be expressed by three polarization bands. Nevertheless, data collected for this thesis shows much higher resolution than the obtained by GPRSIM Software (See Figure 5.26), this illustrates the limitations of the software for radargram resolution analysis. Moreover, the relative permittivity contrast between adjacent materials strongly influences the resolvability of bedding; the 0.5m bed is more clearly detected than the 1m thickness because the 0.5m is surrounded by 3m thick low velocity materials, whereas, the 1m is underlain by a 2m thickness layer producing an overlapping of reflectors that complicates the data interpretation. Figure 5.24d shows a fracture within diamicton which has been represented as a dipping layer with moisture content higher than the host material, as it is expected that water will tend to flow through fractures. The feature is clearly delineated and furthermore, it can be inferred, from the presence of four polarization bands, that the feature depicted is formed from two parallel closely spaced reflectors. Moreover, it can be observed that the dip of the reflector is underestimated, which confirms the dip angle underestimation discussed in Chapter 3. Finally, we have seen before in Figure 5.16 that hyperbola reflections widen with depth, however, the boulders were contained in two different host materials; Figure 5.24d presents two limestone boulders located at different depths enclosed within the same host material. Once more, it is confirmed that the shallower reflector is represented by a narrower hyperbola than the deeper one.

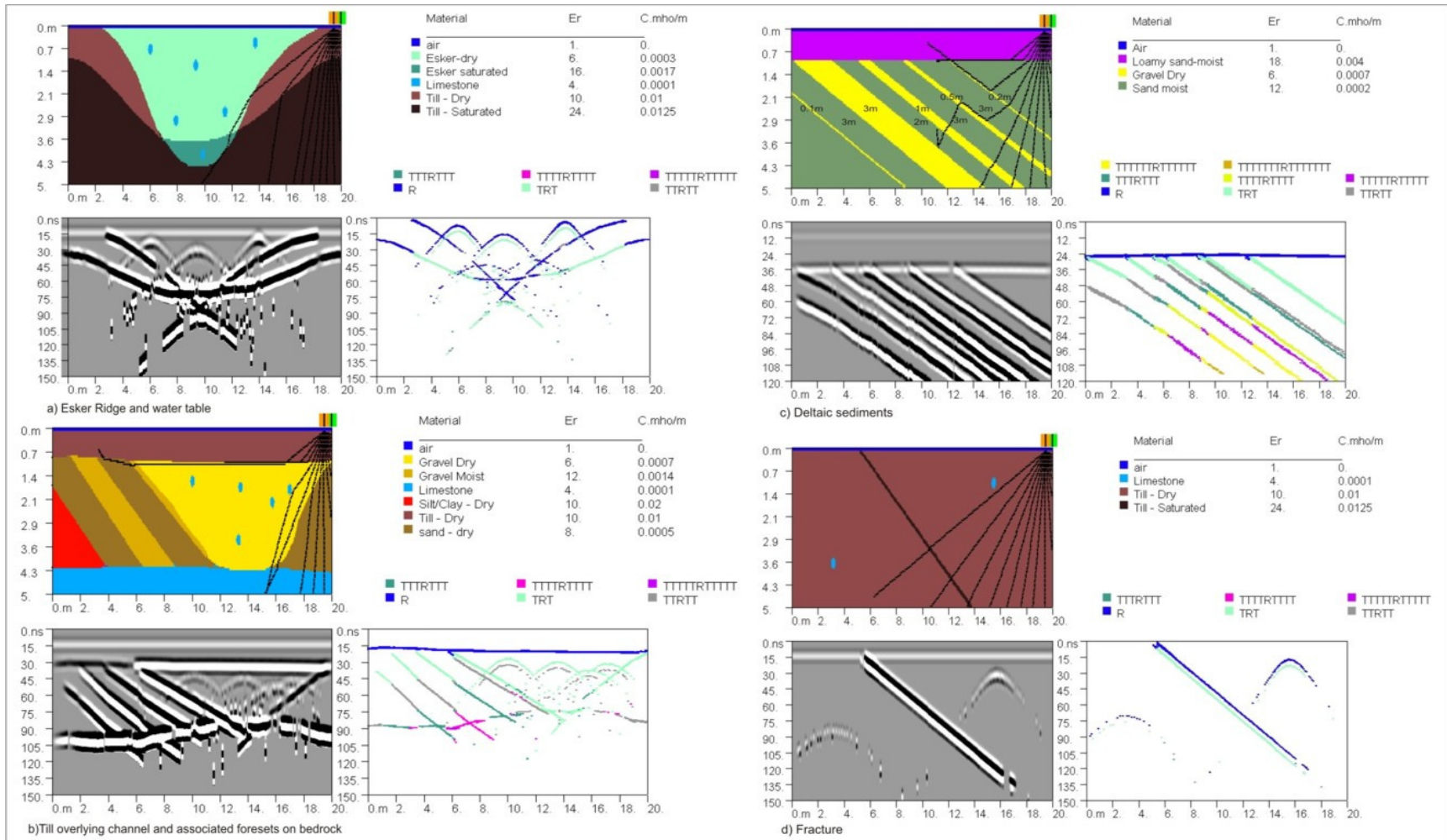


Figure 5.24 – Theoretical models for (a) Esker ridge and water table before topographic correction. (b) Gravel filled channel with boulders overlying limestone bedrock and flanked by foresets. (c) Deltaic sediments composed of topsets overlying foresets and (d) a fracture across a diamicton with two rounded boulders located at different depths.

5.4 – Geophysical techniques Training Sites T1, T2 and T3

Three training sites with exposed sediments have been surveyed to test the capabilities of resolution and penetration of the geophysical systems to detect sedimentological and lithological variations within the subsurface. Thus, various antennae frequencies and orientations could be tested to determine the optimum ones to employ and to allow comparisons between actual geophysical signatures, field exposures of glacial sediments and structures and theoretical models. The exposures selected illustrate examples of glaciodeltaic sediments, esker ridge deposits and glaciofluvial sediments representing a range of glacial deposits commonly occurring in the Irish Midlands. Site T1 is located in the study area. Sites T2 and T3 are located outside the study area 8 Km west-northwest from Horseleap and 6 Km east from Croghan Hill respectively.

Site T1

Site T1 is situated 6 Km south-southwest from Tullamore, in Agall Townland (E 240800, N222800), within an active sand and gravel pit excavated on the north end of a complex glaciodeltaic system occurring along the northeast margin of the Kilcormac Esker. A detailed morphological and geological description of these features was presented in Chapter 4 - Section 4.2.2. A number of exposures were recorded within the site during this research showing development of topsets, foresets and bottomsets characteristic of a deltaic environment. The location of such exposures is presented in Figure 5.25. Exposure ET1-B is shown in Figure 4.5.

A borehole (BH-T1A - E227000, N223000) of 10.5m depth was drilled in 2005 at the base of exposure ET1-C, which is mainly composed of gravel dominated topsets overlying sand and gravel foresets, which are underlain by bottomsets composed of fine sand. The borehole data show soft medium to fine-grained sand with few subangular pebbles (dropstones) with grain size decreasing downwards from 0 - 6.6m. A sample was taken between 2.7 and 3.7m (BH-T1A-1). From 6.6 - 10.5m sediment was described as medium dense to very dense blue-grey clayey silty diamicton with angular subangular limestone

pebbles. A second sample was collected between 7 and 8m (BH-T1A-2). The samples were wet sieved and classified under the Folk (1954) classification scheme. Both samples have been classified as gravelly muddy sand.



Figure 5.25 – Location of GPR survey (brown), borehole (green) and exposures (orange) recorded within site T1.

A GPR geophysical survey was undertaken in 2006 on top of a 70m long exposure occurring 120m south-southwest from BH-T1A; see Figure 5.25. The sedimentological setting within the exposure was recorded in situ; the image and the detailed lithological and sedimentological graphic interpretation are presented in Figure 5.26a/b. The top 1 -

1.5m of the exposure is dominated by interstratified planar cross-bedded sand and gravel which have been interpreted as glaciodeltaic topsets. These are disturbed at five points by vertical features, two of these features cut across the exposure subvertically from top to bottom at 4m and 20m. They are composed of fine sand and have been interpreted as clastic dykes based on the general characteristics described by van der Meer et al. (2009). The other three occur within the first 2m depth at positions 27m and 35m and from 1.5 - 2.5m depth at position 42m; these are shaped as an inverted cone, composed of gravel and have been interpreted ice wedge casts. The topsets are underlain by very well developed foresets dominating most of the exposure. These are alternately composed of sandy gravel, granules, sand and fine sand. The foresets dip 20 - 25° northeast from 0 - 60m. A gradual change in the direction occurs at this point, with dips gradually becoming horizontal and switching to dips of 10 - 20° west-northwest from 60 - 70m. This change in direction of the foresets has also been recorded in Exposure ET1-D. These deposits have been interpreted as a deltaic system composed of a number of coalescing lobes, the change in direction is inferred as the axis of a single lobe migrating northwards during deposition in a glaciolacustrine environment.

The GPR profile was recorded along the top of the exposure, 2 - 3m off its edge using a 50MHz, a 100MHz and a 200MHz antenna frequency. Furthermore, the 100MHz antenna frequency was tested using three antenna orientations: perpendicular broadside (PR-BD), parallel broadside (PL-BD) and cross polarization (XPOL), see Figure 3.21, Chapter 3. The profile runs northeast-southwest for 40m, from this point the recording direction changes to a southeast-east to northwest-west for the last 30m, this change in direction was necessary due to the shape of the exposure at the time of data collection. All the data presented were collected within 5 hours during dry weather conditions and the radargrams processed by means of time zero adjustment, dewow, AGC gain and topographic correction.

Radar surfaces, packages or facies descriptions are based on the terminology illustrated in Figure 3.29 and the coding scheme used is shown in Figure 3.30, Chapter 3.

Figures 5.26c and 5.26d display the radargram collected using a 200MHz antenna and an interpretation of the collected data. Enclosure 2 – E2E shows the interpretation of the dataset as a fence diagram illustrating the true orientation of profile. The topsets facies (L1f3-Dts) in the exposure are less than 1m in thickness on average and their base is delineated by a single continuous subhorizontal reflector (L1s2-be). In the region between 35 and 42m, the topsets package thickens to 1.5m, where part of the internal structure is depicted in form of small low angle dipping reflectors, probably related to a channel feature. Underlying the topsets, a suite of continuous dipping reflectors with toplap contact dominate the profile from 72 - 75.5m O.D. These have been interpreted as foresets. Foresets facies (L1f2-Dfs) are composed of continuous dipping reflectors. These reflectors dip from 10 - 18° northeast between 0 and 20m, they gradually develop into steeper continuous subparallel reflectors reaching maximum dips of 25° between 15 - 45m. From 45m, the dip of the reflectors gradually become flat lying at the 53 - 55m positions, which then change into subparallel continuous reflectors dipping 15° west-northwest from 60 - 70m. These are clearly related to the foresets recorded in the exposure (Figure 5.26b). The foresets overlie a set of gently subhorizontal sinuous subparallel continuous reflectors recorded between 10 and 70m at less than 72m O.D, which have been interpreted as bottomsets (L1f1-Dbs).

Unfortunately the contact detected between the foresets and the bottomsets is not visible on the exposure which would have allowed a good computation of the velocity to estimate the true depth of the profile. However, a lithological contact occurring in the exposure (gravel - Gfo overlying sand - Sfo) between 48 - 57m at around 73m height, is characterised by a strong reflector in the radargram. This contact has been used to compute the velocity to be applied to the profile. Furthermore, the computed velocity has been confirmed by calibrating hyperbolae reflections detected at 45m and at 65m. The velocity computed for this radargram is 0.11m/ns.

The difference in depth of penetration and resolution for different antenna frequencies has been tested for 50MHz, 100MHz and 200MHz antennae using time windows of 320ns, 200ns and 150ns respectively. Figure 5.27 shows GPR data collected with the three

antenna frequencies along the survey line. Topsets are only partially resolved by the 100MHz antenna and can hardly be interpreted as such using the 50MHz antenna, even though a reflector is detected. An almost true representation of the foresets has been attained with the 200MHz antenna profile; these are also partially depicted by the 100MHz antenna and could still be inferred in places from the 50MHz. The main advantage of the low frequency antenna is its superior depth of penetration. Main reflectors within the bottomsets are detected by the three antenna frequencies at different resolution; reflectors detected by the 50MHz have an approximate thickness of 0.7m, which is slightly thicker than the expected minimum vertical resolution of 0.55m calculated from equation 3.15.

The results of a survey carried out with three different orientations of 100MHz antennae relative to the survey line are presented in Figure 5.28. PR-BD is designed to collect *EH* polarization data, PL-BD is designed to collect *EV* polarization data and XPOL is designed to collect *EH* and *EV* polarization data (Baker et al., 2007). Flat-lying reflectors are specially emphasised by PL-BD (Figure 5.28b), while PR-BD (Figure 5.28a) tends to display better the continuity of dipping reflectors, see region from 15 - 25m at 2 - 3m depth. Contact between foresets over bottomsets in the region from 10 - 20m occurs at around 5m depth with PL-BD and PR-BD configurations, while it takes place at 5.75m using the XPOL. Data collected using XPOL (Figure 5.28c) tends to be noisier as both *EH* and *EV* polarization data are collected, this is illustrated by changes in the polarization of the air and surface waves along the profile. Moreover, topsets are not properly detected using this method. The antenna orientation used for this thesis is the PR-BD.

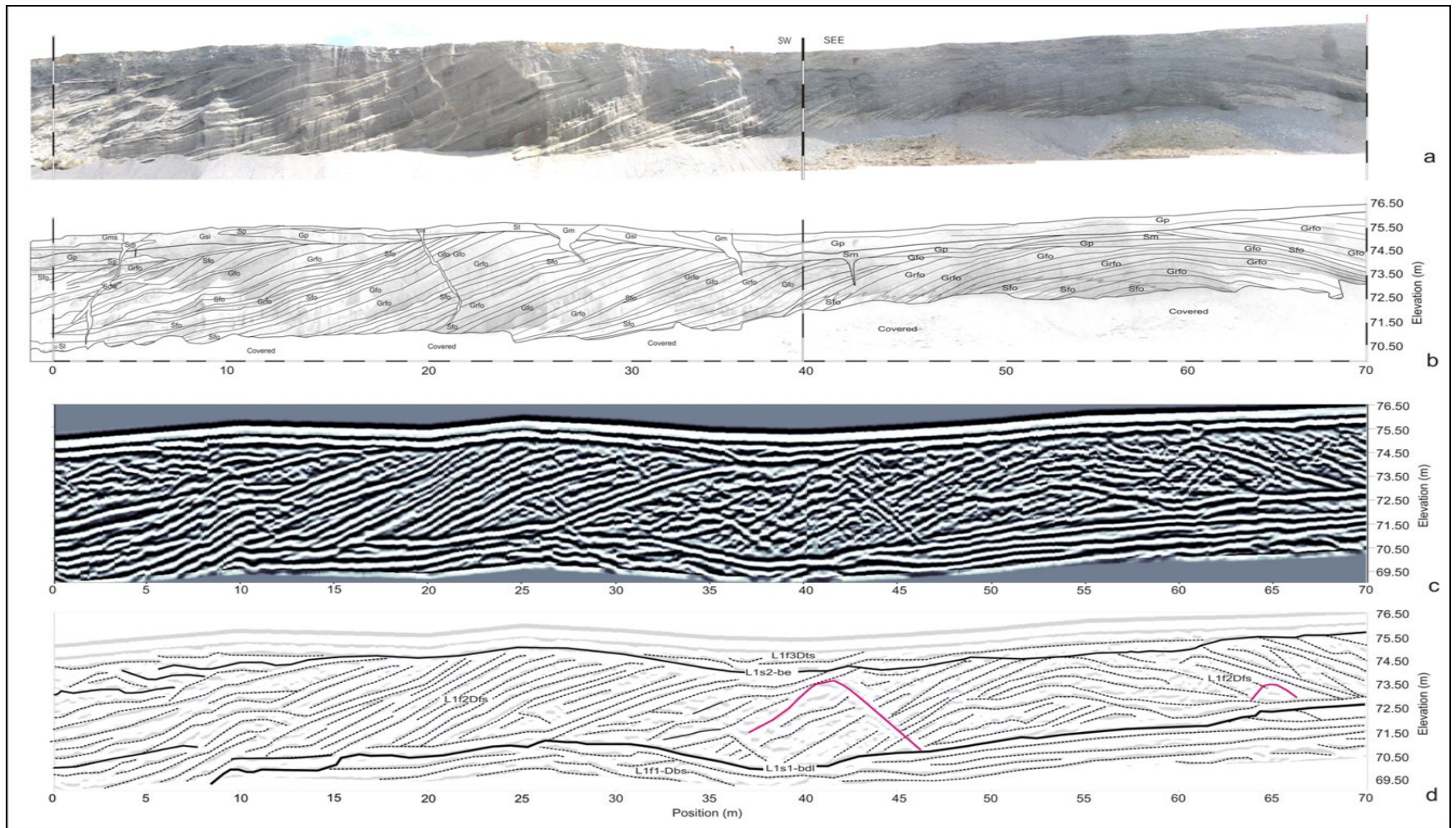


Figure 5.26 – (a) Photo mosaic of exposure ET1 (above), (b) lithological and sedimentological interpretation of exposure. (c) 200MHz GPR radargram recorded on top of the exposure with and AGC gain and topographically corrected. (d) Interpretation of the GPR radargram after an AGC gain and velocity correction.

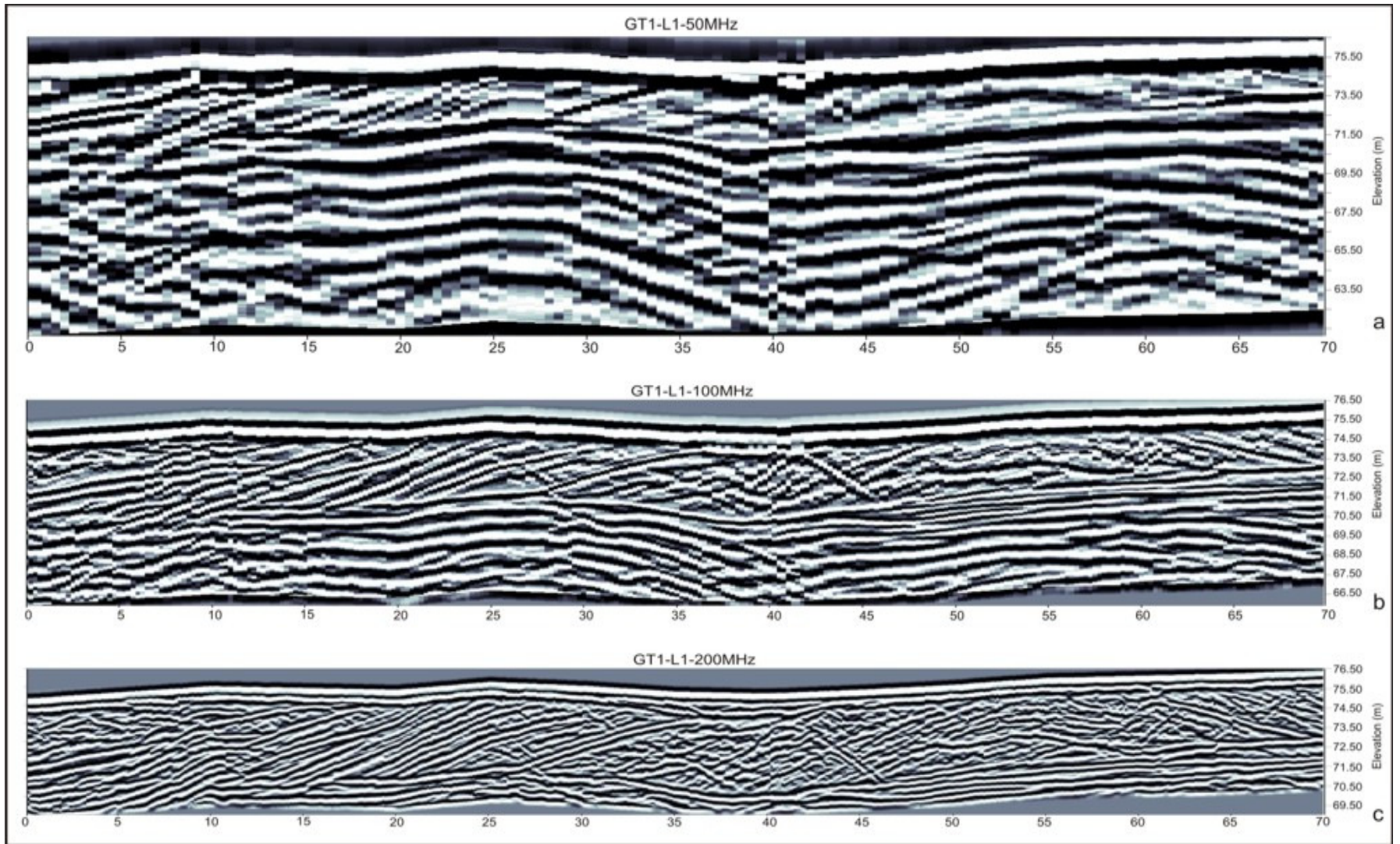


Figure 5.27 – Comparison of radargrams collected in Site T1 recorded by the (a) 50MHz antenna, (b) 100MHz antenna and (c) 200MHz antenna. Resolution decreases and penetration increases with lower antenna frequency.

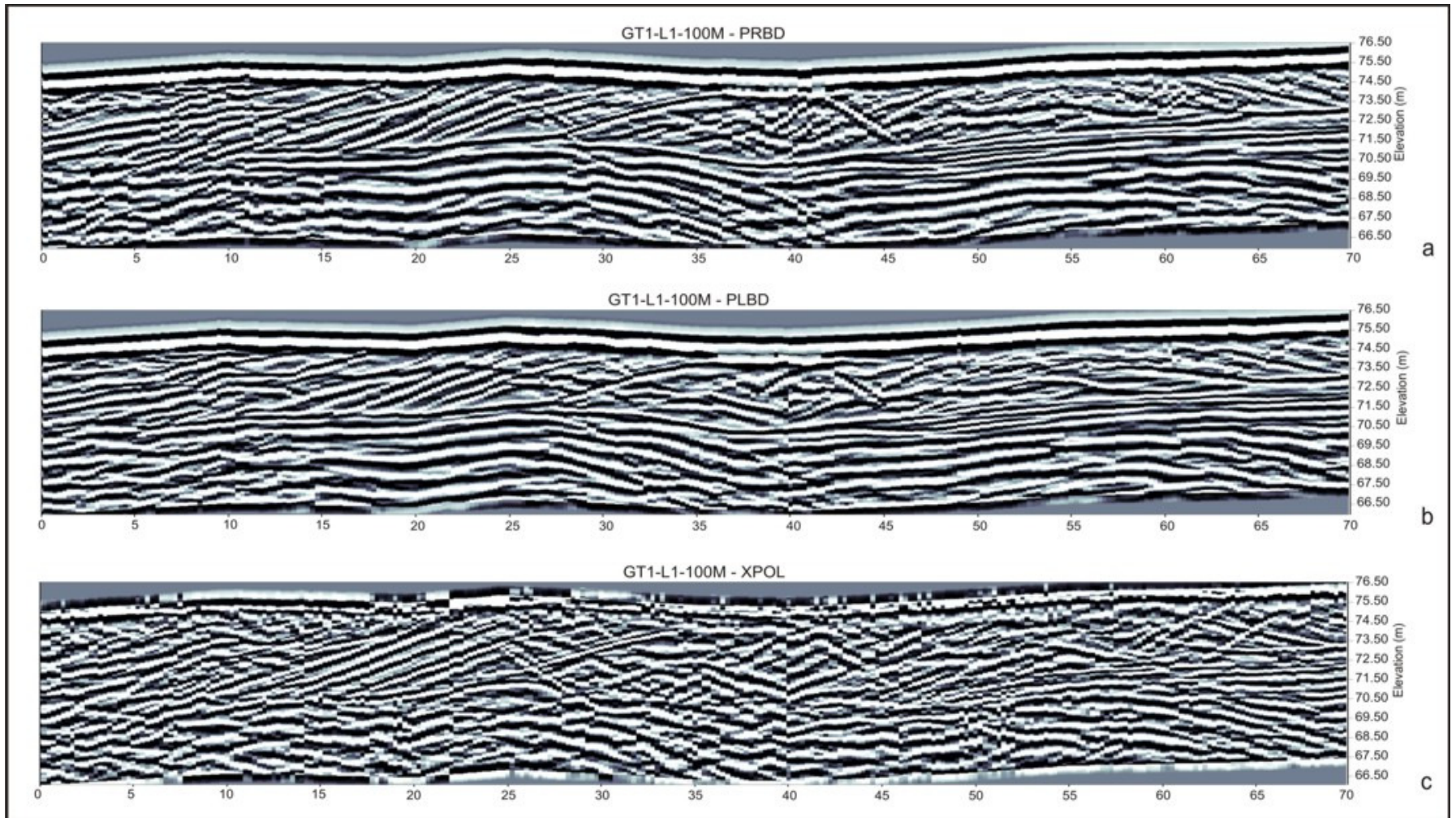


Figure 5.28 – Comparison of results obtained for same profile using three different antenna orientation settings. (a) Perpendicular broadside, (b) Parallel broadside and (c) Cross polarization.

Site T2

Site T2 is located in a disused gravel pit located 15 Km northwest of the study area (E216500, N241200). A detailed description of Moate Esker was presented in Chapter 4. The sedimentological and lithological settings of a number of exposures within Site T2 were surveyed (ET2-A, ET2-B and ET2-C, Figure 5.29).

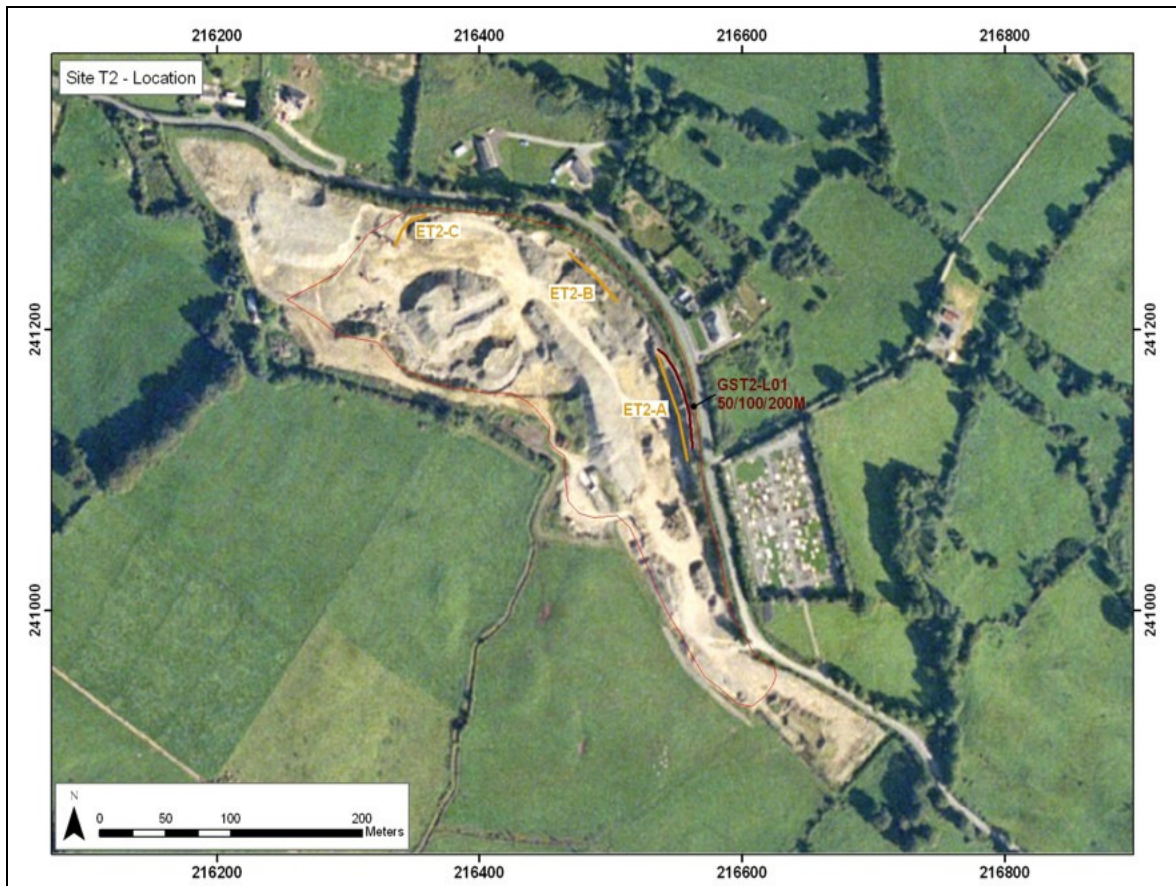


Figure 5.29 – Location of GPR survey (brown) and exposures (orange) recorded within site T2.

The exposures recorded within the gravel pit are dominated by coarse, cobble and boulder gravel. The in situ lithological description of exposure ET2-B shows 3m of crudely horizontally bedded matrix-supported cobble gravel overlying 5 - 6m of foresets composed of boulder gravel generally dipping 10 - 15° northwest. A trench dug at the base of the exposure shows the water table at 3m depth from the surface. Exposure ET2-C is dominated by 4m of cobble gravel gently dipping south-southwest with sand lenses composed of coarse to medium sand. This is underlain by 5m of boulder to cobble gravel

dipping 10 - 15° west-southwest. Large blocks of sand and gravel of up to 10m diameter have been quarried away from this pit face. The exposures are petrologically dominated by Lower Carboniferous limestone.

A GPR survey was undertaken on top of exposure ET2-A in 2006. The recorded exposure is 78m long and approximately 9m high. It runs along the northern margin of the Moate Esker, thus the sediments described would be related to the marginal deposits of a subglacial tunnel infill. Figures 5.30a and 5.30b show an image with a detailed lithological and sedimentological interpretation of exposure ET2-A. The top 3 - 5m are composed of imbricated clast supported pebble to cobble gravel (Gsi) dipping 20 - 30° east-southeast with large lenses of matrix-supported boulder gravel (Bms). These are underlain by massive and horizontally to gently dipping bedded matrix-supported coarse gravel (Gms) dominated by pebbles and cobbles in places. Diamicton (Dms) has been recorded as irregular lenses within the exposures, probably related to frozen sediment carried along the subglacial tunnel and deposited in situ.

The GPR profile was recorded along the top of the exposure, 2 - 3m from its edge using 50MHz, 100MHz and 200MHz antennae frequencies. The exposure is subvertical, thus the sediments recorded within the GPR profile are approximately between 4 - 5m off from the sedimentological structures described within the exposure. The profile was originally collected from the southeast to the northwest for 78m; however, it was subsequently inverted to display it in the same direction as the recorded exposure. The data were collected within 5 hours during dry weather conditions. Furthermore, the 100MHz antenna frequency was tested using three antenna orientations: perpendicular broadside (PR-BD), parallel broadside (PL-BD) and cross polarization (XPOL). All the radargrams presented below have been processed by means of position inversion, time zero adjustment, dewow and AGC gain.

Radar surfaces, packages or facies descriptions are based on the terminology illustrated in Figure 3.29, the coding scheme used for facies and radar surfaces classification is presented in Figure 3.30.

Figures 5.30c and 5.30d display the radargram collected using a 200MHz antenna and an interpretation of the collected data, a larger version of this dataset is presented in Enclosure 2 – E2G. A subhorizontal moderately continuous reflector runs along all the radargram from 80 - 100ns (L1s1-bs), the real depth of this reflector is known as it represents the contact between boulder gravel (Bms) overlying massive sand and gravel (Gms) recorded on the exposure. Therefore, this reflector has been used to estimate an average velocity of 0.11m/ns for the profile. This velocity has subsequently been confirmed by calibration of a number of hyperbolic reflections occurring along the radargram. The top part of the profile is dominated by discontinuous sinuous reflectors dipping in different directions from 0 - 50m (L1f2-Gfc). A curved concave reflector (L1s2-be), located at 10 - 30m, reaches a maximum depth of 4m and enclosing oblique chaotic reflectors (L1f3-Gfch), has been interpreted as a channel feature. From 50 - 78m, the reflectors become more continuous and dipping 20 - 30° east-southeast (L1f3-Gfs). These very clear reflectors show the internal architecture of the esker better than the exposure itself, where dipping reflectors can be hardly depicted from visual analysis alone. The bottom region of the profile (L1f1-Gfc) is dominated by discontinuous sinuous reflectors for the first 40m which gradually evolve into planar/sinuous horizontal or very gently dipping discontinuous reflectors from 40 - 78m.

The difference in depth of penetration and resolution for different antenna frequencies has been tested for 50MHz, 100MHz and 200MHz antennae using time-windows of 330ns, 200ns and 150ns respectively. Figure 5.31 shows GPR data collected with the three antenna frequencies on top of the exposure. 50MHz antenna shows attenuation of the data at the bottom 2-3m of the profile. This could be due to a change of material into diamicton or to the presence of the water table which had been previously recorded at the foot of exposure ET2-B. The channel feature described above is detected by both the 200MHz and the 100MHz antennae, but it is not by the 50MHz. A total of seven dipping reflectors located from 60 - 78m, were detected very crudely by the 50MHz antenna, the 100MHz antenna has recorded fourteen dipping reflectors for the same section, and twenty reflectors were recorded by the 200MHz antenna. Moreover, the 50MHz antenna dataset presents

several artefacts produced by the antenna as it had a poorer coupling with the ground surface, because of the roughness of the surface and the antenna size (2m length). Most of the features detected by the 200MHz antenna are also depicted by the 100MHz, the latter attaining deeper penetration. The 100MHz antenna using a step size between consecutive readings of 25 cm delivers the best trade off between resolution and penetration to map these sediment types.

At site T1, the 100MHz antenna was used to investigate the difference between antenna orientations. At site T2 the 200MHz antenna is tested using the same three antennae orientations relative to the survey line (Figure 5.32). Flat-lying reflectors are specially emphasised by PL-BD (Figure 5.32b), while PR-BD (Figure 5.32a) tends to display better continuity of dipping reflectors - see region from 60 - 78m at 1 - 6m depth. A set of strong flat/gently east-southeast dipping reflectors is depicted by PL-BD from 10 - 50m at around 80ns, these are only partially detected by PR-BD and totally obscured on the X-POL profile (Figure 5.32c). X-POL shows horizontal parallel reflectors at depth, probably related to ringing from the air or surface wave. A 1cm thick electric cable running across the profile has been picked by the PL-BD at 50.9m as a vertical line running all through the profile. As observed before in site T1, data collected using X-POL tends to be noisier as both *EH* and *EV* polarization data are collected. This is illustrated by changes in the polarization of the air and surface wave along the profile. PR-BD provides the best trade off between detection of flat lying and dipping reflectors, however if the objective of the survey is the detection of flat-lying continuous reflectors, the use of the PL-BD setting would be recommended.

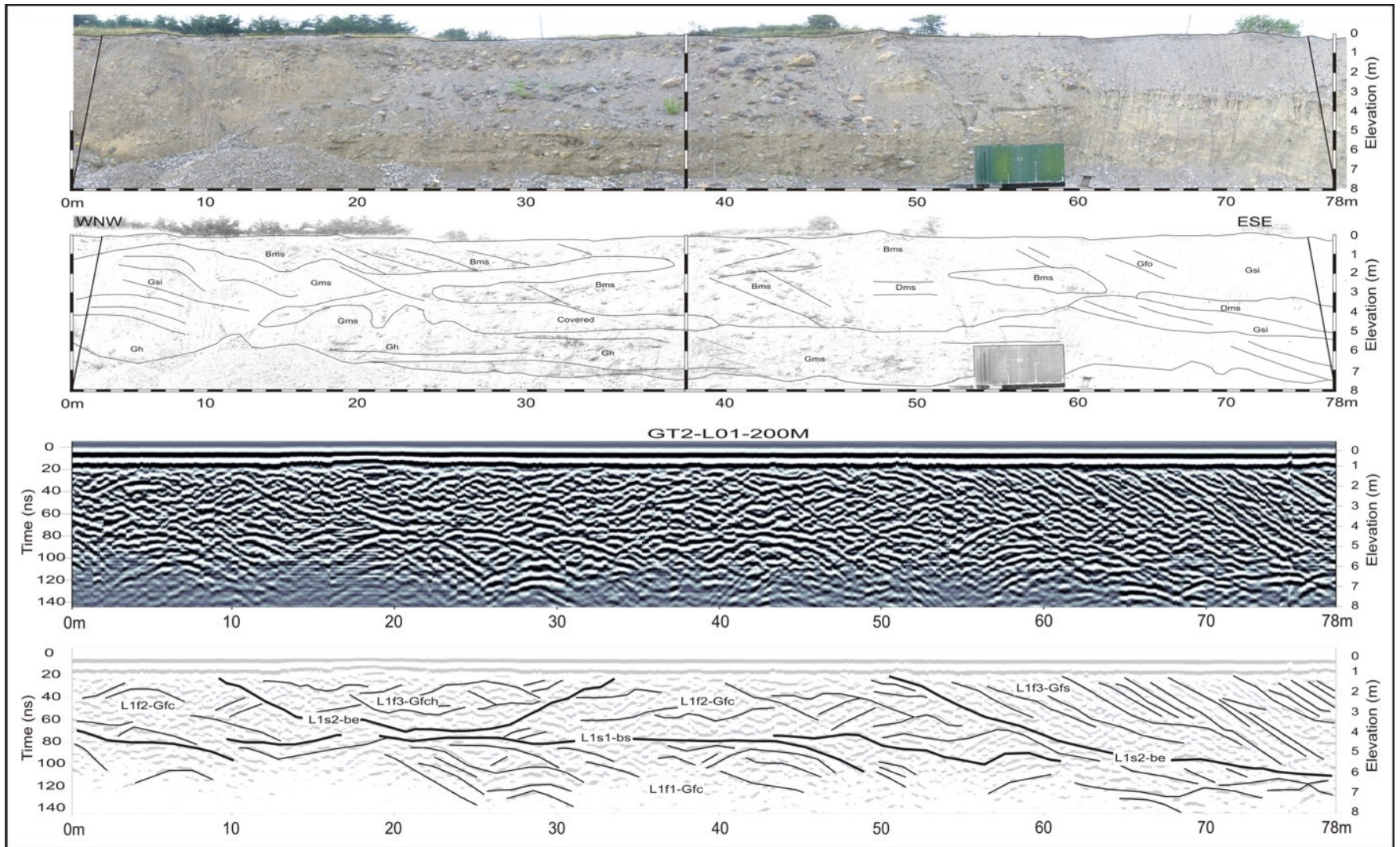


Figure 5.30 – (a) Photo mosaic of exposure T2A (above), (b) lithological and sedimentological interpretation of exposure. (c) 200MHz GPR radargram recorded on top of the exposure with and AGC gain. (d) Interpretation of the GPR radargram.

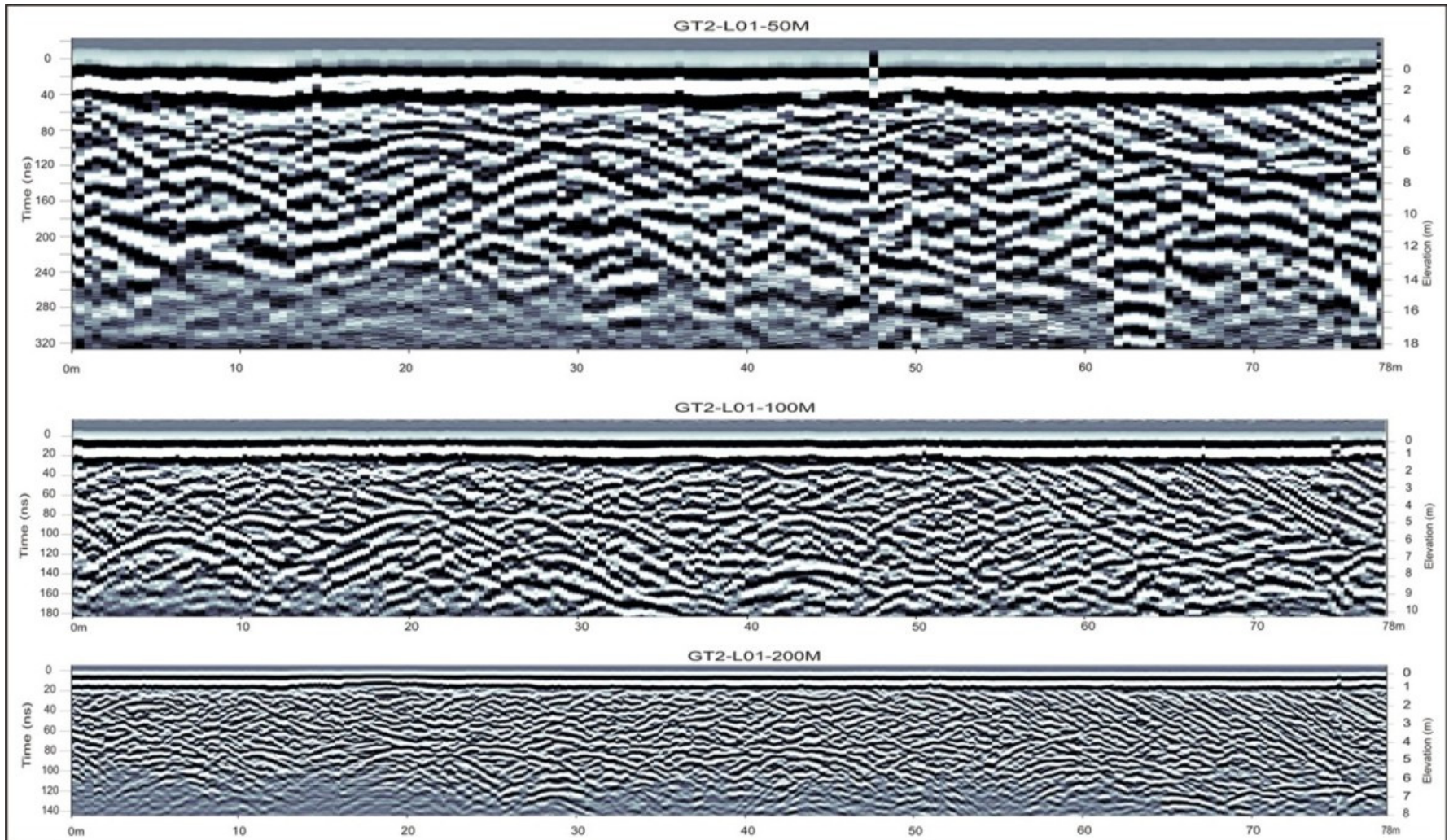


Figure 5.31 – Comparison of radargrams collected in Site T2 recorded by the (a) 50MHz antenna, (b) 100MHz antenna and (c) 200MHz antenna. Resolution decreases penetration increases with lower antenna frequency.

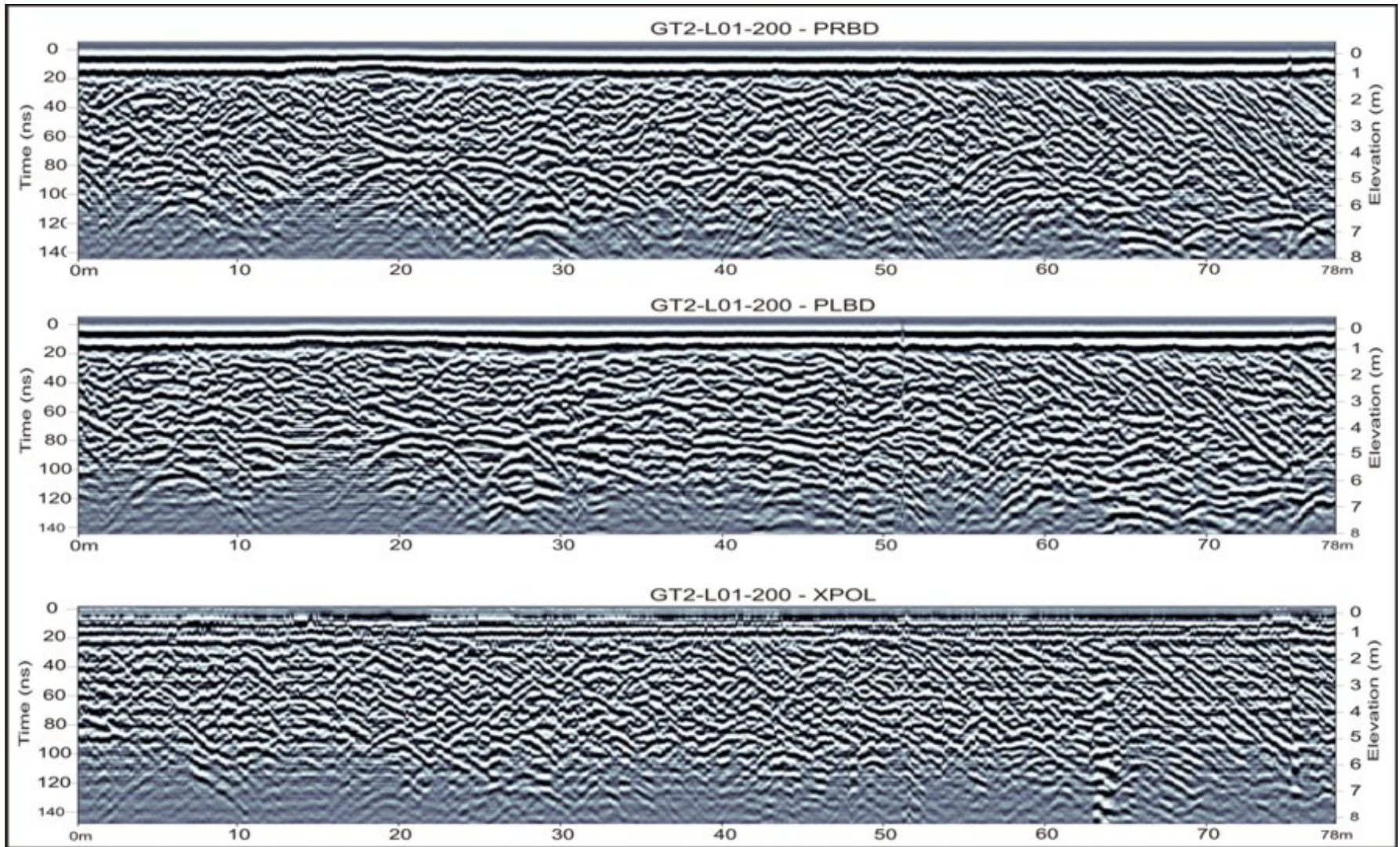


Figure 5.32 – Comparison of results obtained for same profile using three different antenna orientations settings. (a) Perpendicular broadside, (b) Parallel broadside and (c) Cross polarization.

Site T3

Site T3 is located outside the research area in a disused gravel pit approximately 5 Km east of the northeast corner of the study area. Although the site is out of the research area, the top of the exposure is easily accessible and a fine example of a boulder dominated ridge section is presented. The location of the section and the recorded geophysical surveys within the site are presented in Figure 5.33.



Figure 5.33 – Location of GPR profiles (red), resistivity profile and exposure (orange) recorded within site T3.

The site (E255200, N240700) is situated on the southeast end of a 550m long by 250m wide mound running along the southern bank of the Mongagh River which runs towards the southeast at this point. The feature is a gently sloping mound standing 4-5m above the river to the north and about 3m above the landscape to the south. The feature was laid down in a high energy sedimentary environment, as it can be inferred from the boulder gravel composing most of the exposed sediments. Boulders along the top of the section are typically up to 0.5m in diameter. These sediments were probably laid down along a high

energy meltwater outlet close to the ice margin, related to an ice sheet retreating north-eastwards at this point. Furthermore, some exposures surveyed along the river channel situated 200m north of Site T3 show 2m of interstratified sands and fine sand beds underlain by bedrock.

ET3 is a north-northwest south-southeast 31m length 3-4m height exposure excavated along the mound's long axis. It is composed of clast-supported boulder gravel with clayey matrix in places (Figures 5.34a, 5.34b). Crudely imbricated boulders dipping 10° south-southeast are observed in places. Some beds dipping north-northwest have been also recorded. The boulders dominating the exposure are mostly rounded and subrounded between 20 - 40cm in diameter and are formed of Lower Carboniferous limestone.

The Geopulse Tigre resistivity meter has been used to record an Electrical Resistivity Tomography (ERT) profile of 30m length using 1m electrode spacing (RT3-L01-1m). The inversion of the ERT profile (Figure 5.34c) shows a top 0.3 - 0.8m thick layer composed of low resistivity material, which has been interpreted as soil. This is underlain by a continuous 4.3m thick layer with high resistivity values of up to 8000Ωm, which has been interpreted as clast supported boulder gravel. Finally, a layer showing lower resistivity values can be inferred at 4.3 - 5.3m depth. This layer could be related to edge distortion, typical of ERT inversion models (see forward modelling of resistivity data within this chapter –Figure 5.2). However, recent excavations 100m east-southeast from the site reveal the presence of thick sand deposits at depth which supports the view that the boulders are underlain by finer-grained low resistivity sediments. This highlights some limitations of the modelling software.

A 31m long GPR profile (GT3-L01-200M) was recorded along the resistivity survey line. The sedimentological interpretation of the exposure, the radargram recorded with time zero adjustment, dewow, AGC gain and its interpretation are presented in Figures 5.35a, 5.35b and 5.35c. A number of curved continuous reflectors dipping 5 - 10° south-southeast have been recorded along the GPR profile and have been interpreted as different episodes of deposition of glaciofluvial cross stratified sediments (L1f1,2,3,4-Gfc). A number of

reflectors dipping north-northwest are enclosed within these facies. Figure 5.35d shows a migrated version of the radargram using a 0.1m/ns velocity. It is especially noticeable how the dipping reflectors (see line in red correlated to the exposure interpretation) are corrected to their true dip angle subsequent to migration of the dataset using the right velocity.

GPR profile GT3-L02-200M running oblique from the exposure at around the 12m point on the first GPR line was also acquired. The profile has been processed by means of time zero adjustment, dewow, AGC gain and topographic correction. The topographically corrected profile, plus its migrated version and the interpretation are presented in Figure 5.36. Topographic correction and migration have been performed using a velocity of 0.1m/ns, extracted from hyperbola analysis using EkkoView Software. The radargram interpretation has been divided into two main sedimentological episodes. Two depositional episodes of glaciofluvial cross stratified sediments, generally dipping southeast occur from 0 - 15m. From 15 - 50m discontinuous gently dipping northeast subparallel reflectors have been interpreted as glaciofluvial cross stratified sediments (L2f2-Gfc). From 50 - 65m gently dipping northeast subparallel moderately discontinuous to continuous reflectors have been interpreted as cross stratified sediments (L2f4-Fcs) probably related to a later sedimentary episode, as they overly f2-Gfc with an onlap contact (L2s4-bol). The resolution of the radargram is reduced when the data are migrated. However, hyperbolic reflections are eliminated, the dipping reflectors are corrected to their true position and flat lying reflectors are emphasised. The combination of both the migrated and the non-migrated, aids in a better interpretation of the radargram. Therefore, analysis of both migrated and non-migrated radargrams have been incorporated as essential steps in the interpretation of the GPR data collected for this thesis.

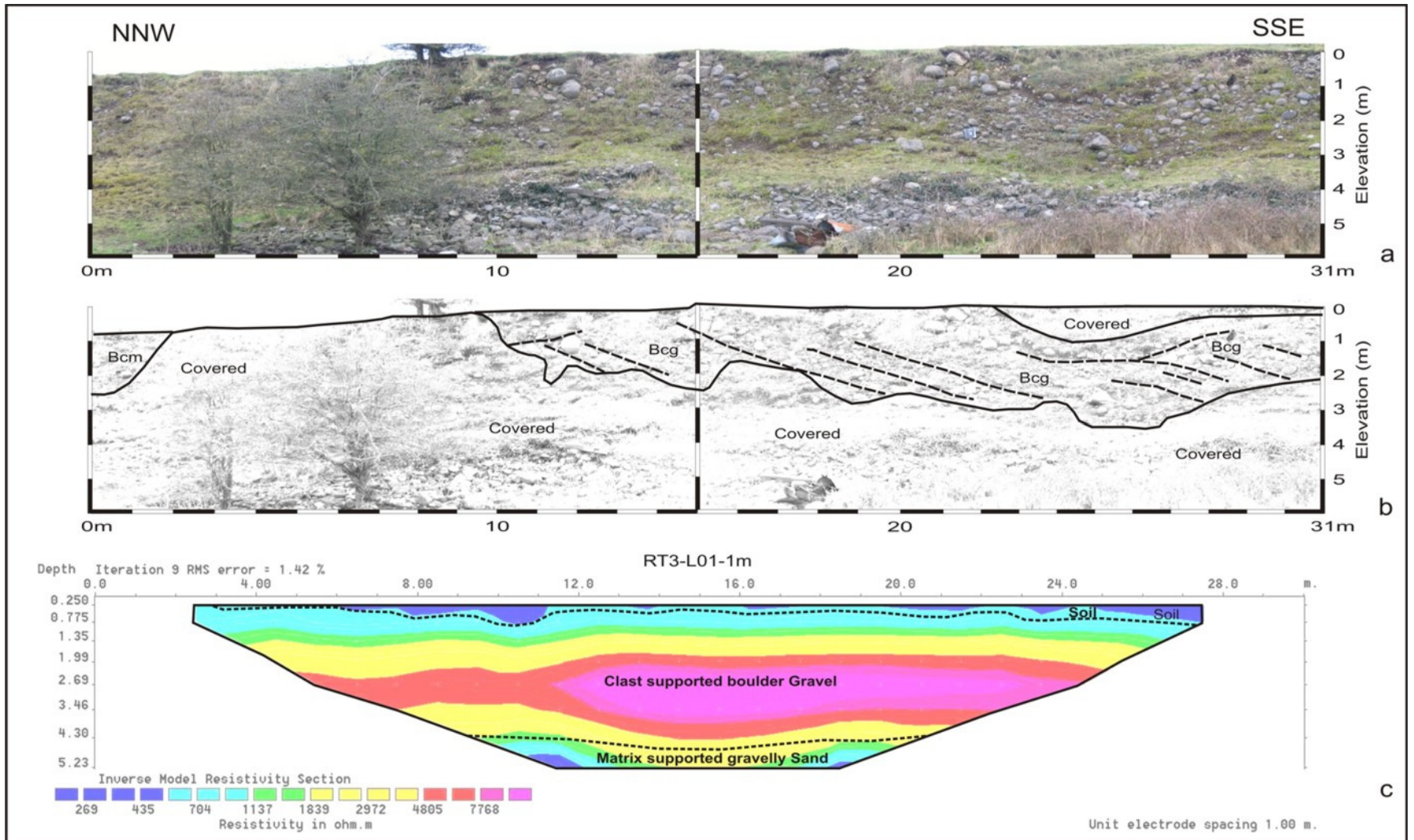


Figure 5.34 – (a) Image of the exposure recorded in site T3. (b) Sedimentological interpretation of the exposure. (c) Inverse model of ERT profile recorded along the top of the exposure at 1m electrode spacing and interpretation.

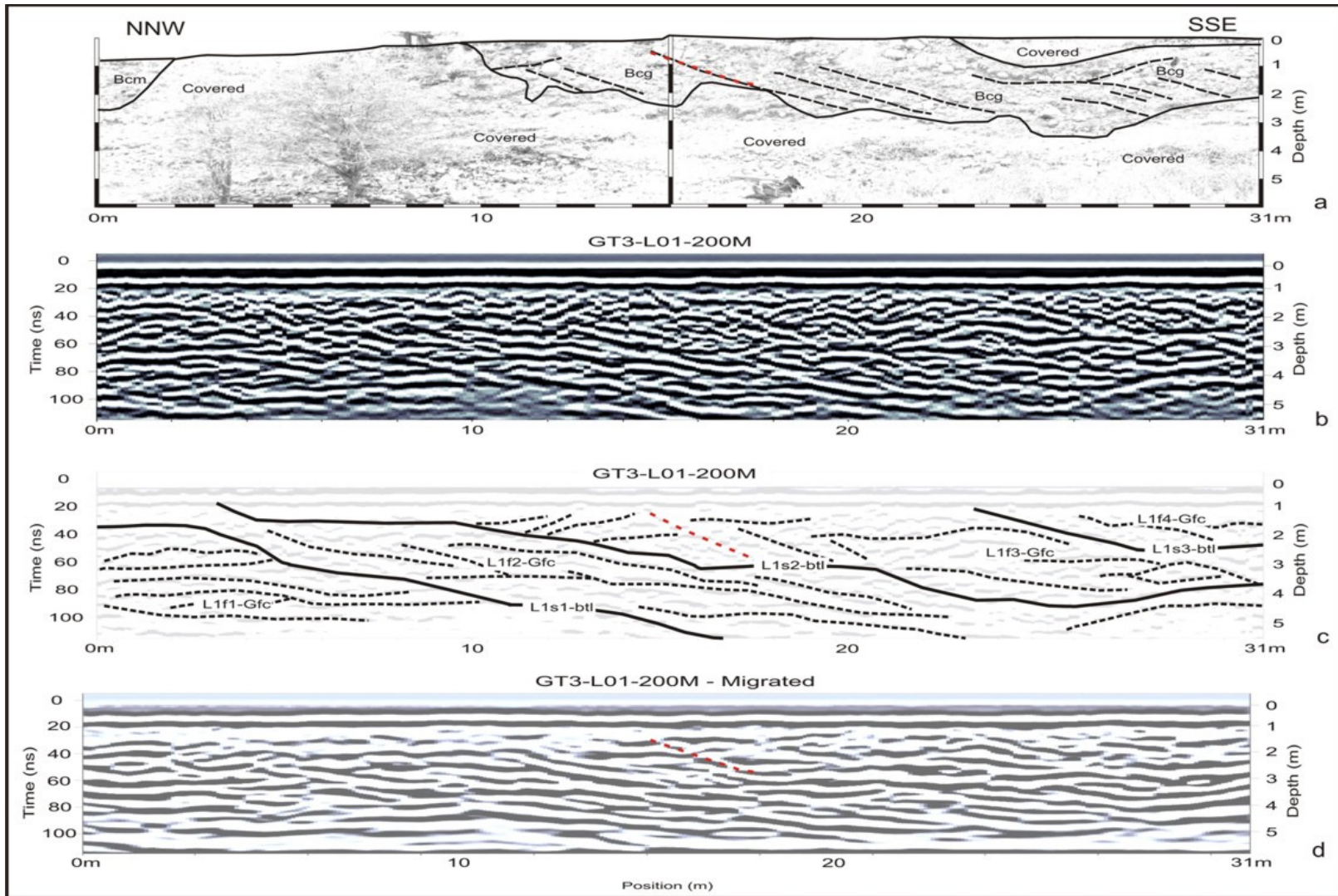


Figure 5.35 – (a) Sedimentological interpretation of the exposure. (b) GPR profile collected along the top of the exposure. (c) Interpretation of the GPR data. (d) Migrated GPR profile, showing correction of dipping reflector in red.

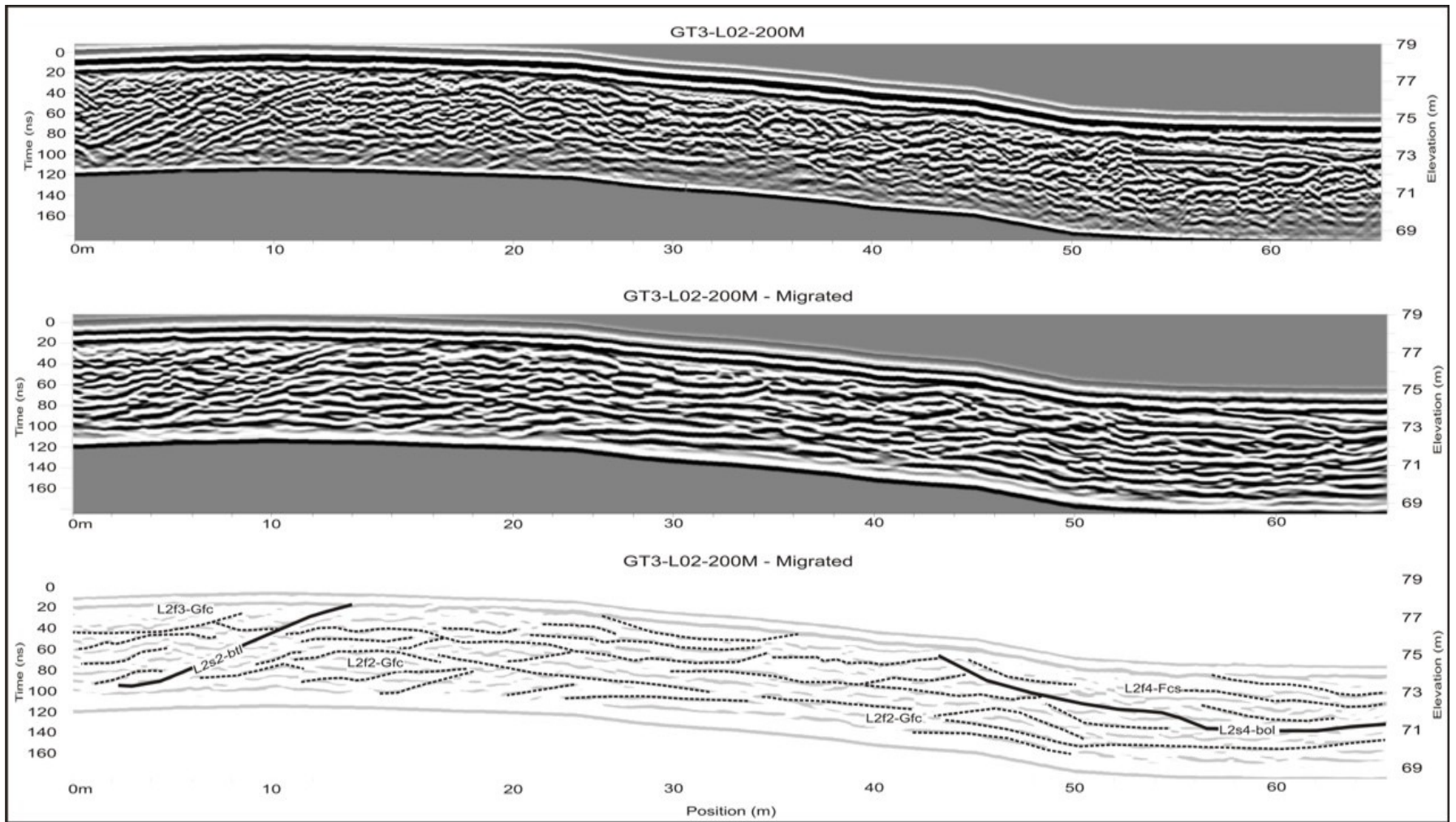


Figure 5.36 – (a) topographically corrected GPR profile GT3-L02-200M, dewow and AGC gain. (b) Migrated profile with a velocity of 0.11 m/ns. (c) Sedimentological interpretation.

5.5 – Summary

RES2DINV software has a large number of possible setting combinations that can be tested to obtain the most accurate final results. The type of inversion method picked for data processing appears to be the main factor to take into account. Features depicted for both inversion methods can be considered real (Loke, 2001). However, the use of the Gauss-Newton robust constraint method is in general the one that provides the most accurate results. A number of theoretical models have been tested using RES2DMOD software; the relative disposition of sediments with differing resistivity, the thickness of the layer and the contrasting resistivity values will highly influence the results obtained on the inverted profile. It has been observed that the accurate thickness of layers is difficult to determine by use of resistivity surveying, the relative resistivity values of neighbouring layers with differing resistivity seems to strongly influence the inverted model outcome, as the resulting profile is the result of interpolation, thus a thin layer presenting very large resistivity values will appear in the inverted model as a much thicker layer than it is.

The production of GPR theoretical subsurface models and their simulation with GPRSIM software before fieldwork will lead to a more accurate interpretation of data collected in this thesis where there are no exposures. Moreover, it can be inferred from the forward modelling exercise that the application of topographic correction and migration techniques greatly assists in minimising some distortions of the collected data, e.g. reflectors usually subparallel to the surface, such as water table are placed on their original position following topographic correction, which aids to their correct interpretation.

Three test sites with good exposures for a range of glacial sediments have been surveyed using GPR and ERT in order to compare the signature obtained from these geophysical techniques against the exposure itself.

In general terms, the 100MHz antenna provides the best trade off between resolution and depth of penetration. Most of the sedimentological structures are depicted using this antenna, whereas some are missed when using the 50MHz antenna. On the other hand, the 200MHz provides a better resolved radargram; however, the depth of penetration is rarely more than 5m, which in many occasions does not provide with a full picture of the surveyed sediments.

The application of migration to GPR data, using the correct velocity, yields a more accurate image of the subsurface and places the underground features at their true position. The velocity of the subsurface is calibrated using EkkoView software based on the shape of the hyperbolae at different velocities or by correlating reflectors observed on the radargram to sedimentological boundaries recorded in the exposure.

The use of different antennae orientations when recording a GPR profile can improve the interpretation of the data recorded. The PRBD antenna setting provides the best trade off between detection of flat lying and dipping reflectors. PLBD should be used if the objective of the survey is detecting flat-lying reflectors.

Detailed sedimentological structures recorded in the exposure are fairly well detected by the use of GPR data, whereas ERT allows the detection of the main lithological changes (grain size) and changes in moisture content. However, the depth of penetration with the GPR antennae employed in this thesis, combined with Irish subsurface conditions limit the depth of penetration to c. 7m whereas ERT can provide information at depths of up to 45m. The combination of both techniques, allied to field mapping, greatly enhances our ability to map subsurface sedimentological variations in the Irish Midlands study area.

CHAPTER 6

Results of Geophysical Surveys

6.1 – Introduction

A total of 17 sites were surveyed in the study area using a number of geophysical techniques. Site S1 was intensively surveyed in order to test a range of geophysical techniques and select the most adequate ones to be used in the remaining sites, thus the results obtained in Site S1 encompass a large portion of this Chapter. The two main techniques employed are Electrical Resistivity Tomography (ERT) and Ground Penetrating Radar (GPR). Other techniques tested in Site S1 were Azimuthal Resistivity and Very Low Frequency Electromagnetics (VLF).

The sites presented cover a broad range of Quaternary sediment types typically encountered in the Irish Midlands. These include postglacial sediments such as peat, lacustrine sediments and alluvium, glacial sediments directly deposited by the ice in both subglacial and proglacial environments, and glacial sediments deposited by meltwater released during deglaciation including glaciofluvial and glaciolacustrine deposits. Sites are named from S1 to S17 and presented in the order the data were collected. Sites S1 to S8 were surveyed from 2006-07, Sites S9 to S12 from 2007-08 and Sites S13 to S17 during 2009. The spatial distribution of the sites is presented in Figure 6.1.

A systematic methodology for processing and interpretation of the data presented below has been followed in order to provide a consistent data interpretation output.

The data collection and processing methods for ERT data were presented in detail in Chapter 3 (Section 3.3.3 – Electrical Resistivity Tomography) and as a schematic flow diagram with emphasis on the data processing stage in Figure 3.13. RES2DINV and RES3DINV Inversion modelling software programs have been used for ERT data processing and display. All the ERT figures presented in this chapter show the inverted model of the pseudosection at the top encompassing: the number of iterations used during

inversion, the standard error, the electrode spacing and a key with resistivity in Ωm with user-defined contour intervals. The interpretation of the profile showing the lithological units identified is presented below the inverted model. The interpretation of the inverted model is based on the resistivity range of the geological materials presented in Figure 3.3, on available borehole data and other sedimentological and geomorphological information collected during the field mapping exercise. A number of the original datasets consisting of the measured apparent resistivity pseudosection on top, the calculated apparent resistivity pseudosection in the middle and the inverse model resistivity section at the bottom are presented in Appendix B.

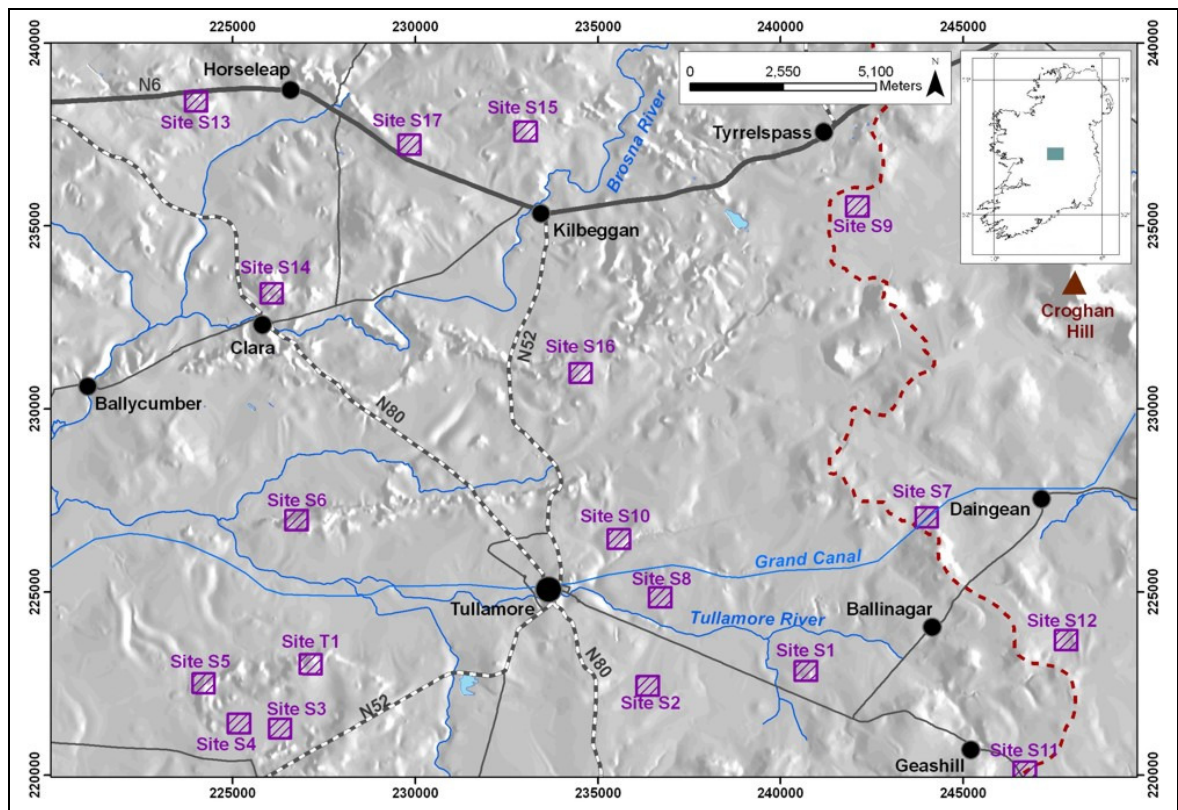


Figure 6.1 – Location of the sites where geophysical surveys have been carried out shown in purple. Main towns, roads, and rivers in study area are also portrayed. Dashed red line indicates location of watershed between the Shannon and the Boyne/Barrow Basins.

The data collection, processing and interpretation methods for GPR data are presented in Chapter 3 (Sections 3.4.3 to 3.4.6) and as a schematic flow diagram with emphasis on the data processing stage in Figure 3.27. All the GPR figures presented in this chapter show a

raw profile with a dewow filter and AGC gain at the top, a migrated profile using the selected velocity in the middle and an interpreted profile at the bottom. Data processing (e.g. migration) may, on occasions, result in the loss of reflectors related to the subsurface architecture, such as, hyperbolae derived from reflections from boulders. Horizontal and subhorizontal reflectors are emphasized and hyperbolae reflectors are collapsed after migration of the dataset using the correct velocity; however, data interpretation is more accurate when using both datasets. On the other hand, migration has been found to be a very useful technique for enhancing the continuity of horizontal and subhorizontal reflectors. Topographic correction is a valuable processing technique, and has helped in understanding the internal sediment architecture or in the identification of water-table levels. The interpreted profiles present the main radar facies with an associated code which are separated by coded continuous thick lines (radar surfaces). The description of the code format used for radar surfaces and radar facies was presented in Figure 3.30. The terminology for description of radar surfaces, radar packages and radar facies has been adapted from Neal (2004) and was presented in Figure 3.29.

Borehole data collected along the profiles presented in this Chapter are integrated into the figures. A systematic colour scheme based on Folk's (1954) classification is used to display the dominant lithology within the borehole log (See Figure 6.2).

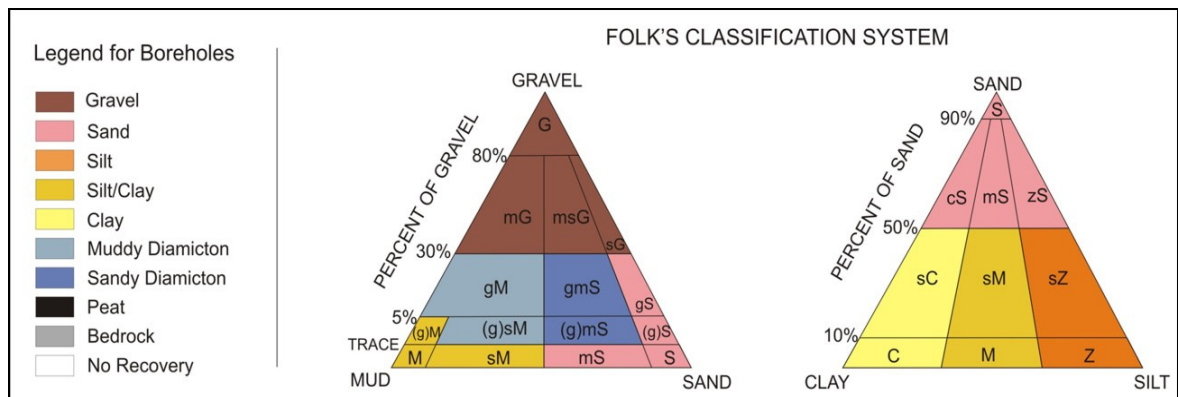


Figure 6.2 – Left - Legend for Borehole data presented in this Chapter to support the GPR and ERT data interpretation. Right – Folk's (1954) clastic sediments classification scheme, colour scheme used in the diagrams correspond to colours used in the legend.

6.2 – Site S1

6.2.1 – Introduction

This site is the one most intensively surveyed by means of geophysical techniques. A broad range of glacial and postglacial sediment types are present in a relatively small area, which allowed testing of the response of a range of geophysical techniques against a number of lithological and sedimentological settings. Furthermore, a comprehensive drilling program has been carried out at the site to refine the geophysical data interpretation. The results obtained at this site have been used as a basis for data processing and interpretation for the other surveyed sites.

Site S1 is located 9 Km east-southeast from Tullamore Town, along the Tullamore to Portarlinton Road (See Map 1). A broad variety of Quaternary sediments occur in this site within a small area of approximately 2 Km². A section of the topographically poorly-expressed Geashill Esker runs along the site's northern margin in an east-northeast to west-southwest direction, reaching a maximum height of 3 - 4m relative to the surrounding landscape and it has a width ranging from 20 - 50m. The esker is bounded to the north by a low lying landscape dominated by peat underlain by lacustrine sediments extending northwards for a few kilometres, and to the south by an east northeast - west southwest flat stretch of poorly-drained low ground dominated by lacustrine silts and clays blanketed by a thin coating of peat (0.3m approx.). This lacustrine stretch is bounded to the south by a well drained, flat-topped elongated fan running east-west for approximately 2 Km, reaching a maximum height of 10m above the surrounding landscape and encompassing widths of 200 - 450m. A maximum height of 72m above Ordnance Datum (OD) is reached by this feature within the site. A number of small 1m high exposures along its flanks show interstratified silt, sand and gravel. The feature is bounded to the south by poorly drained low ground. A 2-3m deep ditch located at the southern margin of the site shows diamicton derived from Lower Carboniferous Limestone and running water at 60m OD, which has been inferred by the author as the approximate level of the water-table in the area. The main geomorphological features in the site are illustrated in Plate 6.1.



Plate 6.1 – Three main morphological features within Site S1. Esker ridge running east-northeast to west-southwest covered with bushes. Perimeter of the lacustrine flat is outlined in yellow. The edge of the glaciofluvial fan can be seen on the right and bottom margin starting on a concave change of slope.

Two exposures have been recorded at the site (Figure 6.3). Exposure ES1A, excavated across the southern margin of the fan, 100m from the west margin of the site (E240500, N222840), is dominated by interstratified sand and gravel (Figure 6.4a). Sand is fine to very fine with some silt component; bedding is deformed, possible due to collapse subsequent to melting of buried ice. Gravel size ranges from medium to coarse and is generally matrix supported with a number of clast supported isolated beds. Trough cross-bedding has been observed in the exposure, indicating that the sediments were most likely deposited in a channel environment at this point. ES1B is a 3-4m high exposure located along the esker ridge (E240900, N223100). The exposure is dominated by crudely bedded matrix supported cobble/boulder gravel with beds dipping 15 - 20 degrees north with a fine to medium sand matrix. Moreover, a small lens of laminated silts and clays (Fld) occurs within the beds. These sediments are draped by a thin coating (0 - 2m) of diamicton, thickening towards the edges of the ridge and thinner on the ridge-top. Lithological and sedimentological descriptions of the sediments are illustrated in Figure 6.4b.

The flight continuous auger method has been used to drill a total of eight boreholes at Site S1 which greatly enhanced the interpretation of data collected at the site for geophysical characterisation. Figure 6.3 exhibits the location of these boreholes within the site. Boreholes BH-S1A, B, C, D, G and H were drilled on the fan, Boreholes BH-S1A, B, D and G are generally dominated by sand and muddy sand with some gravel lenses in places. Boreholes BH-S1D and H located westwards, present a higher content of gravel, indicating

a lithology coarsening westwards. This is confirmed by ESA1, which is dominated by medium and coarse gravel (see Figure 6.4a). The sediments recorded on the fan have been interpreted as glaciofluvial and are underlain by diamicton (glacial till) at depths ranging 8 - 12m. BH-S1E (Figure A1) is located on the boundary between the lacustrine flat and the fan and is dominated by 2.8m of silty clay overlying diamicton. BH-S1F (Figure A2) was drilled on top of the Geashill Esker and it is dominated by boulder/cobble gravel with silty sandy matrix. The description of each borehole individually and their lithological classification (Folk, 1954 classification scheme) of PSA results for a total of 25 samples are presented on Table 6.1. A detailed log for a representative sample of the boreholes described and their PSA distribution analysis results in a cumulative graph format for each sample are illustrated in Appendix A.

The geophysical techniques carried out in the site encompass Electrical Resistivity Tomography (ERT), Azimuthal Resistivity, Ground Penetrating Radar (GPR) and Very Low Frequency Electromagnetics (VLF). A detailed description of all the geophysical surveys is presented below.

- ERT includes two profiles at 5m spacing and three profiles at 10m spacing.
- Two ERT profiles were surveyed at 2m and two at 5m electrode spacing on a monthly basis during a period of 1 year for time-lapse resistivity analysis. Thus in all, 52 resistivity profiles were collected.
- A 3D resistivity model composed of nine profiles at 2m electrode spacing.
- Azimuthal Resistivity was undertaken at four locations, where six Vertical Electrical Survey (VES) lines were recorded at six different azimuths.
- GPR survey includes, five profiles using a 200MHz antenna, two using a 100MHz and one using the 50MHz.
- A 3D model has been constructed using the 200MHz antenna. 61 east-west GPR profiles and 41 south-north GPR lines were collected. Two common mid point surveys (CMP) have also been carried out to estimate EM waves velocity.
- VLF has been surveyed for four lines at 10m spacing across the main geomorphological features occurring on the site.

All these datasets are presented and described separately below. The results are discussed and contrasted with exposure, borehole and geomorphological data, aiming:

- to achieve a better understanding of the value and application of each geophysical technique for soft sediments mapping,
- to determine geophysical signatures for a range of Quaternary sediments, and to arrive at an accurate interpretation of the relative chronological relationship of these deposits with the deglaciation processes in the area.

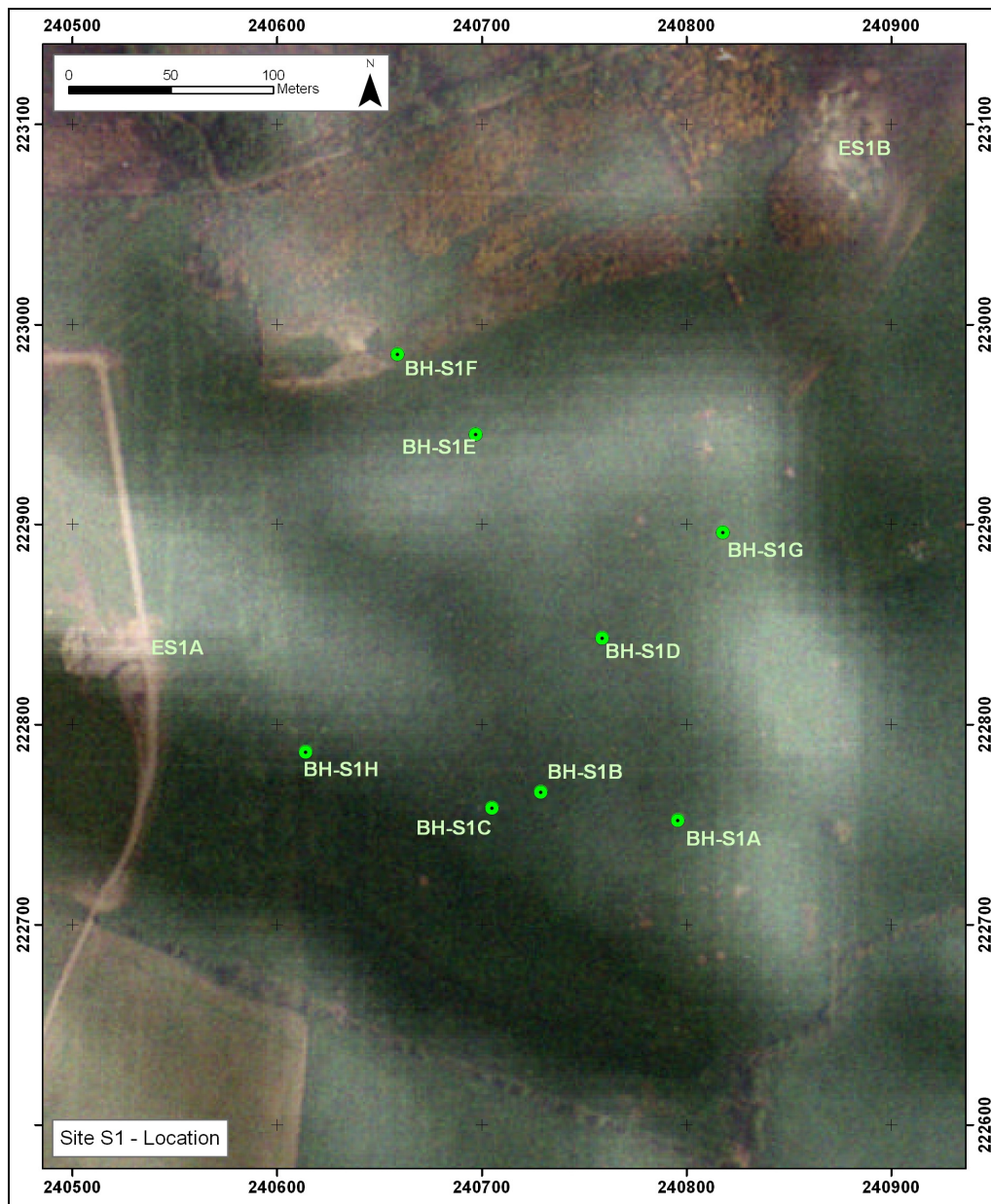
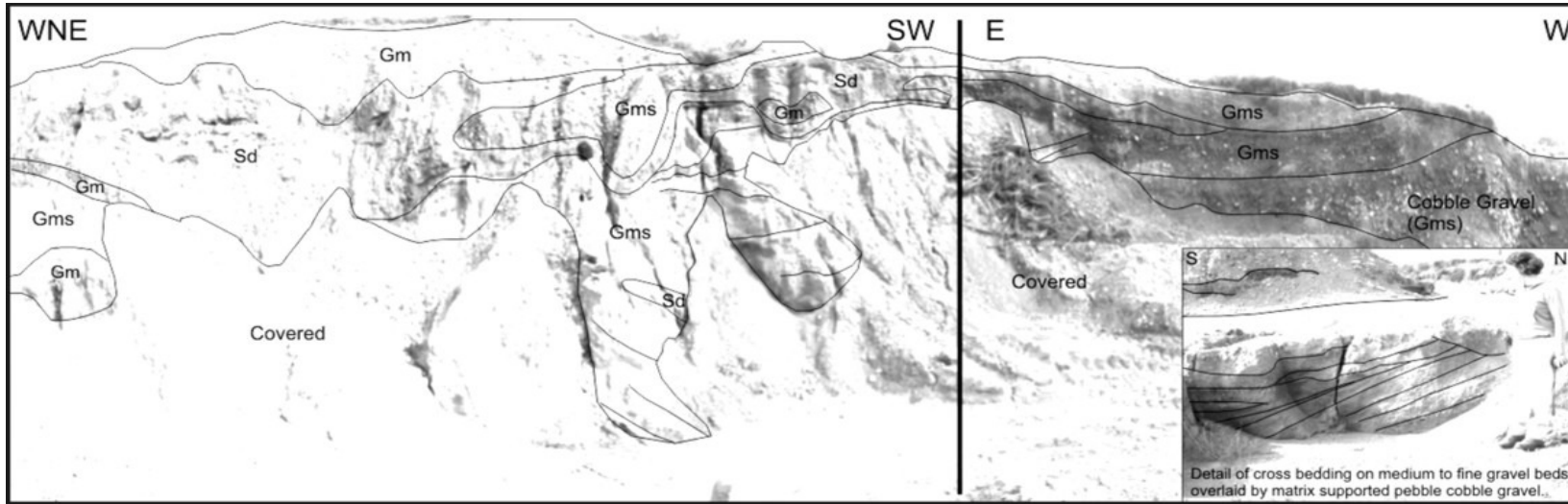
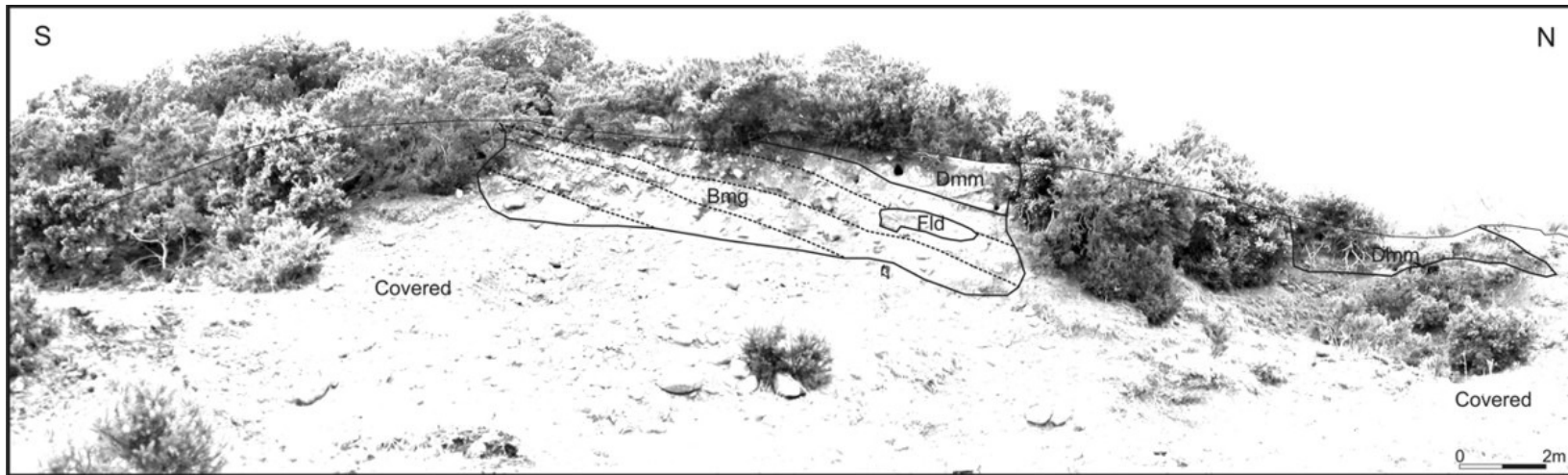


Figure 6.3 – Location of boreholes and exposures described for Site S1.



a



b

Figure 6.4 – (a) Exposure ES1A is dominated by interstratified sands and gravels with deformed bedding. Bottom right corner shows detail of cross bedding. (b) Exposure ES1B shows a cross section of the esker ridge dominated by crudely bedded cobble/boulder gravel.

BH-S1A						
X: 240796		DATE: 14/07/05		MORPHOLOGY: Glaciofluvial fan		
Y: 222752		DEPTH: 13.8m		WATER LEVEL: Not encountered		
LAYER	FROM	TO	FIELD DESCRIPTION	SAMPLE	COLOUR	SAMPLE CLASS (20mm/2mm)
1	0.0	0.3	Topsoil			
2	0.3	1.5	Soft light brown (2.5Y/4/3) silty SAND with Lst. pebbles. GLACIOFLUVIAL			
3	1.5	2.1	Medium soft clayey sandy GRAVEL with rounded to subrounded Lst pebbles (1-10cm diam.). GLACIOFLUVIAL	1	2.5Y-4/3	GRAVELLY SAND
4	2.1	3.8	Medium dense clayey SAND with small Lst pebbles (1-2cm diam.). fining downwards. GLACIOFLUVIAL			
5	3.8	6.8	Soft brown clayey fine SAND with few angular Lst pebbles (1-1.5cm diam.). GLACIOFLUVIAL	2	10YR-3/2	GRAVELLY MUDDY SAND
6	6.8	8.5	Medium dense dark brown sandy CLAY. GLACIOFLUVIAL	3	2.5Y-4/2	SLIGHTLY GRAVELLY MUDDY SAND
7	8.5	11.5	No Recovery			
8	11.5	12.5	Medium dense Grey brown sandy CLAY with isolated Lst pebbles. GLACIOFLUVIAL	4	2.5Y-4/2	SLIGHTLY GRAVELLY MUDDY SAND
9	12.5	13.8	Medium dense Grey brown sandy silty DIAMICTON Lst pebbles. GLACIAL	5	2.5Y-3/5	SLIGHTLY GRAVELLY SANDY MUD / SANDY SILT

BH-S1B						
X: 240729		DATE: 14/07/05		MORPHOLOGY: Glaciofluvial fan		
Y: 222766		DEPTH: 14.7m		WATER LEVEL: Not encountered		
LAYER	FROM	TO	FIELD DESCRIPTION	SAMPLE	COLOUR	SAMPLE CLASS (20mm/2mm)
1	0.0	0.3	Topsoil			
2	0.3	3.5	Soft brown silty clayey SAND with Lst. pebbles. GLACIOFLUVIAL	1	2.5Y-4/3	SLIGHTLY GRAVELLY MUDDY SAND
3	3.5	7.5	Soft to Dense dark brown clayey SAND to Coarse SAND, coarsening downwards with Lst and Sst pebbles (1-2cm diam.). GLACIOFLUVIAL	2	2.5Y-3/1	GRAVELLY MUDDY SAND
3A	7.5	8.5	Coarse SAND, coarsening downwards with Lst and Sst pebbles. GLACIOFLUVIAL	3	2.5Y-3/1	GRAVELLY MUDDY SAND
4	8.5	9.0	Medium dense clayey coarse SAND with Lst/Sst pebbles. GLACIOFLUVIAL			
5	9.0	10.0	Dense sandy clayey DIAMICTON with small Lst pebbles. GLACIAL	4	2.5Y-4/3	GRAVELLY MUD / SANDY MUD
6	10.0	14.7	Dense to very dense, stony sound. No Recovery			

BH-S1C						
X: 240705		DATE: 14/07/05		MORPHOLOGY: Glaciofluvial fan		
Y: 222758		DEPTH: 12.3m		WATER LEVEL: Not encountered		
LAYER	FROM	TO	FIELD DESCRIPTION	SAMPLE	COLOUR	SAMPLE CLASS (20mm/2mm)
1	0.0	0.3	Topsoil			
2	0.3	4.9	Very soft brown clayey fine SAND with very few Lst pebbles (1-2cm diam.). GLACIOFLUVIAL	1	2.5Y-4/3	SLIGHTLY GRAVELLY MUDDY SAND
3	4.9	8.3	Very soft to soft brown SAND with Lst pebbles (1-8cm diam). GLACIOFLUVIAL	2	2.5Y-4/2	MUDDY SANDY GRAVEL
4	8.3	11.0	Medium dense to dense brown clayey SAND with rounded to subrounded Lst pebbles (1-4cm diam). Pebble proportion: 45%. GLACIOFLUVIAL	3	2.5Y-4/2	MUDDY SANDY GRAVEL
5	11.0	12.3	Dense to very dense sandy silty DIAMICTON. GLACIAL	4	2.5Y-4/1	GRAVELLY MUD / SANDY SILT

BH-S1D						
X: 240759		DATE: 14/07/05		MORPHOLOGY: Glaciofluvial fan		
Y: 222843		DEPTH: 14		WATER LEVEL: Not encountered		
LAYER	FROM	TO	FIELD DESCRIPTION	SAMPLE	COLOUR	SAMPLE CLASS (20mm/2mm)
1	0.0	0.3	Topsoil			
2	0.3	1.8	Soft red-brown clayey fine SAND with Lst pebbles (2cm diam). GLACIOFLUVIAL			
3	1.8	5.2	Soft brown fine to medium SAND with no pebbles, Sand coarsening downwards. GLACIOFLUVIAL	1	2.5Y-4/3	SLIGHTLY GRAVELLY MUDDY SAND
4	5.2	8.9	Soft clayey fine to medium SAND with no pebbles. Clay proportion increasing downwards. GLACIOFLUVIAL			
5	8.9	10.8	Medium dense sandy SILT. GLACIOFLUVIAL	2	2.5Y-4/3	GRAVELLY MUD / SANDY SILT
6	10.8	11.5	Medium dense silty clayey SAND. GLACIOFLUVIAL	3	2.5Y-4/3	SLIGHTLY GRAVELLY MUDDY SAND
7	11.5	13.1	No Recovery			
8	13.1	14.0	Dense to very dense grey brown silty sandy DIAMICTON with angular Lst pebbles (3cm diam). GLACIAL	4	5Y-3/1	GRAVELLY MUDDY SAND / SILTY SAND

BH-S1E						
X: 240697		DATE: 14/07/05		MORPHOLOGY: Lacustrine Flat		
Y: 222945		DEPTH: 7.5m		WATER LEVEL: 3m		
LAYER	FROM	TO	FIELD DESCRIPTION	SAMPLE	COLOUR	SAMPLE CLASS (20mm/2mm)
1	0.0	0.7	Peaty Soil			
2	0.7	2.8	Soft fine sand with silt/Clay. No pebbles. LACUSTRINE	1	GLE1-3/1	SLIGHTLY GRAVELLY SANDY MUD
3	2.8	7.5	Medium dense silty sandy DIAMICTON with subangular angular pebbles (0.1-0.5cm diam.). GLACIAL	2		GRAVELLY MUD / SANDY SILT

BH-S1F						
X: 240659		DATE: 14/07/05		MORPHOLOGY: Esker Ridge		
Y: 222985		DEPTH: 11.5m		WATER LEVEL: 5m		
LAYER	FROM	TO	FIELD DESCRIPTION	SAMPLE	COLOUR	SAMPLE CLASS (20mm/2mm)
1	0.0	0.5	Topsoil			
2	0.5	2.2	Dense silty sandy GRAVEL with subrounded subangular Lst pebbles (1-9cm diam). GLACIOFLUVIAL			
3	2.2	4.0	Medium dense silty clayey GRAVEL with subangular subrounded Lst pebbles (1-10cm diam.). GLACIOFLUVIAL	1	2.5Y-4/2	MUDDY SANDY GRAVEL / SILTY SAND
4	4.0	10.0	Soft to medium dense stony sediment (water table) No Recovery.			
5	10.0	11.5	Very dense stony sediment. No recovery			

BH-S1G						
X: 240818		DATE:19/07/05		MORPHOLOGY: Glaciofluvial fan		
Y: 222896		DEPTH: 13.5m		WATER LEVEL: 12m		
LAYER	FROM	TO	FIELD DESCRIPTION	SAMPLE	COLOUR	SAMPLE CLASS (20mm/2mm)
1	0.0	0.2	Topsoil			
2	0.2	1.6	Very soft fine SAND with no pebbles (2.5Y-4/2). GLACIOFLUVIAL			
3	1.6	4.4	Soft Clayey Silty SAND with few (5%) subangular pebbles. GLACIOFLUVIAL	1	2.5Y-4/2	SILTY SAND
4	4.4	8.8	Soft fine SAND with silty nodules and rounded to subangular Lst/Chert pebbles (1-8cm diam.). Pebble proportion: 40%. GLACIOFLUVIAL	2	2.5Y-4/3	GRAVELLY MUDDY SAND
5	8.8	12.2	Soft medium to fine SAND with rounded to angular Lst pebbles. Pebble proportion: 20%. GLACIOFLUVIAL			
6	12.2	13.5	Dense grey blue silty sandy DIAMICTON with angular-subangular Lst pebbles. GLACIAL	3		GRAVELLY MUDDY SAND / MUDDY SAND

BH-S1H						
X: 240614		DATE:19/07/05		MORPHOLOGY: Glaciofluvial fan		
Y: 222786		DEPTH: 14.7m		WATER LEVEL: 12m		
LAYER	FROM	TO	FIELD DESCRIPTION	SAMPLE	COLOUR	SAMPLE CLASS (20mm/2mm)
1	0.0	0.2	Topsoil			
2	0.2	1.6	Medium dense coarse GRAVEL with sandy matrix. Rounded pebbles. Clast supported. GLACIOFLUVIAL			
3	1.6	3.3	Medium dense sandy GRAVEL with rounded Lst pebbles (some Sst pebbles present). GLACIOFLUVIAL	1	2.5Y-3/2	GRAVELLY MUDDY SAND
4	3.3	10.0	Soft gravelly medium SAND with well rounded Lst pebbles. Pebble proportion: 30-50% increasing downwards. Pebble size: 1-12cm diam.	2	10YR-4/2	GRAVELLY SAND
4a	10.0	11.0	Soft Gravelly Sand with Lst and Cherty Lst pebbles. GLACIOFLUVIAL	3		GRAVELLY MUDDY SAND
5	11.0	12.2	Soft sediment, maybe due to water presence. No recovery			
6	12.2	14.7	Dense Silty Clayey DIAMICTON (2.5Y-4/1) with angular-subangular Lst pebbles. GLACIAL			

Table 6.1 – Borehole records for Site S1. Boreholes have been drilled using a Continuous Flight Auger. Sample colour coding is based on the Munsell Colour Scheme. Sample class 20mm indicates samples wet sieved, sample class 2mm indicates samples with Full Particle Analysis. Classes are derived from the Classification Scheme by Folk (1954).

6.2.2 – Electrical Resistivity Data

The electrical resistivity surveys carried out are presented below in four different sections. ERT profiles are firstly presented and discussed followed by the time-lapse resistivity data, the azimuthal resistivity and finally, the 3D Model.

6.2.2.1 – 2D Electrical Resistivity

Five electrical resistivity profiles collected in Site S1 using the Wenner-Schlumberger array with 5m and 10m electrode spacing are presented below. Their relative locations are presented in Figure 6.5.

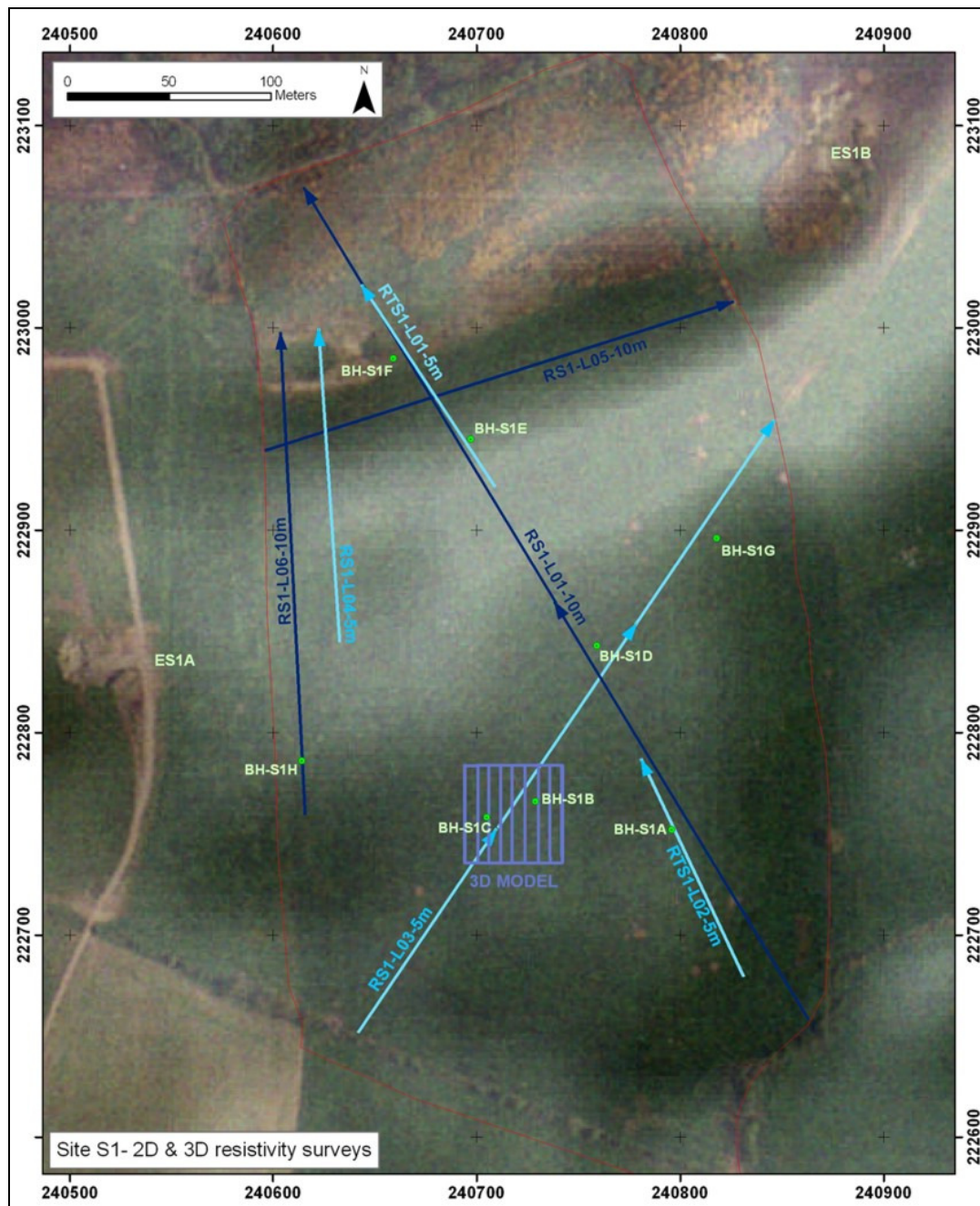


Figure 6.5 – Location of 2D ERT profiles at Site S1 at 10m spacing (dark blue) and at 5m spacing (light blue). The nine profiles used to produce 3D model are displayed in purple.

RS1-L01-10m (Figure 6.6) is composed of two concatenated profiles at 10m electrode spacing. It cuts across the main geomorphologic features in the site approximately in a south-southeast to north-northwest direction. The profile is 460m in length and extends to a depth of 40m. Medium to high resistivity values (400 - 2000 Ω m) occur in places along the surface within the first 10m at 40 - 330m. The areas with higher values (> 800 Ω m) have been interpreted as sandy gravel; the areas with lower values (< 800 Ω m) have been interpreted as gravelly sand and silt, both forming part of a glaciofluvial depositional system. Two boreholes drilled along the line (BHS1A and BHS1D) show gravelly sand and slightly gravelly muddy sand as the dominant lithologies. The section from 330 - 390m is dominated by silts and clays represented by low resistivity values (<120 Ω m) down to a depth of about 5m. Resistivity values (>400 Ω m) occurs from 390 - 410m, and are related to the presence of an esker ridge composed of cobble gravel, approximately 8m thick. The area along the surface 410 - 440m is dominated by low resistivity values interpreted as silts and clays. All the materials described above are underlain by low to medium resistivity values. These have been interpreted as diamicton underlying the sediments described above with varying thickness between 5 to more than 25m. The lower part of the profile is dominated by high resistivity values ranging 1000 - 3000 Ω m. This has been interpreted as the bedrock basement underlying the diamicton with undulating topography. A lower resistivity zone (600 Ω m) occurs at 100 - 125m, the contact with the surrounding high resistivity zone is sharp and vertical, this may be related to the presence of karstified limestone bedrock, consisting either of weathered bedrock or soft sediments infill. Furthermore, the relative location of the time-lapse resistivity profiles collected along this line and described in the next section is illustrated in Figure 6.6.

RS1-L03-5m (Figure 6.7) is composed of three concatenated profiles at 5m electrode spacing which cut obliquely across the main geomorphologic feature in the site (flat topped fan) in a southwest to northeast direction. Four boreholes drilled along the profile have been used to refine the final interpretation. Low resistivity values (< 250 Ω m) occurring on the surface from 0 - 40m and developing towards deeper parts are believed to represent diamicton which has been mapped as a continuous gently undulating layer occurring under 55m OD along the profile. It is underlain in places by higher resistivity values (>1700 Ω m),

which have been interpreted as bedrock. The diamicton is overlain by high resistivity areas ($> 800\Omega\text{m}$) from 40 - 210m and 240 - 360m interpreted as sandy gravel. This sand and gravel body is overlain by a layer presenting low to medium resistivity ($150 - 400\Omega\text{m}$) from 90 - 360m with large variations in thickness interpreted as gravelly sand with silty matrix. The resistivity variation may be related to the percentage of silt in the sediments.

RS1-L04-5m (Figure 6.8) Data were collected using a Geopulse Tigre resistivity meter with 32 electrodes at 5m spacing. The profile runs 50m west of and subparallel to RS1-L01- 10m, showing similar results and displaying a higher resolution resistivity model of the top 35m. A small patch with medium to high resistivity ($700\Omega\text{m}$) at 35m OD at 90m has been interpreted as probable bedrock. A medium low resistivity area ($150 - 300\Omega\text{m}$) overlying the former have been interpreted as diamicton. This is overlain by a section from 0 - 65m reaching a maximum thickness of 15m with resistivity $700 - 1400\Omega\text{m}$ which have been interpreted as gravelly sand. The area 75 - 90m is dominated by $700 - 900\Omega\text{m}$ resistivity values associated with 7 - 8m thick cobble gravel deposited along the esker ridge. A low resistivity zone ($<150\Omega\text{m}$) dominate the surface at 65 - 115m. It has been interpreted as lacustrine silt and clay overlain by a thin coating of peat. The thickness of the postglacial sediments reaches a maximum of 7.5m at 95m.

RS1-L05-10m (Figure 6.9) runs along the silt/clay dominated lowland located at the southern margin of the esker ridge. The profile shows two very high resistivity values dominating the lower areas ($> 1700\Omega\text{m}$) from 50 - 20m OD. These have been interpreted as bedrock. A layer of weathered bedrock occurs from 140 - 210m pinching out westwards with medium high resistivity values ($600 - 1000\Omega\text{m}$). These are overlain by low resistivity values ($< 400\Omega\text{m}$), which have been interpreted as diamicton overlain by lacustrine silt and clay. There is a disagreement between the rock head level portrayed by this profile (50m OD) and the rock head level encountered by profiles L01, L04 and L06 cutting across it at a number of points, which consistently show rock head level at less than 45m OD. A similar situation was analysed in the forward modelling exercise in Chapter 5. However, in the theoretical model, the area dominated by high resistivity values (bedrock) is displaced at lower levels than the known location (Figure 5.5).

RS1-L06-10m (Figure 6.10) profile runs 30m west of and parallel to line L04, and shows similar results. Medium to very high resistivity values (500 - 2000 Ω m) occur along the surface at 0 - 130m, reaching maximums of 15m depth. The area 130 - 210m is dominated by low values (< 150 Ω m) interpreted as lacustrine silts and clays, reaching maximum depth of 8m. The area north of it is dominated by medium resistivity (c. 500 Ω m) interpreted as gravel. These sediments are underlain by low to medium resistivity values (150 - 300 Ω m) interpreted as diamicton, which are underlain by a high resistivity area related to the presence of bedrock underlying the surficial sediments.

Five main lithological categories have been identified in Site S1 by means of ERT surveys and borehole data. Bedrock has been identified in L01, L03, L05 and L06 and inferred in L04; it is characterized by high to very high resistivity values (> 900 Ω m). Depth to bedrock ranges from 20 - 38m, a number of possible weathered bedrock layers have been described in L01 and L05. A layer of diamicton has been identified overlying the bedrock. It is characterized by low to medium resistivity values (80 - 400 Ω m), its thickness varies from less than 1m in areas underlying the fan up to 25m in the low ground where the lacustrine sediments and the esker ridge overly it. A layer described as gravelly sand/silt or as muddy sand (pink colour in L01, L03, L04 and L06) interstratified with a layer of sandy gravel (brown colour in L01 and L03) overlies the diamicton in the area morphologically defined as a fan and it is defined by medium to high resistivity values (300 - 1000 Ω m). These have been interpreted as glaciofluvial sediments reaching a thickness of over 10m in the middle area of the fan and pinching out towards its southern and northern margins. An isolated patch of high resistivity values has been identified in L01, L04 and L06 and has been interpreted as the esker ridge cutting across the site. This is generally composed of boulders and sandy gravel and reaches a maximum thickness of 9m and width of up to 40m. Finally, a lithological category dominated by low resistivity (60 - 120 Ω m) has been recognized in L01, L04, L05 and L06. It has been interpreted as lacustrine silt and clay occurring along the surface at the northern and southern margins of the esker ridge overlying the diamicton. It reaches a maximum thickness of 8m in the middle area of the body located south of the esker and gradually pinches out towards its northern and southern margins.

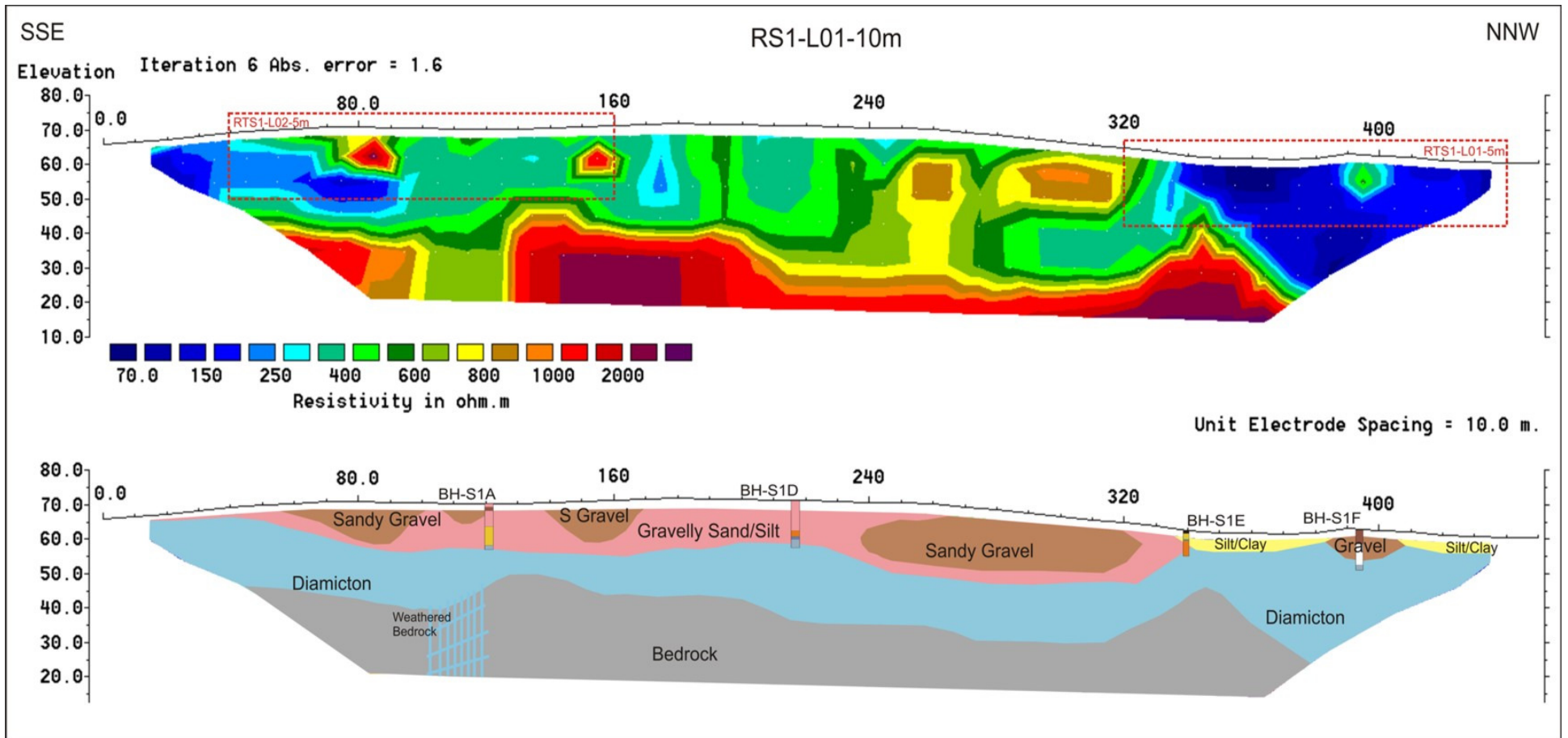


Figure 6.6 – Electrical Resistivity profile RS1-L01-10m collected in Site S1 and its interpretation.

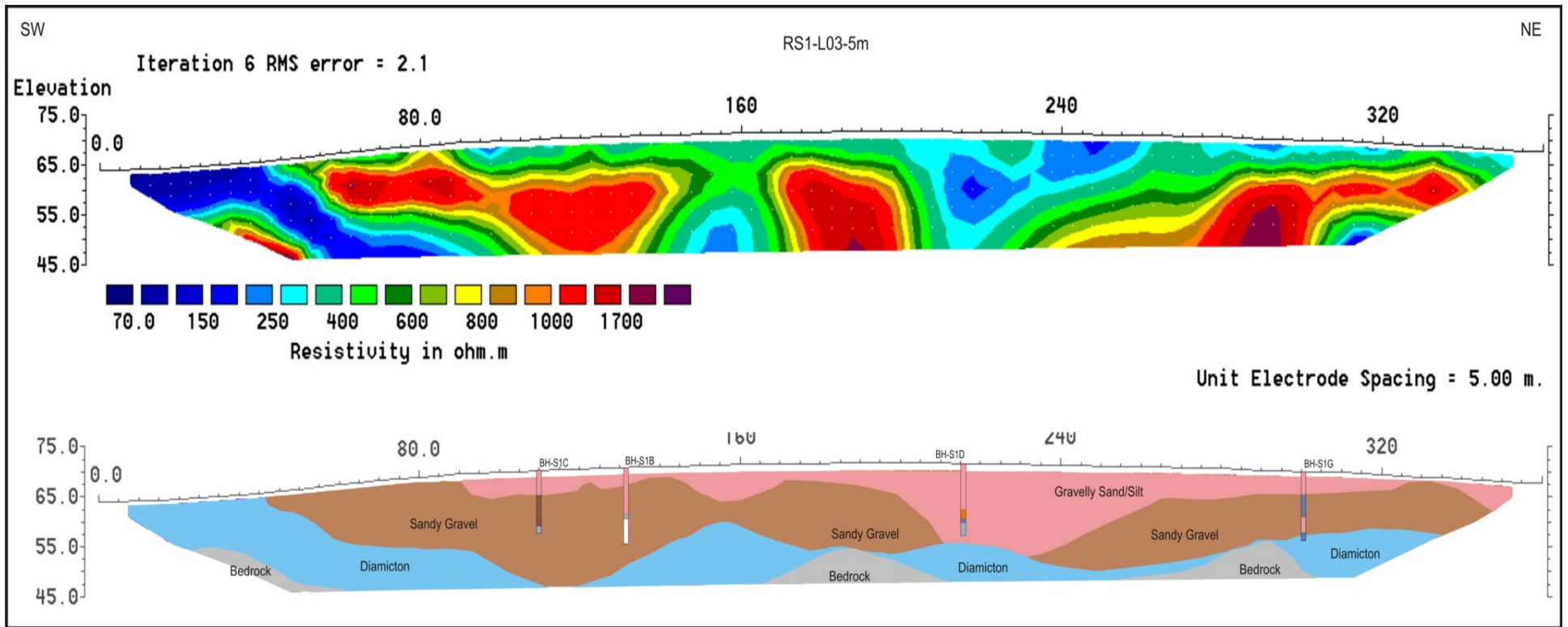


Figure 6.7 – Electrical Resistivity profile RS1-L03-5m collected in Site S1 and its interpretation.

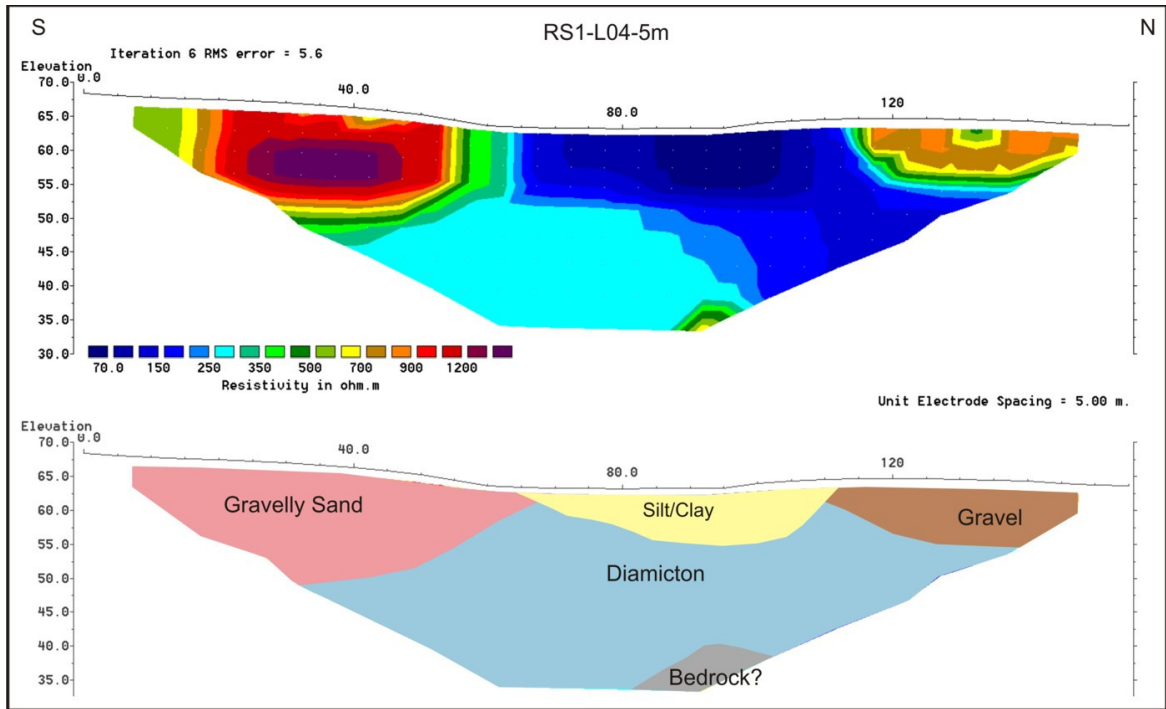


Figure 6.8 – Electrical Resistivity profile RS1-L04-5m collected in Site S1 and its interpretation.

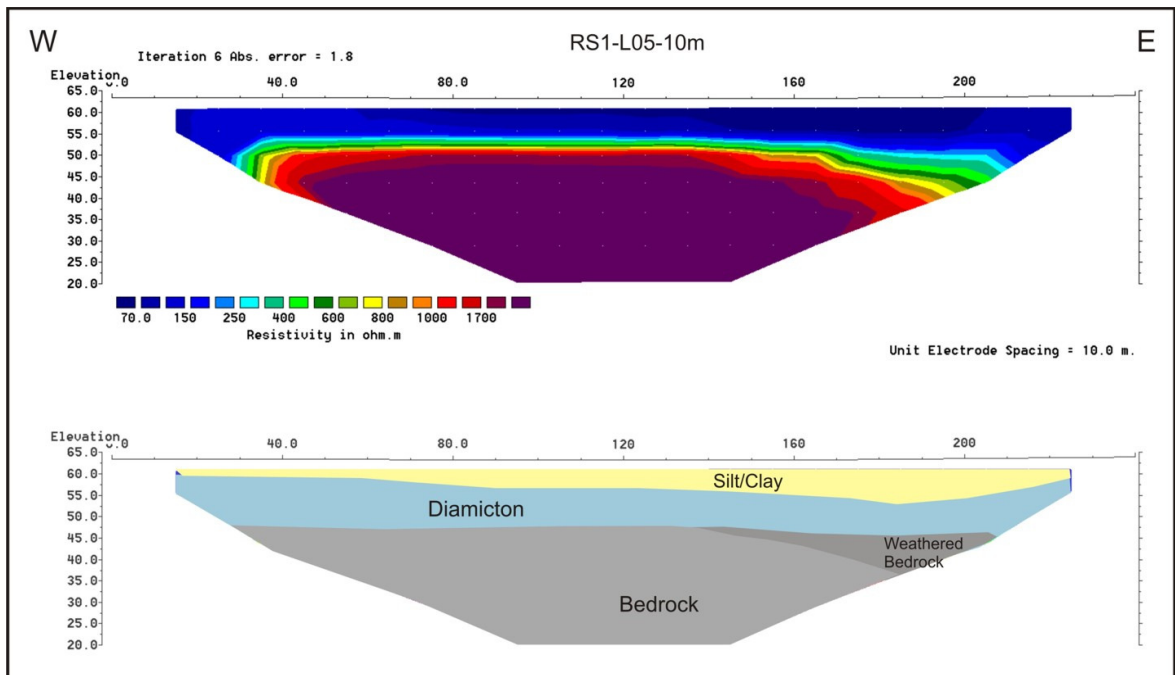


Figure 6.9 – Electrical Resistivity profile RS1-L05-10m collected in Site S1 and its interpretation.

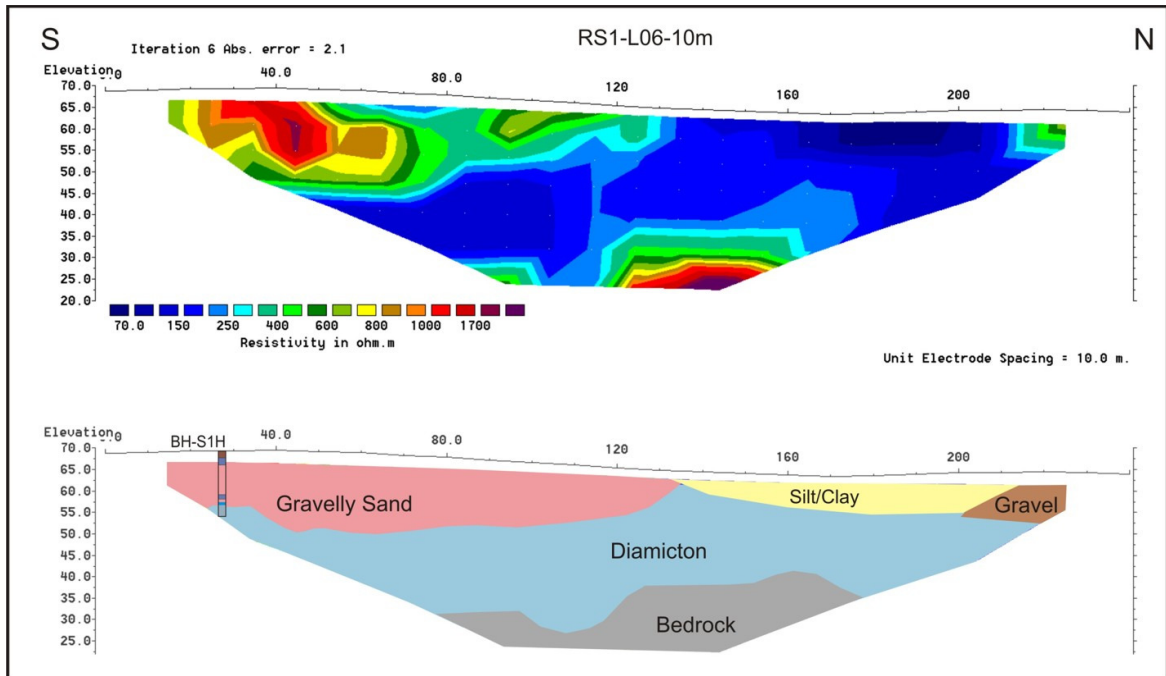


Figure 6.10 – Electrical Resistivity profile RS1-L06-10m collected in Site S1 and its interpretation.

6.2.2.2 – Time-lapse Resistivity

Time-lapse resistivity surveys have been carried out on a monthly basis from January 2006 to January 2007 for four resistivity profiles. The four profiles were surveyed monthly within the same day between 10am and 4pm; the date of the surveys and the weather and ground conditions for the day are presented in Table 6.2. In order to know the exact location of the lines surveyed, two wooden props were placed at both ends of every profile and were left as reference points for the length of the whole survey (14th January 2006 to the 19th of January 2007). The objective was to observe the seasonal variation of resistivity values in a range of glacial and postglacial sediments existing in Site S1 to ascertain the effect of rainfall and temperature on the resistivity of the sediments. This site was considered ideal for this exercise as a large range of sediment types occur within a small area. The locations of the profiles surveyed are presented in Figure 6.11.

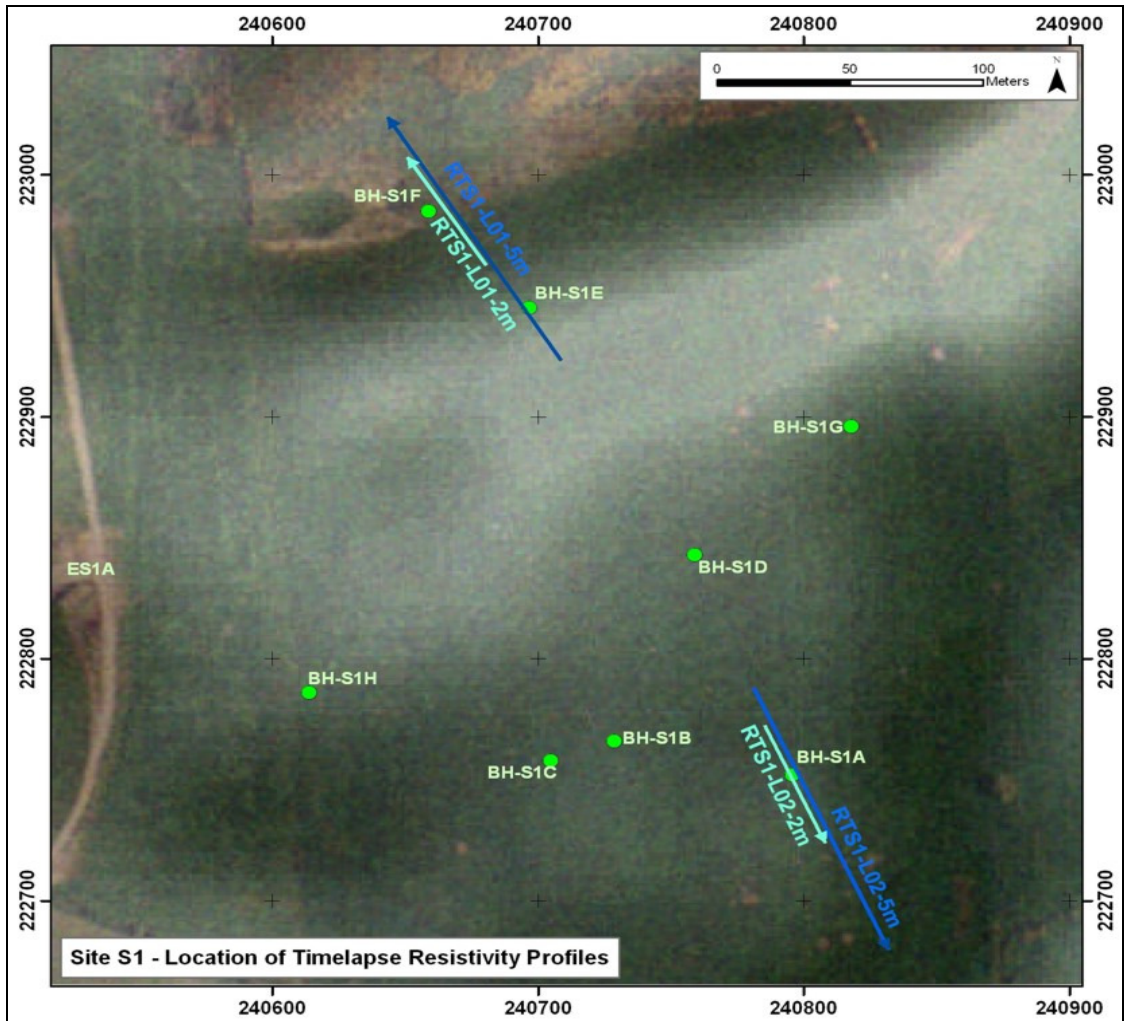


Figure 6.11 – Location of time-lapse resistivity profiles at Site S1. Lines recorded with 2m electrode spacing are displayed in cyan. Lines recorded with 5m electrode spacing are displayed in blue.

Survey Number	Date	Weather	Temperature (°C)	Ground
1	14/01/2006	Sunny	4.1	Wet
2	12/02/2006	Rain	8.5	Wet
3	12/03/2006	Cloudy	7.7	Wet
4	16/04/2006	Cloudy	10.9	Dry
5	12/05/2006	Sunny	13.6	Dry
6	09/06/2006	Sunny	17.3	Dry
7	15/07/2006	Sunny	16.2	Dry
8	14/08/2006	Cloudy	13.8	Very dry
9	16/09/2006	Cloudy	13.6	Wet
10	14/10/2006	Cloudy	13.4	Wet
11	09/11/2006	Sunny	6.6	Wet
12	12/12/2006	Rain	7.5	Wet
13	19/01/2006	Cloudy	8.8	Wet

Table 6.2 – Dates when the time-lapse resistivity surveys were carried out including weather and temperature on the date.

The description and interpretation for the four profiles collected are presented below. The profile collected on the 9th of June of 2006 was selected for this purpose.

RTS1-L01- 5m (Figure 6.12) shows a high resolution section of L01-10m between 320 - 440m, see Figure 6.6. Two low resistivity zones (<100Ωm) dominate the surface from 15 - 72m and from 87 - 115m. These have been interpreted as lacustrine silt and clay overlain by a thin coating of peat (See BH-S1E). These sediments reach a maximum thickness of 7.5m at 45m. The section between 72 - 86m is dominated by 500 - 800Ωm resistivity values associated with cobble gravel with a muddy matrix reaching a thickness of 7 - 8m and forming the core of an esker ridge running across the profile. A zone, close to the surface from 0 - 20m showing medium to high resistivity values (200 - 600Ωm), has been interpreted as gravelly sandy silt (see sample 2 of BH-S1E - Table 6.1) underlying the lacustrine sediments. A low to medium resistivity area (100 - 200Ωm) underlying all the sediments described above has been interpreted as diamicton. Finally, a small area underlying the diamicton from 38 - 57m presenting values higher than 500Ωm has been interpreted as bedrock.

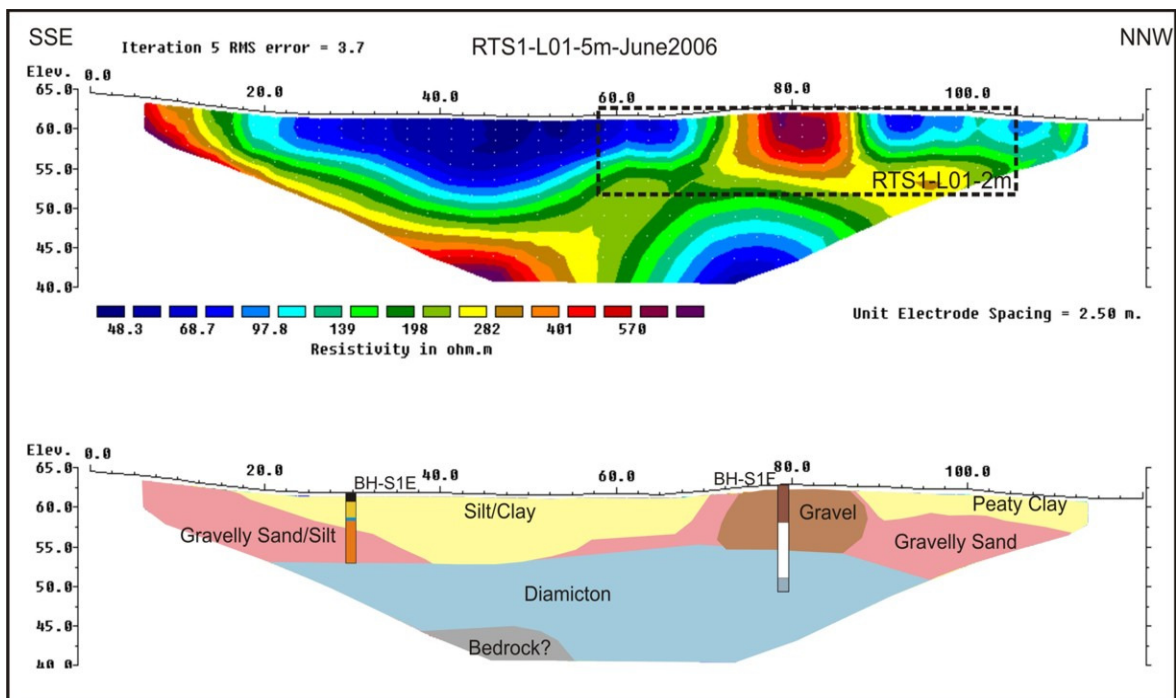


Figure 6.12 – Time-lapse Electrical Resistivity profile RTS1-L01-5m for the month of June 2006 collected in Site S1 and its interpretation. The location of profile RTS1-L01-2m is outlined in black.

RTS1-L01-2m (Figure 6.13) runs inline with L01-5m for 48m, starting at 58m on L01-5m, see Figure 6.12. It provides a high resolution cross-section of the esker ridge. The profile shows medium to high resistivity values ($> 400\Omega\text{m}$) along the surface between 16 - 32m and from 0 - 6m depth, which have been interpreted as cobble gravel with muddy matrix forming the core of the esker ridge. The top two metres, between 0 - 15m and 33 - 48m, are dominated by very low resistivity values ($<60\Omega\text{m}$). These deposits are composed of peat overlying lacustrine silt/clay. Moreover, low to medium resistivity values occurring in the area underlying the lacustrine sediments ranging from 60 to $400\Omega\text{m}$ have been interpreted as gravelly muddy sand associated with the esker. Finally, a small patch of low to medium resistivity ($100 - 300\Omega\text{m}$) underlying the esker may be related to the presence of the diamicton described for line L01-5m.

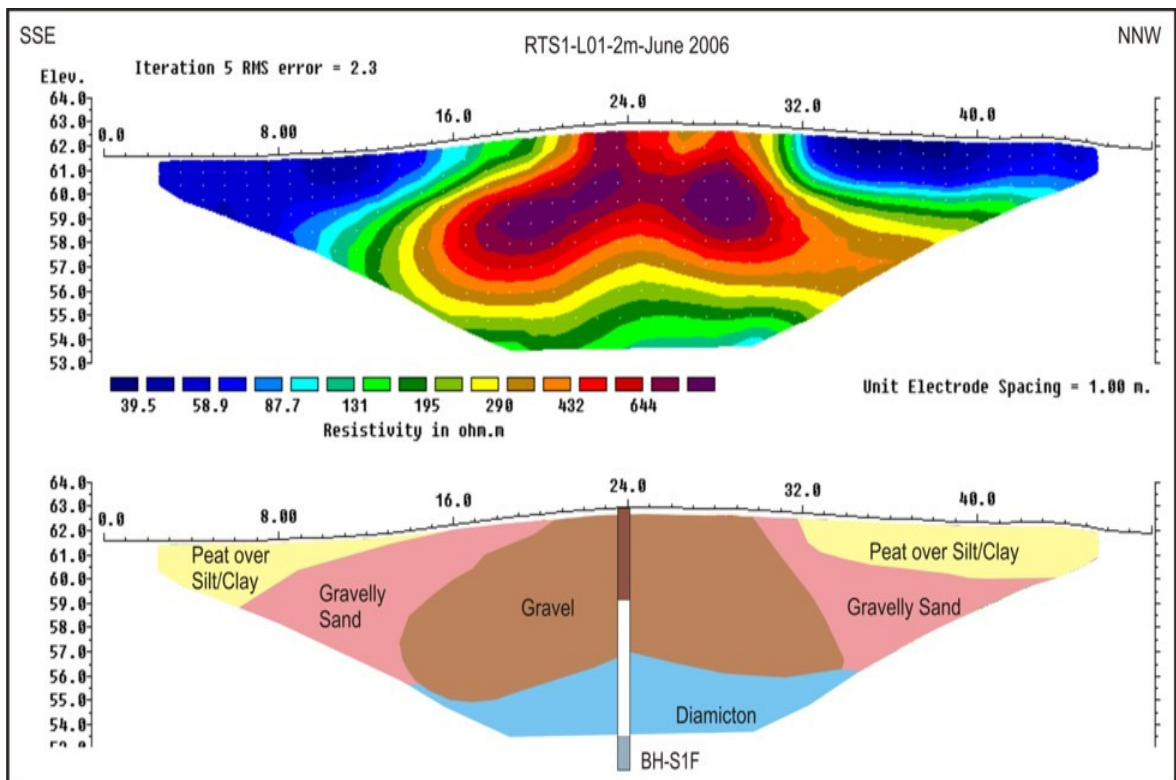


Figure 6.13 – Time-lapse Electrical Resistivity profile RTS1-L01-2m for the month of June 2006 collected in Site S1 and its interpretation.

RTS1-L02-5m (Figure 6.14) shows a higher resolution section of L01-10m from 40 - 160m. Resistivity values higher than 300Ωm dominate the top 10m. Within this section, the areas with values higher than 500Ωm have been interpreted as deposits dominated by sand and gravel. It has been inferred from their shape (see high resistivity areas 38 - 54m and 65 - 100m) that these correspond to infill of buried channel features or lenses running across the profile. The areas dominated by lower resistivity values (300 - 500Ωm) have been interpreted as slightly gravelly muddy sand as recorded in BH-S1A. Resistivity values lower than 300Ωm dominate the lower parts of the profile, which has been interpreted as diamicton. Finally a small area displaying high resistivity occurs at the bottom of the profile between 42 - 56m and it is likely related to the presence of bedrock.

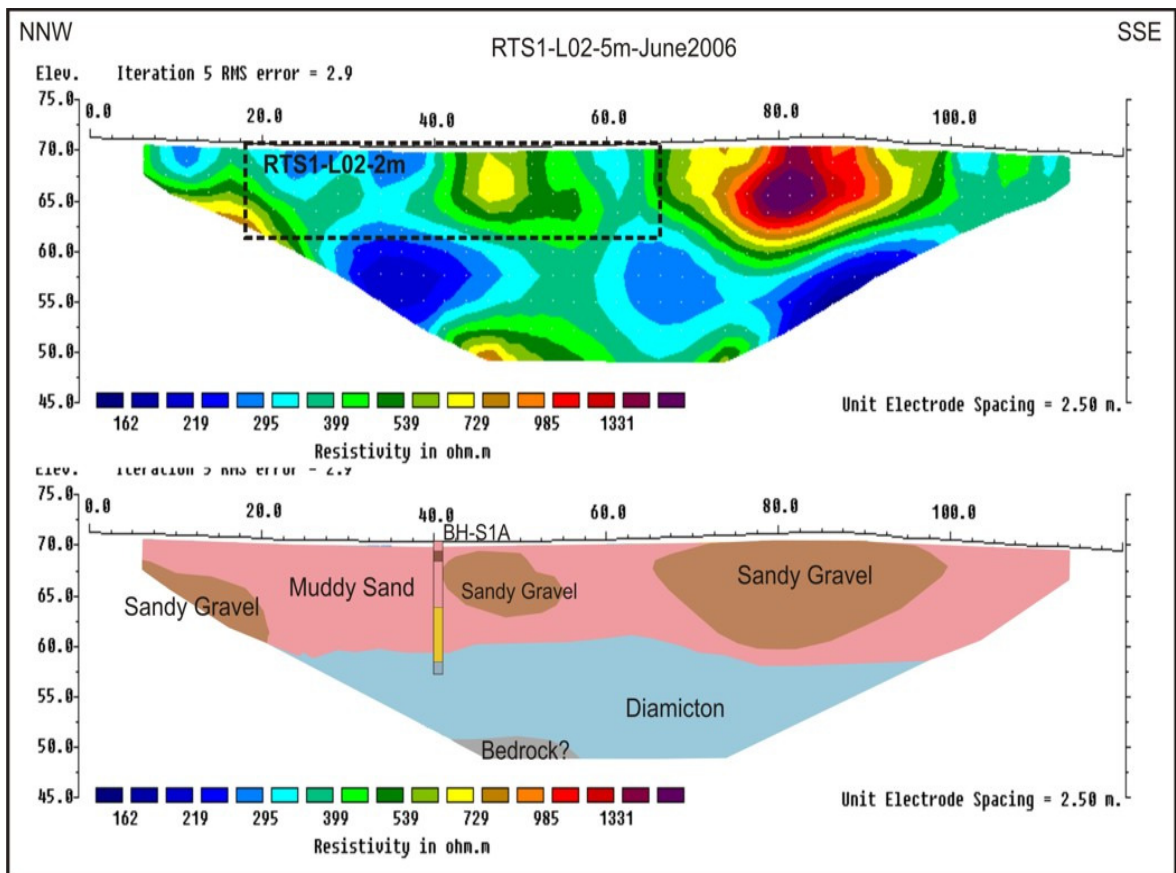


Figure 6.14 – Time-lapse Electrical Resistivity profile RTS1-L02-5m for the month of June 2006 collected in Site S1 and its interpretation. The location of profile RTS1-L02-2m is outlined in black.

RTS1-L02-2m (Figure 6.15) runs inline with L02-5m for 48m, starting at its 18m point. It provides a high resolution cross-section of a small portion of the flat topped area of the fan. The top metre is dominated by values of less than 300Ωm, probably related to presence of muddy sands. Two medium high resistivity values (>400Ωm) occur between 13 - 17m and 22 - 40m. These two areas have been interpreted as sandy gravel related to infill of buried channel features or lenses running approximately orthogonal to the profile. The remaining areas within the profile are dominated by a wide resistivity range, 150 - 400Ωm. These have been interpreted as muddy sand; however, the resistivity values vary within short distances, probably indicating variations in the proportions of sand and mud within the sediments.

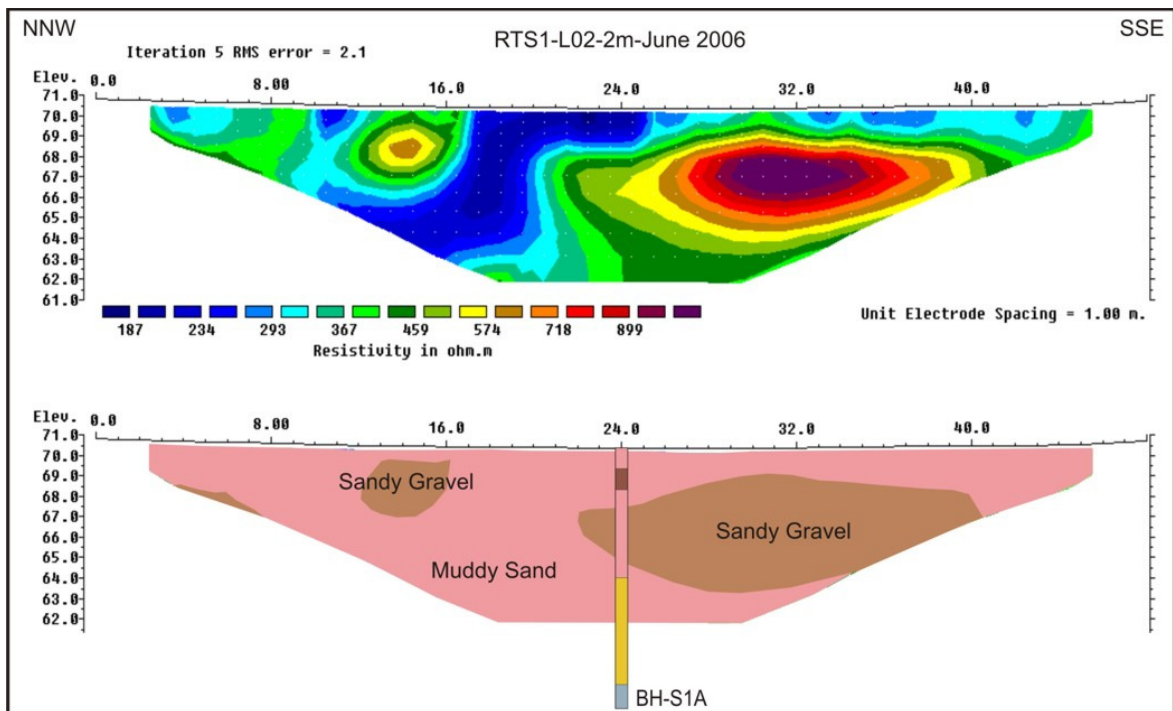


Figure 6.15 – Time-lapse Electrical Resistivity profile RTS1-L02-2m for the month of June 2006 collected in Site S1 and its interpretation.

Two methods have been used to look at the seasonal variation of resistivity data. RES2DINV software provides a tool that compares the seasonal variation between two profiles displaying the percentage variation as a third profile. This has been used to

compare and discuss main seasonal variations. Moreover, the monthly variation of the inverted data for a number of points selected for each profile has been examined.

Seasonal variation in resistivity values is expected to be influenced by the moisture content of the surveyed sediments which can vary by fluctuations of the water-table and by the volume of rainfall water permeating into the subsurface below the root zone (i.e. Effective Recharge). Effective Recharge has been calculated from the rainfall and potential evapotranspiration data obtained from the Mullingar weather station for a number of soils and vegetation cover types using the Penam-Monteith equation. Further details on this equation are presented in Allen et al. (1998) and will not be further discussed in this thesis. Figure 6.16 shows the daily effective recharge in mm for a sandy loam soil vegetated with grass. Sandy loam was chosen as the soil type to model the data as it encompasses the different sediments mapped along the four profiles. Also, grass has been selected as the vegetation type as it overlies over 95% of the ERT profiles surveyed.

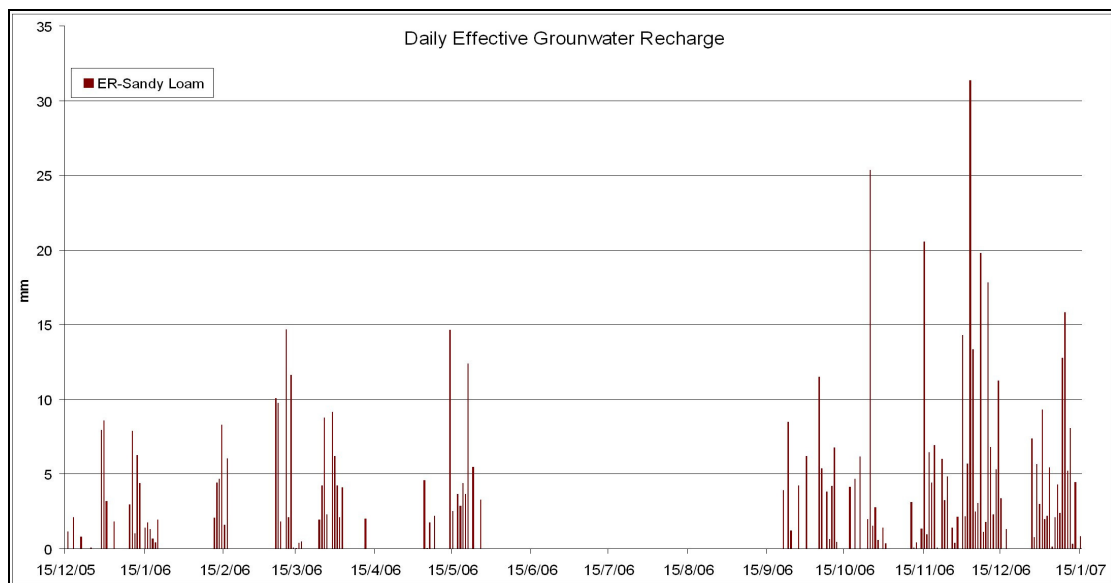


Figure 6.16 – Effective Recharge for sandy loam with grass cover for year 2006. Effective recharge has been estimated from rainfall and potential evapotranspiration data from Mullingar weather stations using the Penam-Monteith equation (Allen et al., 1998).

Five profiles collected from January 06 to January 07 for line **RTS1-L01-5m** are presented in Figure 6.17. It can be observed that all the profiles show a very similar model of the subsurface for the different seasons. However, an increase of the resistivity of areas dominated by sand and gravel and bedrock for the July profile is noticeable. RES2DINV software allows the display of the difference between two profiles by means of percentage variation between them for each point of the model. Figures 6.18a,b,c,d show the percentage difference between the profiles collected in January 06, April 06, July 06, October 06 and January 07. Areas close to the surface mapped as sand and gravel show an important increase in resistivity, especially in July 06 (>50%), while areas greater than 5m depth underlying them exhibit a decrease in resistivity (20-40%). On the other hand, the area dominated by mud between 20 - 70m shows a slight decrease in resistivity along the surface, and some increase in the deeper parts. Also, the area mapped as diamicton (Figure 6.12) shows a decrease in the resistivity during the drier months where overlain by sand and gravel. Figure 6.18e shows the resistivity difference between October 06 and January 07. Resistivity increases slightly (10%) in areas dominated by lacustrine mud and diamicton and decreases significantly (>50%) for the ones dominated by sand and gravel. The profile for July 06 to October 06 (Figure 6.18f) shows a decrease of the resistivity values along the surface in areas dominated by sand and gravel and increase in the ones dominated by mud, However, the areas under 5m depth overlain by sand and gravel show an important increase of the resistivity (>50%), whereas, when overlain by mud a decrease of the resistivity values occur.

Percentage variations for line **RTS1-L01-2m** display similar results to **L01-5m**. Finer detail in the esker area and surroundings shows that the largest resistivity increase during drier seasons concentrates in the central parts and the northern margin of the ridge along the top 2.5 - 4m. A general decrease of the resistivity occurs just underneath the feature below 2.5m) during the drier months (Figures 6.19a,b,c,d. Figure 6.19e shows an increase of the resistivity values along the top 2m, whereas, areas greater than 2m depth are dominated by a broad decrease of the resistivity. Finally, percentage variations between July 06 and October 06 (Figures 6.19f) show a general resistivity decrease along the surface and an important increase of the resistivity values (>100%) for the zone underlying

the esker ridge below 2.5m depth for the October profile. In contrast, areas overlain by mud show a minor decrease in resistivity (<20%).

Seasonal percentage variations of resistivity values for profile **RTS1-L02-5m** present a similar pattern to that discussed above. Drier seasons show a general increase in the resistivity along the top 5m. This increase is quite dramatic in areas dominated by sandy gravel (>100%), and moderate in the ones composed of muddy sand (10-20%), these changes are especially noticeable in Figure 6.20b. The areas at more than 5m depth, overlain by sandy gravel 42 - 52m and 70 - 90m show a large reduction of the resistivity (>50%). A subtler reduction occurs in areas overlain by muddy sand. The contrary is observed when examining the percentage change between July 06 and October 06, an important drop of the resistivity values occurs along the surface (>50%), whereas a significant resistivity increase occurs for the area below 5m depth (>100%), see Figure 6.20f.

Following the same pattern observed above, **RTS1-L02-2m** shows a significant increase in the resistivity values above 3m depth during the drier season and a decrease of the resistivity values in the deeper areas. However, the percentage difference profile between January 06 and July 06 (Figure 6.21b) does not show obvious variations between the areas dominated by gravel from those dominated by muddy sand. Figure 6.21c presents the resistivity contrast between January 06 and October 06 and it shows a decrease in the areas dominated by gravel and a resistivity increase for areas overlain by the gravel bodies. This is even more explicitly illustrated in Figure 6.21f, which illustrates the resistivity contrast between July and October. A large resistivity drop of more than 50% for the top 3 to 4m and a dramatic increase of up to 100% in the area over 3 - 4m depth are observed for this profile.

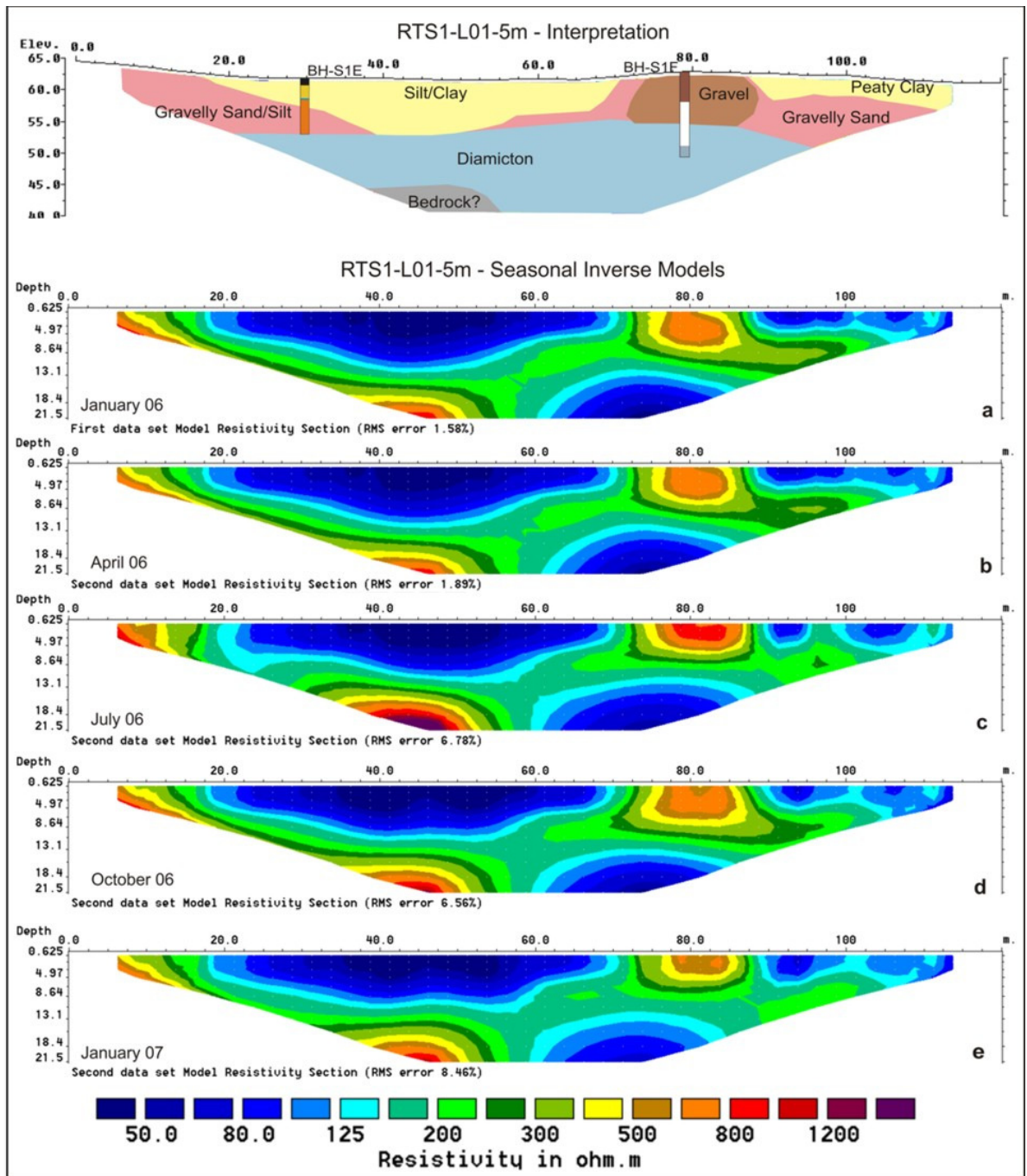


Figure 6.17 – Time-lapse ERT profile RTS1-L01-5m collected for a number of seasons.

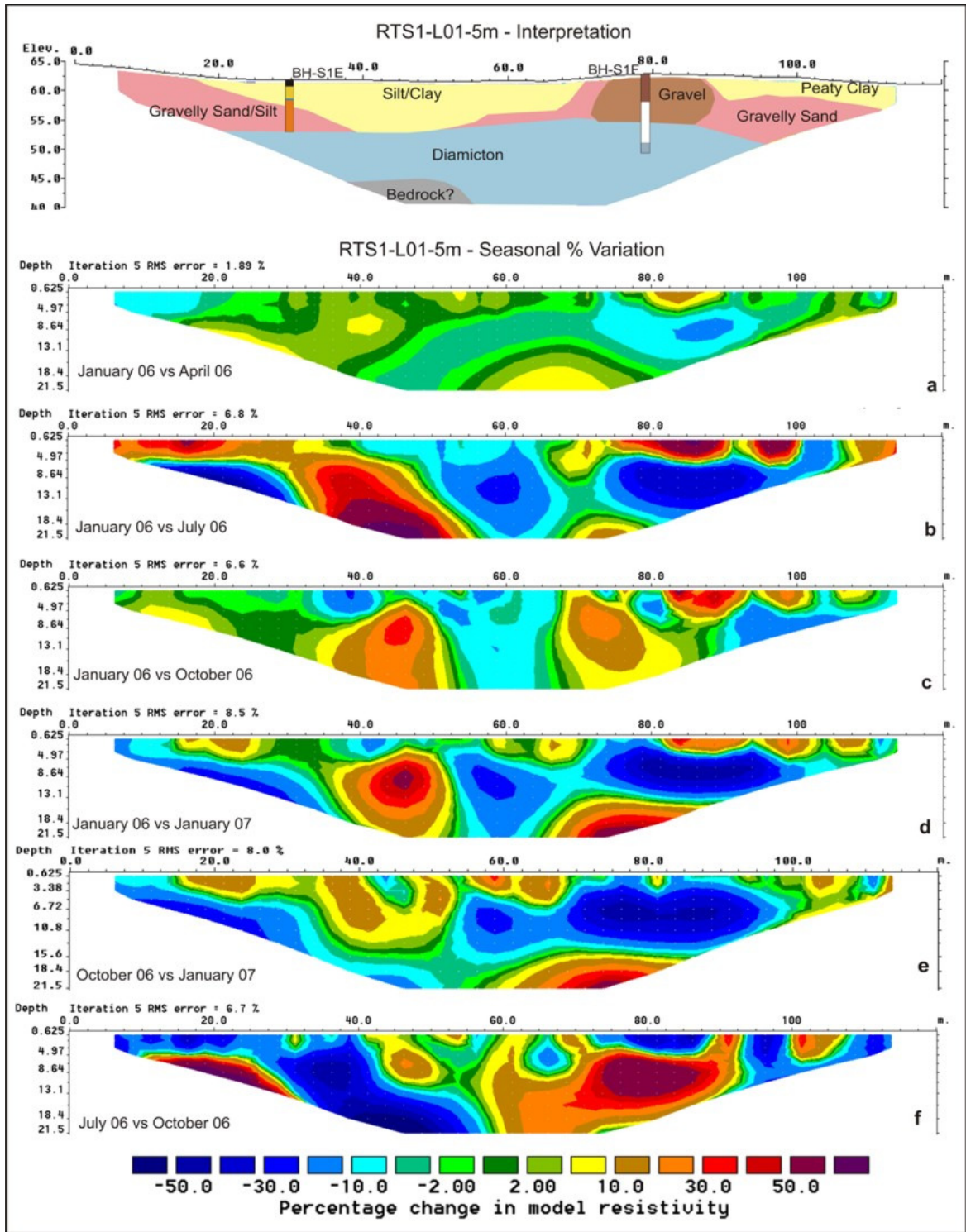


Figure 6.18 – Time-lapse ERT profile RTS1-L01-5m seasonal variation expressed in percentages.

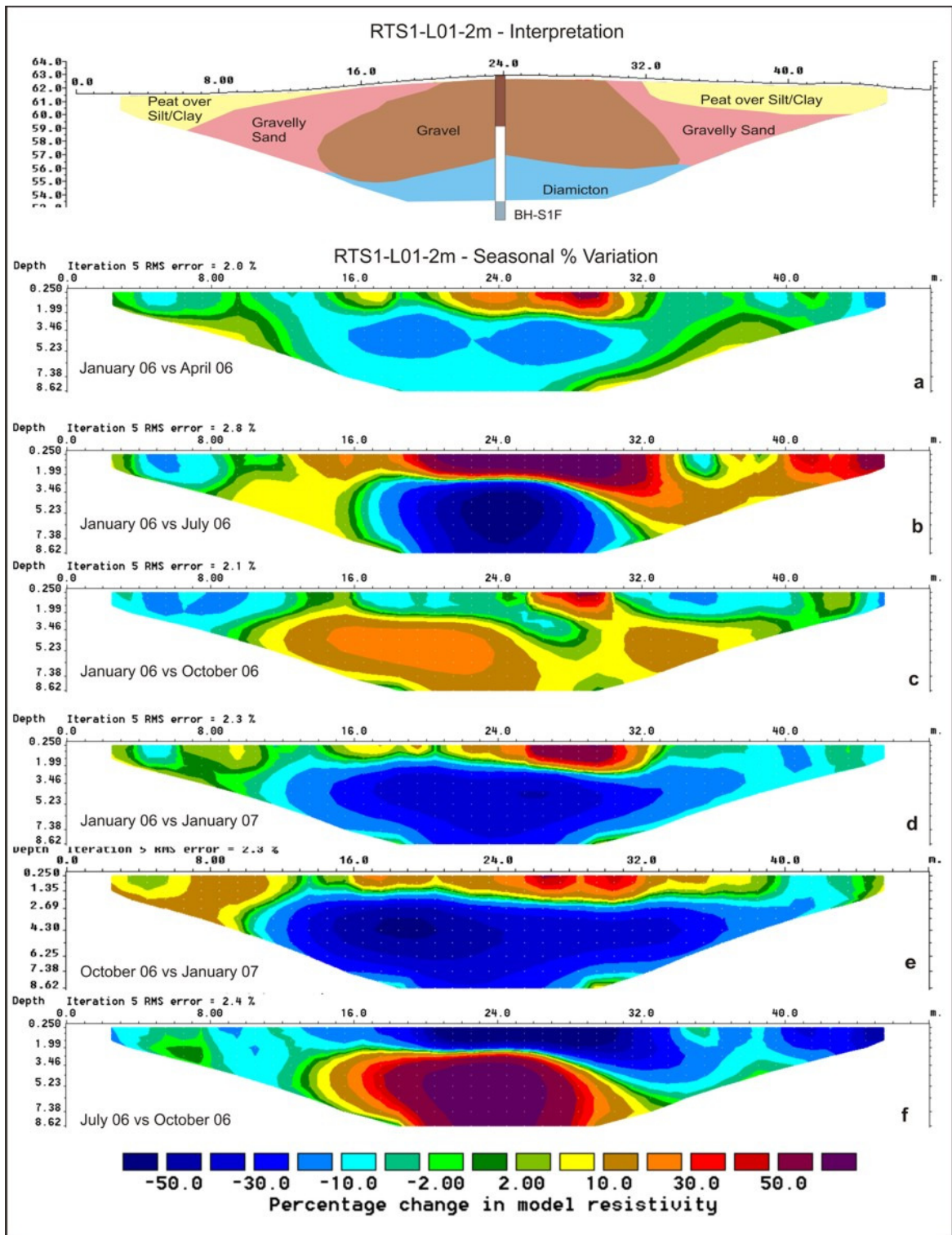


Figure 6.19 – Time-lapse ERT profile RTS1-L01-2m seasonal variation expressed in percentages.

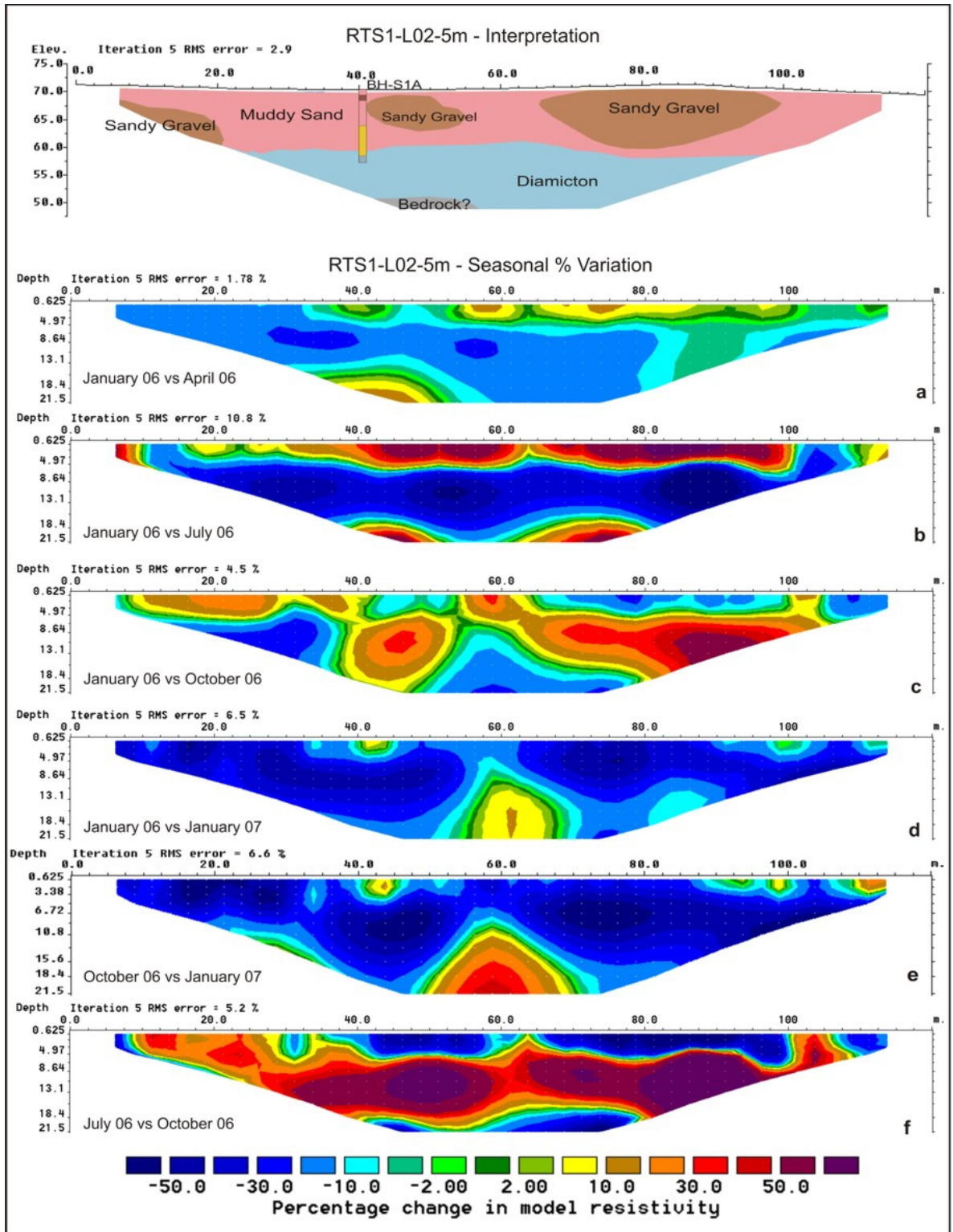


Figure 6.20 – Time-lapse ERT profile RTS1-L02-5m seasonal variation expressed in percentages.

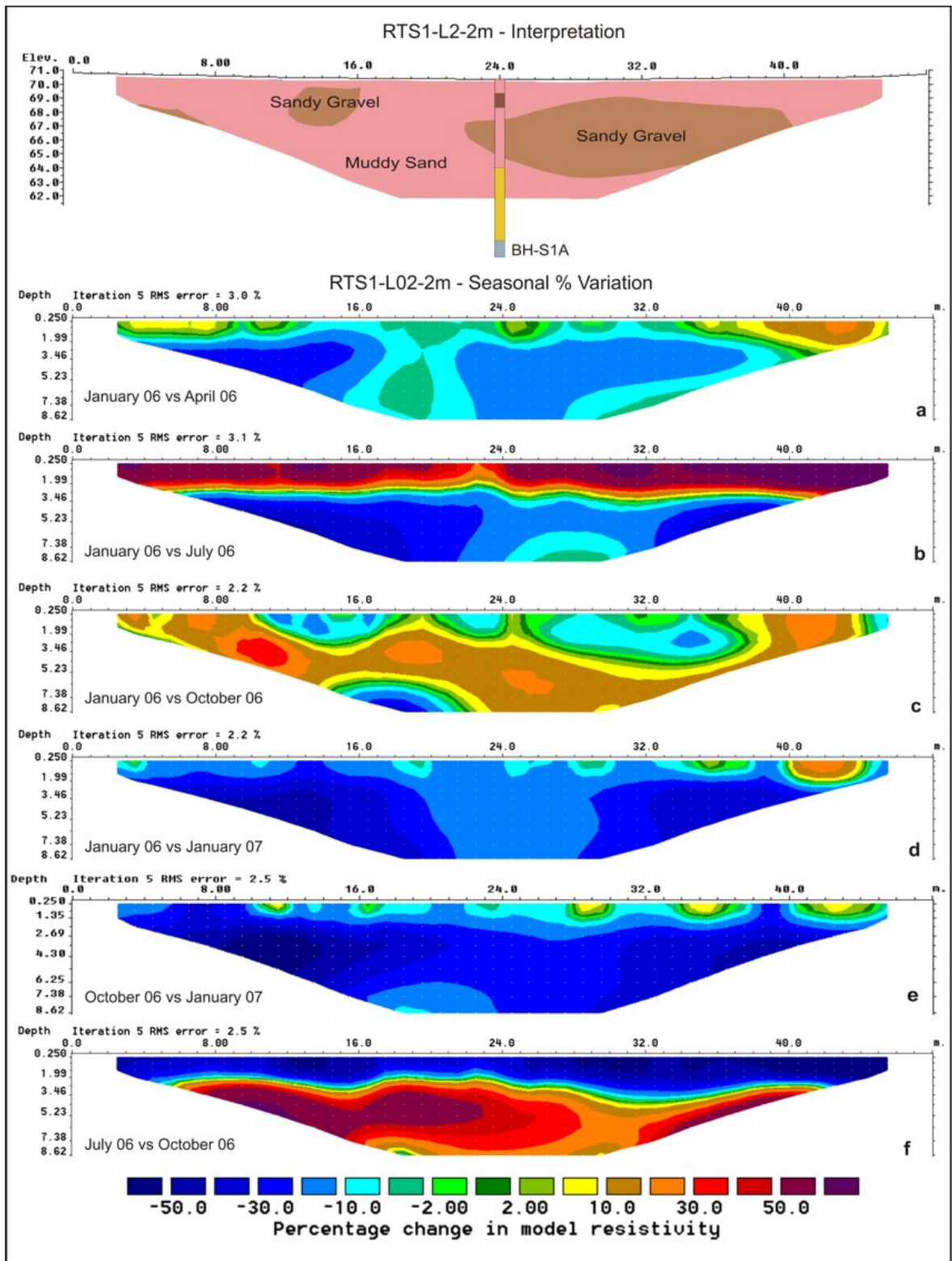


Figure 6.21 – Time-lapse ERT profile RTS1-L02-2m seasonal variation expressed in percentages.

In order to further understand the changes in resistivity through the year for the profiles presented above, the monthly resistivity values for a number of sediment types occurring along the profiles together with the effective recharge have been plotted as Cartesian diagrams. A number of points located at different depths have been selected aiming to recognize the influence of the lithology, the depth and the effective recharge on the observed resistivity variation through a year. Effective recharge values are presented as the sum of the 10, 15, 20 and 30 days period before the data were collected.

Five points have been selected for **RTS1-L01-5m** and their location and lithology are illustrated in Figure 6.22. Resistivity values for gravelly mud (R1) and muddy gravel (R3) show a significant increase during the drier months when no effective recharge has effect, this is followed by a resistivity decrease from September to January 07. R2, located in silt/clay shows small (10%) variations through the year. The resistivity values for the diamicton (R4) underlying the silt/clay fluctuate around the 180 Ω m value. On the other hand, the diamicton underlying muddy gravel (R5) shows an unexpected resistivity decrease during the drier months and an increase from September to January when an important rise of the effective recharge occurs.

Five points have been examined for **RTS1-L01-2m**, their location and lithology are shown in Figure 6.23. Two points recorded at 1m depth in silt/clay (R1 and R2) show an increase in resistivity values during the summer (>15%), while, R3, also recorded at 1m depth, but in muddy gravel, shows an increase of over 100%. The resistivity values recorded for two points (R4 and R5) located below R3 at 3.8 - 8m depth respectively, drop during the drier season indicating an increase of the moisture content in the deeper areas. This is followed by an increase in the resistivity from September to November.

Six points have been selected for **RTS1-L02-5m** and their lithology and location within the profile are illustrated in Figure 6.24. Three points recorded at 4m depth in muddy sand (R1) and gravel (R2, R3) show an increase in their resistivity during the summer and relatively steady values during the rest of the year. This resistivity increase is relatively smaller for the muddy sand (40%) compared to the gravel (55%). Three points have been

recorded at 14m depth. R4 and R5 show a drop in resistivity values from June to September and R6 from June to August. These decrease in resistivity during the summer and are followed by an important increase in resistivity from September to November, which is especially significant for point R6 (>100%).

Five points have been examined for **RTS1-L02-2m**, their location and lithology are illustrated in Figure 6.25. Points R2 and R3 recorded as sandy gravel at 1 - 4m depth respectively show a resistivity increase from July to September (> 100% for R2) and little change for the remaining months. Point R5, dominated by muddy sand, underlying the former at 8m depth shows a steady resistivity decrease from January to June, an increase from June to October and a steady decrease through autumn and winter. R1, at 1m depth, overlies R4 (7m depth), both being muddy sand. The expected increase in resistivity values during the drier months is observed for R1 (>100%), whereas, R4 shows a 30% drop in resistivity values from June to September, an increase from September to November (>30%) and a drop for December and January 07 (>30%).

The analysis of time-lapse resistivity data has revealed a number of patterns. Shallow areas within the profiles appear to respond very rapidly to changes in effective recharge, an increase in the resistivity of 20 - 100% generally occurs in the top 2 - 4m during the months of July, August and September (with zero effective recharge). The percentage variation is influenced by the lithology, sediments with a fine (silt/clay) matrix tend to experience minor changes, whereas, sediments with a coarse matrix (sand and gravel) respond with more significant resistivity variations. In contrast, the deeper areas generally show a decrease of the resistivity values during the drier season (>50%) followed by an increase (>100% in places) of the resistivity immediately after it. The resistivity variation seems to be controlled in this instance by four attributes: the effective recharge, the depth, the lithology of the material and the lithology of the material overlying it. Further discussion of these results is presented in Chapter 7.

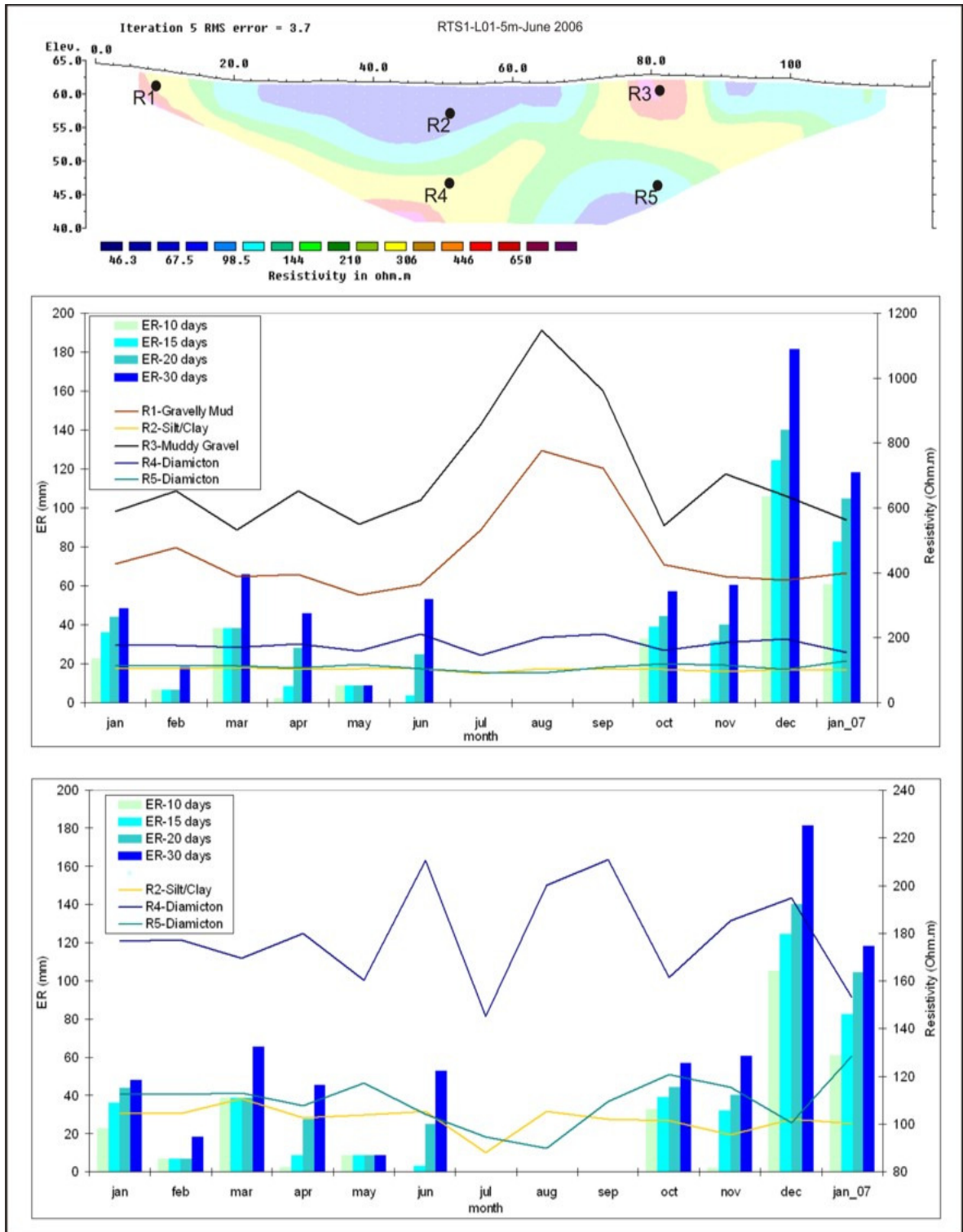


Figure 6.22 – (a) Location of 5 point data of the inverse model of profile RTS1-L01-5m for a number of known sediment types. (b) Plot of the resistivity values of the point data through the year against the cumulative effective recharge (ER in the legend) for 10, 15, 20 and 30 days before the profile was collected. (c) Detail of results for diamicton and lacustrine sediments.

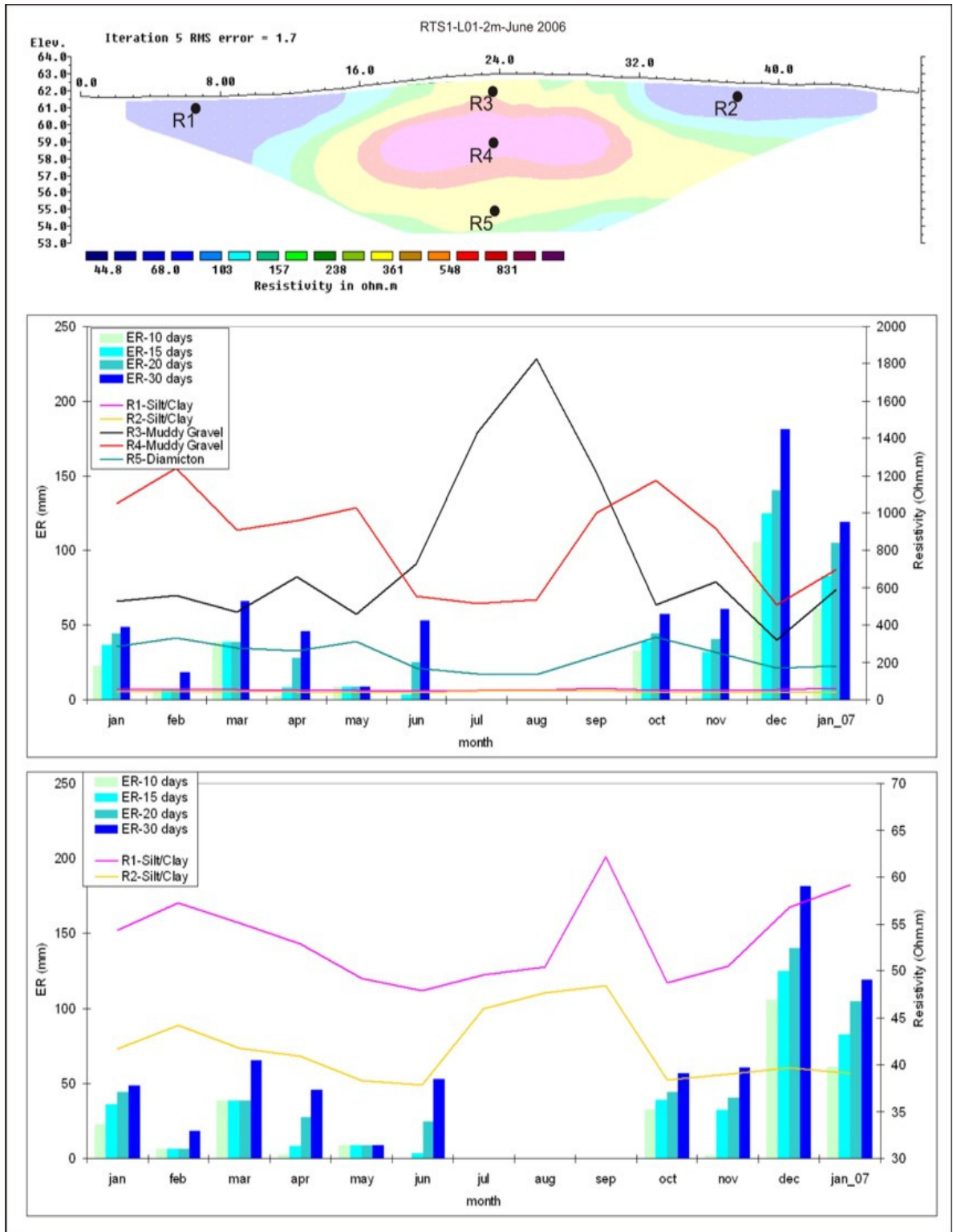


Figure 6.23 – (a) Location of 5 data points of the inverse model of profile RTS1-L01-2m for a number of known sediment types. (b) Plot of the resistivity values of the point data through the year against the cumulative effective recharge (ER in the legend) for 10, 15, 20 and 30 days before the profile was collected. (c) Detail of results for lacustrine sediments.

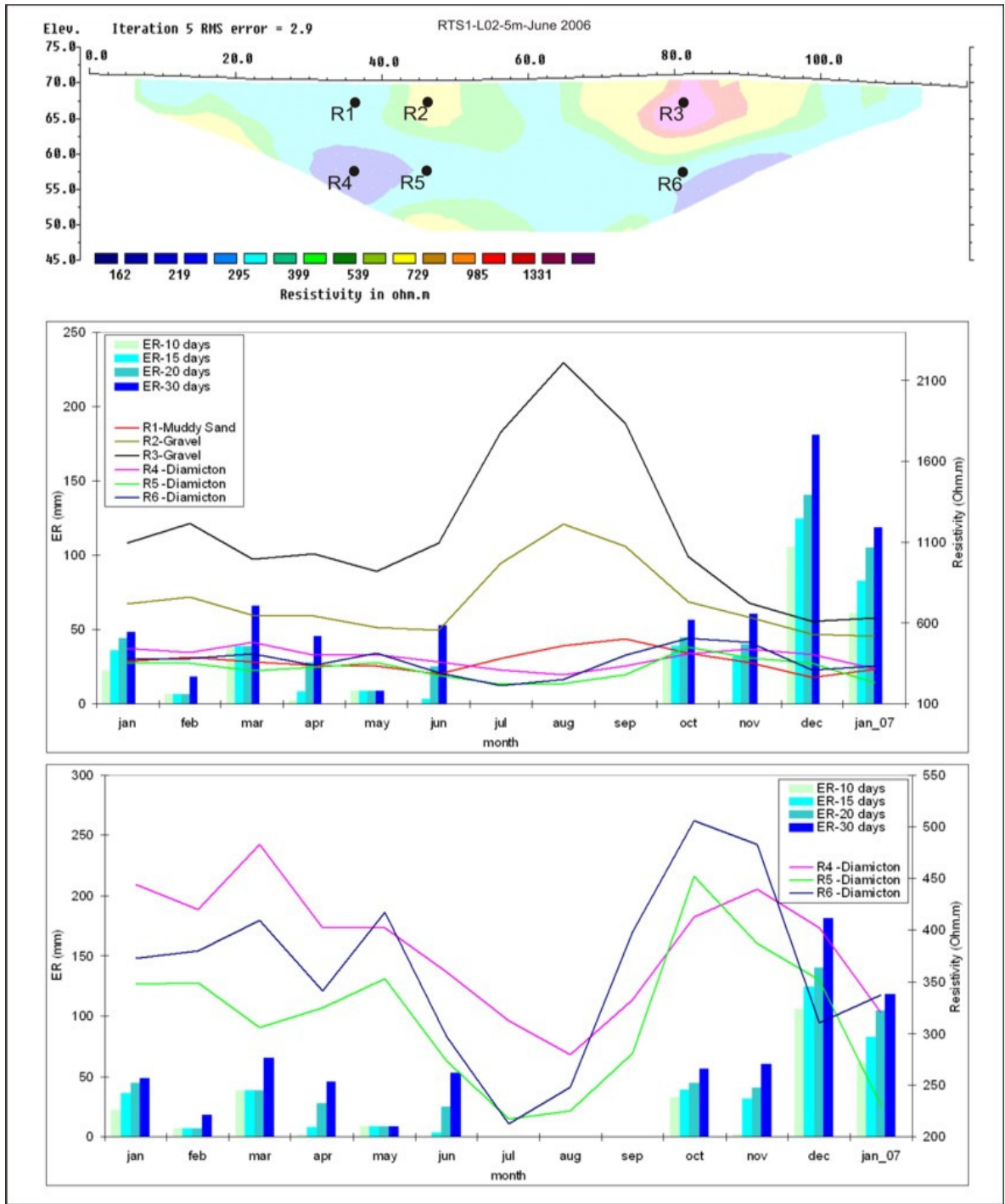


Figure 6.24 – (a) Location of 6 data points of the inverse model of profile RTS1-L02-5m for a number of known sediment types. (b) Plot of the resistivity values of the point data through the year against the cumulative effective recharge (ER in the legend) for 10, 15, 20 and 30 days before the profile was collected. (c) Detail of results for diamicton.

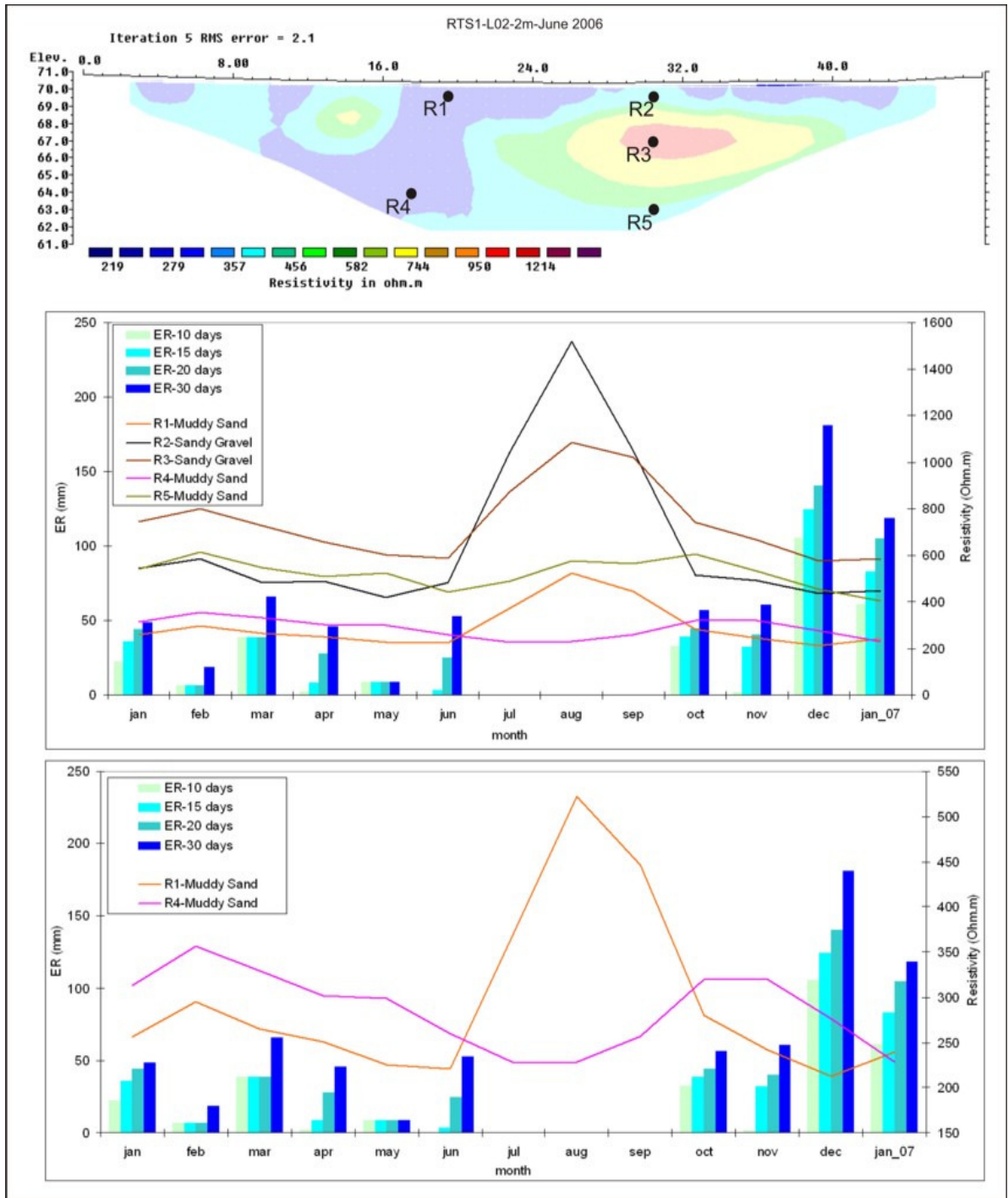


Figure 6.25 – (a) Location of 5 data points of the inverse model of profile RTS1-L02-2m for a number of known sediment types. (b) Plot of the resistivity values of the point data through the year against the cumulative effective recharge (ER in the legend) for 10, 15, 20 and 30 days before the profile was collected. (c) Detail of results for muddy sand at different depth.

6.2.2.3 – Azimuthal Resistivity

Four azimuthal resistivity points were surveyed in Site S1 (Figure 6.26). Six lines were surveyed for each of the four points; the first line is collected in a north to south direction, the following at 30° clockwise and so forth – see Figure 3.16. The Wenner array was used to collect resistance data by using the Vertical Electrical Sounding (VES) method, previously described in Chapter 3 – Section 3.3.6. A total of 12 resistance readings (repeated four times) at increasing electrode spacing were collected for each line, as an example, the data collected for the line with 0° azimuth for Point 1 is presented in Table 6.3. Increasing electrode spacing implies an increase on the depth of penetration (e.g. an electrode spacing of 10m will approximately represent 5m depth). The resistance values obtained were subsequently converted to apparent resistivity using equation 3.7 presented in Chapter 3.

A Cartesian diagram with the electrode spacing on the X-Axis and the obtained apparent resistivity in the Y-Axis is presented for each point, with the six azimuths recorded displayed as different coloured lines. In theory, for a totally homogenous subsurface, the data for the 6 azimuthal lines should be horizontal and plot on top of each other.

Spacing	R1	R2	R3	R4	Average Resistance	Resistivity
1m	85.5	85.5	85.5	85.5	85.50	537.28
2m	42.9	42.9	42.9	42.9	42.90	539.17
4m	32.9	33	33	33	33.00	829.49
6m	24.3	24.2	24.3	24.2	24.23	913.69
8m	16.9	16.9	16.9	16.9	16.90	849.60
10m	11.7	11.8	11.8	11.9	11.83	743.61
16m	5.55	5.94	5.9	5.98	5.94	597.23
20m	4.71	4.82	4.82	4.84	4.83	606.62
26m	2.98	3.76	3.69	3.82	3.76	613.78
30m	2.89	3.29	3.24	3.31	3.28	618.35
36m	1.38	2.19	2.11	2.24	2.18	493.17
40m	1.87	1.87	1.87	1.87	1.87	470.04

Table 6.3 – Azimuthal resistivity data collected for L01 (0 degrees) of Point 1. Resistivity is calculated from the recorded resistance values.

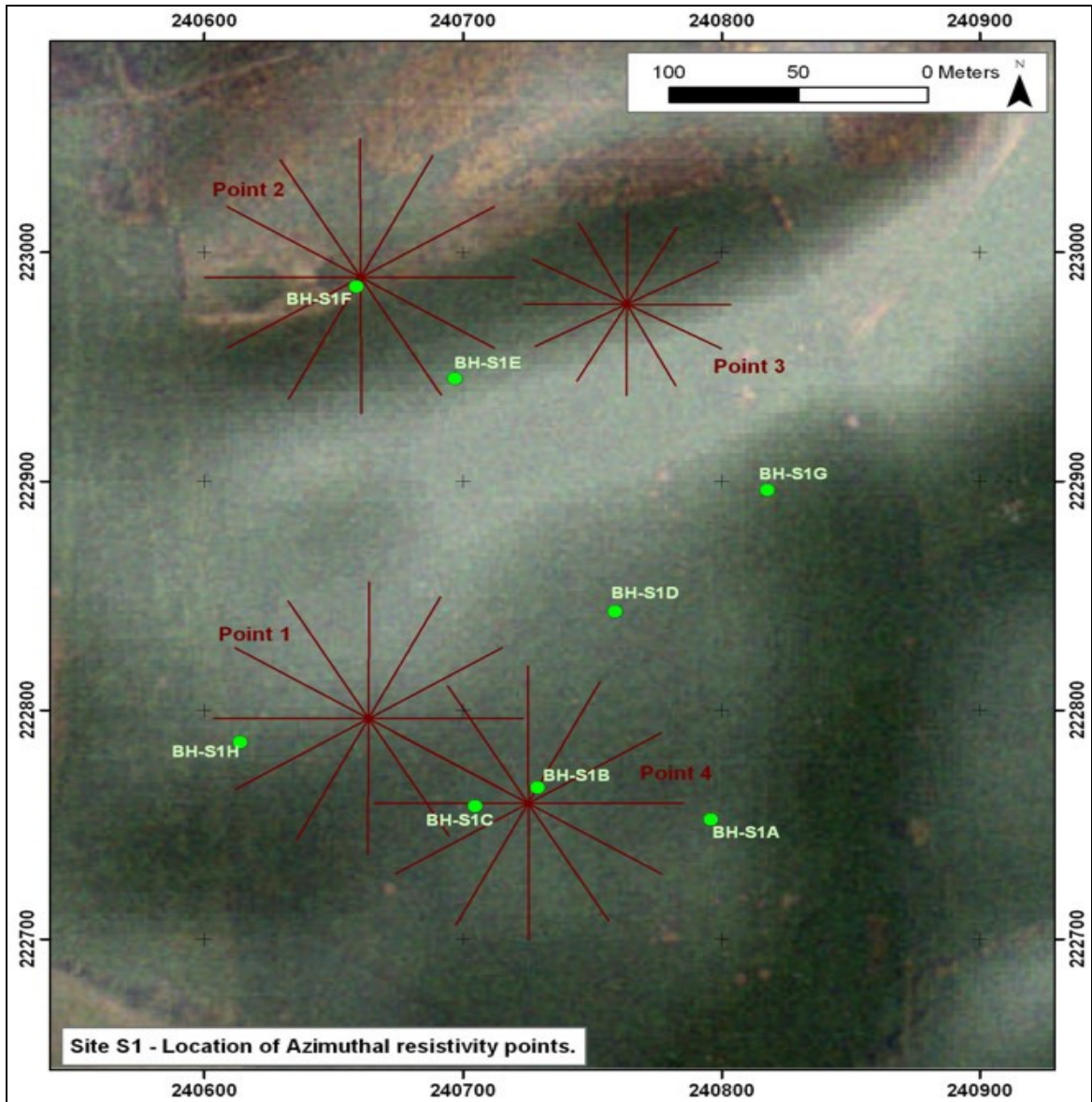


Figure 6.26 – Location of azimuthal resistivity points within Site S1. Six lines at 30° intervals are recorded for each point.

Point 1 (Figure 6.27) was collected in the west central parts of the glaciofluvial fan. Apparent resistivity ranges from 400 - 1200 Ω m. The values remain fairly similar up to 4m spacing (2m depth), however from 4 - 20m (10m depth) the apparent resistivity values of lines at 30° and 60° are a lot larger, twofold in places, than lines running 120° and 150°, especially between 8m (4m depth) and 16m (8m depth). This may be related to the presence of a gravel dominated channel or lens running approximately NE-SW resulting in higher apparent resistivity at this point. On the other hand, electrode spacing over 25m presents opposing results, the lines recorded at 120° and 150° show larger values than the lines running 30° and 60°. It is known from borehole and resistivity data presented above that the glaciofluvial sediments are underlain by diamicton, which is underlain by bedrock. However, the depth to bedrock varies considerably along the profile (see Figure 6.10). The results obtained may indicate that lines running 120° and 150° detect a high resistivity layer, which results in apparent resistivity values of over 600 Ω m, while lines running 30° and 60° show lower values (>450 Ω m). In general terms, the area can be characterized as heterogeneous, as important changes in the apparent resistivity values along the different azimuths occur.

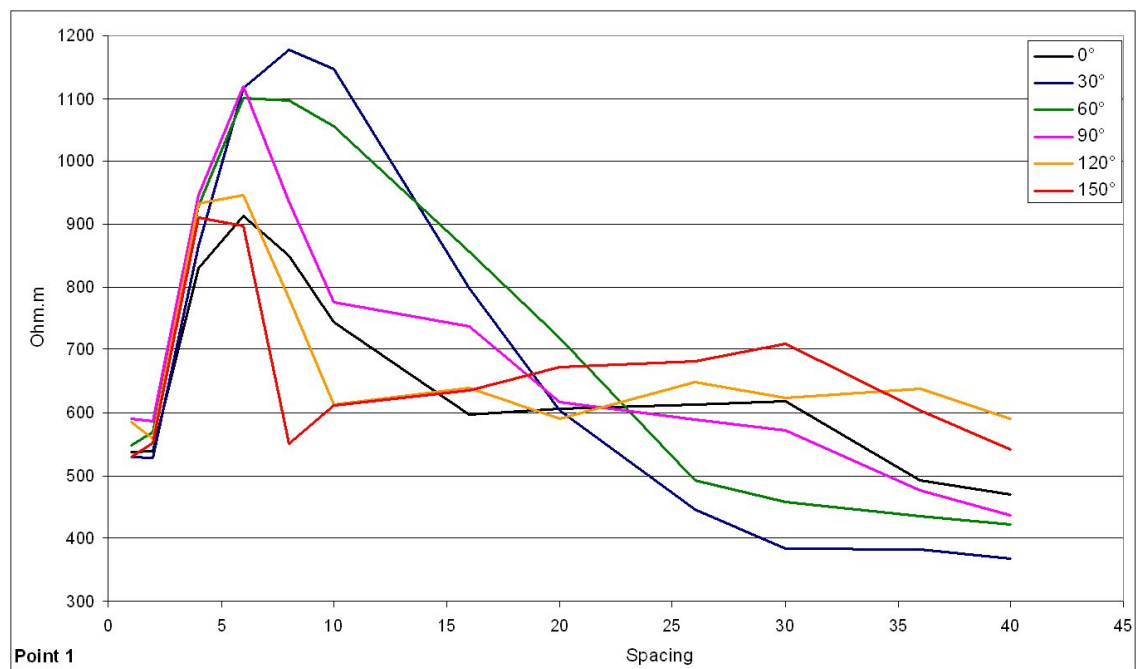


Figure 6.27 – Cartesian plot of the six VES lines collected at Point 1 within Site S1.

Point 2 (Figure 6.28) was collected on top of the esker ridge and exhibits a completely different pattern from Point 1 on the glaciofluvial fan. There is considerably less variation between the lowest and highest values for different azimuths and at spacings greater than about 16m, the acquired values are very similar. Apparent resistivity ranges between 150 and 900Ωm. The values for the six lines decline greatly with increasing depths. Thus, very high apparent resistivity values evolve into low apparent resistivity values, following approximately an exponential curve. This agrees with results obtained in profile RTS1-L01-5m (Figure 6.12 at 80m), showing gravel overlying diamicton. However, the lines with azimuth 60° and 90° between 4m (2m depth) and 16m (8m depth) present relatively higher values than the other lines. This agrees with the esker ridge direction (approx. 70°), these two lines approximately run on top of the gravel dominated ridge for the whole profile, while azimuths cutting across the ridge cover lacustrine sediments, which reduce their final average value. The apparent resistivity values for all the lines converge at 16m (8m depth), which is presumably related to the thickness of the gravel ridge. Furthermore, the apparent resistivity remains approximately horizontal from 20m (10m depth) to 40m (20m depth) and it is fairly consistent for all the azimuths. This could be related to presence of reasonably homogeneous diamicton underlying the gravel.

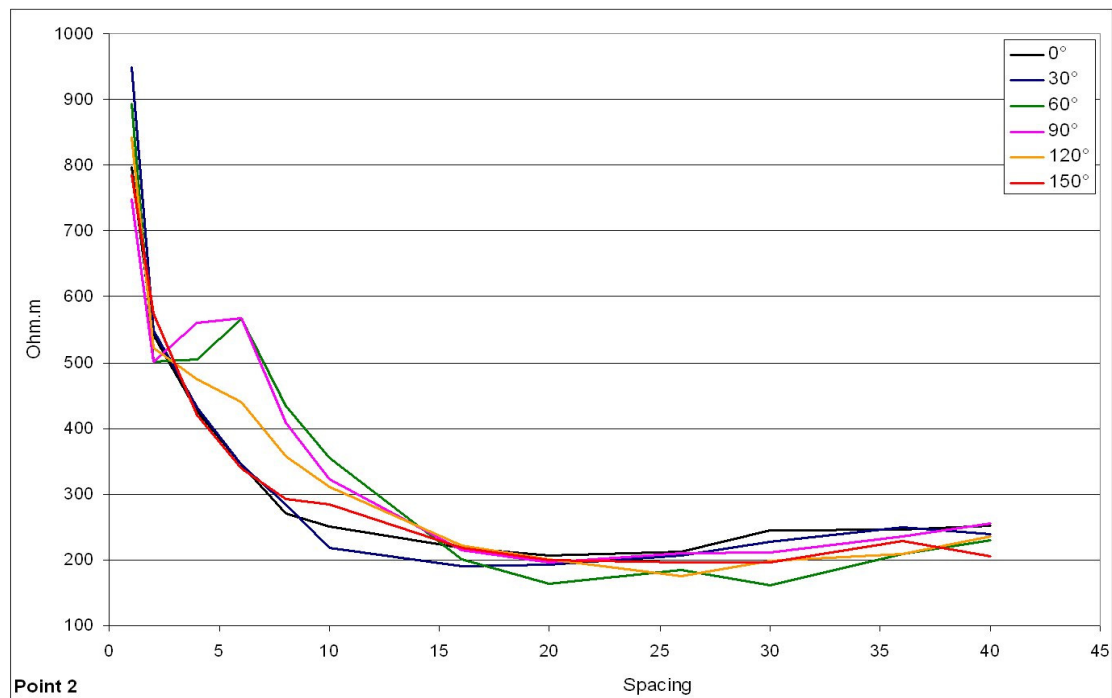


Figure 6.28 – Cartesian plot of the six VES lines collected at Point 2 within Site S1.

Point 3 (Figure 6.29) was collected on the flat low ground area dominated by lacustrine fine sediments overlain by a thin coating of peat and underlain by diamicton at approximately 6m depth. Apparent resistivity values through the profile range 50 - 350Ωm. The values recorded for the six lines drop from 1m (0.5m depth) to 2m (1m depth), this is probably related to the presence of peat in the top layer which increases the apparent resistivity for the shallowest reading; peat has higher apparent resistivity than clays (Figure 3.3). The apparent resistivity increases with a linear positive slope from 2 - 10m (5m depth) for the six azimuths. From 16m spacing to 26m (13m depth) the apparent resistivity for azimuths 30° and 60° gradually develop into relatively lower resistivities, these azimuths approximately follow the area with thickest lacustrine sediments (see Figure 6.12). This is inferred as the cause of a small drop (c. 50Ωm) compared to the other azimuths, which run over thinner lacustrine sediments and also the edges of both glaciofluvial fan and esker sediments with typically higher apparent resistivity. Finally, the apparent resistivity steady positive slope drops at 30m spacing (15m depth) for the 90° and 120° azimuths.

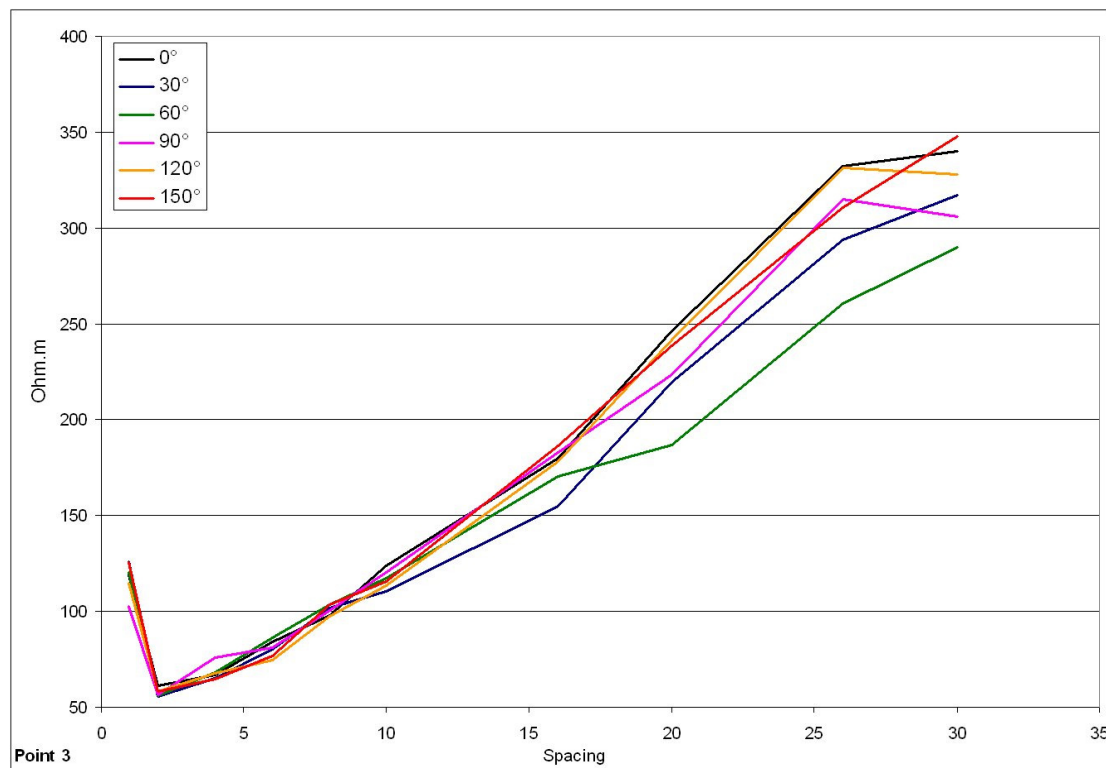


Figure 6.29 – Cartesian plot of the six VES lines collected at Point 3 within Site S1.

Point 4 (Figure 6.30) was collected in the south central part of the glaciofluvial fan, 70m southeast from Point 1. Apparent resistivity ranges 250 - 650 Ω m generally increasing in depth. A dramatic increase of the apparent resistivity (250 - 540 Ω m) occurs from 1 - 8m spacing (0.5 - 4m depth). However, no major changes occur between the different azimuths (<70 Ω m) in this shallow area. The section 8 - 40m spacing shows a less accentuated increase in apparent resistivity. However, the variation in apparent resistivity values between the different azimuths increases. The most significant azimuthal variation within the profile occurs in the 16-30m stretch (8 - 15m depth), maximum differences of 150 Ω m occur in this area, lower values occurring along the 60° azimuth and higher along the 120°, 150° and 0° azimuths. RS1-L03-5m (Figure 6.7) cuts across Point 4 at 135m showing important changes in the gravel body thickness overlying diamicton along a SW-NE direction. This thickness variation of the gravel may be related to the changing apparent resistivity values recorded along the different azimuths.

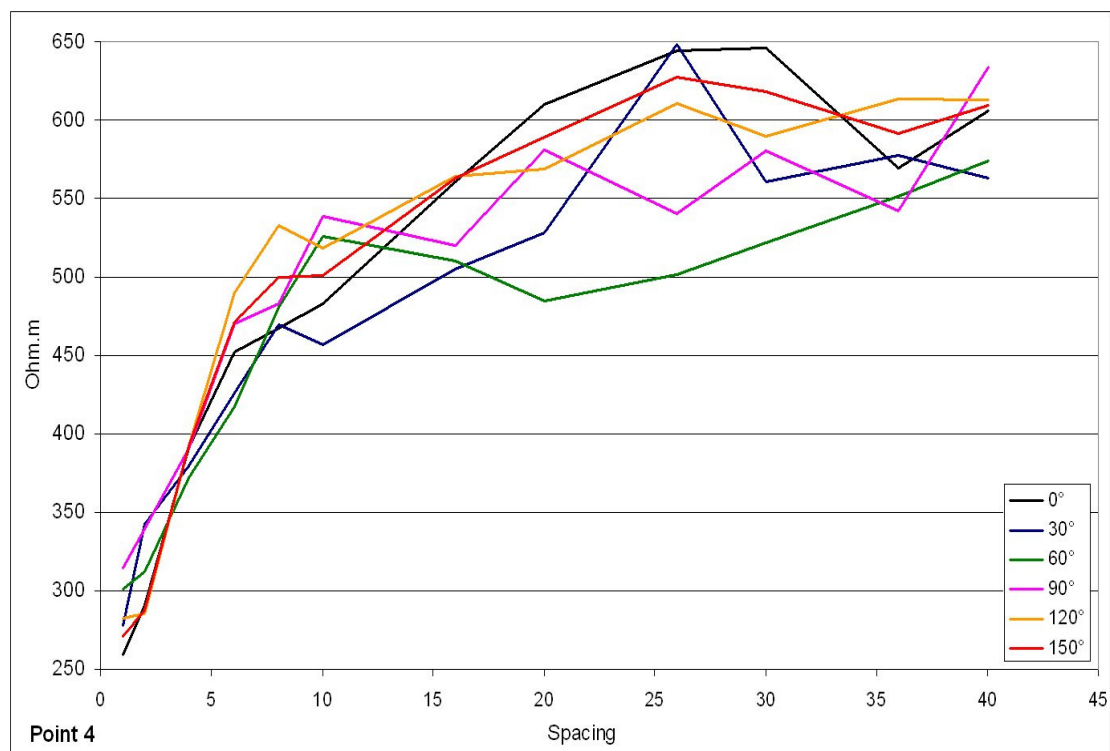


Figure 6.30 – Cartesian plot of the six VES lines collected at Point 4 within Site S1.

A Cartesian diagram illustrating the average values for the six azimuths collected for each point is presented in Figure 6.31. Large variations occur in the top 24m spacing (12m depth) between the two points recorded on the glaciofluvial fan (Points P1 and P4), at depths over 12m the apparent resistivity recorded ranges 500 - 600 Ω m, which agrees with the depth of the diamicton recorded in boreholes BH-S1B/C. At greater depths, the apparent resistivity values are fairly similar. Apparent resistivity recorded on the esker ridge (Point P2) shows values of 450 - 850 Ω m from 0 - 6m spacing, which are in the range of the values encountered in P1 and P4. However, the values drop towards 200 Ω m with depth (considerably less than for the fan), possibly due to a shallower diamicton. Finally, Point P3 shows very small change compared to the other points, the apparent resistivity ranges 80 - 300 Ω m with a steady linear increase in depth related to the presence of lacustrine silts and clays underlain by diamicton.

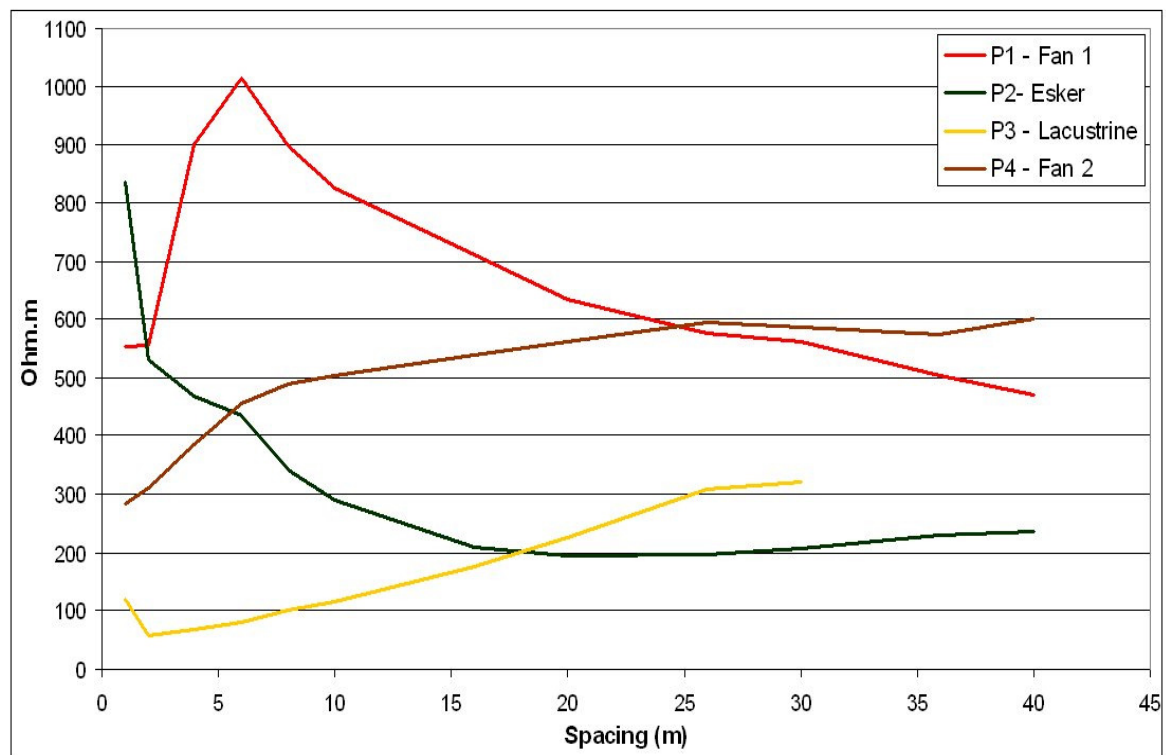


Figure 6.31 – Average values for the four points surveyed with Azimuthal Resistivity in Site S1.

6.2.2.4 – 3D Electrical Resistivity

Nine parallel resistivity lines running south to north spaced six metres apart, were collected at 2m electrode spacing using the Wenner-Schlumberger array, with the objective of producing a 3D model and to determine the heterogeneous nature of the middle of the glaciofluvial fan (see location in Figure 6.5). The total area surveyed was a 48 x 48m (2304 m²) encompassing 1413 resistivity readings. Two boreholes were drilled within this area in order to constrain the model and to provide ground truth (BH-S1B and BH-S1C, see Table 6.1). The location of the dataset relative to other borehole data and other datasets collected in the 3D Model area is presented in Figure 6.32.

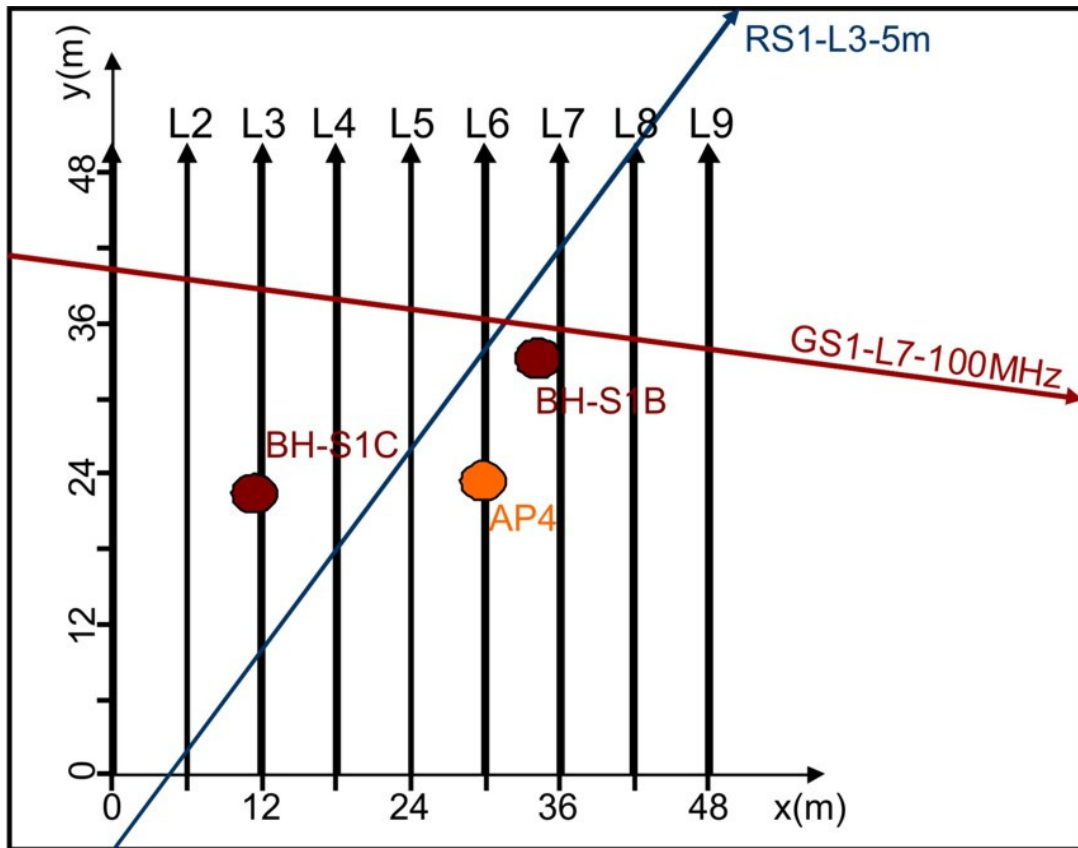


Figure 6.32 – Relative location of the nine ERT profiles recorded to produce the 3D model in Site S1. Borehole data, GPR and ERT profiles and Azimuthal Resistivity Point 4 (AP4).

The data collected were compiled and processed with the RES3DINV software package and depth slices generated for the dataset. Figure 6.33 shows six depth slices derived from

the model. Low to medium resistivity values ($<500\Omega\text{m}$) dominate the top metre, fine sediments appear to dominate this first metre and a linear pattern can be observed from south to north. This may be related to the direction of the recorded lines. Layer 2 (1 - 2.15m depth) is mainly dominated by medium resistivity values with some small patches showing low resistivity extending north from the centre. Layer 3 (2 - 3.5m) shows a medium to high resistivity ($>500\Omega\text{m}$) band stretching from west to east, widening towards the east and flanked to the north and to the south by lower resistivity values. This feature becomes more evident with depth, as it can be observed in layer 5 (4.99 – 6.74m) and layer 6 (6.74 - 8.75m). It has been interpreted as gravel infilled channel/lens (see BH-S1C) running approximately eastwards and flanked by gravelly muddy sand (as recorded in BH-S1B) along both, its northern and southern margins.

A number of vertical profiles extracted from the 3D model are presented in Figure 6.34. The profiles orientated parallel to the X-Axis show high resistivity values ($>800\Omega\text{m}$) dominating the medium and lower parts of the profile at 8 - 22m. This may be associated with the gravel infilled channel/lens described above, which runs subparallel to these profiles. The sections orientated parallel to the Y-Axis show high resistivity values ($>800\Omega\text{m}$) area cutting across all the profiles at 0 - 30m, which gradually turn north as far as the 24 to 30m profile and changes direction again towards the south at 30m.

The 3D Model created with RES3DINV was exported to SlicerDicer software and was used to produce a movie, which was subsequently exported to Windows Multimedia format for presentation of the data. A motion picture was generated which shows the full dataset with all resistivity values, with progressively lower resistivity values being removed from the image, highlighting higher resistivities. Figure 6.35 shows four frames of the motion picture. Figure 6.35a shows the shallow area dominated by low to medium resistivity and higher values occurring in the lower parts at 30 - 48m along the X-Axis and at 0 - 20m along the Y-Axis, Figure 6.35b illustrates the deposits encompassing resistivities of more than $350\Omega\text{m}$, Figure 6.35c shows deposits with resistivity values over $600\Omega\text{m}$, which dominate the south margin of the block. The shape of the channel/lens

feature encompassing resistivities of more than 900Ωm, most likely composed of sandy gravel, is shown in Figure 6.35d

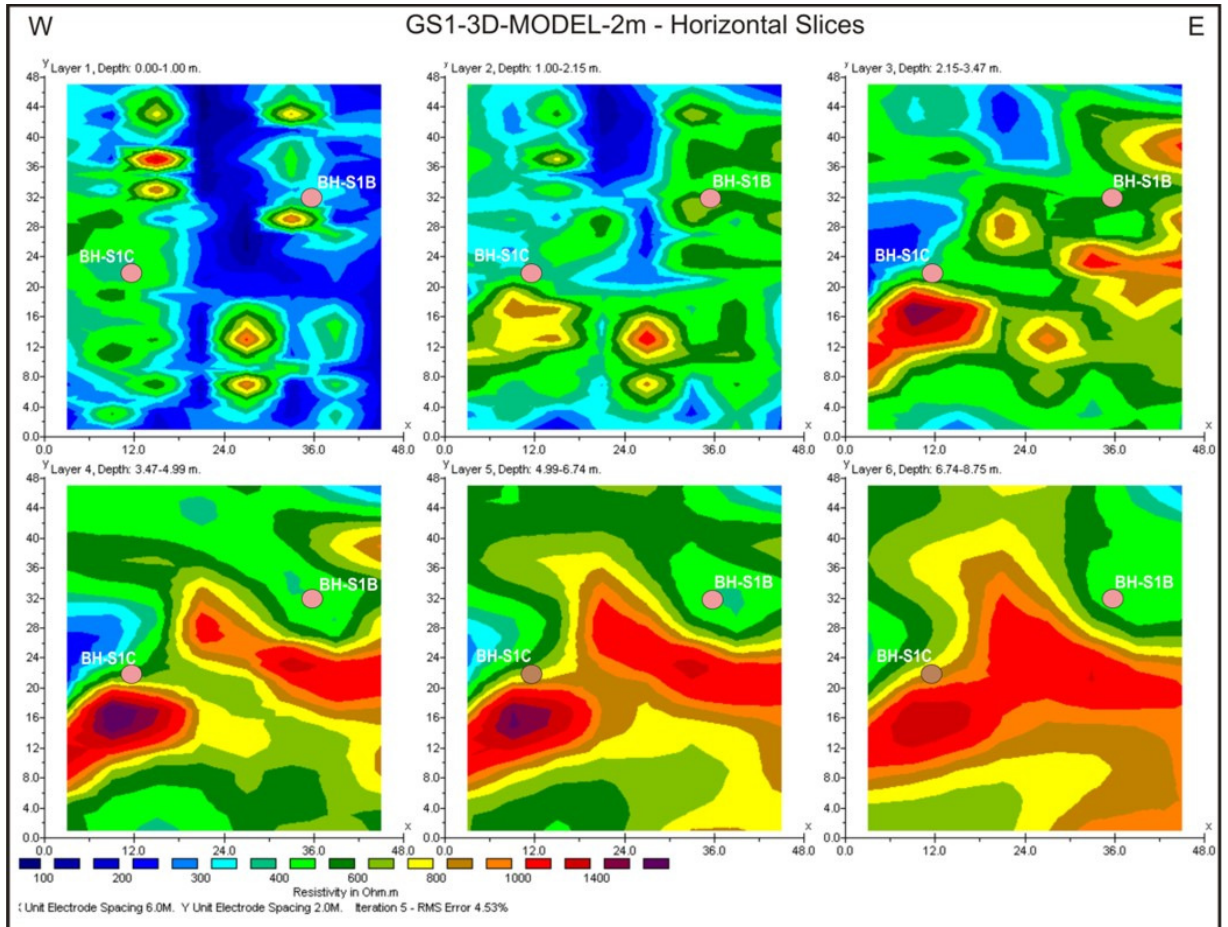


Figure 6.33 – Resistivity 3D model GS1-3D-MODEL-2m horizontal depth slices collected in Site S1.

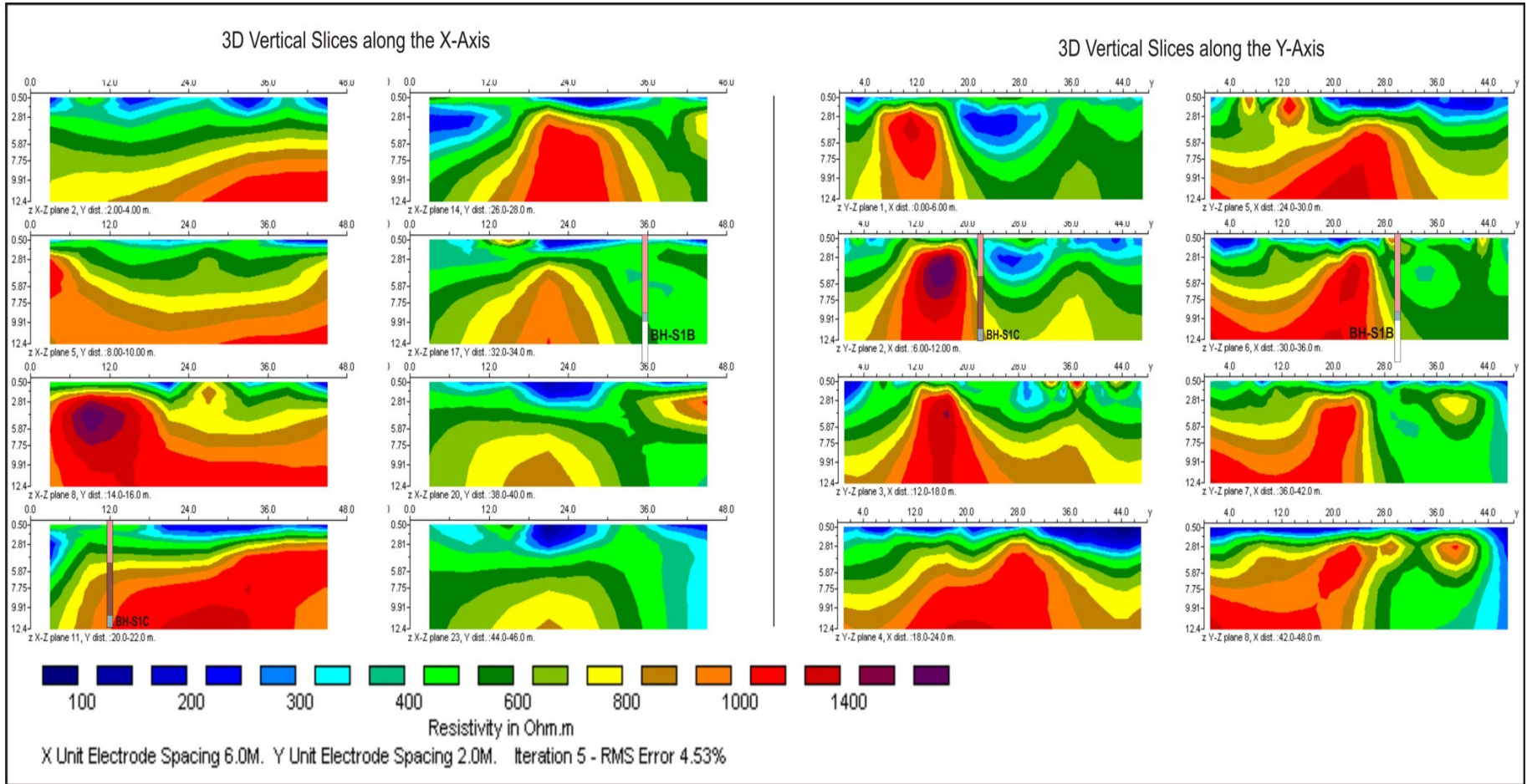


Figure 6.34 – Resistivity 3D model GS1-3D-MODEL-2m vertical slices collected in Site S1 together with borehole data associated with the nearest slice.

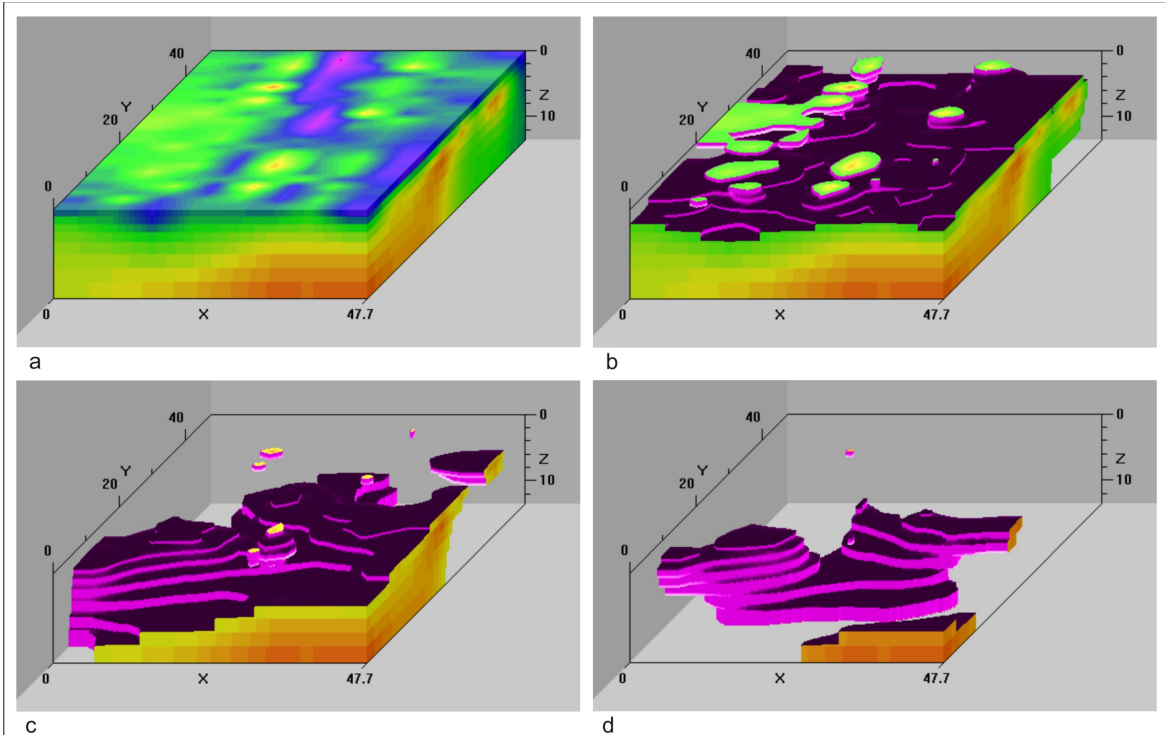


Figure 6.35 – Multi-frame sequence of the resistivity 3D model showing (a) the areas dominated by resistivity values of more than $50\Omega\text{m}$, (b) the areas dominated by resistivity values of more than $350\Omega\text{m}$, (c) the areas dominated by resistivity values of more than $600\Omega\text{m}$ and (d) the areas dominated by resistivity values of more than $900\Omega\text{m}$.

6.2.3 – Ground Penetrating Radar (GPR)

2D GPR Data

Eight GPR profiles collected in Site S1 are presented below. Their relative location is presented in Figure 6.36. The velocity for all the profiles in the site has been estimated from two CMP surveys carried out in the 3D MODEL area. Moreover, the velocity has been ascertained for each profile by means of the hyperbolae calibration tool available in the software package EkkoView DeLuxe. The velocity has been estimated at 0.11m/ns, even though some areas along some of the profiles would be more accurately calibrated with slower velocities (e.g. lacustrine silts and clays). However, the software only allows a single velocity for each individual profile. The selected velocity was considered the best compromise for all the surveyed profiles.

GS1-L01-50MHz (Figure 6.37) runs across the study area from the south-southeast to the north-northwest for 420m, reaching a maximum depth of 14m. Four boreholes were drilled along it and are included in the interpreted dataset. Five radar facies have been identified along the profile. Based on the borehole data, the area along the lower parts of the profile showing poor reflectivity (L1f1-Gm) has been interpreted as undifferentiated glacial diamicton, which contains a high percentage of clay attenuating the EM waves. This is overlain from 380 - 410m by reflectors interpreted as boulder gravel forming the core of an esker ridge with moderate topographic expression (L1f2-Gfm). A number of dipping reflectors spread from both flanks of the ridge have been interpreted as glaciofluvial sands associated with this ridge. The third interpreted radar facies (L1f3-Gcd) was recorded from 0 - 330m. It is composed of discontinuous to moderately continuous wavy reflectors probably indicating cross-stratified sediments. A set of four moderately continuous reflectors dipping 30° NNW at 280 - 340m were interpreted as normal faults related to collapse of sediments supported by ice during deposition. These are overlain by several curved concave reflectors interpreted as cross/oblique sections of channel features (L1f4-Gfch). The features range from 15 - 30m in width and 7 - 4m in depth and present an erosive contact with the underlying sediments. Furthermore, a continuous reflector subparallel to the surface occurs at 330 - 380m (L1f5-Lh). The EM waves are significantly

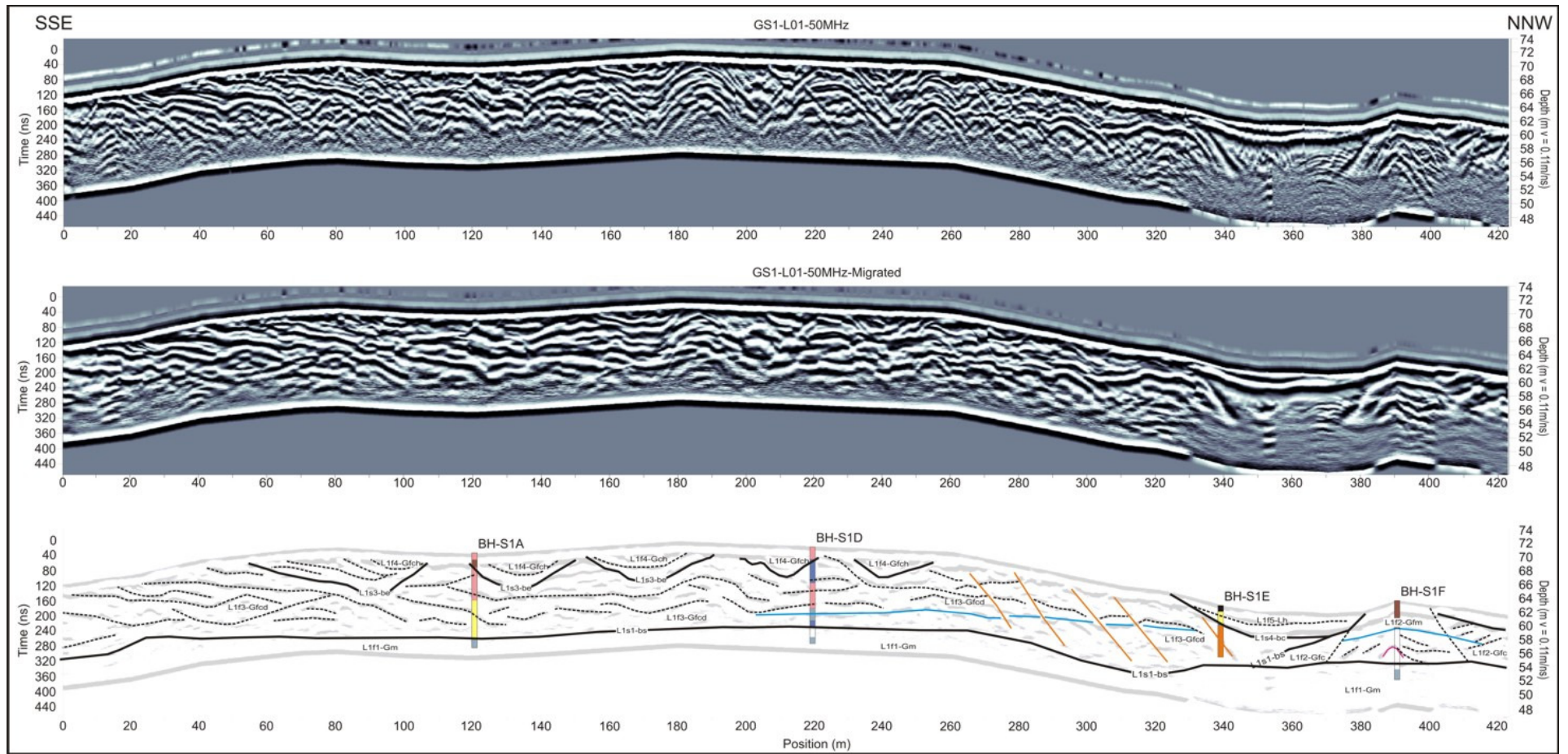


Figure 6.37 – GPR profile GS1-L01-50MHz collected in Site S1. Top – Radargram with AGC Gain and topographically corrected. Middle – topographically corrected migrated radargram using a 0.11m/ns velocity. Bottom – Interpretation of the radargram.

A time slice analysis plot for various time/depth zones is presented for this profile in Figure 6.38 where amplitude variation is plotted on the Y-Axis and position on the X-Axis. A running average filter has been applied to the original data to remove spikes. The methodology to produce these datasets was discussed in Chapter 3 (Section 3.4.5). The amplitude variation for all levels is remarkably similar. The main lithological changes are clearly depicted, fine sediments characterized by high attenuation of the EM waves occurring from 330 - 380m and 405 - 425m show very low amplitude values. The contact between this material and the esker ridge, composed of muddy cobble/gravel, is very well depicted with a sudden increase in the amplitude. Moreover, the amplitude values generally increase from 0 - 130m, remaining reasonably steady from 130 - 270m and dropping from 270 - 325m. This pattern mirrors the topography of the profile across the fan. All the time slices display a pattern of peaks and valleys through the fan. The valley areas located from 20 - 75m and at 120m, 200m, and 240m are interpreted as areas with a higher percentage of fine sediments, whereas high amplitude areas at 80m, 110m, 225m and 260m may be related to presence of coarser sediments e.g. sand and gravel. However, the amplitudes recorded on the fan area are, on average, higher than the ones in the esker, indicating lower attenuation, which may be interpreted as a higher percentage of silt/clay in the esker than in the fan. Finally, a high amplitude signature located from 5 - 15m is non glacial in origin and is related to a large network of rabbit burrows.

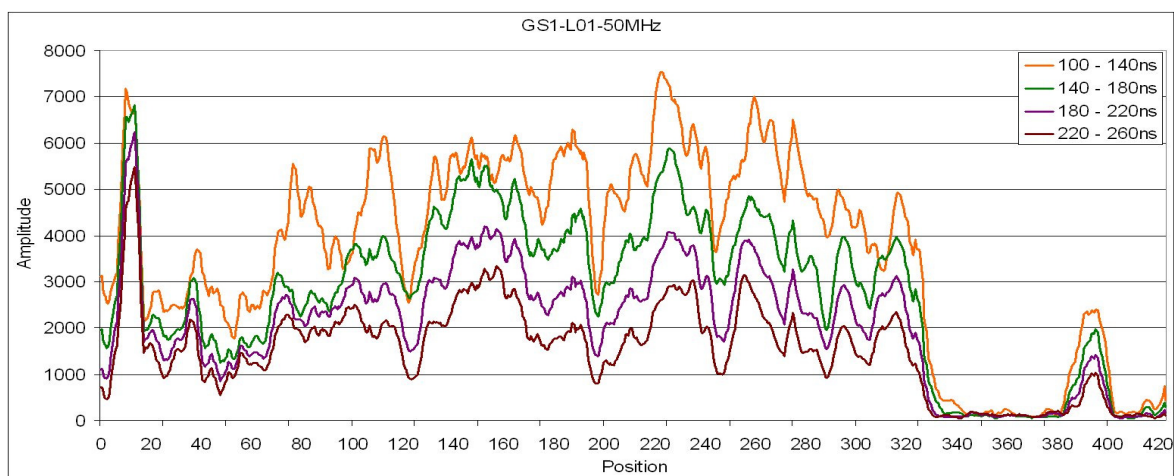


Figure 6.38 – Time slice diagram for radargram GS1-L01-50MHz. Time slices showing the average amplitude variation through the radargram for four 40ns time windows, an average smoothing filter has been applied to the data.

Two radargrams using a 200MHz antenna frequency have been collected inline with L01-50MHz; these are **GS1-L01-200MHz** and **GS1-L02-200MHz** (See Figure 6.36). These radargrams provide a higher resolution profile for the top 8m of sediments and are presented as a single entity in Figure 6.39. The same facies described above in radargram GS1-L01-50MHz were recognized within these two profiles. However the level of detail achieved is higher (see Enclosure 1 – E1B). A number of reflectors gently dipping NNW are detected within the esker (L1f2-Gfm), which can be correlated with gently dipping beds of coarse gravel recorded in exposure ES1B (Figure 6.4b). Moreover, a continuous reflector parallel to the surface is clearly depicted running along in profile GS1-L02-200MHz at 59m OD, which has been interpreted as the water-table. A larger number of normal faulting planes are detected at 240 - 290m, compared to the 50MHz profile. Also, the shape of the channel features (L1f4-Gfch) is more clearly depicted and detailed depositional structures within the channel are sensed (e.g. continuous reflectors dipping SSW interpreted as foresets at 140m). Borehole data recorded along the profiles show reasonable correlation with the GPR data. The main lithological changes recorded in the borehole data correspond to the main radar surfaces (BHS1-A/D) or to subsurface moisture content change (BHS1-E/F), see Figures 6.37 and 6.39.

GS1-L03-200MHz shows a longitudinal section along the crest of the esker ridge running east-northeast for 81m and reaching up to 8m depth. One borehole has been drilled along the line and is included in the interpreted dataset (Figure 6.40). A continuous horizontal reflector running along the whole profile at 59m OD has been inferred as the water-table, the same reflector is clearly depicted along radargram L02 at the same altitude. A set of moderately continuous and discontinuous oblique, non-parallel reflectors underlie it along the whole profile (L3f2-Gfc), these probably correspond to cross-stratified glaciofluvial sediments. These are overlain from 0 - 40m by discontinuous chaotic and hyperbolic reflectors (L3f2-Gfm), probably due to the presence of large boulders recorded in BHS1-F. Moreover, the top 4m from 40 - 80m are dominated by moderately continuous reflectors dipping 10° WSW (L3f2-Gfs). Such reflectors have also been recognised along line L02 and mapped in exposure ES1B dipping north. Therefore, the estimated dip direction of the bedding planes recognised in exposure ES1B may be approximately NW.

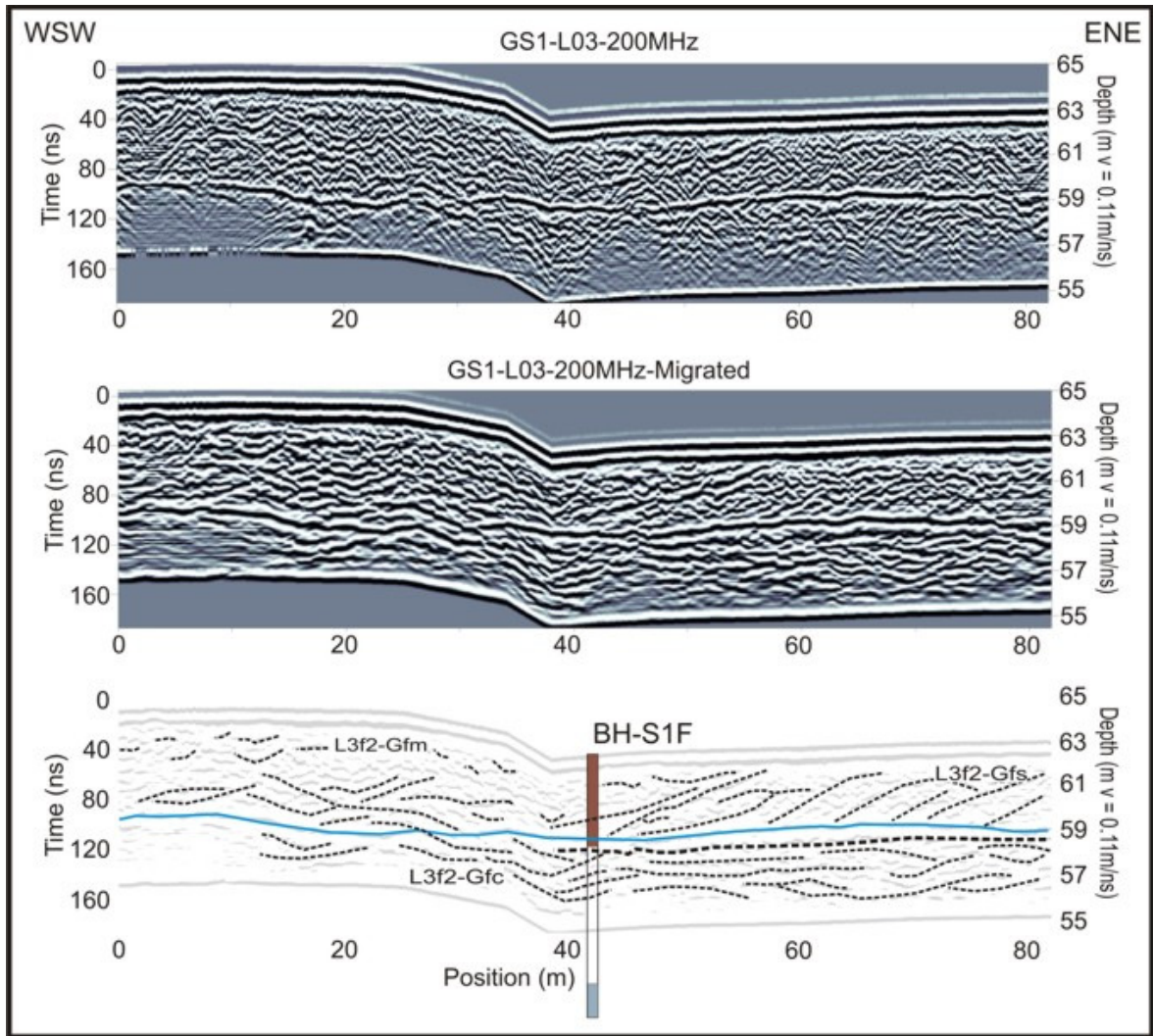


Figure 6.40 – GPR profile GS1-L03-200MHz collected in Site S1. Top – Radargram with AGC Gain and topographically corrected. Middle – topographically corrected migrated radargram using a 0.11m/ns velocity. Bottom – Interpretation of the radargram.

GS1-L04-200MHz shows a cross-section of the southern margin of the fan from its base to the flat top of the feature. One borehole has been drilled along the line and is included in the interpreted dataset (Figure 6.41). An area with very poor reflectivity occurs under 62m OD from 0 - 110m. It shows hyperbolae reflections underlain by multiples which are probably related to sediments with high clay contents (L4f1-Gm), this has been interpreted as diamicton with boulders. These radar facies are overlain from 50 - 70m by discontinuous oblique chaotic reflectors, discontinuous reflectors dipping 30° S and wavy discontinuous reflectors interpreted as deformation by collapse of sediments once

supported by ice. These evolve into moderately continuous subhorizontal parallel reflectors from 70 - 180m, which are probably related to horizontally stratified sand and gravel. These signatures are masked at 120 - 160m by channel features showing a distinctive bow-tie reflector, characteristic of V-shaped channels – see Figure 5.18a. These form part of facies f4, however the channel at 120m is blanketed by 2m of sediments related to the channel at 180m, which indicates that its deposition precedes the channel located at 180m. Data recorded in BHS1-B located at 150m show gravelly muddy sand as the dominant lithology from 0 - 10m depth.

GS1-L05-200MHz shows a cross-section of the northern margin of the fan from its flat top to the lacustrine flat located between the fan and the esker ridge. One borehole has been drilled along the line and is included in the interpreted dataset (Figure 6.42). An area with very poor reflectivity occurring at 60 - 64m OD along the whole profile has been interpreted as diamicton (L5f1-Gm), underlying the fan glaciofluvial sediments from 0 - 150m and lacustrine deposits from 150 - 170m. The diamicton is overlain by moderately continuous to discontinuous sinuous reflectors, these reflectors are distorted from 100 - 150m (L5f3-Gcd) by a set of five discontinuous dipping reflectors interpreted as normal fault planes probably associated with collapse of deposits following melting of the ice. From 0 - 100m, the reflectors are in the main sinuous and moderately continuous, these are overlain in places with an erosive contact by the channel features ((L5f4-Gch) identified in previously discussed radargrams, as in line L04. Two channel features located 10 – 50m are overlain by about 2m of sediments, which dates them as older than the channels occurring along the surface. A channel feature occurring along the surface from 90 - 120m is also distorted by the normal faults referred to above. Channel lithology has been recorded in BHS1-G located at 73m; the radargram shows a channel feature infilled by silty sand underlain by gravelly muddy sand. A small area from 150 - 170m with thickness of 2m and pinching out southwards (L5f5-Lh) has been interpreted as lacustrine sediments.

GS1-L07-100MHz runs west to east along the flat-topped elongated fan for 270m and reaches a maximum of 12m depth. Three boreholes were drilled along the line and are included in the interpreted dataset (Figure 6.43). Three radar facies were identified along

the profile; L7f1-Gm is characterized by very few discontinuous chaotic reflectors and occurs along the whole profile at depths over 6 - 10m. This is overlain along the entire profile by moderately continuous to discontinuous oblique/subparallel reflectors with some occurrences of reflectors dipping east (20 - 50m at 4m depth and 210 - 230m at 5m depth) interpreted as cross-stratified sediments. Continuous curved concave up reflectors overlie the former with an erosive contact. These were interpreted as channel features. The feature interpreted as a channel at 180m along the surface, is shown in the unprocessed profile as a distinctive bow-tie reflector, characteristic of V-shaped channel features. Some of the channels appear to be cut obliquely as their profile is particularly wide (see channels along the surface at 30 - 100m and 100 - 140m). Furthermore, three reflectors dipping 30° E were interpreted as normal faults distorting facies f3 and f4. The main lithological changes recorded in boreholes BHS1-A/B and H between glacial and glaciofluvial sediments correspond to the interpreted radar surface L7s1-bs. Other lithological changes within the glaciofluvial sediments have also been correlated with radar surfaces (e.g. contact between layers 3 and 4 in BHS1-A corresponds to surface L7s1-be).

GS1-L08-100MHz runs southwest to northeast along the flat-topped elongated fan for 250m and reaching 12m depth. Two boreholes were drilled along the line and are included in the interpreted dataset (Figure 6.44). As in line L07, three radar facies were identified along the profile; L8f1-Gm consists of a small number of discontinuous chaotic reflectors, it covers the entire profile at depths over 8 - 10m. This is overlain along the whole profile by moderately continuous to discontinuous sinuous subparallel reflectors, which were interpreted as cross-stratified sediments L8f3-Gfc. Continuous curved concave up, sinuous in places, reflectors overlie the former with an erosive contact. This contact has also been identified in boreholes BHS1-D/G recorded along the profile at 120 and 200m respectively. These were interpreted as channel features, however the profile cuts the channels at oblique angles in places, the area 0 - 180m at 0 - 6m depth was interpreted as a long-oblique section of two channel features (L8f4a/b-Gfch). Another channel feature dominates the top part of the radargram from 200 - 240m. Based on these data and the other the data collected from other channel feature identified in the previously described radargrams the palaeocurrents in the fan area flowed approximately east-northeast.

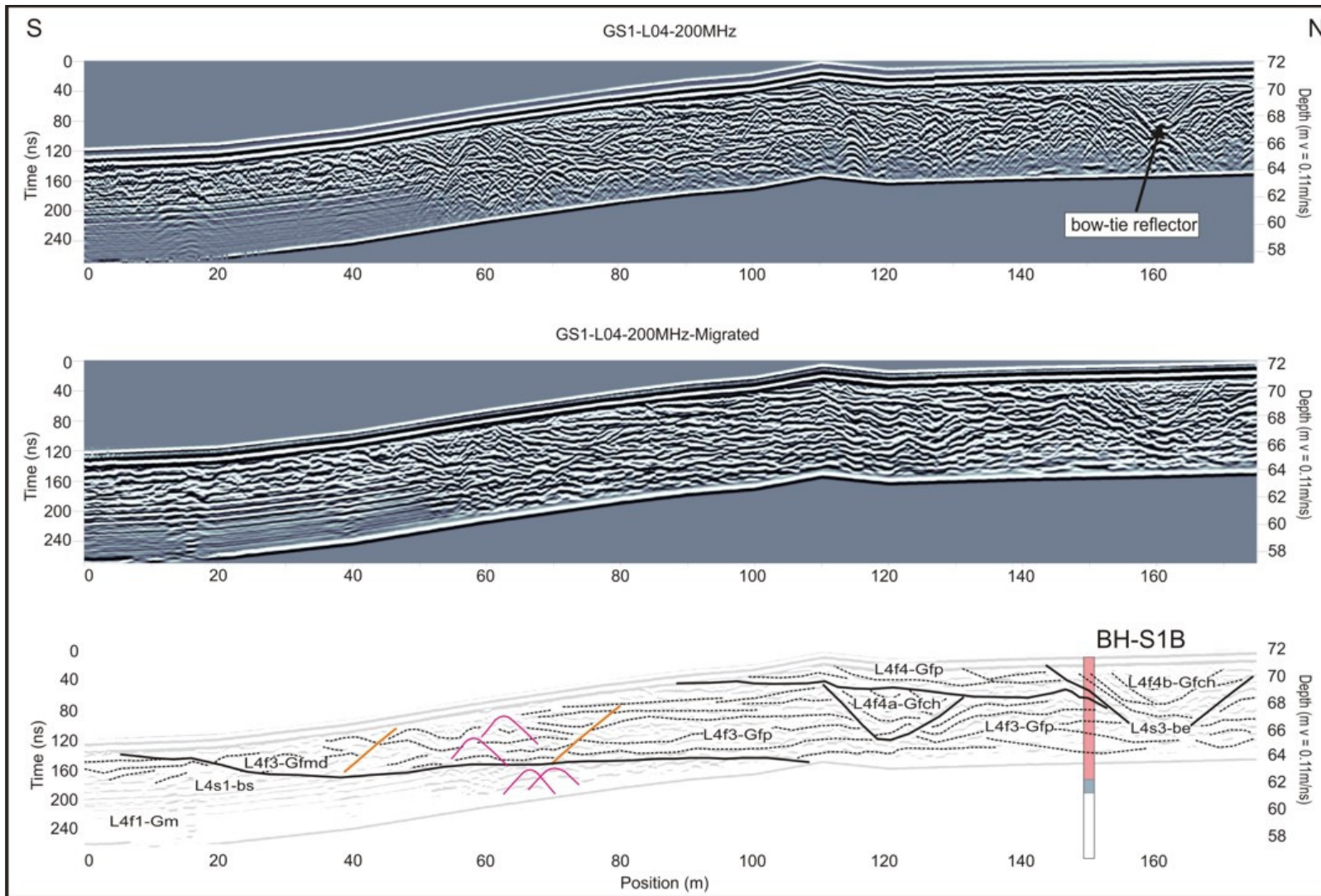


Figure 6.41 – GPR profile GS1-L04-200MHz collected in Site S1. Top – Radargram with AGC Gain and topographically corrected. Middle – topographically corrected migrated radargram using a 0.11m/ns velocity. Bottom – Interpretation of the radargram.

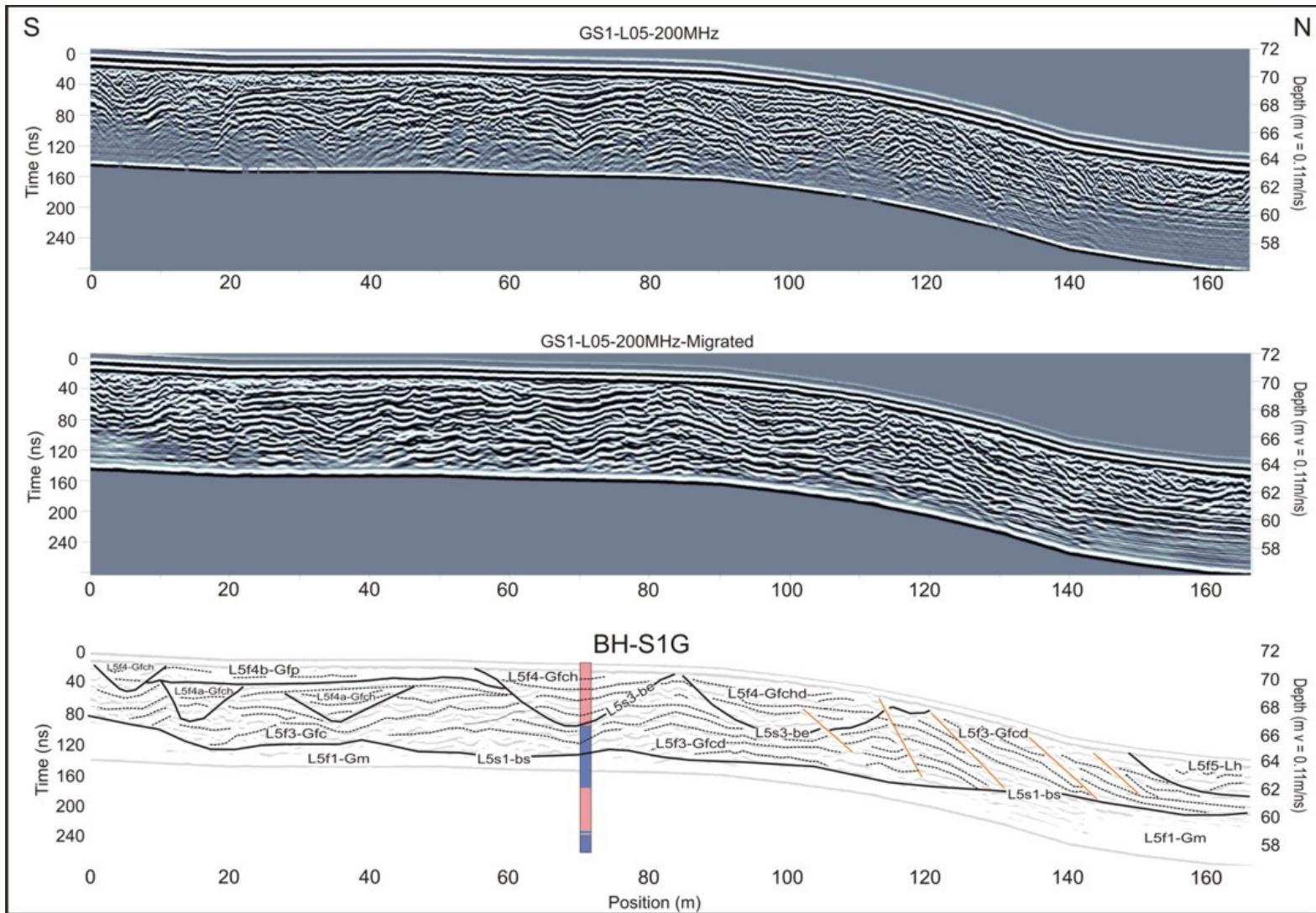


Figure 6.42 – GPR profile GS1-L05-200MHz collected in Site S1. Top – Radargram with AGC Gain and topographically corrected. Middle – topographically corrected migrated radargram using a 0.11m/ns velocity. Bottom – Interpretation of the radargram.

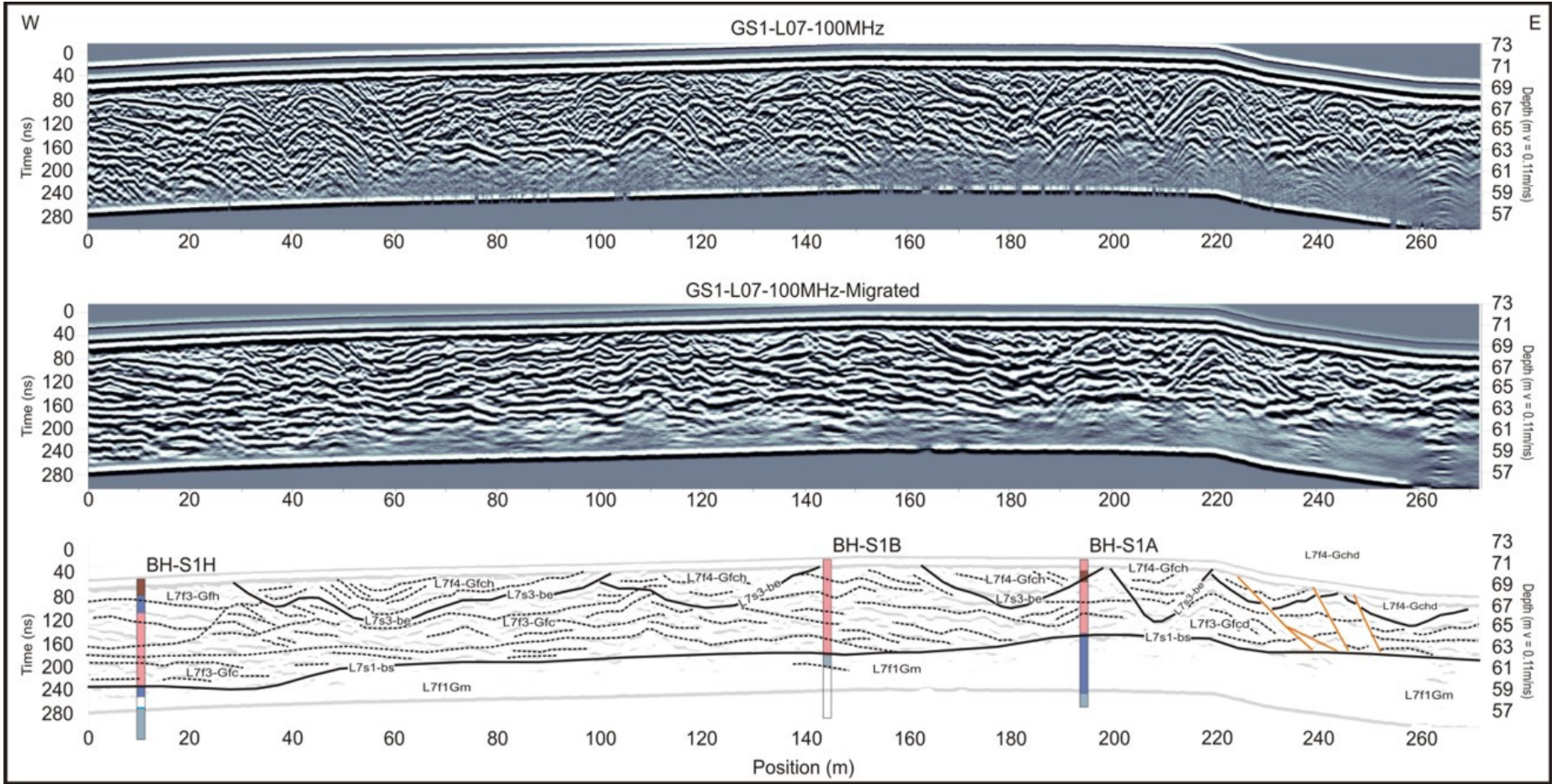


Figure 6.43 – GPR profile GS1-L07-100MHz collected in Site S1. Top – Radargram with AGC Gain and topographically corrected. Middle – topographically corrected migrated radargram using a 0.11m/ns velocity. Bottom – Interpretation of the radargram.

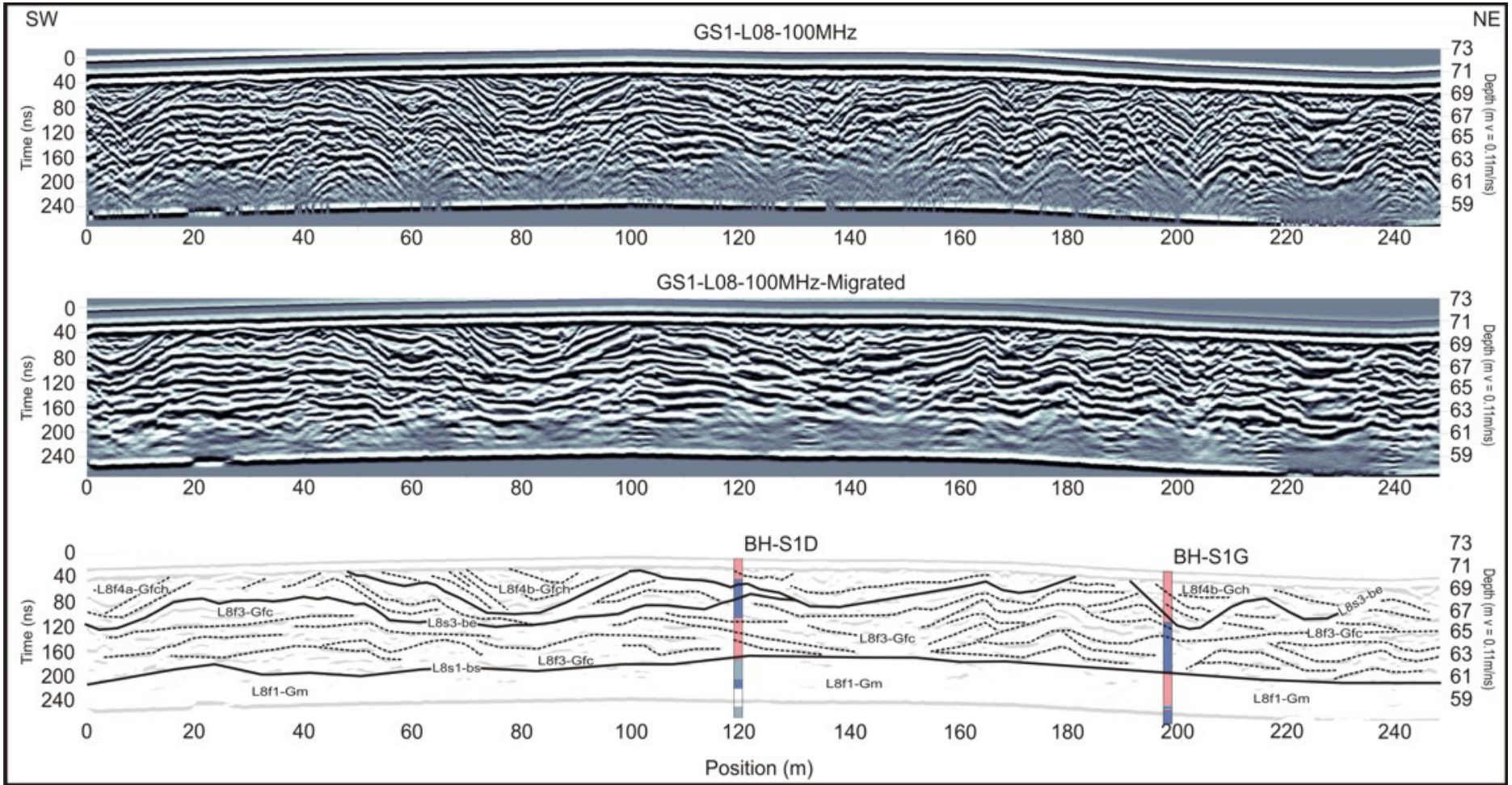


Figure 6.44 – GPR profile GS1-L08-100MHz collected in Site S1. Top – Radargram with AGC Gain and topographically corrected. Middle – topographically corrected migrated radargram using a 0.11m/ns velocity. Bottom – Interpretation of the radargram.

In summary, five radar facies presenting similar reflectivity characteristics were identified in Site S1, they have been numbered by their relative age of deposition from older (f1) to younger (f5). Their main features and spatial distribution within the site are presented below. Radar facies f1 is characterized by its poor reflectivity, it has been identified in all the radargrams presented, and it is commonly placed at the lower parts of the profile underlying f2 or f3. The available borehole data usually indicate that it is a muddy or sandy diamicton (Figure 6.2). Radar facies f2 has been identified in L01, L02 and L03 overlying f1 with an undifferentiated bounding surface, it has been described as discontinuous oblique chaotic reflectors, hyperbolae and as moderately continuous dipping reflectors in places. It corresponds to the deposits forming the core of the esker ridge and associated sediments composed of sand, gravel and boulders. This facies was recorded in exposure ES1B as crudely bedded cobble/boulder gravel and in BH-S1F as muddy sandy gravel. Radar facies f3 has been identified in L01, L04, L05, L07 and L08. It is mainly composed of moderately continuous to discontinuous oblique/subparallel reflectors and sinuous/subhorizontal subparallel reflectors overlying f1 with undifferentiated bounding surface. The borehole data corresponding with this facies generally indicate sand and gravel and sandy diamicton (BH-S1D/G) and silt/clay (BH-S1A). These facies occur only within the fan area. Radar facies f4 has been recognized in L01, L04, L05, L07 and L08. They have been described as continuous curved concave, sinuous in places reflectors generally occurring along the surface, overlying f3 with an erosional bounding surface. Borehole data indicate predominantly sand and gravel, these facies occur only within the fan area. Radar facies f5 was identified in L01, L02 and L05 and described as continuous reflectors subparallel to the surface. This facies covers the lower ground area between the esker ridge and the fan, borehole BHS1-E data indicate slightly gravelly sandy mud. It has been interpreted as lacustrine silts and clays overlain by a thin coating of peat. Finally, a number of sets of discontinuous to moderately continuous dipping reflectors, interpreted as normal faults, have been depicted in L01, L04, L05 and L07. These faults have been associated by the author to collapse structures derived from loss of support of the edges of an ice contact lake acting as a temporary small scale sedimentary basin.

3D GPR Data

A GPR 3D model was constructed for the same area covered by the resistivity 3D block presented in Section 6.2.2. The model is composed of 41 parallel 30m long GPR lines running south to north and 61 lines 20m long running orthogonal to the former (west to east). The total area surveyed was 20 x 30m (600 m²) and the location of the 3D Model within Site S1 is presented in Figure 6.36. All the profiles were collected with the 200MHz antenna using a step size 0.1m and a time window of 150ns and were spaced 0.5m apart. Moreover, two CMP surveys running east-west were carried out within the 3D area to estimate the velocity of the EM waves for the area. Furthermore, two boreholes were previously drilled within this site in order to constrain the model and to provide ground truth (BH-S1B and BH-S1C, see Table 6.1). The location of the GPR 3D Model dataset relative to other borehole data and other geophysical datasets collected in the area is presented in Figure 6.45.

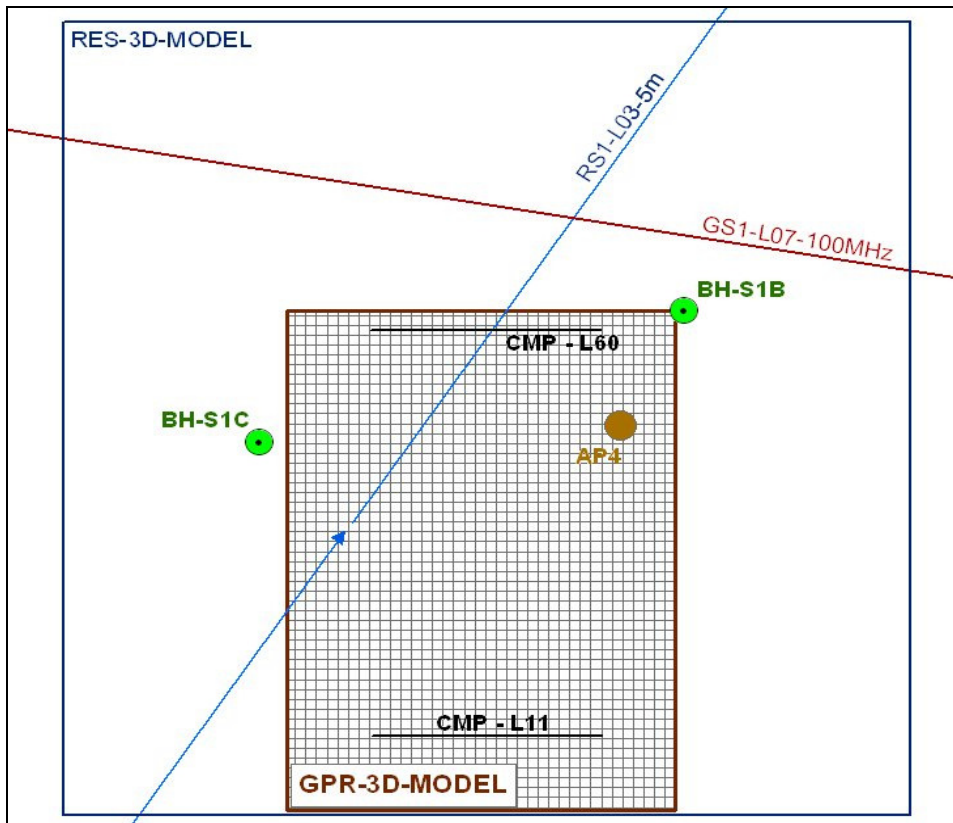


Figure 6.45 – Location of the GPR 3D model recorded in Site S1, relative to borehole data, GPR and ERT profiles Azimuthal Resistivity Point 4 (AP4) and Resistivity 3D Model.

The GPR data were collected as individual profiles. GFP Edit software was used to arrange the individual profiles into a unique dataset in a 3D Model. Ekko Mapper 3 software package was used to process the datasets. The raw data was processed by means of background removal, dewow, migration, envelope and amplitude equalization. Amplitude equalization compensates for the decrease in the amplitude values with depth; the result is analogous to that obtained by a SEC gain. The velocity to be applied to the 3D Model was estimated from two CMP Surveys carried out within the area of study (see Figure 6.45). The two obtained CMP radargrams show the best fit velocity at different depths (Figure 6.46). The velocity obtained ranges between 0.9m/ns and 0.12m/ns and based on these datasets and hyperbolae calibrations carried out in some of the radargrams, the average velocity was estimated at 0.11m/ns.

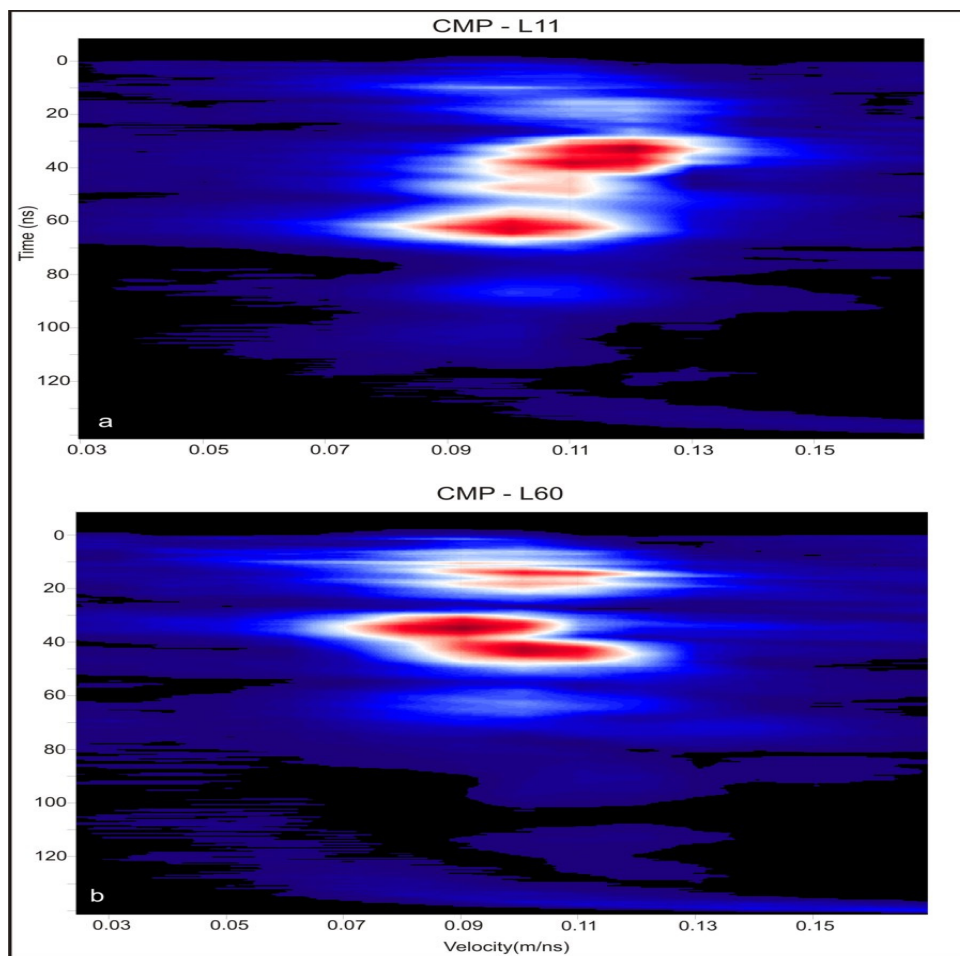


Figure 6.46 – CMP Surveys carried out within the GPR 3D Model area in Site S1. (a) CMP survey for Line CMP – 11 shows an average velocity of 0.11m/ns. (b) CMP survey for Line CMP – 60 shows an average velocity of 0.10m/ns.

Voxler software was used to display the final datasets in a number of forms. A conventional means of presenting a 3D data block is by the systematic removal of depth slices. Figure 6.47 shows eight depth slices at 1m intervals. The top metre has been skipped as it shows horizontal layering related to the air and ground layers. Amplitude values subsequent to amplitude equalization range 300 - 30000 mV. Slices at 1 - 2m are dominated by very high amplitudes. The slice at 3m shows two features cutting the Y-Axis at 2 - 10m running east-west dominated by relatively high amplitudes, Slices 4 - 5m show the two linear features cutting the Y-Axis at 5m and at 10m, respectively, however the second fades out with depth. Depth slice at 5m shows a single linear feature cutting the Y-Axis at 5 - 10m, the feature gradually fades out from slices 6 to 8m.

The data have also been presented as vertical slices of the 3D volume. Figure 6.48 shows two different ways to display the data, an envelope filter has been applied to the dataset on top, the same dataset is shown at the bottom with an AGC gain and no envelope applied to it. The dataset with an envelope filter (Figure 6.48a,b,c) allows the comparison of amplitude values at different positions. On the other hand, the results of the dataset with no envelope (Figure 6.48d,e,f) are comparable to the one obtained with a single radargram, however, the reflectors are the result of averaging within the trace altering the real amplitude values. Vertical slices show a channel-like feature running east-west dominated by relatively high amplitudes, cutting across the Y-Axis from 5 - 10m and reaching a maximum depth of 6.5m.

Fence diagrams may be employed with 3D data and this approach allows the examination of areas of interest within the 3D model from different angles. Figure 6.49 shows four different views of the dataset. View a and b show the channel feature identified before from a south and a north point of view respectively. It is noticed in view b that the channel gently bends northwards near its middle parts and a gradual decrease of the amplitude values occurs northwards. View c shows a close-up of the feature from the east, illustrating the bottom of the channel at 6.3m depth and its cross-section along the Y-Axis. View d shows the feature from underneath, as detected before in view b, the slice at 2m depth

shows the shape of the feature bending slightly north. Furthermore, the cross-section of the channel is well depicted in the two profiles running along the Y-Axis.

A further method to visualize the 3D data is by producing isosurfaces which show the distribution of surfaces with equal amplitudes within an area. Figure 6.50 shows six examples of isosurfaces occurring within the 3D Model. Higher amplitude isosurfaces occur in the shallower areas (Figure 6.50a,b,c). Isosurfaces b and c show the shape of the channel feature described above. Isosurfaces with lower values, less than 4000 mV (Figure 6.50d,e,f) occur at greater depths. This method does not provide any further information for this particular dataset; however, it may be a useful tool for depicting the 3D shape of continuous reflectors such as the water-table or the bedrock interface.

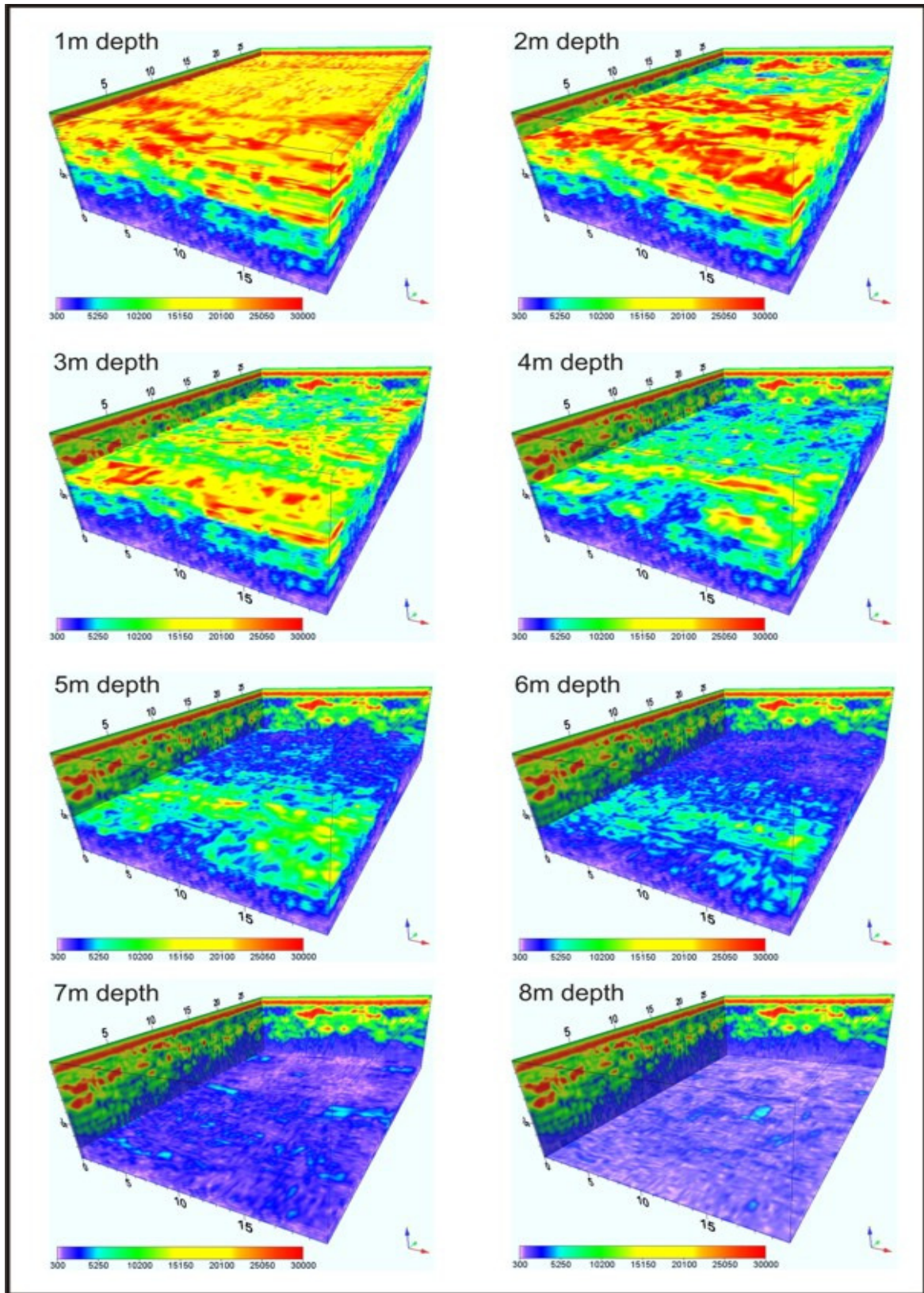
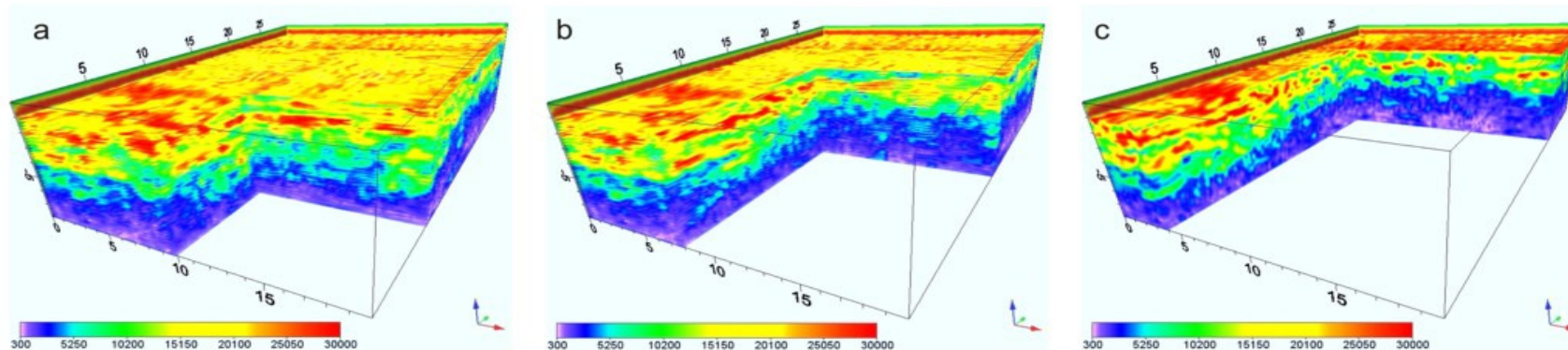


Figure 6.47 – Depth slices at 1m intervals for GPR 3D Model collected in Site S1. Displayed in Voxler software. North direction is illustrated by green arrow.

3D Model with dewow, migration, envelope filters and amplitude equalization



3D Model of with no envelope filter and an AGC Gain

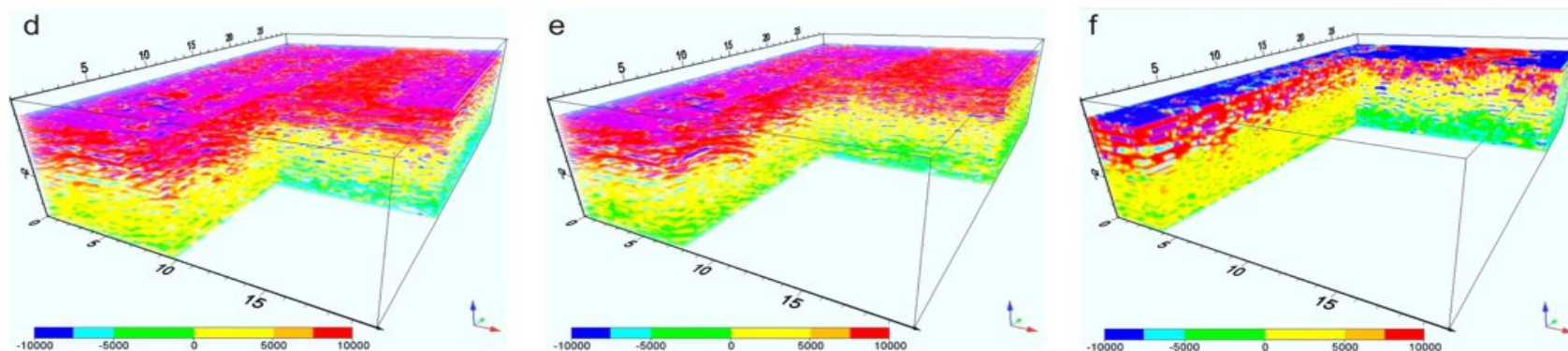


Figure 6.48 – Vertical slices at 1m intervals for GPR 3D Model collected in Site S1. Above the data presented have been processed and an envelope applied to them to normalise amplitude values. Below – The same dataset has not been normalised, thus, dataset encompasses positive and negative amplitude values. Displayed in Voxler software. North direction is illustrated by green arrow.

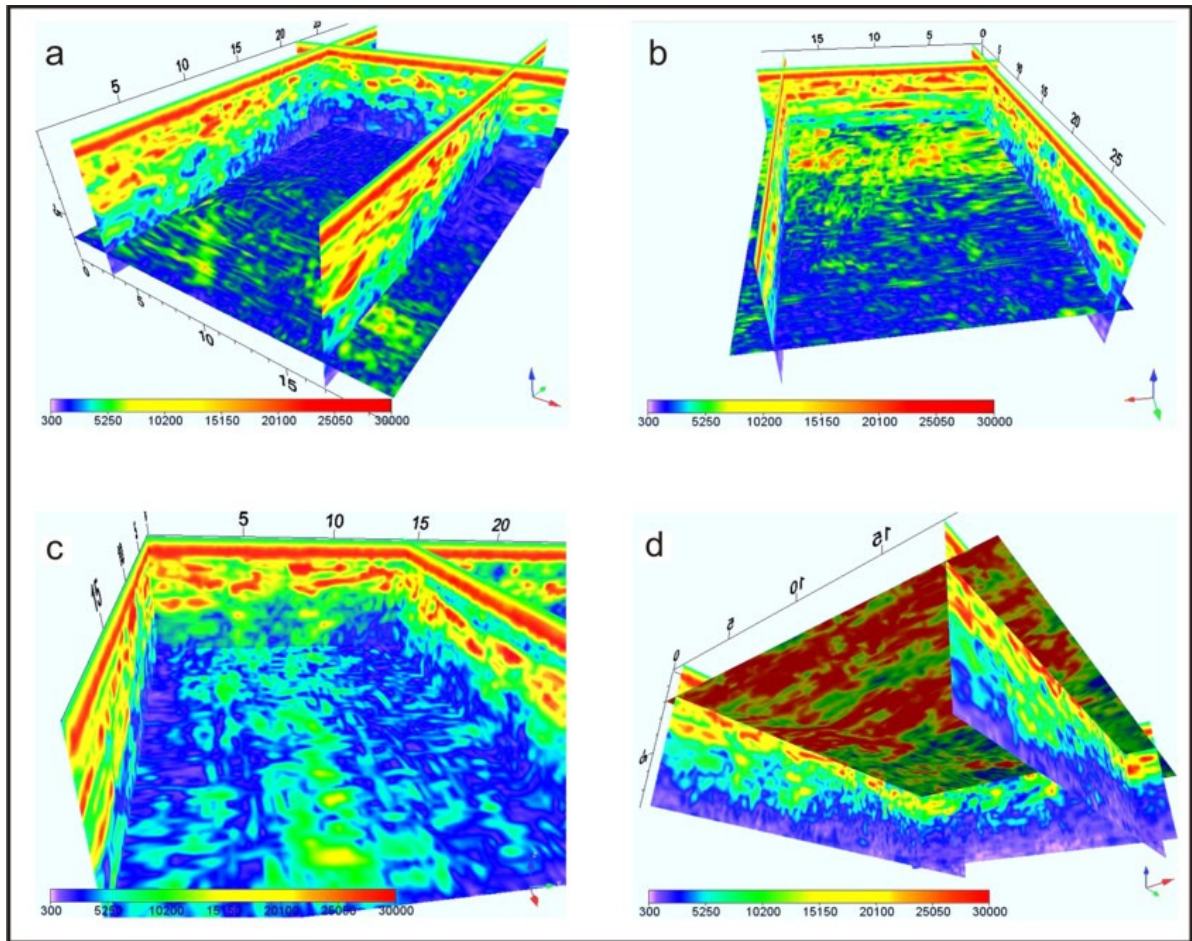


Figure 6.49 – Four views of the GPR 3D Model using fence diagrams. Displayed in Voxler software. North direction is illustrated by green arrow.

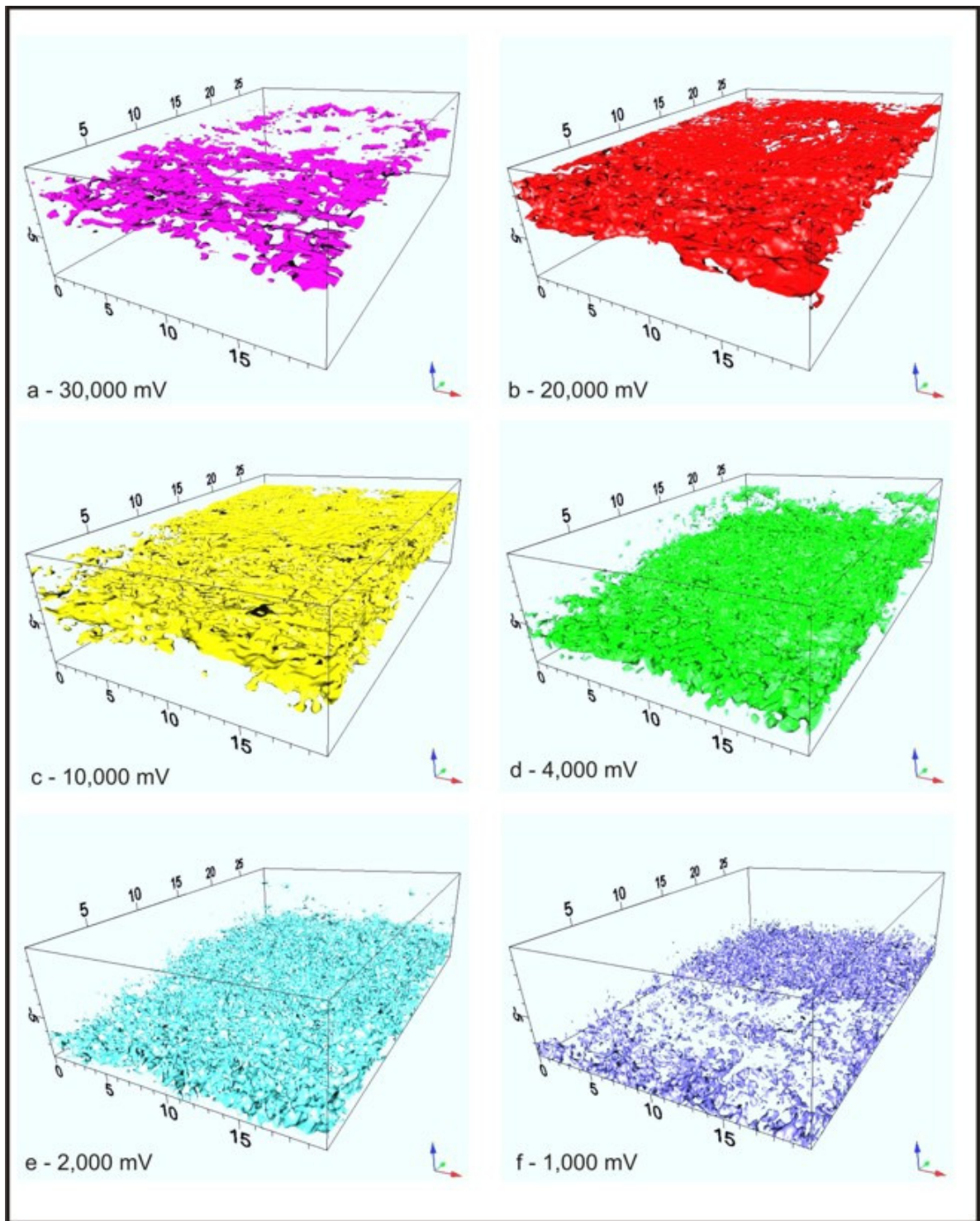


Figure 6.50 – Isosurfaces depicted for GPR 3D Model illustrate areas with similar amplitude values. Displayed in Voxler software. North direction is illustrated by green arrow.

6.2.4 – Very Low Frequency Data (VLF)

Four VLF profiles with a station spacing of 10m were collected in Site S1 using a Abem Wadi VLF system, see location in Figure 6.51. Two readings were collected for each point, the raw in-phase value (R Real) and the raw out-of-phase imaginary (R Imaginary) value. Filtered values were calculated from those using the filter developed by Karous and Hjeltdt (1983) - see Chapter 3 for further details. Using both the Filtered real (FR) and filtered imaginary (FI) fields allows a more precise data interpretation and the location of features within the subsurface is more accurately delineated with the filtered data. Raw and filtered data are presented for profile 1 to illustrate the differences between raw and filtered data. However, filtered data only will be plotted for the remaining profiles.

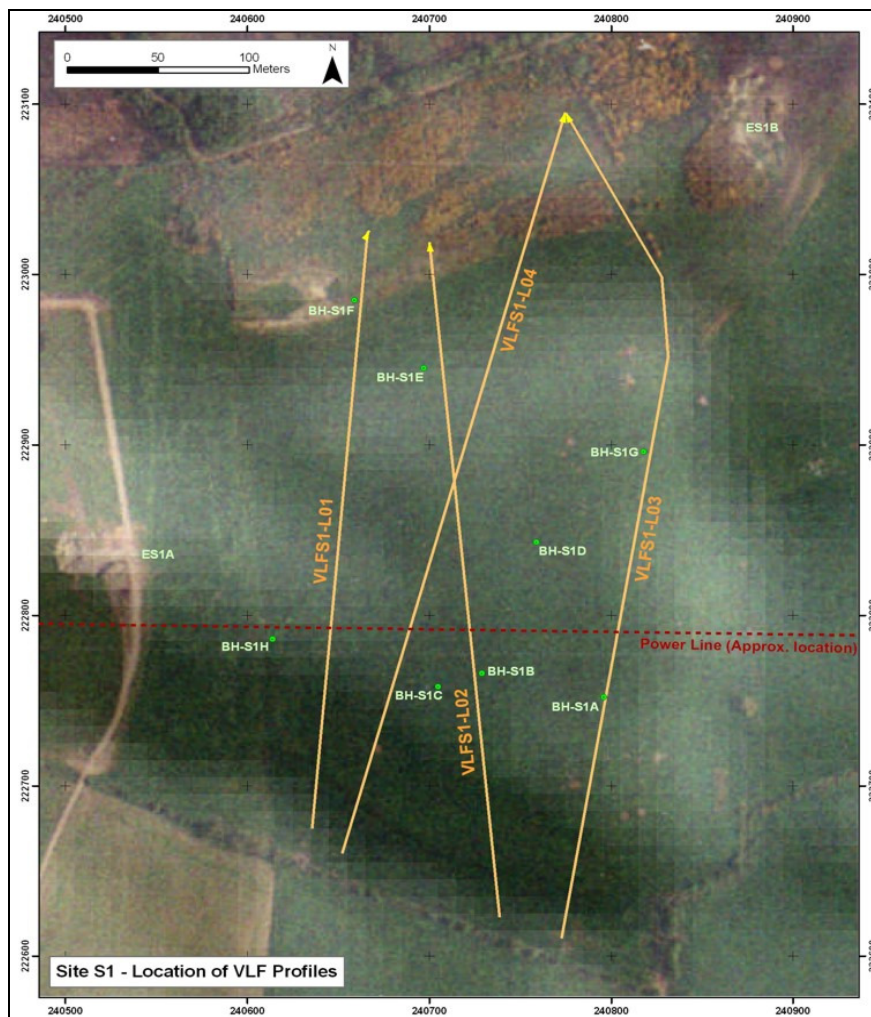


Figure 6.51 – Location of VLF profiles and power line influencing the collected readings.

The data was plotted in a Cartesian diagram with the position in metres on the X-Axis and the variation of the in-phase and out-of-phase components of the vertical magnetic field as a percentage of the horizontal primary magnetic field in the Y-Axis. The shape, depth, orientation and the conductivity of the feature recorded in the subsurface contribute to the final percentage obtained (Gibson and George, 2004).

Profile **VLFS1-L01** runs south to north for 380m cutting across the main geomorphologic features in the site. Figure 6.52 shows both the raw and the filtered datasets. A power line crosses the profile at 120m. It can be observed that the raw data shows major variations at 100 - 110m. However, following the application of the filter the percentage variation caused by the power line is placed in the correct location, this variation will not be counted in the interpretation. Other minor percentage variations were recorded along the profile. The FR field shows positive values from 0 - 20m, which could be related to subsurface dominated by diamicton, this is followed by low negative values from 20 - 270m with minor variations probably associated to the presence of interstratified gravelly sand and muddy sand. A positive percentage variation occurs for the FR field from 270 to 320 representing the lacustrine sediments, the highest value (6.4%) is reached where the clay facies is thickest. This is followed by a slight negative percentage variation associated with the boulders and gravels deposited along the esker ridge.

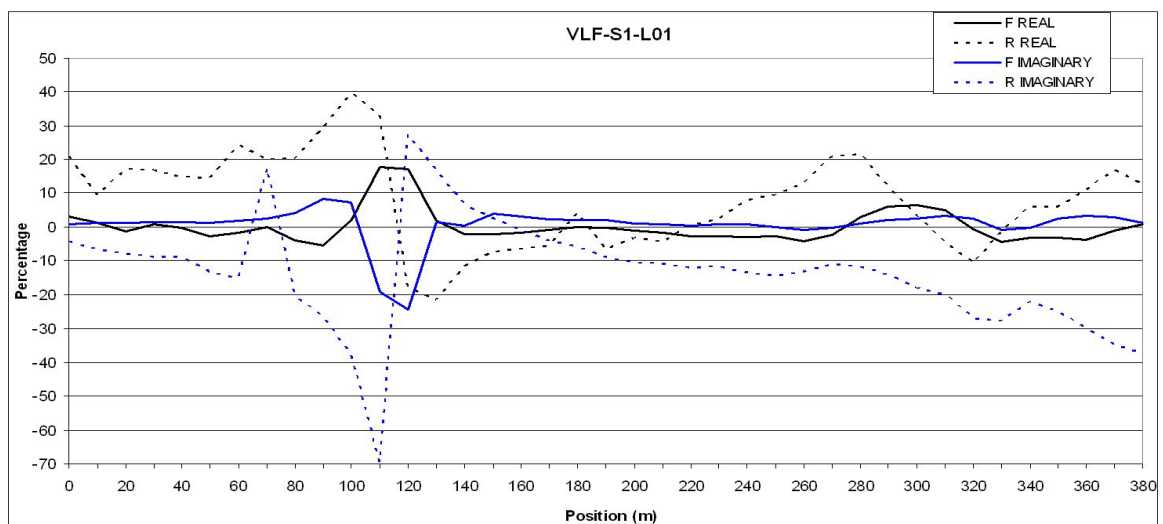


Figure 6.52 – Results of VLF profile VLFS1-L01. Both, the filtered (solid line) and the raw (dashed line) are plotted for the in-phase (black) and out-of-phase (blue) percentage variation.

Profile **VLFS1-L02** was collected from north to south and subsequently reversed for consistency with the remaining datasets, it runs approximately south to north subparallel to L01 for 420m cutting across the main geomorphologic features in the site. Figure 6.53 illustrates the percentage variation of filtered data. The power line crosses the profile at 160m and is expressed as a large anomaly in the data at 160 - 170m. A number of percentage variations were recorded along the profile, the FR field shows negative values from 0 - 20m. This result disagrees with the expected positive percentage variation caused by a diamicton dominated subsurface, however, other factors such as depth, and orientation of the feature may influence the results. This is followed by values very close to 0 from 20 - 270m; a negative percentage variation occurs from 270 - 310m (-6%), possibly due to an increase in the gravel content of the sediments at the northern edge of the fan (see resistivity profile L01-10m from 280 to 310m - Figure 6.6). A positive percentage variation between 310 and 380 (7%) is associated with the presence of lacustrine silt and clay along the surface generally underlain by diamicton. A slight negative percentage variation from 385 - 410m represents the boulder and gravel dominated esker ridge.

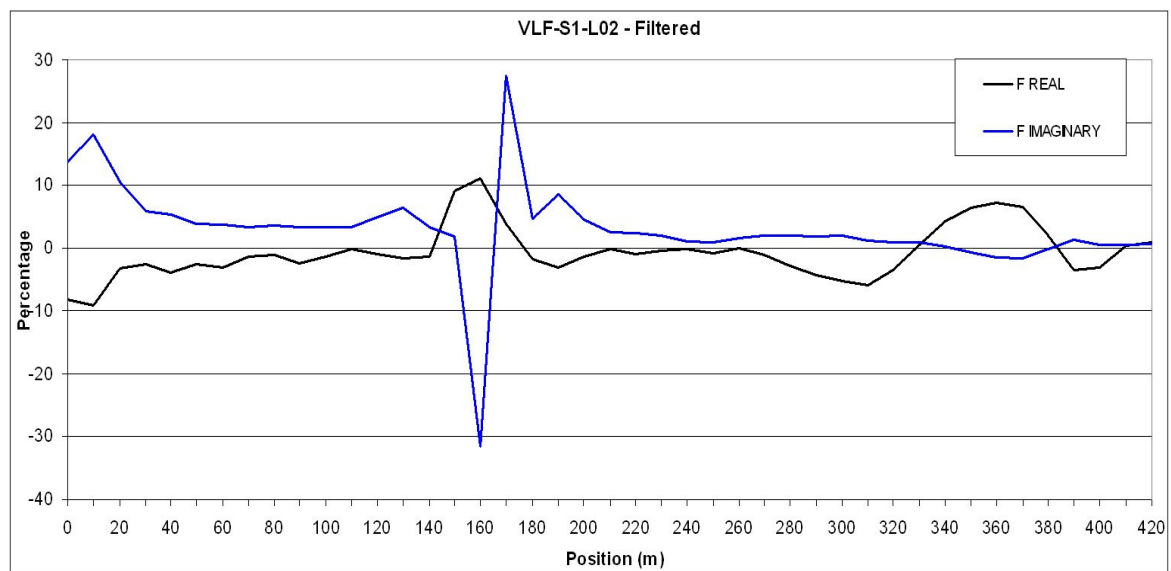


Figure 6.53 – Results of VLF profile VLFS1-L02. The filtered for the in-phase (black) and out-of-phase (blue) percentage variation are plotted.

Profile **VLFS1-L03** runs south to north for 510m cutting across the main geomorphologic features in the site. Figure 6.54 illustrates the percentage variation of the filtered data. The power line crosses the profile at 190m. A number of percentage variations were recorded along the profile. The FR field shows large negative values from 0 - 30m; from 30 - 300m the percentage variation stays close to 0, with minor negative variations of less than 5%. These small variations may be related to presence of sand and gravel dominated areas within the muddy sand, for instance, the percentage variation recorded at 310 - 320m can be correlated with the channel features recorded in GS1-L05-200MHz at 90 - 110m (Figure 6.42). A large positive percentage variation, reaching a maximum of 14.7% occurs for the FR field from 380 – 430m, which yet again indicates the presence of conductive fine lacustrine sediments underlain by diamicton. A significant negative percentage variation of more than 10% occurs over the esker ridge located at 440 – 500m. The FI field shows positive percentage variations from 0 - 30m (20%) related to clay dominated subsurface sediments. Further positive variations recorded 150 - 160m (10.6%) were correlated with a weathered bedrock area identified within resistivity line L01-10m at 100 - 120m, see Figure 6.6. Minor variations of less than 6% occur on the esker ridge area at 440 - 480m.

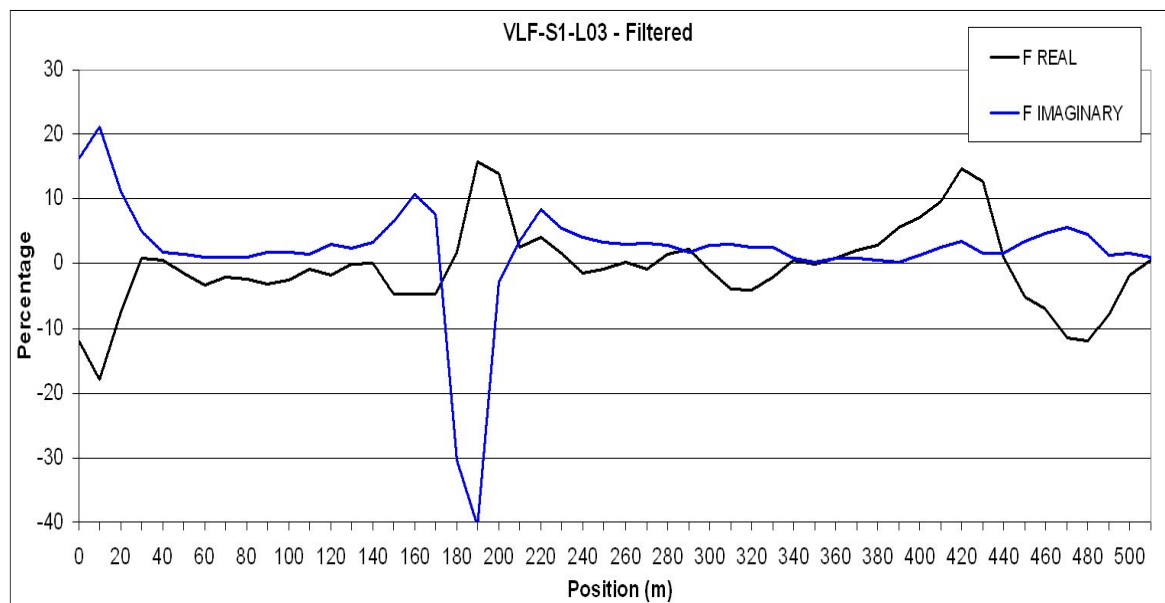


Figure 6.54 – Results of VLF profile VLFS1-L03. The filtered for the in-phase (black) and out-of-phase (blue) percentage variation are plotted

Profile **VLFS1-L04** was collected from north to south and subsequently reversed for consistency with the remaining datasets; it runs approximately south-southwest to north-northeast subparallel to L01 for 440m cutting across the main geomorphologic features in the site. Figure 6.55 shows the percentage variation of the filtered data. The power line crosses the profile at 130m and is expressed as a large anomaly. The FR field shows negative values from 0 - 20m, as in lines L02 and L03 this result disagrees with the expected positive percentage variation caused by diamicton dominated subsurface and may be due to presence of relatively shallow bedrock. The values stay relatively close to 0 from 20 - 240m. A negative percentage variation occurs from 250 - 290m, probably related, as in L02, to a decrease in conductivity caused by the higher proportion of gravel in the deposits occurring at the northern edge of the fan. A high resistivity area close to the surface has been recorded in profile RS1-L01-10m from 280 - 310m, which concurs with such interpretation, see Figure 6.6. A positive percentage variation, reaching a maximum of 9.4%, occurs 300 - 350m, is associated with the area dominated by lacustrine silt and clay. A slight negative percentage variation occurs from 360 - 420m, is correlated with the boulder and gravel dominated esker ridge and a positive percentage variation at 430 - 440m, is most likely related to presence of conductive fine sediments in the area.

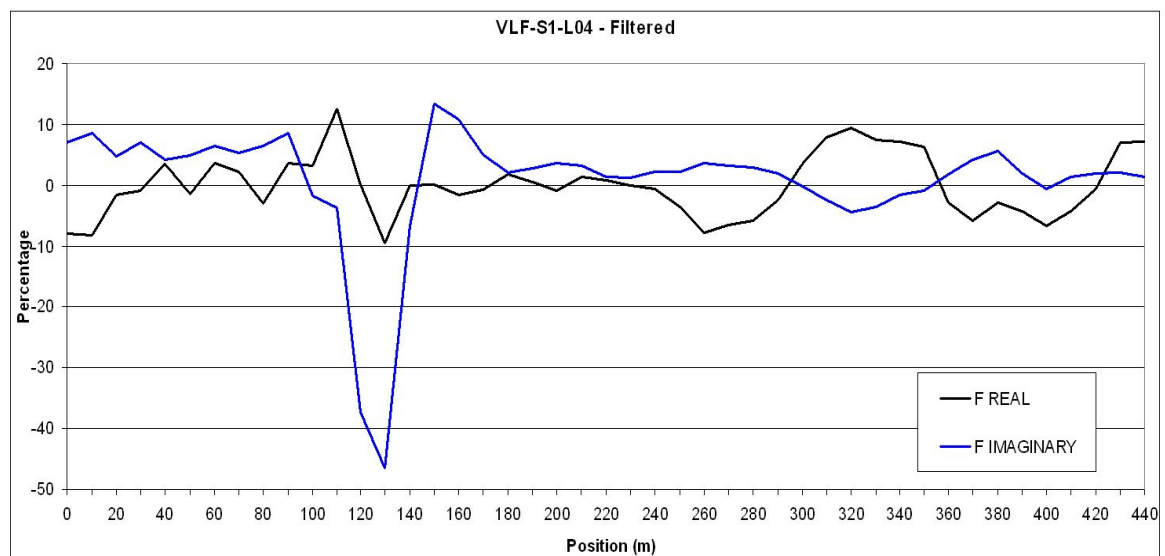


Figure 6.55 – Results of VLF profile VLFS1-L04. The filtered for the in-phase (black) and out-of-phase (blue) percentage variation are plotted.

The VLF data show reasonable correlation with other geophysical data collected in Site S1. The main percentage variation of both the FR and the FI fields is an artefact caused by the overhead power line running across all the VLF profiles. However other percentage variations were recorded and it appears that the surficial sediments seem to be the main factor influencing the negative and positive variations of both the FR and FI fields. In general terms, positive percentage variations are related to the existence of conductive sediments dominating the subsurface (silts and clays and diamicton), on the other hand, low conductivity sediment such as sand and gravel give a negative percentage variations of the FR field. Minor variations of the FR field have also been correlated to subtle lithological changes (muddy sand to sandy gravel) occurring within the fan. Moreover, a fracture previously detected with ERT survey has also been sensed by the FI percentage variation; showing a positive percentage variation over the fracture, see profile VLFS1-L03.

The spatial resolution obtained for the VLF is low and a good knowledge of the main geological settings of the area of study is necessary to produce an accurate interpretation. However, VLF is a rapid data acquisition method and the percentage variations, which, when properly interpreted, allow the broad characterisation of the dominant subsurface lithology for medium to large study areas.

6.2.5 – Evaluation of Geophysical techniques

A broad range of Quaternary deposits were recognised and classified in Site S1 by means of exposure sedimentological analysis, borehole logging and a number of geophysical techniques. This detailed study in such a small area allowed selecting the geophysical methods to be used for the remaining sites and refine the methodology for data acquisition, processing and interpretation.

‘Ground truth’ by means of morphological mapping, exposure assessment and eight boreholes helped improve the interpretation of the geophysical surveying data. The site has

been used to test the potential use of different geophysical techniques for surficial sediments recognition and characterisation.

ERT data proved extremely useful for lithological differentiation of sediments, five lithological classes were differentiated, which in reverse chronological order are:

- lacustrine silt/clay overlain by peat
- gravelly sand/silt and sandy gravel
- esker gravel and boulders
- diamicton
- bedrock

These classes are characterised from the results of resistivity modelling, however, borehole data, geomorphological evidence and results from other geophysical techniques have helped constrain the boundaries between the different lithologies. Moreover, this technique solely has been found highly useful to estimate depth to bedrock within S1.

Important changes in the resistivity values were recorded by means of time-lapse resistivity data. The shallow area of the profiles (0 - 2/4m depth) appears to respond very rapidly to changes in effective recharge, the deeper areas (> 4m depth) show a delay in the response to effective recharge of 2 to 3 months. According to the available data, the seasonal variation of resistivity values is influenced by four attributes: the effective recharge, the depth, the dominant lithology of the material and the lithology of the material overlying it.

The analysis of time-lapse resistivity data has revealed a number of patterns. Shallow areas within the profiles appear to respond very rapidly to changes in effective recharge, an increase in the resistivity of 20 - 100% generally occurs during the drier months. The percentage variation is also influenced by the lithology, fine sediments tend to experience minor changes, whereas, coarser sediments respond with more significant resistivity variations. In contrast, the deeper areas generally show a decrease of the resistivity values

during the drier season (>50%) followed by an increase (>100% in places) of the resistivity immediately after it. Further discussion of these results is presented in Chapter 7.

Azimuthal resistivity data correlated fairly well with ERT data, however, it is a relatively slow data collection method, with fairly limited interpretation outcomes compared to ERT method and is considered rather ineffective as a Quaternary sediment mapping technique.

GPR data have shown a remarkable potential for sedimentological classification. Five radar facies were identified, which in chronological order from older to younger are:

- f1-Gm – glacial massive diamicton,
- f2-Gfm/Gfc – glaciofluvial massive/cross stratified sediments associated with the esker ridge.
- f3-Gcd(d) - glaciofluvial cross-stratified sediments, deformed in places associated with the fan,
- f4-Gch(d) - glaciofluvial channel fill sediments, deformed in places associated with the fan
- f5-Lh – lacustrine horizontally stratified sediments.

VLF data were collected quickly and it is a fairly effective tool for broad classification of the subsurface sediments. The data collected agree reasonably with ERT and GPR data. However, the spatial resolution attained with this method is quite coarse, which makes it not suitable for detailed geophysical characterization.

The radar facies obtained from GPR correlate to a high degree with the lithological classes identified by ERT surveys and reasonably well with VLF data. Table 6.4 shows the approximate correlation between resistivity lithological classes, radar facies and VLF percentage variations. Each technique has its own advantages and drawbacks. GPR data provide, in ideal conditions, a high resolution picture of the internal architecture of the subsurface, however, as shown in the forward modelling exercise presented in Chapter 5, vertical features cannot be depicted using this technique and the maximum depth of penetration attained in the site is 14m. On the other hand, the ERT system allows the

production of profiles of up to 40m depth and clearly detects vertical and horizontal features. However, the level of detail attained is much lower and only lithological changes can be detected using this technique. Finally VLF provides a low resolution dataset and the depth of the features detected can not be clearly stated, however, the data acquisition rate is faster and could be a valuable tool to target the best location for GPR and ERT surveys. The combination of these techniques has allowed the construction of an accurate picture of the distribution and relative chronology of the surficial sediments occurring in the site and to produce a systematic methodological approach for data collection, processing and interpretation for the remaining 16 sites surveyed for this thesis.

Relative chronology	Resistivity (Ωm)	ERT Lithological classes	GPR Radar facies	VLF FR % (+/-)
6	60 to 120 Ω m	lacustrine silt and clay	f5-Lh - lacustrine sediments	Positive
5	600 to 1700 Ω m	gravelly sand/silt	f4-Gch(d) – glaciofluvial channel fill (fan)	Negative
4	300 to 600 Ω m	sandy gravel	f3-Gcd(d) – glaciofluvial cross stratified (fan)	None or Negative
3	500 to 1000 Ω m	esker gravel and boulders	f2-Gfm/Gfc – glaciofluvial massive (esker ridge)	Negative
2	80 to 400 Ω m	Diamicton	f1-Gm – glacial massive	Positive
1	(> 900 Ω m)	Bedrock	Not detected	Negative

Table 6.4 – Correlation between ERT data, GPR and VLF data for Site S1.

6.3 – Site S2

6.3.1 – Introduction

Site S2 (Figure 6.1) is located 3.5 Km southeast of Tullamore (E236000, N222000) and its southern margin is delineated by the Geashill esker (previously described in Chapter 4.3.2) which runs in an east-west direction as a discontinuous ridge with fairly subdued topography. The esker in this area is expressed, from west to east, as three smaller segments with lengths of 500, 700 and 1200m. These reach a maximum height over the surrounding landscape of 5 - 6m and encompass a range in width of about 30 - 50m. Glaciofluvial sediments, associated with the esker, dominate the relatively elevated areas, which also developed in an east-west direction. The lower ground is dominated by partially cut away peat bogs underlain by glaciofluvial sand and gravel and/or diamicton derived from Lower Carboniferous limestone.

Surficial deposit thicknesses of more than 30m were mapped using geophysical techniques in Site S1; thick surficial sediments were also mapped east from Kilcormac Esker (E229000, N220500 – See Map 2), a question about the existence of a channel feature running parallel to Geashill Esker and linking these two areas encompassing thick surficial sediments aroused during the production of the DTB Map. Knowledge of the depth to bedrock in Site S2 was very limited. This motivated to pursue geophysical survey to investigate the presence of a potential channel feature linking the Kilcormac and Geashill eskers. Therefore, two ERT profiles were collected on the site to broadly estimate the surficial deposit thickness in this area. An aerial photograph of the site with the location of the profiles is shown in Figure 6.56.

The underlying sediments are exposed in a 2m deep ditch located in the centre of the site (ES2A). This shows a thin layer of cut away peat overlying 1m thick layer of poorly stratified cobble gravel with sandy matrix, which is underlain by horizontally stratified medium to fine sand (see Plate 6.2).

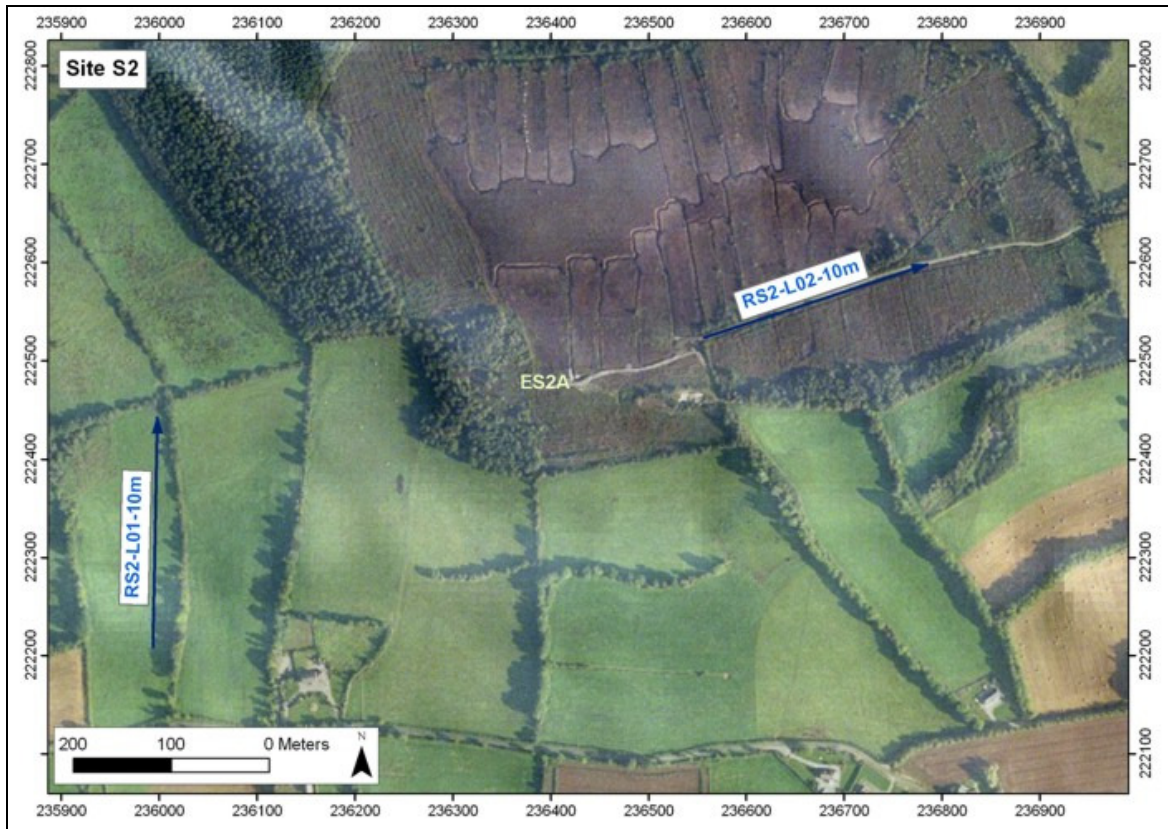


Figure 6.56 – Location of profiles recorded in Site S2.



Plate 6.2 – Exposure ES2A located between profiles 1 and 2 illustrating sediment distribution in this area (E236418, N222482).

6.3.2 – Electrical Resistivity Data

Two electrical resistivity profiles at 10m electrode spacing were collected in Site S2 using the Wenner-Schlumberger array.

Profile **RS2-L01-10m** runs south to north across the location through which the expected channel feature would run. The line runs northwards through gently sloping and well drained ground from 0 to 110m, where a concave change in slope occurs, from this point the landscape changes into flat poorly drained ground underlain by cut away raised bog. Plate 6.3 shows the morphological expression of the area, low flat ground in the foreground and a ridge running east-west on the background. The profile recorded (Figure 6.57) shows low resistivity values of less than 100 Ω m at 0 - 70m and 120 - 240m, reaching maximum depths of 12m. This has been interpreted as poorly sorted sand and gravel/diamicton on the higher ground from 0 - 120m and as peat on the low lying ground. Medium values ranging 100 - 1000 Ω m occur from 60 - 150m at 0 - 20m depth, these values could be interpreted as poorly sorted glaciofluvial sediments. High resistivity values of more than 1000 Ω m dominate the lower parts of the profile; this has been interpreted as bedrock, rock head elevation thus ranges 50 - 58m OD. The depth to bedrock varies along the profile at 10 - 18m depth.

Profile **RS2-L02-10m** (Figure 6.58) runs on cut away peat bog along the potential channel feature on a west to east direction. The topography is flat and fairly depressed compared to the surrounding landscape, with an average altitude of 64.5m OD; therefore, topographic correction has not been applied to the profile. The inverse model of the collected data shows a gradual change from low resistivity values in the shallow subsurface changing into a very sharp contact at 12 - 14m depth. This has been interpreted as a sub-horizontal contact between poorly sorted sand and gravel (less than 500 Ω m) and overlying bedrock (high resistivity values reaching maximums of 6,000 Ω m). The presence of the gravel recorded at ES2A is not clear on the model of the pseudosection presented; this is possibly because of the high water-table level expected in a raised bog, which could reduce the resistivity values for interstratified sand and gravel to less than 100 Ω m.

Both resistivity profiles show glacial/glaciofluvial sediments with 12 - 14m thickness overlying bedrock, the expected channel running west-east has not been depicted. However, thick Quaternary deposits occur in the area.



Plate 6.3 – Morphological expression along profile RS2-L01-10m towards the south seen from the north end of line 1. High well-drained ground dominates the landscape in the background. Flat lying, poorly-drained ground dominates the foreground.

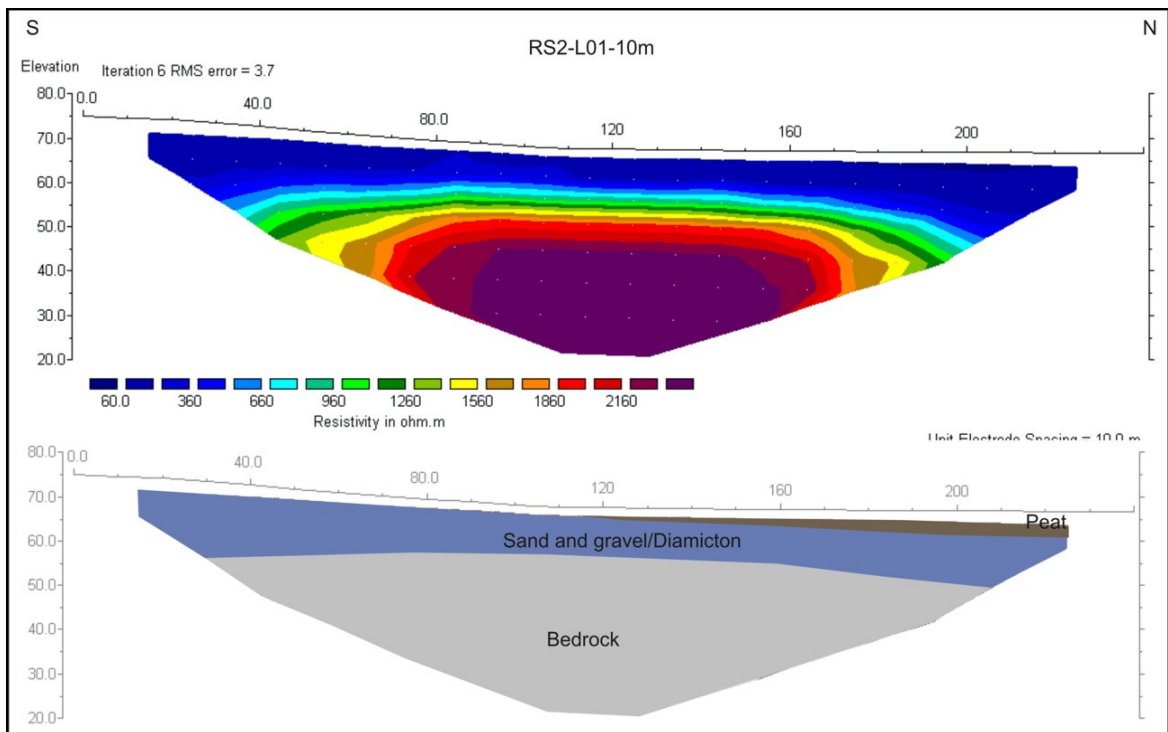


Figure 6.57 – Electrical Resistivity profile RS2-L01-10m collected in Site S2 and its interpretation.

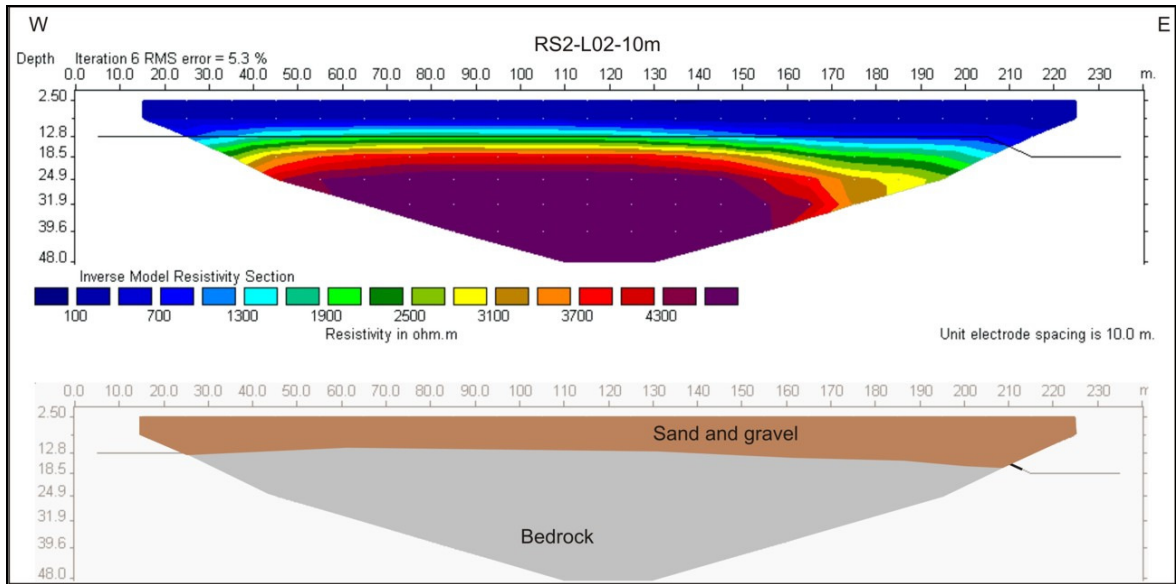


Figure 6.58 –Electrical Resistivity profile RS2-L02-10m collected in Site S2 and interpretation based on resistivity values and exposure ES2A.

6.4 – Sites S3 and S4

6.4.1 – Introduction

Sites S3 and S4 are presented as a one entity (Site S4 is located approximately 1 Km west from Site S3). Both sites form part of an ice marginal ridge complex situated 10 Km southwest-west from Tullamore Town (Figure 6.1 and Map 1). The feature consists of a set of ridges with relatively subdued topographic expression running across the Kilcormac Esker in the area north of Blue Ball (E226000, N221000). The Kilcormac Esker was originally mapped by Sollas (1896) who concluded it was deposited as a subglacial tunnel fill, Charlesworth (1928) interpreted it as a morainic ridge associated to an ice sheet retreating northwards. Farrington and Synge (1970) revisited it and agreed with the first interpretation. Moreover, they identified an assemblage of subparallel end moraines running across the Kilcormac Esker associated to ice retreating southwest. Sites S3 and S4 occur within this morainic system. The two sites were surveyed by means of borehole drilling, electrical resistivity and GPR in order to identify the internal architecture and lithological composition of these features.

Site S3 is located along the northern margin of the Kilcormac Esker. It consists of a series of mounds and ridges running northwest-southeast (see Plate 6.4). Geotechnical and geophysical surveys were carried out on a 800m long ridge, with varying width of 50 - 100m and heights above the surrounding landscape ranging from 3 - 8m. A detailed map of the site with the location of borehole data, electrical resistivity and GPR profiles is presented in Figure 6.59.

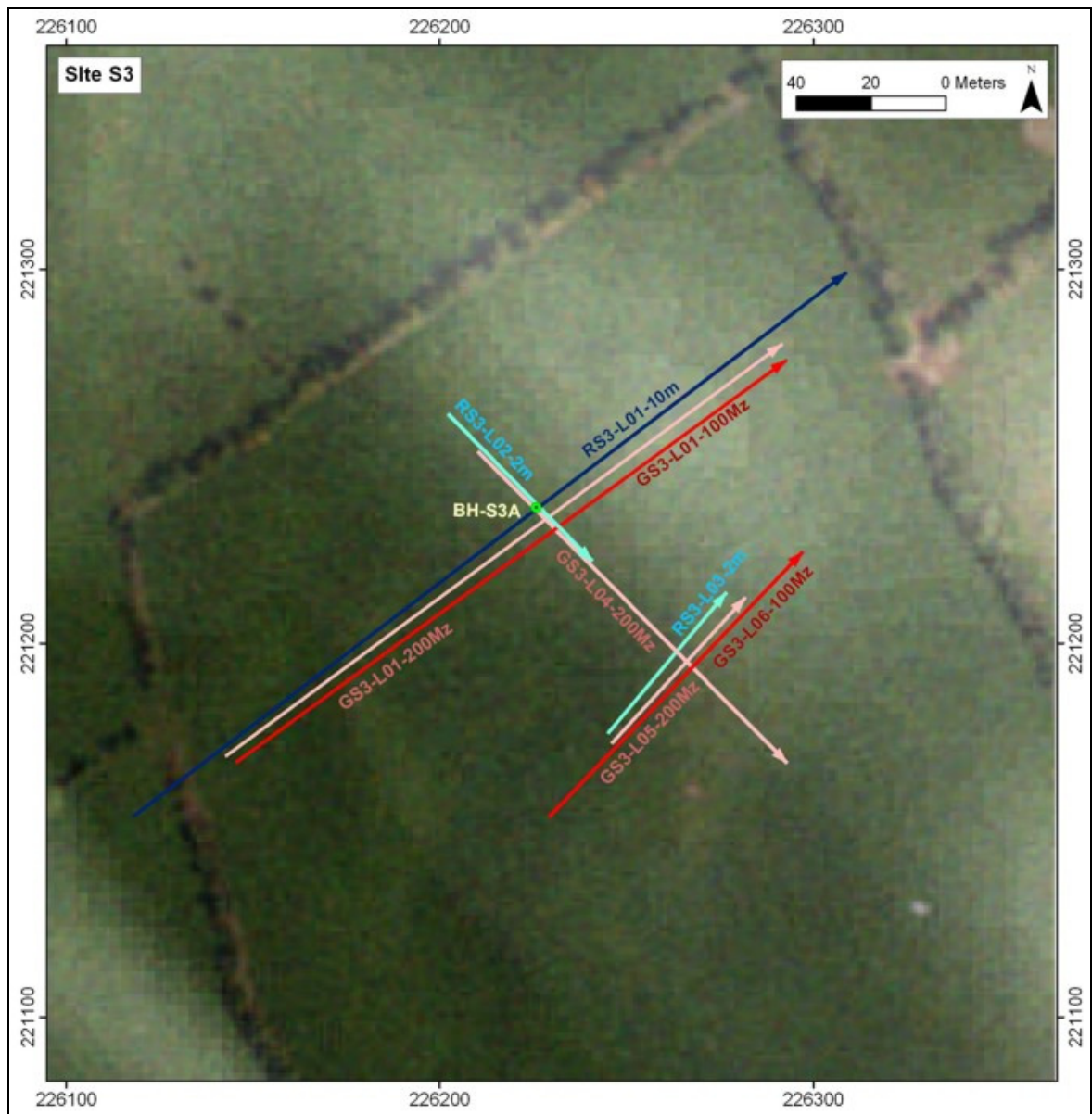


Figure 6.59 – Aerial photograph of site S3 with location and orientation (arrow head indicating end of the profile) of surveyed geophysical profiles. Borehole location is displayed in green, Resistivity profiles are presented in blue, and GPR in red.



Plate 6.4 – Morphological expression of Site S3 showing the main ridge recorded from its southeast margin

A borehole (BH-S3A - E226216, N221242) was drilled but had to be stopped at 4.2m depth due to the presence of large boulders. The log was described in situ as topsoil from 0 - 0.3m and dense to very dense silty gravelly diamicton with subangular/subrounded limestone pebbles from 0.3 - 4.2m. A bulk sample (BH-S3A-1) was collected at 2 - 3m depth, and particle size distribution analysis (PSA) performed on it. The sample has been classified under the Folk (1954) classification scheme as clast supported gravel with sandy silty matrix. The borehole log and the PSA results are presented in Appendix A.

Site S4 consists of low lying to the south ground giving way to a steep slope climbing northwards and reaching a relative height of 8m above the southern landscape, this slope has been interpreted during the field mapping exercise as an ice proximal slope, see Plate 6.5. The feature evolves at its higher area into a gentle slope declining northwards from this point. Although, the feature is part of the morainic complex described in Site S3, its genesis may have been slightly different, as the feature is wider in this area. A map of the site with the location of borehole data, electrical resistivity and GPR profiles is presented in Figure 6.60.

A borehole (BH-S4A - E225193, N221444) was drilled on the site. Its log description shows stiff clast supported silty sandy gravel with subrounded/subangular limestone pebbles from 0 - 3.5 m. A soft layer with no recovery occurs at 3.5 - 4.3 depth. The sediments are described as dense silty clayey gravel with subangular/subrounded limestone pebbles from 4.3 - 7.2m. Two samples collected 3 - 4m (BH-S4A-1) and 6 - 7m (BH-S4A-2) were analysed by PSA. The samples have been respectively classified under the Folk

(1954) classification scheme as muddy sandy gravel and as muddy sandy gravel with sandy silty matrix. The borehole log and the PSA results are available in Appendix A.

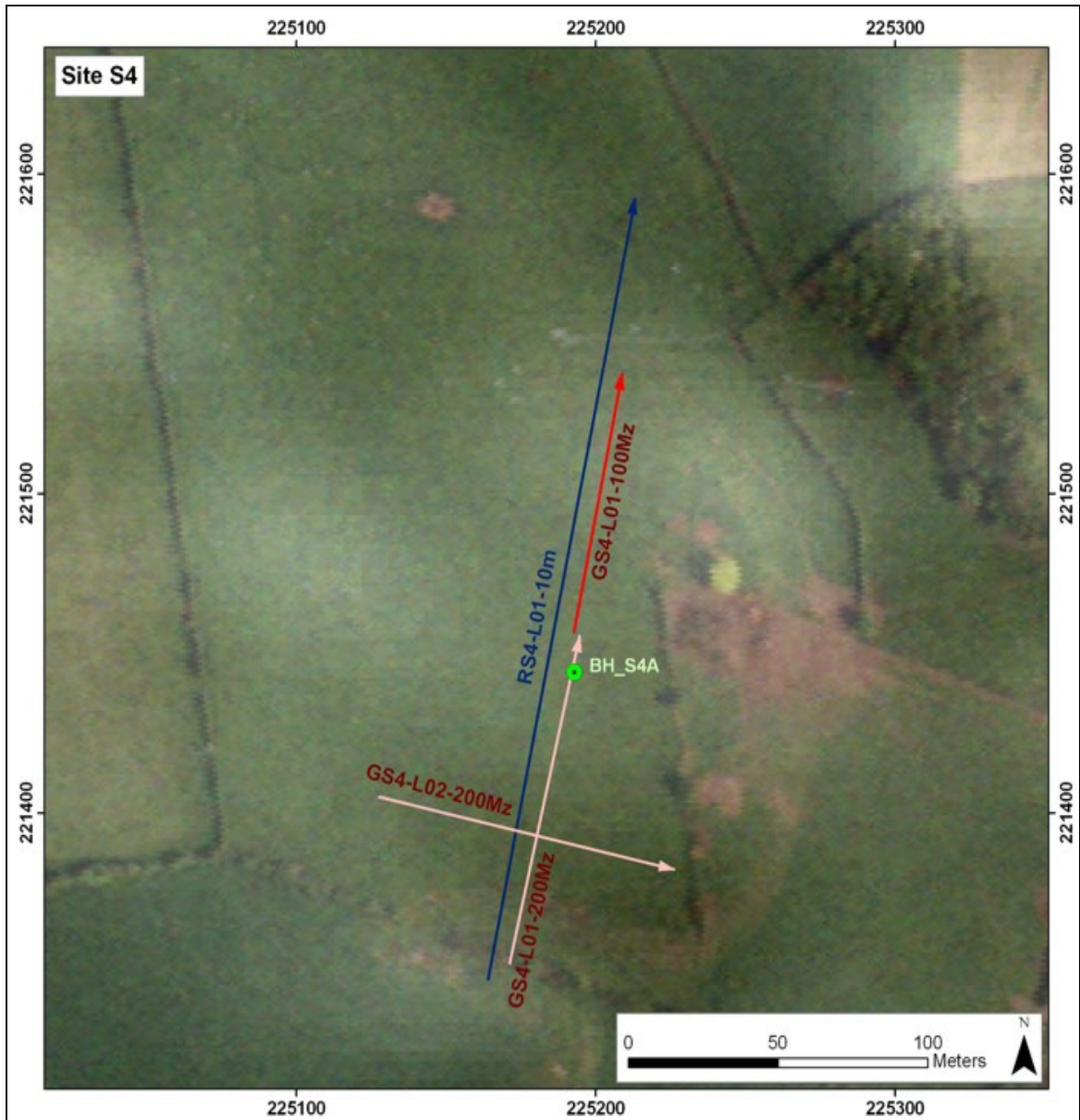


Figure 6.60 – Aerial photograph of site S4 with location and orientation (arrow head indicating end of the profile) of surveyed geophysical profiles. Borehole location is displayed in green, Resistivity profiles are presented in blue, and GPR in red.



Plate 6.5 – Recording a GPR profile in Site S4 using a 200MHz antenna across the ice proximal slope of an ice marginal ridge.

6.4.2 – Electrical Resistivity Data

Three electrical resistivity profiles were collected in Site S3 using the Wenner-Schlumberger array. Two of them were collected with a 2m electrode spacing (RS3-L02-2m and RS3-L03-2m) for detail and one at 10m electrode spacing (RS3-L01-10m) to provide a deeper depth of investigation.

RS3-L03-2m (Figure 6.61a) cuts across the morainic ridge in a southwest-northeast direction. High resistivity values occur all along the profile, representing a stretch of clast supported gravel 3.5m thick in the ice proximal margin of the moraine. The thickness of this gravel body increases to 6m on the ice distal margin of the ridge. A sharp contact separates these high resistivity sediments from the lower deposits encompassing low resistivity values, these were interpreted as diamicton or the presence of the water-table, which could also have caused a dramatic drop in the observed resistivity values.

RS3-L01-10m (Figure 6.61b) presents a very high error (21.6%) due to very dry ground conditions when the profile was recorded, which resulted in excessively high contact resistance values for some of the electrodes used ($>2000\Omega\text{m}$). The profile runs across the morainic ridge in a southwest-northeast direction. It intersects BH-S3A and RS3-L02-2m

at 135m. High resistivity values occur in places along the surface at 0 - 4m depth, most likely related to cobble/boulder gravel from 70 - 190m. Small patches of gravel, reaching a maximum thickness of around 7m, occur 130 - 150m, these deposits have been correlated to the high resistivity gravel recorded in the profile RS3-L02-2m. These well sorted sediments are underlain by lower resistivity values ($<1000\Omega\text{m}$), which were interpreted as diamicton reaching depths 8 - 20m. Finally, very high resistivity values ($>3000\Omega\text{m}$) recorded at the bottom of the profile were interpreted as limestone bedrock.

The profiles presented have different resolutions; however a correlation can be defined between lines **RS3-L01-10m** and **RS3-L03-2m** (Figure 6.61) which illustrates accumulation of thicker sand and gravel deposits occurring on the ice distal slope of the morainic ridge. The profile along the ridge presents no variation in the thickness of these deposits. The differential distribution of sediment at both sides of the ridge agrees with the typical asymmetrical morphological expression expected from ice marginal ridges.

RS3-L02-2m (Figure 6.62) runs along the crest of the morainic ridge on a northwest-southeast direction. The profile intersects BH-S3A at 20m. High resistivity values of up to $6000\Omega\text{m}$ occur from 0 to 3 - 4m depth. These were interpreted as morainic clast supported cobble/boulder gravel, as it has been recorded in BHS3A. Lower resistivity values ranging from 30 - $500\Omega\text{m}$ dominate at depths greater than 4m and were interpreted as diamicton underlying the morainic gravels. Low values also occur in a small pocket along the surface at 3 - 6m, it has also been interpreted as diamicton. A sharp contact between both deposits can be easily delineated from the profile.

An ERT profile at 10m spacing (**RS4-L01-10m**) was collected in Site S4 using the Wenner-Schlumberger array, see Figure 6.63. The profile runs northwards across the ice marginal ridge and close to borehole BH-S4A at 100m. Very high resistivity values occur near the surface at 0 - 120m, reaching depths of 5 - 10m, probably related to well-sorted sand and gravel. Lower resistivity values occur in the middle depth of the profile and were interpreted as diamicton with sandy silty matrix recorded in sample BH-S4A-2. This material presents resistivity values of 300 - $1500\Omega\text{m}$. Another possible interpretation of

this drop in resistivity values could be due to the presence of the water-table at around 10m depth. Finally, these sediments are underlain by a higher resistivity layer ($>2000\Omega\text{m}$), a tentative continuous boundary between these bodies has been delineated and the underlying material has been interpreted as undulating limestone bedrock occurring along the whole profile under depths of 20 - 30m.

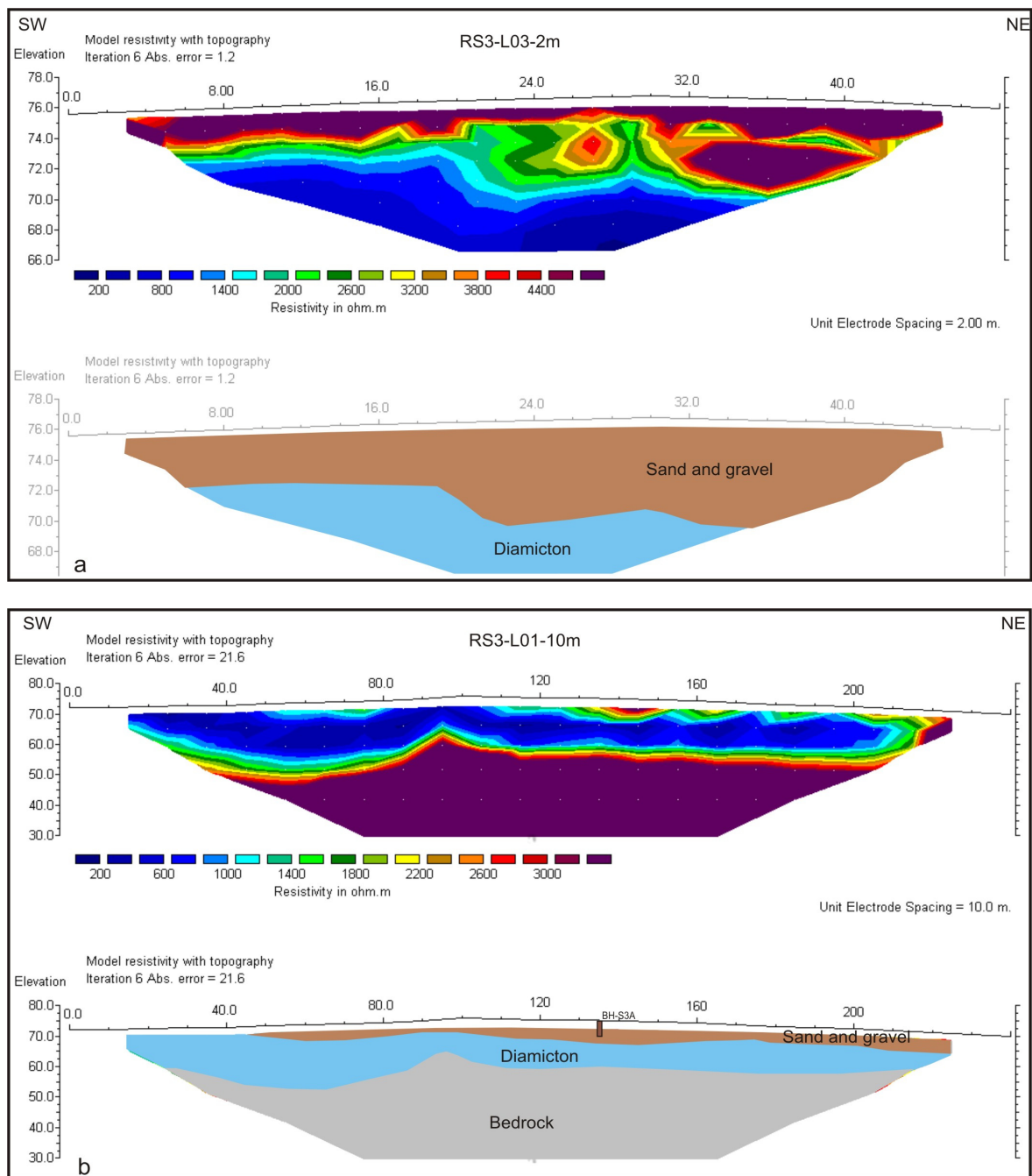


Figure 6.61 – Resistivity profiles RS3-L03-2m and RS3-L01-10m and their interpretation (a) RS3-L03-2m and (b) RS3-L01-10m.

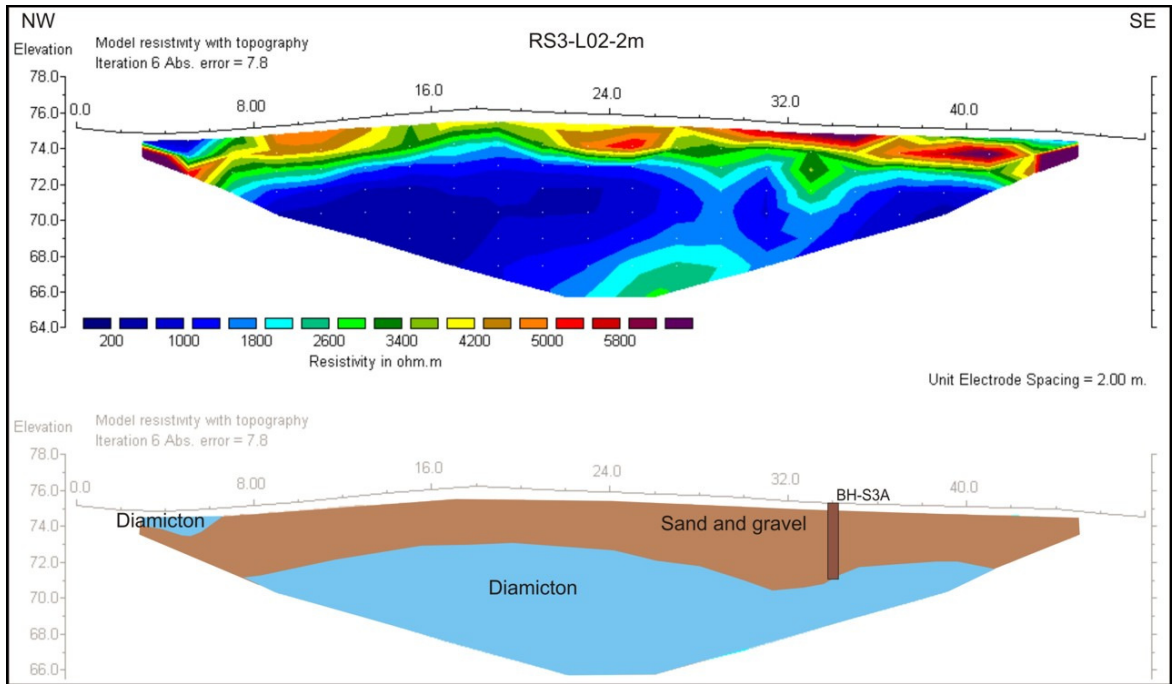


Figure 6.62 – Electrical Resistivity profile RS3-L02-2m collected in Site S3 and its interpretation.

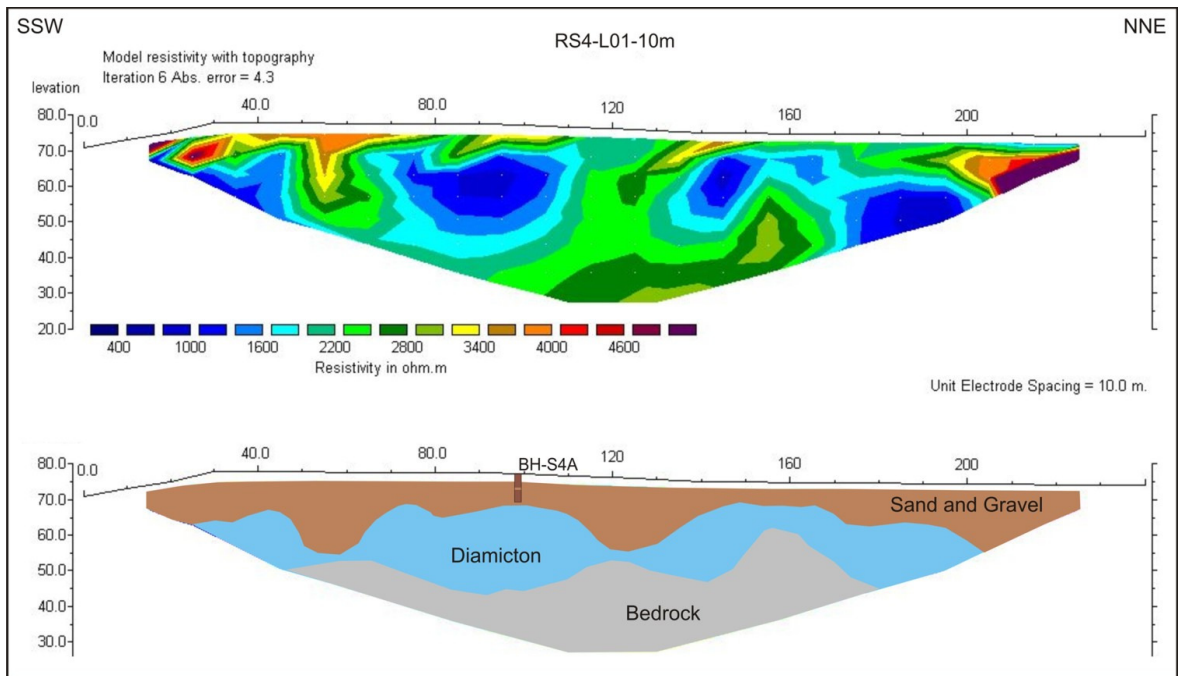


Figure 6.63 – Electrical Resistivity profile RS4-L01-10m collected in Site S4 and its interpretation.

6.4.3 – Ground Penetrating Radar (GPR)

Several GPR profiles were collected in Site S3. Three were collected using a 200MHz antenna and two using a 100MHz antenna. The profiles have been processed when necessary using the methods recommended by Neal (2004) and already discussed in Chapter 3.

GPR Line **GS3-L01-100MHz** runs perpendicular to the ice marginal ridge and its interpretation is presented in Figure 6.64. Four main radar facies were differentiated; these are separated by the primary radar surfaces. The lower facies packages were classified as deformed glaciofluvial cross-stratified sediments (L1f1-Gfcd), the radar surfaces limiting them may be related to changes in lithological content. Secondary reflectors have been depicted within them, which are generally sinuous discontinuous reflectors subhorizontal or dipping slightly northeast. A second facies package occurs at 40 - 200m, it is dominated by moderately continuous reflectors dipping 20 - 15° NE from 40 - 70m, chaotic discontinuous reflectors from 70 - 170m and moderately continuous reflectors dipping 5 - 10° SW. These facies are overlain from 120 - 160m by crude moderately continuous reflectors dipping 20° - 15°, which have been interpreted as foresets. These evolve northeastwards into subhorizontal moderately continuous reflectors cut across by reflectors dipping southwest which were interpreted as thrust faults deforming them. A concave reflector occurring at 1 - 2m depth from 60 - 120m has been interpreted as the lower margin of a thrust plane overlain by discontinuous deformed sub-horizontal reflectors. A large number of hyperbolic reflectors can be observed in the non-processed radargram. These mainly occur on the crest and the northeast margin of the profile, chiefly at depths of more than 3m; and are interpreted as medium sized (c. 500mm diameter) boulders associated with cross-bedded radar facies. A number of subparallel discontinuous reflectors depicted in orange dipping 10° - 15° southwest placed at both margins of the ridge have been interpreted as fault planes, probably associated with ice pushing in a northeast direction. Finally, the water-table has been detected on the left margin of the profile as a flat lying reflector at 64.8m OD, which agrees with the water level of a small lake situated 500m southeast of this profile.

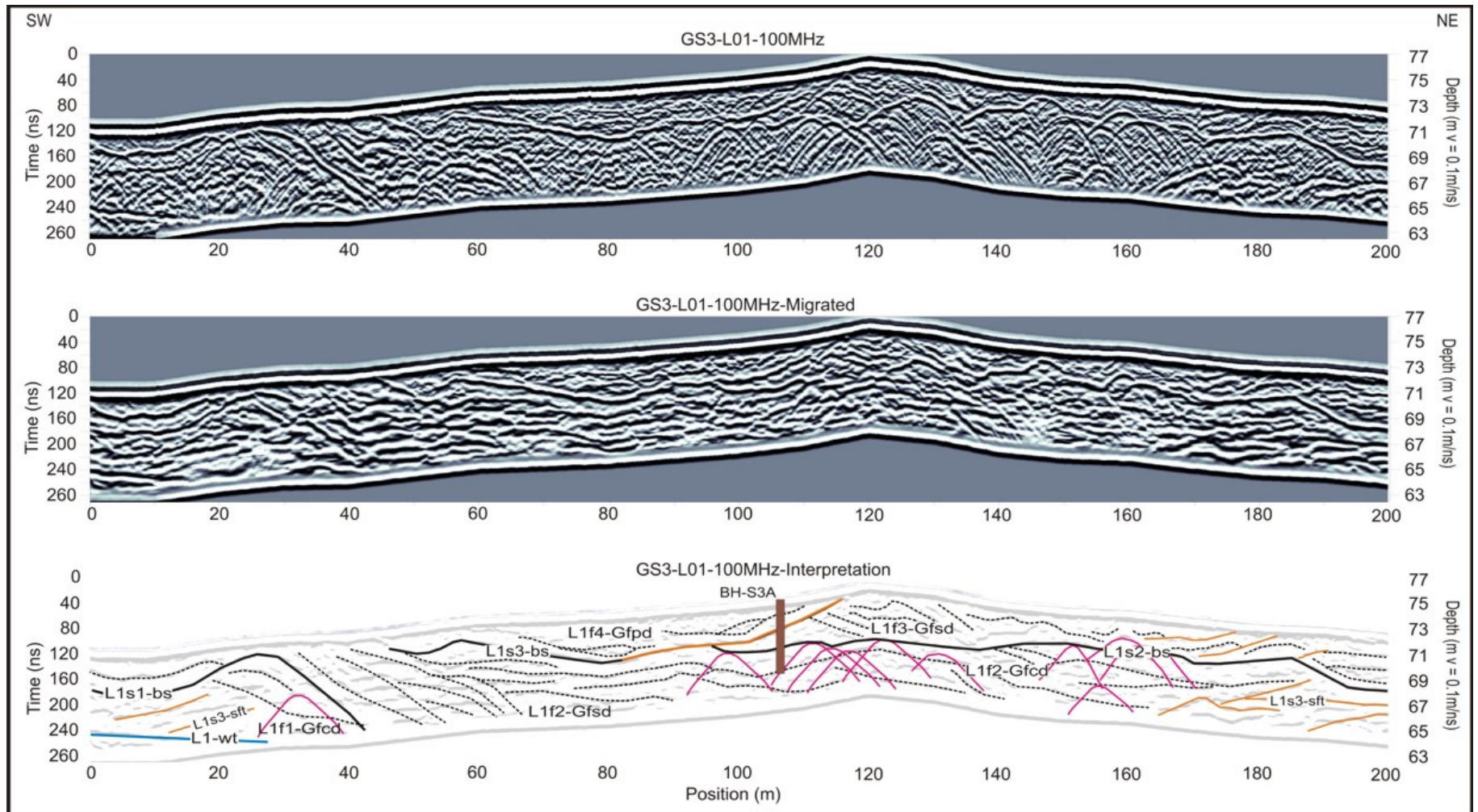


Figure 6.64 – GPR profile GS3-L01-100MHz collected in Site S3. Top – radargram with AGC Gain and topographically corrected. Middle – topographically corrected migrated radargram using a 0.1m/ns velocity. Bottom – Interpretation of the radargram.

Time slice analysis performed on this profile is presented in Figure 6.65. High amplitude values are usually correlated with medium to coarse sediments with low clay contents and amplitude generally decreases with depth as fewer reflections are registered by the receiver. The upper range time slice (20-60ns or 1-3m depth) shows sets of high and low values, which can be inversely correlated with amplitudes obtained in the range 60 - 100ns (3-5m depth.). This probably indicates the presence of well-sorted sediments with no reflectors in the upper section (20 - 60ns) which allows the electromagnetic waves to penetrate freely, followed by a more reflective area at 60 - 100ns reflecting a larger amount of energy at that point than in the surrounding areas. It is inferred from the time slice profile 60 - 100ns that low reflectivity sediments, possibly sand and gravel with high silt/clay contents, occur at 50 - 90m and 130 - 150m. Higher amplitude dominates 0 - 50m, 90 - 130m and 150 - 180m, possibly related to the presence of higher reflectivity sediments such as interstratified sand and gravel. The time slices 100 - 140ns and 140 - 180ns show the highest amplitudes at the positions 0 - 20m, 70 - 120m and 170 - 200m and relatively lower values between them probably related to higher silt/clay contents.

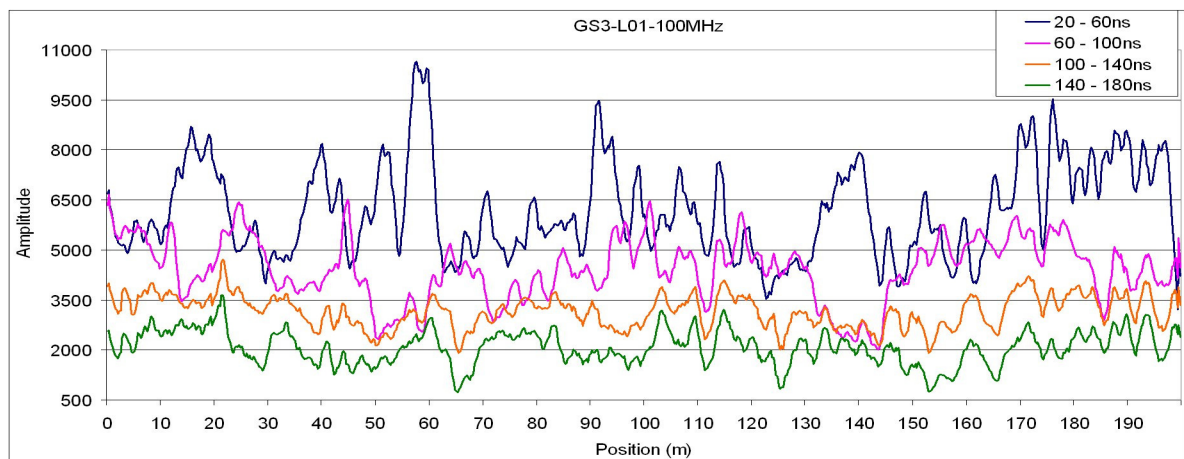


Figure 6.65 – Time-slice analysis for GPR profile GS3-L01-100MHz collected in Site S3.

GS3-L01-200MHz radargram using an antenna with 200MHz frequency was collected inline with L01. This radargram provides a higher resolution for the top 6m of sediments (Figure 6.66). This profile was useful for detection of deformation structures, probably associated to a readvance of the ice. However, main reflectors defining the sedimentological settings of the moraine are equally depicted by the 100MHz antenna.

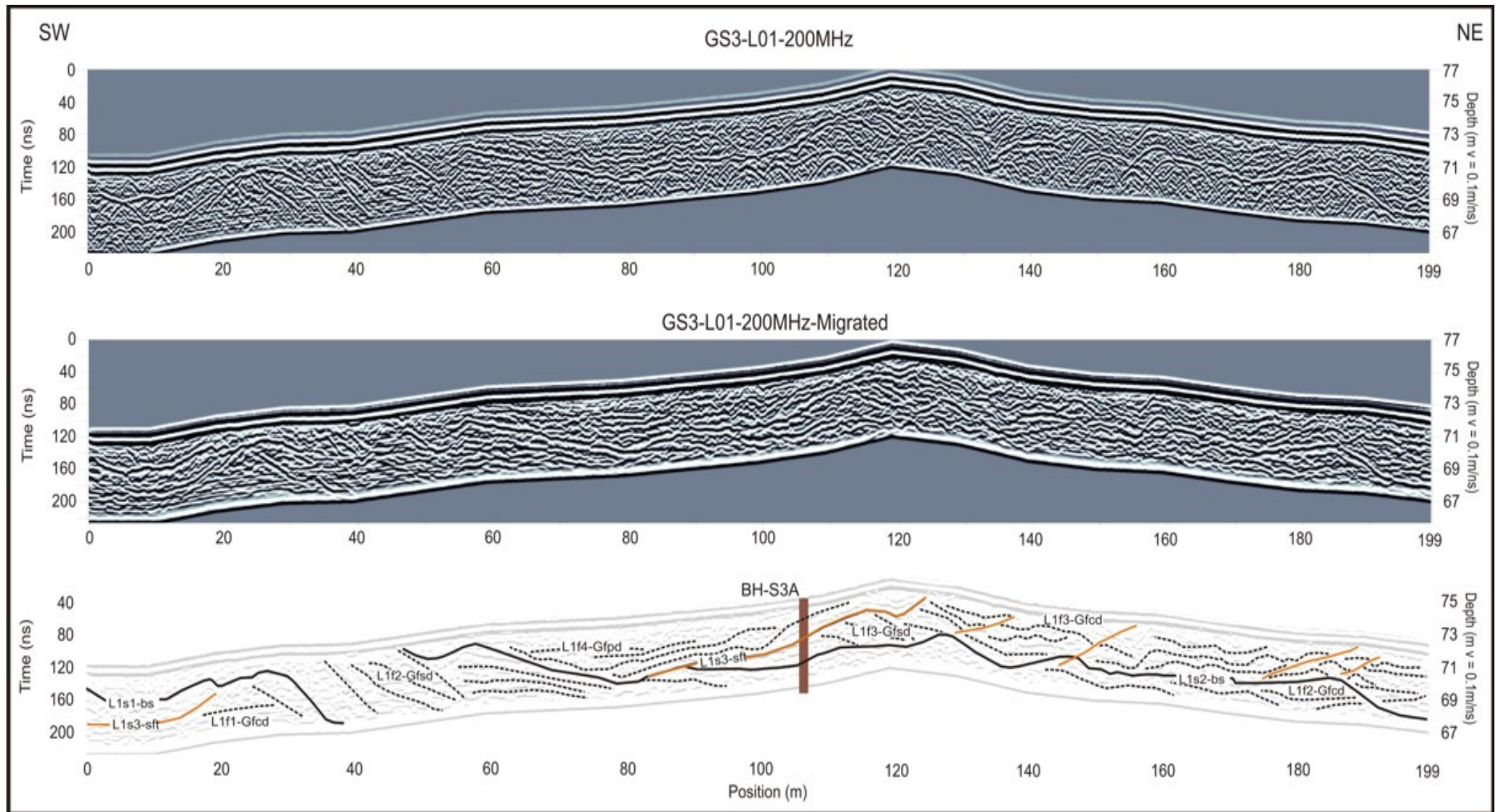


Figure 6.66 – GPR profile GS3-L01-200MHz collected in Site S3. Top – radargram with AGC Gain and topographically corrected. Middle – topographically corrected migrated radargram using a 0.1m/ns velocity. Bottom – Interpretation of the radargram.

Line **GS3-L04-200MHz** runs northwest-southeast, along the crest of the ice marginal ridge. The resulting topographically corrected and migrated radargram and its interpretation are presented in Figure 6.67. Three main radar facies have been differentiated in the radargram, radar facies 1 occurs at the lower parts from 0 - 20m. It is composed of a number of chaotic discontinuous reflectors which have been interpreted as deformed glaciofluvial cross-stratified sediments (L1f1-Gfcd). These are overlain by moderately continuous sinuous reflectors crossing each other from 0 - 50m, which evolve from 60 - 120m into sinuous discontinuous reflectors subparallel to the topography (L1f2-Gfcd). The numerous sinuous discontinuous reflectors may have been caused by collapse structures of the sediments. This may be an indication of ice cored sediments, which would have deformed during the melting of the buried ice. Several moderately continuous dipping reflectors depicted from 50 - 70m dipping SE and NW are interpreted as normal faults probably associated to collapse subsequent to melting of underlying ice. A number of thrust faults depicted in L01 and L05 are also depicted here from 0 - 40m and 70 - 90m.

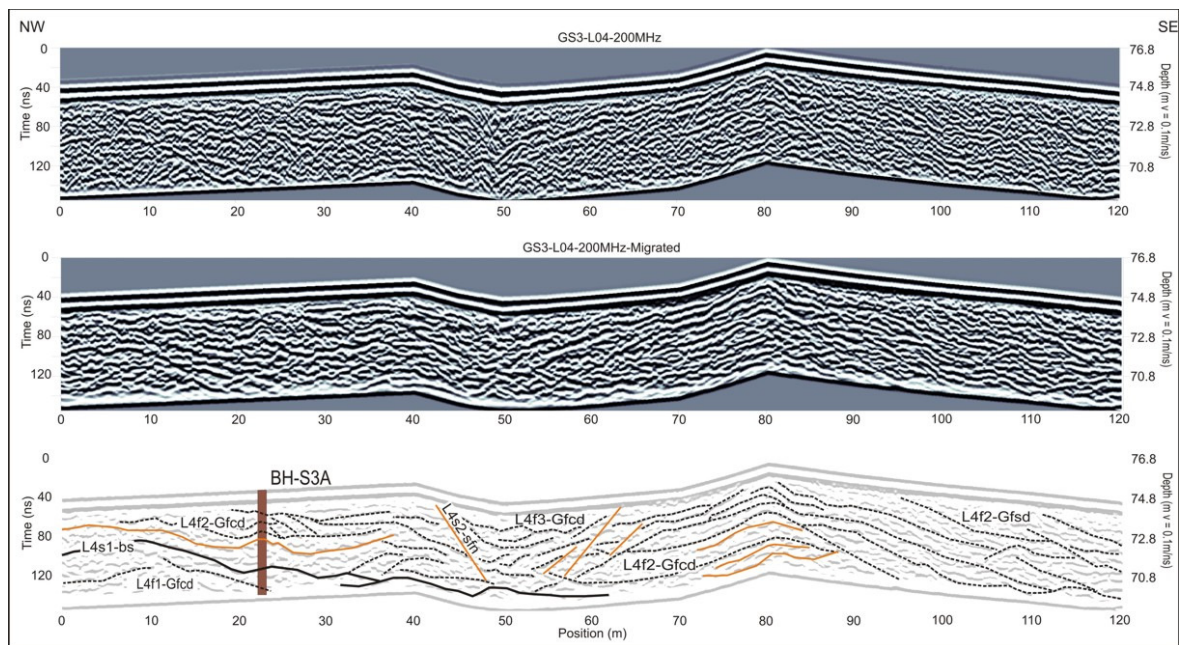


Figure 6.67 – GPR profile GS3-L04-200MHz collected in Site S3. Top – topographically corrected radargram with dewow and AGC Gain. Middle – topographically corrected migrated radargram using a 0.1m/ns velocity. Bottom – Interpretation of the radargram.

Profile **GS3-L06-100MHz** runs southwest-northeast perpendicular to the ice marginal ridge. The interpretation of the radargram is presented in Figure 6.68. A strong continuous sinuous reflector runs along the profile at 3 - 5m depth with secondary associated tangential discontinuous reflectors diverging from it. Hyperbolae occur beneath this main reflector (see top non-processed radargram), which is probably related to a sharp lithological change between the underlying diamicton and the sand and gravel - see resistivity profile RS3-L03-2m. A set of sinuous moderately continuous reflectors dipping 15° - 20° occur within the sands and gravels at 20 - 50m, which end in a downlap contact with the main continuous reflector. A set of divergent, moderately continuous reflectors dipping 5 - 10° displayed in orange at 0 - 40m and 80 - 90m have been interpreted as possible reverse faults or thrusts associated with ice pushing towards the northeast. This profile shows many similarities to L01, and supports a model of glaciofluvial sediments deposited on diamicton subsequently deformed by ice advancing northeastwards.

A radargram using an antenna with 200MHz frequency (Figure 6.69) was collected inline with profile L06 along the section between 15 and 65m (**GS3-L05-200MHz**). The profile has been particularly useful for more accurately detect the presence of deformation structures associated to a readvance of the ice, a number of thrusts and reverse faults have been detected mainly along the up-ice area from 0 - 30m. Dipping reflectors interpreted as partially deformed foreset radar facies (L5f2-GFsd) occur from 25 - 50m, these are overlain from 30 - 50m by flat lying moderately continuous reflectors (L5f3-Gtsd).

The interpreted radargrams for profiles GS3-L01-200MHz, GS3-L04-200MHz and GS3-L05-200MHz are presented as a fence diagram in Enclosure 2 – E2A.

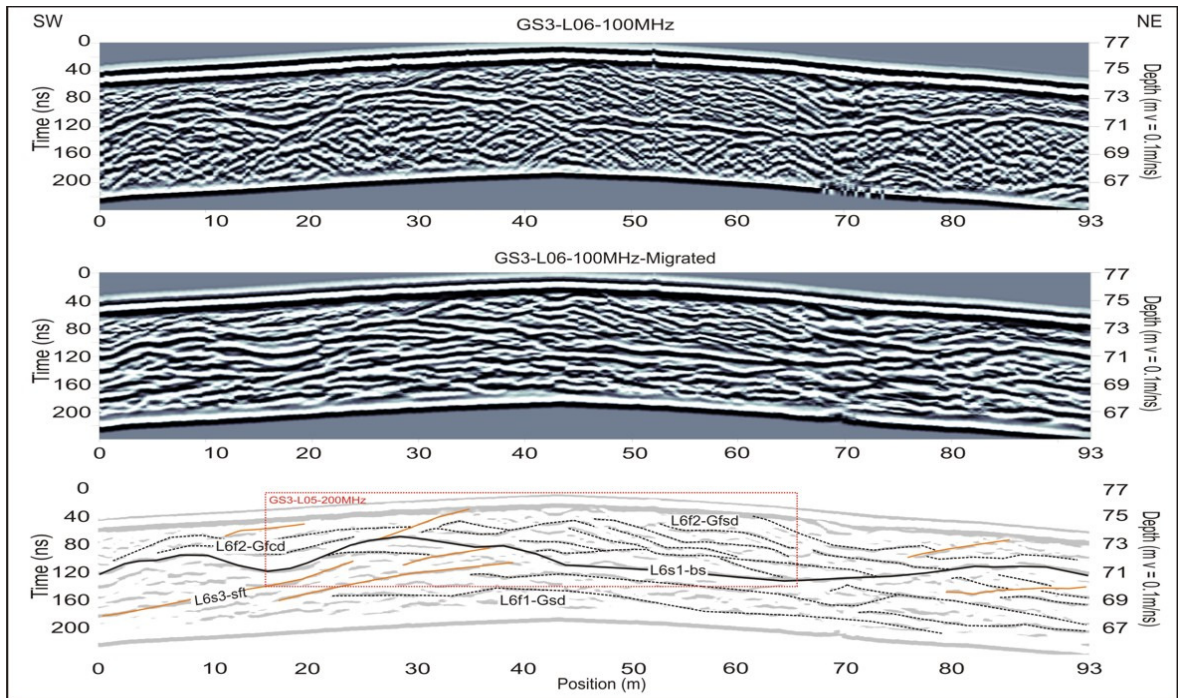


Figure 6.68 – GPR profile GS3-L06-100MHz collected in Site S3. Top – topographically corrected radargram with dewow and AGC Gain. Middle – topographically corrected migrated radargram using a 0.1m/ns velocity. Bottom – Interpretation of the radargram.

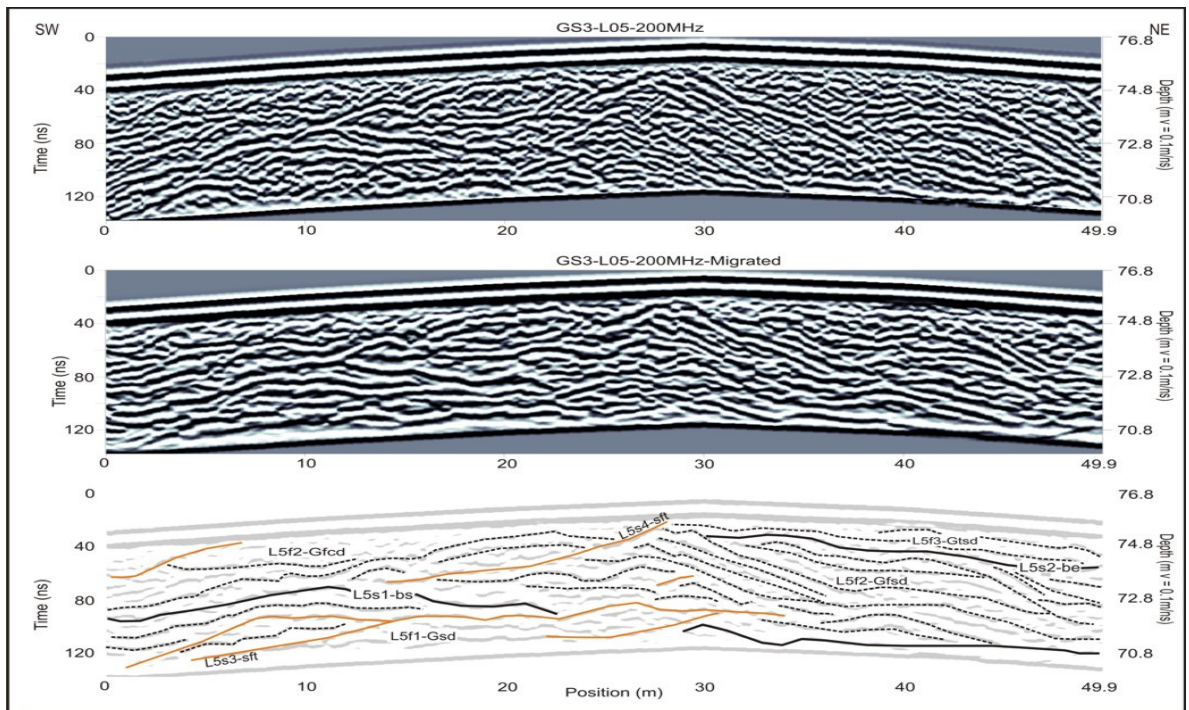


Figure 6.69 – GPR profile GS3-L05-200MHz collected in Site S3. Top – topographically corrected radargram with dewow and AGC Gain. Middle – topographically corrected migrated radargram using a 0.1m/ns velocity. Bottom – Interpretation of the radargram.

Two GPR profiles using the 200MHz and the 100MHz antenna were collected at Site S4. Lines **GS4-L01-200/100MHz** run parallel to the ERT profile shown in Figure 6.63. They have been merged and both are presented and interpreted in Figure 6.70. Subparallel, sinuous moderately continuous reflectors have been depicted subparallel to the slope at 0 - 35m and have been interpreted as faults derived from collapse subsequent to ice withdrawal and/or secondary deformed sedimentological boundaries. A continuous strong reflector oblique to the surface from 0 - 20m has been interpreted as the water-table (delineated in blue). A continuous reflector gently dipping south-southwest runs along the profile from 20 - 120m, it delimits the bottom of foresets dominated facies (L1f3-Gfsd) which pinches out towards the north-northeast. Tangential reflectors dipping 10° - 20° north-northeast occur above it merging in a downlap contact and are interpreted as foresets. A wide shallow channel feature overlies the foresets with an erosive contact between 75 - 100m, probably showing a later channel cutting across the foresets. This assemblage is underlain by a facies 2 - 4m thick occurring at 30 - 180m composed of sinuous moderately discontinuous reflectors interpreted as deformed cross-stratified beds. Deformation may be related either to ice pushing during readvance or collapse subsequent to ice retreat. A very strong continuous subhorizontal reflector from 80 - 180m has been interpreted as a bounding surface; this reflector is underlain by a number of sinuous moderately continuous reflectors interpreted as deformed cross-stratified sediments, some of the reflections at 160 - 180m from 67 - 78m OD could also be interpreted as thrust faults related to ice pushing NNE.

A time slice analysis plot for the 200MHz antenna is presented in profile in Figure 6.71. The 20 - 60ns time slice shows important variability in the 0 - 45m stretch. The profile changes suddenly at this point into a more steady shape in the 45 - 90m section, which probably indicates a change from heterogeneous to homogeneous sediments. Main lithological changes are clearly depicted in the 60 - 100ns and 100 - 140ns slices, low amplitude values recorded from 0 - 5m are associated with diamicton underlying this section of the profile. The amplitude values increase gradually from 5 - 20m as the underlying lithology gradually changes into sand and gravel as the profile climbs the up-ice margin of the morainic ridge. A small decrease in the amplitude is recorded between 25

- 30m and 38 -45m, possibly related to an increase in mud contents within the sand and gravel deposits. The amplitude values remain steady from 45 - 100m with very small variations indicating homogeneous lithology for this section.

Profile **GS4-L02-200MHz** (Figure 6.72) runs along the crest of the feature, intersecting L01 orthogonally at 34m. A set of curved oblique continuous reflectors dipping 2° - 10° ESE occur in the first 80m of the profile (L2f4-Gfsd). These overlie from 30 – 80m with an onlap contact a set of moderately continuous subparallel reflectors dipping 10° ESE (L2f3-Gfsd), which terminate at 4m depth on a downlap contact with a continuous moderately sinuous reflector from 60 - 100m. These two sets of dipping reflectors have been interpreted as foresets, possibly related to the growing stages of an ice marginal subaqueous fan or glaciodelta. The presence of the channel feature depicted in profile L01 points towards a glaciodeltaic interpretation. However, the subaqueous fans can evolve into glaciodelta if they build up sufficiently to reach lake surface (Benn and Evans, 1998), which could be the case for this setting. The two described radar facies dominated by dipping reflectors are underlain by two groups of discontinuous to moderately continuous subhorizontal sinuous reflectors, which have been interpreted as cross-bedding. The dipping reflectors have been interpreted as foresets, which could be related to the deposition of an ice contact subaqueous fan in a proglacial lake probably evolving into a glaciodeltaic system.

The interpreted radargrams for profiles GS4-L01-200/100MHz and GS4-L02-200MHz are presented as a fence diagram in Enclosure 2 – E2B.

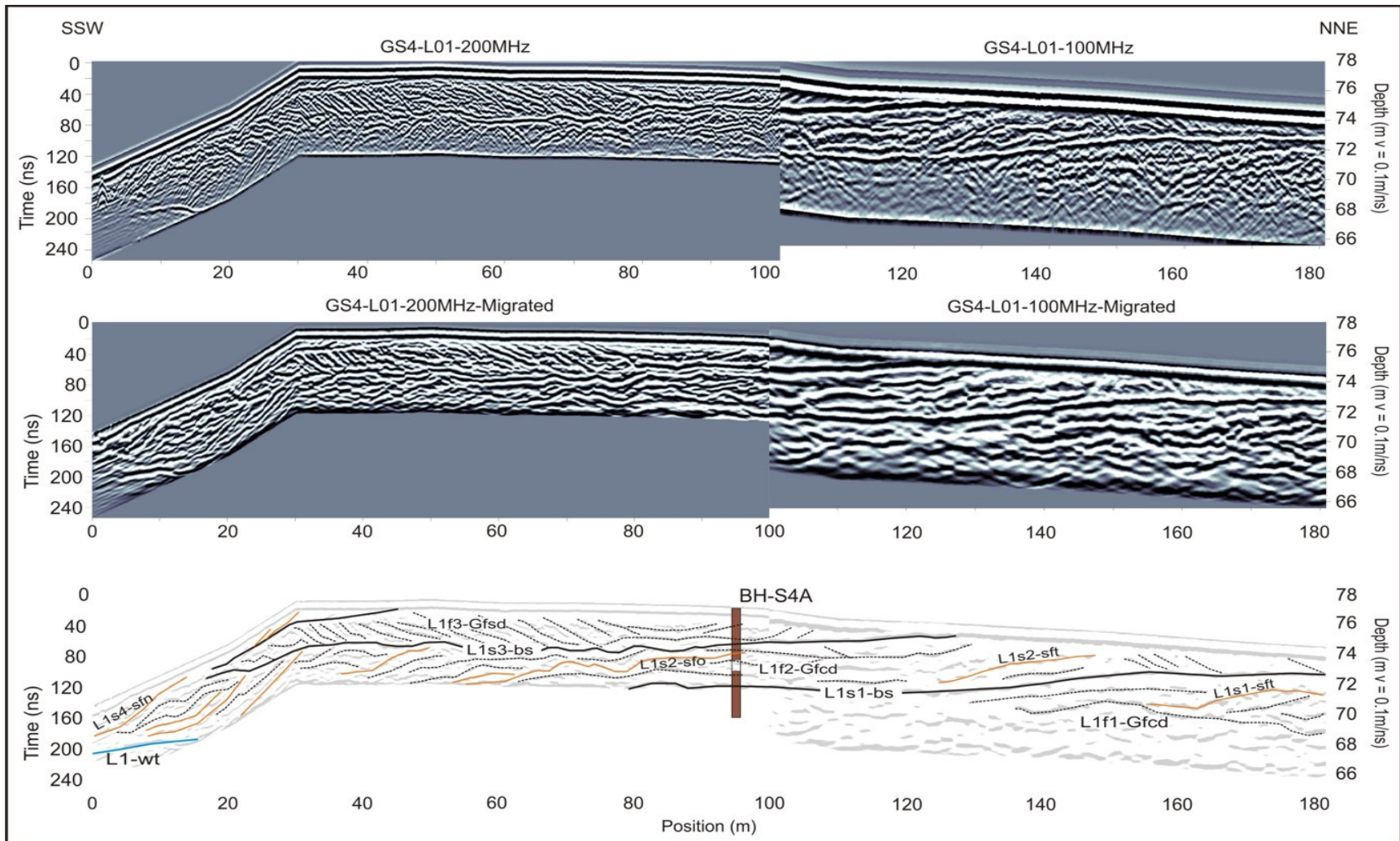


Figure 6.70 – GPR profiles GS4-L01-200MHz and GS4-L01-100MHz collected in Site S4. Top – topographically corrected radargram with dewow and AGC Gain. Middle – topographically corrected migrated radargram using a 0.1m/ns velocity. Bottom – Interpretation of the radargram.

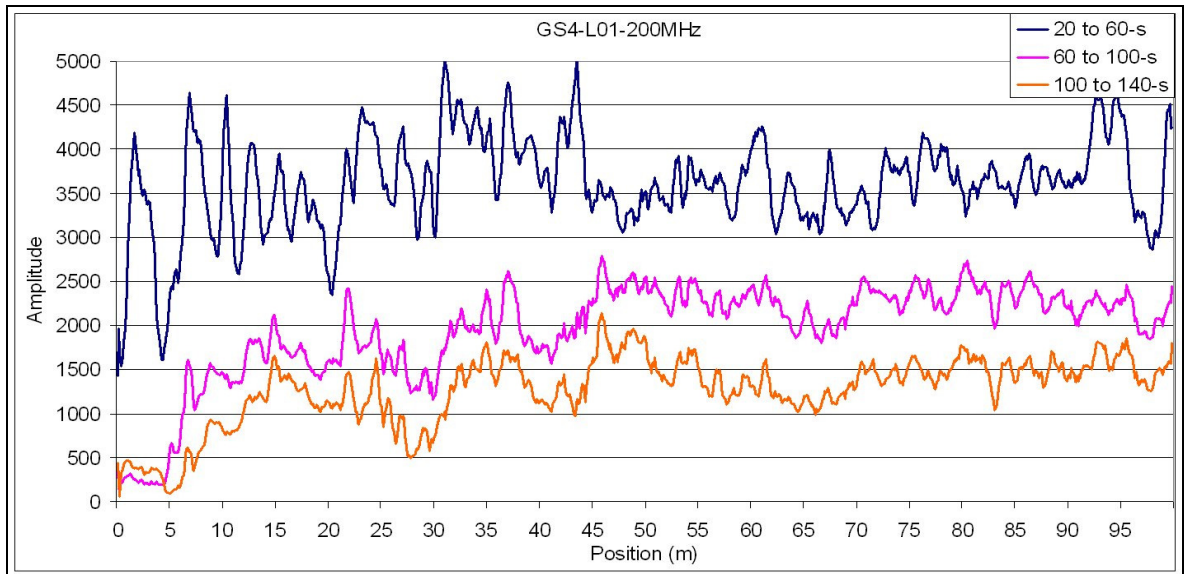


Figure 6.71 – Time-slice analysis for GPR profile GS4-L01-200MHz collected in Site S4.

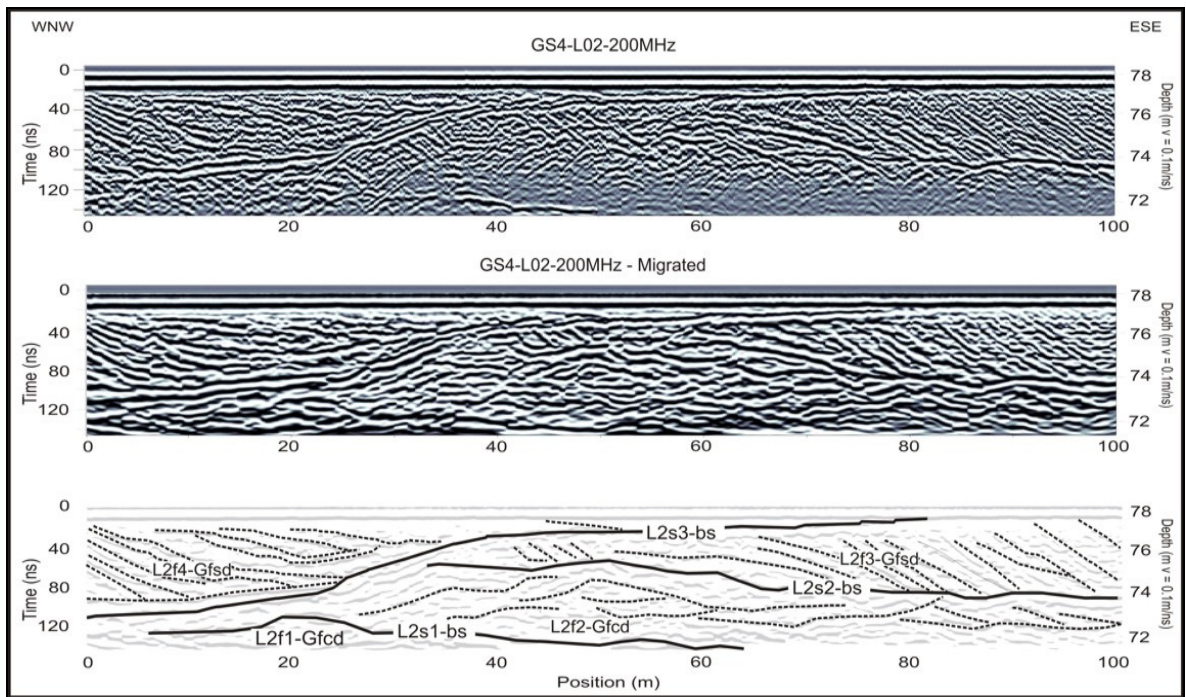


Figure 6.72 – GPR profile GS4-L02-200MHz collected in Site S4. Top – topographically corrected radargram with dewow and AGC Gain. Middle – topographically corrected migrated radargram using a 0.1m/ns velocity. Bottom – Interpretation of the radargram.

6.5 – Site S5

6.5.1 – Introduction

This site forms part of a complex glaciodeltaic system deposited along the northern margin of the Kilcormac Esker (See Map 1). The feature extends northwards for approximately 2Km from the northern end of Kilcormac Esker (E228000, N221000) and it is approximately 5Km wide. A number of exposures recorded in gravel pits in the complex show that the deposits are dominated by well-sorted glaciofluvial sand and gravel (see Kilcormac Esker within section 4.2.2, Chapter 4).

Site 5 occurs on the northwest margin of the glaciodeltaic system and is located in a field on the southwest margin of a 500m elongated mound reaching a maximum height of 72.5m OD. The long axis of the feature runs southwest-northeast and attains a maximum width of 200m. The mound protrudes 10 - 12m above the surrounding landscape and is well drained and dominated by sand and gravel. The more depressed surrounding landscape is dominated by peat on the northwest and the southeast, margins of the feature. Plate 6.6 shows the morphological expression of the mound from its eastern margin.

An exposure (ES5A) in a gravel pit along the northeast edge of the site shows interstratified glaciofluvial sand and gravel with well developed foresets dipping 10° - 15° north-northwest underlain by massive poorly horizontally stratified silty sand forming the bottom sets (see Plate 6.7). This is indicative of sediment deposited in a subaqueous environment, probably evolving into a glaciodelta at the later stages of the development of the feature. However no clear topsets can be observed. The water source may be associated with ice generally withdrawing southwest and related to the Kilcormac Esker.

A borehole (BH-S5A - E224201, N222412) was drilled at the site and it shows soft fine to coarse sand with well rounded limestone pebbles, coarsening downwards, from 0 - 4m. Medium coarse gravelly sand with rounded pebbles occurs 4 - 12.2m. Soft to medium dense fining downwards sand, with very few pebbles occurs 12.2 - 16.8m depth and the sand becomes wet at around 15m depth. Three bulk samples were collected from 2.2 -

3.2m (BH-S5A-1), 7.5 - 8.5m (BH-S5A-2) and 13 - 14m (BH-S5A-3). These have been wet sieved and classified under the Folk (1954) classification scheme. Samples BH-S5A-1 and BH-S5A-3 have been classified as gravelly sand, and sample BH-S5A-2 as sandy gravel. The borehole log and the PSA results are available in Appendix A.

Four GPR radargrams and one resistivity profiles were recorded on the site. An aerial photography of the site with the location of the profiles is presented in Figure 6.73.



Plate 6.6 – Morphological expression of Site S5. Surveyed sand and gravel mound is located at the background. Flat poorly-drained land at the foreground.

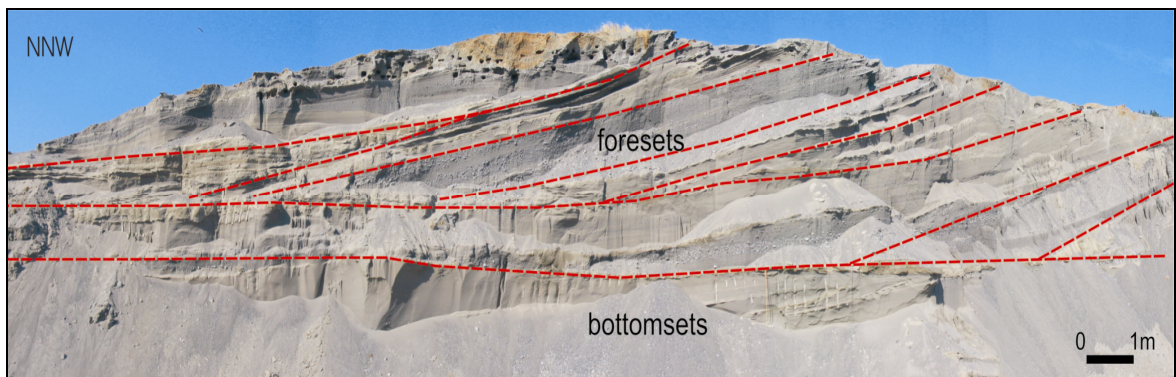


Plate 6.7 – Exposure ES5A located in a gravel pit 100m northwest from site S5. Well developed foresets dipping 8° to 10° north-northwest composed of well-sorted interstratified sand and gravel.

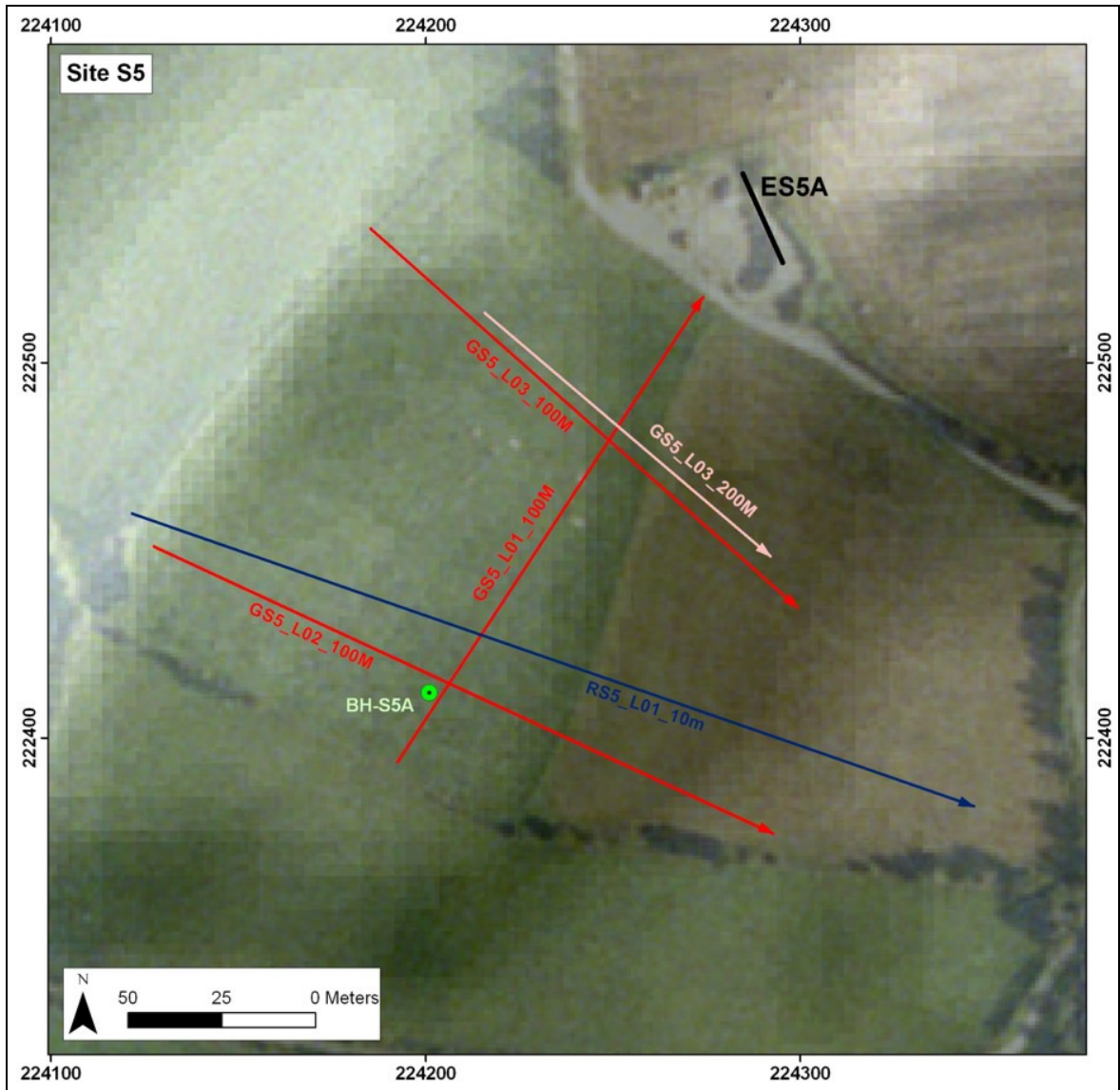


Figure 6.73 – Aerial photography of Site S5 with location and orientation (arrow head indicating end of the profile) of surveyed geophysical profiles. Borehole location is displayed in green, Resistivity profiles are presented in blue, and GPR in red. The exposure ES5A located adjacent to the site is delineated in black.

6.5.2 – Electrical Resistivity Data

One ERT section with 10m electrode spacing was collected in Site S5 using the Wenner-Schlumberger array (RS5-L01-10m). The profile (Figure 6.74) clearly displays a continuous high resistivity area ($>1500\Omega\text{m}$) from 0 - 180m and with thickness ranging 10 - 24m. The area corresponds to the higher ground within the site. This body has been depicted at around 100m within the profile by BH-S5A as sandy gravel and gravelly sand.

Sand and gravel is underlain by a large area dominated by low resistivity values ($>400\Omega\text{m}$) which reaches the surface from 180 - 230m and corresponds with the relatively lower, poorly drained ground and composed of diamicton. The contact between these two resistivity layers seems to be gradational at some points. This may be related to the existence of an increase in the wetness of the sediments detected in BH-S5A at around 15m depth. Finally, a change in resistivity values occurs as a subhorizontal layer at around 40m depth from 90 - 150m. Resistivity values below the contact range 1400 - 1800 Ωm are interpreted as limestone bedrock underlying diamicton.

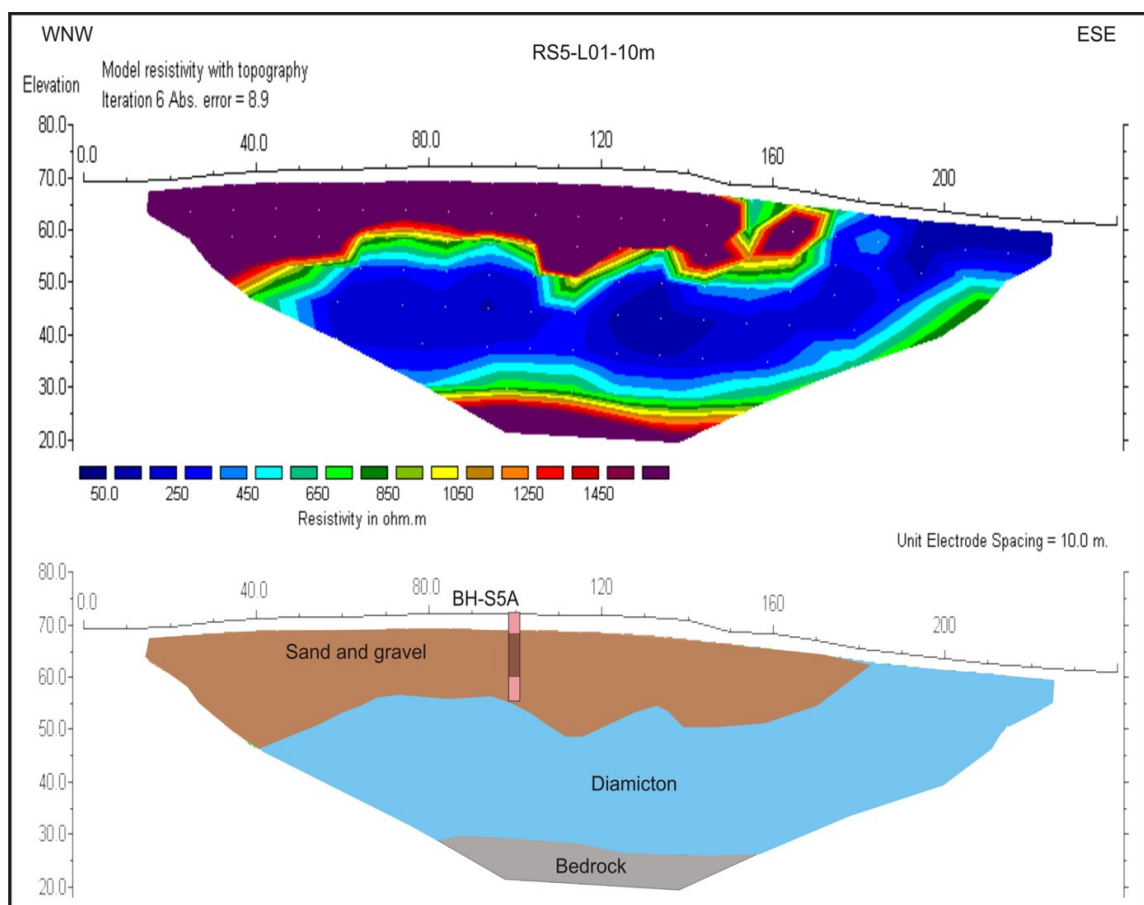


Figure 6.74 – Electrical Resistivity profile RS5-L01-10m collected in Site S5 and its interpretation.

6.5.3 – Ground Penetrating Radar (GPR)

A total of four GPR profiles were collected in this site. Three profiles, two collected with a 100MHz antenna and one with 200MHz, were taken across the shorter axis to yield cross-sections and one along the feature's long axis.

Line **GS5-L01-100MHz** is a 150m long profile running southwest to northeast, parallel to the feature's long axis. The profile topographically corrected and its interpretation is presented in Figure 6.75. Maximum penetration was of the order of 9m. From 0 - 50m the profile displays a series of sinuous, subparallel to oblique, discontinuous reflectors (L1f2-Gfc). A wide homogeneous feature occurs 50 - 100m, it is delineated by a series of parallel, continuous strong reflectors, gently dipping towards the centre of the feature on the edges and planar in the central part (L1f2-Gfpd). A series of dipping chaotic, curved reflectors occur on the right margin of this feature from 100 - 130m (L1f2-Gfc). A channel-like feature with a continuous concave strong reflector delineating its base, probably due to erosional contact has been depicted at 120 - 150m. Moderately continuous sinuous reflectors occur within the channel-like feature (L1f3-Gfcd) and it is underlain by a featureless zone where penetration by the GPR signal is negligible. This zone is almost certainly dominated by silt/clay.

Time slice analysis for this radargram shows three main sections with differentiated amplitude signatures (Figure 6.76). The sector from 0 - 50m is characterized by high amplitudes with a number of peaks and valleys indicating rapid lithological changes through the section, the three time slices show a similar pattern. The amplitude values from 50 - 110m drop gently towards the north; this is possibly due to an increase of the attenuation rate, which may be related to a gradual fining. Finally, the amplitude rises for the top time slice (60 - 100ns) from 110 - 150m and drops for the other two (100 - 140ns and 140 - 180ns), this may be interpreted as presence of reflective well-sorted sand and gravel on the top 3 - 4m overlying sediments with a high attenuation rate, probably silt/clay.

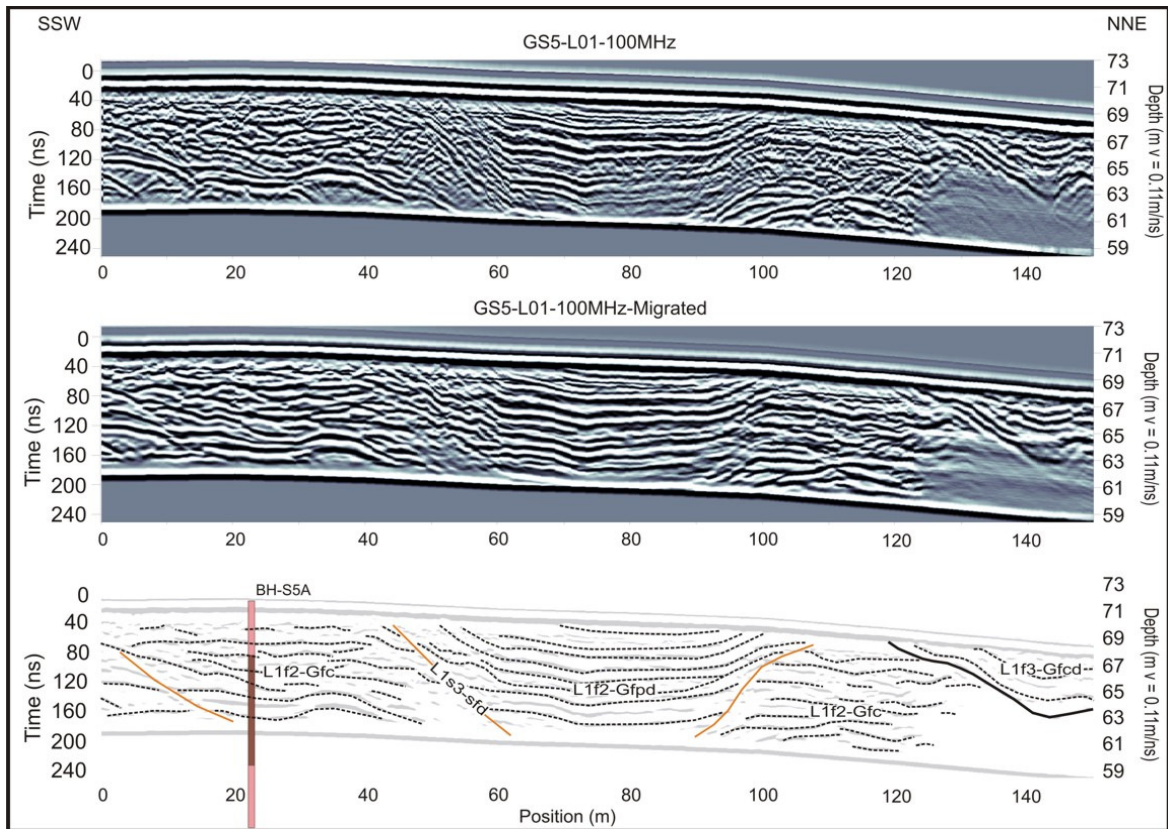


Figure 6.75 – GPR profile GS5-L01-100MHz collected in Site S5. Top – topographically corrected radargram with dewow and AGC Gain. Middle – topographically corrected migrated radargram using a 0.11m/ns velocity. Bottom – Interpretation of the radargram.

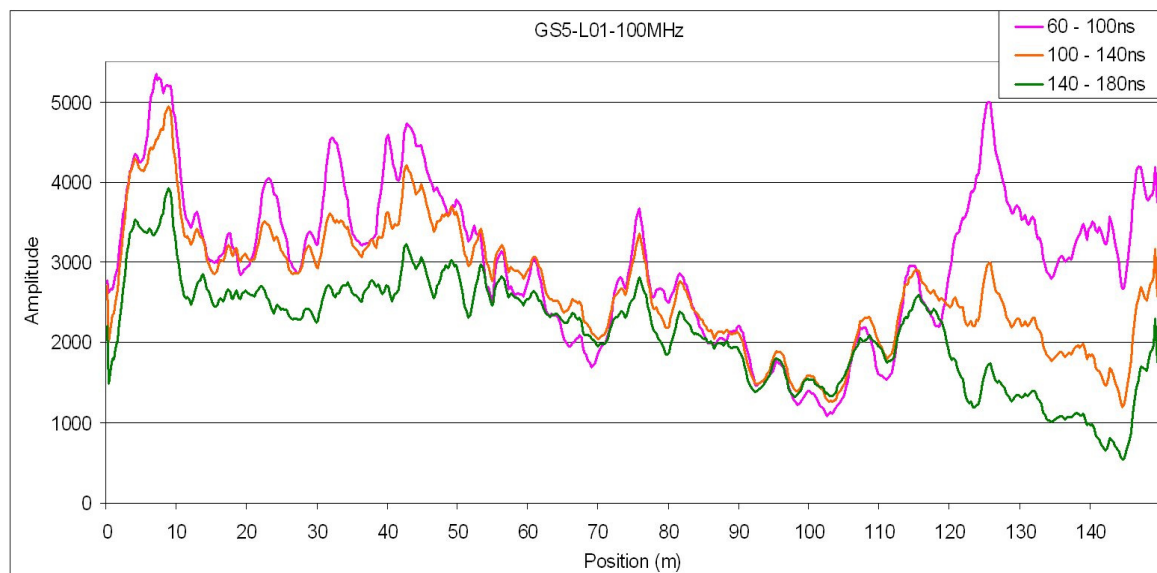


Figure 6.76 – Time-slice analysis for GPR profile GS5-L01-100MHz collected in Site S5.

Line **GS5-L02-100MHz** consists of a 190m profile running northwest to southeast across the long axis of the mound. Figure 6.77 displays the profile topographically corrected, processed and interpreted. A number of sigmoidal, tangential, continuous, dipping 15° - 20° northwest reflectors have been interpreted as foresets along the profile from 0 - 130m (L2f2-Gfs). The dips of the foresets are slightly higher than the ones on the exposure (Plate 6.7), probably due to the slight variation on the orientation of the exposure versus the profile. The foresets occur continuously along the profile as far as a convex change in slope at 130m. Several sinuous, subparallel, moderately continuous reflectors dipping approximately 30° southeast occur 130 - 170m. These have been interpreted as foresets obliterated by normal faults caused by the collapse of the mound subsequent to ice withdrawal (L2f2-Gfsd). The sediments, composing the mound, were probably partially supported by the ice sheet. A continuous reflector subparallel to the topography dipping 5° - 10° south-eastwards has been interpreted as the water-table occurring 5 - 10m from the surface. In humid areas, the water-table generally follows the shape of the surface topography (Fetter, 1980).

Two additional inline radargrams have been recorded in this site, **GS5-L03-100MHz** and **GS5-L03-200MHz** (Figures 6.78 and 6.79) using 100MHz and 200MHz antennae. The 200MHz profile shows a higher resolution profile of the 100MHz radargram from 40 - 140m. These radargrams are approximately 100m apart from L02, run subparallel to it and show similar radar facies. Three main radar facies have been differentiated for profile GS5-L03-100MHz. Moderately continuous subparallel reflectors located 0 - 90m at 5 - 6m from the surface have been interpreted as bottomsets (L3f1-Gbs). These are overlain with a downlap contact by various sigmoidal, tangential, continuous reflectors dipping 10° - 15° west-northwest, which have been interpreted as foresets (L3f2-Gfsd) that suffer some deformation in their east-southeast margin. The foresets are partially overlain with an erosive contact by curved concave moderately continuous reflectors, which have been interpreted as cross bedded sediments (L3f3-Gfcd). These sediments are distorted by a number of normal faults dipping 20° - 30° east-southeast prompted by collapse of ice supported sediment, which indicates as inferred in L02 that this is an ice marginal slope. The water-table or a clear change of the sediments moisture content has been identified at

90 - 150m running subparallel to the topography at around 6m depth. Data collected with the 200 MHz antenna show similar results with a higher resolution but lower penetration. It has been especially useful in detecting the faulting planes and the boundary between facies f1 and f2.

The radargrams for profiles GS5-L01-100MHz, GS5-L02-100MHz and GS5-L03-100MHz are presented as a fence diagram in Enclosure 2 – E2D.

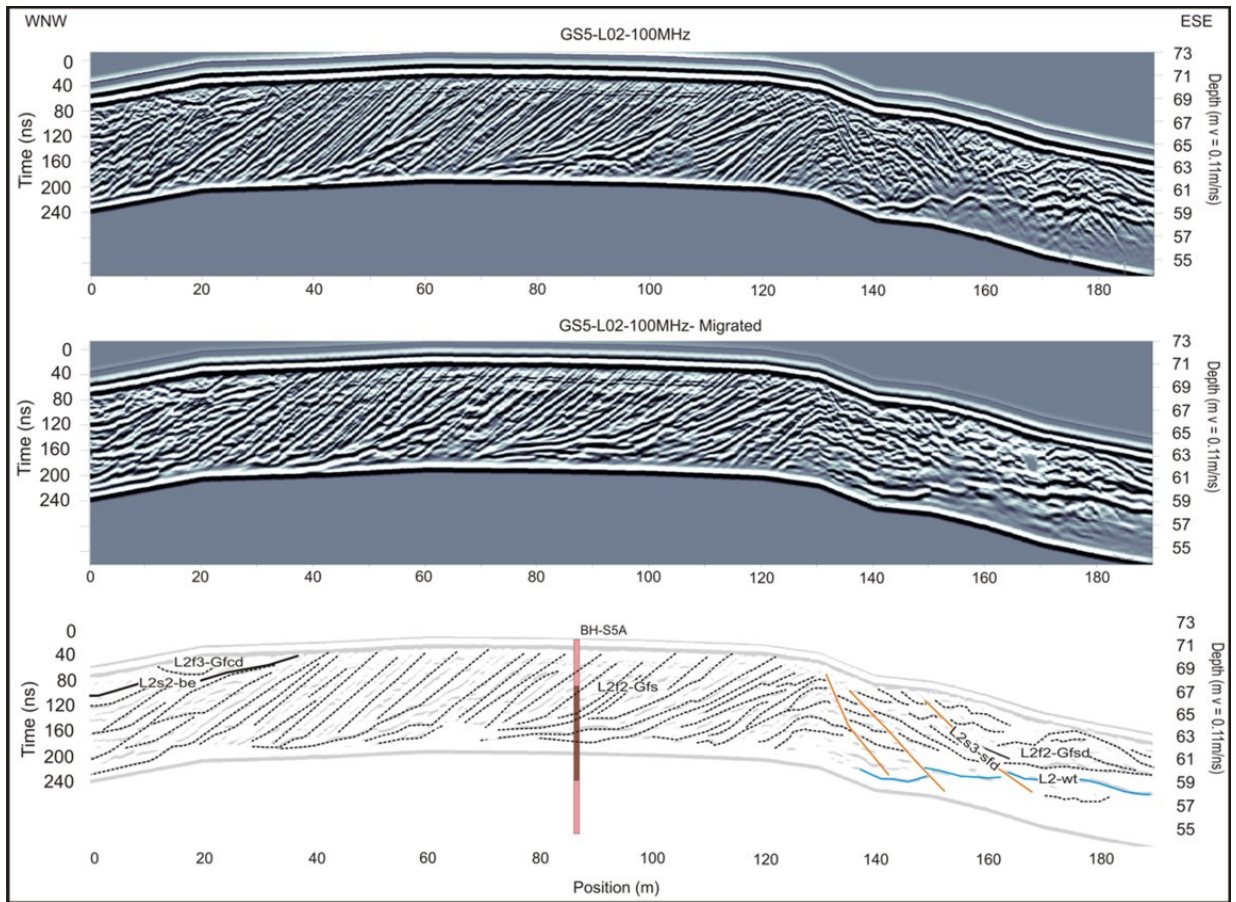


Figure 6.77 – GPR profile GS5-L02-100MHz collected in Site S5. Top – topographically corrected radargram with dewow and AGC Gain. Middle – topographically corrected migrated radargram using a 0.11m/ns velocity. Bottom – Interpretation of the radargram.

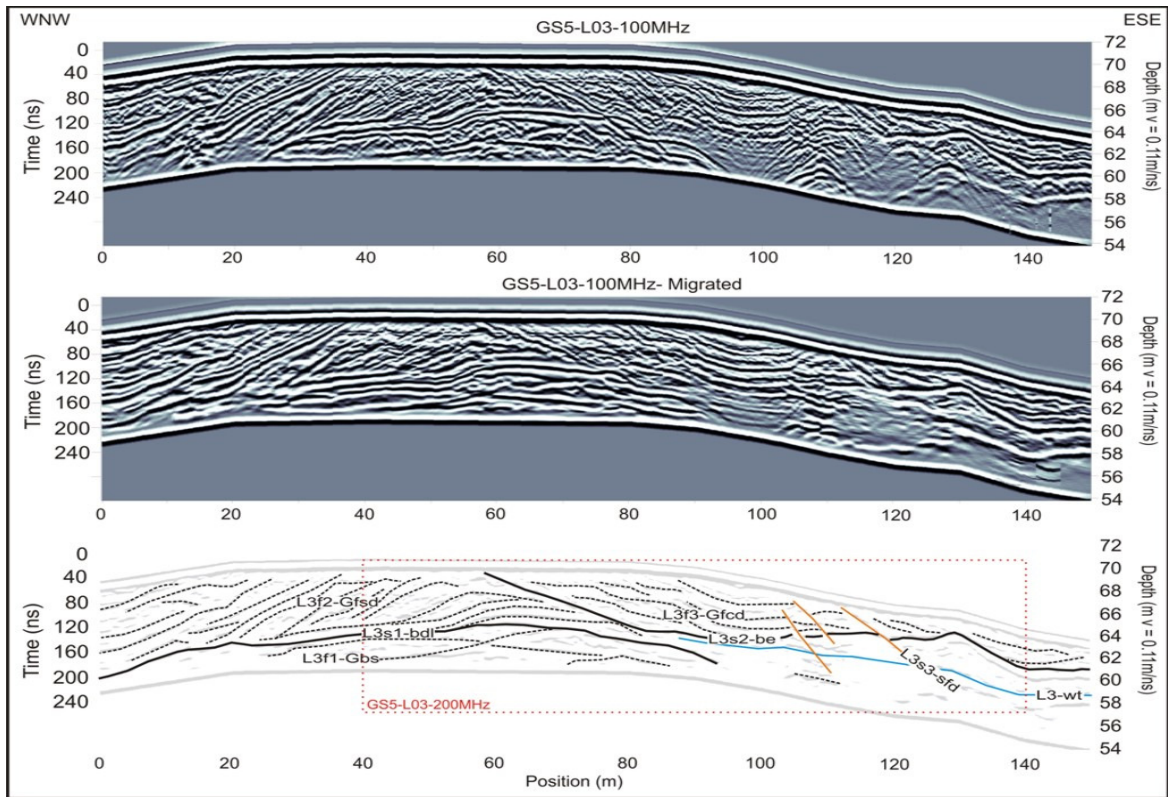


Figure 6.78 – GPR profile GS5-L03-100MHz collected in Site S5. Top – topographically corrected radargram with dewow and AGC Gain. Middle – topographically corrected migrated radargram using a 0.11m/ns velocity. Bottom – Interpretation of the radargram.

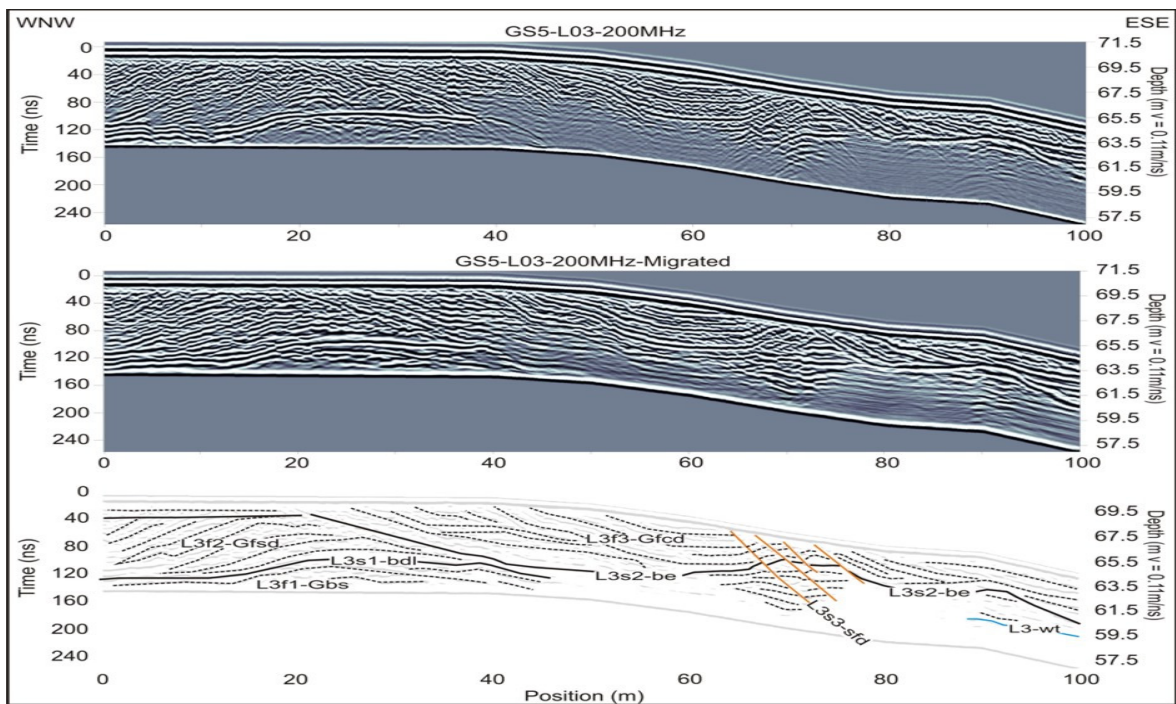


Figure 6.79 – GPR profile GS5-L03-200MHz. Top – radargram with dewow and AGC Gain. Middle – migrated radargram using a 0.11m/ns velocity. Bottom – Interpretation of radargram.

6.6 – Site S6

6.6.1 – Introduction

Site S6 (E226700, N226900) is located 5.5Km south of Clara (Figure 6.1), on top of the Ballyduff Esker complex, which was described in detail in Chapter 4, section 4.2.2. A number of exposures recorded along this feature show glaciofluvial sand and gravel derived from limestone rocks as the dominant lithologies. The Esker complex widens at Site 6 for about 2.5Km. It is up to 200m in width and reaches a maximum altitude of 72m OD within the site. The feature becomes wider and higher east of Site S6, reaching a maximum width of 600m and a maximum altitude of 83m OD on Trumpet Hill, located 800m east of the site (see Map 1).

The field site occurs in an area with an average relative height 20m above the surrounding landscape. The width of the feature at this point is approximately 400m. The esker ridge is here bounded by a steep convex slope to the north, sloping 15° - 20° and by gentle convex slopes to the south ranging 1° - 5°. The feature gently increases in elevation eastwards along the site.

A borehole (BH-S6A - E226965, N226741) was drilled on the site as part of this thesis. It shows medium dense sandy gravel with subangular to rounded limestone pebbles fining downwards to silt and clay with pebbles from 0 - 3m. Soft yellow-brown fine sand with subrounded limestone pebbles develops into sandy gravel coarsening downwards as far as 6m depth. Very soft brown-bluish medium-coarse sand with very few rounded pebbles becomes finer downwards into dense silty gravelly sand as far as 12m, which changes to coarse sand from 12 - 12.8m. Medium dense to dense fine to medium sand with few pebbles dominates from 12.8m. The borehole terminated in dense sediments at 16.5m due to technical problems. Three bulk samples were collected, wet sieved and classified under the Folk (1954) classification scheme. BH-S6A-1 was collected from 3.6 - 4.2m and has been classified as muddy sandy gravel; BH-S6A-2 and BH-S6A-3 gathered from 6 - 6.9m and 12.8 - 13.8m, respectively, are categorized as gravelly muddy sand. The borehole log and the PSA graphs are shown in Appendix A.

The objective at this site was to characterize the internal architecture of the sediments composing a large esker ridge at this point and to identify the potential presence of glaciofluvial sediments overlying the core of the esker and their direction of deposition. Surveying was confined to GPR at this site as the interest was focused on the internal architecture of the sediments.

6.6.2 – Ground Penetrating Radar (GPR)

Three GPR profiles with different orientations, intersecting each other at the borehole location, have been collected in the site (Figure 6.80).

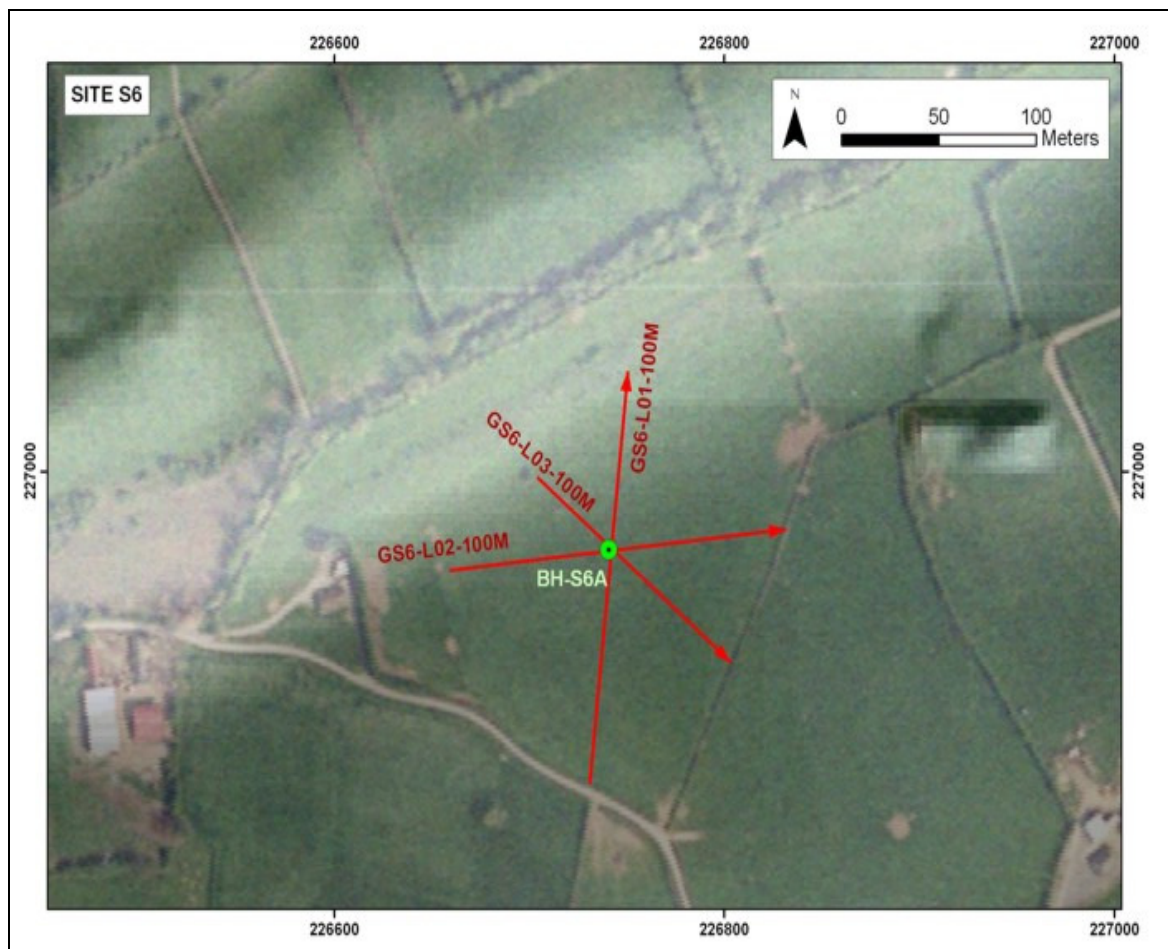


Figure 6.80 – Aerial photograph of Site S6 with location and orientation (arrow head indicating end of the profile) of surveyed geophysical lines. Borehole location is displayed in green. GPR profiles are presented in red.

Line **GS6-L01-100MHz** runs approximately transverse to the esker ridge's long axis from south to north for 180m. A complex sedimentological setting arises from the interpreted profile (Figure 6.81). Several moderately continuous, sinuous, subhorizontal reflectors have been detected at 0 - 60m, which have been interpreted as sedimentological boundaries. These reflectors are truncated by three moderately continuous subparallel reflectors dipping 20° - 30° south, which are interpreted as normal faults indicating collapse of deposits originally supported by ice located at their south margin (L1f2-Gfcd). A set of moderately continuous, subparallel reflectors dipping 10° - 20° north were interpreted as foresets (L1f2-Gfsd) at 60 - 100m. These foresets overlap the oblique chaotic reflectors with an onlap contact, which are represented by a large number of hyperbolic reflections in the non-processed profile. The latter have been interpreted as boulders, probably forming the core of the esker ridge (L1f1-Gfm). Overlying these deposits with an erosive contact, a 2m thickness layer occurs from 80 - 170m. It is composed of a set of discontinuous subparallel reflectors dipping 20° south and interpreted as foresets associated with the development of a meandering channel with its centre at 90 - 110m (L1f3-Gfch).

Line **GS6-L02-100MHz** (Figure 6.82) runs west to east for 170m and the profile encompasses three main radar facies. The area 100 - 170m, dominated by moderately discontinuous reflectors dipping to both east and west, has been classified as massive sand and gravel (L2f1-Gfm). The section 0 - 100m at depths of more than 1m is dominated by moderately discontinuous wavy reflectors, which have been interpreted as cross-stratified sediments (L2f2-Gfcd) which are overlain from 0 - 140m by a shallow, 1 - 2m thick channel feature previously described in L01 (L2f3-Gfch). Subhorizontal reflectors in L02 in radar facies L2f2 and L2f3 are depicted in L01 as reflectors dipping south in facies L1f3 and dipping north in L1f2. This indicates that L02 runs subparallel to the strike of the dipping planes.

Line **GS6-L03-100MHz** (Figure 6.83) is again dominated by three main radar facies. The zone between 0 - 70m is characterised by moderately continuous wavy reflectors gently dipping southeast from 0 - 40m and gently dipping northwest from 40 - 70m. The area between 70 - 130m shows a number of moderately continuous reflectors dipping 15°

southeast. These have been interpreted as massive glaciofluvial sediments (L3f1-Gfm) evolving into more clearly dipping deformed reflectors (L3f2-Gfsd) towards the southeast. A continuous reflector running from 0 - 60 between 0 - 2m depth overlies these deposits. The sediments overlying the reflector are composed of a set of discontinuous subparallel reflectors dipping 15° southeast (L1f3-Gfch). These have been interpreted as the same foresets depicted in L01. Finally, a subhorizontal discontinuous reflector parallel to the surface occurs at about 6m. This reflector, running subparallel to the surface, has been depicted in all three surveyed profiles and could be interpreted as the water-table or a change in moisture content.

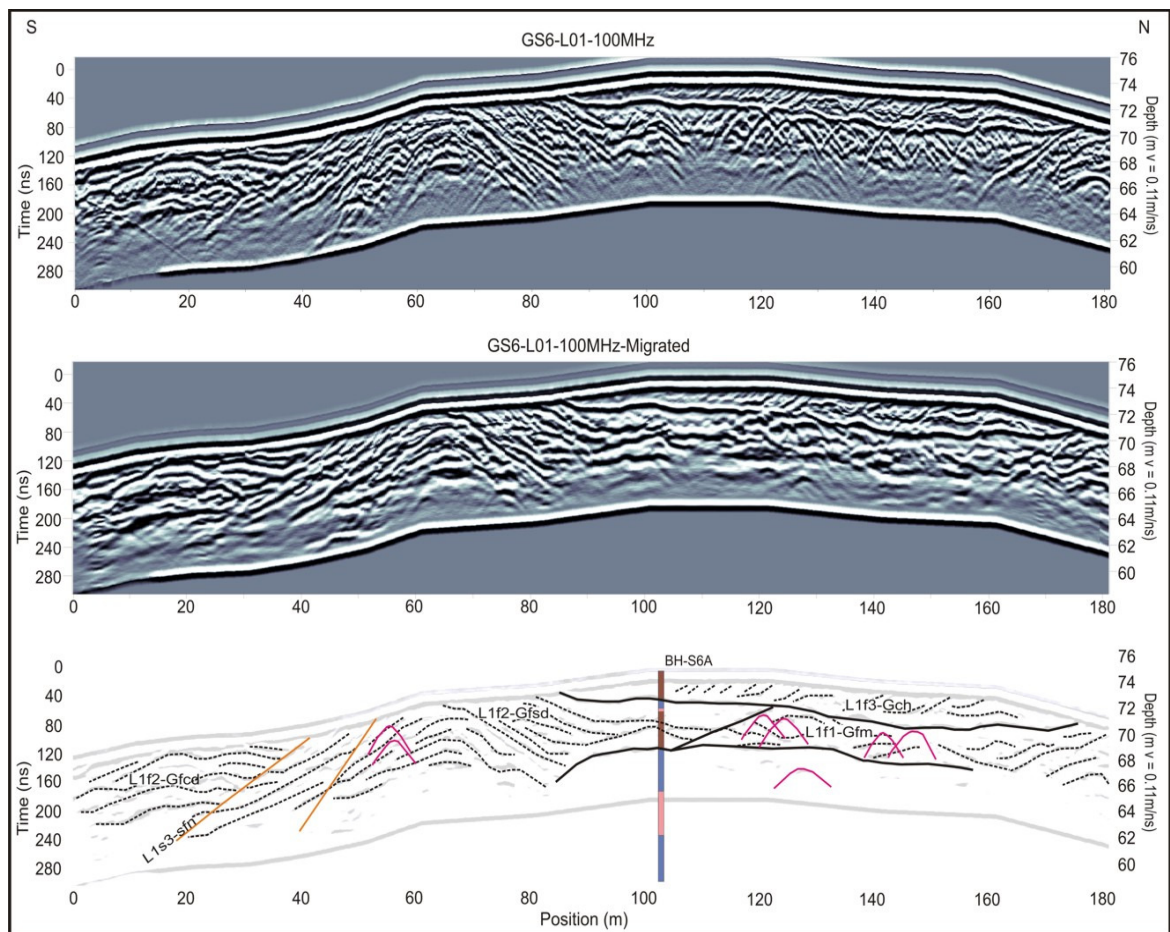


Figure 6.81 – GPR profile GS6-L01-100MHz collected in Site S6. Top – topographically corrected radargram with dewow and AGC Gain. Middle – topographically corrected migrated radargram using a 0.11m/ns velocity. Bottom – Interpretation of the migrated radargram.

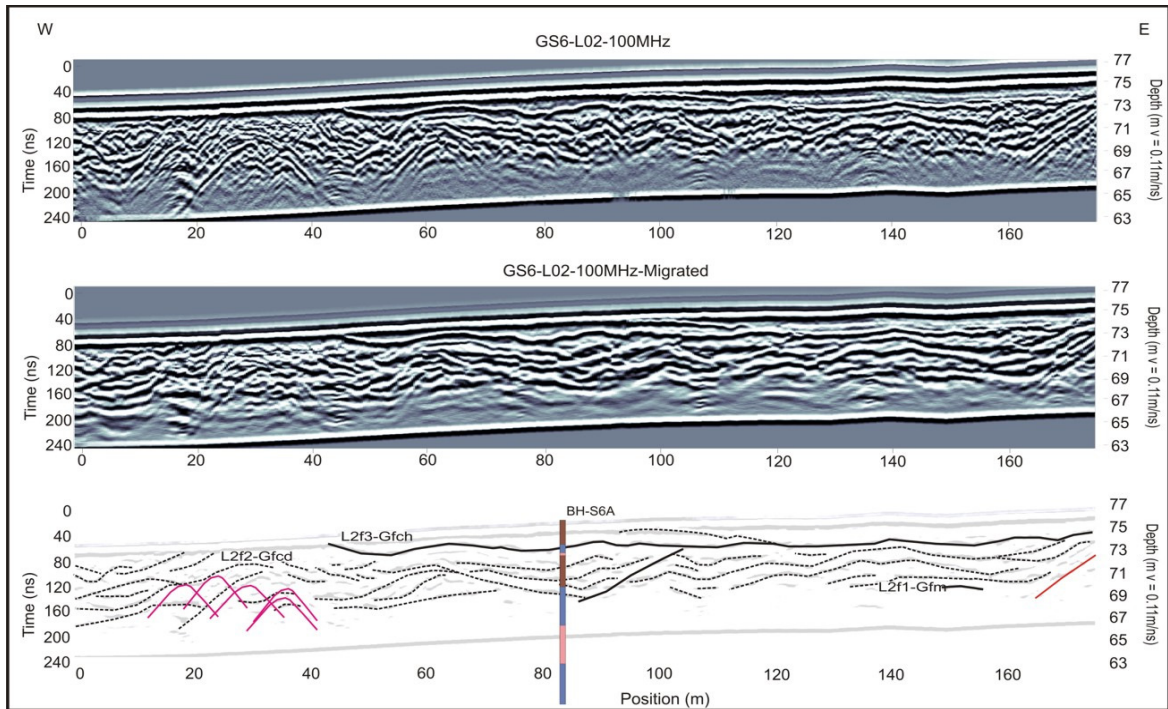


Figure 6.82 – GPR profile GS6-L02-100MHz collected in Site S6. Top – topographically corrected radargram with dewow and AGC Gain. Middle – topographically corrected migrated radargram using a 0.11m/ns velocity. Bottom – Interpretation of the radargram.

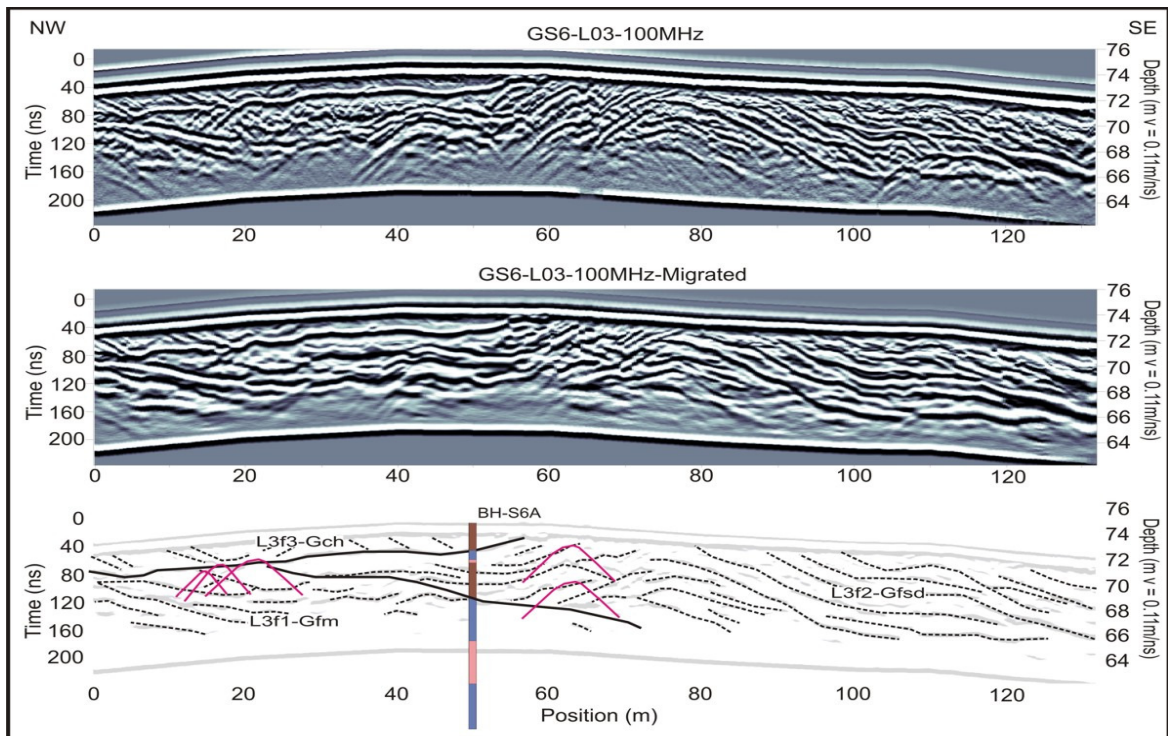


Figure 6.83 – GPR profile GS6-L03-100MHz collected in Site S6. Top – topographically corrected radargram with dewow and AGC Gain. Middle – topographically corrected migrated radargram using a 0.11m/ns velocity. Bottom – Interpretation of the radargram.

6.7 – Site S7

6.7.1 – Introduction

Site S7 is located 2Km west of Daingean, along the Royal Canal (Figure 6.1). This site is one of the potential glacial lake overflow channels running east-northeast across the Shannon - East Basin watershed (See Map 1). This has been identified during the field mapping exercise as one of the lowest channels cutting across the watershed indicating a potential glacial lake overflow level of 83m OD.

Two exposures (ES7A and ES7B) have been recorded in the area (Figure 6.84). ES7A is located along a road cutting 250m south of the resistivity profile; it shows 1m of peat overlying 0.5m of grey silty diamicton with limestone angular-subangular pebbles with some Old Red Sandstone pebbles (see Plate 6.8). ES7B is located 350m north of the resistivity profile. It is a 1m thick exposure along a ditch showing a well consolidated pale brown silty clayey diamicton with limestone (dominant), sandstone and chert pebbles.



Figure 6.84 – Aerial photograph of Site S7 with location and orientation (arrow head indicating end of the profile) of surveyed geophysical lines and exposure ES7A.



Plate 6.8 – Exposure ES7A located 250m southwest from ERT profile L01.

The objective at this site was to identify the main lithological changes and to detect the surficial sediment thickness variation occurring along the channel. Low resolution ERT survey was considered sufficient for this purpose.

6.7.2 – Electrical Resistivity Data

Two inline resistivity profiles at 10m electrode spacing running southwest-northeast along the Royal Canal were collected at Site S7 (Figure 6.84) using the Wenner-Schlumberger array (**RS7-L01-10m** and **RS7-L02-10m**). The profiles have been concatenated into a 480m long line and presented as a single entity. Topographic variation along them is minimal compared to the surrounding landscape, with an average altitude of 83m OD; consequently, topographic correction has not been necessary. The inverse model and its interpretation are presented in Figure 6.85. The profile is dominated by pockets of very low resistivity values (less than 100 Ω m) along the surface interpreted as thin coatings of peat. These pockets are underlain by low to medium resistivity values (100 - 600 Ω m)

interpreted as silty clayey diamicton recorded in the exposures ES7A and B. These sediments would be saturated as the water-table is marked by a stream cutting across the profile and draining into the Royal Canal at 1m depth. The diamicton varies in thickness between a minimum of 3m to a maximum of 15 - 20m in the area between 120 - 280m. This is underlain by high resistivity values reaching maximums of 6,000Ωm, which have been interpreted as limestone bedrock. A section 120 - 320m at 12 - 20m depth is possibly weathered bedrock. It can be inferred from the profile that the basement of the channel feature is infilled by fairly thick diamicton, probably with similar composition to exposures ES7A and B.

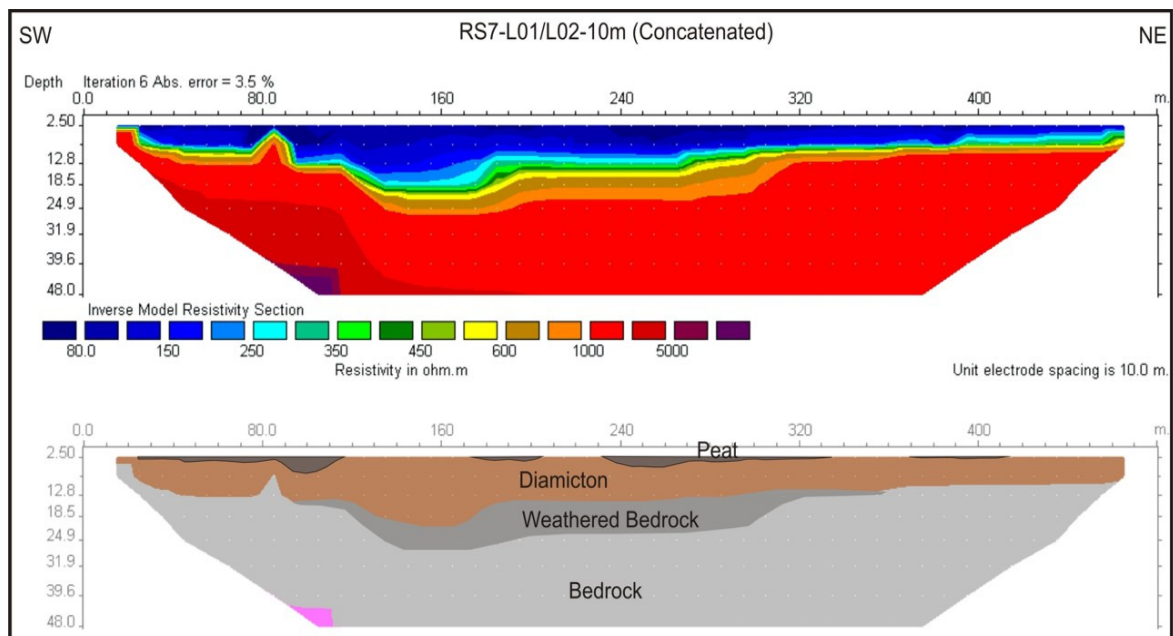


Figure 6.85 – Concatenated Electrical Resistivity profiles RS7-L01-10m and RS7-L02-10m collected in Site S7 with and their interpretation.

6.8 – Site S8

6.8.1 – Introduction

A number of low topographic ridges with their long axis running north-south are located along the road between Tullamore and Ballinagar (see Map 1). The area is dominated by a thin coating of diamicton overlying Lower Carboniferous limestone bedrock, which outcrops in a number of localities. These morphological features have been interpreted in Chapter 4 as recessional moraines related to an ice sheet retreating westwards in this area.

One of these moraines was chosen to characterise their lithological composition, thickness and internal structure. The feature selected for geophysical surveying is a discontinuous ridge running north-south for 1Km; its width in the study area is approximately 130m and it reaches a maximum height of 4m above the surrounding landscape (Plate 6.9). The land along the crest of the feature is well-drained compared to the lower areas. No exposures are available within the site; the closest reference with respect to the composition of the subsurface is a 0.7m high exposure on a morainic ridge located 1Km east of the site. The exposure is composed of well-consolidated silty sandy diamicton with subangular limestone cobbles and pebbles and a few sandstone pebbles (ES8A – Plate 6.10).

An ERT and a GPR profiles have been collected across the feature with the objective of defining its lithological composition, the change in glacial sediment thickness between the lower and the higher ground and its internal architecture (Figure 6.86).



Plate 6.9 – Photograph of site S8. Low, poorly-drained ground in the foreground gradually changes into well-drained higher ground. Tape running across the ridge indicates position of the GPR line.



Figure 6.86 – Location of Electrical Resistivity (blue) and GPR (red) profiles surveyed in Site S8 and exposure ES8A.



Plate 6.10 – Exposure ES8A showing diamicton with subangular/subrounded pebbles and cobbles.

6.8.2 – Electrical Resistivity Data

Line **RS8-L01-10m** at 10m electrode spacing was collected using the Wenner-Schlumberger array (Figure 6.87). Low to medium electrical resistivity values (less than $400\Omega\text{m}$) dominates the top 3 - 9m depth, which has been interpreted as diamicton, probably composed of silty sandy matrix as recorded in exposure ES8A. Surficial sediment thickness increases gradually from east to west and the top 6 - 8m of the profile are dominated by diamicton from 0 - 110m. The ridge-top occurs 110 - 160m, diamicton thickness gradually decreases from west to east. The area between 160 - 240m, located east from the ridge is dominated by very thin diamicton overlying bedrock. A layer showing medium to high resistivity values ($400 - 2000\Omega\text{m}$) occurs from 0 - 160m, which is 7m thick and gradually pinching off eastwards, has been interpreted as weathered bedrock. These two layers are underlain by high resistivity values ($>2000\Omega\text{m}$), which has been interpreted as bedrock. The thickest accumulation of surficial sediments occurs on the stoss side of the ridge, assuming that the ice sheet re-advances eastwards. It is inferred from these results that the ridges could be partially controlled by the shape of the bedrock underlying the surficial sediments.

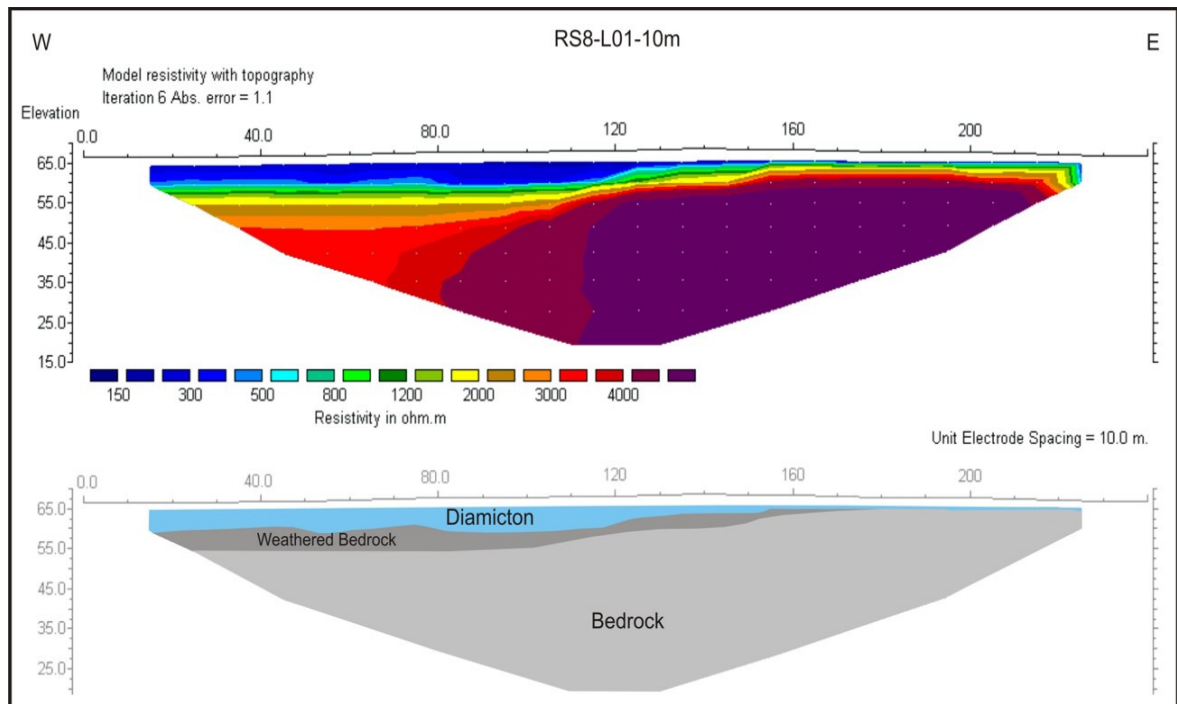


Figure 6.87 – Electrical Resistivity profile RS8-L01-10m collected in Site S8 and its interpretation.

6.8.3 – Ground Penetrating Radar (GPR)

Line **GS8-L01-100MHz** is a 200m long profile running across the ridge from east to west, (Figure 6.88). The crest of the ridge is located at around 100m. A 300ns time window was used for data collection and the maximum depth of penetration attained in this radargram is around 7m. The velocity of the radargram used to estimate depth has been calibrated from hyperbolae reflections in the profile at 0.11m/ns (Figure 6.89a). The non-processed radargram shows a large number of very wide hyperbolic reflections following the topography at around 115ns depth. These reflections are artefacts caused by large trees located parallel to and 17m from the survey line (Plate 6.9). The shape of the hyperbolae agrees with a 0.285 m/ns velocity (Figure 6.89b). In order to eliminate these reflections the radargram has been migrated using a velocity of 0.285 m/ns. Aside from these artefacts, a subhorizontal moderately continuous reflector at around 62.5m OD running along the whole profile has been interpreted as the water-table. This water level agrees with the water recorded along a ditch running north to south at the west end of the site. A number of discontinuous reflectors dipping 5 - 10° west are interpreted as thrust planes associated with an ice sheet pushing eastwards/north-eastwards during an ice readvance stage.

Time slice analysis data for this radargram (Figure 6.90) has a symmetric shape with a high reflectivity in its middle. The profile can be separate into three sections based on amplitude signatures. The first section runs from 0 - 82m, the amplitude gradually drops eastwards with a relatively higher amplitude between 20 - 40m and a sudden drop on the 70 - 82m stretch. The middle section, 82 - 120m, shows a sharply defined increase in the amplitude values, probably related to a sudden lithological change. This coincides with the higher part of the morainic ridge. The 120 - 200m section of the radargram starts with a sudden drop in the amplitude values, possibly related to high silt/clay contents attenuating the EM waves; the amplitude values then gradually increase to 150m and decrease again from 150 - 190m.

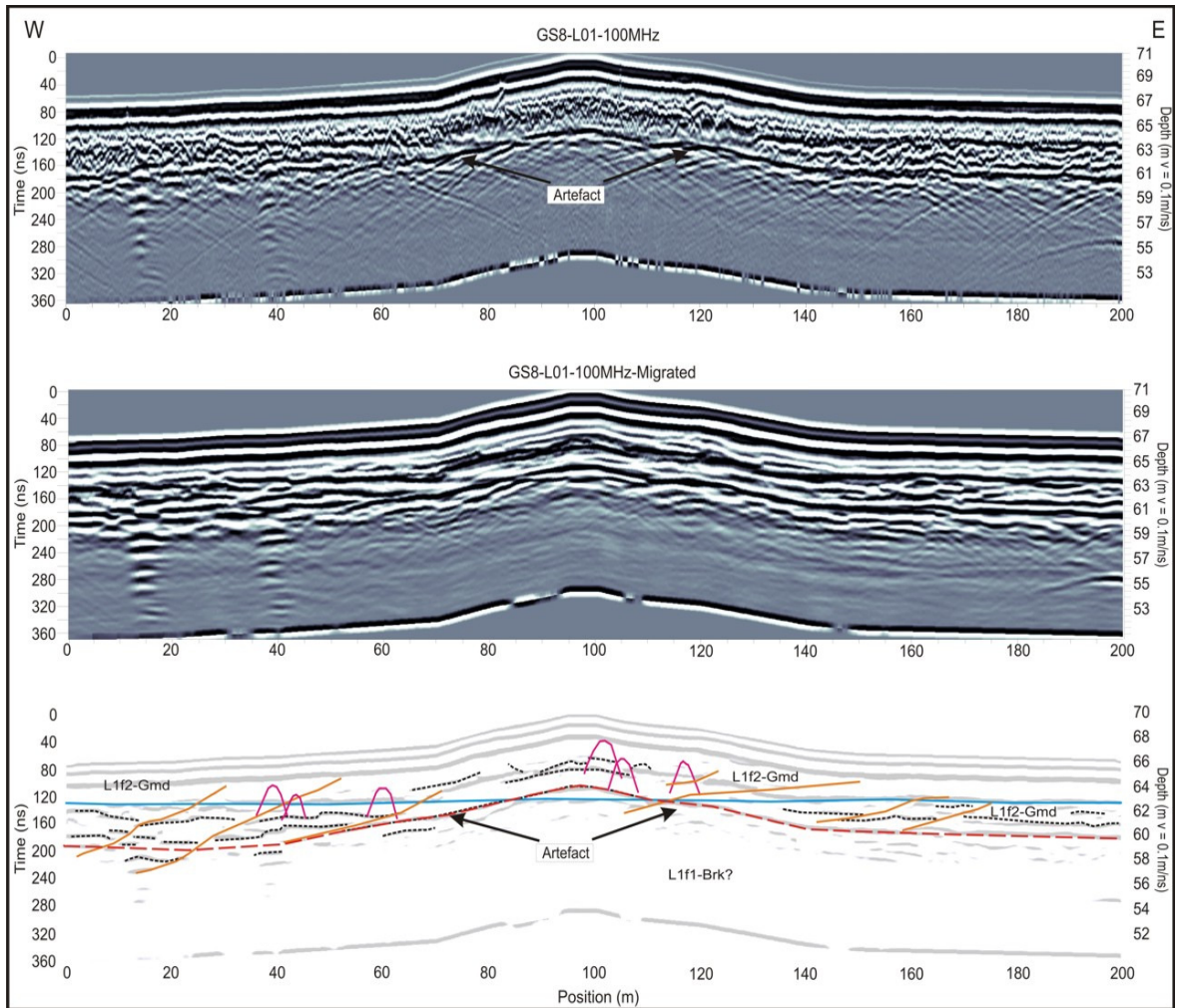


Figure 6.88 – GPR profile GS8-L01-100MHz collected in Site S8. Top – topographically corrected radargram with dewow and AGC Gain. Middle – topographically corrected migrated radargram using a 0.11m/ns velocity. Bottom – Interpretation of the radargram. Tentative water level in blue.

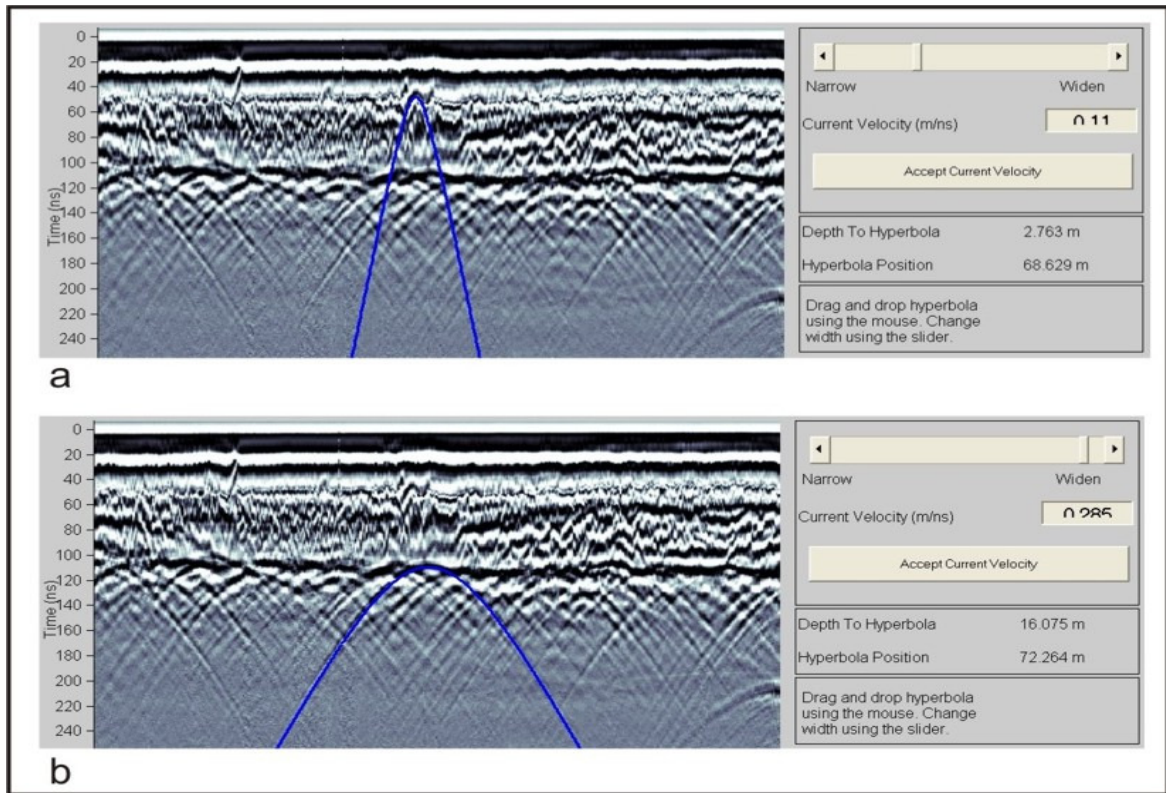


Figure 6.89 – GPR profile velocity calibration using hyperbolae reflections. (a) Velocity of the subsurface calibrated at 0.11m/ns. (b) Hyperbolae at 115ns show a velocity of 0.285m/ns.

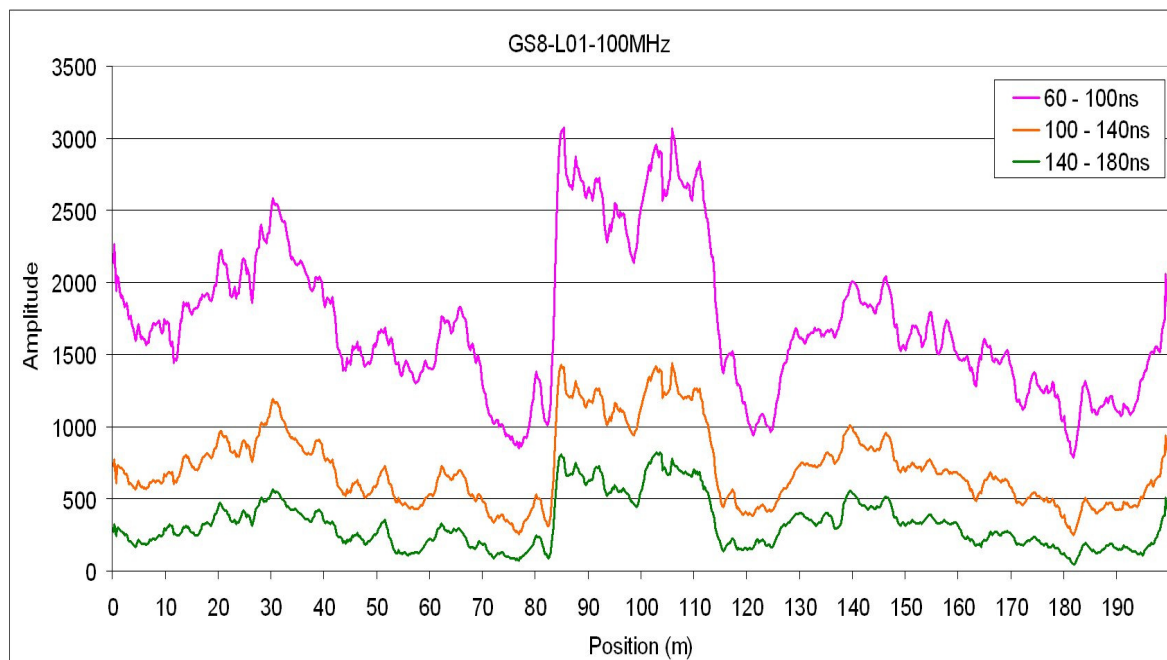


Figure 6.90 – Time-slice analysis for GPR profile GS8-L01-100MHz collected in Site S8.

6.9 – Site S9

6.9.1 – Introduction

Site S9 is situated in the northeast quadrant of the study area (Figure 6.1). It is located in a peat bog, 2Km south from Tyrrelspass, on the watershed between the Shannon and the Barrow/Boyne Basins, along one of the meltwater channels running eastwards across the watershed, see Map 1. It is expected that a cross-section of the channel using GPR will provide information on the peat thickness and the minimum altitude of subglacial sediments or bedrock along the watershed which would correspond with the water level of Glacial Lake Riada, when this channel was acting as the main outlet (Pellicer and Warren, 2005). This will assist in the reconstruction of a more accurate evolutionary model for the study area. The peat bog is currently being harvested on an industrial scale by Bord na Mona. A number of ditches are cut across the bog in a SSW-NNE direction for draining purposes (see Plate 6.11). The site is generally flat with very little topographic variation ranging 93 - 95m OD. A small exposure recorded in a 3m deep ditch running along the northern edge of the bog shows 1m of peat overlying glaciofluvial massive coarse gravel with sandy matrix.



Plate 6.11 – View of Site S9 from the southern margin of the collected datasets.

Location of ERT and GPR surveys is presented in Figure 6.91. It was intended to identify the peat thickness, the lithological composition of the underlying sediments and the morphology of the underlying bedrock.

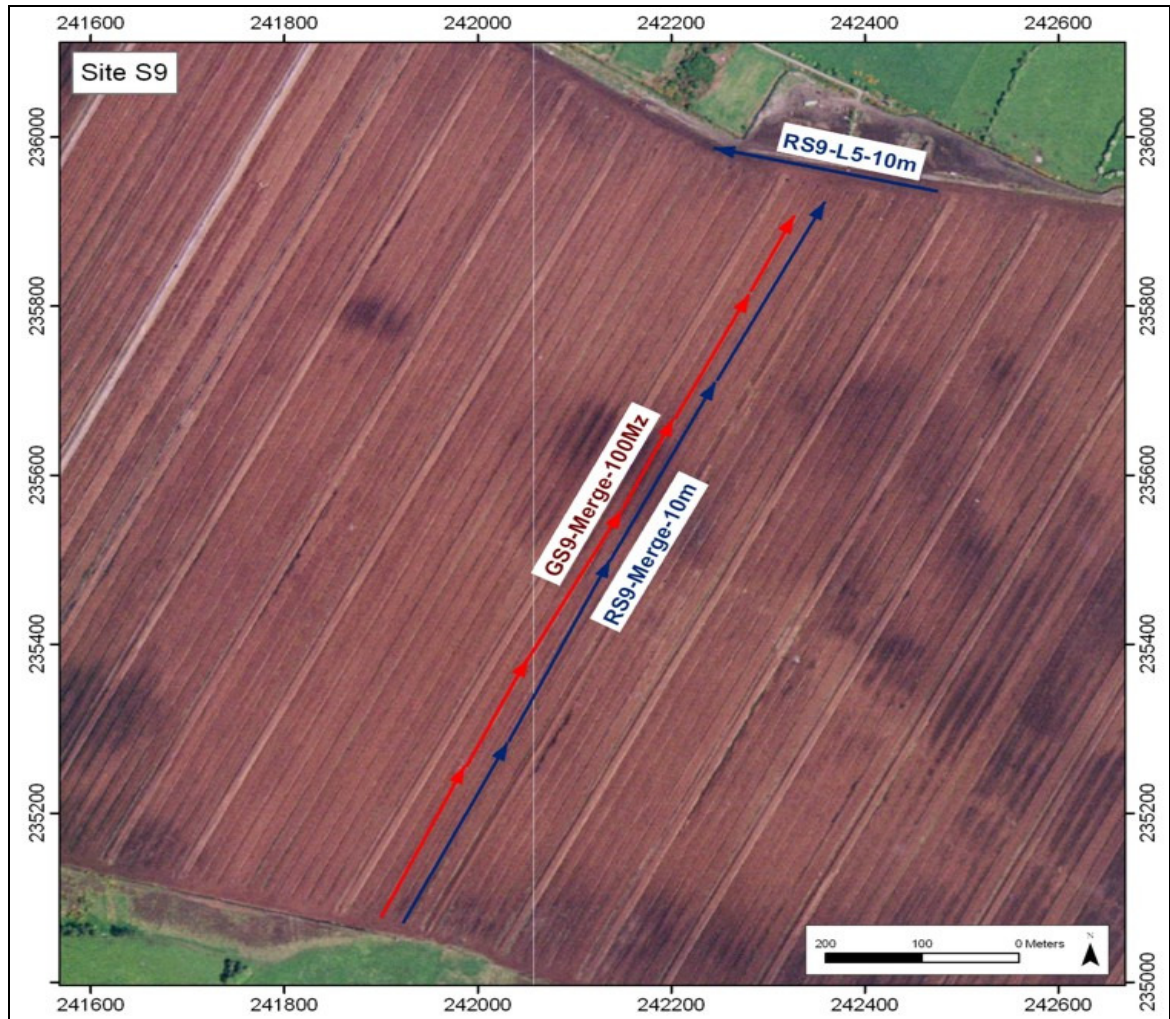


Figure 6.91 – Location of Electrical Resistivity (blue) and GPR (red) profiles surveyed in Site S9.

6.9.2 – Electrical Resistivity Data

A set of four inline electrical resistivity profiles at 10m electrode spacing have been collected across the bog on a south-southwest to north-northeast direction using the Wenner-Schlumberger array. The profiles have been merged using the software RES2DINV and are presented as a single resistivity profile, just less than 1km in total

length. Moreover, an additional profile has been collected parallel to the northern margin of the bog.

Figure 6.92 shows the resulting resistivity values and the interpretation of a merged profile of resistivity lines 1 to 4 (**RS9-Merge-10m**). The profile runs across the peat bog for 960m. The results show low resistivity values of less than $150\Omega\text{m}$ along the surface for the profile, which has been interpreted as peat reaching a maximum thickness of around 7m in the section 570 - 780m. A continuous layer underlying the peat presenting slightly higher resistivity values, ranging between $150 - 600\Omega\text{m}$, occurs along the whole profile. It varies in thickness from 3 - 15m, and has been interpreted saturated sands and gravel/diamiction. This layer is underlain by high resistivity values increasing downwards reaching more than $3000\Omega\text{m}$, which has been interpreted as bedrock underlying the whole profile. A drop of the bedrock head elevation occurs in a wide section from 420 - 630m, the lower parts of this deep show resistivity values of $700 - 1000\Omega\text{m}$, which has been interpreted as weathered bedrock. This may possibly correspond to the location of the former overflow channel illustrated in Map 1.

Figure 6.93 shows the resulting resistivity values and the interpretation of resistivity line 5 (**RS9-L5-10m**). The profile runs from east to west along the northern edge of the peat bog. The inverse model also shows low resistivity values of less than $150\Omega\text{m}$ along the surface through all the profile, which has been interpreted as peat with a thickness of 5 - 6m. A continuous layer underlying it shows medium to high values ($150 - 1000\Omega\text{m}$) with thickness varying between 5 - 20m gently increasing towards the west. This is a layer of water saturated glaciofluvial sands and gravels. Finally, this layer is underlain by a high resistivity values reaching more than $4000\Omega\text{m}$, which are believed to be bedrock.

6.9.3 – Ground Penetrating Radar (GPR)

A set of six inline GPR radargrams were collected using the 100MHz antenna. The profiles have been merged to produce a single GPR profile, which has subsequently been processed as a unique entity using the methodology presented in Chapter 3.

The merged profile (**S9-Merge-100MHz**) attains a total length of 930m, Figure 6.94 shows the radargram with dewow and an AGC gain. Migration has been applied to the dataset for velocity calculation; however the non-migrated profile displays a more comprehensible picture of the subsurface and is the one presented in Figure 6.94. Topographic correction has not been considered necessary on this occasion as it is generally flat, with gentle changes along the profile no larger than 1.5m. EM wave velocity in peat has been calibrated using the hyperbolic reflections. Two plastic pipes running across the profile located at 440m and 660m, have been clearly depicted as hyperbolic reflections by the GPR survey and velocity has been estimated from them at 0.048m/ns, see Figure 6.95a. However, velocity calibration by means of other hyperbolae reflections encountered along the radargram (probably related to tree trunks) show a velocity of 0.037m/ns as the correct one (Figure 6.95b), this velocity agrees with velocity in peat estimated by Trafford (2009) and Murphy and Clark (2009), the faster velocity encountered with the pipes may be related with the disruption of the peat internal structure when laying the pipes. The dataset has been migrated using a velocity of 0.037m/ns and most of the numerous hyperbolic reflections detected have been collapsed, which validates it as the correct velocity. Reflectors portrayed in black are related to lithological boundaries, in red to hyperbolic reflections and in blue to water-table level. A long discontinuous sinuous reflector (L1s1-bol) occurs 0 - 930m, it has been interpreted as the boundary between the peat and the underlying sand and gravel. Possible changes in the texture or type of peat are detected by two continuous reflectors marked as discontinuous lines (L1s2-bs), probably related to changes in their degree of humification. A continuous reflector occurring along the profile at 2 - 3m depth has been interpreted as the water level, this agrees with the depth to the recorded drainage pipes. A number of other hyperbolic reflections enclosed in the peat are most likely related to presence of tree trunks preserved within the peat. The region with the thickest peat is located 570 - 720m, reaching a thickness of at least 5.5m. The altitude recorded by the 10m resolution DEM at this location is 95m OD. This indicates that a potential glacial lake overflow channel draining eastwards across the watershed at this point was at most at an altitude of 89.5m OD. A larger version of the radargram GS9-Merge-100MHz-B and its interpretation is presented in Enclosure 2 – E2J.

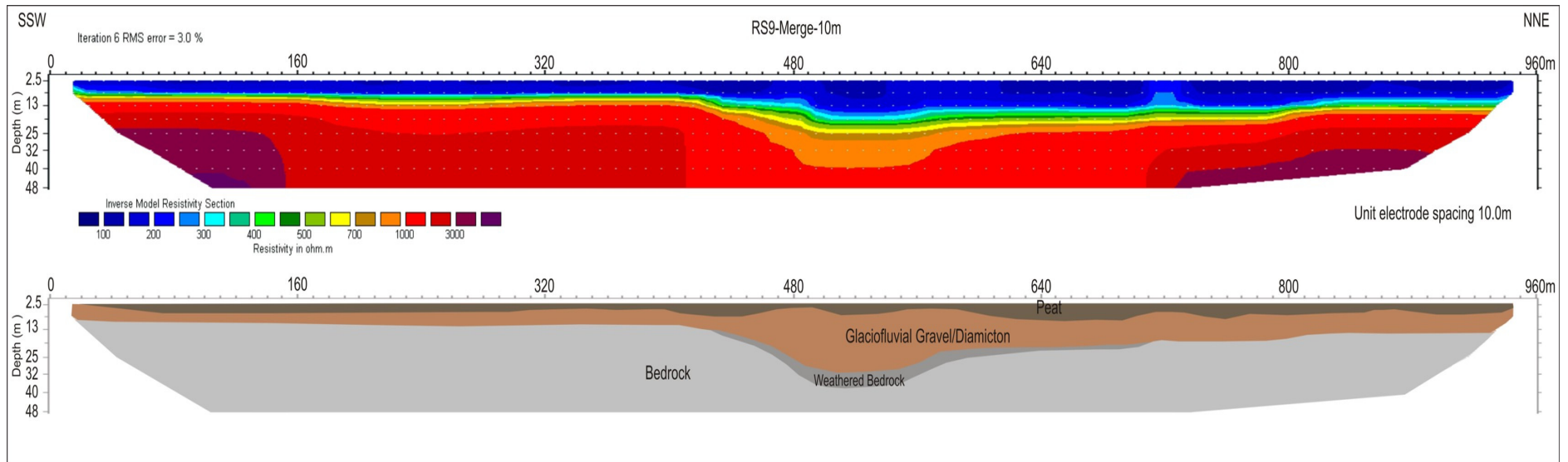


Figure 6.92 - Resistivity profile RS9-Merge-10m collected in Site S9 and its interpretation.

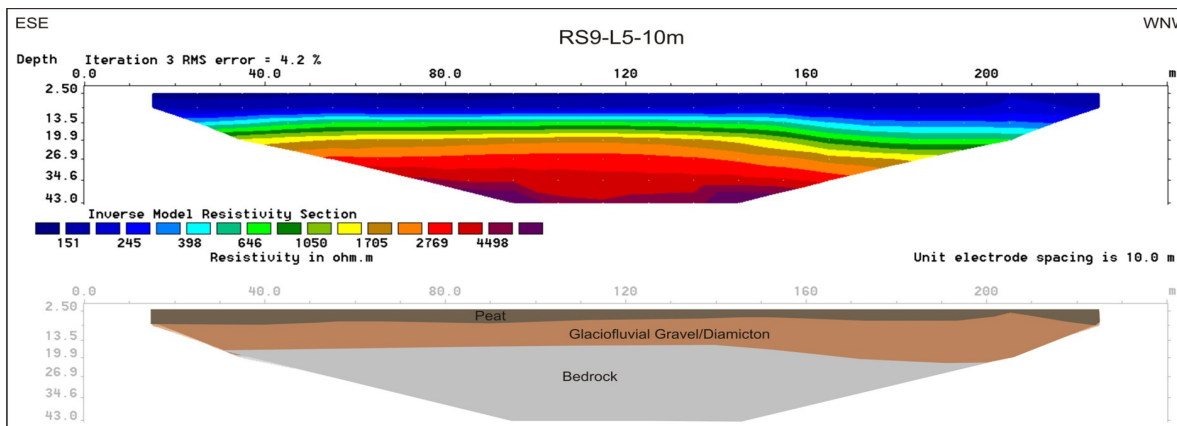


Figure 6.93 - Resistivity profile RS9-L5-10m collected in Site S9 and its interpretation.

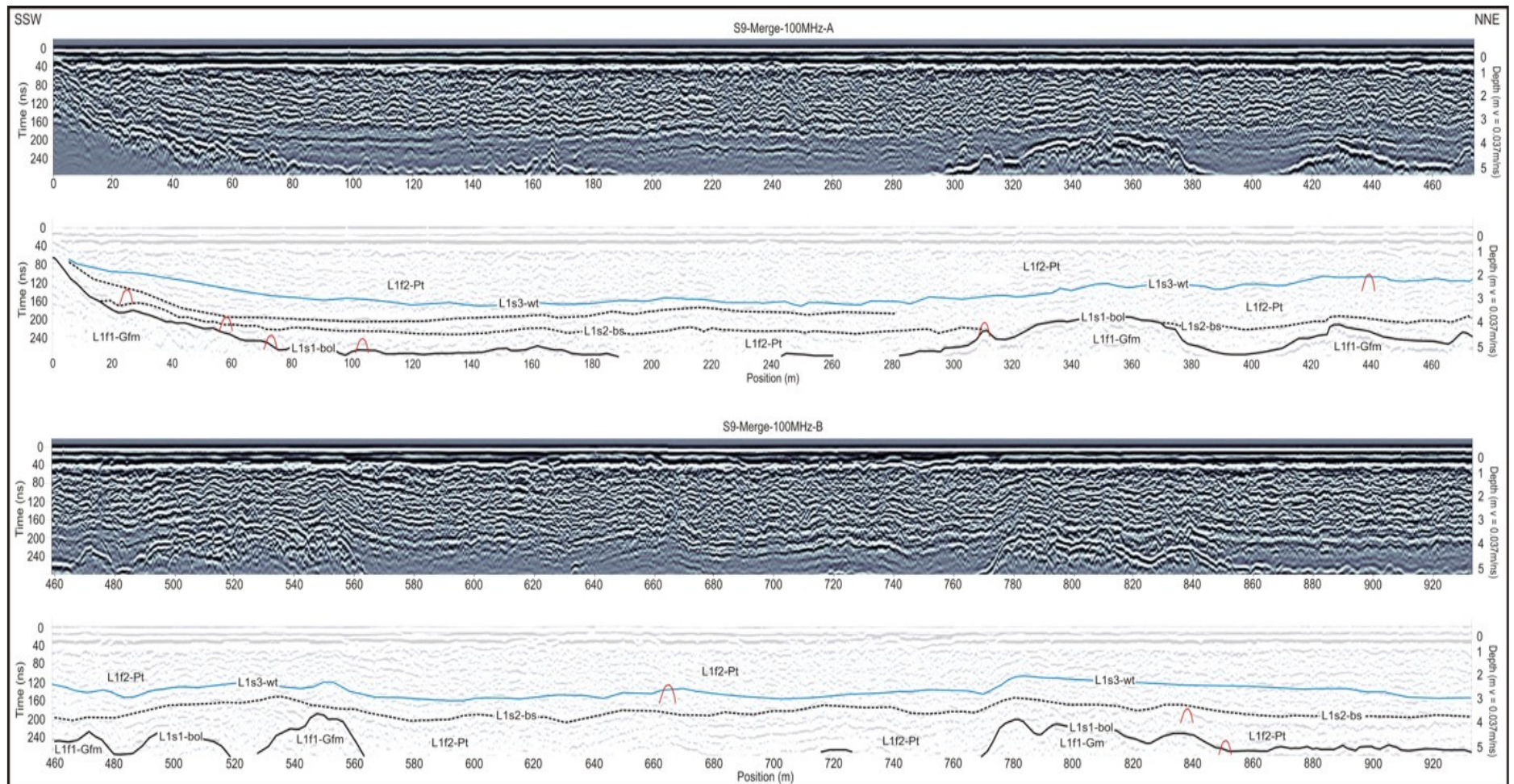


Figure 6.94 – GPR profile GS9-Merge-100MHz collected in S9. Top –radargram with dewow and AGC Gain calibrated using a velocity of 0.048 m/ns. Middle – topographically corrected migrated radargram using a. Bottom – Interpretation of the migrated radargram.

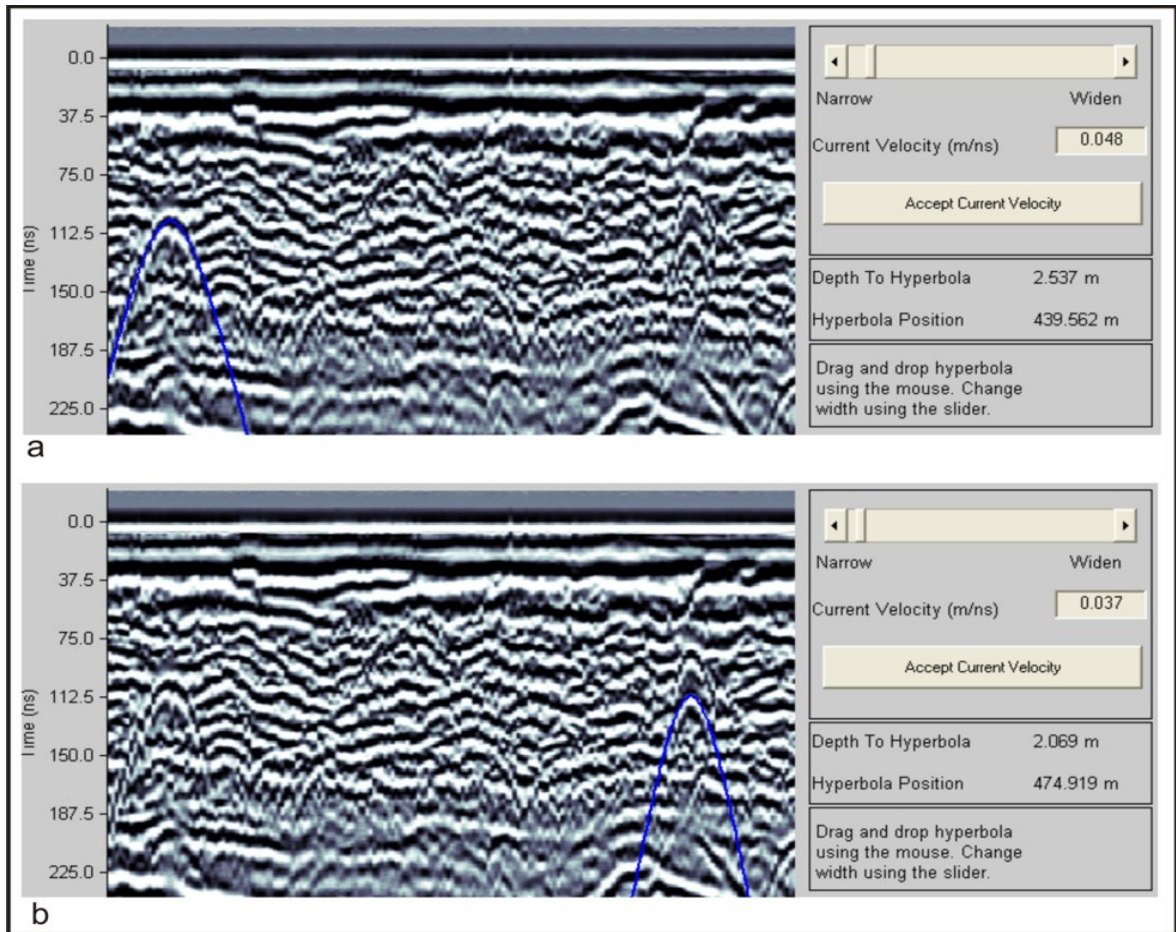


Figure 6.95 – GPR profile velocity calibration using hyperbolae reflections. (a) Velocity of the peat over drainage pipe is calibrated at 0.048m/ns. (b) A number of hyperbolae occurring along the profile however, show a velocity of 0.037m/ns.

6.10 – Site S10

6.10.1 – Introduction

Site S10 is located 1.5Km northeast from Tullamore (Figure 6.1), on the western end of a wide ridge running southwest-northeast along the southern margin of the Ballyduff Esker complex for more than 2.5 Km at altitudes ranging 77 - 84m OD. The feature widens north-eastwards attaining a maximum width of 1 Km. Its average height above the surrounding landscape varies 8 - 12m (See Map 1).

An exposure (ES10A) recorded 100m west from the site shows well sorted stratified fine to medium sand with interstratified gravel lenses derived from lower Carboniferous limestone and showing minor deformation structures. These have been interpreted as faults related to sediment deposition on buried ice and water escape structures. Two samples of the exposure are shown in Plate 6.12.

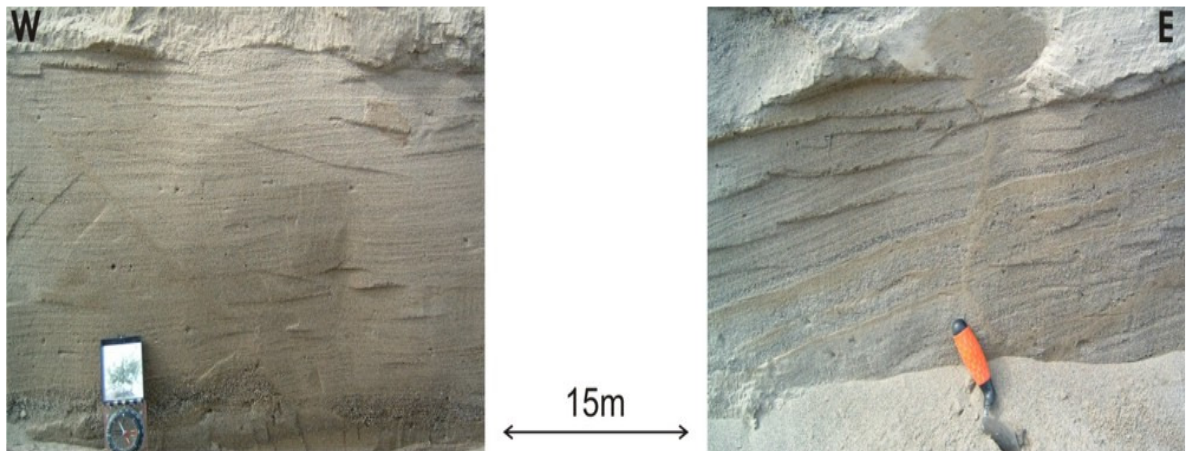


Plate 6.12 – Exposure ES10A showing well sorted stratified sand and gravel with minor deformation structures.

A borehole (BH-S10A - E235427, N226485) shows dense silty sandy gravel with rounded to subangular pebbles from 0 to 3.2m. Medium dense to soft silty clayey diamicton changes downwards to sandy silty diamicton with subangular and subrounded limestone and chert pebbles dominate from 3.2 - 12m. This is underlain by a 1.5m thickness layer of soft blue sandy clayey silt with no pebbles overlying very dense silty clayey diamicton with angular to subrounded pebbles.

Three GPR profiles using the 100MHz frequency antenna were recorded on the site. An aerial photograph of the site, with the location of the profiles is presented in Figure 6.96.

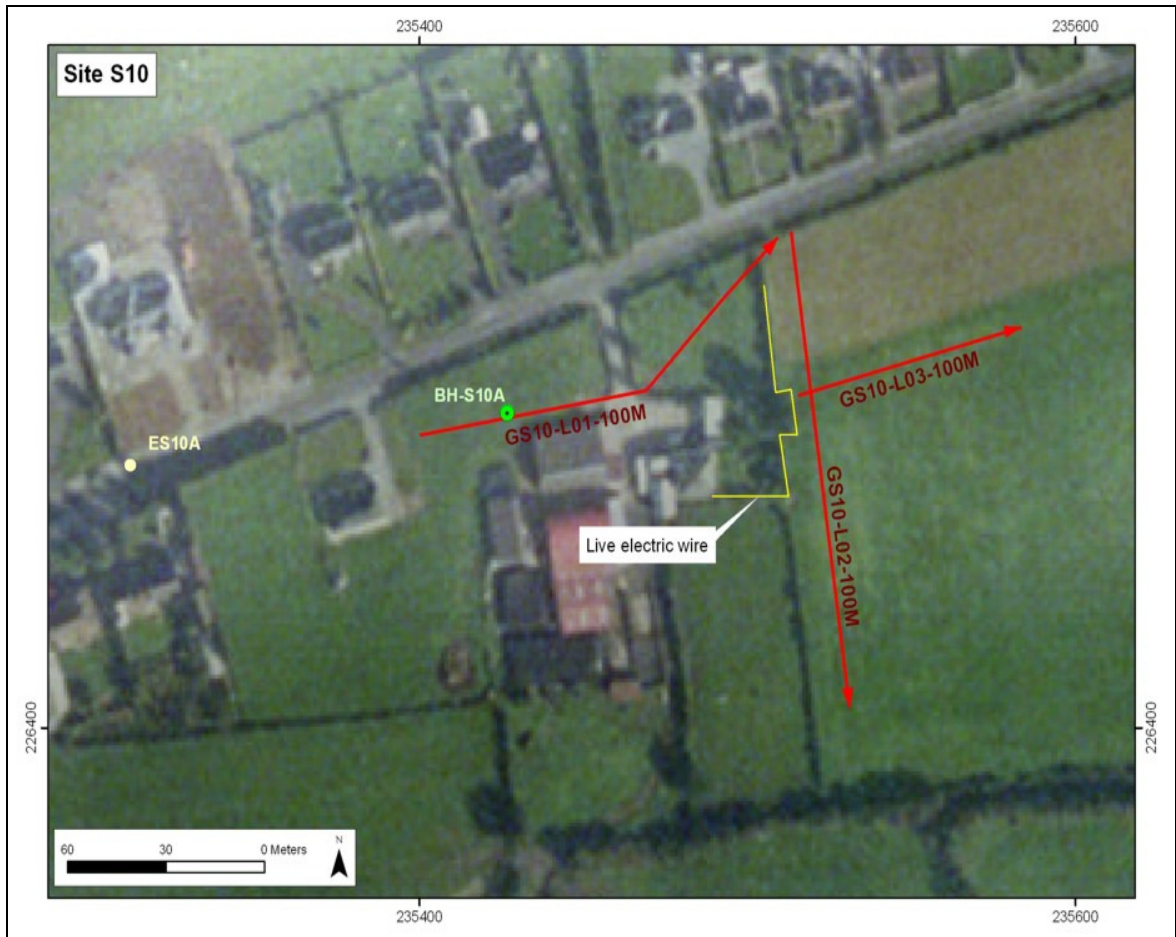


Figure 6.96 – Location of exposure ES10A, borehole BH-S10A and GPR profiles surveyed in site S10.

6.10.2 – Ground Penetrating Radar (GPR)

Prior to data processing, a velocity calibration exercise was performed using hyperbolae reflections detected on the radargrams (Figure 6.97). The velocity was estimated as 0.09m/ns. This velocity was the one used for migration and topographic correction of the data.

Line **GS10-L01-100M** runs approximately along the long axis of the feature and changes direction at 70m to the northwest (Figure 6.98). A moderately continuous, subhorizontal reflector runs parallel to the surface at 3 - 4m depth. This reflector has been interpreted as

the contact between silty sandy gravel (L1f3-Gfc) overlying gravelly sand (L1f2-Gfm) recorded in BH-S10A, which intersects the radargram at 27m. L1f3-Gfc is dominated by sinuous, discontinuous/moderately continuous reflectors; interpreted as cross-bedded deformed gravels.

The profile collected runs on grass from 0 - 35m and 80 - 120m, and on stripped ground from 35 - 80m and 120 - 127m. This is depicted on the radargram with a change in the polarization of the top reflector. Moreover, a number of reflectors occur below 4m from 35 - 80m and 120 - 126m, coupling of the antennae with bare ground seems to be enhanced, which gives better penetration in these areas. Reflectors depicted under 69m OD have been interpreted as multiples of the top layer.

Line **GS10-L02-100M** runs north to south across the long axis of the feature, its radargram topographically corrected, migrated and interpreted is presented in Figure 6.99. A moderately continuous reflector running subparallel to the surface at 3 - 4m depth is believed to be the contact (L2s2-bs) between silty sandy gravel overlying silty clayey diamicton recorded in BH-S10A. Very poor reflections have been depicted below this reflector, mostly a number of multiples. The artefact, portrayed in red is a hyperbolic reflection from a live electrical wire running parallel to the line at 40 - 50m (See Figure 6.96). Above the main reflector, a number of discontinuous to moderately continuous sinuous reflectors have been interpreted as cross-bedding in sand and gravel. Profile **GS10-L03-100M** is presented in Figure 6.100 and it displays a similar radargram to the previous one. A main moderately continuous reflector subparallel to the surface at 3 - 4m depth and a number of discontinuous to moderately continuous sinuous reflectors, which are interpreted as cross-bedding in sand and gravel (L2f3-Gfc). The artefact recorded in L02 is also shown in this line at 80ns depth.

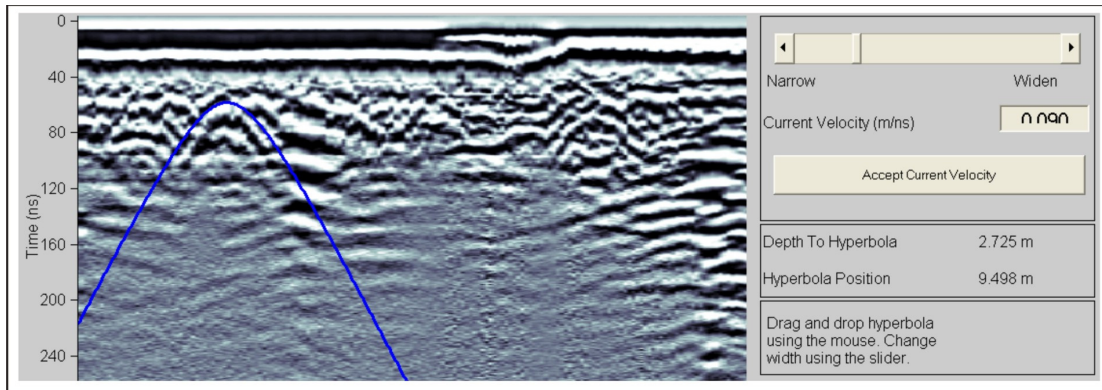


Figure 6.97 – GPR profile velocity calibration using hyperbolae reflections. Velocity of the subsurface along profile L01 has been estimated at 0.09m/ns.

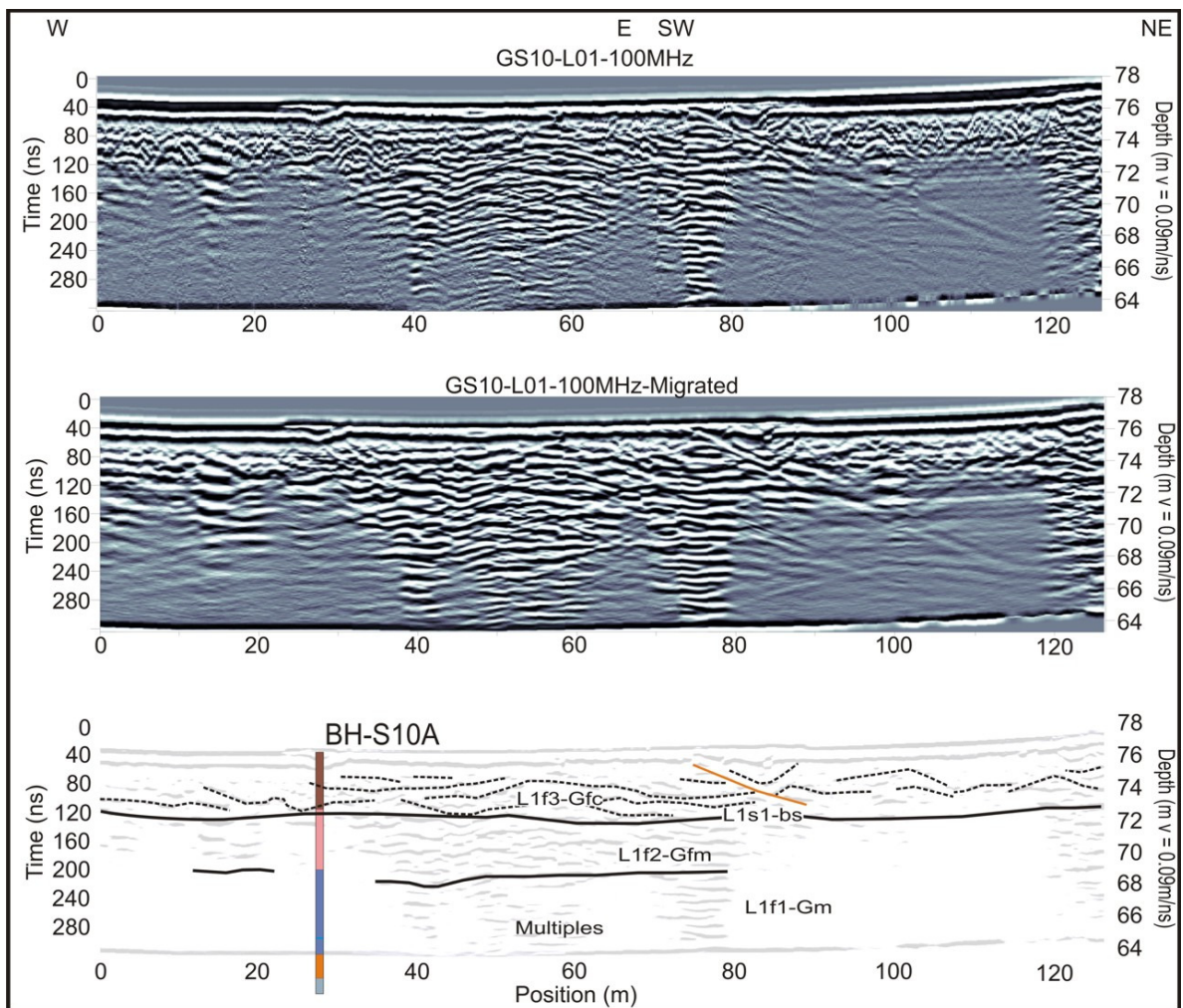


Figure 6.98 – GPR profile GS10-L01-100MHz collected in S10. Top – topographically corrected radargram with dewow and AGC Gain. Middle – topographically corrected migrated radargram using a 0.09m/ns velocity. Bottom – Interpretation of the radargram.

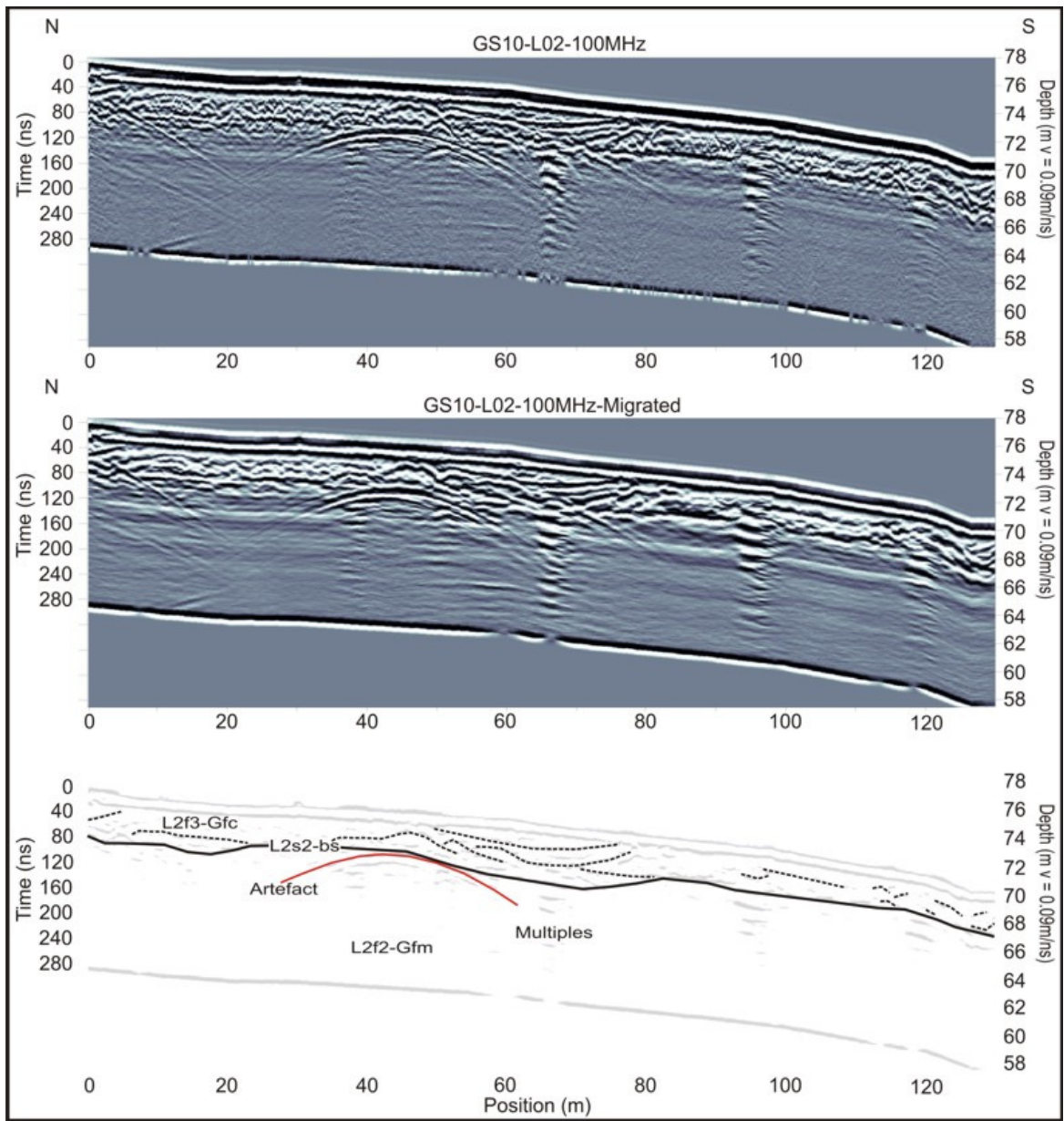


Figure 6.99 – GPR profile GS10-L02-100MHz collected in S10. Top – topographically corrected radargram with dewow and AGC Gain. Middle – topographically corrected migrated radargram using a 0.09m/ns velocity. Bottom – Interpretation of the radargram.

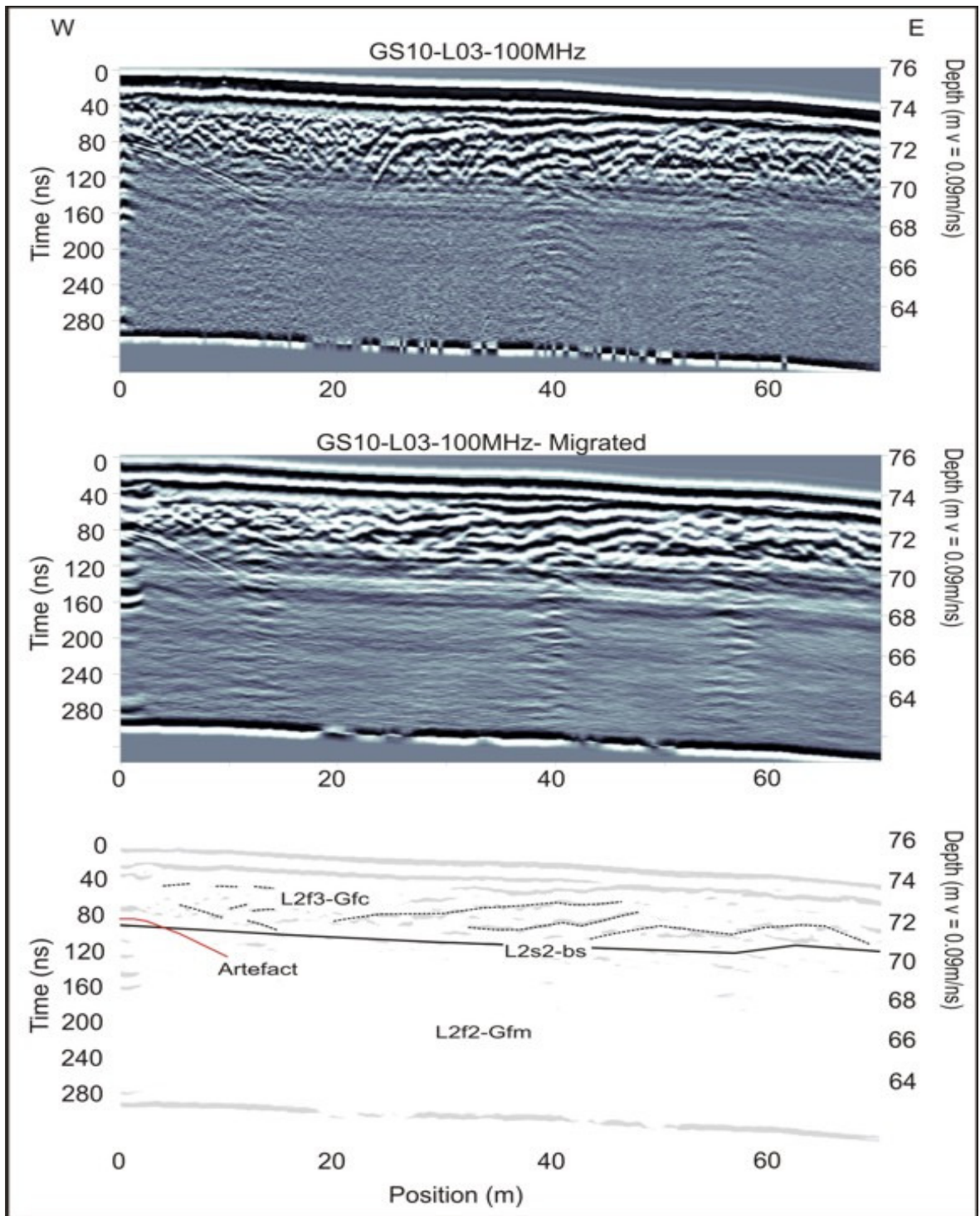


Figure 6.100 - GPR profile GS10-L03-100MHz collected in S10. Top – topographically corrected radargram with dewow and AGC Gain. Middle – topographically corrected migrated radargram using a 0.09m/ns velocity. Bottom – Interpretation of the radargram.

6.11 – Site S11

6.11.1 – Introduction

The site is located southeast of Geashill, in the southeastern part of the study area (Figure 6.1), along the watershed area between the Shannon and the Barrow Basins (E246800, N220000). The site is situated along one of the lowest points on the watershed between the Shannon and the Barrow Basins (83m OD). Geashill Esker runs across the watershed at this site in a south-southeast to north-northwest direction.

Two exposures have been recorded in the area close to the site – see Figure 6.101 for location. Exposure ES11A is 4 - 5m high and 18m long and is located in a gravel pit along the main ridge of the Geashill Esker (Plate 6.13). The top metre is dominated by massive cobble gravel. These are underlain by poorly stratified boulder/cobble gravel with crude bedding generally dipping 20° - 25° east. Most of the exposure is covered by slumped material. Exposure ES11B is located in a disused gravel pit along the east side of the Geashill Esker. The exposure (Plate 6.14) is 30m long and 6 - 8m high. A 0.3 - 0.7m thick layer of poorly stratified coarse gravel with sandy matrix dominates the top part of the section. It is underlain by a 1m thick layer of silty diamicton which overlays a c. 2m thick massive layer of cobble/boulder gravel.

Two ERT profiles were recorded on the eastern margin of the Geashill Esker and two more across the watershed to determine the surficial sediment thickness in the area and their lithological composition - see Figure 6.101. GPR data was not necessary for this purpose.



Plate 6.13 – Exposure in Site 11 (ES11A) showing poorly sorted massive cobble/boulder gravel with sandy matrix.



Plate 6.14 – Exposure in S11 (ES11B) in disused Gravel Pit shows coarse gravel overlying diamicton overlying cobble/boulder gravel with sandy matrix.

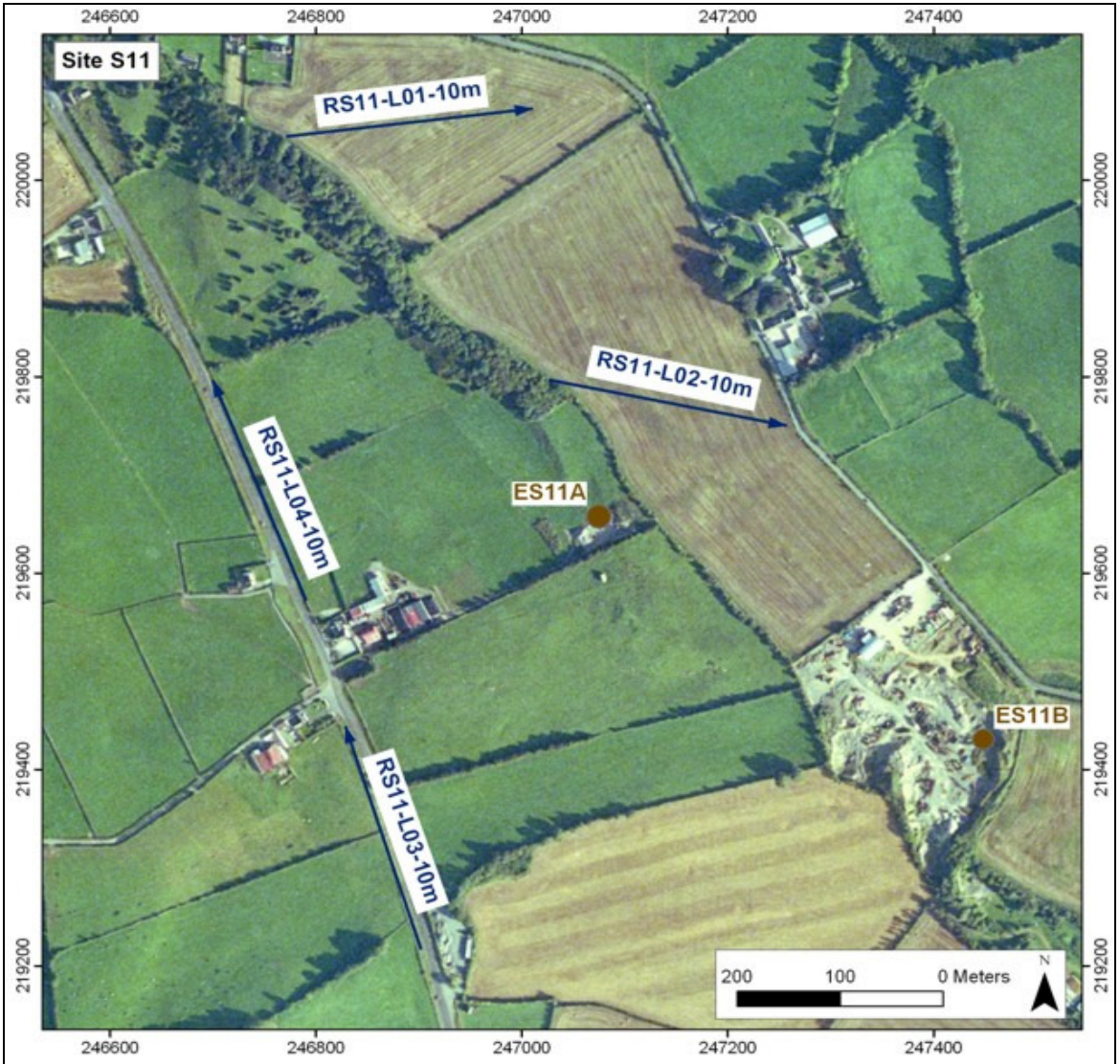


Figure 6.101 – Location of surveyed profiles and exposures recorded in Site S11.

6.11.2 – Electrical Resistivity Data

RS11-L01-10m (Figure 6.102) and **RS11-L02-10m** (Figure 6.103) are located at the eastern margin of Geashill Esker and run eastwards from the foot of the ridge. L02 is located 300m south of L01 and both profiles present similar resistivity values. The upper part of L01 is dominated by low resistivity values ($<400\Omega\text{m}$) interpreted as diamicton. A sharp sinuous high resistivity values ($>1000\Omega\text{m}$) contact occurs at 14 - 22m depth which has been interpreted as bedrock. L02 presents a very similar inverted model to L01 with high resistivity values interpreted as bedrock overlain by lower resistivity values interpreted as diamicton. The diamicton is overlain at 0 - 100m by a 1 - 4m thick layer presenting relatively higher resistivity values ($>400\Omega\text{m}$), which has been interpreted as sand and gravel.

RS11-L03-10m and **RS11-L04-10m** (Figure 6.104) run northwards, along a potential glacial lake overflow channel running along the western margin of Geashill Esker. The profiles have been collected inline at 100m distance from each other. The resulting models of the pseudosections show analogous results. The top region of the profile is dominated by medium to high resistivity values ranging between 500 - 1500 Ωm ; these have been interpreted as glaciofluvial sand and gravel with a varying thickness from 2 - 19m in L03. The average thickness of this deposit is 8m in L03 and around 4m in L04. These deposits are underlain by lower resistivity values ($<500\Omega\text{m}$), which have been interpreted as diamicton. High resistivity values ($>1000\Omega\text{m}$) occur along the lower region of both inverted models presenting an uneven and sharp contact with the overlying sediments - these high resistivity values have been interpreted as bedrock.

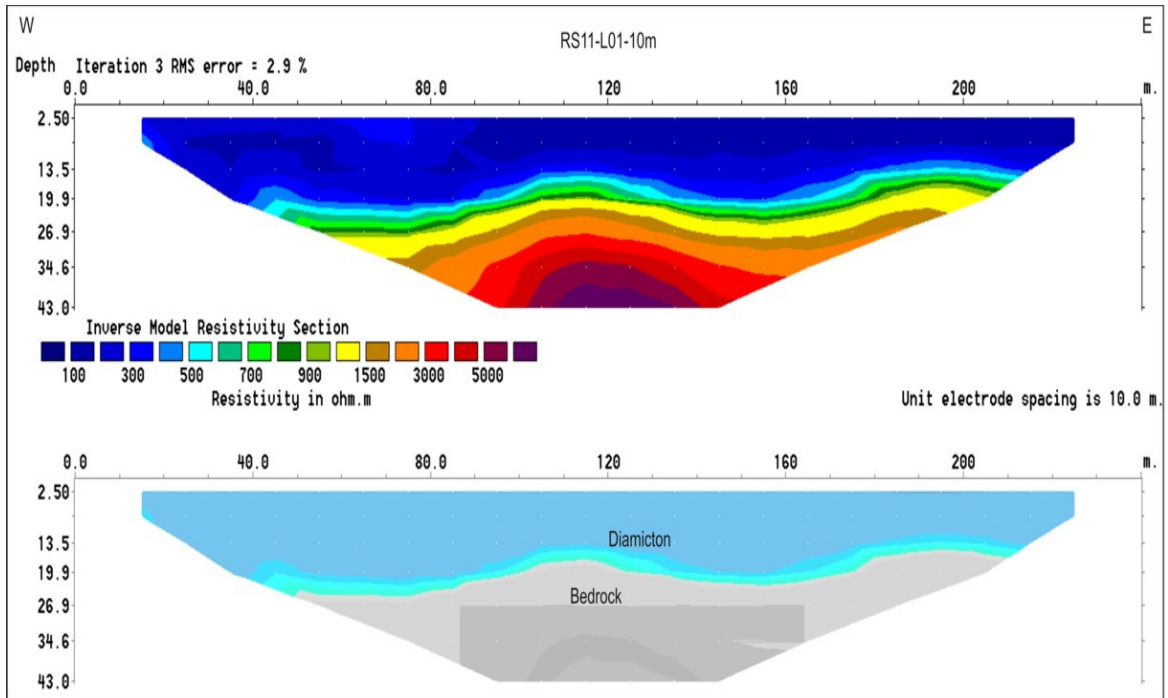


Figure 6.102 – Electrical Resistivity profile RS11-L01-10m collected in S11 and its interpretation.

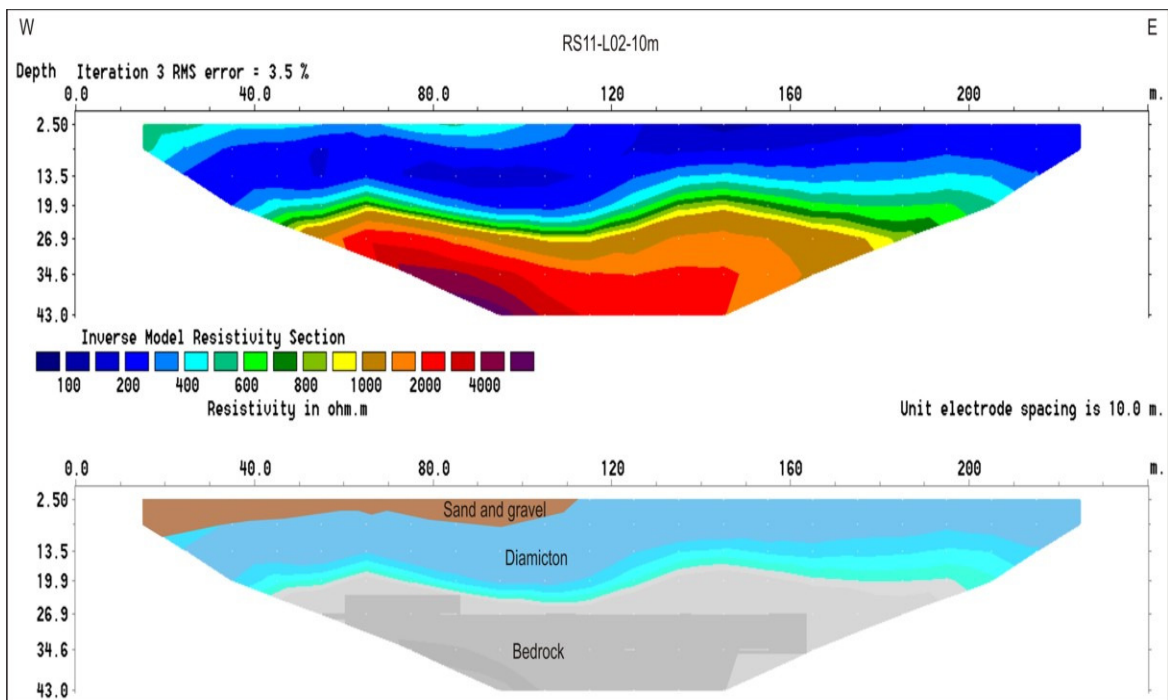


Figure 6.103 – Electrical Resistivity profile RS11-L02-10m collected in S11 and its interpretation.

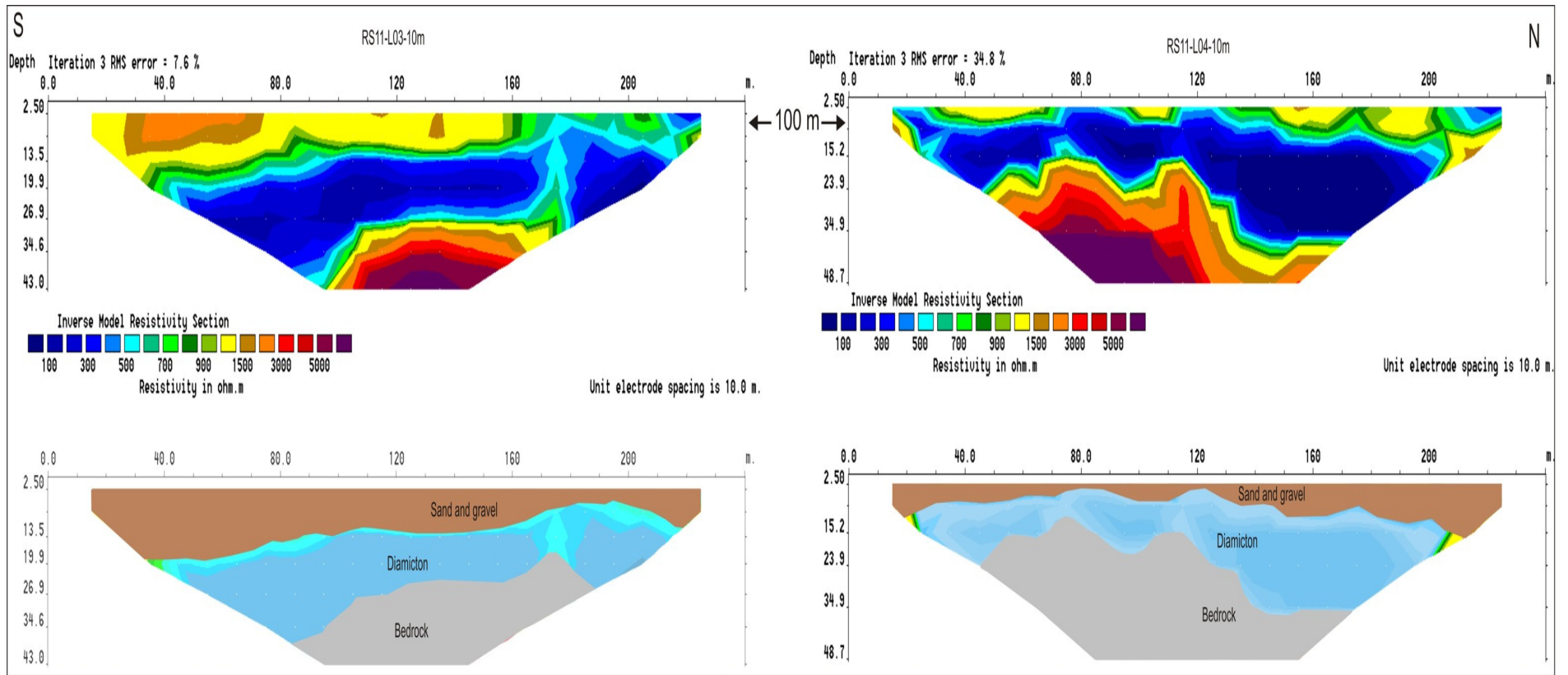


Figure 6.104 – Electrical Resistivity profiles RS11-L03-10m and RS11-L04-10m collected in S11 and their interpretation.

6.12 – Site S12

6.12.1 – Introduction

This site is located 3 Km east of Ballinagar (Figure 6.1), in a peat bog east of the watershed between the Shannon and the Barrow Basins (E247500, N223500). A meltwater channel incised in bedrock has been mapped south of Ballinagar, see Plate 4.2. The prolongation of this channel feature to the east is uncertain as it is covered by peat. A number of drainage ditches cut across the bog in a SSW-NNE direction (See Plate 6.15), these are underlain at one point by a drainage pipe buried at a depth of 2.5m marking the water-table. The site is generally flat with very little topographic variation ranging 79 - 83m OD. Lower ground occurs in the middle section of the profiles and higher ground at the margins. A number of shallow exposures recorded along the ditches show peat overlying massive waterlogged till derived from Lower Carboniferous limestone with silty clay matrix and subangular to rounded pebbles.



Plate 6.15 – Ongoing GPR data collection in Site S12.

ERT and GPR surveys have been carried out in order to determine the peat thickness, lithological composition and the depth to bedrock across the channel. The locations of the geophysical lines are presented in Figure 6.105.

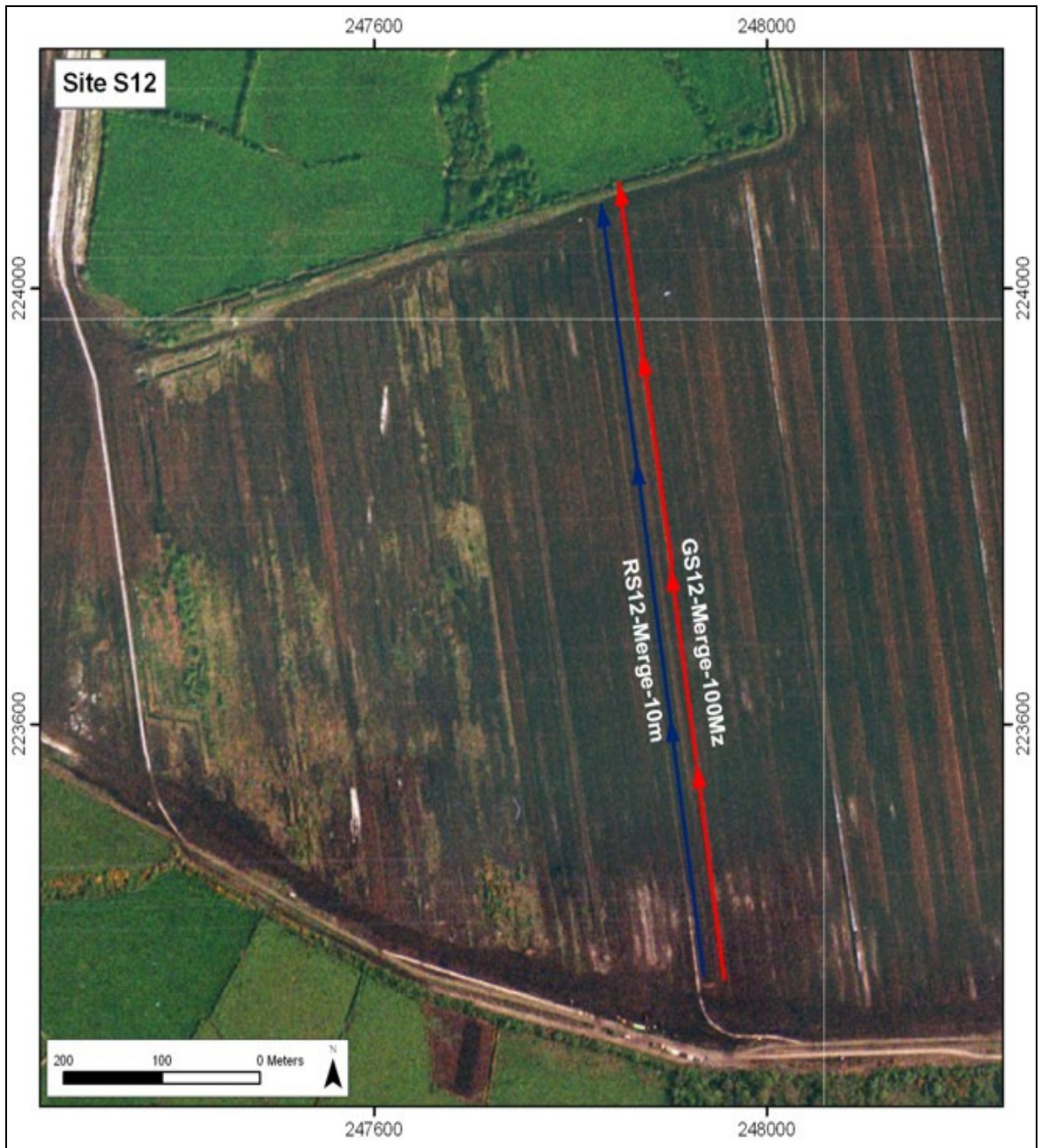


Figure 6.105 – Location of Electrical Resistivity (blue) and GPR (red) profiles surveyed in Site S12.

6.12.2 – Electrical Resistivity Data

A set of three inline electrical resistivity profiles at 10m electrode spacing have been collected across the bog on a south to north direction using the Wenner-Schlumberger array. The profiles have been merged using the software RES2DINV and are presented as a single resistivity profile. Moreover, an additional profile has been collected parallel to the northern margin of the bog.

Figure 6.106 shows profile **RS12-Merge-10m**, it runs south to north across the expected channel feature. The line runs across the peat bog for 720m. The profile recorded shows low resistivity values of less than 400Ωm throughout all the profile. Resistivity values lower than 100Ωm are recorded from 300 - 720m along the surface with increasing thickness towards the end of the profile. This has been interpreted as clayey glacial till overlain by peat. Peat thickness can hardly be depicted with this electrode spacing, however it has been included in the interpretation as a thin layer as its presence is obvious from visual analysis. The till shows variations in its resistivity values from 80 - 300Ωm, values higher than 140Ωm have been tentatively interpreted as glacial till with sandy matrix, in contrast with lower resistivity values interpreted as till with clayey matrix. Till reaches a surprising thickness of 48m along most the profile. A small area of higher resistivity values located at 40m depth between 560 - 640m has been interpreted as possible bedrock, however further surveying should be carried out to confirm it as such.

6.12.3 – Ground Penetrating Radar (GPR)

A set of four inline GPR radargrams were collected using the 100MHz antennae. The profiles have been merged to produce a single GPR profile, which has subsequently been processed as a unique entity using the methodology presented in Chapter 3.

The merging of the collected profiles yielded an overall length of 708m, (**S12-Merge-100MHz**) and is presented in Figure 6.107. The figure shows two sections of the profile with their respective interpretation. The dataset presented has not been migrated nor topographically corrected. Topographic correction has not been considered necessary in

this site as it is fairly flat. Migration has been applied to the dataset for velocity estimation; however the non-migrated profile presents a clearer picture of the subsurface. EM wave velocity in peat has been calibrated from numerous hyperbolae reflections, related to the presence of tree trunks buried in the peat occurring along the profile (Plate 6.16). The calibrated velocity has been estimated at 0.037m/ns. Reflectors portrayed in black are related to lithological boundaries, in red to hyperbolic reflections and in blue to the estimated water-table level. A continuous sinuous reflector (L1s1-bol) running along all the profile from 1 - 4m depth has been interpreted as the boundary between the peat and the underlying till. A number of discontinuous dipping reflectors in places underlying the former have been interpreted as unclassified lithological boundaries within the till. The water-table has been detected as a continuous reflector running at 1 - 2m depth, this water level agrees with water in the ditches running parallel to the profile, which drain towards a pipe cutting across the profile at 400m (see hyperbolic reflection in Figure 6.107). Other unclassified continuous reflectors parallel to the surface have been interpreted as changes on the degree of humification of the peat.

A possible channel feature at 112 - 130m is overlain by 3m of peat. Moreover, 3m of peat thickness occurs from 320 - 380m. These are the lowest points in the area potentially acting as meltwater channels during deglaciation.



Plate 6.16 – Tree trunks buried under more than 1m of peat.

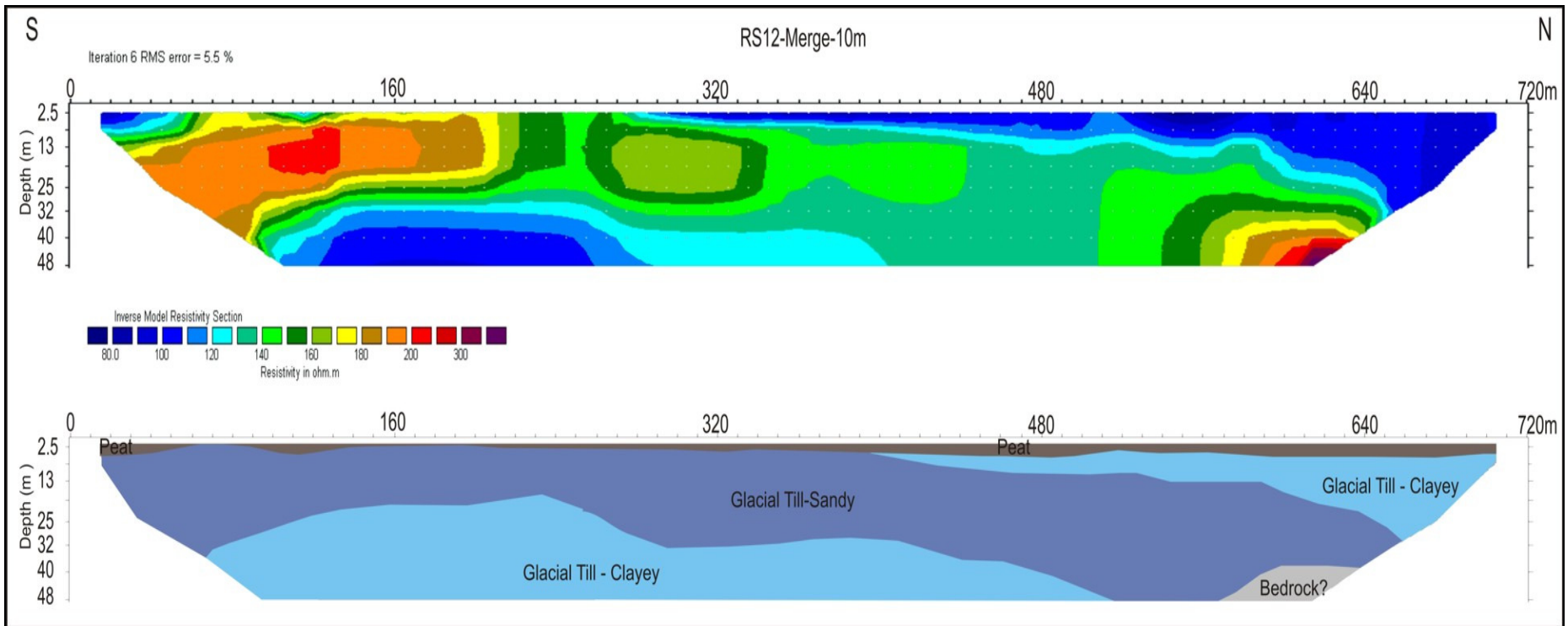


Figure 6.106 - Electrical Resistivity profile RS12-Merge-10m collected in S12 and its interpretation.

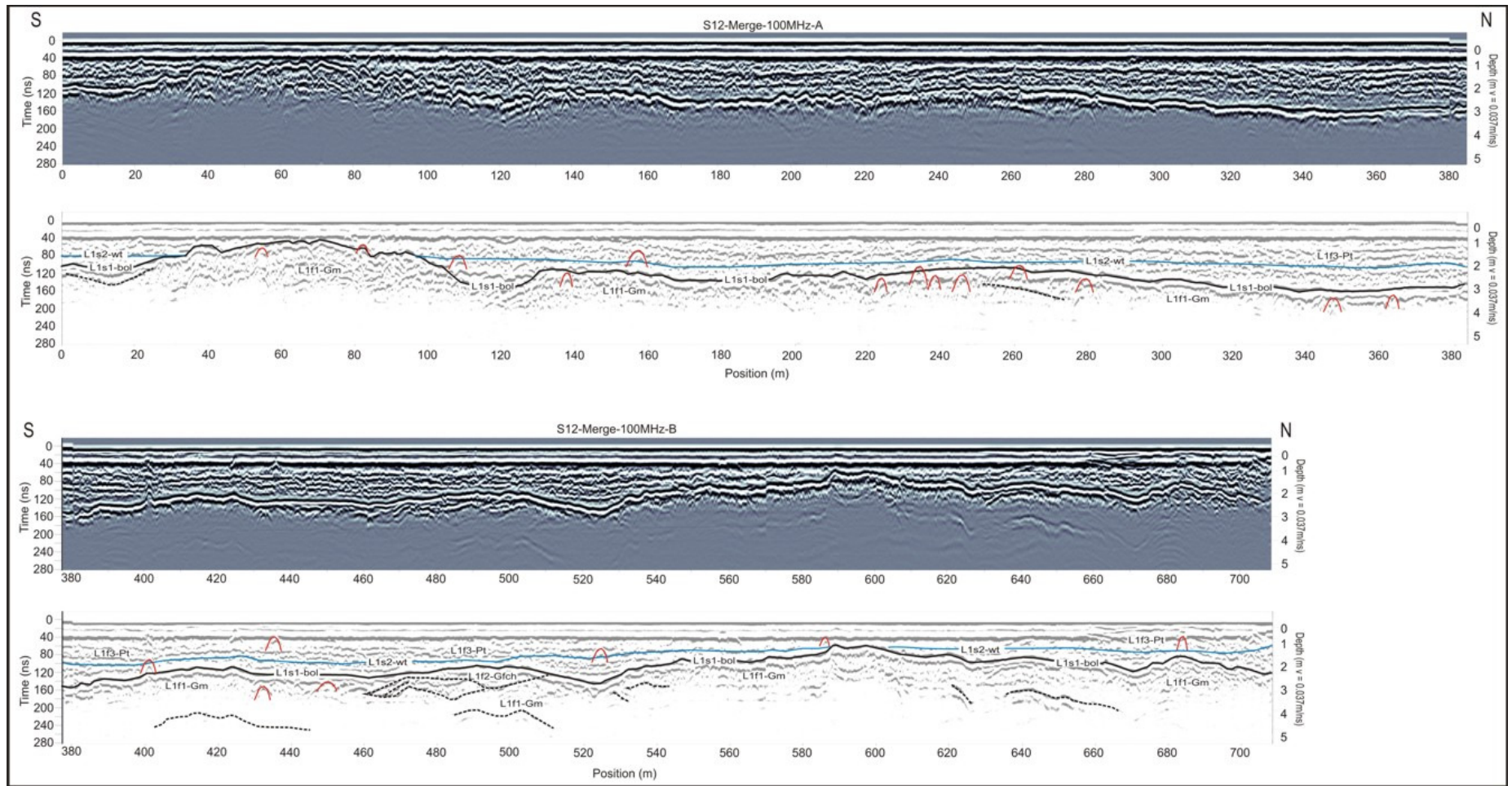


Figure 6.107 - GPR profile GS12-Merge-100MHz collected in S12. Radargram processed with dewow and AGC Gain and its interpretation. Estimated water level is displayed in blue, hyperbolae reflections in red.

6.13 – Site S13

6.13.1 – Introduction

The site is located 4 Km west of Horseleap on top of a fan-shaped feature near the eastern margin of the Moate Esker and widening in a east-southeast direction for 1.4 Km, Figure 6.1. The feature reaches a maximum altitude of 85m OD, protrudes 15 - 20m above the surrounding ground and has been interpreted as a glaciolacustrine fan/delta associated with the Moate Esker. It ranges between a minimum width of 400m at its western end and a maximum width of 800m at its eastern margin (see Map 1). The relatively depressed surrounding landscape is dominated by marl, peat and alluvium at the fan's southern margin and by alluvium and diamicton at its northern margin. The site is mainly flat with a depression located at its western margin that has been interpreted as a kettle hole; Plate 6.17 shows the site from the starting point of the resistivity profile.



Plate 6.17 – View of Site 13. Depression in the top left corner has been interpreted as a kettle hole.

A small exposure (ES13A) recorded in a talus excavated for construction of a house, located at the northern margin slope of the feature shows massive sandy gravel with no clear structure (Plate 6.18).



Plate 6.18 – Exposure in S13 (ES13A) in excavation on slope behind house shows coarse gravel with sandy matrix.

A borehole (BH-MBR28 - E224075, N238150), at 77.8m OD was drilled 250m south of the site by Northwest Holst Soil Engineering LTd. (2001) as part of the site investigation for the construction of the M6 Motorway. The borehole is dominated by gravelly fine to medium sand from 0.8 - 10.5m. From 10.5 - 16.2 the recorded dominant lithology was sandy silt, increasing its density with depth. This is underlain by silt becoming slightly sandy with increasing depth from 16.2 - 20m. The water level was recorded at 10.6m depth (67.14m OD).

An ERT profile at 5m electrode spacing and three GPR radargrams using the 100 MHz antennae were recorded on the site. An aerial photograph of the site with the location of the profiles is presented in Figure 6.108.

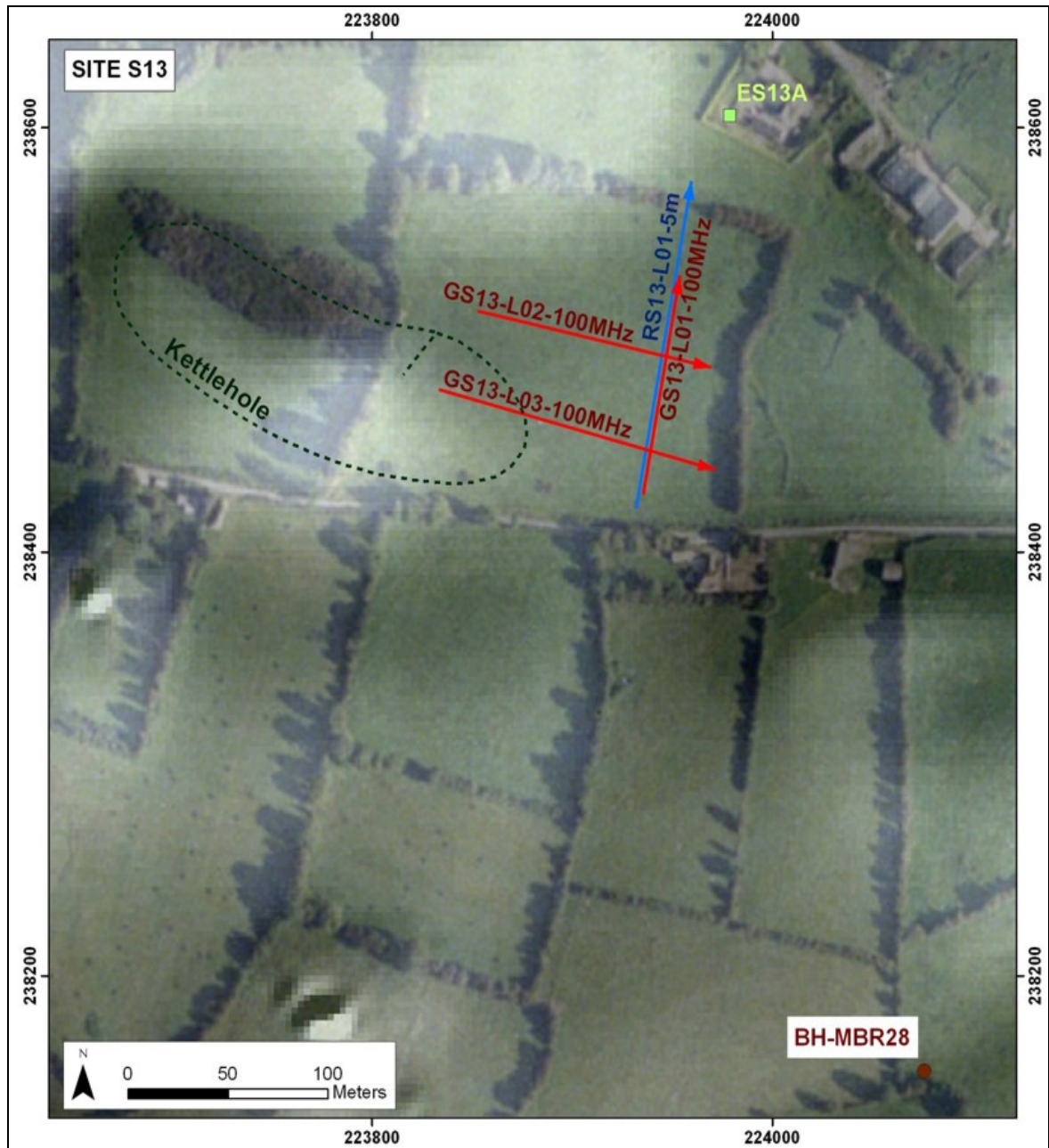


Figure 6.108 – Location of Electrical Resistivity (blue) and GPR (red) profiles surveyed in Site S13.

6.13.2 – Electrical Resistivity Data

The Geopulse Tigre resistivity meter with 32 electrodes was used to collect an ERT section using the Wenner-Schlumberger array (RS13-L01-5m). The profile runs from south to north for 160m, reaching a maximum depth of about 30m (Figure 6.109). It displays a generally continuous medium - high resistivity area ($>500\Omega\text{m}$) along the top 6 - 10m. These values correspond to the sandy gravel recorded in exposure ES13A, recorded 40m north of the end of the ERT profile at approximately 76m OD altitude. The layer is underlain by a continuous low resistivity layer (70 - 200 Ωm) running across the whole profile, which correlates with the saturated sandy silt recorded at BH-MBR28 at depths of more than 10.5m (67.1m OD). A medium resistivity layer (300 - 500 Ωm) underlies the former at approximately 26m depth (60m OD); BH-MBR28 records an increase in the sand contents of the sandy silt within the last 2m of the borehole. The increase in resistivity values at the lower parts of the profile may be related to an increase on the grain size from this point downwards.

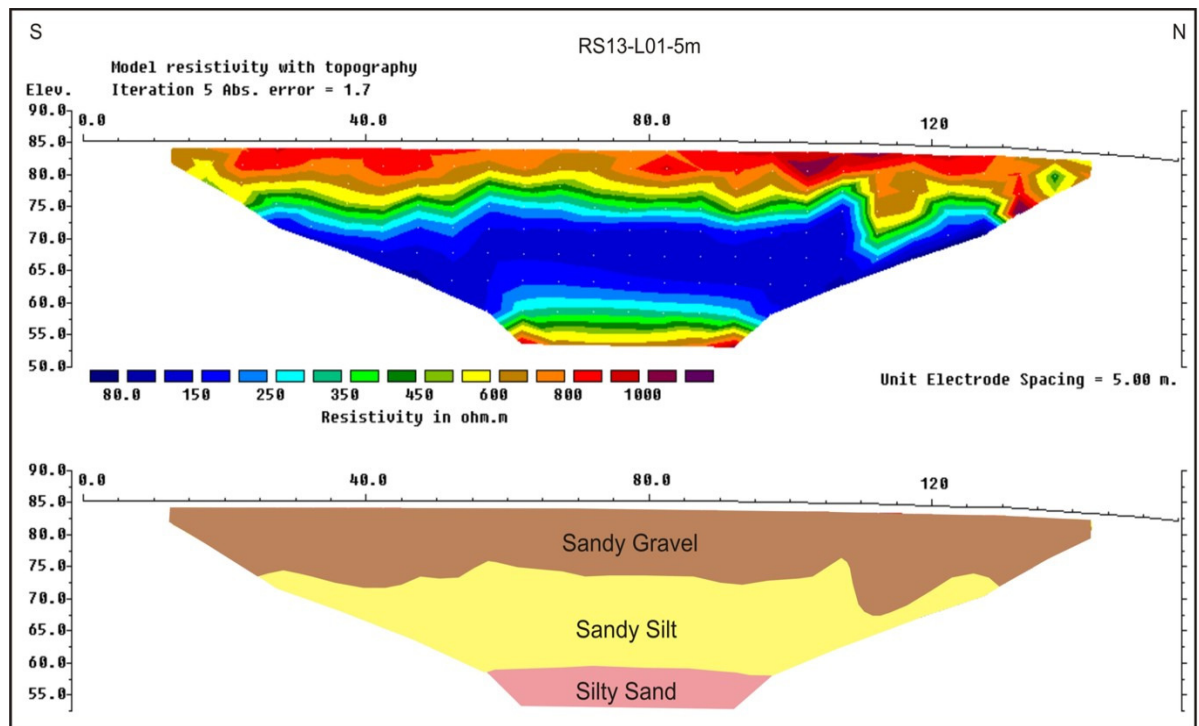


Figure 6.109 - Electrical Resistivity profile RS13-L01-5m collected in S13 and its interpretation

6.13.3 – Ground Penetrating Radar (GPR)

A number of hyperbolic reflections were recorded along the three radargrams, which were used to estimate the velocity in the sediments as 0.078m/ns.

Line **GS13-L01-100MHz** is a 91m length profile approximately running south to north, orthogonal to the fan's long axis. The original and migrated profiles topographically corrected together with the interpretation of the main reflectors are presented in Figure 6.110. Maximum penetration was of the order of 8m. The profile displays a series of sinuous, subhorizontal, moderately continuous reflectors along the bottom, below 80m OD (L1f1-Gfm). These are overlain by 3 - 4m thickness layer (L1f2-Gfp) comprised of continuous reflectors, subhorizontal from 0 - 60m evolving into moderately sinuous from 60 - 91m. This layer underlies a set of sinuous reflectors dipping 10° north from 0 - 60m and south from 60 - 91m. A set of discontinuous chaotic reflectors and a number of hyperbolae have been interpreted as boulders and gravel dominating this layer (L1f3-Gfm).

Line **GS13-L02-100MHz** consists of a 105m profile running approximately west to east, along the long axis of the fan. Figure 6.111 displays the profile topographically corrected, processed and interpreted. Maximum penetration was of the order of 8m. A 3 - 4m thickness layer composed of oblique tangential, moderately continuous reflectors dipping between 5° - 15° east depicted between 0 - 70m, which evolve eastwards into horizontal sinuous subparallel continuous reflectors, have been interpreted as possible foresets (L2f2-Gfs). These are overlain by a 3 - 4m thick layer (L2f3-Gts) composed of a set of discontinuous chaotic reflectors and two hyperbolae, which are interpreted as topsets overlying the foresets.

Line **GS13-L03-100MHz** consists of a 135m profile running 45m south of and parallel to L02. The interpreted radargram is presented in Figure 6.112. Maximum penetration was of the order of 7m. This profile runs eastwards upslope from the edge of a kettle hole to higher flat-topped ground. A 3 - 5m thickness layer has been recorded along the whole profile (L3f2-Gfs). It is composed of moderately continuous reflectors dipping 10° - 20°

east from 0 - 20m evolving into subhorizontal ones from 20 - 40m; these are overlain by reflectors dipping 15° east from 30 - 50m. The described reflectors are distorted from 30 - 70m by a number of normal fault planes associated with melting of the dead ice formerly underlying the existing kettle hole. From 70 - 135m, the reflectors are continuous, sinuous, subhorizontal and dipping east in places. A layer, not more than 2m thick, overlies L3f2-Gfs from 0 - 80m, pinching out towards the east. A number of chaotic reflectors and hyperbolae were depicted along it. This radar facies (L3f3-Gts) was also identified from 95 - 135m as a set of moderately continuous sinuous chaotic reflectors overlying L3f2-Gfs with an erosive contact.

A fence diagram showing the three radargrams is presented in Enclosure 2 – E2F.

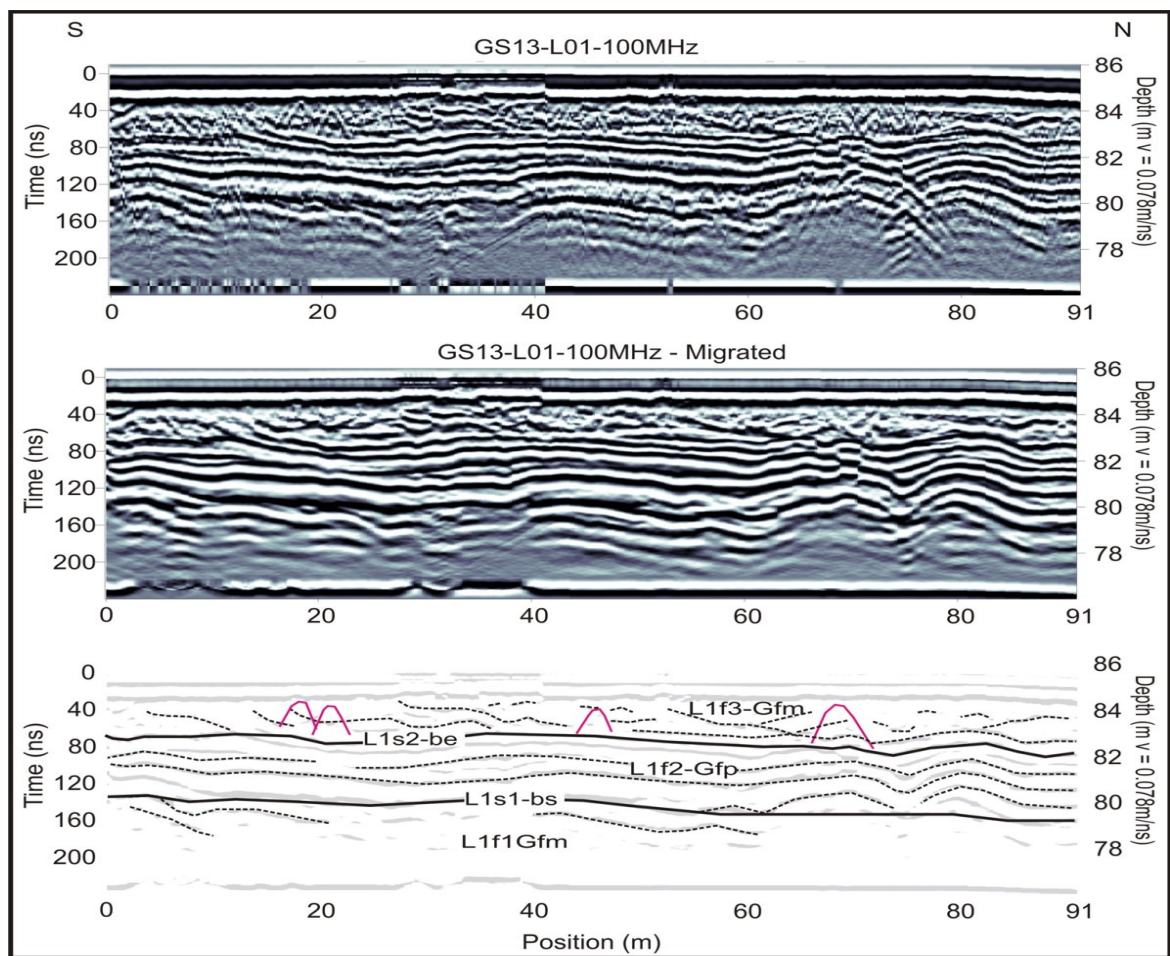


Figure 6.110 – GPR profile GS13-L01-100MHz collected in S13. Top – topographically corrected radargram with dewow and AGC Gain. Middle – topographically corrected migrated radargram using a 0.078 m/ns velocity. Bottom – Interpretation of the radargram.

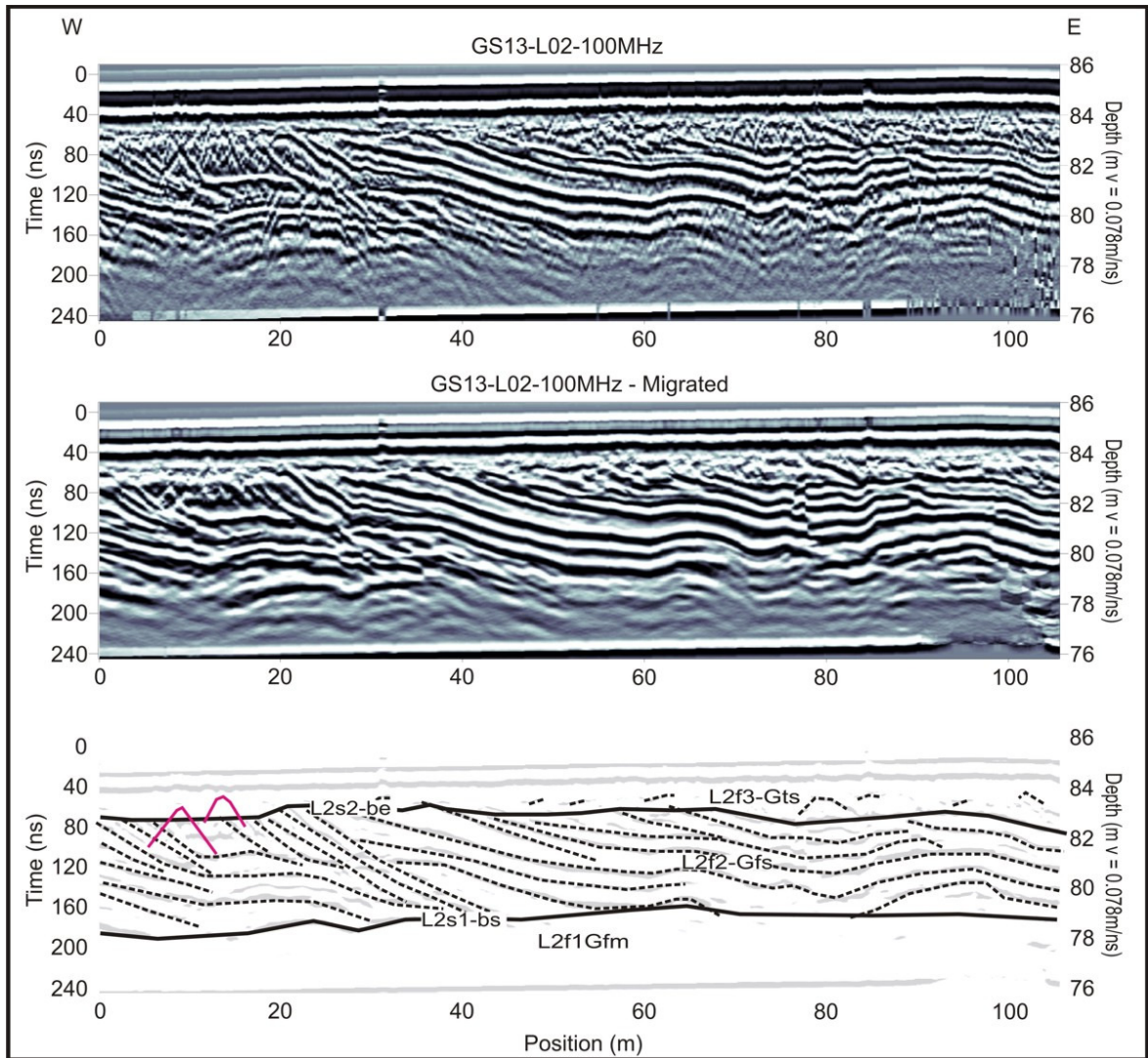


Figure 6.111 – GPR profile GS13-L02-100MHz collected in S13. Top – topographically corrected radargram with dewow and AGC Gain. Middle – topographically corrected migrated radargram using a 0.078 m/ns velocity. Bottom – Interpretation of the radargram.

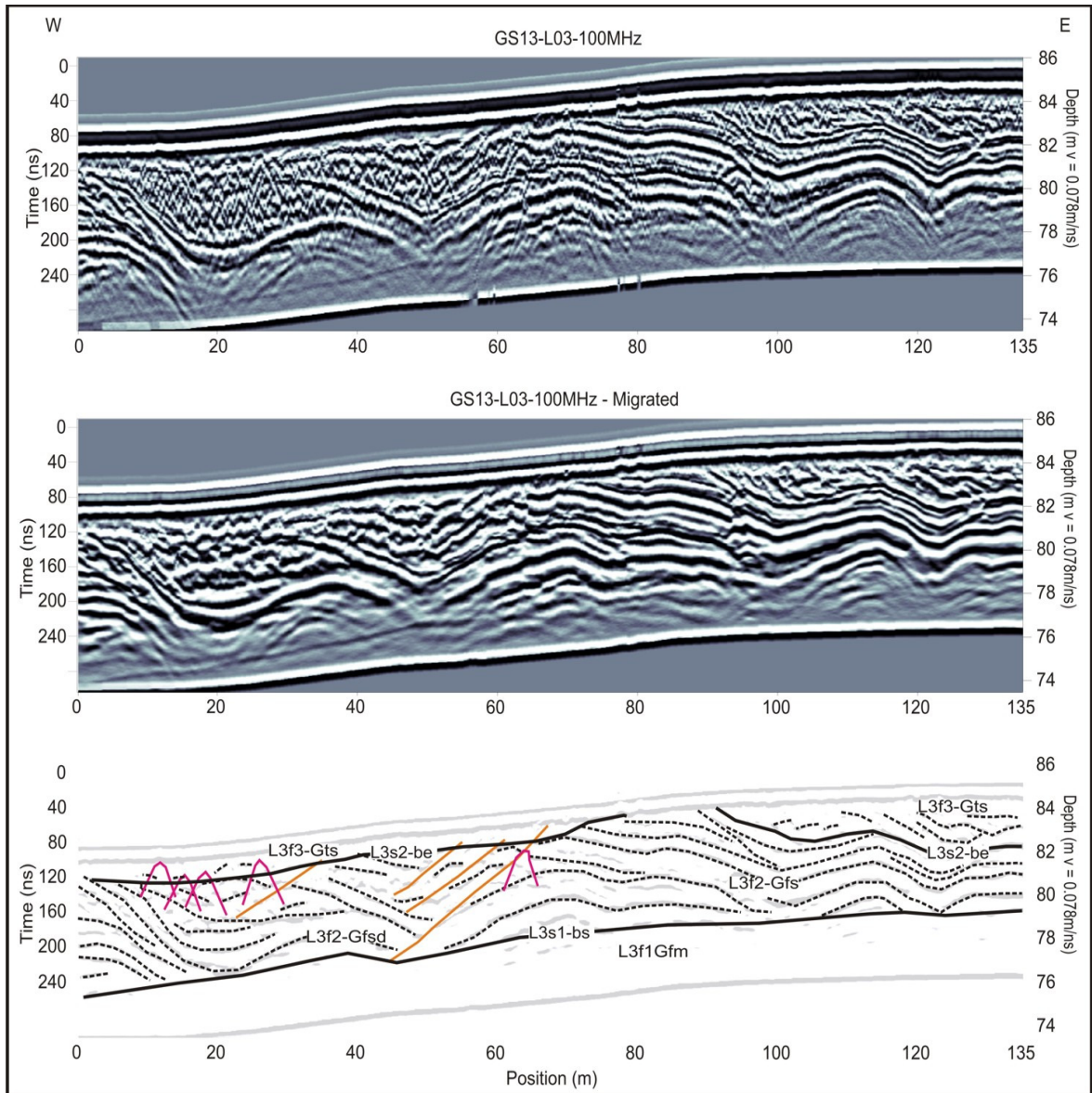


Figure 6.112 – GPR profile GS13-L03-100MHz collected in S13. Top – topographically corrected radargram with dewow and AGC Gain. Middle – topographically corrected migrated radargram using a 0.078 m/ns velocity. Bottom – Interpretation of the radargram.

6.14 – Site S14

6.14.1 – Introduction

The site is located on a flat topped isolated hill (Plate 6.19) reaching a maximum altitude of 95m OD and located at the northern margin of Clara Town, Figure 6.1. The hill is a slightly elongated feature running west-northwest to east-southeast for 1.5 Km, reaching a maximum width of 600m at its central part and protruding from the surrounding landscape 20 - 40m. A number of exposures recorded along the margins of the feature during the field mapping exercise show sand and gravel as the dominant lithologies. The relatively depressed surroundings are dominated by diamicton to the south, west and east margins and by peat to the north, (See Map 1).



Plate 6.19 – View of Site 14 from the end point of the collected ERT profile. The site is fairly flat.

An exposure running northwest-southeast (ES14A) recorded in an excavation approximately 300m southwest from the site is dominated by silty sand with silty clayey lenses, overlain by medium sand for 0.6m with a conformal contact. This is overlain by fine sand with silty clayey lenses for 1.2m, which in turn is overlain with an erosive contact by crudely bedded boulders, cobbles and gravel for 3 - 4m (Plate 6.20).

Two GPR profiles and one ERT line were recorded on the site. An aerial photograph of the site with the location of the profiles is presented in Figure 6.113.



Plate 6.20 – Exposure in S14 (ES14A) in excavation on slope behind house shows coarse gravel with sandy matrix.

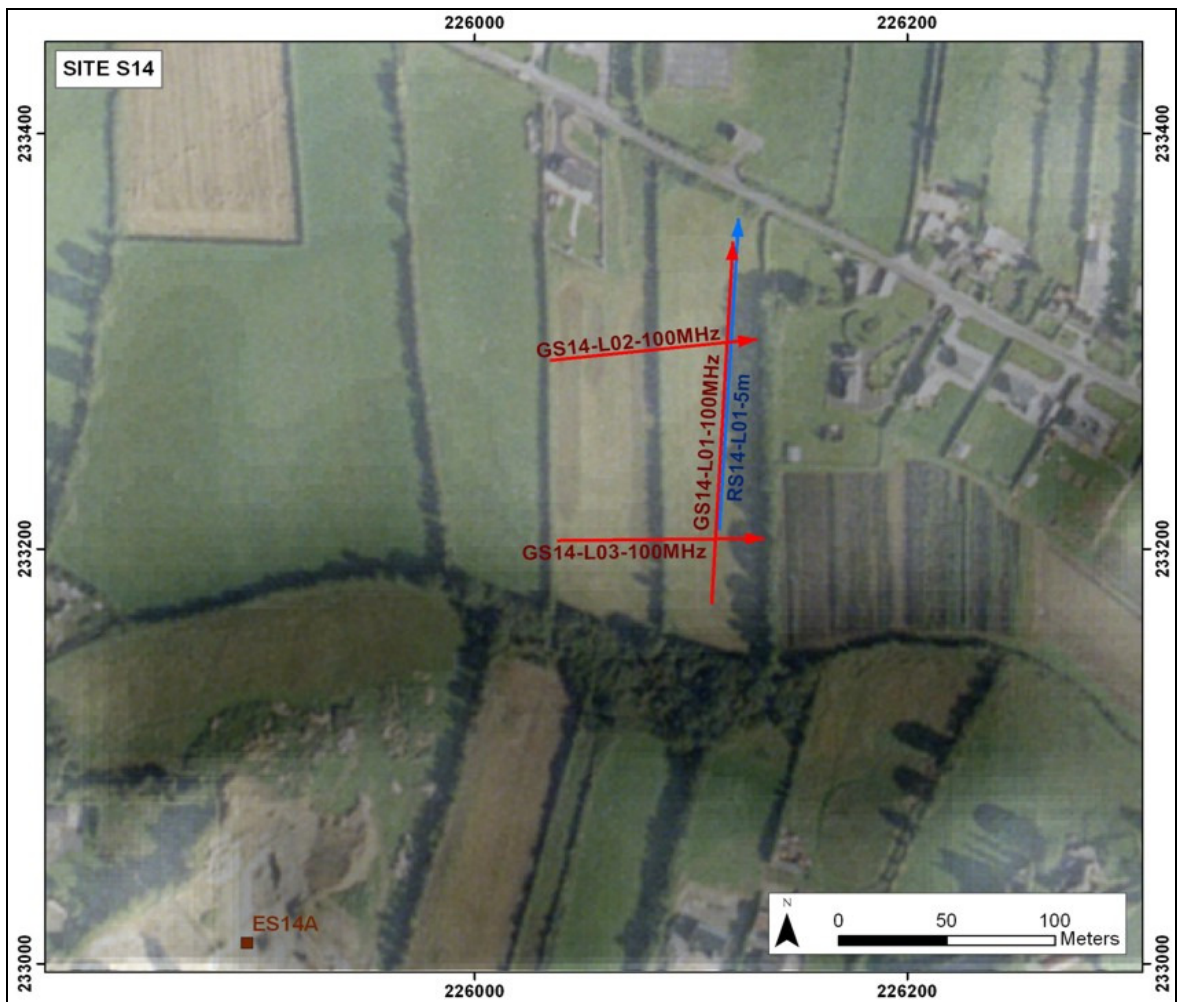


Figure 6.113 – Location of Electrical Resistivity (blue) and GPR (red) profiles surveyed in Site S14.

6.14.2 – Electrical Resistivity Data

An ERT section with 5m electrode spacing was obtained using the Wenner-Schlumberger array (RS14-L01-5m). The profile (Figure 6.114) displays a generally continuous low - medium resistivity ($< 500\Omega\text{m}$) along the top 4 - 6m. These values may correspond to saturated silty sand, as the profile was recorded just after a period of heavy rainfall in the study area. These are underlain by high to very high resistivities ($1200 - 5000\Omega\text{m}$) from 4 - 6m to near 30m depth, and such high values would be expected from bedrock. However, exposures recorded along the edge of the hill show gravel as the dominant lithology and no sign of bedrock has been encountered in the area, so, the very high resistivity values could be related to presence of the boulder/cobble gravel recorded in ES14A. Medium to high resistivity values ($900\Omega\text{m}$) occur at depths of more than 30m. This layer may be related to the sands underlying the boulder, cobble and gravels recorded in ES14A. The contact in the exposure is approximately at 66m OD, which agrees with the depth at which the change in resistivity from high to very high occurs. The expected values for silty sand recorded in the exposure would be lower than those obtained in the inverse model, however, as shown in the forward modelling exercise in Chapter 5, in a situation of high resistivity layers overlying medium resistivities, the boundary of the inverse model tends to be in the middle range between the two, which would be around $1500\Omega\text{m}$.

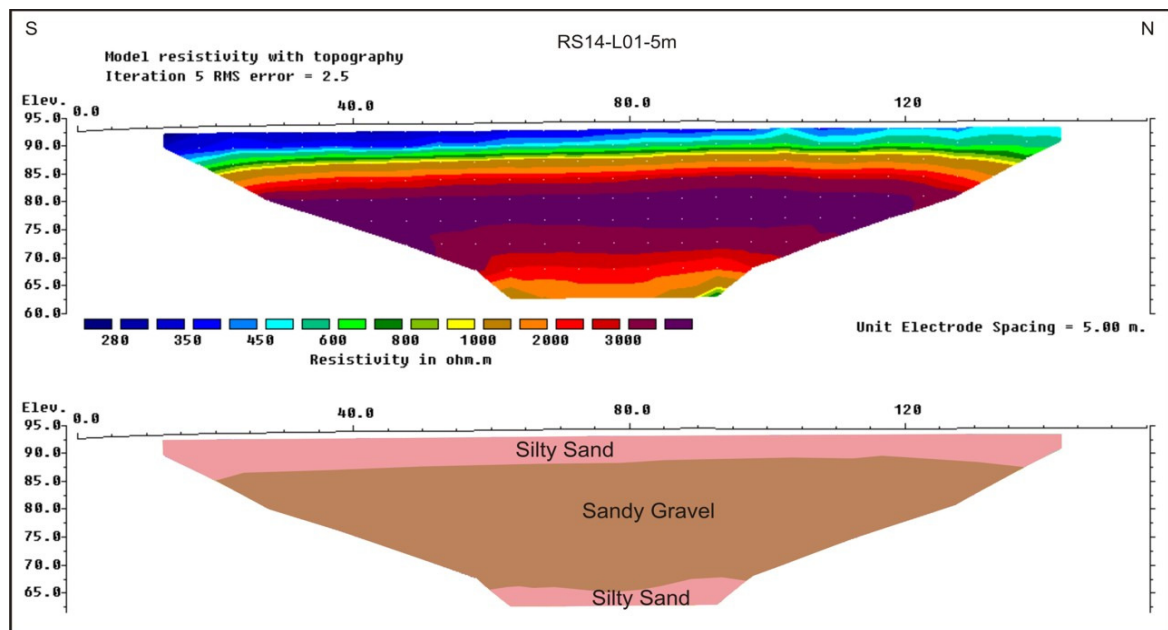


Figure 6.114 - Electrical Resistivity profile RS14-L01-5m collected in S14 and its interpretation.

6.14.3 – Ground Penetrating Radar (GPR)

A number of hyperbolic reflections were imaged along the three radargrams, These were used to estimate the velocity of the material underlying the subsurface at 0.082m/ns.

Line **GS14-L01-100MHz** is a 172m long profile running approximately south to north, at right angles to the flat topped hill's long axis. The topographically corrected original and migrated profiles, together with the interpretation of the main reflectors, are presented in Figure 6.115. Maximum penetration was of the order of 8m. A set of subhorizontal moderately continuous to discontinuous reflectors dominate the lower 3 - 4m of the radargram (L1f1-Gfp). These are overlain by a continuous layer 2 - 3m in thickness showing moderately continuous reflectors, subhorizontal or gently dipping southwards (L1f2-Gfc). A channel feature has been identified within the layer from 15 - 25m. This layer is overlain by one running the length of the whole profile (L1f3-Gfm). Its lowermost reflector is continuous and subparallel to the surface, however, reflectivity within the layer is very poor.

Line **GS14-L02-100MHz** consists of a 96m long profile running approximately west to east, along the flat topped hill's long axis. Figure 6.116 displays the profile topographically corrected, processed and interpreted. Maximum penetration was of the order of 8m. The lower radar facies located below 89m OD is dominated by discontinuous to moderately continuous subhorizontal reflectors (L2f1-Gfm). These are overlain by a 3 - 4m thick layer (L2f2-Gfc) dominated by moderately continuous oblique non-parallel and a number of curved concave up reflectors, which have been interpreted as cross-bedding and channel features. This layer, in turn, is overlain by a radar facies consisting of few chaotic discontinuous reflectors (L2f3-Gfm). The contact between both facies is depicted as a continuous reflector subparallel to the surface as recorded in L01.

Line **GS14-L03-100MHz** consists of a 97m long profile running west to east parallel to and 90m south of L02. Figure 6.117 displays the profile topographically corrected, processed and interpreted. Maximum penetration was of the order of 8m. The lower layer (below 89m OD) is characterised by discontinuous to moderately continuous subhorizontal

to oblique non-parallel reflectors (L3f1-Gfm). These are overlain by a 2 - 3m thick layer (L3f2-Gfc) dominated by moderately continuous oblique non-parallel and two curved concave up reflectors. As in L02, these have been interpreted as cross-stratified sediments with two channel features probably running oblique to the profile. This is overlain by a layer running along the whole profile (L3f3-Gfm) with a continuous reflector subparallel to the surface marking its lower contact and within which there are a few chaotic discontinuous reflectors.

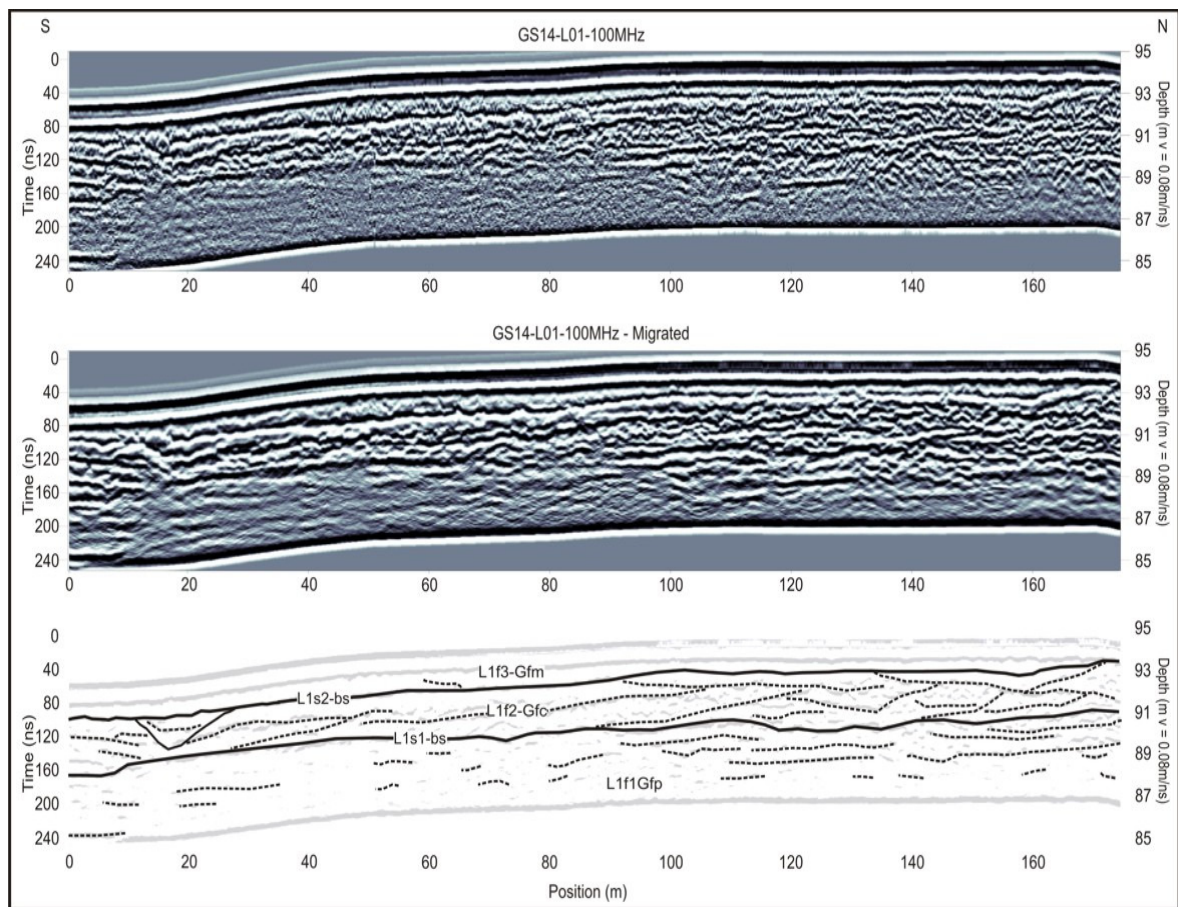


Figure 6.115 – GPR profile GS14-L01-100MHz collected in S14. Top – topographically corrected radargram with dewow and AGC Gain. Middle – topographically corrected migrated radargram using a 0.078 m/ns velocity. Bottom – Interpretation of the migrated radargram

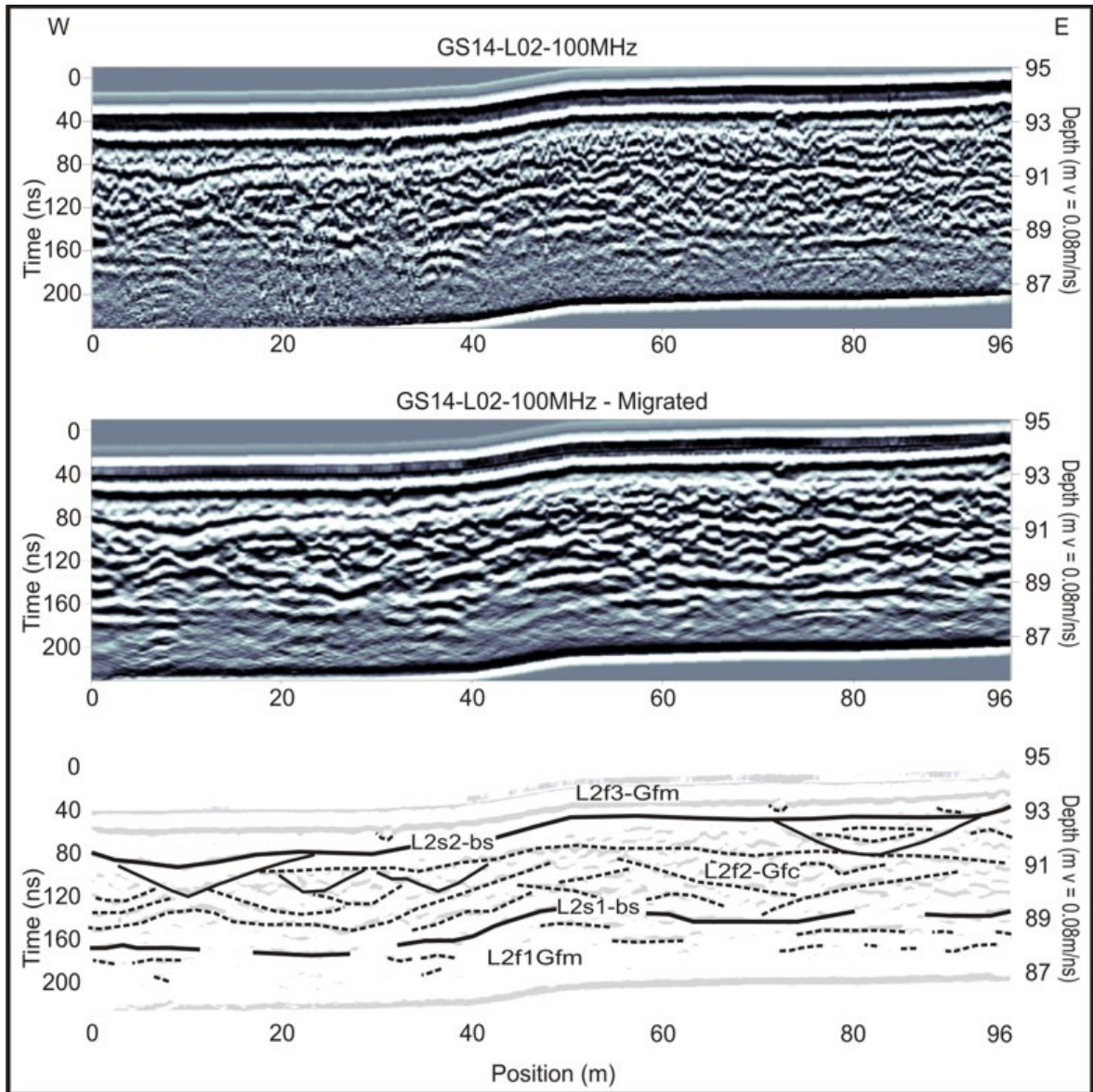


Figure 6.116 – GPR profile GS14-L02-100MHz collected in S14. Top – topographically corrected radargram with dewow and AGC Gain. Middle – topographically corrected migrated radargram using a 0.078 m/ns velocity. Bottom – Interpretation of the radargram.

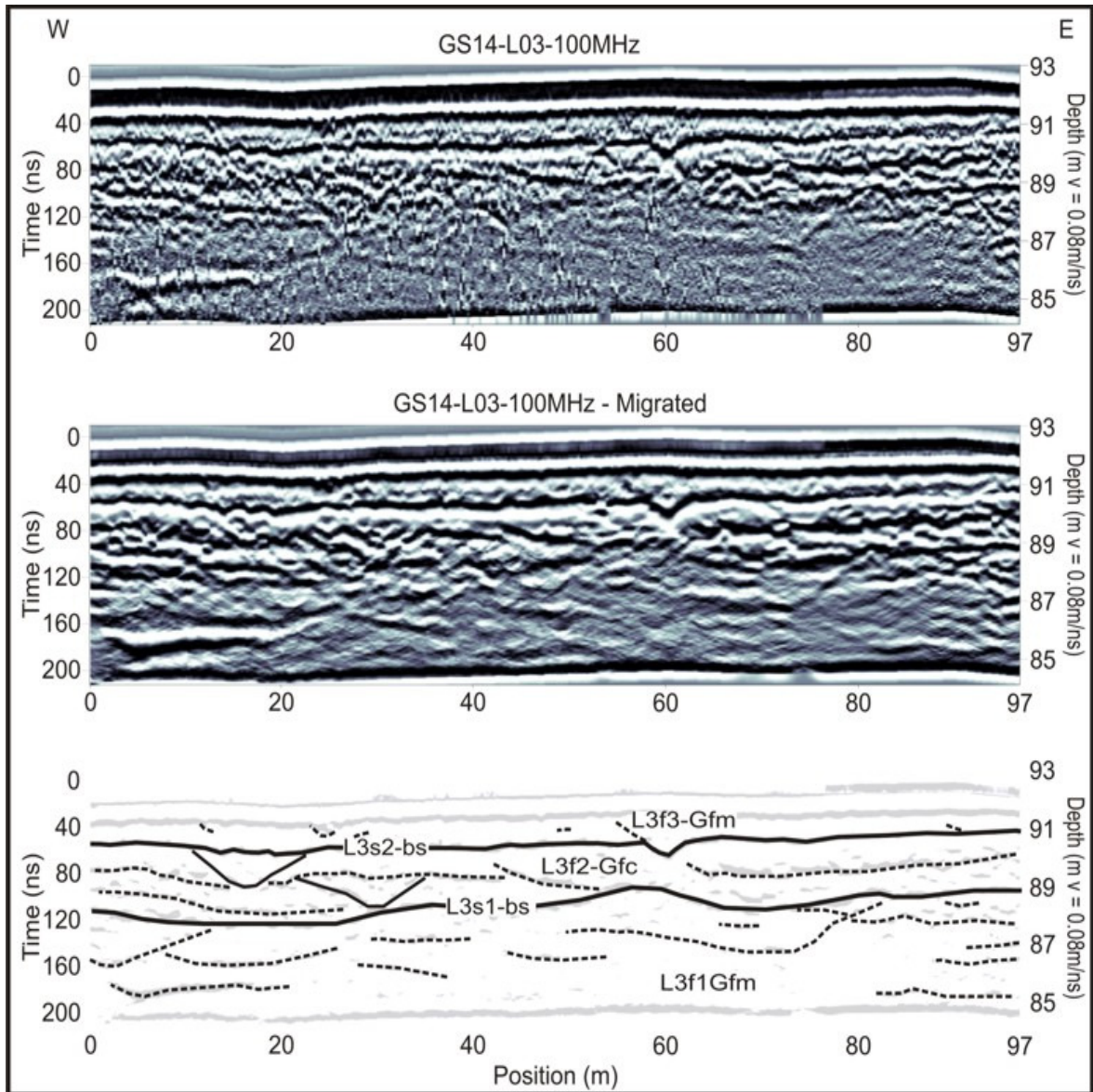


Figure 6.117 – GPR profile GS14-L03-100MHz collected in S14. Top – topographically corrected radargram with dewow and AGC Gain. Middle – topographically corrected migrated radargram using a 0.078 m/ns velocity. Bottom – Interpretation of the radargram.

6.15 – Site S15

6.15.1 – Introduction

The site is located 2 Km north of Kilbeggan in a gently undulating area along the southern margin of one of the ridges composing the Split Hill Esker (Figure 6.1). The Esker, along the northern margin of the site, reaches a maximum height of 10m above the site (see Plate 6.21). The surrounding landscape to the south is composed of diamicton (See Map 1) and is depressed relative to the site. The east and west margins are 2 - 3m relatively higher and were mapped as sand and gravel. A gentle depression within the site was interpreted as a shallow kettle hole of irregular shape. Its perimeter is delineated in Figure 6.118.



Plate 6.21 – View of Site 15 from the end point of the collected ERT profile, see Split Hill Esker running approximately east-west in the background.

No exposure or borehole data were recorded within the site. It is known from the field mapping that the ridge feature running along the northern margin is mainly composed of cobbles and gravel. An ERT survey and two GPR surveys were carried out in the site to determine the nature of the sediment composing the site and any associated sedimentological structures. The locations of the survey lines are presented in Figure 6.118.

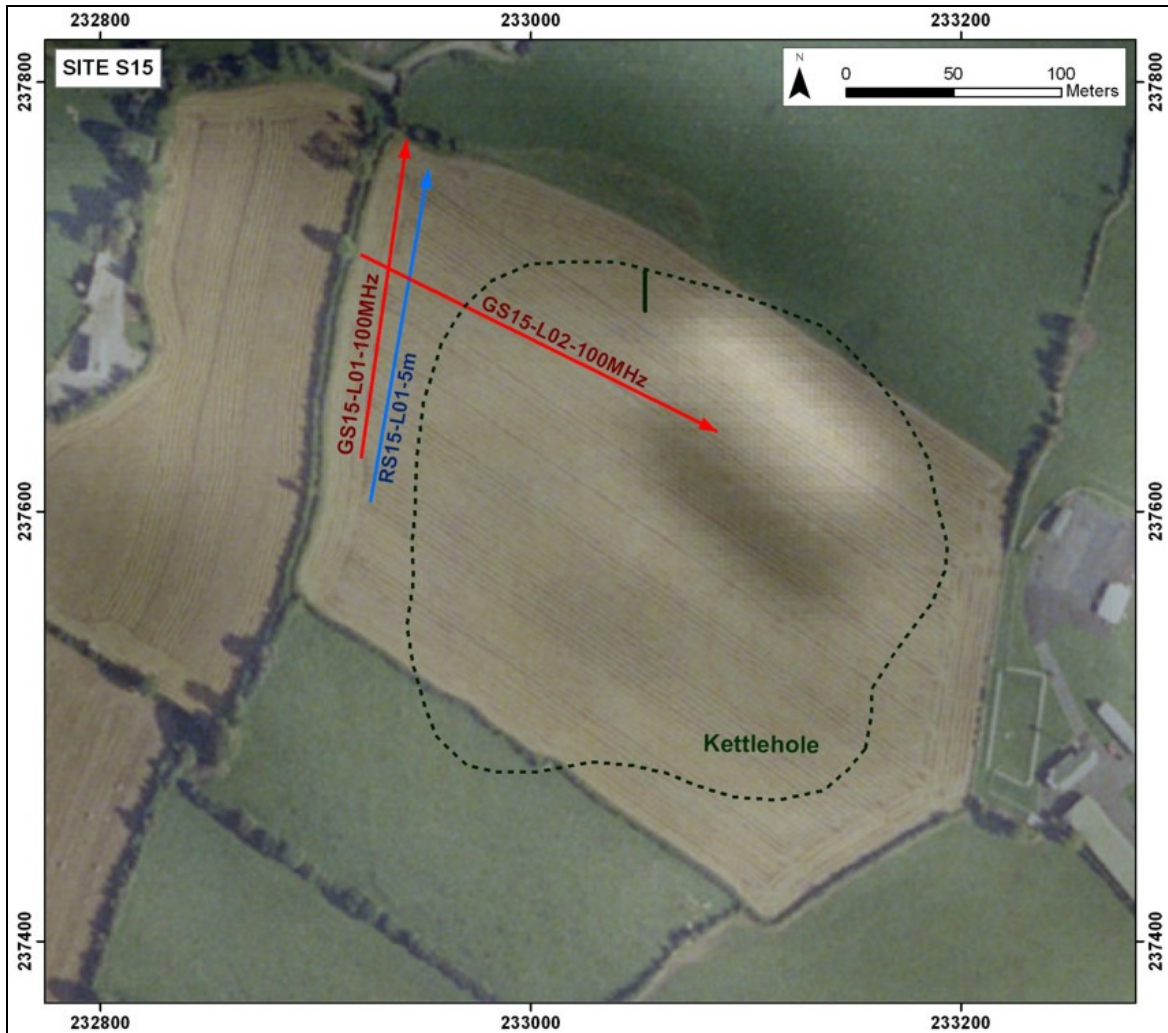


Figure 6.118 – Location of Electrical Resistivity (blue) and GPR (red) profiles surveyed in Site S15.

6.15.2 – Electrical Resistivity Data

The Geopulse Tigre resistivity meter with 32 electrodes was used to collect an ERT section with 5m electrode spacing using the Wenner-Schlumberger array (**RS15-L01-5m**). The profile (Figure 6.119) displays a number of shallow, channel like features showing low to medium resistivity values ($< 250\Omega\text{m}$), which have been interpreted as fine sediments, probably sandy silt or silty sand. The area presenting these low resistivity values attains a maximum thickness of around 5m at about the 110m position and gradually pinches out towards the north and south. These sediments are underlain by a continuous zone extending across the entire profile for approximately the top 10m with medium to high

resistivity values (300 - 1000Ωm), which has been interpreted as sandy gravel. Very high resistivity values dominate the areas greater than 10m depth, reaching up to 7000Ωm along the edges of the profile. These values have been interpreted as bedrock.

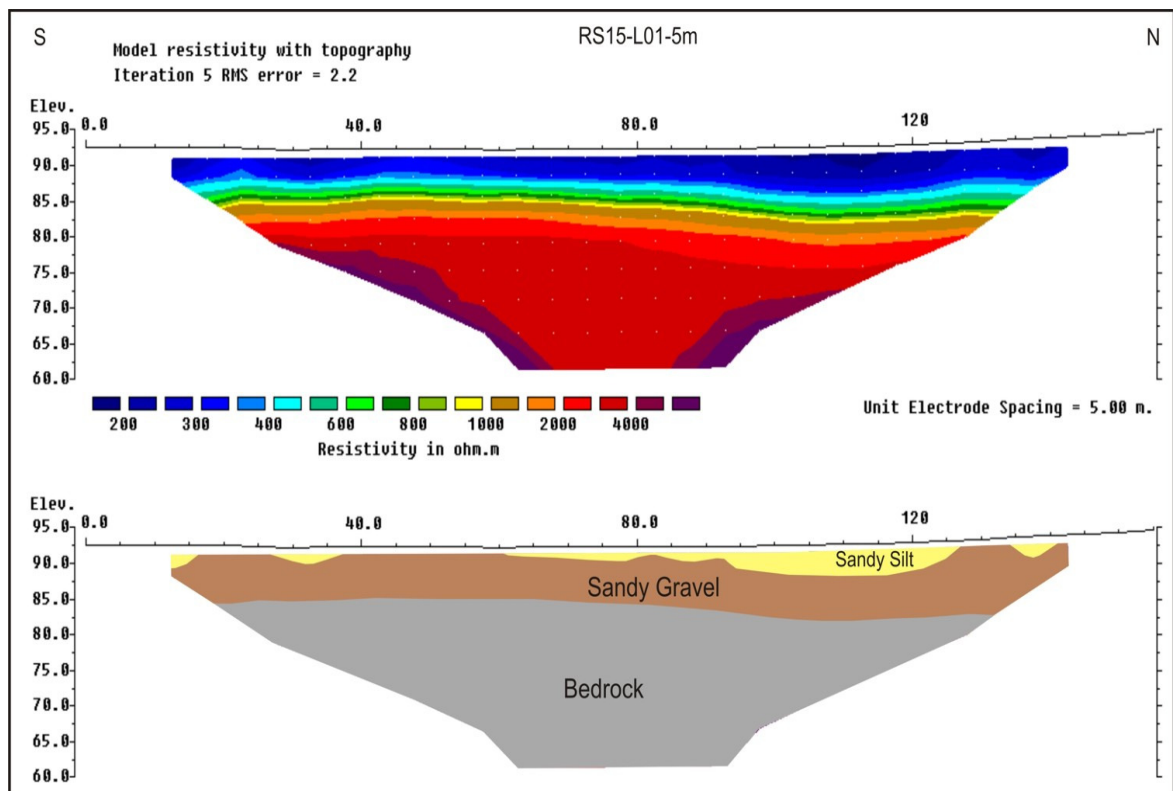


Figure 6.119 - Electrical Resistivity profile RS15-L01-5m collected in S15 and its interpretation.

6.15.3 – Ground Penetrating Radar (GPR)

A number of hyperbolic reflections were recorded for the two recorded radargrams. It can be observed from Figure 6.120 that the hyperbolae are characterised by different reflection amplitudes at the same depth, indicating different velocities occurring within the same profile. It was previously illustrated in Chapter 5 that distortions of the radargram should be expected when using the incorrect velocity (Figure 5.17). However, the processing software used for this thesis allows a unique velocity to be used for each profile, thus, an average velocity of 0.095m/ns has been estimated for the two profiles.

Line **GS15-L01-100MHz** is a 145m length profile running approximately south to north, at right angles to the esker running along the northern margin of the site. The original and migrated topographically corrected profiles together with the interpretation of the main reflectors are presented in Figure 6.120. Maximum penetration was of the order of 7m. Discontinuous reflectors dominate the lower parts of the radargram (L1f1-Gfm). These are overlain by a continuous layer 5 - 6m in thickness pinching out northwards from 0 - 90m. A number of reflectors dipping north occur from 0 - 20m, however, moderately continuous reflectors dipping 5° - 10° south dominate this radar facies (L1f2-Gfs). A 5 - 6m thick layer overlies f2 from 60 - 90m and f1 from 90 - 145m. This is dominated by moderately continuous sinuous reflectors dipping in different directions (L1f3-Gfc) and has been interpreted as cross-stratified sediments.

Line **GS15-L02-100MHz** consists of a 184m long profile running approximately west to east, along the southern margin of the esker ridge and crossing the kettle hole illustrated in Figure 6.118. Figure 6.121 displays the profile topographically corrected, processed and interpreted. Maximum penetration was of the order of 8m. The signal is mostly attenuated when reaching the lower radar facies (L2f1-Gfm), which is illustrated by a few discontinuous reflectors at the 140m position. It is overlain from 30 - 150m by a layer (L2f2-Gfs) dominated by moderately continuous reflectors dipping 10° ESE, which are separated from 80 - 150m by sets of minor reflectors gently dipping WNW. This layer is overlain by an onlap contact by a 4 - 5m thick layer (L2f3-Gfc) wedging out from 40 - 80m and mainly composed of moderately continuous oblique non-parallel reflectors crossing each other and possibly related to cross-stratified sediments. A layer, pinching out WNW (L2f4-Gfm), overlies f2 from 150 - 184m. A single continuous reflector parallel to the surface dominates this layer. Penetration is very poor in this area, probably due to high silt/clay contents of the sediments.

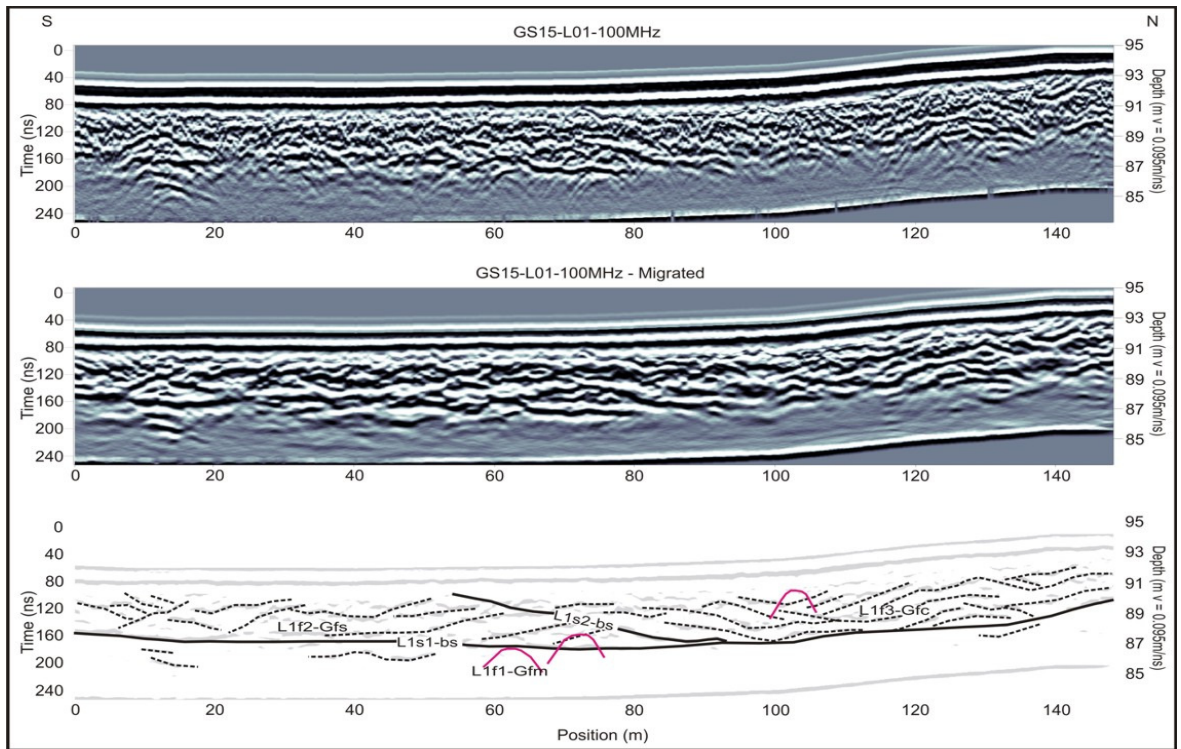


Figure 6.120 – GPR profile GS15-L01-100MHz collected in S15. Top – topographically corrected radargram with dewow and AGC Gain. Middle – topographically corrected migrated radargram using a 0.095m/ns velocity. Bottom – Interpretation of the radargram.

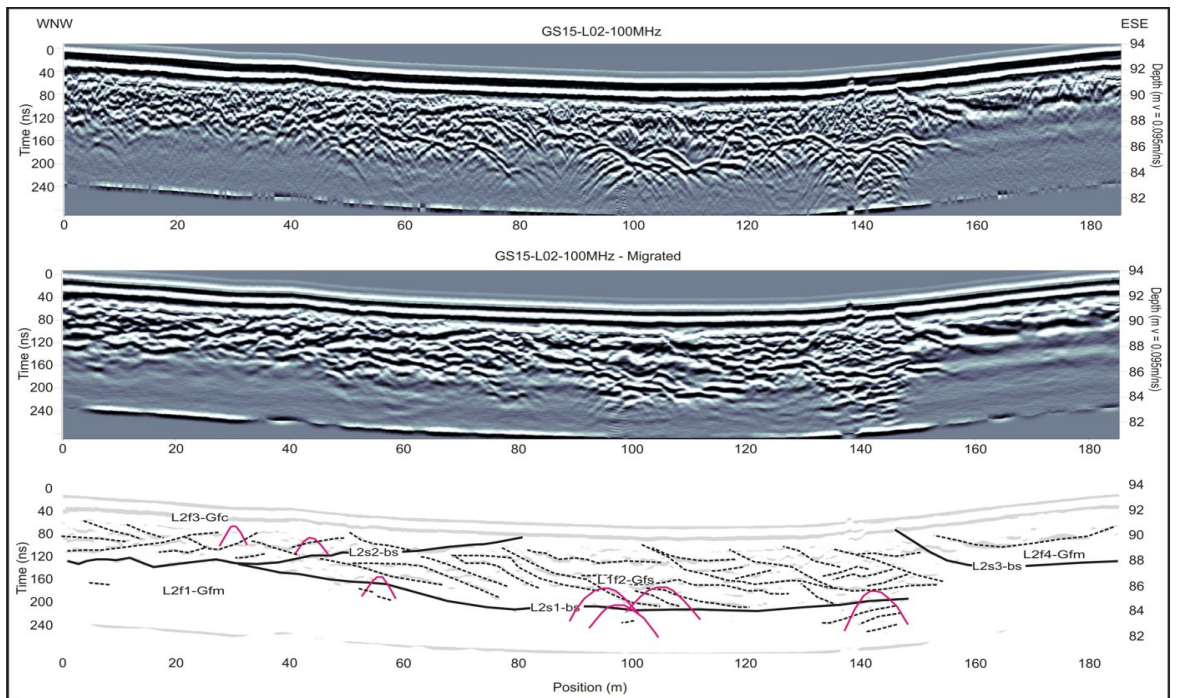


Figure 6.121 – GPR profile GS15-L02-100MHz collected in S15. Top – topographically corrected radargram with dewow and AGC Gain. Middle – topographically corrected migrated radargram using a 0.095m/ns velocity. Bottom – Interpretation of the radargram

6.16 – Site S16

6.16.1 – Introduction

The site is located approximately 4 Km south of Kilbeggan along the southern margin of Clara Esker (Figure 6.1). The area has been mapped as hummocky terrain dominated by kame and kettle topography (Plate 6.22) underlain by glaciofluvial sand and gravel associated with the Esker (see Map 1). A ridge feature cuts across the site in a southwest to northeast direction and joins the southern flank of the main Clara Esker ridge which runs west-east at this point. This feature is approximately 1000m in length, 300m in width and 5 - 7m relatively higher than the surrounding landscape. It ranges in altitude between 87 and 93m OD.



Plate 6.22 – View of Site 16 from the end point of the collected ERT profile, The landscape is very undulating.

No exposure or borehole data were recorded within the site. It is known that the Clara Esker is mainly composed of gravel, cobbles and boulders in this area. An ERT survey and two GPR surveys were carried out to determine the internal characteristics of the site. The location of the survey lines is presented in Figure 6.122.

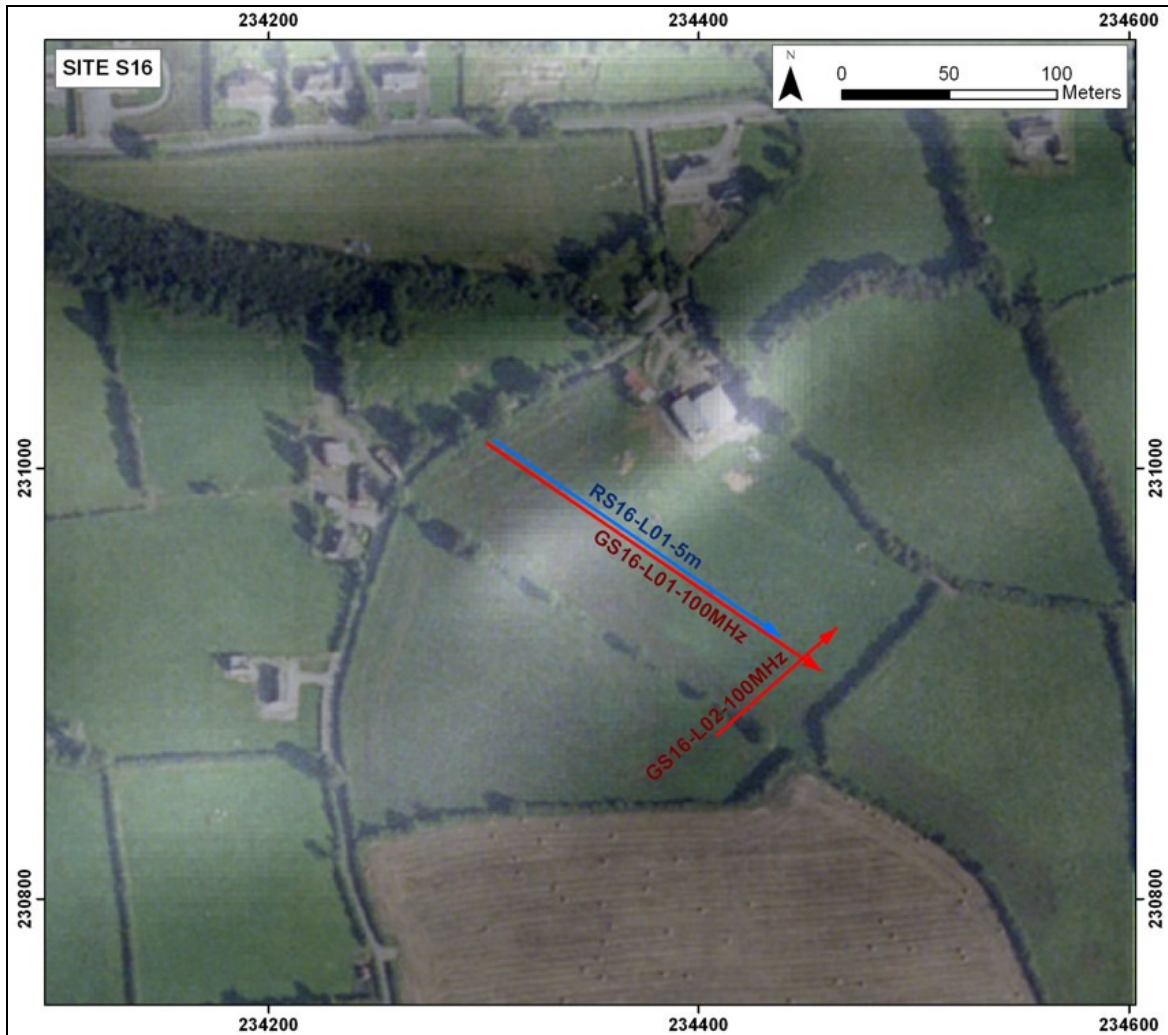


Figure 6.122 – Location of Electrical Resistivity (blue) and GPR (red) profiles surveyed in Site S16.

6.16.2 – Electrical Resistivity Data

An ERT section using 5m electrode spacing was obtained using the Wenner-Schlumberger array (**RS16-L01-5m**). The profile (Figure 6.123) displays a number of shallow depressions dominated by low to medium resistivity values ($< 250\Omega\text{m}$), which have been interpreted as fine sediments, probably silt/clay. These sediments occur in relatively depressed parts of the hummocky landscape and the depressions are probably related to the presence of former buried ice. They are underlain in places by a 7 – 10m thick layer running along the whole profile with medium to high resistivity values (400 to $1500\Omega\text{m}$), which has been interpreted as sandy gravel. A low resistivity layer underlies it with an

undulating contact and is dominated by resistivities ranging 120 - 500Ωm and is thought to be diamicton. A medium to high resistivity (650 - 750Ωm) layer is located along the lower parts of the profile from 57 - 61m OD. This is interpreted as bedrock, probably weathered, as the resistivity expected from fresh limestone would typically be higher.

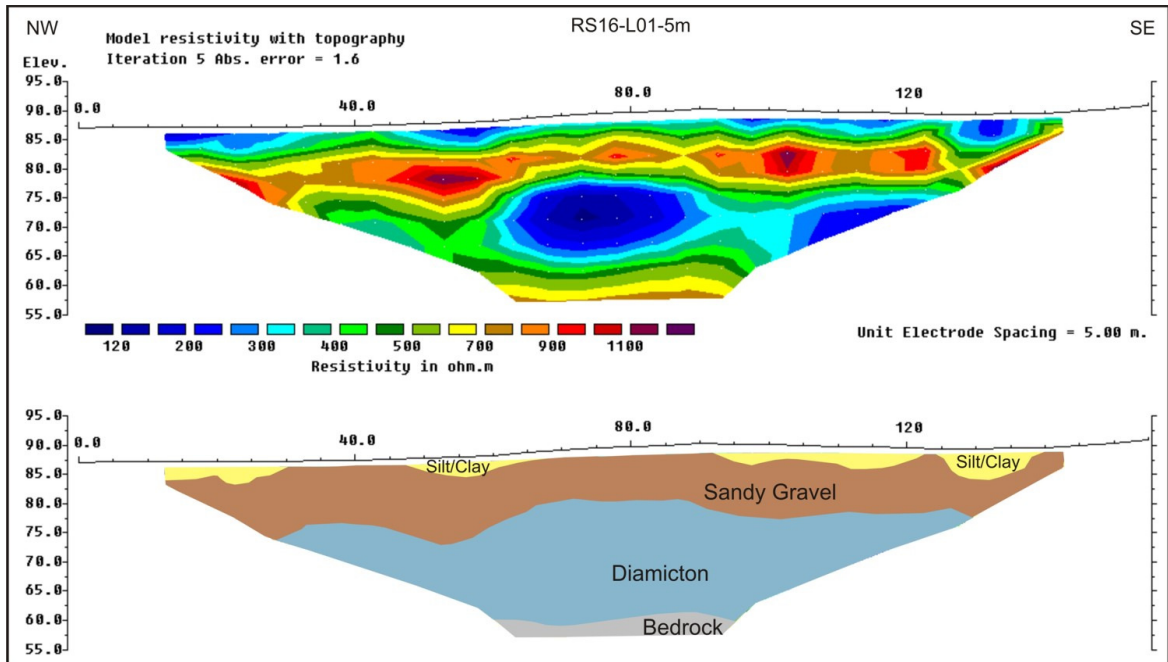


Figure 6.123 - Electrical Resistivity profile RS16-L01-5m collected in S16 and its interpretation

6.16.3 – Ground Penetrating Radar (GPR)

A number of hyperbolic reflections were recorded for the two radargrams and an average velocity of 0.092m/ns has been estimated for them.

Line **GS16-L01-100MHz** is a 165m length profile running northwest to southeast along the southern margin of Clara Esker. The topographically corrected original and migrated profiles together with the interpretation are presented in Figure 6.124. An expanded version of this radargram is presented in Enclosure 2 – E2C. Maximum penetration was of the order of 8m. Very poor reflectivity was recorded in the lower parts of the radargram (L1f1-Gfm) as most of the energy has been attenuated at this depth, though some oblique discontinuous reflectors occur in this radar facies from 30 - 80m. This is overlain along the whole profile by moderately continuous and discontinuous sinuous reflectors, which are

distorted in some areas. These reflectors are distorted from 50 - 70m by a set of three moderately continuous reflectors dipping 20° - 30° NW and from 110 - 140m by two sets of reflectors dipping 20° - 30° SE and NW, respectively. These reflectors have been interpreted as normal faults possibly associated with the collapse of sediments during melting of buried ice. Several hyperbolae indicating the presence of large boulders have been identified in this layer. An artefact caused by a telephone pole located at the start of the line is shown in red at 0 - 10m.

Time slice analysis for this radargram (Figure 6.125) shows very low amplitudes from 0 - 12m, indicating the presence of fine sediments with a high attenuation rate. These increase from 12 - 35m, especially around 30m possibly related to the presence of sand and gravel. A drop in the values occurs between 35 - 60m, which agrees with the presence of silt/clay detected in RS16-L01-5m (Figure 6.123). Higher amplitudes are registered from 60 - 90m and are probably related to the presence of sand and gravel identified in the ERT profile. The amplitude decreases again from 90 - 125m, agreeing with the lower ground area dominated by fine sediments along the surface, which attenuate the signal. The amplitude signature for the last 45m increases dramatically, this corresponds to the topographically higher area within the profile and probably with coarsening of the sediments.

Line **GS16-L02-100MHz** consists of a 71m long profile running southwest to northeast, cutting across L01 at 155m as illustrated in Figure 6.122. Figure 6.126 displays the profile topographically corrected, processed and interpreted. Maximum penetration was of the order of 8m. The lower layer (L2f1-Gfm) shows a few moderately continuous reflectors from 40 - 65m. It is overlain by a layer (L2f2-Gfcd) dominated by discontinuous to moderately continuous reflectors subparallel to the subsurface, oblique to each other and distorted in places by a number of reflectors dipping less than 15° NE. As in L01, these reflectors have been interpreted as normal faults associated with the collapse of sediments during the melting of bodies of buried ice. A number of hyperbolae have been identified indicating presence of large boulders along the profile.

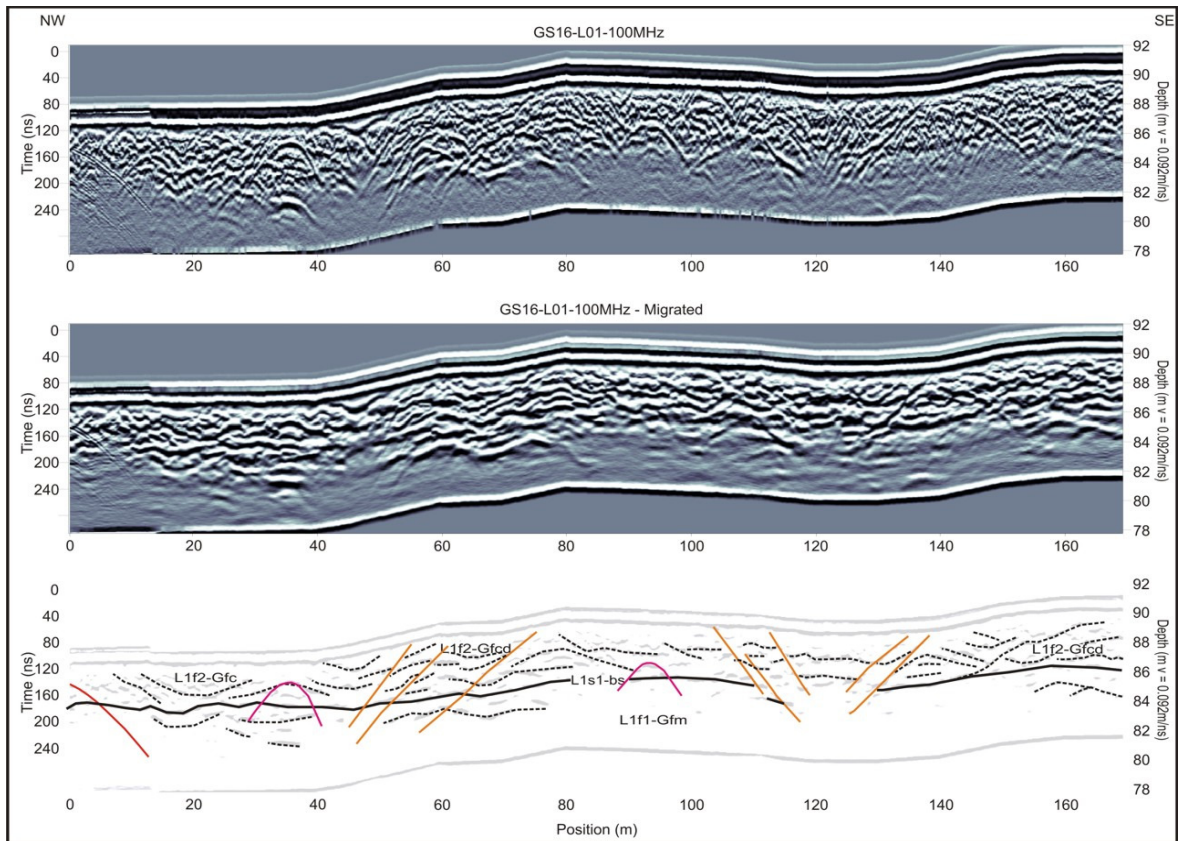


Figure 6.124 – GPR profile GS16-L01-100MHz collected in S16. Top – topographically corrected radargram with dewow and AGC Gain. Middle – topographically corrected migrated radargram using a 0.092m/ns velocity. Bottom – Interpretation of the radargram.

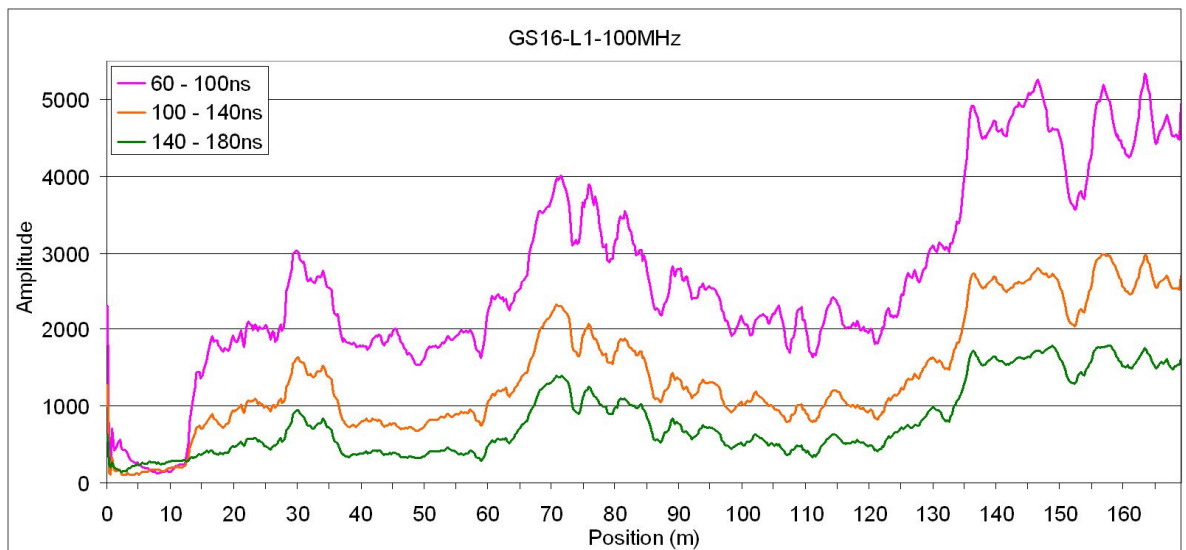


Figure 6.125 – Time-slice analysis for GPR profile GS16-L01-100MHz collected in Site S16.

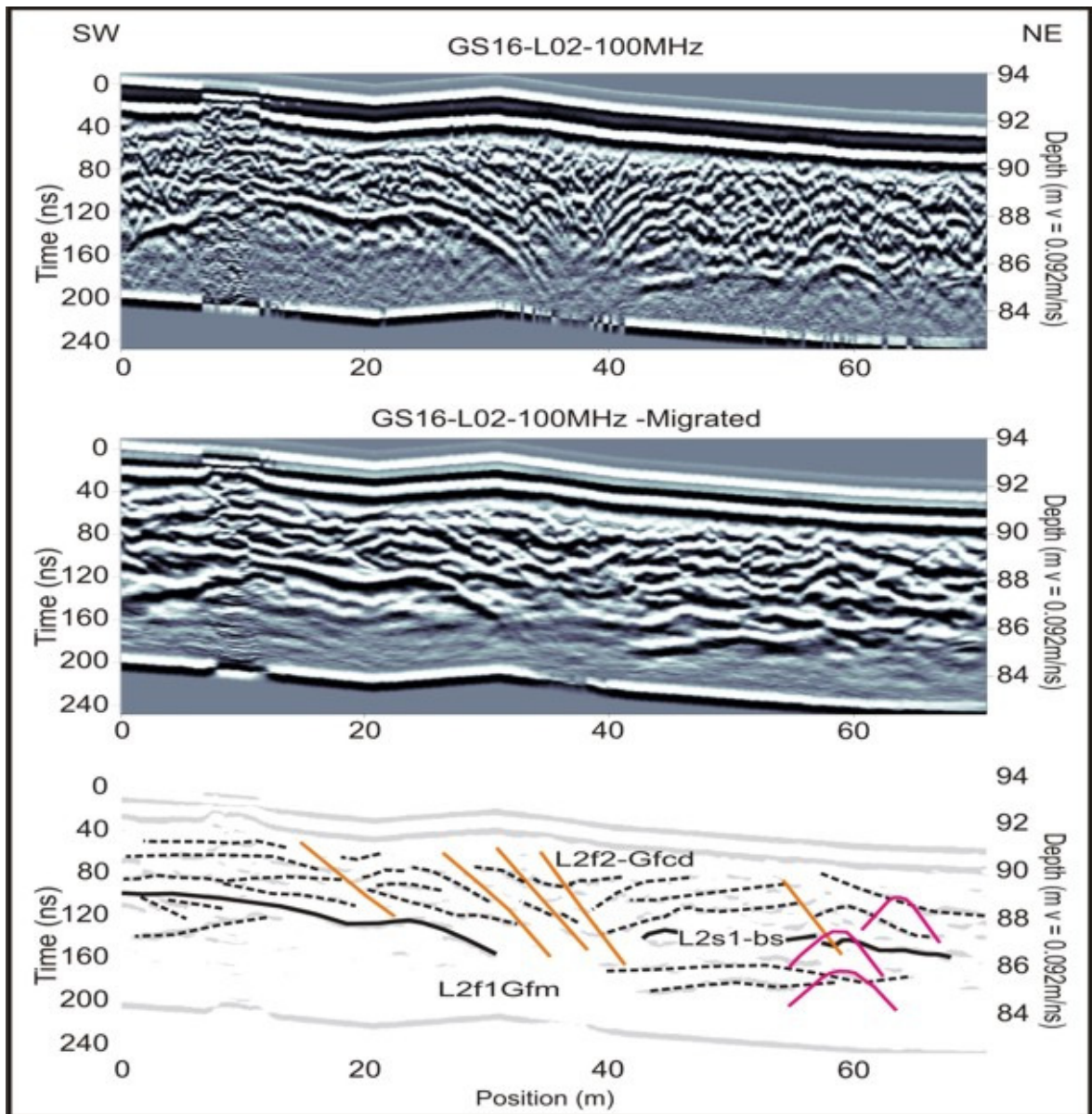


Figure 6.126 – GPR profile GS16-L02-100MHz collected in S16. Top – topographically corrected radargram with dewow and AGC Gain. Middle – topographically corrected migrated radargram using a 0.092m/ns velocity. Bottom – Interpretation of the radargram.

6.17 – Site S17

6.17.1 – Introduction

This site is located along the N6 between Horseleap and Kilbeggan, 3Km west of Site S15 (Figure 6.1). The area has been described in Chapter 4 as a fan/glaciodeltaic complex fed by a meltwater subglacial conduit associated with the Horseleap Esker. The fan reaches a width of more than 500m, length over 700m and 10 - 15m height above the surrounding landscape and altitude ranges 88 - 93m OD. The feature has been mapped as glaciofluvial sand and gravel associated with esker gravel. The relatively depressed landscape to its north, south and east margins is dominated by diamicton and glaciofluvial sand and gravel, the west margin is relatively higher and has been mapped as the start of Horseleap Esker (see Map 1). No exposure or borehole data were recorded within the site. The site has been mapped as sand and gravel deposits during field mapping based on its fan shape and its close morphological association with Horseleap Esker. The locations of the survey lines are presented in Figure 6.127.

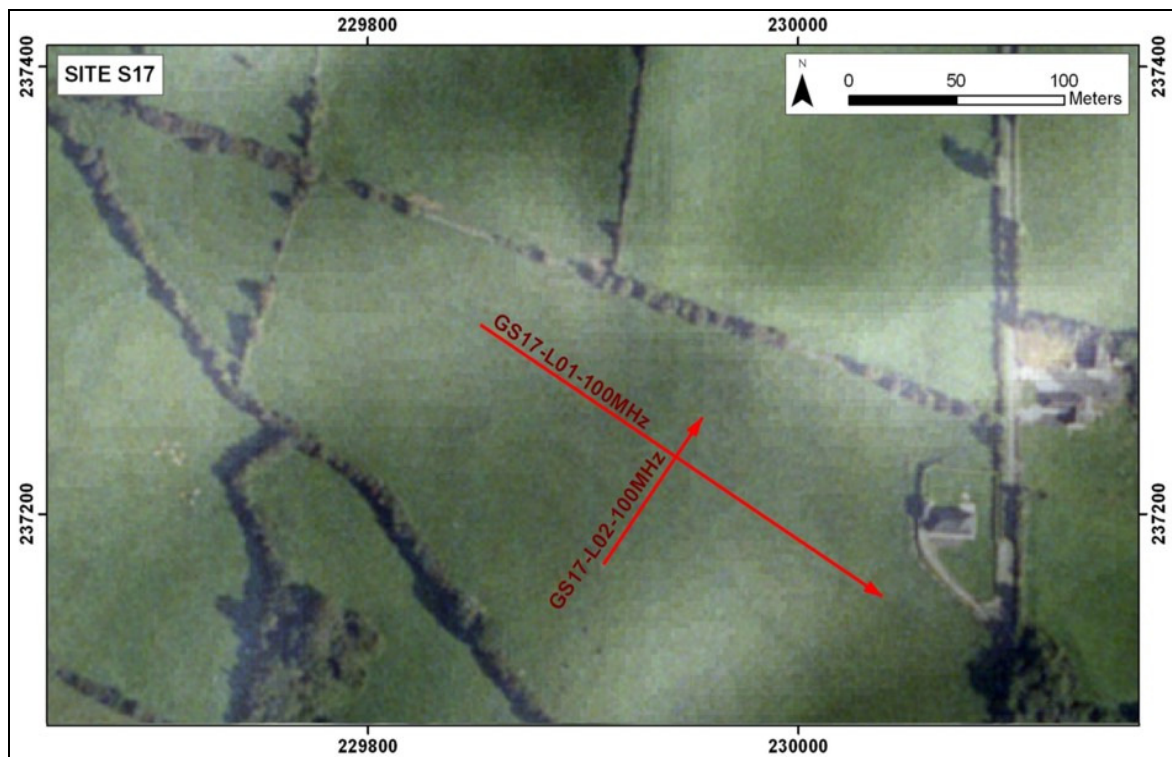


Figure 6.127 – Location of Electrical Resistivity (blue) and GPR (red) profiles surveyed in Site S17.

6.17.2 – Ground Penetrating Radar (GPR)

A number of hyperbolic reflections were recorded for the two radargrams, and were used to estimate the subsurface velocity at 0.082m/ns.

Line **GS17-L01-100MHz** consists of a 218m long profile running west-northwest to east-southeast, along the long axis of the fan. Figure 6.128 displays the profile topographically corrected, processed and interpreted. Maximum penetration was of the order of 8m. The lower part of the profile (> 150ns) from 0 - 140m shows very poor penetration, probably due to high silt/clay contents (L1f1-Gfm). This is overlain from 15 - 50m by an area dominated by hyperbolae and discontinuous chaotic reflectors (L1f2-Gfm). This, in turn, is overlain from 15 - 20m with an onlap contact by a set of moderately continuous reflectors dipping 5 - 20° ESE (L1f3-Gfs). Moreover, it is overlain from 50 - 120m with a downlap contact by a set of continuous sinuous reflectors dipping 10 - 15° ESE from 50 - 60m and 90 - 120m (L1f3-Gfs). Radar facies f2 and f3 are overlain from 0 - 110m with an erosive contact by a 1 - 2m thick layer (L1f4-Gts) dominated by discontinuous chaotic reflectors. A 4 - 7m thick layer overlies f3 with an onlap contact with moderately continuous reflectors dipping 5 - 10° ESE from 110 - 160m (L1f4-Gfs). These reflectors evolve into discontinuous oblique non-parallel reflectors from 160 - 218m (L1f4-Gfc). Hyperbolic reflections increase in this area indicating the presence of boulders. All these facies are overlain by a 1 - 2m thick layer dominated by discontinuous chaotic reflectors (L1f5-Gts) with its baseline between 90 and 91m OD.

Line **GS17-L02-100MHz** is a 78m long profile running south-southwest to north-northeast, orthogonal to the fan's long axis. The topographically corrected original and migrated profiles together with the interpretation are presented in Figure 6.129. Maximum penetration recorded is of the order of 6m. The profile displays a continuous subhorizontal sinuous reflector running at 90m OD underlain by a series of multiples and few discontinuous reflectors dipping in a number of directions (L2f3-Gfm). The reflector is overlain by a layer 1 - 2m in thickness composed of a series of discontinuous oblique reflectors (L2f4-Gfc). Also, hyperbolae indicate presence of boulders along the radargram.

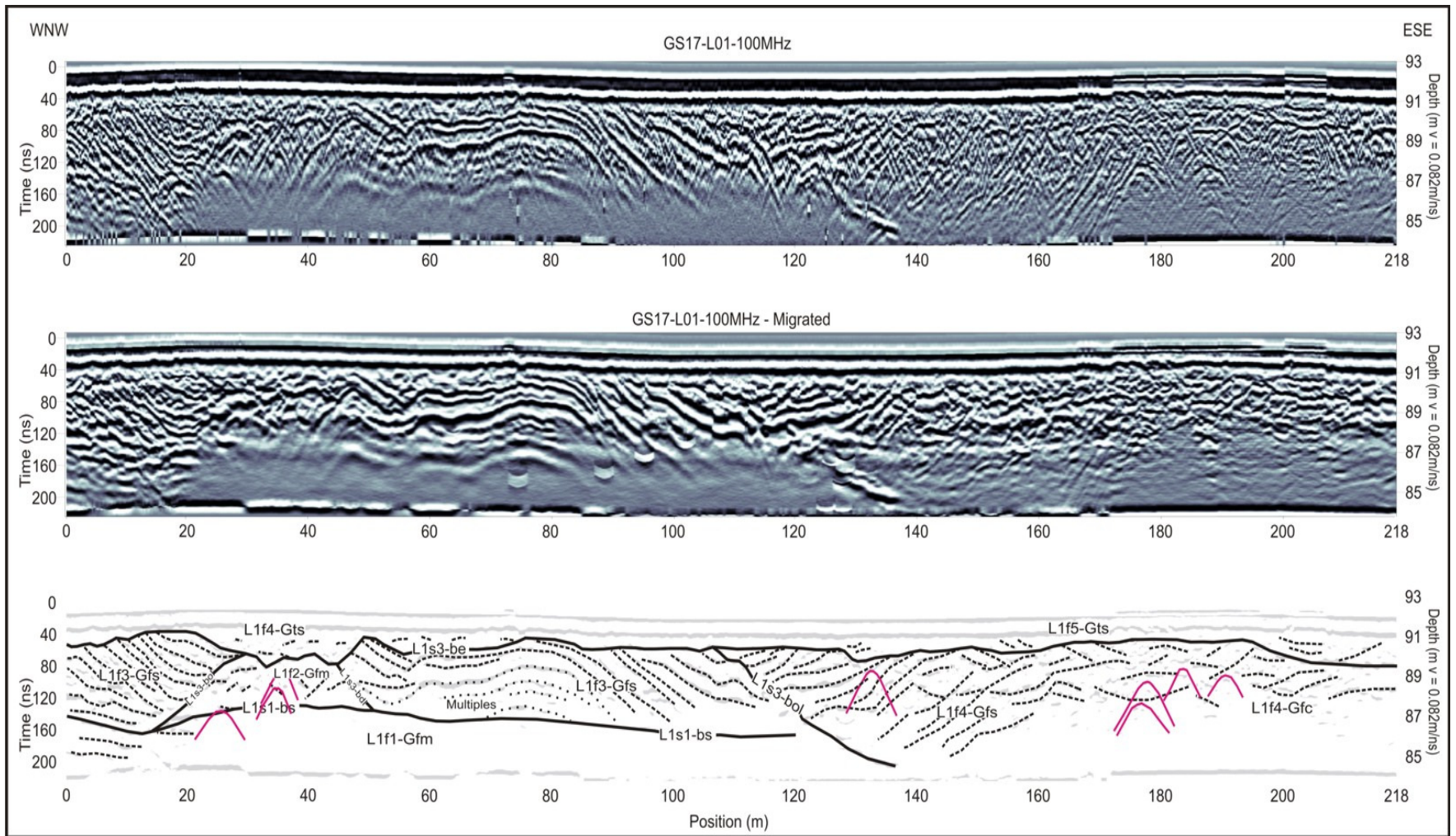


Figure 6.128 – GPR profile GS17-L01-100MHz collected in S17. Top – topographically corrected radargram with dewow and AGC Gain. Middle – topographically corrected migrated radargram using a 0.092m/ns velocity. Bottom – Interpretation of the radargram.

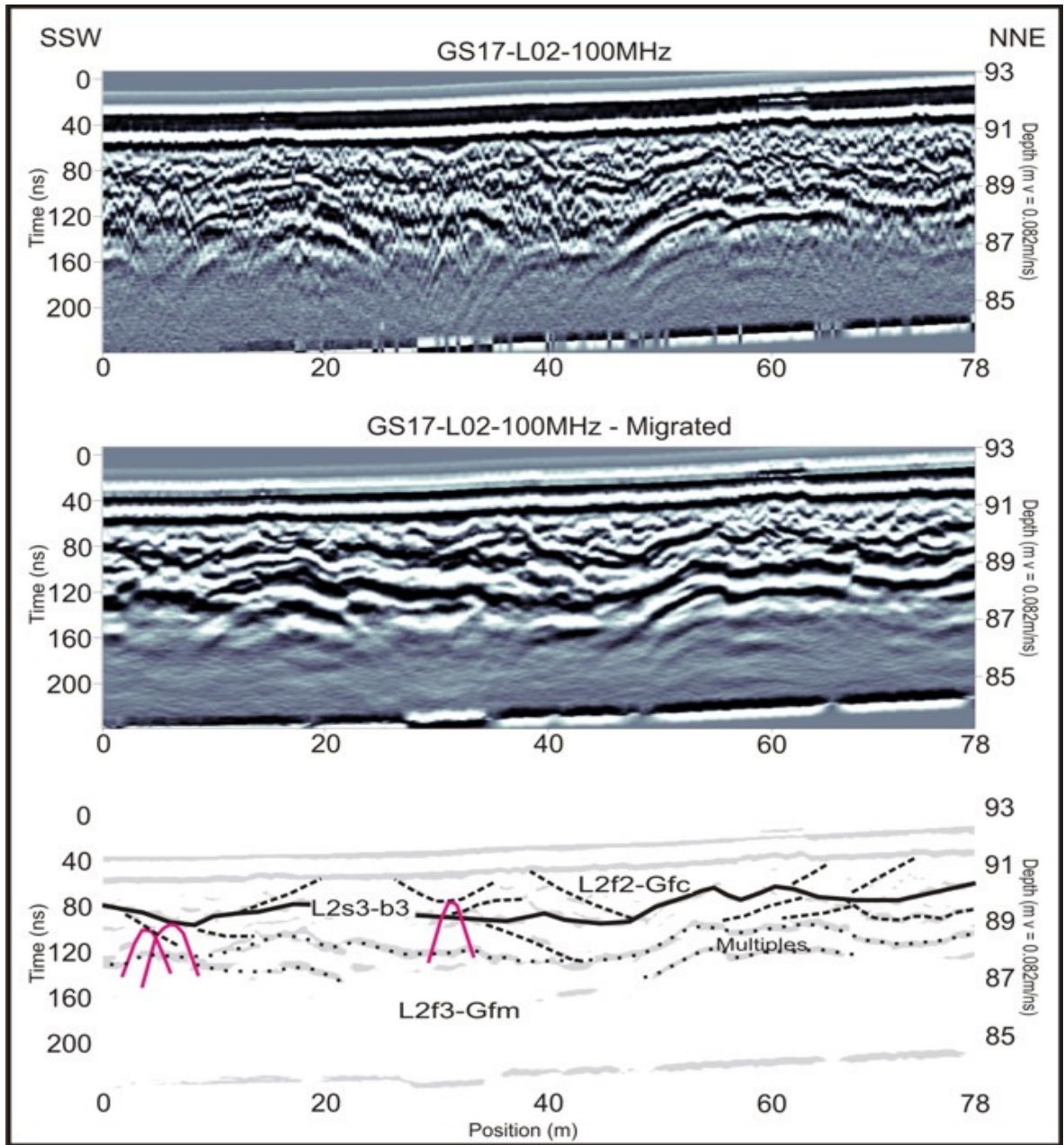


Figure 6.129 – GPR profile GS17-L02-100MHz collected in S17. Top – topographically corrected radargram with dewow and AGC Gain. Middle – topographically corrected migrated radargram using a 0.092m/ns velocity. Bottom – Interpretation of the radargram.

6.18 – Summary

Three geophysical techniques (Electrical Resistivity, GPR and VLF) have been used for the recognition and classification of Quaternary sediments in 17 sites located in the study area, Figure 6.1.

Site S1 was surveyed intensively with a range of geophysical methods. It has been used as a test area to refine the data collection, processing and interpretation methods for the remaining sites. Electrical Resistivity methods encompass Electrical Resistivity Tomography (ERT) and Azimuthal Resistivity. ERT has also been used for the production of a 3D model for a part of Site 1 and for time-lapse data analysis. Six lithological types have been differentiated by means of ERT surveys and borehole drilling, these are in chronological order from older to younger, bedrock ($>1000\Omega\text{m}$), weathered bedrock (600 - 1200 Ωm), diamicton (100 - 300 Ωm), esker muddy boulders/cobbles/gravel (500 - 1000 Ωm), glaciofluvial sand and gravel (400 - 1500 Ωm) and lacustrine silt/clay (40 - 150 Ωm). Important seasonal variations in the resistivity values for a range of sediment types has been estimated by means of time-lapse resistivity analysis. Increases in the resistivity values of over 100% have been detected in glaciofluvial sand and gravel and esker muddy gravel during the dry season. These changes are usually less drastic in silt/clay ($<30\%$) and diamicton ($<50\%$). The production of a 3D Model has been useful for the depiction of channel features within the glaciofluvial fan. Azimuthal resistivity has proved useful in understanding the heterogeneous nature of the Quaternary sediments. Both, 2D GPR data have been collected in the site and a 3D model has been generated from them. GPR has been proven to be a powerful tool for the delineation of the detailed internal architecture of the Quaternary sediments and main lithological variations when used in combination with time-slice analysis. Very Low Frequency Electromagnetics (VLF) has been tested and the results showed reasonable correlations with the other methods. The areas underlain by sediments with large matrix contents (lacustrine mud and diamicton) show a positive percentage variation of the filtered real field (FR), well sorted sediment with low conductivity values such as sand and gravel are generally characterised by negative percentage variation of the FR. The VLF vertical resolution is low as it is

dependent on the frequency used, and thus it does not provide substantially more additional information for the reconstruction of the geology of the site.

Morainic ridges recognised during the mapping exercise were surveyed at three sites (Sites S3, S4 and S8). Borehole drilling, ERT and GPR surveys carried out in the three sites have been useful in the identification of depth to bedrock, main lithological types and the major sedimentological and structural settings across and along the features. Deformation structures recorded in the GPR profiles for sites S3 and S8 were inferred as thrust planes related to ice pushing northeast and east, respectively. The ridges have been classified as push moraines in both sites. In contrast, the radar facies recorded in Site S4 seem to be related to a depositional environment. Several deformation structures depicted have been interpreted as normal faults associated with collapse of sediments subsequent to ice front retreat, thus the ridge has been classified as an ice front depositional moraine.

A number of sites were surveyed to locate depositional environments constraining the position and water level of the glacial Paleolake Riada presented in Chapter 4. Site 5 shows glaciofluvial sediments morphologically expressed as a ridge overlying diamicton on bedrock. GPR data illustrate the internal architecture of the top 10m displaying very well developed foresets and normal faulting associated with collapse of formerly ice-marginal supported sediments, which indicate paleocurrents running northwest. Site S6, located on the Ballyduff Esker, was surveyed using borehole drilling and GPR. The site is dominated by interstratified sand, gravel and muddy sand. No clear evidence of glaciolacustrine deposition was found in this site. A fan-shaped feature at the eastern margin of Moate Esker has been surveyed in Site S13. A range of glaciofluvial sediments with thicknesses of over 30m was depicted using ERT. GPR data showed collapse structures associated to the formation of a kettle hole and possible foresets overlain by topsets inferring paleocurrents towards the east. A flat-topped isolated hill located north from Clara has been recorded at Site S14. ERT data show interstratified sand and gravel occurring from 0 - 30m depth. GPR data show three main radar surfaces and some channel features running south to north. However, there is no clear evidence of a glaciolacustrine environment. Site S15 is in an area located along the southern margin of Split Hill Esker.

An ERT profile shows sandy gravel underlain by bedrock and overlain by pockets of fine sediments. GPR data attain fairly poor penetration though a number of radar facies with chaotic reflectors and cross-bedding provide some evidence of a glaciolacustrine environment. A fan shaped feature at the eastern end of Horseleap Esker has been recorded in Site S17. GPR data show a set of reflectors dipping east interpreted as foresets overlain by a thin coating of chaotic reflectors for the first 120m. These may be related to a glaciolacustrine environment at the mouth of Horseleap Esker with paleocurrents indicating deposition east-southeastwards.

Geophysics has been used to survey the main overflow channels mapped during fieldwork (Map 1) located along the watershed between the Shannon and Boyne/Barrow Basins. A long ERT profile (Site S7) was used to determine the lithology of the sediments underlying the channel. It is mainly underlain by diamicton overlying bedrock, weathered in places. A further lake overflow channel has been inferred during field mapping in an area currently covered by peat. A long geophysical line, running across the feature has been recorded using ERT and GPR in Site S9. Peat and diamicton/glaciofluvial sediment thickness variations overlying bedrock have been determined. Moreover, a potential lake overflow channel has been located and its height estimated at 89.5m. Four ERT profiles were collected in Site S11. The results show the presence of glaciofluvial sand and gravel overlying diamicton and underlain by bedrock along the potential overflow channel and diamicton underlain by bedrock along the margins of the feature. The eastern margin of the Shannon Basin watershed has been surveyed in a peat bog at Site S12. ERT data show very low resistivity values indicating a depth to bedrock of over 40m in the area. GPR data show a peat thickness of 0.5 - 3m with some chaotic reflectors within the sediments underlying them. Two potential lake overflow channels were inferred running across the profile.

Two ERT surveys were carried out in Site S2 to add to the limited knowledge of lithological types and depth to bedrock in this area. Glacial diamicton and glaciofluvial sand and gravel reaching thickness of over 12m and overlying bedrock have been recognised in the site. Borehole drilling and GPR were used to investigate a site (Site S10)

located on a wide ridge of glaciofluvial sediments running parallel to the Ballyduff Esker. Borehole data show interstratified sand/gravel and diamicton. GPR L01 illustrates the remarkable difference of depth of penetration from data collected in a grassed field (5m) to data collected on bare ground (>10m), which illustrates the limitations of this technique in grassed areas. Hummocky terrain has been investigated in Site S16. ERT data show pockets of fine sediments underlain by sand/gravel overlying diamicton underlain by bedrock. GPR data indicate cross-bedding and a number of normal faults at the edges of the relatively depressed terrain. Time-slice analysis of the data shows low amplitudes in depressed areas indicating the presence of fine sediments attenuating the EM waves.

CHAPTER 7

Discussion of results and Evolutionary Model

7.1 – Geophysical methods

Electrical resistivity and electromagnetic geophysical methods were used in this thesis to characterise Quaternary sediments. Data collection, processing and interpretation methodologies were established, in detail for ERT and GPR, and were presented in Chapter 3 and the results from the geophysical surveys were presented in Chapter 6. Discussion on the methods and results obtained, comparative assessment of the different techniques and a geological characterisation of the surveyed sites based on the geophysical data supported by field mapping data are presented below.

7.1.1 - Electrical Resistivity Methods

The depth of investigation attained by **Electrical Resistivity Tomography (ERT)** is dependent on the electrode array and spacing used and the number of electrodes available for the profile. A number of electrode arrays were investigated in Chapter 3 and the Wenner-Schlumberger was considered the most suitable for this research.

Forward modelling and data collected for this thesis showed that the level of spatial resolution depends on three factors: the electrode spacing used, the resistivity contrast between the different lithologies and the relative position between these features. It was established by forward modelling that horizontal layers/lenses thinner than the electrode spacing are on occasions detected. However, the size of the feature is distorted and often major artefacts are detected in the inverse model (see Figures 5.8 and 5.11). Channel features or esker ridges were depicted even if smaller than the electrode spacing. This is supported by data collected for this thesis which showed that an esker (600Ωm) 16m wide and 7m thick was detected with 10m electrode spacing (Figure 6.6). However, artefacts are often generated in the lower parts of the inverse model (see Figure 5.12). Furthermore, care

has to be taken with the interpretation of such features, channel features and eskers show similar resistivity outcomes in the inverse model (Figures 5.24a,b), knowledge of the profile topographic expression and local geomorphology is required to properly distinguish them.

Forward modelling was used to replicate the inversion model obtained from gathered data. Figure 5.14 is a theoretical model produced for the data collected for profile RTS1-L01-5m (Figure 6.12). It was observed that a high resistivity area generated by the inversion model in the lower parts of the profile from 45 - 65m is not present in the original theoretical model (Figure 5.14). The use of this approach allowed artefacts produced by the inversion process to be detected and led to a more correct final interpretation.

A range of lithologies in the study area were differentiated using ERT ((Enclosure 1 – E1A). The range of resistivities recorded for the classified materials is presented in Table 7.1. Bedrock has been recorded in 11 sites with resistivity values ranging from 1000 - 10,000 Ω m, which fall within the resistivity range proposed by Palacky (1987), see Figure 3.3. Moreover, a number of areas displaying resistivities of 600 - 1200 Ω m overlying or flanking bedrock have been classified as weathered bedrock at 3 sites. Diamicton has been recorded overlying bedrock at 7 sites. Resistivity values for diamicton consistently range from 100 - 500 Ω m, regardless of the morphology associated with the material or its relative location within the subsurface. Several sources from the literature show discrepancies in the resistivities of soft sediment, especially sand and gravel (Palacky 1987, Reynolds 1997 and Gerin et al. 2004). Sand and gravel deposits mapped for this thesis show a resistivity range of 200 - 5000 Ω m (Table 7.1). Dry morainic sand and gravel recorded in Sites S3 and S4 during the summer present large resistivities values of 1400 - 5000 Ω m, whereas, sand and gravel recorded in winter for Site S16 and classified as hummocky moraine shows resistivity values ranging 600 - 1500 Ω m. Saturated sand and gravel underlying peat recorded in Sites S2 and S9 display resistivities ranging from 200 - 1000 Ω m. Muddy sandy gravel recorded within an esker ridge recorded in Site S1 has a resistivity range of 500 - 1800 Ω m.

Morphology	Lithology	Sites	Recorded PSA Class Folk (1954)	Resistivity range (Ω m)	GPR Max. Penetration of EM waves	GPR Amplitude 100Mz (60-100ns)	Radar facies
Several	Bedrock	S1, S2, S3, S4, S5, S7, S8, S11, S15	n/a	1,000 – 10,000	n/a	n/a	n/a
Several	Weathered Bedrock	S1, S7, S8	n/a	600 – 1,200	n/a	n/a	n/a
Several	Overlain Diamicton	S1, S3, S4, S5, S7, S11, S12, S16	Slightly gravelly sandy mud Gravelly muddy sand	100 - 500	3m (S12) – 100Mz	n/a	Gm
Flat plain	Diamicton	S1, S7, S8, S12	n/a	100 - 500	3m (S1) – 200Mz 6m (S8) – 100Mz	800 - 2500	Gm
Moraine	Diamicton	S8	n/a	100 - 500	6m (S8) – 100Mz	2200 - 3100	Gm, Hyp
Moraine	Sandy gravel (dry)	S3, S4, T3	Gravel Muddy sandy gravel	1400 – 5,000	> 5m – 200MHz > 8m (S3) – 100Mz	2000 - 6000	Gfc, Gfs, Gfp, Gfm, Hyp
Moraine	Sandy gravel (moist)	S16	Gravel Muddy sandy gravel	600 – 1,500	6.3m – 100Mz	2500 - 5000	Gfc, Gfs, Gfp, Gfm, Hyp
Glaciofluvial fan	Sand and gravel	S1, S5, S10, S11, S13, S14, S15, S17, T1	Muddy sandy gravel Gravelly sand	600 – 5,000	> 15m – 50Mz 11.5m – 100Mz 7.5m – 200Mz	3000 – 10000 (dry) 500 – 3000 (moist)	Gfc, Gfs, Gfp, Gfch, Gm, Hyp
Flat plain	Sandy gravel (Saturated)	S2, S9	n/a	200 - 1000	2m (S9) – 100Mz	400 - 900	Gfm
Esker Ridge	Muddy gravel/ boulders	S1, S6, T2	Muddy sandy gravel	500 – 1,800	12m (S1) – 50Mz 8.5m (S6) – 100Mz 7m (S1) – 200Mz	1500 – 4000	Gfc, Gfs, Gfm, Hyp
Glaciofluvial fan	Muddy sand /Sandy Mud	S1, S13, S14, S15, S17	Gravelly sand / Silty sand Slightly gravelly muddy sand	80 – 500		2000 – 4000 (dry) 400 – 2000 (moist)	Gfc Gfp, Gm
Kettle hole	Silt/Clay	S16	n/a	80 – 200	>2.5 – 100Mz	500 - 2000	
Lacustrine Flat	Silt/Clay	S1	Slightly gravelly sandy mud	38 – 120	3.5m – 50Mz 2.5m – 200Mz	100 - 800	Lh
Flat	Peat	S2, S7, S9, S12	n/a	50 - 150	5m (S9) – 100Mz	800 - 1500	Pt

Table 7.1 – A range of lithologies were identified in the research area expressed as different geomorphological features. Resistivity values compiled from ERT surveys plus amplitude values and radar facies identified with GPR related to each lithology are presented.

Resistivity values for sediments recorded in glaciofluvial sediments classified as muddy sand/sandy mud at Sites S1, S13, S14 and S15 range from 80 - 500 Ω m. Fine sediments have been recognised in Site S1 as lacustrine silt/clay and in Site S16 as kettle hole infill, these are characterised by resistivity values ranging 38 - 120 Ω m and 50 - 200 Ω m, respectively. Finally, peat has been surveyed at a number of sites and is associated with resistivities ranging from 50 - 150 Ω m. The results presented in Table 7.1 show that the range of resistivities encountered for different materials overlap each other. Knowledge of the local geology (geomorphology, lithology and hydrogeology) is necessary to complement an accurate interpretation of the ERT data.

Time-lapse ERT data (Chapter 6) illustrates important variations in the resistivity values for a range of materials. The variation recorded is generally larger for well-sorted sediments (sand and gravel) and smaller for poorly-sorted (diamicton) and fine sediments. Materials lying close to the surface seem to react rapidly to changes in effective recharge, this is illustrated by the rapid increase of the resistivity values during the summer months. However, there is an increasing time lag with depth between the effective recharge and its influence on the resistivity values recorded. This time lag is illustrated in Figure 7.1. Resistivities recorded for resistivity profile RTS1-L02-5m at point 57.5m at 10 different depths (Figure 7.1a) are presented. The data show an increase of the resistivity from July for data recorded in the top 6 - 7m, the resistivity increase is postponed to August from 9 - 12m depth and to September from 14 - 20m depth. On the other hand, increase of the effective recharge in October triggers a rapid decrease in the resistivity values for the top 6m; whereas, points recorded at 7.6m and 9.6m depths react to the increasing effective recharge in November and December, respectively. Furthermore, points at depths over 11m still show an increase of the resistivity after 3 months of increasing effective recharge. Resistivities recorded for profile RTS1-L02-2m at point 19m at 10 different depths (Figure 7.1b) for the same period of time show a similar pattern to the former, however in this instance the spatial resolution is higher and a month time lag in resistivity response to dry weather is recorded at a shallower depth (4.7m). Seepage of water through the subsurface results in a time lag of at least a month for sediments at depths over 5.7m. These results

show that weather conditions previous to the survey have to be accounted for in the interpretation of ERT data and emphasize the potential of this technique for the study of infiltration rates in soft sediments. A higher resolution dataset (spatial and temporal) covering a longer time period would be recommended for an accurate estimation of water infiltration rates.

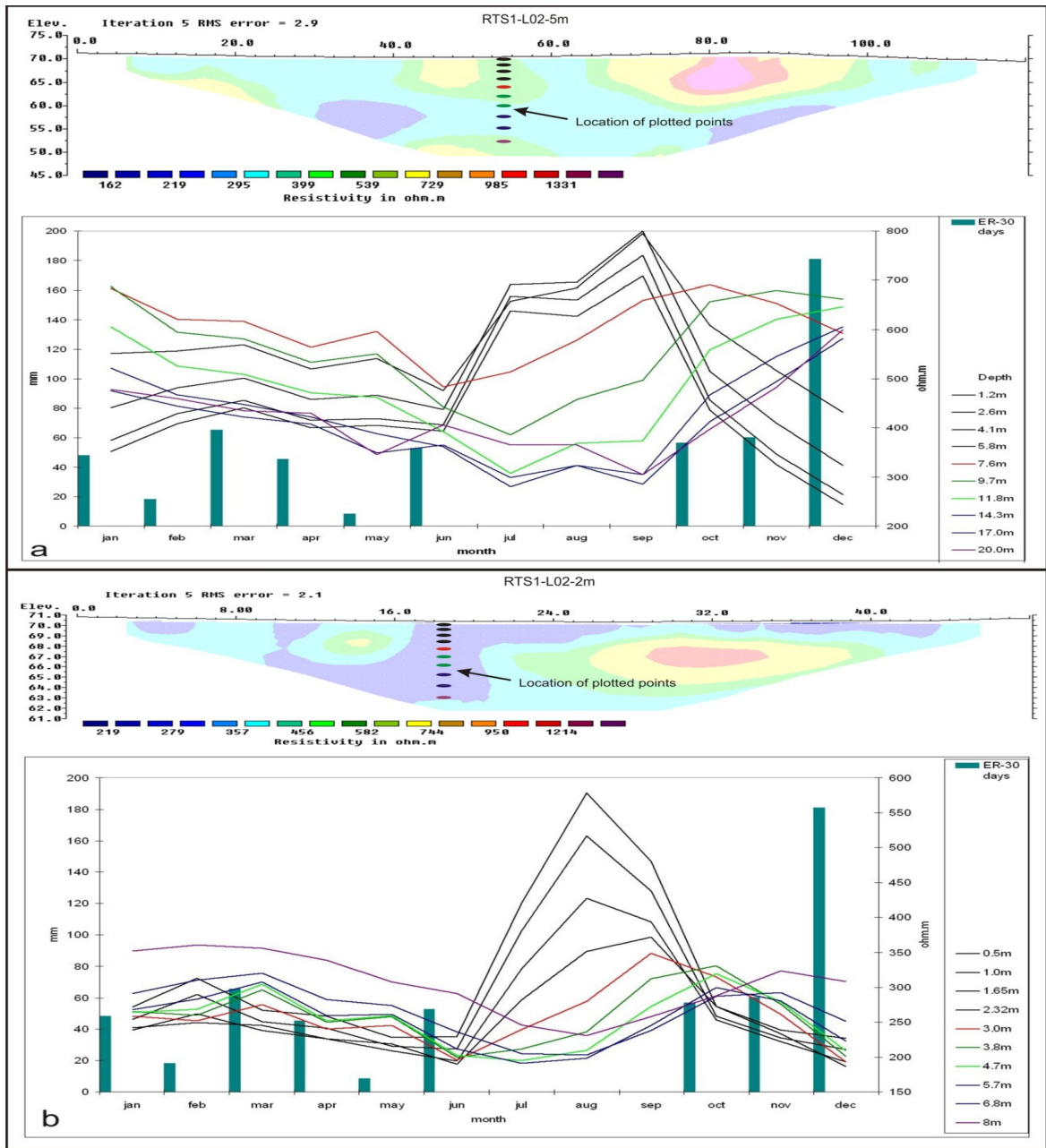


Figure 7.1 – Variation in depth of the resistivity values through 2006 for (a) time-lapse profile RTS1-L02-5m at point 57.5m and (b) time-lapse profile RTS1-L02-2m at point 19m.

The construction of a **3D Model using ERT** is a time-consuming process. The 3D Model produced for this thesis is presented in (Enclosure 1 – E1C). Data collected for the 3D model (Chapter 6 – Section 6.2.2.4) aided an understanding of the spatial distribution of different lithological types and the interpretation of their sedimentological relationships.

Azimuthal resistivity data proved useful in understanding the lithological variations within the subsurface. The graphs for different types of glacial feature show different shape characteristics and the apparent resistivity ranges often vary greatly (Figure 6.31). Glaciofluvial sediments show large azimuthal variations in apparent resistivity, which agrees with their expected heterogeneous nature. On the contrary, diamicton and/or lacustrine silts and clays present a fairly homogeneous response for the six azimuths recorded. The graphical output, shape, range of values and gradient breaks provided reasonably useful information on the subsurface. However, ERT profiling allows the collection of data with finer spatial and depth resolutions over a shorter period of time.

ERT profiling has proved to be a valuable tool for the characterisation of the subsurface lithological composition for soft sediments and also gives a broad depiction of the sediments internal architecture when using 3D data. Time-lapse ERT data showed the influence of Effective Recharge on the resistivities recorded. Soft sediments in water saturated conditions display very similar resistivities for different lithologies, whereas, resistivities obtained in a relatively dry subsurface allow more accurate lithological characterisation.

7.1.2 - Electromagnetic Methods

Ground Penetrating Radar (GPR) allows the identification of radar facies which provide information on the internal architecture of the subsurface. Theoretical spatial resolution of Ground Penetrating subsurface features was presented in Chapter 3. Assuming an average velocity of the subsurface of 0.1m/ns, the vertical resolution (Equation 3.15) obtained with a 100MHz antenna is 0.25m and the horizontal resolution for an object at 2m depth (Equation 3.16) is 1.5m. Resolution, both vertical and horizontal, is dependent upon the

velocity of the subsurface. The resolution obtained in this thesis with a 100MHz antenna frequency for high velocity materials (e.g. sand and gravel - 0.11m/ns) is c. 0.7m (see example in Figure 6.75). Whereas, features 0.25m thick are resolved in low velocity materials, such as peat (0.037m/ns), see Figure 6.94.

Forward modelling of GPR data using GPRSIM software allowed the response of a range of subsurface features within in the study area to be determined (channels, boulders, esker ridges, dipping sediments, etc). However, this software gave misleading results when testing spatial and relative permittivity resolution (Chapter 5 - Section 5.3). Spatial resolution analysis carried out with GPRSIM disagreed with theoretical values obtained from equations 3.15 and 3.16 and with ground truth evaluation data collected in Site T1 (Figure 5.26). Another failing of the software was that unrealistic results were produced when investigating the minimum relative permittivity contrast needed to differentiate neighbouring materials.

Three parameters seem to control the depth of penetration of EM waves into the subsurface in the study area: the type of material, the moisture content and the surface vegetation. The depth of penetration for 50, 100 and 200MHz antennae for a range of materials encountered is presented in Table 7.1. The minimum depth of penetration was found in lacustrine silt/clay, diamicton and peat, never reaching more than 6m depth. Maximum penetration was recorded in sand and gravel deposits, either in moraines, eskers or glaciofluvial fans; it reached a maximum of over 15m in Site T1 (Figure 5.27) using a 50MHz antenna and 11.5m in Site S1 with the 100MHz antenna. However, depth of penetration for sand and gravel deposits with high moisture content diminishes significantly. Sand and gravel recorded in winter with a 100MHz antenna in Sites S13, S14, S15, S16 and S17 show penetration of less than 8m. Moreover, the vegetation coverage seems to play an important role in the depth of penetration. L01 collected in Site S10 (see Figure 6.98) shows a dramatic change in the depth of penetration recorded when passing from a grass vegetated section recorded from 0 - 28m to a section of stripped soil (28 - 80m). Depth of penetration of the EM waves in the non-vegetated ground is nearly twice the depth of penetration obtained in vegetated ground.

Time-slice analysis of GPR data illustrated that amplitude values recorded are often related to the lithological composition of the materials surveyed. The 60 - 100ns time section for a number of profiles collected with the 100MHz antenna were analysed. The amplitude range characterising a number of lithologies, has been extracted from the time-slice data, see Table 7.1. Diamicton in flat landscape and in a moraine shows range 800 - 3100mV. Glaciofluvial sediments present an amplitude range (400 - 10,000mV). An increase in moisture contents produces a decrease in the amplitude (3000 - 10000mV for dry, 500 - 3000mV for moist and 400 - 900mV for saturated sand/gravel). Amplitude for muddy sand/sandy mud ranges 400 - 4000mV, depending on their moisture contents. Silt/clay recorded ranges 500 - 2000mV for infill of kettle hole and 100 - 800mV for lacustrine sediments. Finally, peat shows an amplitude range 800 - 1500mV.

Visual analysis of the radargrams was used to group similar patterns of reflection as radar facies (see Figure 3.30). Glacial massive diamicton (Gm) is characterised by poor reflectivity and development of multiples when clay rich (Figure 6.41). Glaciofluvial massive sediments (Gfm) are represented by chaotic short reflectors with no definite structure but good reflectivity. These are often associated with the presence of hyperbolae and are related to poorly sorted sand/gravel deposited in high energy environments such as eskers and moraines. Glaciofluvial plane stratified sediments (Gfp) are characterised by horizontal/sub-horizontal continuous to moderately continuous reflectors. These radar facies were identified in glaciofluvial fans and in glaciodeltaic foresets when recorded along their strike direction. Glaciofluvial cross-stratified sediments (Gfc) are characterised by discontinuous to moderately continuous wavy to subhorizontal reflectors, these facies have been encountered in moraines, eskers, glaciofluvial fans and glaciodeltaic environments. They are related to moderate to high energy depositional environments and are on occasions associated with hyperbolae indicating the presence of boulders. Glaciofluvial channel infill (Gfch) is characterised by continuous concave surfaces infilled with chaotic, planar or dipping reflectors. A bow-tie pattern (Figure 5.18a) is characteristic of V-shaped channel features. These are recorded in glaciofluvial fans and are often associated with cross/planar stratified radar facies. Glaciodeltaic/subaqueous fans recorded

encompass at least one of the following radar facies; topsets (Gts) characterised by chaotic discontinuous wavy reflectors. These have been identified along the surface of glaciodeltaic sediments and are often overlying foresets. Foresets (Gfs) are defined by continuous dipping reflectors parallel to each other, dipping direction indicating paleocurrents. Bottomsets (Gbs) occur beneath them and are defined by sub-horizontal continuous reflectors. Peat is mainly characterised by planar continuous to moderately continuous reflectors, probably related to different degrees of humification of the peat. Bedrock could not be characterised using GPR in the surveyed sites. Surficial sediments are fairly thick in the study area and bedrock is mainly overlain by diamicton, which attenuates the EM waves.

The Very Low Frequency Electromagnetic (VLF) technique was tested in Site S1. The results obtained showed some correlation with the data collected with ERT and GPR (Table 6.4). The lacustrine clays yielded a positive VLF anomaly which contrasted with the esker and glaciofluvial fan. However, the obtained data did not greatly help in the interpretation of the subsurface. The low spatial resolution attained with this method meant it was relatively ineffective at a local scale. However, VLF is a rapid data acquisition method, which could make it suitable for broad characterisation of Quaternary sediments for bigger sites than the ones surveyed for this thesis.

7.1.3 - Comparative analysis of GPR and ERT

The use of a combination of geophysical techniques for geological mapping has been found to be successful for characterising the internal structure of Quaternary sediments in central Ireland. Data collected for this thesis show that ERT is a valuable tool for the characterisation of the subsurface lithologies, meanwhile, GPR data greatly helps in understanding the internal architecture of the subsurface sediments. A comparative discussion of both techniques is presented below.

Spatial resolution is considerably higher for GPR data. In order to attain high resolution using ERT data, the electrode spacing would have to be reduced considerably, which

reduces the depth of investigation and increases the survey time (Enclosure 1 – E1A). As presented in Chapter 3, resolution and penetration of GPR data is also influenced by the antenna frequency (see Enclosure 1 – E1B); however, the increase in survey time is less significant than for ERT. GPR data are constrained to sediment types with small attenuation rates. Sediments with large attenuation rates, such as fine lacustrine deposits, impede the penetration of the EM waves and thus the underlying material cannot be characterised. On the other hand, ERT surveys deliver results for all the materials recognised in the area. However, some sediments present a similar range of resistivity values (Table 7.1 - e.g. saturated sand/gravel and diamicton). The use of GPR or traditional mapping techniques can in these situations help differentiate the lithologies. Depth to bedrock has been identified in nine of the surveyed sites using ERT. GPR has been used for bedrock detection in other settings (Ayotte 1994, Lombard 2009); however, characterisation of the bedrock interface using GPR was not possible in the surveyed sites. The bedrock in the study area is generally covered by thick soft sediments, which are often underlain by diamicton, which encompasses high attenuation rates, impeding penetration of EM waves. In general terms, the two techniques support each other. The weakness of ERT surveying, such as spatial resolution can be compensated for by GPR data. Also, the limitations of GPR, such as poor penetration in conductive sediments and incapacity to detect vertical contacts and the bedrock interface are counteracted to some extent by the ERT data. ERT data provided good lithological information, penetrated conductive sediments, showed vertical contacts and provided accurate bedrock detection (Figure 6.6).

It has been found that there is some level of correlation between resistivity (ERT data) and amplitude values from time-slice analysis of GPR data (Table 7.1). Fine sediments (silt/clay) show low resistivity values and low amplitude values, while coarser sorted sediments (sand/gravel) encompass high resistivity values and high amplitude values. This is illustrated in the two 3D models collected at the same location with both techniques (Enclosure 1 – E1c,d,e). As discussed in Chapter 6, both models have been interpreted as a lens/channel of sandy gravel enclosed in muddy sand. Moreover, the sandy gravel area is dominated by high resistivities and amplitudes, while the muddy sand area is dominated by

low values for both resistivity and amplitude. The lens/channel feature is better defined by the GPR data as the spatial resolution is finer. This emphasises that amplitude analysis can provide some information of the main lithological variations in the subsurface. It has to be taken into account that the level of confidence of these data is not as reliable as that obtained with ERT. EM wave amplitude variation with depth can be largely affected by amplitudes obtained from overlying materials.

Test sites surveyed (Sites T1, T2 and T3, Chapter 5) helped greatly in understanding the response of geophysical methods for a range of lithologies and sedimentological settings. Additionally, forward modelling of theoretical data helped in understanding the response of subsurface features encountered during geophysical surveying. The use of both, traditional field mapping data and forward modelling are necessary to properly interpret geophysical data. Forward modelling has been integrated in the methodology for data processing and interpretation of both GPR and ERT data (see Figures 3.13 and 3.27). The use of this technique can significantly enhance the understanding of the survey outcomes. It was useful in identifying artefacts generated by the software processing of ERT data (e.g. lower level artefacts), to recognise the response of GPR EM waves to external artefacts (e.g. wide hyperbolae reflections derived from tree trunks located along the GPR profile in Site S8) and to understand the deformation of the subsurface caused by changes in the velocity of the GPR EM waves.

7.2 – Geological characterisation of sites

The geophysical characterisation of the sediments at the 17 sites surveyed assisted in the production of an evolutionary model of deglaciation for the research area. ERT and GPR data, together with geomorphological mapping and borehole and exposure data (when available), helped identify the geological settings in the sites surveyed. This aided to reconstruct the glacial history of the study area, see below.

Site S1 is composed of a flat topped elongated fan running parallel to the lower lying Geashill Esker. These features are separated by a stretch of lacustrine sediments in the site

area, but merge east of the site as a single entity. The fan is wedge shaped, widening to the east. Borehole, GPR and ERT data show that the fan is mainly composed of gravelly sand to muddy sand fining eastwards with a number of cut-and-fill channel features running west-east and filled with sandy gravel (Enclosure 1 - E1A,B). The esker is dominated by crudely bedded muddy boulder gravel (Enclosure 2 - E2H). The geological settings encountered in the site are complex, subaerial conditions would allow their simplest interpretation. However, the existence of Glacial Lake Riada requires these features to form either under subglacial or subaqueous conditions. A subglacial setting is contemplated as the most plausible. The fan is interpreted as an abandoned subglacial conduit of the Geashill Esker drainage system. This drainage system diverted to a lower subglacial tunnel (Geashill Esker), leaving a large subglacial cavity where the fan is located. At some stage, the Geashill Esker started to fill in with muddy boulder gravel, indicative of a high energy depositional system, this cavity located at a higher level started to fill in a relatively low energy depositional environment composed of gravelly sand at its west margin fining to muddy sand eastwards. The numerous channel features identified by GPR running west to east are indicative of a very dynamic pulse-like depositional system, which was intermittently reactivated. In order for the fan to be filled in, its outlet to the east was previously blocked by deposition along the subglacial conduit expressed by Geashill Esker, thus deposition along the Geashill Esker was most likely contemporaneous to the fan. Lacustrine deposits between the features, are composed of silt/clay with some pebbles and were deposited at a later stage (Figure 7.3e) under subaqueous conditions in a glacial lake environment. A thin coating of peat developed on top of these sediments within the site and as thicker deposits along the northern margin of Geashill Esker. Peat deposits suggest the presence of a shallow lake covering the most depressed areas of the site during postglacial times.

Unexpectedly thick surficial sediments were identified at Site S1 (20 -30m), and in an area at the east end of Kilcormac Esker (E229000, N221000). These data suggested the possible presence of a channel feature running along the Kilcormac and Geashill Eskers. ERT profiling was carried out at Site S2 to recognise this feature. Approximately 15m thick glaciofluvial sediments were identified in the site. These data allowed to the DTB map

presented in this thesis to be refined (Map 2). However, the expected channel feature was not located and may not be present.

Morainic sediments mapped in the area expressed as ridges were recognised during field mapping and subsequently surveyed with geophysics in an attempt to determine their origin. A set of ridges at Site S3 and Site S4 are associated with ice receding west-southwestwards. ERT data for Site S3 shows gravel deposits overlying diamicton, the gravel deposits being considerably thicker at the down-ice side of the ridge (Figure 6.62a). The internal architecture depicted from GPR data (e.g. Figure 6.64a) of the sand and gravel deposits shows areas dominated by hyperbolae indicating presence of boulders within diamicton. These are overlain in places by dipping and planar stratified sediments probably related to small scale subaqueous fans. These sediments are largely obliterated by thrust planes suggesting ice readvance towards the east-northeast. These ridges have been interpreted as push moraines (Enclosure 2 – E2A).

Morainic sediments at Site S4 are interpreted as push moraine overlain by subaqueous fan moraine (Enclosure 2 – E2B). ERT shows thick sand and gravel deposits overlying diamicton, which is underlain by bedrock. Three radar facies depicted in L01 (Figure 6.70) delimited by strong continuous reflectors may be related to different depositional stages. Facies 1 and 2 consist of cross-stratified sediments showing evidence of deformation in the form of thrust faults, associated with an ice readvance north-northeastwards. These are overlain by foresets dipping north and east deposited as a subaqueous fan during a standstill of the ice sheet. Normal faults recorded along the up-ice slope of the moraine are probably due to collapse after ice withdrawal and illustrate that this was an ice contact margin.

The moraine recorded at Site S8 was classified as a push moraine composed of a thin coating of diamicton overlying bedrock, evidence of deformation was depicted as moderately continuous reflectors dipping west and obliterating flat lying less prominent reflectors. A further ten morainic ridges with similar morphological expression running

south to north have been recorded for 5Km east from the site. These are indicative of ice retreating westwards in this region.

Geophysical data collected at Site S16 illustrates the sedimentological architecture of a hummocky moraine (Enclosure 2 – E2C). Fine sediments on the topographically depressed areas overlying sand/gravel depicted from ERT (Figure 6.123) and collapse structures identified with GPR data (Figure 6.124) illustrate that these sediments were deposited in association with dead ice. Deformed cross-stratified sediments are the dominant facies recorded; a number of hyperbolae are interpreted as boulders indicating a high energy depositional environment.

Glaciolacustrine sediments identified during the field mapping exercise were surveyed in order to identify depositional environments associated with glacial paleo-lake Riada (Delaney, 2002). Site S5 is located on an isolated mound stretching WSW-ENE and reaching an altitude of 73m OD. ERT data show sand/gravel deposits underlain by diamicton thickening towards the west-northwest. Two GPR sections across the mound show very well expressed foresets dipping west-northwest indicative of paleocurrents in this direction ((Enclosure 2 – E2D). Topsets have not been identified overlying these sediments, which suggest that they were probably deposited in subaqueous conditions. The east-southeast slope is interpreted as an ice-contact slope; normal faults recorded by GPR dipping towards it were generated after the ice margin withdrew from this position.

GPR data collected along the Ballyduff Esker at Site S6 show three main radar facies, possibly associated with the infill of a subglacial tunnel forming the esker. F1 occurs along the ridge-top (77m OD) and is dominated by hyperbolae and cross-bedded sediments. These are overtopped to the south by f2, dominated by hyperbolae in its central part and flanked by foresets dipping north and south. The hyperbolae are caused by boulders associated with a high energy depositional phase forming the core of two eskers whereas, the stratified sediments are associated with a lower energy depositional phase within the subglacial tunnel. A shallow channel feature with associated foresets, possibly indicating

low energy conditions, runs on top of the core of the eskers. The sediments illustrate three depositional episodes of the infill of a subglacial tunnel draining eastwards.

Data collected in Site S10 provided very little information on the depositional environment. It is known from borehole (BHS10A – Appendix A) and exposure data (Plate 6.12) that glaciofluvial sediments dominate the area. GPR reflectors were interpreted as cross-stratification. However, the depositional environment can not be defined from these data alone.

A good example of a glaciodeltaic depositional system was recorded in Site S13. Thick surficial sediments composed of sandy gravel overlying sandy silt was recognised from ERT data on a fan-shaped flat-topped hill at the eastern margin of Moate Esker. GPR data depicted chaotic discontinuous reflectors overlying reflectors gently dipping eastwards. These are interpreted as foresets dipping towards the east and overlain by topsets. The contact between the two layers marks the water level of a glacial lake at the time these sediments were deposited (83m OD). Recorded profiles are presented as a fence diagram in Enclosure 2 – E2F. Additionally, a kettle hole within the site indicates deposition associated with buried ice in an ice marginal environment.

An isolated flat topped hill has been surveyed at Site S14, ERT data show that the hill is composed of thick surficial sediments of silty sand overlying sandy gravel. Dense grass vegetation impeded good penetration of GPR EM waves. The data collected up to 6m depth show planar bedding overlain by cross-stratified beds and small cut-and-fill channel features running north-south. These beds could have been deposited as thick topsets in a glaciolacustrine environment or as tunnel infill in a large subglacial cavity, knowledge on the internal architecture of deeper sediments is necessary to properly reconstruct the geological history of the site.

Site S15 is located in a relatively elevated flat topped region along the southern margin of Split Hill Esker. ERT show that the site is composed of gravel 10m thick overlain in places by a layer of sandy silt and underlain by bedrock. Poorly-developed deformed foresets

dipping southeast overlain by cross-stratified sediments are inferred from two GPR radargrams. The transition zone between the foresets and cross-stratified sediments (88m OD) is interpreted as the water level of a former glacial lake.

A flat topped fan has been surveyed with GPR at the eastern end of Horseleap Esker in Site S17. A profile running WNW-ESE shows foreset beds, generally dipping east-southeast overlain by cross-stratified sediments interpreted as topsets. The fan has been interpreted as a glaciodelta deposited at the mouth of Horseleap Esker marking a lake level, inferred from the transition zone between the foresets and the topsets ranging 87 - 90m OD.

Potential **Glacial lake overflow channels** identified during the field mapping (Map 1) were surveyed along the watershed area between the Shannon and the Boyne/Barrow Basins to geologically characterise them. An ERT survey carried out at Site S7 along the Royal Canal shows 5 - 15m thick diamicton overlying bedrock. This is one of the lowest overflow channels (82.5m OD). However, its level was probably lowered during the works carried out to build the Royal Canal.

ERT data for Site S9 show a large sand/gravel channel feature infill (Figure 6.92) cutting across the watershed in a WNW-ESE direction. This is overlain by 4 - 6m of peat. GPR profiling of the peat basement (Enclosure 2 – E2J) illustrates the presence of a possible overflow channel from 560 - 760m marking a lake level of less than 89.5m OD.

Another potential lake overflow channel running along the west margin of Geashill Esker was surveyed in Site S11. Several ERT profiles collected show glaciofluvial sediments overlying diamicton, which overlies bedrock. The presence of glaciofluvial sediments suggest that this was acting at some stage as a meltwater channel. This channel acted at a later stage as an overflow channel of Glacial Lake Riada (Figure 7.3d). The approximate lake level at the time is marked by the highest point recorded along the channel, which is approximately 84m OD.

Site S12 occurs along a potential overflow channel. Very thick surficial deposits (> 40m) overlain by 1 - 3m of peat were recognised using ERT. These unexpectedly thick surficial sediments were deposited on the lee side of a drumlinoid orientated northwest-southeast, 2Km northwest from the site (see Map 1). Peat basement profiling using GPR shows a maximum peat thickness of 3m at 300 - 390m (Figure 6.107). This section could have been acting as the overflow channel flowing eastwards; however, the shape of the feature is not clearly depicted.

7.3 – Quaternary Geology and evolutionary model of deglaciation

The study area is located in a relatively depressed region flanked to the south by the Slieve Bloom Mountains and to the north by a relatively higher drumlin/crag and tail landscape. Over 98% of the sediments mapped along the surface (top 1m) within the study area were deposited during the Quaternary period. These deposits reach a maximum thickness of over 40m in places and have an average thickness throughout the whole area of 7.38m. The topographic setting and the ice advance and retreat, during Weichselian times, in the Irish Midlands seem to have strongly influenced the spatial distribution (Map 1) and the thickness (Map 2) of Quaternary sediments in the research area.

The sediment types recognised (Map 1) present distinctive lithological characteristics which have been identified from their particle size distribution and petrography analysis. Their lithological type has been classified under the Folk (1954) classification scheme (Figure 6.2) and the dominant petrology from the petrography analysis. A summary of the lithologies represented in Map 1 is presented below.

Three types of diamicton were recognised. Diamicton derived from Lower Carboniferous limestone covers 41.8% of the area, 62 samples show gravelly mud with sandy silty matrix as the dominant lithology. Diamicton derived from Devonian sandstone approximately covers 0.2% of the area, it has been visually assessed during fieldwork and classified as

gravelly muddy sand. Diamicton derived from basic igneous rocks covers about 1.2% of the area. It has been classified at one location as gravelly mud with a sandy muddy matrix.

Glaciofluvial sediments, all derived from Lower Carboniferous limestone, were classified by the dominant lithology. Glaciofluvial sand and gravel covers 21.1% of the area, 61 samples show silty sandy gravel/gravelly muddy sand with silty sandy matrix as the dominant lithologies. Esker gravel covers 2.3% of the area, 9 samples analysed show muddy sandy gravel with silty sandy matrix as the dominant lithology. Glaciofluvial sand was mapped at two locations (0.5% of the area) and its lithology is dominated by slightly gravelly muddy sand with sandy silty matrix. Interstratified diamicton and gravel covers 2.6% of the area, 9 samples analysed show either mud, sand or gravel as dominant lithologies.

Postglacial sediments recorded are alluvium, lacustrine, peat and marl. Lacustrine sediments approximately cover 1% of the area. 3 samples analysed show mud and sandy mud as the dominant lithologies. About 9% of the area is overlain by alluvium, it has been classified at one location using PSA and by visual assessment during fieldwork as silt/clay slightly sandy/gravelly in places. Peat occurs over 17.8% of the area and has been classified as raised bog. It is underlain by a range of materials: lacustrine silt/clay, alluvium, diamicton and glaciofluvial sand and gravel and bedrock. Marl covers 1.2% of the region and has been visually classified as organic rich silt/clay. Finally, small patches of made ground (<0.05%) have also been recorded.

Some evidence for ice advance direction was found in the study area, some drumlinoid features have been identified indicating ice movement towards the southeast and east-southeast (Map 1). Greenwood and Clark (2008) produced a subglacial bedforms map for Ireland, which illustrates ice direction towards the southeast north of the study area and towards the east-southeast south of the study area. Ice direction indicators extracted from erratic carriage are quite weak. Petrography analysis shows limestone pebbles as the dominant petrology (Figure 4.7) in the study area, however, this rock type could not be used as an ice direction indicator. On the other hand, percentage of sandstone pebbles in

samples collected in diamicton is highest in samples collected southeast of sandstone bedrock located northwest of the study area. This indicates erratic carriage towards the southeast, which agrees with the orientation of the drumlinoids. No other erratic carriage ice movement indicators were identified in the area.

Four physiographic units (Figure 4.1) with distinctive geomorphological characteristics were recognised during the mapping exercise. The spatial and chronological distribution of the sediments composing each physiographic unit provides good evidence of the deglaciation processes in the research area.

The East Basin physiographic unit is located within the Boyne and Barrow Basins. A schematic cross-section diagram illustrating the depositional history of the area is presented in Figure 7.2a. The largest feature in this area is Croghan Hill reaching 234m OD around which some bedrock is exposed. Bedrock is mostly overlain by diamicton, derived from Lower Carboniferous limestone and by diamicton derived from basic igneous rocks around Croghan Hill. It also occurs underlying glaciofluvial sand and gravel as kame terraces along the Croghan Hill slope and underlying peat in Derrygreenagh. The diamicton is almost certainly of glacial origin, erratic carriage in analysed samples shows the presence of limestone, chert, sandstone and basic igneous pebbles. It is morphologically expressed by flat to gently undulating landscape. Sand and gravel has also been mapped along the Croghan Hill slope as a number of terraces, interpreted as kame terraces. These terraces mapped at different altitudes illustrate an ice sheet thinning as it was retreating towards the west-northwest (Figure 7.3a). Glaciofluvial sediments, composed of a mixture of sand and gravel interstratified with diamicton in places, are recognised on the lower ground areas and overlie diamicton at a number of locations (Figure 7.2a). These are morphologically expressed as gently undulating landscape in areas east of Geashill and north of Daingean and are composed of sand and gravel fed from an ice sheet located to the west. In the area north of Croghan Hill, the landscape is mainly flat with few isolated hummocky areas. A large body of glaciofluvial sand and gravel identified in this area is composed of coarse sandy gravel gradually fining eastwards into fine sand. This has been interpreted as a sandur encroaching a lacustrine water body from

west to east. The three described bodies of gravel were fed by subglacial tunnels from an ice sheet with its margin approximately located along the watershed between the Shannon and Boyne/Barrow Basins (Figure 7.3b). Lacustrine mud is quite extensive in the area and overlies most of the sandur. However, it outcrops in very few locations as it is often covered by peat. The deposits are generally composed of silt/clay, but have been mapped as marl south of Daingean. Alluvial sediments occur along few river beds draining eastwards. Peat is the dominant postglacial deposit in the area and it occurs in the most depressed areas, generally overlying lacustrine mud and alluvium.

The Shannon/East Basins watershed physiographic unit is topographically higher than the other three units. A schematic diagram illustrating the depositional history of the area is presented in Figure 7.2b. This unit encompasses the highest concentration of bedrock outcrops, often glacially smoothed. Diamicton, derived from Lower Carboniferous limestone, is generally expressed as gently undulating ground and in three locations as drumlinoids indicating ice advancing southeast and east-southeast (Map 1). It is quite thin in the relatively higher areas where seems to adapt to the original ice moulded bedrock topography. A number of abandoned channels running west to east dominate the most depressed areas within this unit (Map 1). These channel features are covered by peat in places, which masks their original morphology. Four of these channels have been surveyed with geophysics in Sites S7, S9, S11 and S12. Channels at Sites S9 and S11 are underlain by gravel indicating deposition along them, whereas channels along Sites S7 and S12 are underlain by diamicton. The maximum altitude at which the channels cut across the watershed may indicate the level of the former Glacial Lake Riada (Delaney, 2002; Pellicer and Warren, 2005). The northernmost channel cuts across the watershed at 107m OD, the channel identified in Site S9 (Figure 6.94) at 89.5m OD and a channel feature south of it at less than 95m OD. These channels acted as glaciofluvial meltwater channels feeding the sandur deposits located in the East Basin physiographic unit when the ice margin was located along the watershed. Subsequent to retreat of the ice sheet, the channel identified in Site S9 acted as the outlet of Glacial Lake Riada (starting to form within the Shannon Basin), with a water level of 89.5m OD or less (Figure 7.3b). A meltwater channel was recorded northwest from Daingean (Map 1). This was identified as a possible lake

overflow channel (Figure 7.3c) marking a lake water level of 88m OD. The channel recorded in Site S7 acted as a meltwater channel supplying the glaciofluvial sand and gravel deposits identified north of Daingean. This channel, which runs along the Royal Canal, could have also acted as a glacial lake outlet at 82m OD. However, this altitude should be taken with caution as its original topography was most likely lowered during the construction of the Royal Canal. The channel cutting across Site S12 (Figure 6.107) runs across the watershed at less than 88m OD, peat thickness is unknown at this location, so the altitude of the channel feature is unknown. Another channel feature recorded at Site S11 runs along the west margin of Geashill Esker. Glaciofluvial sand and gravel mapped along the channel (Figure 6.104) and a glaciofluvial fan composed of sand and gravel mapped by Warren and Hammond (1999) south of the study area, indicate that it acted as a meltwater channel feeding these deposits. The channel cuts the watershed at 84.5m OD and probably marks a lower water level of Glacial Lake Riada as the ice sheet retreated west and northwest exposing this lower ground outlet (Figure 7.3d). Peat is the dominant postglacial deposit in the area; it has been mapped in Sites S9 and S12 as raised bog overlying glaciofluvial sediments and diamicton. It covers the relatively depressed landscape and is underlain by lacustrine sediments in places. These deposits formed during postglacial times developing from lake basins left behind after ice retreated.

The Shannon Basin esker-dominated landscape encompasses a range of geomorphological features providing evidence for ice retreat direction and the formation of Glacial Lake Riada. A schematic diagram illustrating the depositional history of the area is presented in Figure 7.2c. Bedrock is generally fairly deep (>10m) in the Shannon Basin region within the study area (Map 2), however, it outcrops in a number of places around Tullamore and north of Kilbeggan (Map 1). Diamicton is generally derived from Lower Carboniferous limestone with the exception of a small area north of Clara, where it is derived from Devonian sandstone. Petrographic analysis shows the presence of a range of petrologies (limestone, chert, sandstone and acid volcanic pebbles), which indicates that these deposits are most likely of glacial origin. These sediments are generally expressed by flat to very gently undulating ground. A set of morainic ridges, located east of Tullamore, are composed of diamicton. The ridges run north-south and are parallel to each other

indicating a series of standstill phases of an ice sheet retreating westwards in this area (Map 1). One of these features was surveyed in Site S8 and shows thrust faults produced by an ice sheet pushing east in this area illustrating local ice sheet readvance in this area.

Glaciofluvial and glaciolacustrine sand and gravel, morphologically expressed as esker ridges, morainic fans, glaciodeltas and subaqueous fans are the dominant morphological features in this unit. The cores of the esker ridges are lithologically characterised by large boulders, cobbles and coarse gravel with muddy matrix (Figure 4.4). The size of these boulders, more than 1m in places, indicates an extremely high energy depositional environment. The sediments composing these ridges are generally deposited within subglacial meltwater conduits from west to east, but young from east to west. Their subglacial origin is inferred from the eskers climbing the landscape from west to east, which would only be feasible in an ice confined environment. Geashill Esker cuts across the Shannon Basin watershed and was deposited as a tunnel infill of a subglacial meltwater conduit flowing approximately west from Kilcormac Esker to the east of Site S1 (See Map 1) and turning southwest from there. This is indicative of an ice sheet retreating northwestwards and gradually changing to a westwards direction. Kilcormac, Ballyduff, Clara, Moate, Horseleap and Split Hill Eskers are particularly well preserved and occur only west of the Shannon/East Basin watershed. The presence of a Glacial Lake Riada in this area during deglaciation is supported by the exceptional preservation of these features as continuous subglacial conduit infill. A number of subaqueous fans associated with the eskers have also been mapped in the area. They were described in detail by Warren and Ashley (1994) and also support the presence of a glacial lake in this area during deglaciation. Morainic ridges and fans associated with an ice marginal environment were identified during the mapping exercise (Map 1) and surveyed with geophysics in Sites S3, S4 and S16. These features are often morphologically expressed by kame and kettle topography and can be classified as hummocky moraine (Site S16). The front margins of these morainic sediments are portrayed as a brown line in Map 1. Their spatial distribution and orientation indicate the existence of two ice sheets in the area, one in the north area retreating northwest and the other dominating the southern areas of the study area retreating south-southwest. Glaciolacustrine sediments deposited in Glacial Lake Riada

composed of glaciodeltas and subaqueous fans were identified in a number of locations. These sediments are also related to two separate ice sheets, one retreating south and southwest and another retreating northwest. Geophysical data from Sites T1, Site S4 and Site S5 and Quaternary mapping of glaciolacustrine deposits, overtopping the Clara and Ballyduff Eskers in some locations, (Figure 4.3 and Plate 4.5) show paleocurrents inferred from foresets pointing north and northwest, these sediments are associated with the ice sheet retreating southwest (Figure 7.3d,e). Geophysical data from Sites S13, Site S15 and Site S17, show paleocurrents inferred from foresets dipping east and southeast and are associated to an ice sheet retreating northwest.

A clear pattern of deglacial sedimentation into the expanding interdomal glacial Lake Riada has been depicted. Two main directions of ice retreat are identified from the pattern of esker and ice-marginal delta and subaqueous fan sedimentation. Initially two conjoined ice dome fronts decayed westward forming the western wall of the ice-dammed lake (Figure 7.3b). The two domes then began to separate opening an ever-widening inlet, which progressed westward to separate the domes (Figure 7.3c). This resulted in a profound change in the pattern of ice retreat, with two ice fronts, one decaying toward the northwest and the other to the southwest. The eastern margin of Glacial Lake Riada was estimated on the basis of concordant levels of ice-marginal fan/delta surfaces and meltwater overflow channels on the eastern watershed of the Shannon Basin (Figure 7.3d,e).

Finally, postglacial sediments including lacustrine mud, peat and alluvium were mapped in this unit. These cover the lowest parts of the landscape and were deposited after the withdrawal of the two ice sheets.

The Brosna River Basin physiographic unit occupies the relatively most depressed region within the study area and is dominated by postglacial sediments. A schematic diagram illustrating the depositional history of this unit is presented in Figure 7.2d. Bedrock outcrops in few locations within the area and is generally overlain by diamicton derived from Lower Carboniferous limestone. Small scale esker ridges, with associated

glaciofluvial sediments, cut across this unit. Extensive marl deposits were mapped in the area east of Tullamore (Map 1). Alluvial sediments are fairly extensive in the area, especially along the Brosna River flood plain. Extensive peat deposits overly all these sediments in some locations. Geophysical surveys have not been carried out in this area as glacial sediments are very scarce. However, as a physiographic unit it provides insight into the evolution of the landscape during postglacial times. The large areas of peat seem to indicate the presence of numerous postglacial lakes, gradually occupied by peat and subsequently drained by deepening of the main drainage system by the Shannon River. Feehan and Dunne (2003) located and classified a number of mushroom stones east and west of the Shannon River, and concluded that these mark the water-table of a large postglacial lake occurring in the area (Figure 7.3f). The extensive marl deposits overlain by peat recorded in the area supports the existence of a higher level water-table. It is not clear whether this water level is related to the expanding glacial lake or to a postglacial lake. Warren and Ashley (1994) illustrated that a small ice cap blocking the current outlet of the Shannon River would produce a large lake in the Irish Midlands. However, formation of mushroom stones requires a stable lake water level for a long period of time. Additionally, the Irish Midlands remained isostatically depressed during a long period after deglaciation (Warren, 2008), which supports high water table levels during postglacial times.

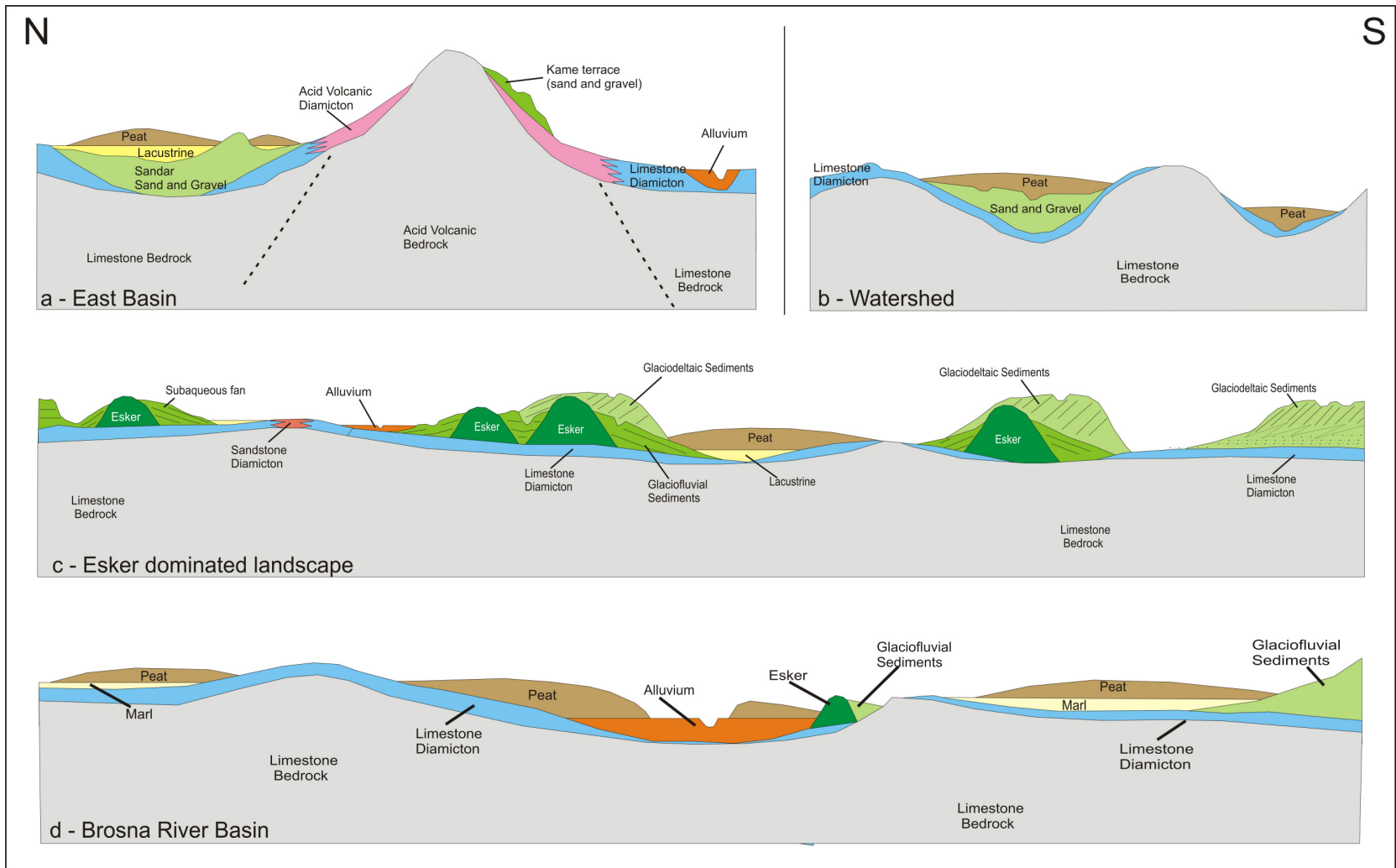


Figure 7.2 – Schematic cross-section illustrating the sequence of deposition in (a) East Basin Physiographic Unit, (b) Shannon/East Basins watershed unit, (c) Basin esker-dominated landscape unit and (d) Brosna River Basin unit.

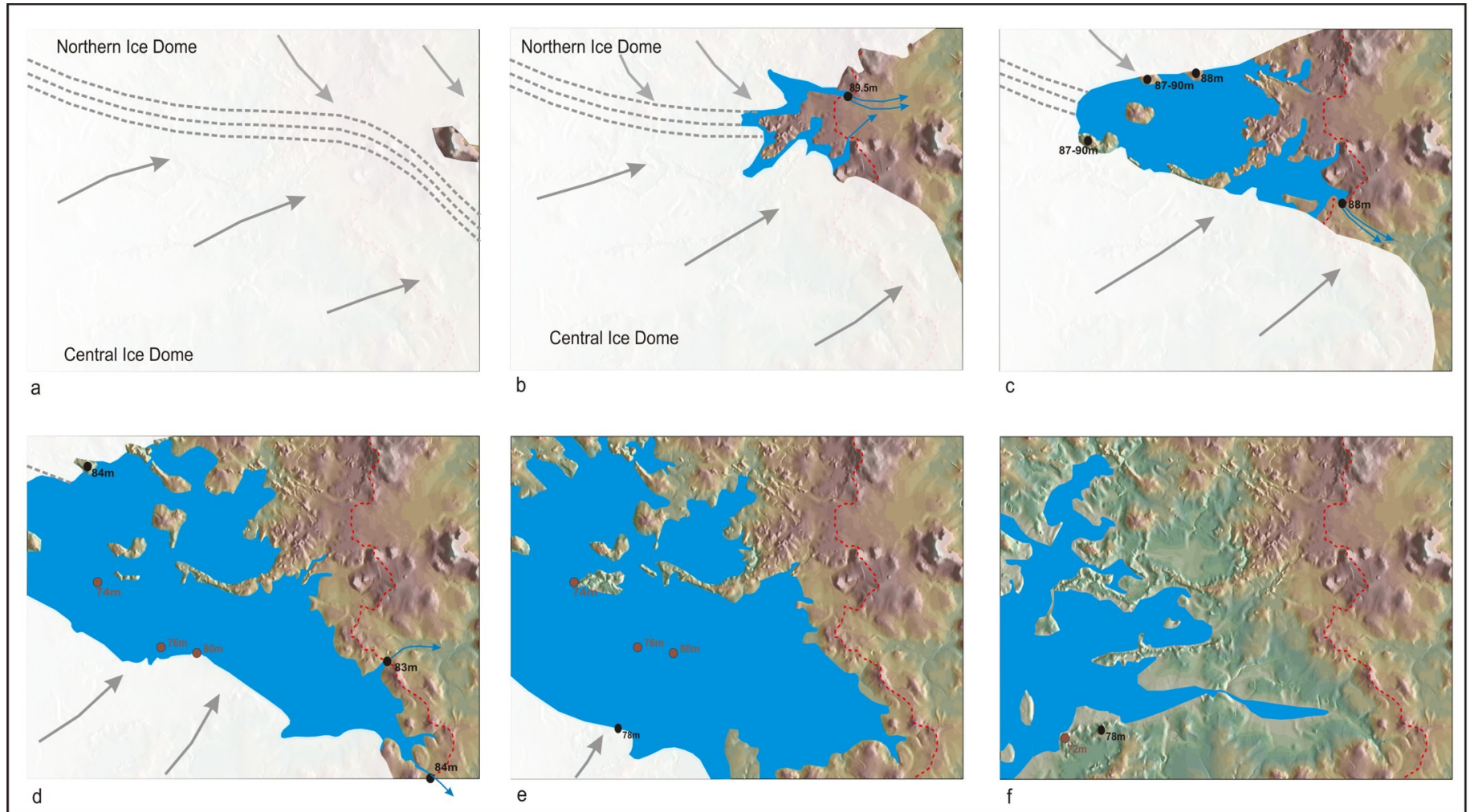


Figure 7.3 – Proposed evolutionary model of deglaciation for the study area. Dashed grey lines indicate the estimated position of the suture zone between the Central and Northern Dome ice sheets. Arrows in grey illustrate ice movement. Arrows in blue indicate glacial lake active outlets. Dots in black show locations showing evidence for lake level (Channels and Glaciodeltas). Dots in brown show location of subaqueous fans.

CHAPTER 8

Conclusions and further research

8.1 – Concluding Remarks

This thesis had three aims, all of which were successfully fulfilled:

The first aim of the research was to produce a Quaternary geological map for the 600 Km² study area located in the south County Westmeath and northeast County Offaly region. The second aim was to assess the potential of Electrical Resistivity Tomography (ERT) and Ground Penetrating Radar (GPR) for mapping Quaternary sediments in Ireland. The third aim of the research was the construction of an evolutionary model of deglaciation for the North County Offaly – South County Westmeath region of the Irish Midlands.

Assessment of a range of geophysical techniques was carried out in Site S1. ERT and GPR survey were selected as the most useful techniques to assist in the production of Quaternary geology (Map 1) and depth to bedrock (Map 2) maps. Other geophysical methods tested gave poor spatial resolutions (VLF), encompassed impractically slow data collection modes (production of 3D models with ERT and GPR) or both (azimuthal resistivity).

The Wenner-Schlumberger array was selected as the most efficient data collection mode for ERT. It allowed deeper penetration and higher sensitivity in areas close to the recorded point. Forward modelling of the data allowed a better final interpretation where there was no ground truth, the identification of artefacts and the selection of the most efficient inversion method for each profile. A methodology for ERT data processing was established (Figure 3.13) based on forward modelling and surveys carried out in Sites S1 and T3.

It was found that an accurate lithological characterisation of the subsurface using ERT data alone could be misleading. A combination of these data with forward modelling, field mapping and other geophysical data is essential to obtain an accurate interpretation.

Time-lapse resistivity showed that moisture content influences resistivity variation. The shallow subsurface (<4m depth) showed a direct relationship between resistivity variation and effective recharge. However, an increasing time-lag between effective recharge and resistivity was recorded at increasing depths resulting in an inverse relationship. Resistivity values obtained for the Quaternary sediments within the study area were given in Table 7.1, Chapter 7.

A systematic methodology for GPR data collection, processing and interpretation was established for this thesis (Figures 3.27 and 3.30). Data processing encompassed data filtering, topographic correction and time-slice analysis. Visual interpretation was performed in raw and filtered radargrams. GPR proved invaluable for depicting the internal architecture of low-loss materials such as esker and morainic gravel and glaciolacustrine sediments. However, penetration in high conductivity sediments, such as clays, was very poor. The radar facies approach used for data interpretation allowed patterns encountered in the radargrams to be related to sedimentological properties of the subsurface. Furthermore, time-slice analysis data greatly helped in understanding the subsurface lithological composition.

ERT and GPR data complemented each other and together provided a fuller understanding of the subsurface geology. In general, GPR provides a more detailed picture of the subsurface architecture whereas ERT gives an accurate estimation of depth to bedrock and allows lithological characterisation of surficial sediments. Particle size analysis carried out in samples collected from the boreholes helped further refine the interpretation of the geophysical data. The use of both techniques together highly improved the understanding of the subsurface internal architecture and lithological composition. The seventeen sites investigated with geophysics were essential to the construction of an evolutionary model of deglaciation for the study area. Conventional field mapping alone would not have been sufficient to create the model.

Six prominent esker ridges generally running east-west are the dominant geomorphological features encountered in the study area. These features fan out westwards from an area south of Tyrrellspass. The eskers are indicative of a large subglacial draining system generally flowing eastwards probably merging into a single

tunnel where these converge. The outstanding preservation of these features is controlled by three factors:

- large boulders dominating the lithological composition of the core of the esker, often located with GPR.
- The disposition of the eskers climbing the topography, which would impede their subsequent erosion after ice retreat.
- The presence of a glacial lake during ice retreat preserving most depositional features.

The former presence of a Glacial Lake Riada is illustrated by glaciolacustrine deposits in the area, which overlie the eskers in places. These are morphologically expressed as flat-topped/rounded hills and indicate the following:

- that Glacial Lake Riada had to be in place during the deposition of these sediments. Topsets, foresets and bottomsets have been recognised within some of the geophysically surveyed glaciodeltaic sediments
- palaeocurrents inferred from foreset orientation point to sediments deposited from two separate ice-sheets, one retreating northwest and another retreating west-southwest.

An objective of the research was to test the deglacial model for the midlands of Ireland proposed by Warren and Ashley (1994) over a broad area east of the River Shannon. Geophysics was deemed an essential tool in the widespread absence of adequate exposure of the sediments. Analysis of the data collected confirms the model which involves the gradual separation of two conjoined ice sheets or domes which supported an expanding interdomal lake (Warren and Ashley, 1994) and added substantial refinement to it in terms of the relative positions of correlative ice fronts and the water level of the interdomal lake as deglaciation progressed. Glaciolacustrine sediments associated to two separate ice-sheets had also been proposed by Glanville (1997) east from the study area. Evidence of the existence of an expanding glacial lake in the study area associated to two separate ice-sheets had also been indicated in studies by van der Meer and Warren (1997) and Delaney (2008).

Geophysics permitted a further refining of the model of deglaciation for the area. It was found that the water level of Glacial Lake Riada was related to a number of glacial lake outlets identified along the east watershed of the Shannon Basin (Map 1). These agree with the altitude of the transition zone from topset to foreset identified in several glaciodeltaic deposits and often discovered using GPR. Based on these data, three water levels for Glacial Lake Riada are proposed. The highest level is at 89.5m OD with an outlet south of Tyrrelspass. A second lake level related to an outlet occurring at 88m OD located south from the first and a third water level at 84m OD marked by an outlet mapped parallel to Geashill Esker. These outlets and a number of glaciodeltas and subaqueous fans delineate the approximate shape of an expanding interdomal glacial lake (Figure 7.3). As the ice-sheets retreated northwest and west-southwest, lower lake outlets opened; glaciolacustrine sediments recognised in Site T1 indicate a later water level at 78m OD, the potential lake outlet controlling this water level is located south of the study area and has not been surveyed for this study. Mushroom stones mapped by Feehan and Dunne (2003) may indicate progressive lowering of the lake water level as the ice-sheets receded.

8.2 – Further Research

This thesis has demonstrated the way in which geophysical surveying using ERT and GPR as pursued in this thesis should be used to target geomorphological features occurring west, north and south of the study area and generate sufficient data to construct a detailed regional evolutionary model of deglaciation for the Irish Midlands, which could be reinforced by lake levels inferred from mushroom stones mapped by Feehan and Dunne (2003). Further research using geophysics could help to confirm the existence of a glacial lake in the area to the east of the study area where Glanville (1997) found evidence of substantial glaciolacustrine sediments.

Absolute dates for deglaciation in the area are not available. A range of techniques could be used in the study area for this purpose:

- The luminescence dating technique could be attempted on sand/silt deposits composing the bottomsets of some of the glaciodeltaic deposits identified.
- Extensive lacustrine silt/clay deposits underlay most of peat deposits in the study area. This would be an excellent location to expand the varve chronology proposed by Delaney (2008), which could ultimately yield absolute dates.
- Conglomerate boulders spread in an area north of Ballycumber contain large quartz pebbles. The cosmogenic exposure dating technique could be attempted in those.

Finally, estimation of in situ water infiltration rates for a range of soft sediments could be attempted using time-lapse resistivity.

APPENDIX A

This appendix shows a representative sample of the detailed borehole logs and Particle Size Analysis (PSA) data presented in this thesis. Boreholes presented below were drilled with the flight continuous auger drilling method (Figures A1 - A8). The data collected from particle size analysis are plotted on cumulative logarithmic graphs to illustrate the grain size distribution (Figures A9 – A16).

BOREHOLE LOGS

Project: Sheet 48		Method: Continuous Flight Auger		1 to 50K: 48		BH-S1E		
		Diameter: 15.2 Centimeters		Easting: 240697		Logged by: XMP		
		County Offaly-Westmeath		Northing: 222945		Date 14/7/05		
		Townland		Elevation: Meters		Page. 1		
Legend	Description	Depth	Sample				Test	
			Num.	Color	Class	Depth	PSA	St Count
	Peaty Soil							
	Soft fine sand with silt/Clay. No pebbles. LACUSTRINE		1	GLEY1-3/I	Sandy silty CLAY	█		
	Medium dense clayey sandy DIAMICTON with subangular angular pebbles (0.1-0.5cm diam.). GLACIAL	5						
			2		Sandy CLAY	█		
Remarks: Borehole completed at 7.5 metres. Hard Till or Bedrock		Topography: Low ground		Drainage: Poor		Water level 2.7 Meters		
				Veg/Crops: Grass		DTB: >7.5 Meters		
						BH depth: 7.5 Meters		

Figure A1 - Borehole BH-S1E collected in Site S1.

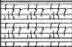




		Method: Continuous Flight Auger	1 to 50K: 48	BH-S1F			
		Diameter: 15.2 Centimeters	Easting: 240659				
Project: Sheet 48		County Offaly-Westmeath	Northing: 222985	Logged by: XMP			
		Townland	Elevation: Meters	Date 14/7/05			
				Page. 1			
Legend	Description	Depth	Sample			Test	
			Num.	Color	Class	Depth	PSA
	Topsoil						
	Dense silty sandy GRAVEL with subrounded subangular Lst pebbles (1-9cm diam). GLACIOFLUVIAL						
	Medium dense silty clayey GRAVEL with subangular subrounded Lst pebbles (1-10cm diam.). GLACIOFLUVIAL		1	2.5Y-4/2	silty clayey GRAVEL		
	Soft to medium dense stony sediment (maybe due to water table) No Recovery.	5					
	Very dense stony sediment. No recovery						
Remarks: Borehole completed at 11.5 metres. Hard Till		Topography: Esker ridge		Drainage: Medium		Water level 5 Meters	
				Veg/Crops: Grass		DTB: >11.5 Meters	
						BH depth: 11.5 Meters	

Figure A2 - Borehole BH-S1F collected in Site S1.

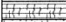


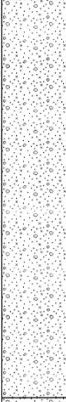
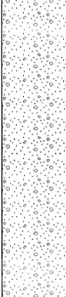

Project: Sheet 48		Method: Continuous Flight Auger Diameter: 15.2 Centimeters County Offaly-Westmeath Townland	1 to 50K: 48 Easting: 240818 Northing: 222896 Elevation: Meters	BH-S1G		Logged by: XMP Date 19/7/05 Page. 1	
Legend	Description	Depth	Sample			Test	
			Num.	Color	Class	Depth	PSA
	Topsoil						
	Very soft fine SAND with no pebbles (2.5Y-4/2). GLACIOFLUVIAL						
	Soft Clayey Silty SAND with few (5%) subangular pebbles. GLACIOFLUVIAL		1	2.5Y-4/2	Silty SAND		
	Soft fine SAND with silty nodules and rounded to subangular Lst/Chert pebbles (1-8cm diam.). Pebble proportion: 40%. GLACIOFLUVIAL	5	2	2.5Y-4/3	fine SAND		
			3		Clayey DIAMI CTON		
	Soft medium to fine SAND with rounded to angular Lst pebbles. Pebble proportion: 20%. GLACIOFLUVIAL						
	Dense grey blue Clayey DIAMICTON with angular-subangular Lst pebbles. GLACIAL						
Remarks: Borehole completed at 13.5 metres. Hard Till or Bedrock. BH collapsed, water level couldn't be measured, expected to be around 12 metres.		Topography: Glaciofluvial Fan		Drainage: Good		Water level 12 Meters	
				Veg/Crops: Grass		DTB: >13.5 Meters	
						BH depth: 13.5 Meters	

Figure A3 - Borehole BH-S1G collected in Site S1.




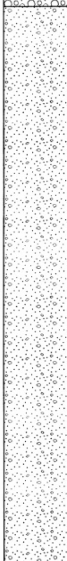
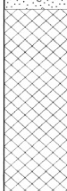

		Method: Continuous Flight Auger	1 to 50K: 48	BH-S1H				
		Diameter: 15.2 Centimeters	Easting: 240614				Logged by: XMP	
Project: Sheet 48		County Offaly-Westmeath	Northing: 222786	Date 19/7/05				
		Townland	Elevation: Meters	Page. 1				
Legend	Description	Depth	Sample				Test	
			Num.	Color	Class	Depth	PSA	St Count
	Topsoil							
	Medium dense coarse GRAVEL with sandy matrix. Rounded pebbles. Clast supported. GLACIOFLUVIAL							
	Medium dense sandy GRAVEL with rounded Lst pebbles (some Sst pebbles present). GLACIOFLUVIAL		1	2.5Y-3/2	sandy GRAVEL			
	Soft gravelly medium SAND with well rounded Lst pebbles. Pebble proportion: 30-50% increasing downwards. Pebble size: 1-12cm diam. GLACIOFLUVIAL	5	2	10YR-4/2	Gravelly SAND			
	Soft sediment, maybe due to water presence. No recovery							
	Dense Silty Clayey DIAMICTON (2.5Y-4/1) with angular-subangular Lst pebbles. GLACIAL							
		15						
Remarks: Borehole completed at 14.7 metres. Hard Till or Bedrock.		Topography: Glaciofluvial Fan		Drainage: Good		Water level 12 Meters		
				Veg/Crops: Grass		DTB: >14.7 Meters		
						BH depth: 14.7 Meters		

Figure A4 - Borehole BH-S1H collected in Site S1.

		Method: Continuous Flight Auger	1 to 50K: 48		BH-S3A			
		Diameter: 15.2 Centimeters	Easting: 226216					
Project: Sheet 48		County Offaly-Westmeath	Northing: 221242		Logged by: XMP			
		Townland	Elevation: Meters		Date 13/7/05			
				Page. 1				
Legend	Description	Depth	Sample				Test	
			Num.	Color	Class	Depth	PSA	St Count
	Topsoil							
	Dense to very dense Silty Gravelly DIAMICTON with subangular subrounded Lst pebbles (0.5-5cm diametre). GLACIAL		1	10YR_5/3	Silty GRAVEL			
		5						
Remarks: Borehole completed at 4.2 metres. Boulder		Topography: Moraine		Drainage: Medium		Water level Meters		
				Veg/Crops: Grass		DTB: >4.2 Meters		
						BH depth: 4.2 Meters		

Figure A5 - Borehole BH-S3A collected in Site S3.

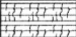



		Method: Continuous Flight Auger		1 to 50K: 48		BH-S4A		
		Diameter: 15.2 Centimeters		Easting: 225193				
Project: Sheet 48		County Offaly-Westmeath		Northing: 221444		Logged by: XMP		
		Townland		Elevation: Meters		Date 13/7/05		
						Page. 1		
Legend	Description	Depth	Sample				Test	
			Num.	Color	Class	Depth	PSA	St Count
	Topsoil							
	Very dense clast supported silty sandy GRAVEL with subrounded subangular pebbles (1-5cm diam.)		1	10YR_4/3	silty GRAVEL			
	Soft layer. No recovery							
	Dense Silty clayey GRAVEL (Diamict) with subangular subrounded Lst pabbles.	5	2	10YR_4/3	silty clayey GRAVEL			
Remarks: Borehole completed at 7.2 metres. Boulder or Bedrock		Topography: Moraine		Drainage: Medium		Water level Meters		
				Veg/Crops: Grass		DTB: >7.2 Meters		
						BH depth: 7.2 Meters		

Figure A6 - Borehole BH-S4A collected in Site S4.

Project: Sheet 48		Method: Continuous Flight Auger	1 to 50K: 48	BH-S5A			
		Diameter: 15.2 Centimeters	Easting: 224201	Logged by: XMP			
		County Offaly-Westmeath	Northing: 222412	Date 13/7/05			
		Townland	Elevation: Meters	Page. 1			
Legend	Description	Depth	Sample			Test	
			Num.	Color	Class	Depth	PSA
	Topsoil						
	Soft fine to coarse sand with well rounded Lst pebbles. Coarsening downwards. GLACIOFLUVIAL		1	2.5Y-3/2	pebbly SAND		
	Medium coarse gravelly sand with rounded Lst pebbles (0.5-6cm diam.). GLACIOFLUVIAL	5					
	Soft medium to fine sand finning downwards with very few Lst pebbles. GLACIOFLUVIAL		2	2.5Y-3/2	Gravelly SAND		
	Soft medium to fine sand finning downwards with very few Lst pebbles. GLACIOFLUVIAL		3	2.5Y-4/2	pebbly SAND		
	Soft wet fine SAND with no pebbles. GLACIOFLUVIAL	15	4		SAND		
Remarks: Borehole completed at 16.8 metres. Due to lack of augers		Topography: Esker ridge	Drainage: Good		Water level Meters		
			Veg/Crops: Grass		DTB: >16.8 Meters		
					BH depth: 16.8 Meters		

Figure A7 - Borehole BH-S5A collected in Site S5.

PARTICLE SIZE ANALYSIS RESULTS

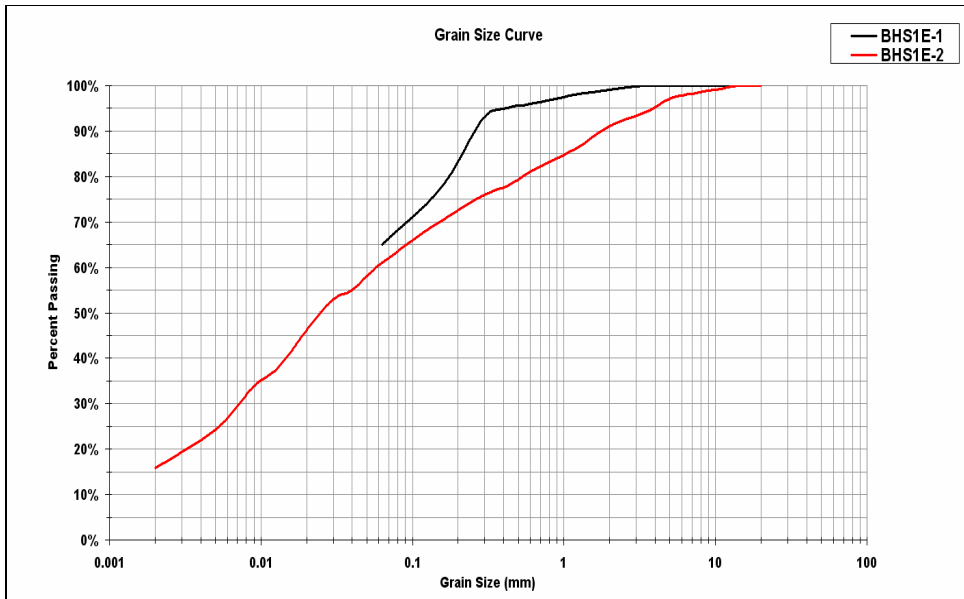


Figure A9 – PSA cumulative graph for samples collected in BH-S1E.

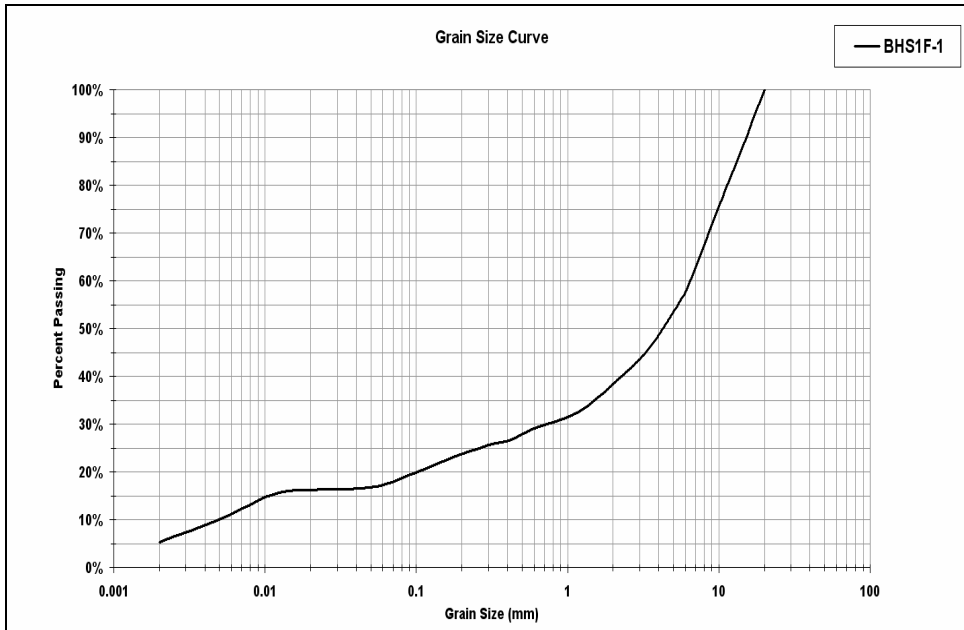


Figure A10 – PSA cumulative graph for samples collected in BH-S1F.

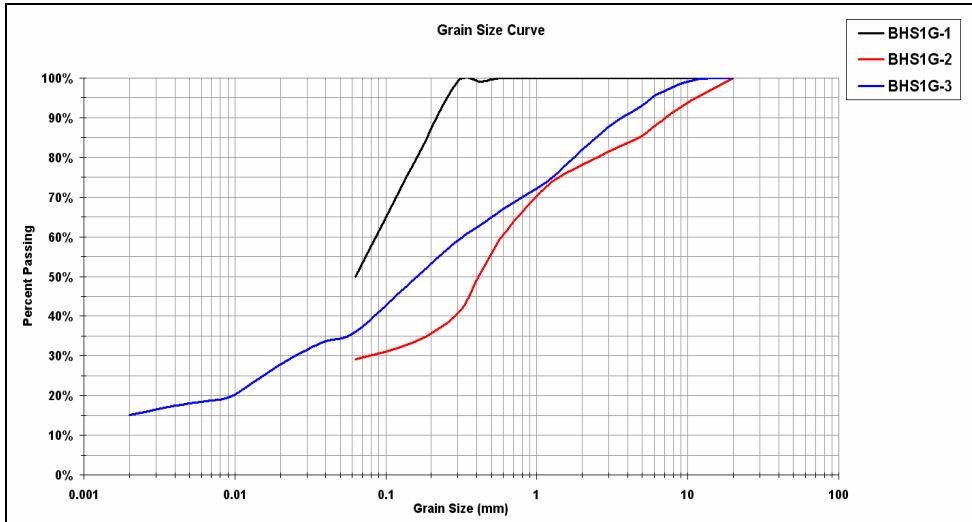


Figure A11 – PSA cumulative graph for samples collected in BH-S1G.

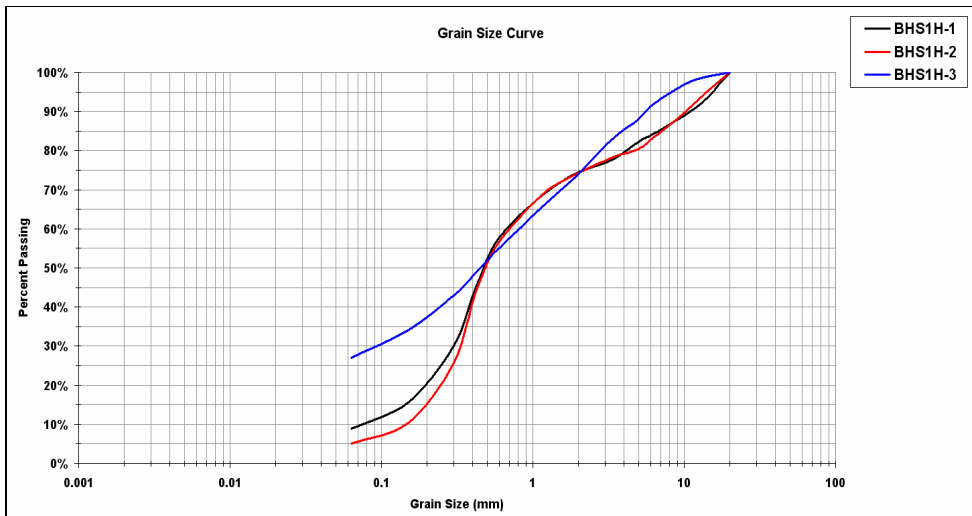


Figure A12 – PSA cumulative graph for samples collected in BH-S1H.

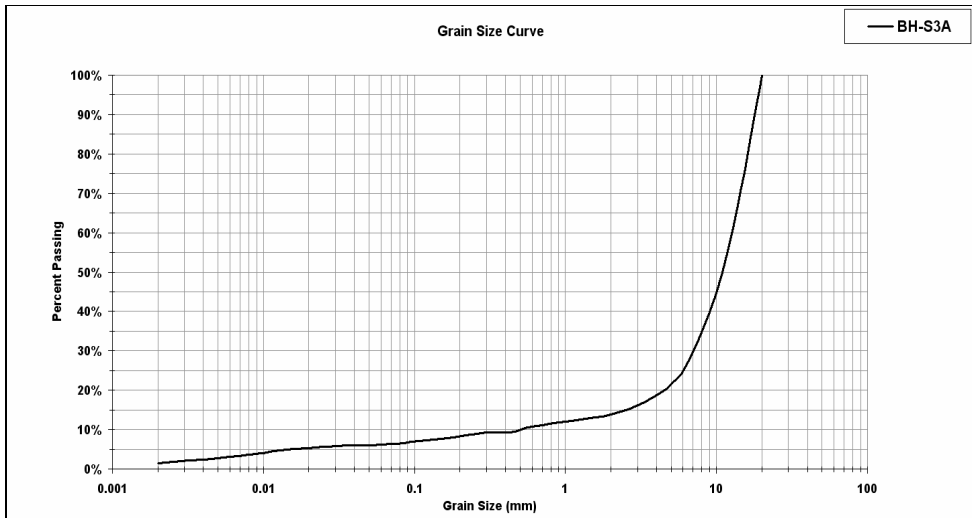


Figure A13 – PSA cumulative graph for samples collected in BH-S3A.

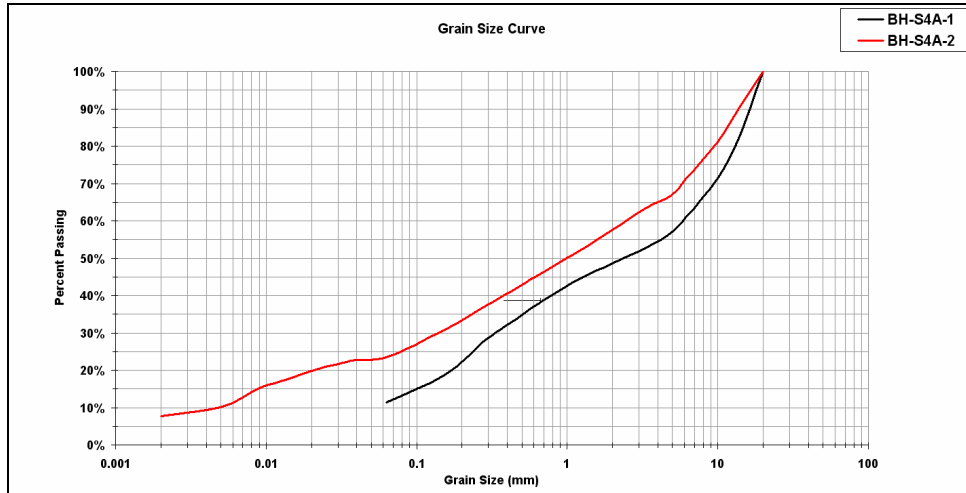


Figure A14 – PSA cumulative graph for samples collected in BH-S4A.

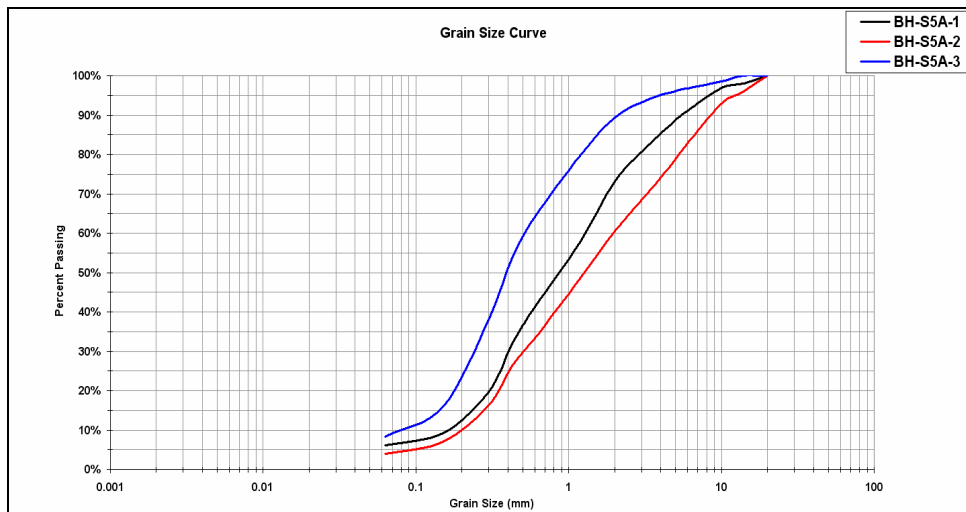


Figure A15 – PSA cumulative graph for samples collected in BH-S5A.

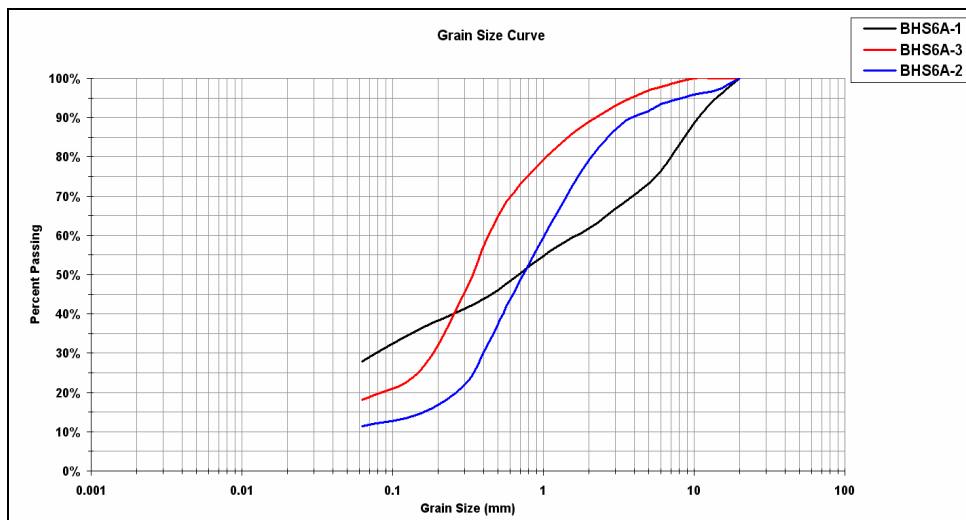


Figure A16 – PSA cumulative graph for samples collected in BH-S6A.

APPENDIX B

This appendix shows a representative sample of the ERT profiles presented in this thesis after processing with RES2DINV Inversion modelling software. This software uses the apparent resistivity values that have been measured in the field (top) to produce an inverse model resistivity section (bottom), which shows the real resistivity values for the materials surveyed. A calculated apparent resistivity pseudosection (middle) is computed from the inverse resistivity model (bottom) and the RMS error calculated between the measured (top) and the calculated (middle) apparent resistivity pseudosections.

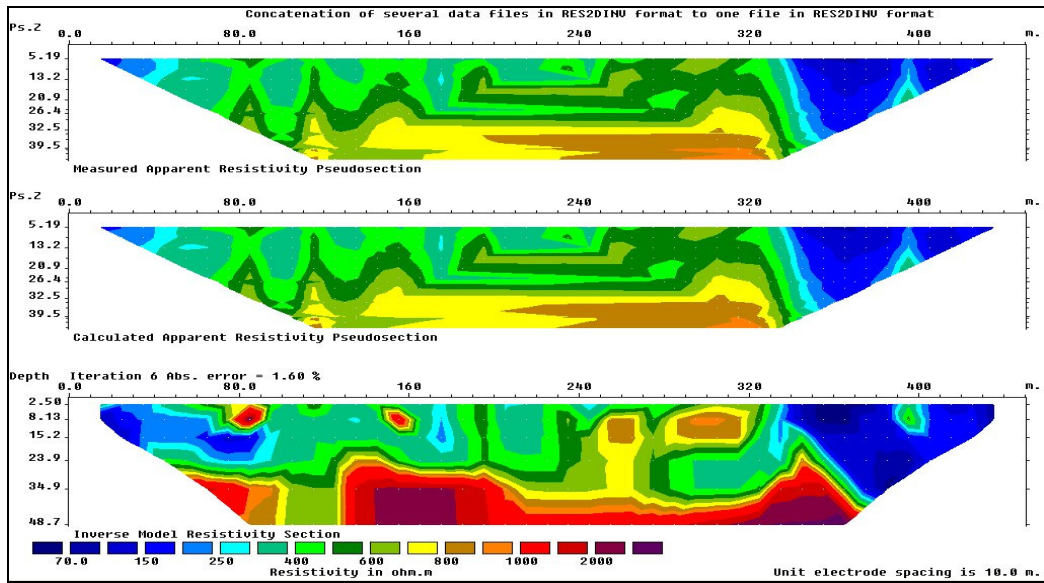


Figure B1 – Measured and Calculated apparent resistivity pseudosection and Inverse model resistivity of profile RS1-L01-10m (Figure 6.6).

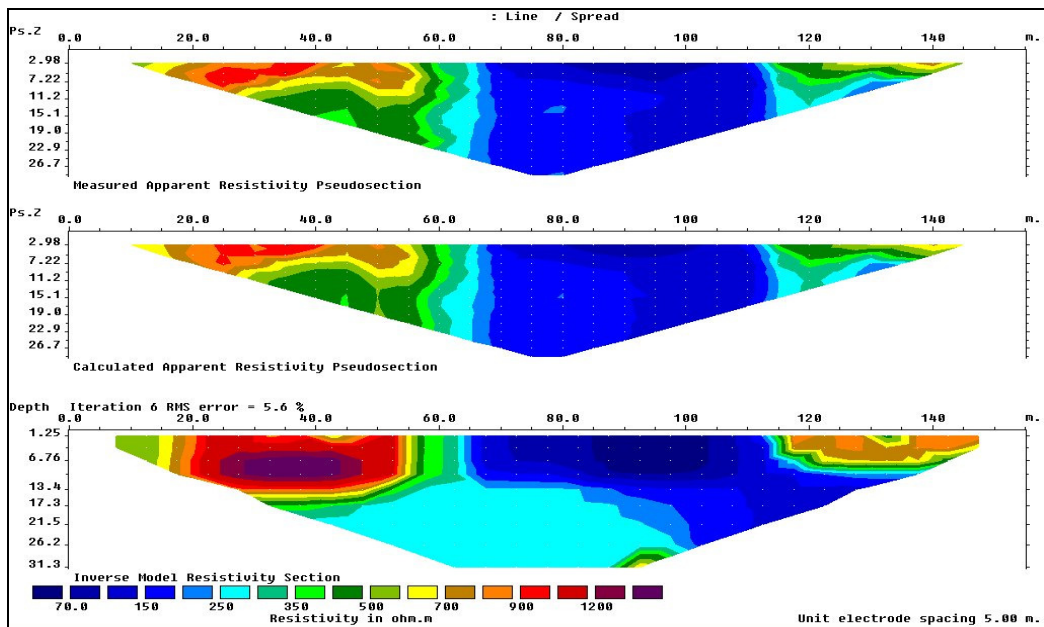


Figure B2 – Measured and Calculated apparent resistivity pseudosection and Inverse model resistivity of profile RS1-L04-5m (Figure 6.8)

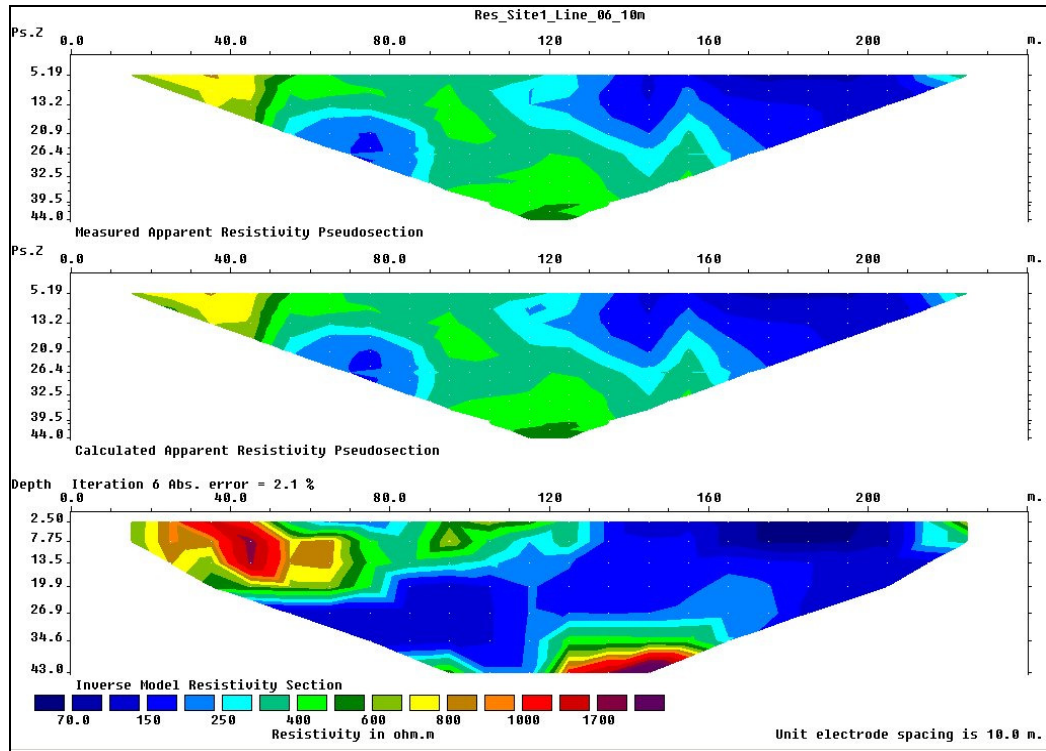


Figure B3 – Measured and Calculated apparent resistivity pseudosection and Inverse model resistivity of profile RS1-L06-10m (Figure 6.10).

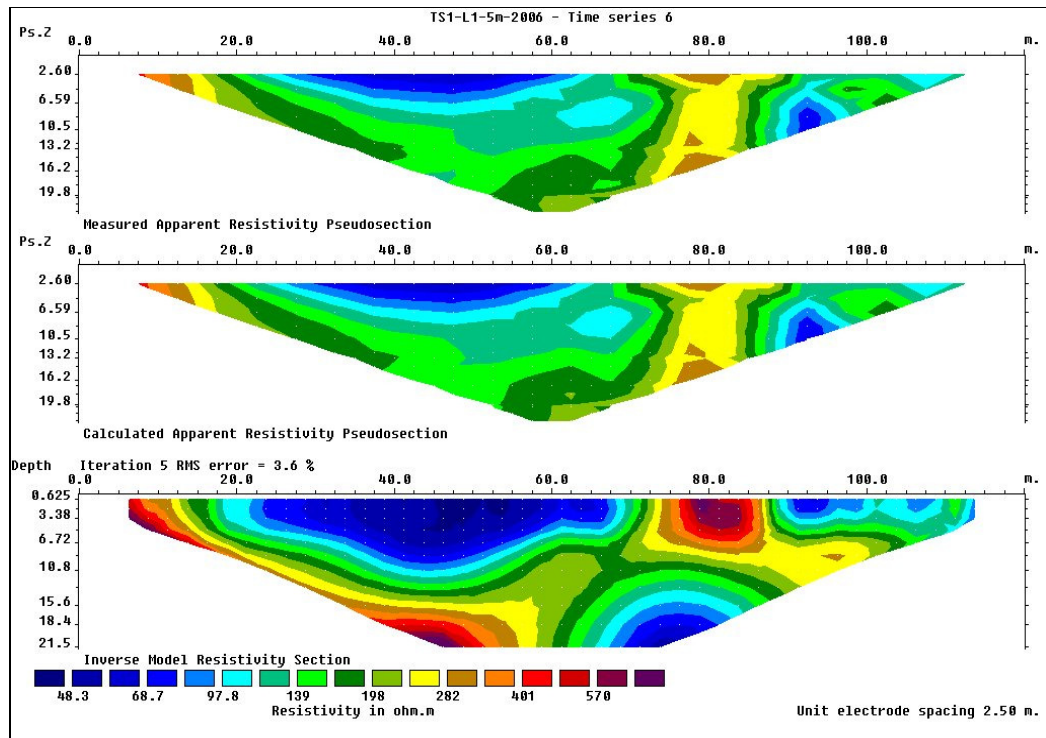


Figure B4 – Measured and Calculated apparent resistivity pseudosection and Inverse model resistivity of profile RTS1-L01-5m (Figure 6.12).

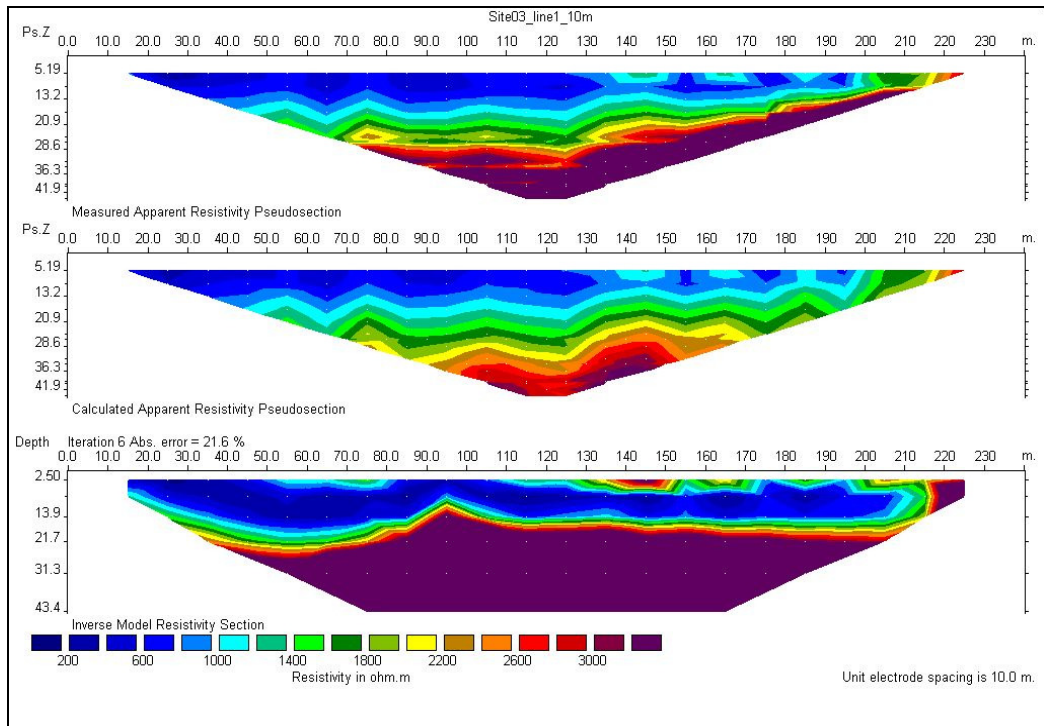


Figure B5 – Measured and Calculated apparent resistivity pseudosection and Inverse model resistivity of profile RTS3-L01-10m (Figure 6.62b).

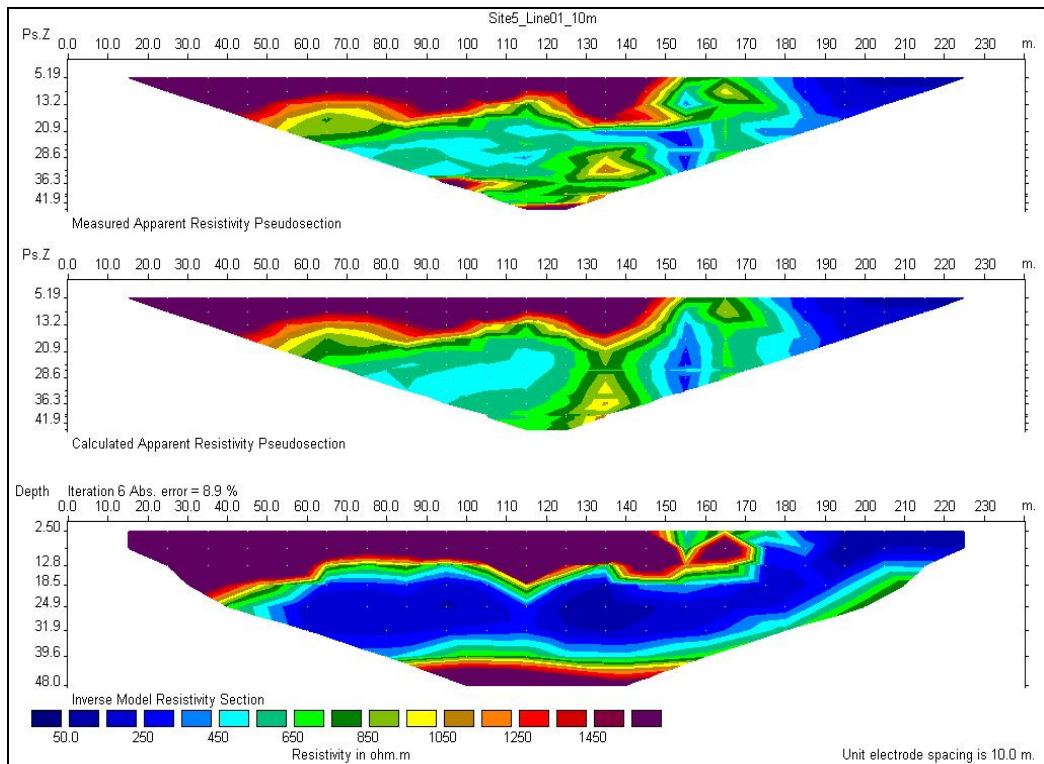


Figure B6 – Measured and Calculated apparent resistivity pseudosection and Inverse model resistivity of profile RTS5-L01-10m (Figure 6.74).

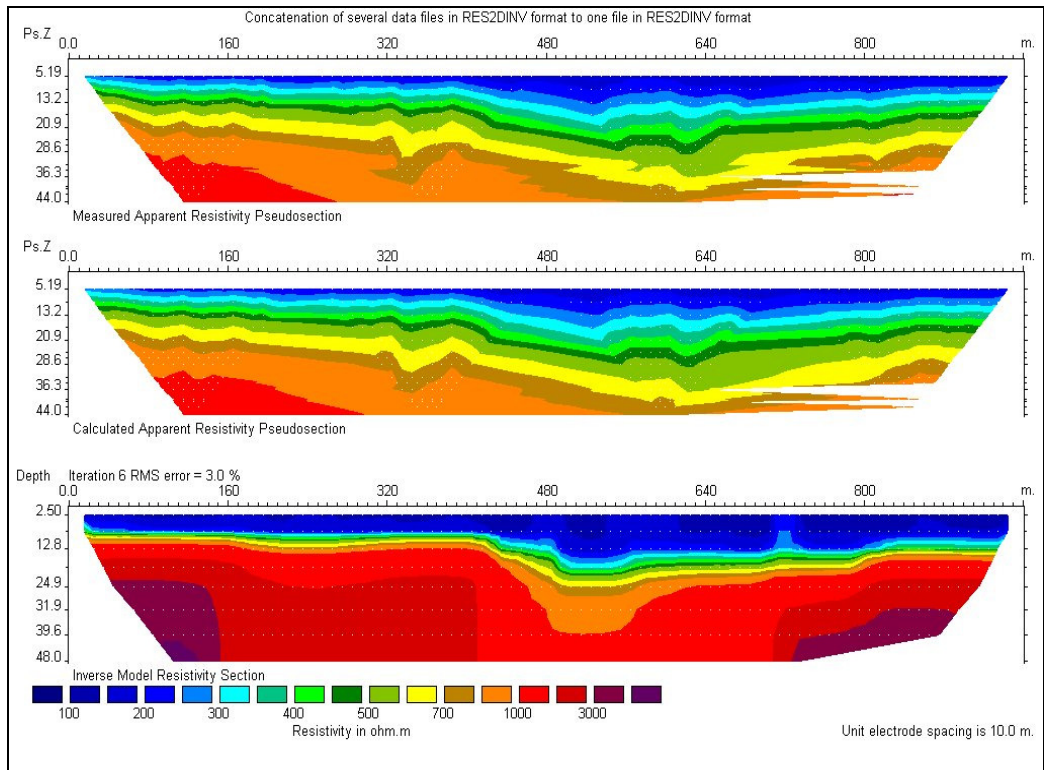


Figure B7 – Measured and Calculated apparent resistivity pseudosection and Inverse model resistivity of profile RS9-Merge-10m (Figure 6.92).

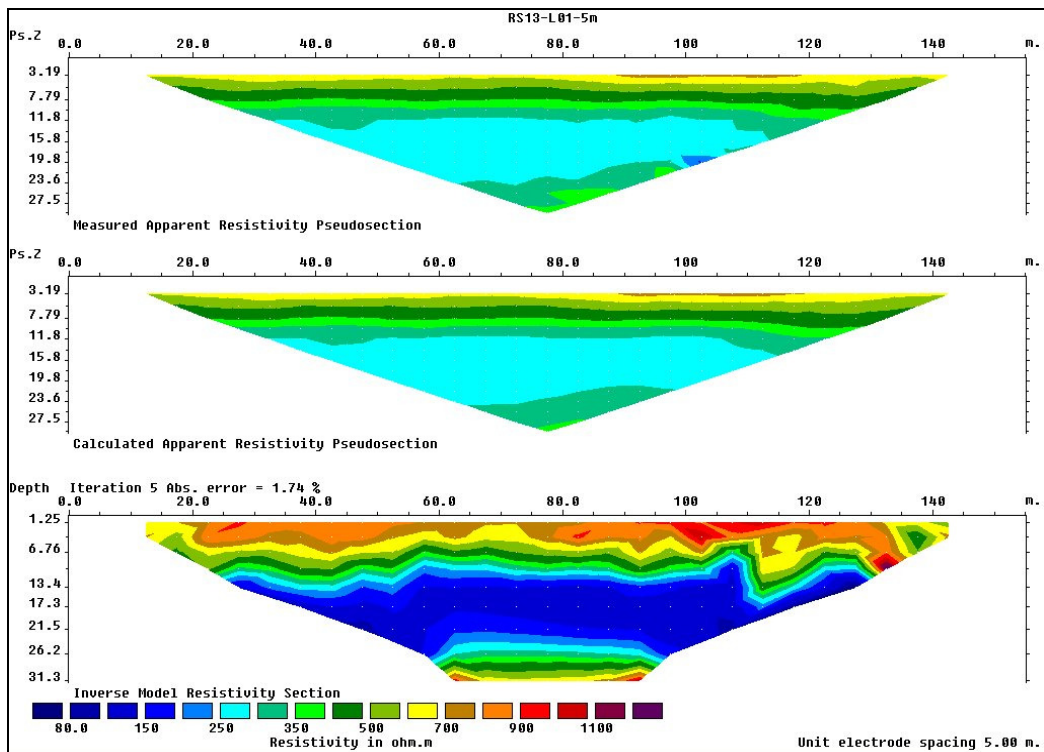


Figure B8 – Measured and Calculated apparent resistivity pseudosection and Inverse model resistivity of profile RS13-L01-5m (Figure 6.109).

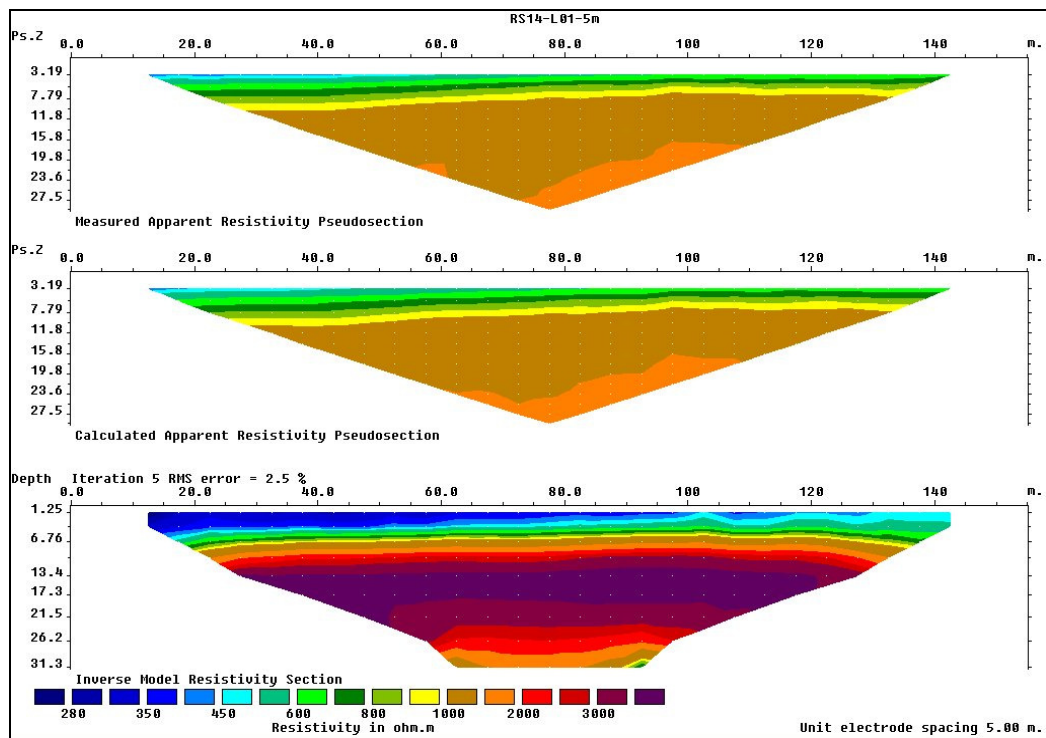


Figure B9 – Measured and Calculated apparent resistivity pseudosection and Inverse model resistivity of profile RS14-L01-5m (Figure 6.114).

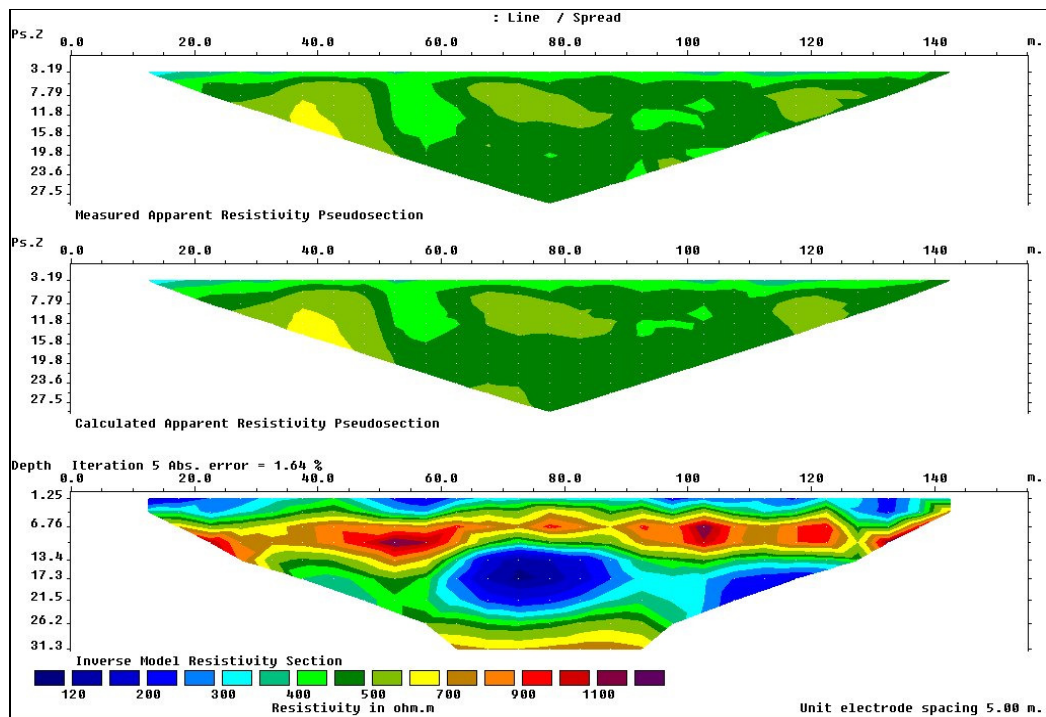


Figure B10 – Measured and Calculated apparent resistivity pseudosection and Inverse model resistivity of profile RS16-L01-5m (Figure 6.123).

Bibliography

- Allen, R.G., Pereira L.S., Raes, D. and Smith, M. (1998) Crop evapotranspiration – Guidelines for computing crop water requirements - FAO Irrigation and drainage paper 56. FAO - Food and Agriculture Organization of the United Nations, Rome.
- Annan, A.P. (1999) Practical processing of GPR data. Proceedings of the second government workshop on Ground Penetrating Radar. Sensors and Software Inc.
- Annan, A.P. (2002) GPR – History, Trends, and Future Developments. *Subsurface Sensing Technologies and Applications* 3 (4), 253 – 270.
- Annan, A.P., Cosway, S.W. and Redman, J.D. (1991) Water table detection with ground penetrating radar. *Expanded Abstracts Soc. Explor. Geophysicists Annual Meeting, SEG, Tulsa, OK*, 494-496.
- Ashley, G.M. (1995) Glaciolacustrine environments. (ed.) Menzies, J. *Modern Glacial Environments - Processes, dynamics and sediments; Glacial Environments Series: Vol. 1, Butterworth Heinemann, Oxford.*
- Ashley, G.M. and Warren, W.P. (1995) Irish Eskers/Origins of ice-contact stratified deposits. *INQUA Commission on Formation and Properties of Glacial Deposits. Symposium and Field Excursion 21-28 May 1995. 59pp.*
- Ayotte, J.D. (1994) Use of Ground Penetrating Radar to determine the depositional environment of glacial deposits in Southern New Hampshire. *Proceeding of the symposium on the application of geophysics to engineering and environmental problems. EEGS.*
- Baker, P.L. (1991) Response of ground-penetrating radar to bounding surfaces and lithofacies variations in sand barrier sequences. *Explor. Geophysics* 22, 19-22.
- Baker, G.S., Jordan, T.E. and Pardy, J. (2007) An Introduction to Ground Penetrating Radar (GPR). In: Baker, G.S. and Jol, H.M.; *Stratigraphic Analyses Using GPR. Geological Society of America Special Paper 432, 181 pp.*
- Bakker, M.A.J. and van der Meer, J.J.M. (2003) Structure of a Pleistocene push moraine revealed by GPR: the eastern Veluwe Ridge, The Netherlands. In: Bristow, C.S., Jol, H.M. (Eds.), *Ground Penetrating Radar in Sediments. Geol. Soc. London Spec. Publ. 211, 143-151.*
- Ballantyne, C.K. (2008) Extent and deglacial chronology of the last British-Irish Ice Sheet: implications of exposure dating using cosmogenic isotopes. *Journal of Quaternary Science. 27, 185–200.*
- Ballantyne, C.K., McCarroll, D. and Stone, J.O. (2006) Vertical dimensions and age of the Wicklow Mountains ice dome, Eastern Ireland, and implications for the extent of the last Irish ice sheet. *Quaternary Science Reviews* 25, 17-18, 2048-2058.

- Ballantyne, C.K., McCarroll, D. and Stone, J.O. (2007). The Donegal ice dome, northwest Ireland: dimensions and chronology. *Journal of Quaternary Science* 22, 773-783.
- Ballantyne, C.K., Stone, J.O. and McCarroll, D. (2008) Dimensions and chronology of the last ice sheet in Western Ireland. *Quaternary Science Reviews* 27, 3-4, 185-200.
- Bano, M., Marquis, G., Niviere, B., Maurin, J.C. and Cushing, M. (2000) Investigating alluvial and tectonic features with ground penetrating radar and analysing differentiations patterns. *Journal of applied geophysics*, 43, 33-41.
- Barker, R.D. (1981) The offset system of electrical resistivity sounding and its use with a multicore cable: *Geophysical Prospecting*, 29, 128-143.
- Barker, R.D. (1989) Depth of investigation of collinear symmetrical four-electrode arrays. *Geophysics* 54, 1031-1037.
- Barker, R.D. and Moore, J. (1998) The application of time-lapse electrical tomography in groundwater studies. *Leading Edge* 17, 10, 1454-1458.
- Beamish, D. (1998) Three-dimensional modelling of VLF data. *Journal of Applied Geophysics* 39. 63-76.
- Beamish, D. (2000) Quantitative 2D VLF data interpretation: *Journal of Applied Geophysics*, 45, 33-47.
- Benn, D.I. and Evans D.J.A. (1998) *Glaciers and Glaciation*. Arnold. London.
- Beres, M., Green, A.G., Huggenberger, P. and Horstmeyer, H. (1995) Mapping the architecture of glaciofluvial sediments with three-dimensional georadar. *Geology* 23, 1087-1090.
- Beres, M., Huggenberger P., Green A.G. and Horstmeyer, H. (1999) Using two and three-dimensional georadar methods to characterize glaciofluvial architecture; *Sedimentary Geology* 129, 1-24
- Bernstone C., Dahlin T., Ohlsson T. and Hogland W. (2000) DC-resistivity mapping of internal landfill structures: two pre-excavation surveys. *Environmental Geology* 39, 3-4, 360-368.
- Blackford, J.J. and Chambers F.M. (1995) Proxy climate record for the last 1000 years from Irish blanket peat and a possible link to solar variability. *Earth and Planetary Science Letters* 133, 1-2, 145-150.
- Boris, M. and Merriam, J. B., (2002) Azimuthal Resistivity to Characterize Fractures in Glacial Till. *Symposium on the Application of Geophysics to Environmental and Engineering Problems*, Las Vegas, Nevada, 10 pp.

- Boulton, G.S. (1970) On deposition of subglacial and melt-out tills at the margins of certain Svalbard glaciers. *Journal of Glaciology* 9, 231-246.
- Boulton, G. S. and Eyles, N. (1979) Sedimentation by valley glaciers: a model and genetic classification. In Schlüchter, C. (ed.): *Moraines and Varves*, 11-23. Balkema, Rotterdam.
- Bowen, D.Q., Phillips, F.M., McCabe, A.M., Knutz, P.C. and Sykes, G.A. (2002) New data on the Last Glacial Maximum in Great Britain and Ireland. *Quaternary Science Reviews* 21, 89-101.
- Breen, R. (2003) A geophysical investigation of glacial sediments in the Galtrim region of Co. Meath. M. Sc. Thesis, Department of Geography, Environmental Geophysics Unit, NUI, Maynooth.
- Brigland, D.R. (1986) *Clast Lithological Analysis*. Quaternary Research Association Technical Guide No. 3.
- Bristow, C.S. (1995). Facies analysis in the Lower Greensand using ground-penetrating radar. *J. Geol. Soc.* 152, 591-598.
- Bristow, C.S., Pugh, J. and Goodall, T. (1996) Internal structure of aeolian dunes in Abu Dhabi determined using ground-penetrating radar. *Sedimentology* 43, 995-1003.
- Bristow, C.S., Skelly, R.L. and Etheridge, F.G. (1999) Crevasse splays from the rapidly aggrading, sand-bed, braided Niobrara River, Nebraska: effect of base-level rise. *Sedimentology* 46, 1029-1047.
- Bristow, C.S., Best, J.L. and Ashworth, P.J. (2000) The use of GPR in developing a facies model for a large sandy braided river, Brahmaputra River, Bangladesh. In: Noon, D.A., Stickley, G.F., Longstaff, D. (Eds.), *Proceedings of the Eighth International Conference on Ground Penetrating Radar*. SPIE, Billingham 4084, 95-100.
- BS 5930. (1999) *Code of Practice for Site Investigations, Section 3. Field Investigations*. Mechanical Augers, 25-26.
- BS EN ISO 22476-2:2005. (2006) *Geotechnical investigation and testing. Field testing. Dynamic probing*. ISBN. 0 580 47636 7.
- Busby, J.P. and Merritt, J.W. (1999) Quaternary deformation mapping with ground-penetrating radar. *Journal of Applied Geophysics* 41, 75-91.
- Busby, J.P. (2000) The effectiveness of azimuthal apparent-resistivity measurements as a method for determining fracture strike orientations. *Geophysical Prospecting* 48, 677-695.

- Busby, J.P. and Jackson, P. (2005) The application of time-lapse azimuthal apparent resistivity measurements for the prediction of coastal cliff failure. *Journal of Applied Geophysics* 59, 4, 261-272.
- Callaghan, L. (2002) The geophysical characteristics of glacial deposits in County Meath. M. A. Thesis, Department of Geography, Environmental Geophysics Unit, NUI, Maynooth.
- Caloca, S. (2006) Geophysical investigation of Quaternary glacial sediments in South Co. Westmeath and North Co. Offaly. Unpublished Master thesis, Environmental Geophysics Unit, NUI Maynooth.
- Carpenter, P.J. (1996) Detection and mapping of mine subsidence fractures in glacial drift using surface electrical methods. Proceedings of the symposium on the application of geophysics to engineering and environmental problems. EEGS.
- Cassidy, N.J., Russell, A.J., Marren, P.M., Fay, H., Knudsen, O., Rushmer, E.L. and van Dijk, T.A.G.P. (2003) GPR derived architecture of November 1996 jökulhlaup deposits, Skeidara ársandur, Iceland. In: Bristow, C.S., Jol, H.M. (Eds.), *Ground Penetrating Radar in Sediments*. Geol. Soc. London Spec. Publ. 211, 153-166.
- Charlesworth, J.K. (1928) The glacial retreat from central and southern Ireland. *Quarterly Journal of the Geological Society of London* 84, 293-344.
- Charlesworth, J.K. (1963) Some observations on the Irish Pleistocene. *Proceedings of the Royal Irish Academy* 62B, 295-322.
- Charlesworth, J.K. (1973) Stages in the dissolution of the last ice sheet in Ireland and the Irish Sea region. *Proceedings of the Royal Irish Academy* 73B, 79-85.
- Claerbout, J.F. and Muir, F. (1973) Robust modelling with erratic data. *Geophysics* 38, 826- 844.
- Clayton L. (1964) Karst topography on stagnant glaciers. *Journal of Glaciology* 5, 37, 107-112.
- Clark, C.D. and Meehan, R.T. (2001) Subglacial bedform geomorphology of the Irish Ice Sheet reveals major configuration changes during growth and decay. *Journal of Quaternary Science* 16, 483-496.
- Clark, I. (2004) The advance geostatistics course. Bring your own data for geostatistical evaluation. Geostokos (Ecosse) Ltd. Scotland.
- Close, M.H. (1867) Notes on the General Glaciation of Ireland, *Journal of the Royal Geological Society of Ireland* 1, 207-242.
- Comas, X., Slater, L. and Reeve, A. (2004) Geophysical evidence for peat basin morphology and stratigraphic controls on vegetation observed in a Northern Peatland. *Journal of Hydrology* 295, 173-184.

- Conyers, L.B. (2004) *Ground Penetrating Radar for Archaeology*. Rowman and Littlefield Publishers Inc. Lanham.
- Coxon, P. and Brown, P. (1989) Glacial deposits and landforms of central and western Ireland. Pp 355-365 in Ehlers, J., Gibbard, P.L. and Rose, J. (eds) *Glacial Deposits in Great Britain and Ireland*. Balkema, Rotterdam.
- Coxon, P. (1993) Irish Pleistocene Biostratigraphy, *Irish Journal of Earth Sciences* 12, 83-105.
- Dahlin, T. (1996) 2D resistivity surveying for environmental and engineering application. *First Break* 14, 275-284.
- van Dam, R.L. and Schlager, W. (2000) Identifying causes of ground-penetrating radar reflections using time-domain reflectometry and sedimentological analyses. *Sedimentology* 47, 435-449.
- Daniels, J.J., Roberts, R. and Vendl, M. (1995) Ground penetrating radar for detection of liquid contaminants. *Applied Geophysics* 33 195-207.
- Davis, J. L. and Annan A. P. (1989) Ground-penetrating radar for high-resolution mapping of soil and rock stratigraphy. *Geophysical Prospecting* 37, 5.
- Dehls, J., Olesen, O., Olsen, L. and Blikra, L.H. (2000) Neotectonic faulting in northern Norway; the Stuoragurra and Nordmannvikdalen postglacial faults. *Quaternary Science Reviews* 19, 1445-1460.
- Delaney, C.A. (2002a) Esker formation and the nature of deglaciation: the Ballymahon esker, Central Ireland. *North West Geography*, 1, 23-33.
- Delaney, C.A. (2002b) Sedimentology of a glaciofluvial landsystem, Lough Ree area, Central Ireland: implications for ice margin characteristics during Devensian deglaciation. *Sedimentary Geology*. 149, 111-126.
- Delaney, C.A. (2008) Seasonal controls on deposition of Late Devensian glaciolacustrine sediments, Central Ireland. In M. Hambrey, P. Christoffersen, N. glasser, P. Jansen, B. Hubbard and Siegert, M. (eds). *Glacial Sedimentary Processes and Products*, 146-163. Special Publication. International Association of Sedimentologists. Oxford. Blackwells.
- Diefendorf, A.F., Patterson, W.P., Mullins, H.T., Tibert, N. and Martini A. (2006) Evidence for high-frequency late Glacial to mid-Holocene (16,800 to 5,500 cal yr B.P.) climate variability from oxygen isotope values of Lough Inchiquin, Ireland. *Quaternary Research* 65, 78-86.
- Diefendorf, A.F., Patterson, W.P., Holmden, C., and Mullins, H.T. (2007) Carbon isotopes of marl and organic lake sediment record terrestrial landscape change during the late glacial and early Holocene (16,800 to 5,540 cal yr BP): a multiproxy study of lacustrine sediments at Loch Inchiquin, western Ireland. *Journal of Paleolimnology* 39, 101-115.

- Doughan, T. (2004) A geophysical investigation of glacial sediments in the Ballinakill region of County Laois. M. A. Thesis, Department of Geography, Environmental Geophysics Unit, NUI, Maynooth.
- Dreimanis, A. (1988): Till: Their Genetic Terminology and Classification; in Genetic Classification of Glaciogenic Deposits, R.P. Goldthwait and C.L. Matsch, Editors, Balkema, 17-67.
- Edwards, K.J. and Warren W.P. 1985. The Quaternary History of Ireland. Academic Press, London.
- Ehlers, J. 1996; Quaternary and Glacial Geology, John Wiley & Sons, Chichester.
- Evans, D.J.A. and Benn D.I. 2004. Practical guide to the study of glacial sediments. Arnold, London.
- Eyles, N. (1979) Facies of supraglacial sedimentation on Icelandic and Alpine temperate glaciers. Canadian Journal of Earth Sciences 16, 1341-1361.
- Farrington, A. (1947) Unglaciaded areas in southern Ireland. Irish Geography I, 89-97.
- Farrington, A. and Synge, F.M. (1970) Three local studies of the Irish Pleistocene, The Eskers of the Tullamore District. (Stephens, N. and Glassock, R., eds.) Irish Geographical Studies, Queens University of Belfast, 49-52.
- Feehan, J. and Dunne, L. (2003) Ireland's Mushroom Stones. Relics of a Vanished Lakeland. Environmental Resource Management, University College Dublin.
- Fetter, C. W. Jr. (1980) Applied Hydrogeology, Charles E. Merrill and Co., Columbus, Ohio, 488 (p 79).
- Fisher, E., McMechan, G.A. and Annan, A.P. (1992) Acquisition and processing of wide-aperture ground-penetrating radar data. Geophysics 57, 495-504.
- Flemming, A. (1986) The Determination of Joint System Characteristics from Azimuthal Resistivity Surveys. Published by University of Wisconsin-Madison.
- Flint, R.F. (1930) The origin of the Irish "eskers": Geographical Review, 20, 615-630.
- Flint R.F. (1957) Glacial and Pleistocene geology: John Wiley & Sons, New York.
- Flint, R.F. (1971) Glacial and Quaternary Geology. Wiley, New York.
- Folk, R.L. (1954) The distinction between grain size and mineral composition in sedimentary-rock nomenclature, Journal of Geology 62, 344-359.
- Fowler, C. M. R. (1990) The Solid Earth. An Introduction to Global Geophysics. Cambridge University Press.

- Gawthorpe, R.L., Collier, R.E.L., Alexander, J., Leeder, M. and Bridge, J.S. (1993) Ground penetrating radar: application to sandbody geometry and heterogeneity studies. In: North, C.P., Prosser, D.J. (Eds.), *Characterization of Fluvial and Aeolian Reservoirs*. Geol. Soc. Lond. Spec. Publ. 73, 421-432.
- Glanville, C. (1997) Glaciolacustrine and glaciofluvial deposits defining the margins of uncoupling ice lobes in the southeastern Midlands of Ireland. *Quaternary Science Reviews*. 16, 685-703.
- George, D. M. and Gibson, P. J. (2000) Application of geophysical techniques for groundwater investigations and waste disposal site contamination studies in Co. Monaghan, Republic of Ireland. Report No: EGU001/2000. Interreg 4 - programme.
- Gerin R., Munoz M.L. Christophe A., Laperrelle C., Hidra M., Drouart, E. and Grellier, S. (2004) Leachate recirculation: moisture content assessment by means of a geophysical technique. *Waste Management* 24, 785-794.
- Gibbard, P.L. and Cohen, K.M. (2008) Global chronostratigraphical correlation table for the last 2.7 million years. *Episodes* 31, 2.
- Gibson, P.J. (1991) An integrated investigation of the Tow Valley fault system (Ireland) with particular emphasis on remote sensing techniques. Unpublished D. Phil. Thesis. University of Ulster. 385pp.
- Gibson, P. J. (2003) Seasonal effects on two dimensional time-lapse subsurface resistivity imaging. Proceedings of the Geophysical Association of Ireland /Irish Association of Hydrogeologists conference 28/5/03 'Geophysical applications in hydrogeological investigations', 1-4.
- Gibson, P. J. (2005) Proceedings of the International Association of Hydrologists meeting: "Groundwater in Ireland", Tullamore 19-20th April. "Advances in Geophysics – time-lapse resistivity imaging – location and movement of landfill plumes. 117-121.
- Gibson, P. J. (2007a). Heritage Landscape of the Irish Midlands and selected itineraries. Geography Publications, Dublin, Ireland.
- Gibson, P. J. (2007b) Integrated geophysical study of the former monastic site, Rahan, Co. Offaly. Phase I and II. EGU 01/07.
- Gibson, P. J. (2007c) Archaeo-magnetic investigation of the former monastic site at Kilskyre, Co. Meath. Riocht na Midhe. Records of the Meath Archaeological and Historical Society. V. XXVIII 33-38.
- Gibson, P. J. and George, D. M. (2001) Electrical resistivity and VLF investigations of potential water bearing structures on extension of North Campus of NUIM, Maynooth, Co. Kildare. Report No: EGU01/01 24pp.

- Gibson, P.J. and George, D.M (2004) Environmental applications of geophysical surveying techniques. Nova Science Publishers Inc. New York.
- Gibson, P.J., Lyle, P. and George D.M. (2004) Application of resistivity and magnetometry geophysical techniques for near-surface investigations in karstic terranes in Ireland. *Journal of Cave and Karst Studies*, 66, 2, 35-38.
- Gibson, P. J. and George, D. M. (2006) Geophysical Investigation of the former monastic settlement, Clonard, Co. Meath, Ireland. *Archaeo. Prosp.* 13, 45-56.
- Goodman, D. (2007) Ground Penetrating Radar Simulation v3.0 (GPRSIM), User Manual, www.GPR-SURVEY.com.
- Goodman, D., Nishimura, Y. and Tobita, K. (1994) GPRSIM forward modeling software and time slices in ground penetrating radar surveys, in *Proceedings of the Fifth International Conference on Ground Penetrating Radar (GPR '94)*, June 12-16, Kitchener, Ontario, Canada, 31-43
- Gracia, V.P., García, F.G. and Abad, I.R. (2008) GPR evaluation of the damage found in the reinforced concrete base of a block of flats: A case study. *NDT & E International*, 41, 5, 341-353.
- Greenwood, S.L. and Clark, C.D. (2008) Subglacial bedforms of the Irish Ice Sheet. *Journal of Maps*, 332-357.
- Greenwood, S.L. and Clark, C.D. (2009a) Reconstructing the last Irish Ice Sheet 1: changing flow geometries and ice flow dynamics deciphered from the glacial landform record. *Quaternary Science Reviews* 28, 3085-3100.
- Greenwood, S.L. and Clark, C.D. (2009b) Reconstructing the last Irish Ice Sheet 2: a geomorphologically-driven model of ice sheet growth, retreat and dynamics. *Quaternary Science Reviews* 28, 3101-3123.
- Griffiths, D.H. and Turnbull, J. (1985). A multi-electrode array for resistivity surveying. *First Break* 3, no. 7, 16-20.
- deGroot-Hedlin, C. and Constable, S. (1990) Occam's inversion to generate smooth, two-dimensional model from magnetotelluric data. *Geophysics* 55, 1613-1624.
- Guglielmin, M., Biasini, A. and Smiraglia, A. (1997) The Contribution of Geoelectrical Investigations in the Analysis of Periglacial and Glacial Landforms in Ice Free Areas of the Northern Foothills (Northern Victoria Land, Antarctica) *Geografiska Annaler, Series A: Physical Geography* 79, 1-2, 17-24.
- Haberjam, G.M. and Watkins, G.E. (1967) The use of an square configuration in resistivity prospecting. *Geophysical Prospecting*. 20, 249-266.
- Hauck, C., Vonder Mühl, D. and Maurer, H. (2003) Using DC resistivity tomography to detect and characterize mountain permafrost. *Geophysical Prospecting* 51, 4, 273-284.

- Hegarty, S., (2004) Limits of Midlandian glaciation in south-eastern Ireland. *Irish Geography* 37, 60-76.
- Heinz, J. and Aigner, T. (2003) Three-dimensional GPR analysis of various Quaternary gravel-bed braided river deposits (southwestern Germany). In: Bristow, C.S., Jol, H.M. (Eds.), *Ground Penetrating Radar in Sediments*. Geol. Soc. London Spec. Publ. 211, 99-110.
- Hitzman, M.W. (1992) Bedrock geological map of the Carboniferous of Central Ireland (1:100,000 Scale, O.S.Sheets 12,13,15, 16, 18 and 19. Geological Survey of Ireland.
- Holmes, C.D. (1947) Kames. *American Journal of Science* 245, 240-249.
- Hull, E. (1878) *Physical Geology and Geography of Ireland*. London: Edward Stanford.
- Jackobsen, P.R. and Overgaard, T. (2002) Georadar facies and glaciotectionic structures in ice marginal deposits, northwest Zealand, Denmark. *Quaternary Science Reviews* 21, 917- 927.
- Jeng, Y., Lin, M.J. and Chen, C.S. (2004) A very low frequency-electromagnetic study of the geo-environmental hazardous areas in Taiwan. *Environmental Geology* 46, 784-795.
- Johansson, S and Dahlin, T. (1996) Seepage monitoring in an earth embankment dam by repeated resistivity measurements. *European Journal of environmental and engineering geophysics* 1, 229-247.
- Jol, H.M. (1995) Ground penetrating radar antennae frequencies and transmitter powers compared for penetration depth, resolution and reflection continuity. *Geophysical Prospection* 43, 693-709.
- Jol, H.M. and Smith, D.G. (1991) Ground penetrating radar of northern lacustrine deltas. *Canadian. Journal of Earth Science*. 28, 1939-1947.
- Jol, H.M. and Bristow, C.J. (2003) GPR in Sediments: advice on data collection, basic processing and interpretation, a good practice guide. Pp. 9-29 in Bristow, C. J. and Jol, H.M. (Eds) *Ground Penetrating Radar in Sediments*, The Geological Society, London.
- Jordan, C. (2002) An holistic approach to mapping the Quaternary geology and reconstruction of the Last Glaciation of west County Mayo, Ireland, using satellite remote sensing and 'conventional' mapping techniques. Unpublished Ph.D. Thesis, Queen Mary, University of London.
- Karous, M. and Hjelt, S.E. (1983) Linear filtering of VLF dip-angle measurements, *Geophysical Prospection* 31, 782-894.
- Kathage, A. (2008) The resolution and detection ability of ground penetrating radar (GPR). Geophysical Survey Systems, Inc.

- Kilner, M., Westa, L.J. and Murray, T. (2005) Characterisation of glacial sediments using geophysical methods for groundwater source protection; *Journal of Applied Geophysics*, 57, 4, 293-305.
- Knight, J., Coxon, P., McCabe, A.M. and McCarron, S.G. (2004) Pleistocene glaciations in Ireland. In: Ehlers, J. and Gibbard, P.L. (eds) *Quaternary Glaciations - Extent and Chronology: Part 1: Europe*. Elsevier, Amsterdam, 183-191.
- Koefoed, O. (1979) *Geosounding principles I, resistivity sounding measurements*: Elsevier Scientific Publ. Co.
- Kostic, B., Becht, A. and Aigner, T. (2005) 3-D sedimentary architecture of a Quaternary gravel delta (SW-Germany): Implications for hydrostratigraphy. *Sedimentary Geology* 181, 143-171.
- Krahn, H. (2009) Geophysical Investigation for a Proposed Landfill Site in NW Ireland. Near Surface 2009 – 15th European Meeting of Environmental and Engineering Geophysics Dublin, Ireland.
- Larsson, T.H. (1995) Revisiting a 1955 resistivity survey over a buried bedrock valley aquifer. Proceedings of the symposium on the application of geophysics to engineering and environmental problems. EEGS.
- Lees, A. (1964) The structure and origin of the Waulsortian “reefs” (Lower Carboniferous) of West-Central Ireland. *Phil. Trans. R.Soc.* B247, 483-521.
- Lehmann, F. and Green, A.G. (2000) Topographic migration of georadar data: implications for acquisition and processing. *Geophysics* 65, 836-848.
- Leopold, M. and Volkel, J. (2003) GPR images of periglacial slope deposits beneath peat bogs in the Central European Highlands, Germany. In: Bristow, C.S., Jol, H.M. (Eds.), *Ground Penetrating Radar in Sediments*. Geol. Soc. London Spec. Publ. 211, 181-189.
- Leroux, V. and Dahlin, T. (2006) Time-lapse resistivity investigations for imaging saltwater transport in glaciofluvial deposits. *Environmental Geology* 49, 347-358.
- Lewis, H.C. (1894) *The Glacial Geology of Great Britain and Ireland*. Longman, Green, London.
- Loke, M. H (2001) Electrical imaging surveys for environmental and engineering studies, A practical guide to 2-D and 3-D surveys: RES2DINV Manual, IRIS Instruments, www.iris-instruments.com.
- Loke, M.H. (2002) Rapid 2-D Resistivity forward modelling using the finite difference and the finite-element methods. Wenner (a,b,g), dipole-dipole, inline pole-pole, poledipole, equatorial dipole-dipole, Wenner-Schlumberger. RES2DMOD ver. 3.01 Manual. Geotomo Software.

- Loke, M.H. (2004) Rapid 2-D Resistivity & IP inversion using the least-squares method. Wenner (a,b,g), dipole-dipole, inline pole-pole, poledipole, equatorial dipole-dipole, Wenner-Schlumberger and non-conventional arrays on land, underwater and cross-borehole surveys. RES2DINV ver. 3.54 Manual. Geotomo Software.
- Loke, M.H. (2005) Rapid 3D Resistivity & IP inversion using the least-squares method (For 3-D surveys using the pole-pole, pole-dipole, dipole-dipole, rectangular, Wenner, Wenner-Schlumberger and non-conventional arrays) On land, underwater and borehole surveys. RES3DINV ver. 2.15 Manual. Geotomo Software.
- Loke, M.H. and Barker, R.D. (1995) Least-squares deconvolution of apparent Resistivity pseudosections. *Geophysics* 60, 1682-1690.
- Loke, M.H. and Barker, R.D. (1996) Rapid least squares inversion of apparent Resistivity pseudosections by a quasi-Newton method. *Geophysical Prospecting* 44, 131-152.
- Lombard, T. (2009) The Role of Selected Geophysical Methodologies in Protection and Development Investigations in Irish Peat Areas. Near Surface 2009 – 15th European Meeting of Environmental and Engineering Geophysics Dublin, Ireland.
- Lønne, I. and Lauritsen, T. (1996) The architecture of a modern pushmoraine at Svalbard as inferred from ground-penetrating radar measurements. *Arctic and Alpine Research* 28, 488-495.
- Martinho, E. and Alomeida, F. (2006) 3D behaviour of contamination in landfill sites using 2D resistivity/IP imaging: case studies in Portugal. *Environmental Geology* 49, 1071-1078.
- Maule, J.A, Nyquist, J.E. and Roth J.S. (2000) A comparison of 2D and 3D resistivity soundings in shallow karst terrain, Easton, PA. Proceedings of the symposium on the application of geophysics to engineering and environmental problems. EEGS.
- McCabe, A.M. (1985) Glacial Geomorphology. In *The Quaternary History of Ireland*. Eds K.J. Edwards and W.P. Warren, 67-93. Academic Press, London.
- McCabe, A.M. (1987) Quaternary deposits and glacial stratigraphy in Ireland. *Quaternary Science Reviews* 6, 259-299.
- McCabe, A.M. (2008) *Glacial Geology and Geomorphology. The landscapes of Ireland*. Dunedin Academic Press Ltd. Edingburgh, Scotland.
- McCabe, A.M and Clark, P.U. (2003) Deglacial chronology from County Donegal, Ireland: implications for deglaciation of the British-Irish ice sheet. *Journal of the Geological Society of London*, 160, 1-9.
- McConnell, B. and Philcox, M.E. (1994) Bedrock geological map of Kildare-Wicklow (1:100,000 Scale, O.S.Sheets 16) Geological Survey of Ireland.

- McGillivray, P., and Oldenburg, D., 1990. Methods for calculating Frechet derivatives and sensitivities for the Non-linear inverse problem: A comparative study: *Geophysical Prospecting* 38, 499-524.
- Meehan, R., Bulfin, M., Cronin, C., Farrelly, N., Fealy, R., Green, S., Loftus, M. and Radford, T. (2006) The EPA Soil and Subsoil Mapping project, Teagasc, Kinsealy.
- van der Meer, J.J.M. and Warren, W.P. (1997) Sedimentology of Late Glacial clays in lacustrine basins, Central Ireland. *Quaternary Science Reviews* 16, 779-791.
- van der Meer, J.J.M., Kjær, K.H., Kruger, J., Rabassa, J. and Kilfeather, A.A. (2009) Under pressure: clastic dykes in glacial settings. *Quaternary Science Reviews* 28, 708-720.
- Menzies, J., Meer, J.J.M. van der & Rose, J. (2006) Till – as a glacial “tectomict”, its internal architecture, and the development of a “typing” method for till differentiation. *Geomorphology* 75, 1-2, 172-200.
- Miall A. D. (1992) Alluvial deposits. In Walker R.G. and James, N.P. (Ed), *Facies Models, Response to Sea Level Change*. Geological Association of Canada, Toronto, 119-142.
- Mitchell, G.F. (1976) *The Irish Landscape*. Collins, London.
- Mitchell, F. (2006) Where did Ireland’s trees come from? *Biology and Environment: proceedings of the Royal Irish Academy*, 106B, 3, 251-259.
- Mitchell, G.F., Penny, L.F., Shotton, F.W. and West, R.G. (1973) A correlation of Quaternary deposits in the British Isles. *Geological Society of London Special Publication* 4. (199pp).
- Mitchum, R.M., Vail, P.R. and Sangree, J.B. (1977) Stratigraphic interpretation of seismic reflection patterns in depositional sequences. In: Payton, C.E. (Ed.), *Seismic Stratigraphy – Applications to Hydrocarbon Exploration*. AAPG Mem. 16, 117- 123.
- Møller, I. and Sørensen, K. (1998) A new approach for fast 2D geoelectrical mapping of near-surface structures. *European Journal of Environmental and Engineering Geophysics* 2, 247-261.
- Monteiro Santos, F.A., Mateus, A. Figueiras, J. and Gonçalves, M.A. (2006) Mapping groundwater contamination around a landfill facility using the VLF-EM method – a case study. *Journal of Applied Geophysics* 60, 2, 115-125.
- Morard, S., Delaloye, R. and Lambiel, C. (2008) Time-lapse electrical resistivity tomography (ERT) to estimate temperature changes at depth in a low elevation ventilated cold talus slope (Dreveneuse, Swiss Prealps). *Geophysical Research Abstracts*, 10, EGU2008-A-09521.

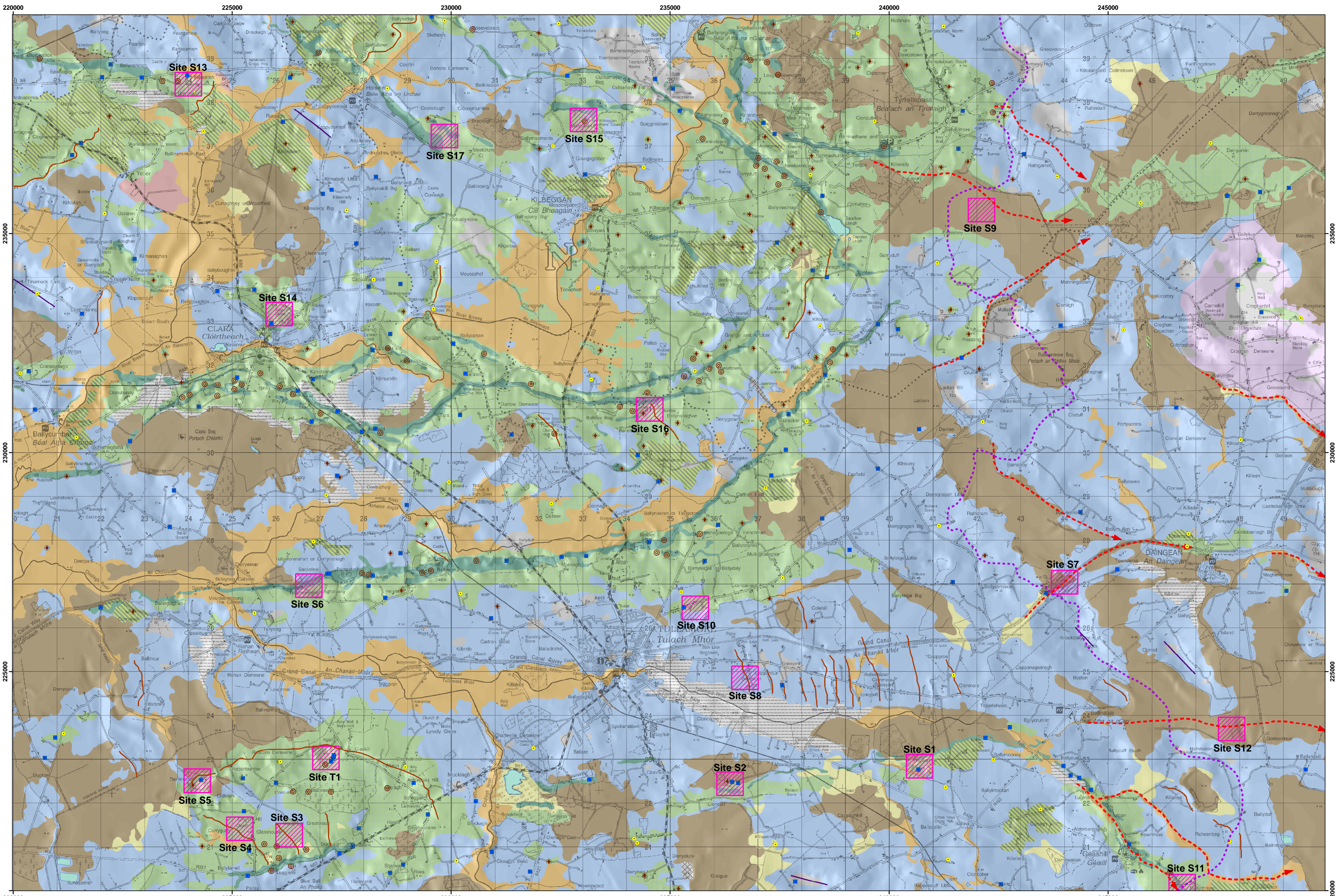
- Munsell (2000); Soil Color Chart. GretagMachbeth.
- Murphy, S. and Clark, R. (2009) A Geophysical Investigation of Imaging Stability Features in Peat. Near Surface 2009 - 15th European Meeting of Environmental and Engineering Geophysics Dublin, Ireland.
- Neal, A. (2004) Ground Penetrating Radar and its use in sedimentology: principles, problems and progress. *Earth-Science Reviews* 66, 261-330.
- Neal, A., Richards, J. and Pye, K. (2002) Structure and development of shell cheniers in Essex, southeast England, investigated using high-frequency ground-penetrating radar. *Marine Geology* 185, 435-469.
- Neal, A., Richards, J. and Pye, K. (2003) Sedimentology of coarseclastic beach-ridge deposits, Essex, southeast England. *Sedimentary Geology* 162, 167-198.
- Northwest Geophysical Associates, Inc. 2000; VLF Method.
- Northwest Holst Soils Engeeniring Ltd. (2001) Report on a Ground Investigation at N6 Kinnegad – Athlone, Vol. 1. Westmeath County Council.
- Ó Cofaigh, C. and Evans, D.J.A.(2007) Radiocarbon constraints on the age of the maximum advance of the British-Irish Ice Sheet in the Celtic Sea. *Quaternary Science Reviews* 26, 9-10, 1197-1203.
- Oldenborger, G.A., Knoll, M.D., Routh, P.S. and LaBrecque, D.J. (2007) Time-lapse ERT monitoring of an injection/withdrawal experiment in a shallow unconfined aquifer. *Geophysics* 72, 4, 177-187.
- O'Rourke, S. and O'Connor, P. (2009) A Geographical Information Systems based Analysis of Resistivities of Carboniferous Lithologies in Ireland. Near Surface 2009 – 15th European Meeting of Environmental and Engineering Geophysics Dublin, Ireland.
- Oskooi, B. and Pedersen, L.B. (2005) Comparison between VLF and RMT methods. A combined tool for mapping conductivity changes in the sedimentary cover. *Journal of Applied Geophysics* 57, 227-241.
- Oskooi, B. and Pedersen, L.B. (2006) Resolution of airborne VLF data. *Journal of Applied Geophysics* 58, 158-175.
- O'Sullivan, J. J., Lyle P., Bean, C. J, Gibson, P. J. and McCloskey, J. (2004) To develop an integrated geophysical approach to the preliminary assessment of potential waste disposal sites. DOE Interreg Report No: 1544. 110pp.
- Overgaard, T. and Jakobsen, P.R. (2001) Mapping of glaciotectonic deformation in an ice marginal environment with ground penetrating radar. *Journal of Applied Geophysics*, 47, 3, 191-197.

- van Overmeeren R.A and Ritsema, I.L. (1988) Continuous electrical vertical sounding. *First Break*, 6, 10, 313-324.
- van Overmeeren R.A (1994) Georadar for hydrology. *First Break* 12, 401-408.
- Palacky, G.J. (1987) Resistivity characteristics of geologic targets, *in* Nabighian, M.N., ed., *Electromagnetic Methods in Applied Geophysics Theory*: Tulsa, Okla., Society of Exploration Geophysicists, v. 1, p. 53-129.
- Paul, M.A. (1983) Supraglacial landsystem. In: Eyles, N. (ed.): *Glacial geology*, Pergamon Press, Oxford, 71-90.
- Pellicer, X.M. and Warren W.P. (2005) Eskers and associated landforms and deposits: the key to the pattern of deglaciation in the midlands of Ireland. 6th International Conference Geomorphology, Poster presentation.
- Pilcher J.R. (1973) Pollen Analysis and Radiocarbon Dating of a Peat on Slieve Gallion, Co. Tyrone, N. Ireland ;*New Phytologist* 72, 3, 681-689.
- Pringle, J.K., Clark, J.D., Westerman, A.R. and Gardiner, A.R. (2003) Using GPR to extract 3-D turbidite channel architecture from the Carboniferous Ross Formation, County Clare, Western Ireland. In: Bristow, C.S. and Jol, H. (eds), *Geological Society Special Publication, GPR in Sediments* 211, 309-320.
- Poppe, L.J., Eliason, A.H., and Hastings, M.E. (2003) A Visual Basic program to classify sediments based on gravel-sand-silt-clay ratios: *Computers and Geosciences* 29, 6, 805-809.
- Postma, G. (1990) Depositional architecture and facies of river and fan deltas: a synthesis. In: *Coarse-grained Deltas*, A. Colella and D.B. Prior (eds.), International Association of Sedimentologists, Special Publication 10, 13-27.
- Pozdnyakova, L.A. (2002) Electrical fields and soil properties. 17th WCSS, 14-21 August, Thailand. Oral Presentation.
- Rabassa, J., Rubulis, S. and Suarez, J. (1979) Rate of formation and sedimentology of push moraines, Frias Glacier, Mount Tronador (42°10'S; 71°53'W), Argentina. In Schluster, C. (Ed), *Moraines and Varves*, Balkema, Rotterdam, 65-79.
- Radulescu, M., Valerian, C. and Yang, J. (2007) Time-lapse electrical resistivity anomalies due to contaminant transport around landfills. *Annals of Geophysics* 50, 3, 453-468.
- Reynolds, John M. (1997) *An Introduction to Applied and Environmental Geophysics*; John Wiley and Sons Ltd.
- Rial F.I., Pereira, M., Lorenzo, E, Arias P. and Novo, A. (2008). Vertical and Horizontal Resolution of GPR bow-tie antennas. *Natural Resources and Environmental Engineering*, University of Vigo.

- Risk, G.F. (1975) Detection of buried zones of fissured rock in geothermal fields using resistivity anisotropy measurements, in Geophysical papers submitted to the second U.N. symposium on the development and use of geothermal resources. San Francisco, California. 78-100.
- Sensors and Software. (1999) Technical Manual 25. Pulse Ekko 100 Run. User's guide Version 1.2. Sensors and Software. Ontario.
- Sensors and Software. (2001) Ekko for DVL, Pulse Ekko 100. User's guide Version 1.0. Sensors and Software. Ontario.
- Sensors and Software. (2003) Ekko View Enhance and deLuxe, User's guide. Sensors and Software. Ontario.
- Sensors and Software. (2007) Ekko Mapper, User's guide. Sensors and Software. Ontario.
- Sheriff, R.E. (1977) Limitations on resolution of seismic reflections and geologic detail derivable from them. In: Payton, C.E. (Ed.), Seismic Stratigraphy—Applications to Hydrocarbon Exploration. AAPG Mem. 16, 3-14.
- Smith, D.G. and Jol, H.M. (1992) Ground-penetrating radar investigation of a Lake Bonneville delta, Provo level, Bingham City, Utah. *Geology* 20, 1083-1086.
- Smith, D.G. and Jol, H.M. (1995) Ground-penetrating radar: antenna frequencies and maximum probable depths of penetration in Quaternary sediments. *Journal of Applied Geophysics* 33, 93-100.
- Smyth, M. (1994) Quaternary Geology and Geophysical Studies of Clara and Raheenmore Bogs, Co. Offaly, Ireland. Unpublished PhD thesis, National University of Ireland.
- Sollas, W.J. (1896) A map to show the distribution of eskers in Ireland, *Sci. Trans. Royal Dublin Society* 2, 5, 785.
- Soocochof, L. (1979) VLF- EM Survey on the Ashnola River Property. A Geophysical report for Great Pacific Resources.
- Sørensen K.I. (1996) Pulled Array Continuous Electrical Profiling. *First Break* 14, 85-90.
- Steinen, R., Liu, L., and Guo, T., (2001) Anatomy of an ice-contact ridge (ice channel/esker?), revealed by ground penetrating radar (gpr) and confirmed by excavation: Jordan ridge, north Windham, Ct. The Geological Society of America. Northeastern Section - 36th Annual Meeting.
- Synge, F. M. (1950). The glacial deposits around Trim, Co. Meath. *Proceedings of the Royal Irish Academy* 53, 99-110.

- Synge, F.M. and Stephens, N. (1960) The Quaternary period in Ireland-an assessment, *Irish Geography* 4, 121-130.
- Synge, F.M. (1979) Quaternary glaciation in Ireland. *Quaternary Newsletter* 28, 1-18.
- Taylor, R.W. and Fleming, A.H. (1988) Characterizing jointed systems by azimuthal resistivity surveys. *Ground Water* 26, 4, 464-474.
- Telford, N.W. Geldart, L.P., Sheriff, R.S. and Keys, D.A. (1976) *Applied Geophysics*. Cambridge University Press.
- Trafford, A. (2009) Mapping Thickness of Raised Peat Bog Deposits Using GPR. Near Surface 2009 – 15th European Meeting of Environmental and Engineering Geophysics, Dublin, Ireland.
- Ulriksen, C.P. (1982) The application of impulse radar to civil engineering. Unpubl. PhD thesis, Univ. Lund.
- Urbini, S., Vittuari, L. and Gandolfi, S. (2001) GPR and GPS data integration: examples of application in Antarctica. *Annali di Geofisica* 44, 687-702.
- Warren, W.P. (1979) The stratigraphic position and age of the Gortian interglacial deposits. *Geological Survey of Ireland* 2, 1979, 315-332.
- Warren, W.P. (1985) Stratigraphy. In *The Quaternary History of Ireland*. Eds K.J. Edwards and W.P. Warren, 39-65. Academic Press, London.
- Warren, W.P. (1991) Fenitian (Midlandian) glacial deposits and glaciation in Ireland and the adjacent offshore regions. Pp 79-88 in Ehlers, J., Gibbard, P.L. and Rose, J. (eds) *Glacial Deposits in Great Britain and Ireland*. Balkema, Rotterdam.
- Warren, W.P. (1992) Drumlin orientation and the pattern of glaciation in Ireland. *Sveriges Geologiska Undersokning, Research Papers, Series Ca* 81, 359-366.
- Warren, W.P. (2008) After wise use - The future of peatlands. *Proceedings of the 13th International Peat Congress*. Tullamore, Ireland. *International Peat Society* 1, 95-99.
- Warren, W.P. and Ashley, G.M. (1994) Origins of the ice-contact stratified ridges (Eskers) of Ireland. *Journal of Sedimentary Research*. A64, 433-449.
- Warren, W.P. and Hammond, R.F. (1999) Surficial Glacial and Postglacial deposits Map - Co. Offaly. To accompany soil Survey bulletin n. 43. National Soil Survey. Teagasc.
- Watson, K.A. and Barker, R.D. (1999) Differentiating anisotropy and lateral effects using azimuthal resistivity offset Wenner soundings: *Geophysics*, 64, 739-745.
- Watts, W.A. (1964) Interglacial deposits at Baggotstown near Bruff, Co. Limerick. *Proceedings of the Royal Irish Academy* 63B, 9, 167-189.

- Wenner, F. (1915) A method of measuring Earth's resistivity. US. Dept. Com. Bur. Standards Sci. Paper 258.
- Woodward, J., Ashworth, P.J., Best, J.L., Sambrook Smith, G.H. and Simpson, C.J. (2003) The use and application of GPR in sandy fluvial environments: methodological considerations. In: Bristow, C.S., Jol, H.M. (Eds.), Ground Penetrating Radar in Sediments. Geol. Soc. London Spec. Publ. 211, 127-142.
- Wright, W.B. (1914). The Quaternary Ice Age, first ed. MacMillan, London, 464pp.
- Yaramanci, U. (2000) Geoelectric exploration and monitoring in rock salt for the safety assessment of underground waste disposal sites. *Journal of Applied Geophysics* 44, 181-196.



Quaternary Geology Map Legend

- Water body
- River
- Watershed

Glacial sediments

- Till derived from Lower Carboniferous Limestone
- Till derived from Devonian Sandstone
- Till derived from Basic Igneous Rocks

Glaciofluvial

- Glaciofluvial Sands derived from Lower Carboniferous Limestone
- Glaciofluvial Gravel derived from lower Carboniferous Limestone
- Interstratified Tills and Gravels derived from lower Carboniferous Limestone

Postglacial Sediments

- Alluvium
- Lacustrine
- Peat
- Marl

Other deposits

- Bedrock within 1 meter of the surface
- Man made ground

Morphology

- Linear features
- Esker Ridge
- Drumlinoid Hills
- Ice Marginal Ridge
- Meltwater Channel

Other Symbolology

- Borehole Location
- Exposure Location

Point Features

- Kame Mound
- Kame Terrace
- Kettle Hole

- Geophysics Site

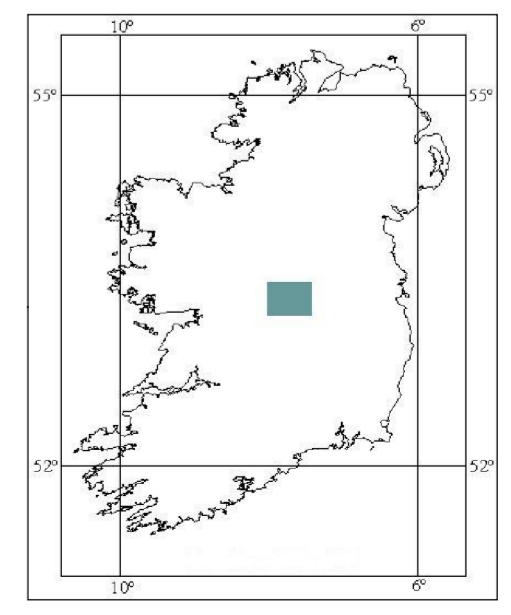
**MAP 1:
Quaternary Geology Map
Geophysics Sites Location**

To accompany PHD Thesis by Xavier Pellicier (NUI, Maynooth)

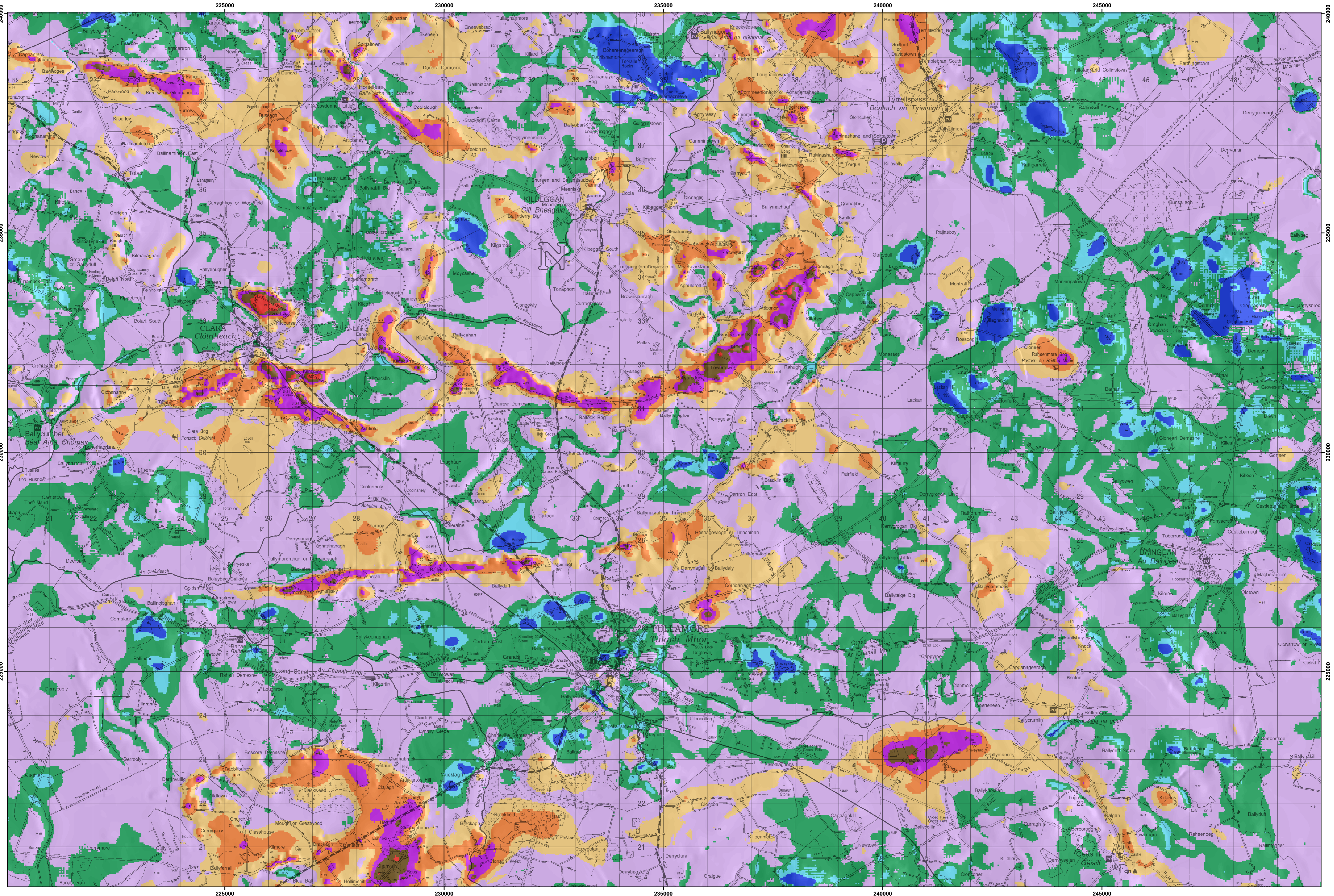
SOURCES OF INFORMATION:
 Geological Survey of Ireland
 Quaternary Field Sheets at 1:10560 scale.
 Surficial Glacial and Postglacial deposits
 Map for County Offaly
 GSI Bedrock Field Sheets at 1:10560 scale.
 Field mapping, sampling and drilling.

The Quaternary Geology map presented shows the distribution of sediments within 1m of the Surface. Local details have been generalised to fit the map scale.
 Sun illuminated topographic background has been derived from the Environmental Protection Agency (EPA) Digital Elevation Model at grid resolution of 20m.
 Discovery Series Map of the Ordnance Survey of Ireland at 1:50,000 scale used as a cartographic base map.
 Map Produced by Xavier Pellicier (c)

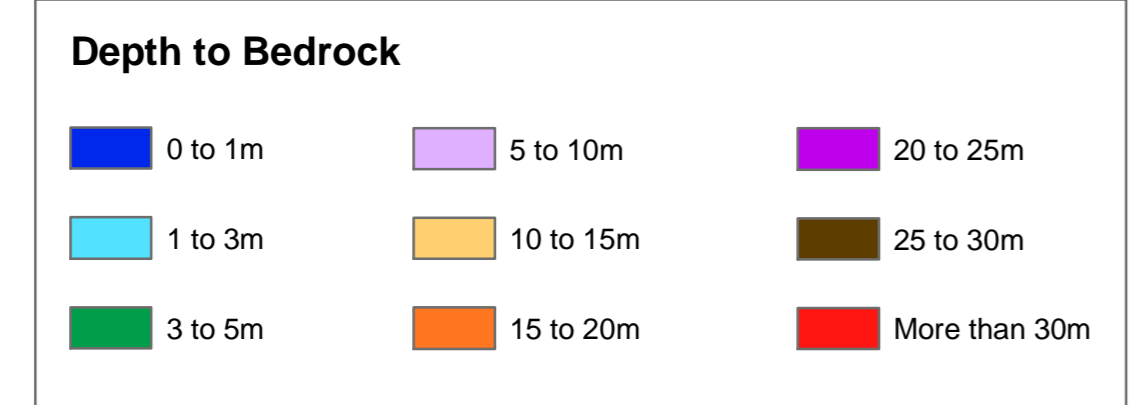
0 1,000 2,000 Meters



Location of the Study Area



MAP 2:
Depth to Bedrock Map
1:40,000 Scale



This map is the result of an interpolation exercise using the krigging geostatistical method. This is a prediction map of the Depth to Bedrock within the research area. Evaluation of specific sites and circumstances will normally require further detailed assessments, and will frequently require site investigations.

Sun illuminated topographic background has been derived from the Environmental Protection Agency Digital Elevation Model at grid resolution of 20m.

The Discovery Series Map sheet 48 of the Ordnance Survey of Ireland at 1 to 50,000 scale has been used as a cartographic base map.

SOURCES OF INFORMATION:

- Geological Survey of Ireland Borehole Database
- Offaly County Council percolation test database
- Borehole data from private surveys (N6, Gas Pipeline...)
- Field mapping and drilling
- Bedrock outcrop and Bedrock close to the surface data extracted from Quaternary Geology Map.

